BLACK SEA JOURNAL OF ENGINEERING AND SCIENCE

(BSJ ENGIN SCI)

BS Journals

OWNER

Assoc. Prof. Dr. Uğur ŞEN

DIRECTOR IN CHARGE

Prof. Dr. Hasan ÖNDER

Assist. Prof. Dr. Adil AL-SAIDI, Al-Nahrain University, Department of Architecture, Architecture, IRAQ

Assist. Prof. Dr. Batıkan Erdem DEMİR, Karabük University, Department of Mechatronics Engineering, Control Theoryand Applications, TÜRKİYE

Assist. Prof. Dr. Bilgehan ERKAL, Karabük University, Department of Electrical and Electronics Engineering, Electrical Engineering, TÜRKİYE

Assist. Prof. Dr. Can AKPOLAT, Fenerbahçe University, Department of Biology, Microbiology, TÜRKİYE

Assist. Prof. Dr. Cemil ALTIN, Yozgat Bozok University, Department of Electrical and Electronics Engineering, Electrical Engineering, TÜRKİYE

Assist. Prof. Dr. Deniz KATİPOĞLU, Erzurum Technical University, Department of Electrical and Electronics Engineering, Electrical Engineering, TÜRKİYE

Assist. Prof. Dr. Dilara ÖRGÜL, Selçuk University, Department of Pharmaceutical Biotechnology, Pharmacology and Pharmaceutical Sciences, TÜRKİYE

Assist. Prof. Dr. Engin BAYSOY, Bahçeşehir University, Department of Biomedical Engineering, Biomedical Imaging, TÜRKİYE

Assist. Prof. Dr. Esra DEMIRTÜRK, Çukurova University, Department of Pharmaceutical Technology, Pharmaceutical Biotechnology, TÜRKİYE

Assist. Prof. Dr. Esra KASAPGİL, İzmir Bakırçay University, Department of Biomedical Engineering, Biomedical Engineering, TÜRKİYE

Assist. Prof. Dr. Fatih TOPALOĞLU, Malatya Turgut Özal University, Department of Computer Engineering, Decision Support and Group Support Systems, TÜRKİYE

Assist. Prof. Dr. Gizem KEZER, Kırşehir Ahi Evran University, Department of Agricultural Biotechnology, Food Sciences, TÜRKİYE

Assist. Prof. Dr. Gökhan GÖKÇE, Çukurova University, Department of Animal Science, Stock Farming and Treatment, TÜRKİYE

Assist. Prof. Dr. Güneş MUTLU AVİNÇ, Muş Alparslan University, Department of Engineering and Architecture, Built Environment and Design, TÜRKİYE

Assist. Prof. Dr. Hacer KAYA ÇAKIR, Bilecik Şeyh Edebali University, Department of Molecular Biology and Genetics, Epigenetics, TÜRKİYE

Assist. Prof. Dr. Hasan Hüseyin BİLGİÇ, Necmettin Erbakan University, Department of Aircraft Engineering, Artificial Intelligence, TÜRKİYE

Assist. Prof. Dr. Hürol KOÇOĞLU, Bolu Abant İzzet Baysal University, Department of Mechanical Engineering, Polymer Technologies, TÜRKİYE

Dr. Abdulhamit SEVGİ, Ostim Technical University, Department of Mechatronics Engineering, Machine Learning, TÜRKİYE

Dr. Cansu SCHMUNK, Ege University, Department of Civil Engineering, Hydromechanics, TÜRKİYE

Dr. Emad Majeed HAMEED, Gujarat University, Department of Computer Science, Machine Learning, INDIA

Dr. Erman ÇAVDAR, Karadeniz Technical University, Department of Civil Engineering, Transportation Engineering, TÜRKİYE

Dr. Esen BİLGE BİÇER, Sivas Cumhuriyet University, Department of Food Processing, Food Sciences, TÜRKİYE

Dr. Gözde ALTIN, Çukurova University, Department of Civil Engineering, Hydromechanics, TÜRKİYE

Dr. İrem ACER, Kütahya Health Sciecnes University, Department of Biomedical Engineering, Biomedical Engineering, TÜRKİYE

Dr. Muyiwa OKUSANYA, School of Engineering the Federal Polytechnic, Department of Agricultural and Bio-Environmental Engineering, Oil Technology, NIGERIA

Dr. Sayed AHMED, Anhalt University of Applied Sciences, Department of Architecture, Architecture, GERMANY

Dr. Yusuf Alperen ŞİŞMAN, Ondokuz Mayıs University, Department of Design, Composites, TÜRKİYE

Dr. Zaid ALAARAJI, Al-Hadba University, Department of Computer Sciecnes, Artificial Intelligence, IRAQ

* The ranking is arranged alphabetically within the academic title

Volume 7, Issue 5 (2024)

Table of Contents

Reviews

SYNTHESIS AND EVALUATION OF PH AND TEMPERATURE STIMULI-RESPONSIVE MAGNETIC NANOHYDROGELS FOR GENE DELIVERY

Ferzane VALİOĞLU[1,3]*, Fereshteh VALIPOUR[2], Sibel SÜMER[3], Mustafa TÜRK[4], Soodabeh DAVARAN[2]

[1]Sakarya University, Technology Development Zones Management CO, 54050 Sakarya, Türkiye
[2]Tabriz University of Medical Sciences, Faculty of Pharmacy, Department of Medicinal Chemistry, Tabriz, Iran
[3]Hacettepe University, Faculty of Sciences, Department of Molecular Biology, 06800, Ankara, Türkiye
[4]Kırıkkale University, Faculty of Bioengineering, Department of Bioengineering, 71451, Kırıkkale, Türkiye

Abstract: The offer of gene delivery technologies as a promising approach to treating a variety of diseases has revolutionized human medicine over the last two decades. So, the application of suitable vectors, particularly polymers with substrates with unique physicochemical properties for the transfer of targeted genes to logical sites for effective treatment, plays an indispensable role for more personalized medicine and improves the safety profile in response to continuing to use new medical technologies. For this purpose, we synthesized nanocarriers with a two-block cationic hydrogel, magnetic and non-magnetic, based on N-isopropyl acrylamide (NIPAM) and quaternary alkyl ammonium halide salts of DMAEMA (DMAEMAQ) with pH and temperature responsiveness via the free radical polymerization technique. The bulk properties of these co-polymers were characterized by using Fourier transform infrared spectroscopy, ^{1}H NMR spectroscopy, zeta potential, lower critical solution temperature (LCST), and gel electrophoresis to show the loading of nanoparticles with the gene. In the results, magnetic P[NIPAM-DMAEMAQ] hydrogel showed controllable responsive properties determined by the nature of the cationic charge +24.7 mV incorporated, nanosize around 86.95 and 91.22 nm, and efficiency loaded with the gene more than 95%. As well, the synthesized nanohydrogel exhibited a sharp volume-phase transition in water at a LCST of ~40 °C. So, the combination of both monomers yielded an interesting system with high transfection efficiency and compliant biocompatibility characteristics, which could effectively achieve gene loading. Also, the magnetic potential of nanohydrogel was determined as a vector to deliver genes to localized sites. Notably, the synthesized combination P[NIPAM-DMAEMAQ] nanohydrogel has been considered a transfection of the biodegradable and biocompatible magnetic nanoparticle sensitive to tunable pH and temperature responsiveness, demonstrating that it will hold a promising approach as a potential carrier to improve gene delivery therapeutic efficacy in cancer and different disease treatments.

Keywords: Gene delivery, Biodegradation, Magnetic P(NIPAM-DMAEMAQ), pH and thermoresponsive hydrogels

1. Introduction

The delivery issue of genes (nucleic acids) and gene therapy in the biomedical field is a hopeful strategy with futuristic applications in the treatment of illnesses ranging from tumors to infectious diseases to genetic syndromes and a crucial role in the treatment of numerous ailments, including cancer, malignant tumors, hereditary diseases, and neurodegenerative diseases (Sung and Kim, 2019). Nevertheless, there are several disadvantages, such as no targeted delivery (Sayed et al., 2022), fast degradation (Shahryari et al., 2021), inadequate effectiveness, and many adverse effects following nucleic acid entry into the bloodstream. In the last few years, significant advancements in knowledge of the importance of effective specific gene transfer at its

origin site through different vectors have drawn attention, and numerous carriers have been introduced. In stimuli-responsive gene delivery systems, targeted delivery and application of biodegrading nanoparticle-based carriers are one of the most important treatment strategies in delivery applications is to ferry genes into the target site with minimizing the side effects and maximizing their therapeutic effects while protecting the gene from nucleases during transit, providing an option for a substantial increase in treatment efficiency compared to conventional methods (Hamimed et al., 2022; Zhang et al., 2023). Because improving transcript splicing, inhibiting or regulating gene expression, and restoring the expression of a damaged protein are all effective methods that might have a significant impact on

biological research and therapy (Shillitoe, 2009; Yang et al., 2020).

Nanocarrier systems could be developed to generate coating NPs using a variety of materials, including polymeric nanoparticles (Rai et al., 2019), inorganic nanoparticles (Lin et al., 2021), metals (He et al., 2023), semiconductors, and other substances, so that these features can be used for specific purposes and are possible to attach to a targeted therapeutic gene to correct a genetic defect (Jacob et al., 2024). A type of nanocarrier system such as hydrogels, by crosslinking water-soluble polymers into a network, can create hydrogels' porous and hydratable structure in order to deliver genes to specific sites in response to external stimuli such as temperature, magnetic field, pH, ionic strength, or electric field (Thang et al., 2023). Also recently in nanomedicine, nanoparticulate systems have seen considerable improvement in the development of an assortment of nanoparticles known as magnetic nanoparticles (MNPs) that are produced with a blend of metal ions and polymer coatings. Magnetic cores could be functionalized or made of porous polymers loaded with magnetic nanoparticles (Bi et al., 2020; Materon et al., 2021). One of the most significant components of magnetic nanoparticles as superparamagnetic iron oxide nanoparticles (SPIONs) is oxidized iron, which has a primarily crystalline core made of Fe_3O_4 or Fe_2O_3 with a dimension of 10–100 nm. These particles can be guided by an outside magnetic field, and nanoparticle-based gene delivery can deliver them to the target origins, which creates promising therapeutic effects for a wide range of diseases (Roy, 2022). Therefore, magnetic nanoparticles have been created to improve the essential features and attributes of capability applications for carrying active biomolecules and gene delivery systems and play a critical role in advance stability, controlling their release, and giving higher curative effects in biomedical applications. Moreover, the nanoscale dimension includes a high surface area-to-volume ratio, which is an important characteristic of nanoparticles (NPs), and in order to qualify as nanoparticles, they have to possess at least one dimension in the nanometer range, up to around 100 nm, that improves their therapeutic and diagnostic forms (Satalkar et al., 2016). Hence, the significance and nano-biotechnology's demand for magnetic nanoparticles due to their potential to improve treatment techniques and bring up new avenues for biomedicine have enabled us to produce and create the magnetic pH and thermosensitive nanohydrogel in this study. So, we initially created a copolymer of 2-(dimethylamino)ethyl methacrylate (DMAEMA) with poly (N-isopropylacrylamide) and its quaternary ammonium quart salt (DMAEMAQ). Next, we synthesized a magnetic P(NIPAM-co-DMAEMAQ) nanohydrogel that could react to temperature and pH stimuli simultaneously. The effect of PNIPAM-co-DMAEMA content was assessed in terms of surface charge features, particle size, construction, and loading of

copolymers with the gene. NIPAM, as a temperature-responsive hydrogel, is a nonionic polymer, but loading a gene into nanomateriyal needs a positive charge because acidic nuclease groups have negative charges (Fussell et al., 2019). So, cationic copolymers of P[DMAEMAQ] with strong positively charged groups that could condense genes through electrostatic adsorption have been used as transfectants in which protonated amines of their capability to bind the desired gene into submicron complexes, which safeguard and preserve the gene from nucleases during transfer (Manouras et al., 2021). In addition, in order to use PNIPAM in gene delivery processes, it is necessary to improve its swelling value by copolymerizing it with hydrophilic and/or ionic comonomers such as poly (PDMAEMAQ). Also, when NIPAM is copolymerized with an ionic monomer, the resultant copolymer reacts to pH and temperature (Fussell et al., 2019; Kim et al., 2019). Thus, cationic polymer-poly (PDMAEMAQ) is utilized as a regulator of the binding or release of genes due to its satisfactory loading capacity. These unique characteristics contribute to targeted and controlled gene release in tumor cells (Yang et al., 2015). Overall, the aim herein was to synthesize and describe the biomedical potential of cationic stimuli-responsive thermo-responsive hydrogels with potential positive charge and magnetic properties for gene delivery to provide for the development of nanoplatforms that will be clinically applicable in medicine. Besides, synergistic therapy could be achieved when combined with other therapeutic regimens. The uniqueness of this study offers the possibility of creating intrinsic magnetic hydrogels through the copolymerization of a quart salt of dimethylaminoethyl methacrylate (DMAEMAQ) with a well-known thermoresponsive monomer, N-isopropylacrylamide (NIPAM), to create hydrogels via precipitation polymerization (radical polymerization) for gene delivery. As a result of this study, we determined that magnetic proportion with dual thermo-pH-sensitive potential copolymer hydrogels could load gene activity and have good physical properties besides maintaining thermos-responsiveness. Also, nano-vectors for gene therapy can be extensively researched and used owing to their facile application, targeting ability, high bioavailability, and good biocompatibility in biomedicine. Finally, by mentioning this case, the in-vitro investigation of these studies in breast cancer cells has been done and will be published soon.

2. Materials and Methods

2.1. Materials

N-isopropyl acrylamide (NIPAM) was obtained at Acros Organics and purified by recrystallization from n-hexane-toluene (90:10 v/v) under vacuum at 25 °C. 2-(Dimethylamino)ethyl methacrylate (DMAEMA) monomers (Sigma–Aldrich Co., Steinem, Germany) were distilled under reduced pressure in nitrogen atmosphere. Tin (II) 2-ethyl hexanoate (stannous octoate, $Sn(Oct)_2$),

benzoyl peroxide (BPO), ferrous chloride tetrahydrate ($FeCl_2.4H_2O$), ferric chloride hexahydrate ($FeCl_3.6H_2O$), ammonium hydroxide (32 wt %), N,N'-methylenebisacrylamide (MBA), tetrahydrofuran (THF), dimethyl sulfoxide (DMSO), sodium monohydrogen phosphate, dihydrogen phosphate, methyl iodide (CH_3I), and ethidium bromide (EtBr) were from Sigma-Aldrich, n-hexane, 1, 4 dioxan, and diethyl ether were obtained at Merck Chemical Co. Distilled deionized (DDI) water was prepared with a Millipore system and used for dilution purposes throughout. Other chemicals were reagent-grade commercial materials and used without further purification.

2.2. Synthesis of Magnetic P(NIPAM-CO-DMAEMAQ) Hydrogel Copolymers

2.2.1. Synthesis of superparamagnetic magnetite nanoparticles

Superparamagnetic magnetite nanoparticles were prepared via the improved chemical co-precipitation method. According to this method, 3.1736 g of $FeCl_2 \cdot 4H_2O$ (0.016 mol) and 7.5684 g of $FeCl_3 \cdot 6H_2O$ (0.028 mol) were dissolved in 320 mL of deionized water. The mixed solution was stirred under N_2 at 80 °C for 1 h. Then, 40 ml of $NH_3 \cdot H_2O$ was injected into the mixture, rapidly stirred under N_2, then cooled to room temperature as shown in Figure1. The precipitated particles were washed five times with hot water and separated by magnetic decantation. Finally, magnetic nanoparticles were dried under vacuum at 70 °C (Wulandari et al., 2022).

$$2\ FeCl_3 + FeCl_2 + 4\ H_2O + 8\ NH_3 \rightarrow Fe_3O_4 + 8\ NH_4Cl$$
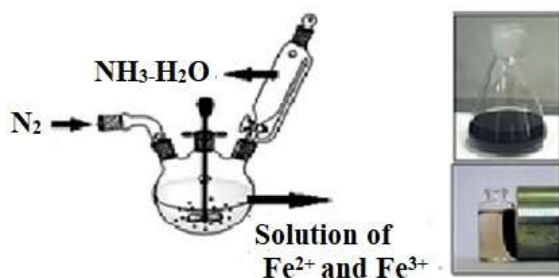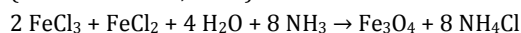
Figure 1. Schematic synthesis of superparamagnetic magnetite nanoparticles.

2.2.2. Synthesis of cationic quaternary ammonum alkyl halide monomers (Q)

Quaternary ammonium alkyl halide monomer (DMAEMAQ) was prepared by dissolving 19.1 mmol of DMAEMA in 5 mL of dry THF under stirring. The next step is the quaternization of the tertiary amine of DMAEMA by addition of 22 mmol of CH_3I, dissolved in 5 mL of THF, via the N-alkylation reaction using methyl iodide, as shown in Figure 2. The reaction was carried out at room temperature with magnetic stirring (Moselhy et al., 2009). The crude products were filtered, washed twice with 10 mL aliquots of cold hexane, and dried in vacuum to yield the DMAEMAQ products (white crystalline solid, yield: 90%).
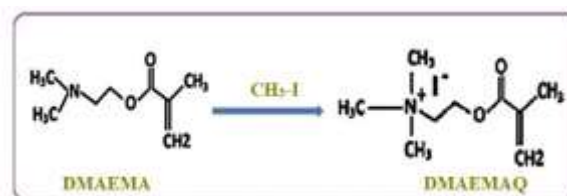
Figure 2. Synthesis scheme of quaternary ammonium alkyl halide monomers (DMAEMAQ).

2.2.3. Synthesis of magnetic P(NIPAM-DMAEMAQ) nanohydrogel

Magnetic thermoresponsive cationic nanogel networks P(NIPAM-DMAEMAQ) based on N-isopropylacrylamide (NIPAM) and quaternary alkyl ammo-nium halide salts of 2-dimethylaminoethyl methacrylate (DMAEMAQ) by molar ratio of 80:20, respectively, Fe_3O_4 nanoparticles, N,N′-methylene-bis-acrylamide (MBA) as a crosslinking agent, and benzoyl peroxide (BPO) as a copolymerization initiator (0.5% w/w) were synthesized by free radical copolymerization of monomers in 1,4-dioxane (50 ml) under nitrogen atmosphere. The specified quantity of reagents and Fe_3O_4 nanoparticles (1% of the total weight monomers) were sonicated with 1,4-dioxane for about 30 min to prepare magnetic nanocomposites. The mixture added to the flask was magnetically stirred and degassed under a nitrogen atmosphere for 30 minutes before polymerization. The reaction was carried out at 70 °C for 18 h under a nitrogen atmosphere. After polymerization, the synthesized polymer was cooled, and the resultant polymers were purified by dissolution/precipitation with a tetrahydrofuran (THF)/diethyl ether solution and dried in a vacuum. Then the purified solution was frozen in liquid nitrogen and then lyophilized to obtain dry powder with a yield of 87%.

2.2.4. Characterization of P(NIPAM- DMAEMAQ) nanohydrogel

Fourier transforms infrared (FT-IR) spectroscopy

The chemical structures of the synthesized polymers were investigated by FT-IR spectroscopy. Upon having the synthesized product, all samples were mixed with the dry potassium bromide (KBr) powders and pressed to the disk. Infrared (IR) spectra of the samples were scanned in the range of 400 to 4000 cm^{-1} at a resolution of 4 cm^{-1}, with a minimum of 256 scans per spectrum at room temperature (Nicolet-Fisher Scientific, Inc., USA). The spectra of water, CO_2, and KBr were subtracted from the sample spectrum, and the procedure was done under nitrogen gas to prevent humidity interference.

Hydrogen nuclear magnetic resonance (^1HNMR) spectroscopy

The chemical composition of the synthesized polymers was determined by ^1H NMR in DMSO at 300 MHz by using Gemini 300 NMR Spectrometer (Varian, Palo Alto, CA, USA).

Particle size and zeta potential measurements

The analysis of the Zeta potential for size-distribution

and surface charge of PNIPAM-DMAEMAQ nanoparticules were performed using a Zetasizer Nano series ZS Dynamic Light Scattering (DLS) (Malvern. Instruments Ltd., UK). The sample of nanoparticules were dissolved in deionized water and ultrasonicated for 5 minutes. It was measured using a Zetasizer Nano Z at 37 °C and at a neutral pH. (Malvern Instruments, UK). The measurement was repeated in triplicate per sample, and measurements were reported as mean ± S.D.

Scanning electron microscopy studies

The size, surface morphology and appearance of the cationic NIPAM-DMAEMAQ hydrogels were assessed by using a scanning electron microscope (JEOL, JSM 5600). Before investigation, the hydrogels were dried at -45 °C and 38.10^{-3} mmHg using a vacuum freeze-dryer (Armfield SB4), and then powder sample was spread on a SEM stub and sputter-coated with gold. Particle size was obtained by measuring the diameters of at least 300 particles shown in SEM using image analysis software (Image-Pro plus 4.5; Media Cybernetics, Silver Spring, USA).

Measurement of LCST of P[NIPAM-DMAEMAQ] nanohydrogel

The phase transition temperature of aqueous P[NIPAM-DMAEMAQ] nanohydrogel was determined using a UV-visible spectrophotometer (UV-160 Shimadzu) at the wavelength of 500 nm over the temperature range (18–50 °C) by using cloud point measurement (turbidimetry) method. The heating rate was 1 °C/min. At each step, the samples were stabilized for 10 min before the next measurements (Valipour et al., 2011). Values for the LCST of polymeric solution were determined as the temperature at the inflection point in the normalized absorbance versus the temperature curve.

Evaluation of the binding P(NIPAM-DMAEMAQ) nanoparticles with the gene

The binding and interaction abilities of the gene with the magnetic P(NIPAM-DMAEMAQ) nanohydrogels of the complex formed by using the negative charge of the gene and the positive charge of the nanoparticle were determined using agarose gel electrophoresis. For this, firstly, nanoparticles (magnetic and non-magnetic) in non-toxicity concentration proportions were prepared. The prepared NP and MNP nanoparticles were loaded with 1 µg of the desired gene (Bcl-2 siRNA) mix in the RPMI 1640 medium without FBS by stirring for 30 min at 37 °C. It was left at room temperature for half an hour for the gene to interact with the nanoparticle. Then, 15 µL of the NP-gene and MNP-gene samples were mixed with 5 µL of 6× loading dye, and the final volume was made up to 20 µL, respectively. The naked gene was used as the control. The complexes were loaded onto a 4% agarose gel of EtBr and run using Tris-Agarose EDTA (TAE) buffer at 100 V for 45 min. The experiments were performed in triplicate. The gene bands were visualized by irradiation with UV light using the ChemDoc™ XRS Gel Documentation System (BioRad, California, USA).

3. Results and Discussion

3.1. Magnetic P(NIPAM-DMAEMAQ) Nanohydrogel

The synthesized bases of magnetic P (NIPAM-DMAEMAQ) and non-magnetic P (NIPAM-DMAEMA) are demonstrated schematically in Figure 3. Co-polymer magnetic P(NIPAM-co-DMAEM) nanohydrogels were synthesized using a radical polymerization process in order to create magnetic and thermoresponsive PNIPAM-based nanocomposites with quaternary alkyl ammonium halide salts of DMAEMA (Kim et al., 2019). Superparamagnetic magnetite nanoparticles were created in the first stage, and then, via the amend chemical co-precipitation technique, cationic quaternary ammonium alkyl halide monomers were synthesized by reacting methyl iodide (CH_3I) and the amine moiety of DMAEMA. Next, in the presence of NIPAM monomers, graft-free radical polymerization was initiated by using the vinyl bond of the DMAEMAQ moiety of a cationic monomer. Subsequently, copolymer P(NIPAM-DMAEMAQ) was mixed with superparamagnetic magnetite nanoparticle polymers. Poly (N,N dimethylaminoethyl methacrylate) (PDMAEMA) carries secondary amine groups that are both thermos-sensitive and pH-sensitive. Then in this way, the cationic magnetic nanoparticulated hydrogels that are pH- and thermos-sensitive were made ready for gene delivery. As known, magnetic nanoparticles, also known as iron oxide nanoparticles, have been shown to be more effective as gene delivery vehicles due to their stronger proton relaxation properties, reduced toxicity, lower detection limit, and active biomolecules tailored to their particular uses (Patra et al., 2018). As shown in Figure 3, the successful synthesis of P(NIPAM-DMAEMAQ) was confirmed by FT-IR spectroscopy. PNIPAM chain was grafted onto the nanogels to serve as pH sensitive and thermos-sensitive nanovalves (Liu et al., 2009). DMAEMAQ as a cationic polymer can condense negatively charged gene into nano sized particles through electrostatic interactions. In the result of nanocomplex formation, the polymers can protect gene from nuclease degradation and facilitate cellular uptake to induce high gene transfection.

3.2. Characterization

3.2.1. Fourier-transform infrared spectroscopy (FT-IR) analysis

FT-IR was first performed to confirm that the copolymerization of NIPAM and DMAEMAQ was successfully achieved. The FT-IR spectrum of the P(NIPAM-DMAEMAQ) polymer network are presented in Figure 4 the range of 4000 to 400 cm^{-1}. The spectrum exhibited two characteristic absorption signals of amide functional groups of poly(NIPAM) at 1650 cm^{-1} (NH-CO stretching) and 1550 cm^{-1} (N-H bending). Additionally, the broad absorption band at 3284 cm^{-1} referred to (−NH secondary amid stretching), and an absorption band at 2960 cm^{-1} (−CH_3 asymmetric stretching) of NIPAM was observed.
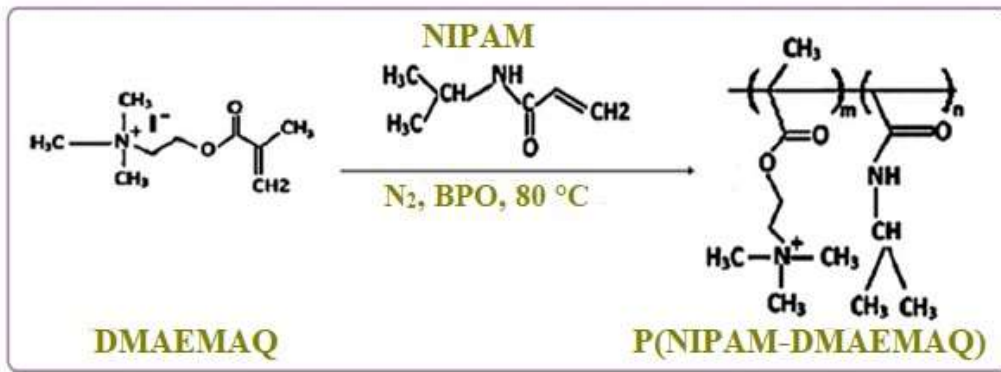
Figure 3. Synthesis scheme of P(NIPAM-DMAEMAQ) copolymer.
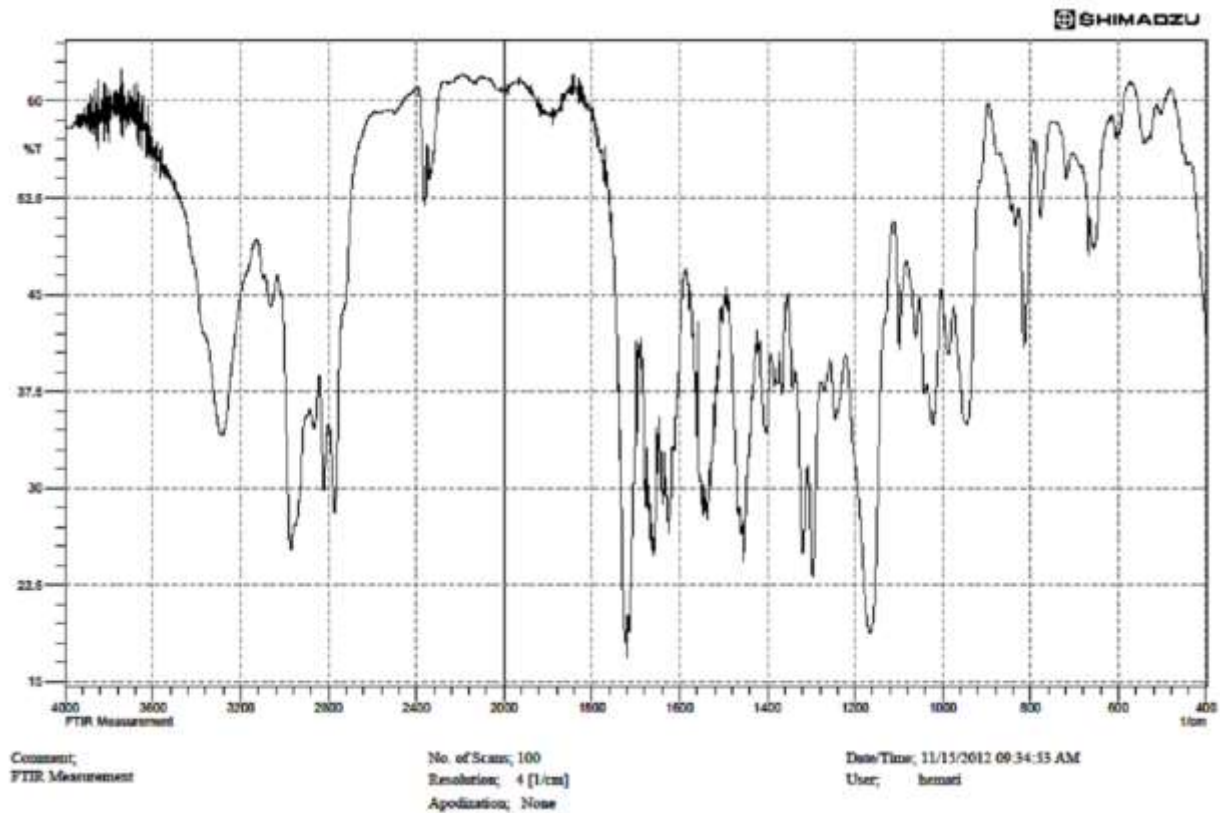
Figure 4. FT-IR spectrum of P(NIPAM-DMAEMAQ) nanohydrogel.

Finally, a characteristic stretching vibration peak for the ester carbonyl (C=O) at 1735 cm^{-1}, which confirms the successful copolymerization of PNIPAM with DMAEMA.

3.2.2. Hydrogen nuclear magnetic resonance (^{1}HNMR) spectrum

The ^{1}HNMR spectrum (in DMSO) of the P(NIPAM-DMAEMAQ) copolymer was used to determine the structure and composition of the copolymer (Figure 5). The chemical shifts at 1.16 ppm (6H, -CH-($\underline{CH_3}$)$_2$), 3.89 ppm (1H, -$\underline{CH}$-(CH$_3$)$_2$), and 7.42 ppm (1H, $\underline{NH}$-C=O) correspond to protons in the PNIPAAm segment. The signals appearing in 2.58 ppm (9H, -N$^+$-(CH$_3$)$_3$), 3.89 ppm (2H, -O-CH$_2$-CH$_2$-N(CH$_3$)$_2$), 2.82 ppm (2H, CH$_2$-N(CH$_3$)$_2$) related to protons of DMAEMA moiety of polymer, respectively (De Jesus-Tellez et al., 2020). The removal of the vinyl protons peaks at 5.58 ppm and 6.11 ppm demonstrates that end double bonds were converted into carbon-carbon signal bonds to form the main chain during polymerization (Valipour et al., 2021). All the evidence proved a graft copolymer was successfully synthesized.

3.2.3. Zeta potential (ζ) measurements

After magnetic copolymer P(NIPAM-DMAEMAQ) nanohydrogels were created, measurements of the surface charge distribution of the nanoparticles were taken with the Zeta-Sizer device (3000 HSA model MALVERN). Figures 6 and 7 show the surface charge graph of nanoparticles measured with the Zeta-Sizer. Initially, we analyzed the produced microgels and ascertained how the NIPAM affected their surface charge density (zeta potential). The PNIPAM hydrogel zeta potential has been shown to be near the isoelectric point (ISP = 0 mV). Then we determined the effect of DMAEMAQ content on the surface charge density of the

prepared microgels and analyzed how the queerization of the tertiary amine of the DMAEMA with different alkyl agents affects the hydrogel's surface charge. When DMAEMAQ was incorporated into the system, as observed in Figure 6, surface charge became positive and increased in value as the content of DMAEMAQ increased, and quaternized hydrogels with methyl showed even higher values of zeta potential: 12 mV. So, it was seen that the zeta potential of non-magnetic P(NIPAM-DMAEMAQ) nanoparticles had a positive surface charge in the surface charge analysis results. This could be caused by the increased carboxyl groups of DMAEMAQ in P (NIPAM-DMAEMAQ). Also, it was seen that the nanoparticles combined with magnetite had a more

positive surface charge of +24.7 mV as shown in Figure 7. This difference could be caused by the Fe^{+3}-containing groups interacting between the polymer layers, which have the most positive charge in magnetic P(NIPAM-DMAEMAQ) hydrogel. It was remarkable that the high zeta potential value was indicative of the colloidal stability of NPs. Thus, magnetic and non-magnetic nanoparticles, which are determined to have a positive surface charge by zeta-potential analysis, will be able to bind and interact with negatively charged genes. Thus, magnetic and non-magnetic nanoparticles, which are determined to have a positive surface charge by zeta-potential analysis, will be able to bind and interact with negatively charged genes.
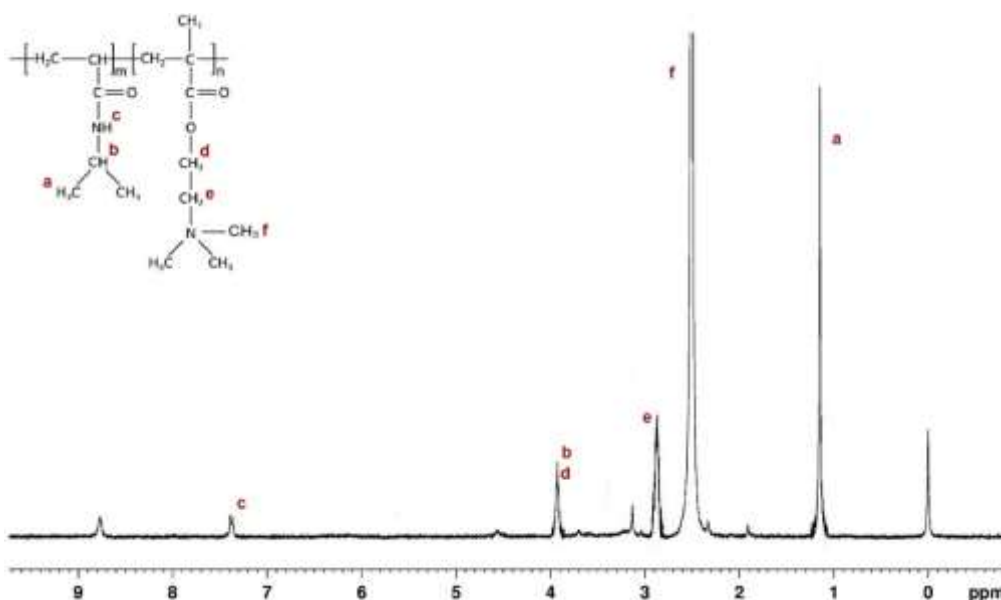
Figure 5. ^{1}HNMR spectrum of P(NIPAM-DMAEMAQ) nanohydrogel.
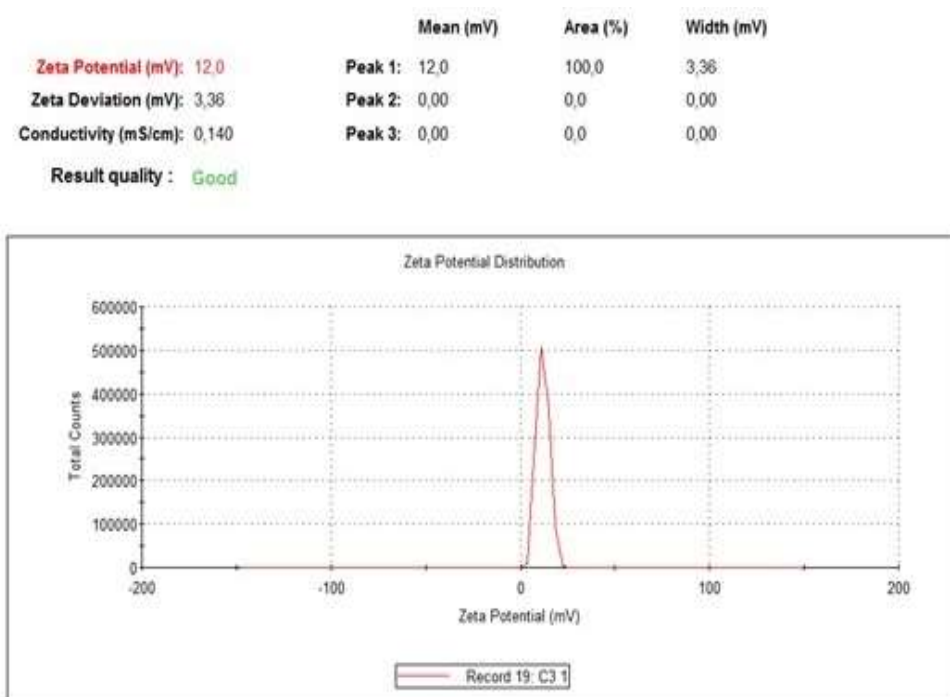
Figure 6. Surface charge distribution of P(NIPAM-DMAEMA) nanoparticles by zeta potential analysis.

	Mean (mV)	Area (%)	Width (mV)
Zeta Potential (mV): 24,7	Peak 1: 25,5	96,5	5,37
Zeta Deviation (mV): 6,98	Peak 2: -0,989	3,5	3,30
Conductivity (mS/cm): 1,22	Peak 3: 0,00	0,0	0,00
Result quality : Good			
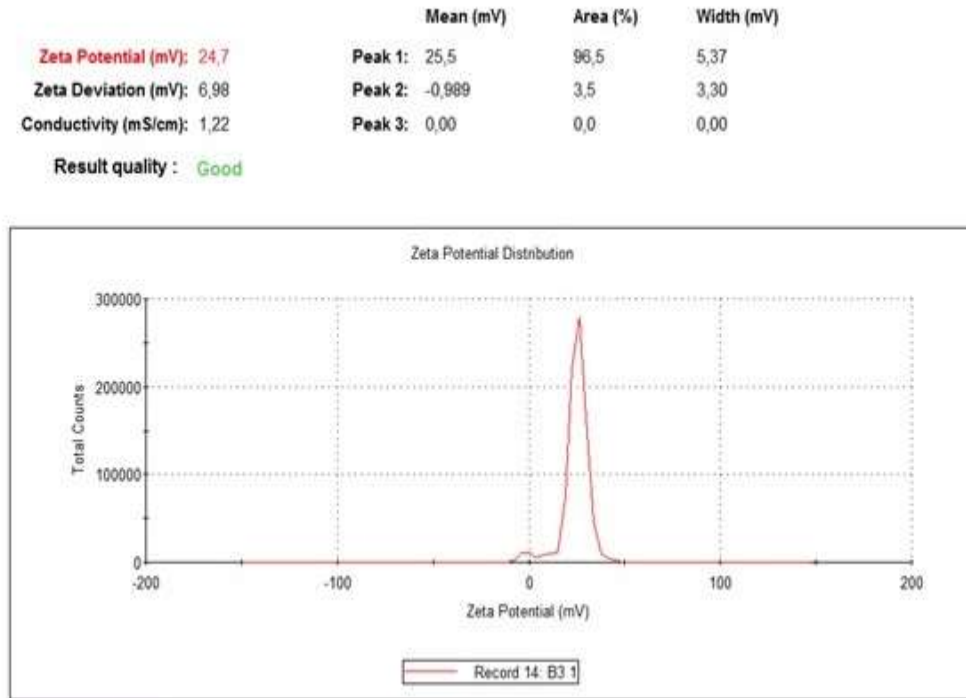
Figure 7. Surface charge distribution of magnetic P(NIPAM-DMAEMAQ) nanoparticles by zeta potential analysis.

3.2.4. Morphology with SEM

The structural morphology of non-magnetic P(NIPAM-co-DMAEMAQ) and magnetic P(NIPAM-co-DMAEMAQ) hydrogels was investigated by scanning electron microscopy (SEM) after the hydrogels in the swelling state were freeze-dried. Figure 8 shows that the interior morphology of the hydrogels clearly exhibits a macro-nano structure. And the particle size and distribution of both copolymer nanohydrogels were porous, with a relatively uniform pore size distribution and a similar trend. Additionally, although there is no apparent difference between the SEM micrographs of both of the magnetic and non-magnetic copolymers, in Figure 9, the SEM results of the nanoparticles' dimensions in non-magnetic nanoparticles were approximately around 77.06 and 77.16 nm, and magnetic nanoparticles were around 86.95 and 91.22 nm. So, the size of magnetic-loaded P(NIPAM-DMAEMAQ) increased slightly, indicating that the magnetic particles were loaded in P(NIPAM-DMAEMAQ) nanocomposites. As a result, it was confirmed that the synthesized P(NIPAM-DMAEMAQ) particles are nanosized.

3.2.5. Phase transition behavior and LCST of the P(NIPAM-DMAEMAQ) nanohydrogel

Cloud point measurements were utilized for determination of LCST of P(NIPAM-DMAEMAQ) nanohydrogel by the turbidity method via monitoring the change in the optical absorbance as a function of temperature. Figure 10 exhibits the typical cloud point measurement of hydrogel with sharp phase transition for hydrogel with a small temperature change. The sharp

reduction in UV transmittance indicates that the hydrogels become increasingly turbid with shrinking on increasing at higher temperatures, and the LCST is the point at which the network structure of polymer collapse and water expelled of the hydrogel. As depicted in Figure 10, P(NIPAM-DMAEMAQ) exhibited sharp volume phase transition at 40 °C, so the LCST of the hydrogel solution was about 40 °C, which was between the LCST of poly(NIPAM) (32 °C) (Lanzalaco and Armelin, 2017) and poly(DMAEMA) (50 °C) (Gutarowska et al., 2015). In general, incorporation of hydrophilic monomers shift the hydrogel toward a more hydrophilic nature and the LCST should shift to a higher temperature. An admitted mechanism of the phase separation of PNIPAM as a thermo-sensitive moiety in the polymer backbone, is described as resulting from the breakdown of hydrogen bonds and the enhancement of hydrophobic interactions. Generally, a hydrophilic/hydrophobic balance exists in PNIPAM side chains. At room temperature, favorable hydrogen bonding interactions between hydrophilic amide groups in the polymers and water molecules result in the good solubility of PNIPAM. With further increasing temperature, the hydrophilic/hydrophobic balance shifts to a more hydrophobic nature, the hydrogen bonds are broken and the aggregation process takes place at around LCST. In addition, copolymerization of hydrophilic DMAEMAQ moiety with NIPAM may increase the LCST value, which caused by the changes of the hydrophilic/hydrophobic ratio and formed more hydrogen bonds between the polymer chains and water molecules (Huang et al., 2017).
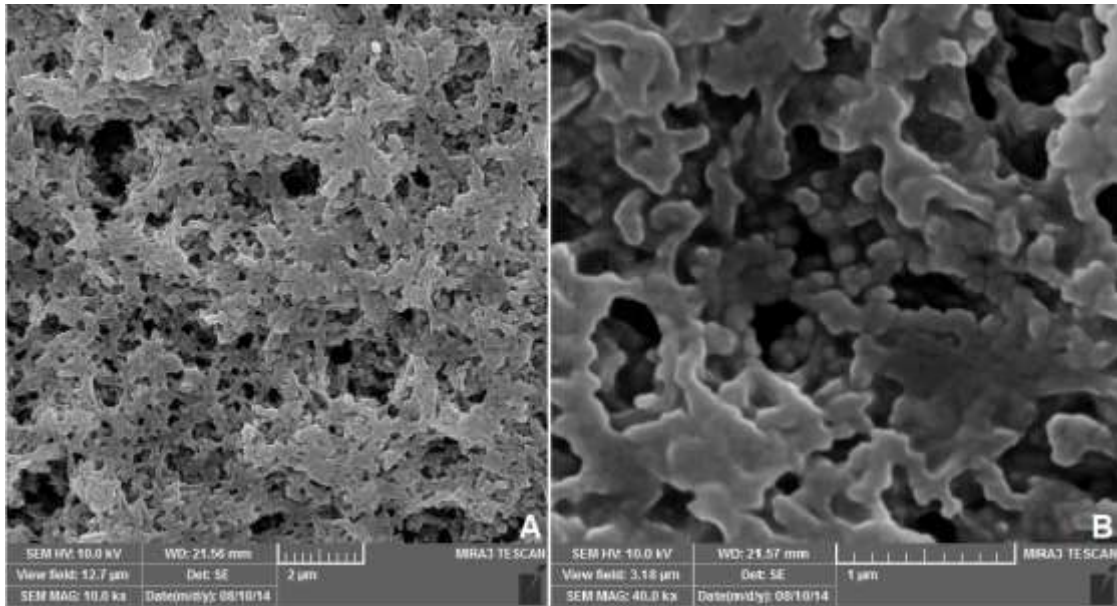
Figure 8. Surface image of the synthesized P(NIPAM-DMAEMAQ) nanohydrogel using SEM.
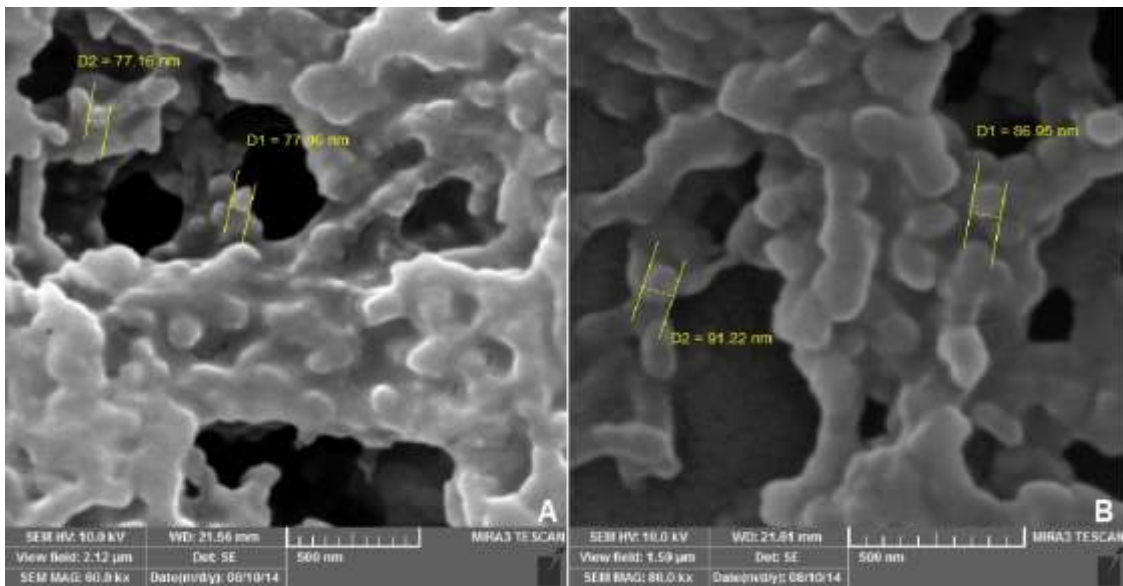
Figure 9. Demonstration of the dimensions of the synthesized P(NIPAM-DMAEMAQ) nanohydrogel using SEM. (A): Size of non-magnetic nanoparticle, (B): Size of magnetic nanoparticle.
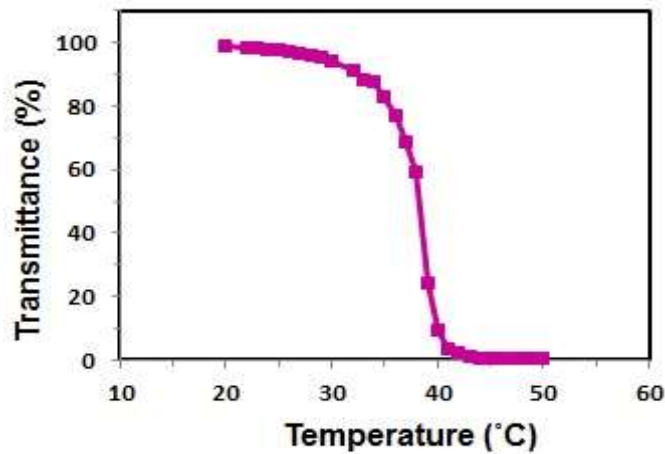
Figure 10. Transmittance-temperature curve of the P(NIPAM-DMAEMAQ) nanohydrogel determination by UV–Vis spectrum.
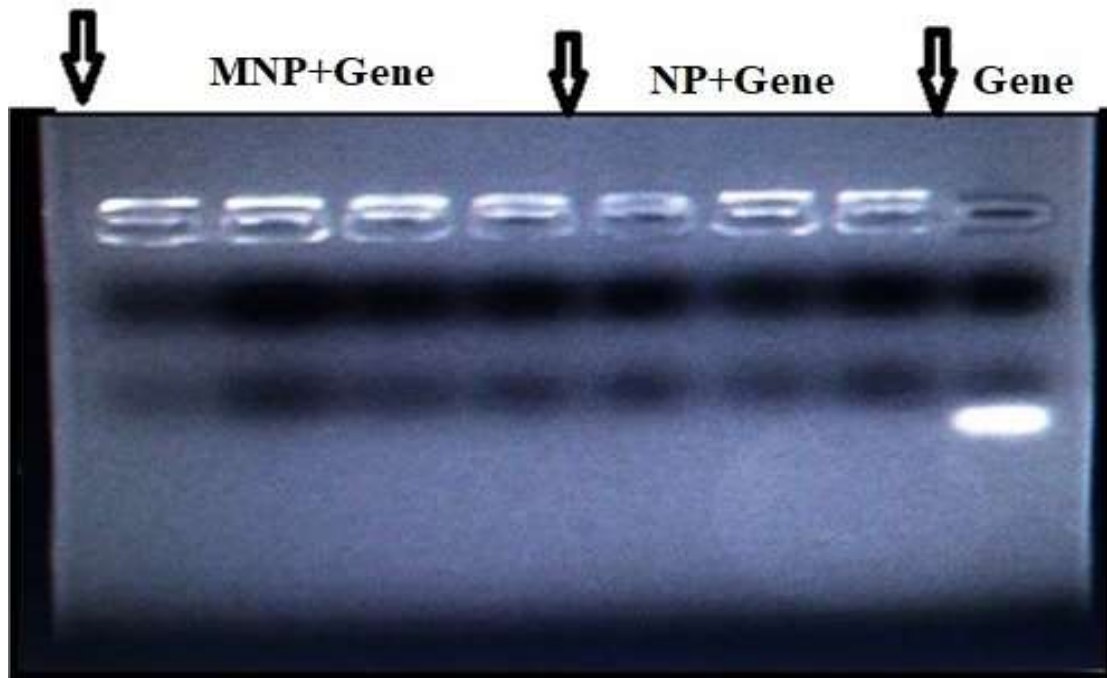
Figure 11. Demonstration of loading MNP and NP with the gene through an agarose gel electrophoresis assay.

3.3. Investigation of the P(NIPAM-DMAEMAQ) Nanohygrogel Loading with the Gene through Agarose Gel Electrophoresis Assay

In this stage of the research to confirm the application of NIPAM-DMAEMAQ-based nanocomposites with loading by gene, the interaction properties between magnetic and non-magnetic NIPAM-DMAEMAQ nanocomposites and the gene were examined by gel electrophoresis assay. As observed in Figure 11, wells 1–7 represent the presents of the gene and NIPAM-DMAEMAQ complex inside the well itself. The wells of 1-4 represent the presents of the gene with MNP, the wells of 5-7 represent the presents of the gene with NP, and well 8 presents the naked gene. The naked gene was used as the control group. As the results showed in well 8, the band didn't exist in the wall, indicating no banding of the naked gene in the well. So the naked gene has not shown any absorbance in the 8-well region. In the case of NP via gene for the wells (5, 6, and 7), a light band is observed. This clearly showed a weak interaction between nonmagnetic NP and the gene, but in the case of MNP with the gene for the wells (1, 2, 3, and 4), a potent band is observed. So, the complete binding of the gene to magnetic P[NIPAM-DMAEMAQ] nanoparticles clearly demonstrates a strong interaction between magnetic NP and the gene in wells 1–4, which has prevented the release of genes in the presence of the electrophoresis buffer. Also, due to the presence of Fe_3O_4, it causes a very positive charge and demonstrates a potent interaction between magnetic NP and gene. So that, the positive charges of magnetic P[NIPAM-DMAEMAQ] could neutralize the negative charges of the phosphate groups in the gene backbone, thus retarding gene mobility. This clearly suggests that the charge of nanoparticles plays a significant role in the loading and delivery of gene

products (negative charge due to the presence of a phosphate group).Therefore, P[NIPAM-DMAEMAQ] NPs are more effective in the intracellular delivery of genes (nucleic acids) (Yang et al., 2015). On the other hand, non-magnetic versus magnetic samples were also tested to check the bonding pattern of nanoparticles with genes. Electrophoresis with gene-loaded NPs demonstrated a weak interaction between the NPs and genes. As a result, the high gene loading in nanoparticles can be attributed to the interaction between the positively charged group of the magnetic P(NIPAM-DMAEMAQ) and the negative charge part of the gene through electrostatic adsorption. Hence, according to the results, we chose the magnetic P(NIPAM-DMAEMAQ) due to its strong adsorption capabilities as a gene carrier, their magnetic properties to achieve control over the delivery of the gene, and their capacity for satisfactory loading to continue our research.

4. Conclusion

In gene delivery systems, the precise control of gene delivery and the right site-selective capability accompanying it are still a big challenge. Currently, the development of functional biosynthesis nanocarriers with safety, good biocompatibility, low cost of production, and effectiveness is of intense focus and importance for the delivery of the gene (nucleic acid) for gene therapy. According to the importance of the issue, our main goal herein was to build up a cationic carrier for targeted, specific gene delivery to maximize efficiency and minimize nano-related toxicity. For these purposes, we copolymerized NIPAM with a basic monomer quaternary ammonium quart salt of DMAEMA. Then, two kinds of dual temperature and pH-responsive polymer-coated magnetic nanohydrogels composed of magnetic P(NIPAM-DMAEMAQ) and non-magnetic P(NIPAM-

DMAEMAQ) polymers were successfully synthesized at an approximate size of nano. The nanoparticles' dimensions in non-magnetic nanoparticles were approximately around 77.06 and 77.16 nm, and magnetic nanoparticles were around 86.95 and 91.22 nm. As a result, MNPs with hyperthermia properties were loaded with specific genes as nanocarriers and used for targeted delivery. The resultant nanocarriers with positive charge were able to be efficiently loaded with the specific gene (more than 95%). Thanks to these unique properties, magnetic nanoparticles with metal-based configurations could be controlled by a varying external magnetic field current for various purposes, such as targeting nano-based genes or medications, promoting specific site targeting, and slowing tumor development. Therefore, combined with the specific gene release behavior and high loading capacity of genes, the present magnetic P (NIPAM-DMAEMAQ) could resolve the difficulties in loading and uncontrolled release of genes in cancer cells and different diseases. As a result, the targeted delivery of genes and drugs with smart nanocarriers could be used to treat different diseases and tumors and will be a promising alternative to cancer and other diseases.

Author Contributions

The percentage of the author(s) contributions is presented below. All authors reviewed and approved the final version of the manuscript.

	F.Valio.	F.Valip.	S.S.	M.T.	S.D.
C	50	15	20	10	5
D	50	35	5	5	5
S	25	5	35	25	10
DCP	50	35	5	5	5
DAI	50	35	5	5	5
L	50	35	5	5	5
W	50	30	10	5	5
CR	50	35	5	5	5
SR	50	35	5	5	5
PM	50	5	20	20	5
FA	40	5	25	20	10

C=Concept, D= design, S= supervision, DCP= data collection and/or processing, DAI= data analysis and/or interpretation, L= literature search, W= writing, CR= critical review, SR= submission and revision, PM= project management, FA= funding acquisition.

Conflict of Interest

The authors declared that there is no conflict of interest.

Ethical Consideration

Ethics committee approval was not required for this study because of there was no study on animals or humans.

Acknowledgment

References

Bi Q, Song X, Hu A, Luo T, Jin R, Ai H, Nie Y. 2020. Magnetofection: Magic magnetic nanoparticles for efficient gene delivery. Chin J Chem, 31: 3041-3046.

De Jesus-Tullez MA, Sanchez-Cerrillo DM, Quintana-Owen P, Schubert US, Contreras-Lopez D, Guerrero-Sanchez C. 2020. Kinetic investigations of quaternization reactions of poly [2-(dimethylamino) ethyl methacrylate] with diverse alkyl halides. Macromol Chem Phys, 221: 1900543.

Fussell SL, Bayliss K, Coops C, Matthews L, Li W, Briscoe WH, Faers M, Royall C, Van Duijneveldt JS. 2019. Reversible temperature-controlled gelation in mixtures of pNIPAM microgels and non-ionic polymer surfactant. Soft Matter, 15: 8578-8588.

Gutarowska B, Stawski D, Sknra J, Herczynska L, Pielech-Przybylska K, Połowinski S, Krucinska I. 2015. PLA nonwovens modified with poly (dimethylaminoethyl methacrylate) as antimicrobial filter materials for workplaces. Text Res J, 85: 1083-1094.

Hamimed S, Jabberi M, Chatti A. 2022. Nanotechnology in drug and gene delivery. Naunyn Schmiedebergs Arch Pharmacol, 395: 769-787.

He Y, Li D, Wu L, Yin X, Zhang X, Patterson LH, Zhang J. 2023. Metal-Organic Frameworks for Gene Therapy and Detection. Adv Funct Mater, 33: 2212277.

Huang Y, Yong P, Chen Y, Gao Y, Xu W, Lv Y, Yang L, Reis RL, Pirraco RP, Chen J. 2017. Micellization and gelatinization in aqueous media of pH-and thermo-responsive amphiphilic ABC (PMMA 82-b-PDMAEMA 150-b-PNIPAM 65) triblock copolymer synthesized by consecutive RAFT polymerization. RSC Adv, 7: 28711-28722.

Jacob S, Kather FS, Morsy MA, Boddu SH, Attimarad M, Shah J, Shinu P, Nair AB. 2024. Advances in nanocarrier systems for overcoming formulation challenges of curcumin: Current İnsights. Nanomater, 14: 672.

Kim YK, Kim E-J, Lim JH, Cho HK, Hong WJ, Jeon HH, Chung BG. 2019. Dual stimuli-triggered nanogels in response to temperature and pH changes for controlled drug release. Nanoscale Res Lett, 14: 1-9.

Lanzalaco S, Armelin E. 2017. Poly (N-isopropylacrylamide) and copolymers: a review on recent progresses in biomedical applications. Gels, 3: 36.

Lin G, Revia RA, Zhang M. 2021. Inorganic nanomaterial-mediated gene therapy in combination with other antitumor treatment modalities. Adv Func Mater, 31: 2007096.

Liu R, Cellesi F, Tirelli N, Saunders B. 2009. A study of thermoassociative gelation of aqueous cationic poly (N-isopropyl acrylamide) graft copolymer solutions. Polymer, 50: 1456-1462.

Manouras T, Platania V, Georgopoulou A, Chatzinikolaidou M, Vamvakaki M. 2021. Responsive quaternized PDMAEMA copolymers with antimicrobial action. Polymers, 13: 3051.

Materon EM, Miyazaki CM, Carr O, Joshi N, Picciani PH, Dalmaschio CJ, Davis F, Shimizu FM. 2021. Magnetic nanoparticles in biomedical applications: A review. Appl Surf Sci Adv, 6: 100163.

Moselhy J, Vira T, Liu FF, Wu XY. 2009. Characterization of complexation of poly (N-isopropylacrylamide-co-2-(dimethylamino) ethyl methacrylate) thermoresponsive cationic nanogels with salmon sperm DNA. Int J Nanomed, 2009: 153-164.

Patra JK, Das G, Fraceto LF, Campos EVR, Rodriguez-Torres MDP, Acosta-Torres LS, Diaz-Torres LA, Grillo R, Swamy MK, Sharma S. 2018. Nano based drug delivery systems: recent developments and future prospects. J Nanobiotechnol, 16: 1-33.

Rai R, Alwani S, Badea I. 2019. Polymeric nanoparticles in gene therapy: New avenues of design and optimization for delivery applications. Polymers, 11: 745.

Roy I. 2022. Therapeutic applications of magnetic nanoparticles: recent advances. Mater Adv, 3: 7425-7444.

Satalkar P, Elger BS, Shaw DM. 2016. Defining nano, nanotechnology and nanomedicine: why should it matter? Sci Eng Ethics, 22: 1255-1276.

Sayed N, Allawadhi P, Khurana A, Singh V, Navik U, Pasumarthi SK, Khurana I, Banothu AK, Weiskirchen R, Bharani KK. 2022. Gene therapy: Comprehensive overview and therapeutic applications. Life Sci, 294: 120375.

Shahryari A, Burtscher I, Nazari Z, Lickert H. 2021. Engineering gene therapy: advances and barriers. Adv Therap, 4: 2100040.

Shillitoe EJ. 2009. Gene therapy: the end of the rainbow?. Head Neck Oncol, 1: 1-5.

Sung YK, Kim S. 2019. Recent advances in the development of gene delivery systems. Biomater Res, 23: 8.

Thang NH, Chien TB, Cuong DX. 2023. Polymer-based hydrogels applied in drug delivery: An overview. Gels, 9: 523.

Valipour F, Esmhosseini M, Nejati K, Kianfar H, Pasdaran A, Davaran S. 2011. Synthesis and antibacterial activity of silver nanoparticles embedded in smart poly (N-isopropylacrylamide)-based hydrogel networks. J Nanotechnol Eng Med, 2: 041001.

Valipour F, Valipour F, Rahbarghazi R, Navali AM, Rashidi MR, Davaran S. 2021. Novel hybrid polyester-polyacrylate hydrogels enriched with platelet-derived growth factor for chondrogenic differentiation of adipose-derived mesenchymal stem cells in vitro. J Biol Eng, 15: 1-14.

Wulandari AD, Sutriyo S, Rahmasari R. 2022. Synthesis conditions and characterization of superparamagnetic iron oxide nanoparticles with oleic acid stabilizer. J Adv Pharm Technol Res, 13: 89-94.

Yang HY, Van Ee RJ, Timmer K, Craenmehr EG, Huang JH, Oner FC, Dhert WJ, Kragten AH, Willems N, Grinwis GC. 2015. A novel injectable thermoresponsive and cytocompatible gel of poly (N-isopropylacrylamide) with layered double hydroxides facilitates siRNA delivery into chondrocytes in 3D culture. Acta Biomater, 23: 214-228.

Yang R, Chen F, Guo J, Zhou D, Luan S. 2020. Recent advances in polymeric biomaterials-based gene delivery for cartilage repair. Bioact Mater, 5: 990-1003.

Zhang Q, Kuang G, Li W, Wang J, Ren H, Zhao Y. 2023. Stimuli-responsive gene delivery nanocarriers for cancer therapy. Nanomicro Lett, 15: 44.

İŞİTME ENGELLİ BİREYLERİN HAREKETLERİNİ SINIFLANDIRMAYA YÖNELİK YAPAY ZEKA MODELİNİN GELİŞTİRİLMESİ

Ahmed KASAPBAŞI[1]*, Hüseyin CANBOLAT[1]

[1]*Ankara Yildirim Beyazit University, Faculty of Engineering and Natural Sciences, Department of Electrical and Electronics Engineering, 06760, Ankara, Türkiye*

Özet: İşaret Dili, işitme engelli bireyler için hayati bir iletişim aracıdır. Farklı ülkelerde kendi ihtiyaçlarına geliştirilmiş birçok işaret dili vardır. Bu çalışma, Türk İşaret Dili (TİD) jestlerini derin öğrenme teknikleriyle metne dönüştürmeyi amaçlamaktadır. Bu amaçla, arka planlar, aydınlatma koşulları ve işaret pozisyonları gibi çeşitli çevresel faktörler açısından çeşitlilik gösteren yeni bir veri kümesi oluşturulmuştur. Daha sonra, TİD alfabesini algılamak ve sınıflandırmak için Evrişimli Sinir Ağları (CNN'ler) kullanılmıştır. Ayrıca, geliştirilen modellerin performansını optimize etmek için çeşitli hiperparametreler araştırılmıştır. En iyi CNN mimarisi, beş evrişimli katmanı içerir ve Adam öğrenme hızı optimizasyon yöntemini kullanır; 80 epoch'tan sonra yaklaşık %98'lik bir doğruluk (başarı) elde edilmiştir. Sonuç olarak, zorlu bir veri kümesi üzerinde eğitilen önerilen modeller, işaret dili tanıma alanında önemli bir ilerleme temsil etmektedir.

Anahtar kelimeler: Yapay zeka, Jest, Tanımlama, İşitme engelli

Development of an Artificial Intelligence Model for Classification of the Movements of Hearing Impaired Individuals

Abstract: Hearing impaired individuals utilize a crucial communication tool called sign language. There are numerous sign languages across different countries such as natural languages. This study proposes leveraging deep learning (DL) advancements to facilitate the conversion of sign language gestures into text. To this end, a novel dataset is curated under various environmental factors such as backgrounds, lighting conditions, and sign positions. Subsequently, Convolutional Neural Networks (CNNs) are employed to detect and classify twenty-three gestures of Turkish sign language alphabet. Furthermore, various hyperparameters are explored to optimize the performance of the developed models. The best model relies on a five-layer convolutional network coupled with the Adam optimization algorithm. This model approximately achieves a commendable accuracy of 98% after 80 epochs. As a result, the proposed models and dataset represent a significant advancement in the field of gestures recognition.

Keywords: Artificial intelligence, Gesture, Recognition, Hearing impaired

1. Giriş

İşitme engelli bireyler, işaret dili aracılığıyla sadece birbirleriyle değil, aynı zamanda bu engeli paylaşmayanlarla da iletişim kurabilirler. Her toplumun kendi belirgin ulusal işaret dili vardır ve ülkeden ülkeye farklılık gösterir (Karaca ve Bayır, 2018). İletişimin önemli bir yönü, bireylerin birbirleri arasındaki etkileşimi kolaylaştırmak için sıkça kullandığı dilde yatar (Thomas ve Mcdonagh, 2013). Her toplumun kendine özgü konuşulan dili vardır ve bireylerin kendilerini ifade etmeleri için doğrudan veya dolaylı bir araç olarak hizmet eder (Alshehri, 2023). Ancak, bazı bireyler çeşitli faktörlerden dolayı işitme kaybı yaşayabilir ve bu durum onları sosyal ortamlarda etkili bir şekilde iletişim kuramaz hale getirebilir. Sonuç olarak, işitme engelliler için her toplumda işaret dili geliştirilmiştir ve işitsel ipuçlarından olmaksızın el, parmak ve kol hareketlerini kullanılır (Vijayalakshmi ve Aarthi, 2016). İşaret dili, işitme engelli bireylerin sayıların, harflerin ve özel karakterlerin jestleriyle vasıtasıyla kendilerini ifade etmelerine ve başkalarıyla iletişim kurmalarına yardımcı olur (Oktekin, 2018).

2015 yılı istatistiklerine göre Türkiye'de yaklaşık 836 bin işitme engelli vatandaş bulunmaktadır (Yıldız ve ark., 2018). İşitme engelliler için kullanışlı olmasına rağmen, toplumun bazı kesimleri için işaret dili hala yabancıdır. Bu nedenle, gerektiğinde işaret dilinin kullanımını sağlayan akıllı araçların teknolojik araçlarla sunulması mümkün bir çözüm olarak görülmektedir (Jantunen ve ark., 2021). Yapay zeka, tanıma ve sınıflandırma alanında

önemli ilerlemeler kaydetmiştir (Anand ve ark., 2021; Machiraju ve ark., 2021; Singh ve ark., 2021). Bu nedenle, işaret dili tanıma sistemleri, işitme engelli bireylere yardımcı olmak için bu ilerlemeyi kullanır. İşaret dili tanıma için iki ana yöntem bulunmaktadır. İlk yöntem, veri eldivenleri (Lu ve ark., 2016) ve elektromiyografi (Qi ve ark., 2020) gibi giyilebilir cihazları içerir, ancak bu cihazlar genellikle kullanışsız ve maliyetlidir. İkinci yöntem ise, yalnızca el hareketi görüntülerini yakalamak için bir kamera gerektirdiğinden ek ekipman ihtiyacını ortadan kaldıran bilgisayarla görme tabanlı yöntemdir.

Araştırmamızın temel amacı, işitme engelli bireylerin hareketlerini algılayan ve bu hareketleri metne dönüştüren bir teknoloji geliştirmektir. Bu, işaret dilini bilmeyen kişilerin bu hareketleri anlamasına yardımcı olacaktır. Bu yaklaşım, işitme engelli bireyler ile toplum arasında kesintisiz iletişimi kolaylaştırmayı hedeflemektedir. Bu kapsamında, bu araştırma, Türk işaret dili karakterlerini sınıflandırmak için gelişmiş bir veri kümesi ve model önermektedir. Bu model, çeşitli işaretleri karşılık gelen Türkçe metne sınıflandırır. Bu sistem, işaretleri Türk alfabesine çevirerek işitme engelli bireylerin etkili bir şekilde iletişim kurmasını sağlar. Dahası, bu çalışmada önerilen modeller, geliştirilen veri kümesini yaklaşık %98'lik bir doğruluk oranıyla işleyebilmektedir.

Bu çalışmanın geri kalanı aşağıdaki gibi yapılandırılmıştır: İkinci bölümde konuyla ilgili bir literatür taraması sunulurken, üçüncü bölüm sistem mimarisi ve veri kümesini içeren metodolojiyi açıklar. Son olarak, dördüncü bölüm çalışmayı sonuçlandırır ve üçüncü bölümde sunulan sonuçların tartışmasını içerir.

1.1. İlgili Çalışmalar

Addepalli ve ark. (2023), Amerikan İşaret Dili (AİD) alfabelerini ve rakamlarını tanıyan ve bunları metne çeviren bir sistem önermişlerdir. Bir AİD veri seti oluşturmuşlar ve kapsamlı bir analizden sonra, özellik çıkarımı için AlexNet'i kullanan transfer öğrenimi ile AİD'yi metne dönüştürmenin optimal tekniğini belirlemişlerdir. AlexNet'i Naive Bayes, SVM ve KNN gibi sınıflandırma algoritmalarıyla birleştirmişler ve Naive Bayes %97.92'lik en yüksek doğruluğa ulaşırken, SVM ve KNN sırasıyla %96.98 ve %96.97 doğruluk oranlarına erişmişlerdir.

Shanmuga Priya ve ark. (2023), işaret dilini sese dönüştürmek için özel bir CNN algoritması önermektedir; bu algoritma, kullanıcıların işaret dilini "duymasını" sağlamaktadır. Bu amaçla on hareketten oluşan bir veri seti toplamışlar ve veri seti oluşturma, görüntü ön işleme ve etiketleme, veri artırma, sinir ağı eğitimi ve doğrulama verileri ile test etme gibi adımları takip etmişlerdir. Hareket tanıma sistemleri %90'ın üzerinde bir doğruluk oranına ulaşmıştır.

Shokoori ve ark. (2022), Pashto İşaret Dili'nin on alfabesi üzerine odaklanarak, engelli bireylerin toplumla iletişim kurmalarını sağlayan bir sistem önermişlerdir. Önerilen sistem, işaretleri ve hareketleri yakalar ve bunları Pashto alfabesine dönüştürür. El hareketlerini tanımak için bir

CNN modeli tasarlamışlar ve %98 doğruluğa erişmişlerdir.

Öztürk ve ark. (2021) çalışmalarında işaret dili parmak alfabesi hareketlerini tanımak için derin öğrenme ve görüntü işleme tekniklerini kullanmış, bunları metne dönüştürmüştür. Sistemi, el görüntülerini derin öğrenme yöntemleri kullanarak yorumlar, onları alfabedeki harflerle eşleştirir ve tahmin edilen harfi metin olarak görüntüler; böylece 1300 fotoğraftan oluşan bir veri kümesiyle %88 doğruluk oranı elde etmişlerdir. Toğaçar ve ark. (2021), Türk İşaret Dili (TİD) için rakam işaretlerini belirlemek için Siamese sinir ağı kullanarak, %98.16'lık eşleştirme başarısına'ya ulaşmıştır.

Katılmış ve Karakuzu (2020), Leap Motion ile çift eli kullanarak TİD alfabesini tanıyan bir sistem aracılığıyla tanıma performansını geleneksel sınıflandırıcılar ve özellik seçme algoritmalarını kullanarak analiz etmişlerdir. Bantupalli ve Xie, 2019, işaret dili işaretlerini metne çevirmek için görüntü tabanlı bir sistem önermişler, videolardan çıkarılan mekansal ve zamansal özellikleri ile Inception ve CNN yapılarını kullanarak AİD veri kümesiyle başarılı bir şekilde jest tanımlamışlardır.

Hurroo ve Walizad (2020), bir AİD alfabesi tanıma sistemi tasarlamıştır. Kendi AİD veri setlerini on statik alfabe işareti ile oluşturmuşlardır. Yaklaşımları, özellik çıkarımı (ikili pikseller) için görüntüleri 64 piksele normalleştirme ve yeniden ölçeklendirme, el hareketlerini algılamak için HSV renk algoritmasını kullanma ve siyah bir arka plan kullanma gibi adımları içermektedir. İlgi bölgesi olan el hareketi, çeşitli bilgisayar görme teknikleri (gri tonlama, genişletme ve maskeleme) kullanılarak segmentlenir ve özellikler çıkarılır. Eğitme ve sınıflandırma için bir CNN kullanarak %90'ın üzerinde doğruluğa ulaşmışlardır.

Sabeenian ve ark. (2020), AİD alfabelerini metne çevirmek için özel bir CNN kullanarak bir sistem geliştirmişlerdir. MNIST AİD veri seti üzerinde eğitilen modelleri, %93'ün üzerinde doğruluğa ulaşmıştır.

Sevli ve Kemaloğlu (2020), Türk işaret dili rakamlarını sınıflandırmak için bir CNN modeli önermiş, Adam optimizatörü kullanarak eğitim için %98.42, test doğruluğu için %98.55 doğruluk oranı elde etmişlerdir. Yalçın ve ark., 2018, esnek sensörler ve bir jiroskop kullanarak Türk İşaret Dili (TİD) harflerini tespit edip çeviren bir veri eldiveni tasarlamışlar, 18 TİD alfabesi harfini tanımayı başarmışlardır.

Arora ve Roy (2018), Bhattacharyya Mesafe Metriği ve OpenCV kullanarak AİD jestlerini tanımayı ve metne çevirmeyi sağlayan bir teknik sunmuşlar. Bu teknik, jestlerin histogram benzerliklerine dayanmaktadır. Unutmaz ve ark. (2019), Kinect cihazından iskelet bilgilerini kullanarak Türk işaretlerini kelimelere dönüştürmek için CNN tabanlı bir sistem önerisiyle, veri kümesi ve CNN yapısına bağlı olarak %80 ila %93 arasında değişen doğruluk değerlerine erişmişlerdir.

Nguyen ve Do, 2019, yapay zeka kullanarak geliştirdikleri bir işaret dili parmak alfabesi tanıma sistemini kullanarak Çok Sınıflı Destek Vektör Makineleri (SVM'ler)

ve CNN yapıları ile tatmin edici sonuçlar elde etmişlerdir. Kaya ve ark., 2018, Türk İşaret Dili (TİD) kullanarak sayıları ve harfleri tespit etmeyi amaçlar, sensörlerle donatılmış bir veri eldiveni kullanarak başarılı bir şekilde 1 ile 5 arasındaki sayıları tespit etmişlerdir.

2. Materyal ve Yöntem

2.1. Veri Kümesi

Bu çalışma, Türk İşaret Dili (TİD) de dahil olmak üzere çeşitli işaret dilleri için kısıtlı sayıdaki veri setlerine ilaveten TİD alfabesinin yirmi üç harfine odaklanan yeni bir veri seti sunmaktadır. Bu araştırmanın temel amacı, TİD alfabesinin jestlerini metne dönüştürmektir. Bunun için TİD harflerinin görüntülerinden oluşan bir veri seti önerilmektedir. Şekil 1, TİD alfabesinin yirmi üç harfini göstermektedir.

Veri setini derlemek için, OpenCV kütüphanesini kullanarak eşik teknikleri kullanılmış ve görüntü boyutları 224x224 piksel olarak ayarlanmıştır. Ortaya çıkan veri seti, kamera mesafelerindeki değişimler, aydınlatma koşulları ve arka planlar gibi çeşitli faktörleri de içeren çeşitli koşullar altında yaklaşık 10,000 görüntü içeren zorlu bir veri setidir. Kullanıma hazır hale getirilmeden önce, görüntüler önerilen modele uygun şekilde 64x64 boyutuna yeniden boyutlandırılır. Daha sonra, veri seti eşit olarak bölünür ve %80'i eğitim için ayrılırken geri kalan %20'si doğrulama ve test amaçları için kullanılır. Dahası, veri artırma teknikleri, veri setinin çeşitliliğini artırmak ve model performansını iyileştirmek için uygulanır. Oluşturulan yeni veri seti, özellikle işaret dili tanıma araştırmaları alanında, yeni derin öğrenme uygulamalarına ilham verebilir.
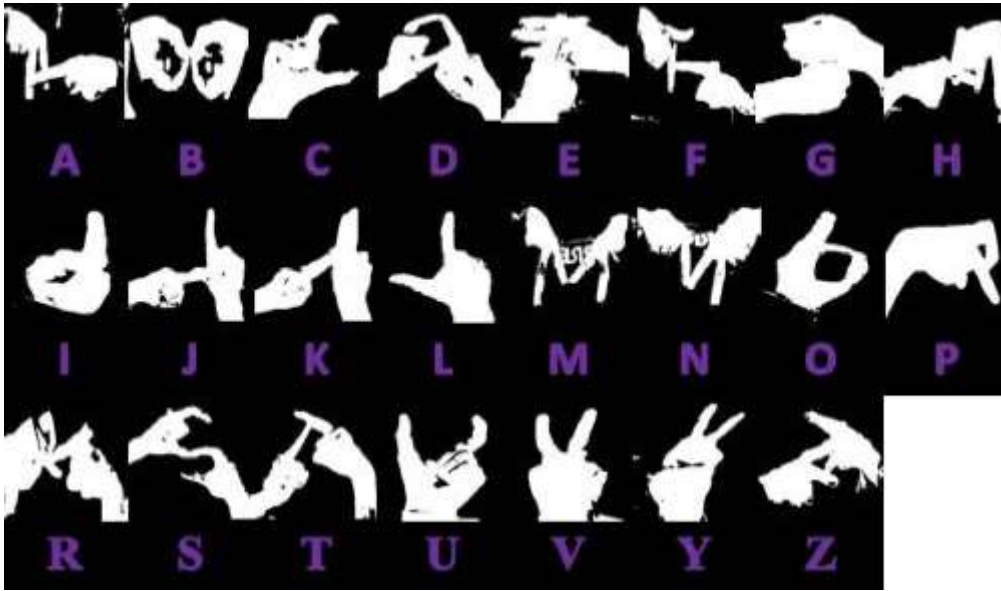
Şekil 1. Yeni Veri Setinde TİD Alfabesinin Jestleri.

2.2. Model Yapısı

Yapay zeka ile donatılmış akıllı bilgisayarlar, doğal dil işleme, karar verme ve konuşma tanıma gibi tipik olarak insan zekası gerektiren görevleri yerine getirmek üzere geliştirilmektedir (Shanmuga Priya ve ark., 2023). Gelişmiş bir sinir ağı mimarisi olan Konvolüsyonel Sinir Ağları (CNN'ler), canlı organizmalarda gözlemlenen karmaşık görsel algı sürecinden esinlenmiştir. Dolayısıyla, günümüz araştırmalarının çoğu, tanıma sistemlerinde CNN tabanlı model yapıları kullanmaktadır (Sadeddine ve ark., 2021; Tan ve ark., 2021). Konvolüsyonel Sinir Ağları (CNN'ler), canlı organizmalarda gözlemlenen karmaşık görsel algı süreçlerinden ilham alan gelişmiş bir sinir ağı mimarisini temsil eder. Canlıların görsel bilgiyi nasıl tanıdığı ve yorumladığını taklit etmek üzere tasarlanan CNN'ler, verileri çok katmanlı olarak işleyerek ve modelleyerek görüntülerdeki karmaşık desenleri ve özellikleri tanıyabilir ve öğrenebilir. Bu nedenle, bu yapılar, nesne tespiti ve görüntü sınıflandırma gibi bilgisayarla görme görevleri için oldukça uygundur.

Son yıllarda, CNN'ler, el yazısı rakamları sınıflandırmak için kullanılan ilk yaygın olarak tanınan derin öğrenme mimarisi olan LeNet'in icadıyla başlayan çeşitli hesaplama zorluklarını çözmede son derece etkili olduklarını kanıtlamıştır. Bu zorluklar, nesne yeniden tanımlama (Khan ve ark., 2022) ve güç tahmini (Khan ve ark., 2023) gibi çeşitli bilgisayarla görme görevlerini içerir. CNN'ler, büyük ölçekli veri kümeleriyle çalışırken, geleneksel özellik tabanlı yaklaşımlara göre üstün performansları sayesinde görüntü sınıflandırmada önemli bir ivme kazanmıştır. Başarıları, ham verilerden doğrudan karmaşık ve çok ölçekli özellikler öğrenme yeteneklerine de bağlanabilir. Dolayısıyla, CNN'ler, görüntülerdeki karmaşık desenleri ve özellikleri tanımlamalarını sağlayan yerleşik yeteneklere sahip olup, bilgisayarla görme ve diğer alanlarda kullanılmaktadır. CNN'ler, bir görüntüde çeşitli işlemler gerçekleştiren ve ağa giriş sağlayan birden çok katmandan oluşur. Bu katmanlar arasında, evrişimli katmanlar, küçük filtreler kullanarak giriş görüntüsünden özellikler çıkaran ve görüntü içinde farklı desenleri vurgulayan özellik

haritaları oluşturarak önemli bir rol oynar. Ayrıca, CNN'deki iki önemli katman arasında, özellik haritası boyutunu belirlenen bir alandaki maksimum değeri seçerek azaltan Havuzlama katmanları ve önceki katman çıkışlarına doğrusal olmayan fonksiyonlar uygulayan aktivasyon katmanları bulunur (Kaiming ve ark., 2016; Alzubaidi ve ark., 2021).

CNN'lerin sonunda, bağlantılı katmanlar, önceki katmanlarda çıkarılan özellikleri bir boyuta indirilmiş bir vektöre indirgeyerek, giriş görüntüsünü sınıflandırmak için kullanır. Son tam bağlı (FC) katmanın çıktısı, sınıf olasılıklarını belirlemek için "softmax" aktivasyon fonksiyonuyla işlenir. Evrişimli Sinir Ağları'nın (CNN'ler) eğitimi genellikle gradyan inişi veya türevlerini kullanarak öngörülen sınıf olasılıkları ile gerçek etiketler arasındaki farkı ölçen bir kayıp fonksiyonunu özyinelemeli olarak geliştirmek için kullanılır. CNN'ler, görüntü sınıflandırma faaliyetlerinde dikkate değer bir performans sergiler ve çeşitli uygulama alanlarında yaygın olarak kullanılır (Alzubaidi ve ark., 2021).

2.2.1. Önerilen CNN yapısı

Bu çalışmanın amacı, yeni bir veri kümesinin gereksinimlerini karşılamak için özelleştirilmiş bir CNN yapısı geliştirmektir. Bu doğrultuda, Model1, Model2 ve Model3 olmak üzere üç CNN modeli önerilmektedir. Araştırmacılar, model performansını optimize etmek için hiperparametreler de dahil olmak üzere farklı parametrelerde ayarlamalar yaparlar. CNN sonuçlarının karşılaştırmalı analizi, bu önerilen modelleri, veri kümeleriyle başa çıkmak için umut verici başlangıç noktaları olarak ortaya koymaktadır.

2.2.1.1. ilk yapı (Model1)

Bu mimaride, başlangıç katmanı, boyutu (3,3) olan 32 filtre ile bir evrişimli katman (Conv2D) içerir. Giriş şekli, 64x64 piksel boyutlarındaki gri tonlamalı bir görüntüyü belirtir. Doğrusal Doğrultulu Birim (ReLU) aktivasyon fonksiyonu kullanılmıştır. Ardından, bir max-havuzlama katmanı (MaxPool2D) boyutu (2,2) olan bir havuzlama boyutu ile, birinci Conv2D katmanı tarafından oluşturulan özellik haritalarının mekansal boyutlarını azaltmak için uygulanır; bu, veri boyutunu minimize ederken temel özellikleri çıkarır. İkinci Conv2D katmanı, boyutu (3,3) olan 32 filtre ile 'aynı' olarak ayarlanmış dolgu ile birlikte gelir, böylelikle çıktı özellik haritalarının girişle aynı mekansal boyutları korunur. ReLU aktivasyon fonksiyonu kullanılarak, katman daha sonra daha fazla mekansal boyut azaltımı için (2,2) boyutunda bir başka max-havuzlama katmanı (MaxPool2D) ile devam eder. Bunun ardından, üçüncü Conv2D katmanı 'aynı' dolgu ile birlikte boyutu (3,3) olan 64 filtre içerir ve ReLU aktivasyon fonksiyonunu kullanır. Daha sonra, üçüncü havuzlama katmanı (MaxPool2D) boyutu (1,1) olan çıktı özellik haritalarına uygulanır, böylelikle soyut özellikler çıkarırken mekansal boyutlar korunur.

Bir Düzleştirme katmanı, üçüncü havuzlama katmanının çıktısını 1-D vektöre dönüştürür. Ardından, iki Tam Bağlı (FC) Yoğun katman tanıtılır. İlk katmanda, CNN içinde doğrusallığı tanıtan "ReLU" ile 256 birim bulunmaktadır.

İkinci Yoğun katman veya son katman, sınıflandırma problemi içindeki 23 birime sahiptir. softmax aktivasyon fonksiyonu, ağ çıkışını sınıflandırma görevlerine göre olasılık dağılımına dönüştürür.

Bu mimari, özellik haritalarının mekansal boyutlarını azaltmak için takiben "ReLU" aktivasyon fonksiyonları kullanan üç evrişimli katman (Conv2D) içerir. Son olarak, softmax aktivasyon fonksiyonu aracılığıyla final sınıflandırma çıkışına ulaşmak için iki FC Yoğun katmanıyla sonuçlanır. Model1'in yapısının grafik temsilini görmek için Şekil 2a'ye bakınız.

2.2.1.2. ikinci yapı (Model2)

Bu mimari, bir Evrişimli Sinir Ağı (CNN), dört evrişimli (Conv2D) katman, üç maksimum havuzlama (MaxPool2D) katmanı ve üç tamamen bağlı (FC) katman içerir. Başlangıçta, birinci katman, boyutu (3,3) olan 32 filtreye sahip bir Conv2D katmanını içerir ve 'aynı' dolgu ile birlikte Doğrusal Doğrultulu Birim (ReLU) aktivasyon fonksiyonunu kullanır. Devamında, ikinci katman, boyutu (3,3) olan ve 64 filtre içeren bir Conv2D katmanını tanıtarak işlemi sürdürür. Bu katman aynı dolguyu ve ReLU aktivasyon fonksiyonunu kullanır. Daha sonra, üçüncü katman, (2,2) boyutunda bir havuzlama boyutu ve (2,2) adımlı bir MaxPool2D katmanı içerir. Dördüncü katman, %25'ini rastgele düşürmek için uygulanan 0.25'lik bir düşme oranına sahip bir Düşme katmanıdır, bu da aşırı uyumlanmayı azaltır. Devamında, beşinci katman, boyutu (3,3) olan 64 filtreye sahip başka bir Conv2D katmanını, 'aynı' dolgu ve ReLU fonksiyonunu içerir. Bunu, (2,2) boyutunda bir havuzlama boyutu ve (2,2) adımlı bir MaxPool2D katmanı olan altıncı katman takip eder. Daha sonra, yedinci katman, %25'ini rastgele düşürmek için uygulanan 0.25'lik bir düşme oranına sahip bir Düşme katmanını içerir. Sekizinci katman, 128 filtre ve (3,3) boyutunda Conv2D katmanını içerir. Bu katmanda aynı dolgu ve ReLU aktivasyon fonksiyonu kullanılır. MaxPool2D (2,2) dokuzuncu katmandır. Sonrasında, onuncu katman, 2D özellik haritalarını 1D özellik vektörüne dönüştüren bir Düzleştirme katmanını içerir. Bunun ardından, on birinci katman, 256 nöron ve bir ReLU fonksiyonu ile Tam Bağlı yoğun katmanları içerir. Aşırı uyumlanmayı önlemek için 0,5'lik bir düşme oranıyla bir Düşme katmanı daha sonradan uygulanır Son olarak, son katmanda, sınıflandırma problemindeki çıkış sınıflarının sayısına eşit olan 23 birimden oluşan bir tam bağlı yoğun katman bulunmaktadır. Sınıflandırma için softmax aktivasyon fonksiyonu kullanılır ve sınıf olasılıkları üretilir. Model2'nin detaylı yapısını Şekil 2b'de gösterilmiştir.

| a | b | c |

Şekil. 2. Model yapısı. a) Model 1, b) Model 2, c) Model 3.

2.2.1.3. üçüncü yapı (Model3)

Üçüncü model, her birinin boyutu (3,3) olan 32 filtre kullanarak giriş görüntüsü üzerinde evrişim işlemleri uygulayan bir evrişimli sinir ağı (CNN) mimarisiyle başlar. Bu katman, 'aynı' olarak ayarlanmış bir dolgu parametresi kullanır ve aktivasyon fonksiyonu olarak Doğrusal Doğrultulu Birim (ReLU) kullanır. Ardından, ikinci katman olarak başka bir Conv2D katmanı kullanılır, her birinin boyutu (3,3) olan 32 filtre içerir ve 'aynı' dolgu ile birlikte ReLU fonksiyonunun çıktısına uygulanır. Üçüncü Conv2D katmanı, boyutu (3,3) olan 64 filtre ve

'aynı' dolgu işlemi için 'aynı' değeri korur ve tekrar ReLU aktivasyon fonksiyonunu kullanır. Conv2D katmanlarını takiben, maksimum havuzlama işlemini uygulamak için (2,2) boyutunda bir havuzlama boyutuna ve adımlara sahip bir MaxPooling2D katmanı tanıtılır. Devamında, beşinci katman olarak, boyutu (3,3) olan 64 filtre ve 'aynı' dolgu kullanılan başka bir Conv2D katmanı, ReLU fonksiyonuyla birlikte kullanılır. Sonrasında, altıncı katman, önceki ile aynı havuzlama boyutu ve adımlara sahip bir MaxPooling2D katmanını içerir. Yedinci katman, boyutu (3,3) olan ve 128 filtre ile donatılmış bir Conv2D

katmanını barındırır. Bu katman, aynı dolgu işlemini korur ve ReLU aktivasyon fonksiyonunu benimser. Ardından gelen MaxPooling2D katmanı, önceki havuzlama katmanlarının parametrelerine uyumlu olarak tasarlanmıştır. Önceki katmanlardan sonra bir Düzleştirme katmanı, çok boyutlu özellik haritalarını bir 1-D vektöre dönüştürmek için eklenir. Daha sonra, 256 birime sahip bir Yoğun katman ve ReLU fonksiyonu tanıtılır. Aşırı uyumlanmayı önlemek için 0,5'lik bir düşme oranıyla bir Düşme katmanı uygulanır. Modelin sonunda sınıflandırma görevi için 23 nöronlu bir Yoğun katman bulunmaktadır. Bu nedenle bu katman Softmax aktivasyon fonksiyonunu kullanır. Model3'ün yapısına ilişkin kapsamlı bir genel bakışı Şekil 2c'de verilmiştir.

3. Bulgular ve Tartışma

Bu bölüm, yeni veri kümesinin önerilen modellerde (Model1, Model2 ve Model3) eğitilmesinin sonuçlarını, Veri Artırma, Düzenleme ve hiperparametre ayarlama gibi çeşitli tekniklerle sonuçları geliştirme stratejileriyle birlikte sunar.

Veri Artırma teknikleri, yansıtma, döndürme ve ölçekleme gibi, eğitim veri kümesini genişletmek için kullanılır ve modellerin yeni veri örneklerine daha iyi genelleme yapmasını sağlar. Ayrıca, aşırı uydurmayı azaltmak ve modellerin genel genelleme yeteneğini güçlendirmek için özellikle düşme gibi Düzenleme teknikleri uygulanır.

Ayrıca, Ön Ayarlama Teknikleri, öğrenme hızı ve epok (epoch) sayısı gibi parametrelerdeki ayarlamaları içerir ve modeller için en uygun yapılandırmanın belirlenmesi için yapılır.

Önerilen modeller başlangıçta 100 epok için eğitilir, daha sonra performans iyileştirmeleri için 500 epoka kadar uzatılabilir. Ancak, etkili model eğitimi için yaklaşık 150 epokun yeterli olduğu gözlemlenmiştir.

Adam optimizer, en çok tercih edilen optimizer yapısıdır, 0.001 öğrenme oranı en umut verici sonuçları verir. 0.01 ve 0.0001 gibi alternatif öğrenme oranları, seçilen yapılandırmanın sağlamlığını gösterebilir fakat önemli bir iyileşme sağlamaz. Ayrıca, Stokastik Gradyan İnişi (SGD) gibi diğer optimizasyonlarla yapılan denemeler tatmin edici sonuçlar vermez.

Özetle, Veri Artırma, Düzenleme ve Hiperparametre Ayarlama kombinasyonu, CNN modellerinin performansını artırmaya önemli ölçüde katkı sağlar. Modeller arasında, en yüksek doğruluğu %98 ve 0,097 kayıpla elde eden Model3 öne çıkmıştır. Bu model, istenen doğruluğa sadece 80 epok sonunda ulaşarak etkili bir eğitim gösterir.

3.1. Model 1

Bu yapılandırmada, adaptif öğrenme oranı optimizasyon algoritması Adam kullanılarak öğrenme oranı 0.001 olarak belirlendiğinde araştırma en iyi sonuçları verir. Genellikle çoklu sınıflandırma senaryolarında kullanılan kayıp fonksiyonu 'categorical_crossentropy' olarak adlandırılır. Değerlendirme metriği 'doğruluk'tur ve modelin doğrulama veya test verileri üzerindeki tahmin

doğruluğunu değerlendirir. Bu ayarlar altında, Model 1, 300 epok sonrasında %88 doğruluk oranı ve 0.413 kayıp, ve 500 epok sonrasında %89.72 doğruluk oranı ve 0.42 kayıp elde edilmiştir. Özellikle, epok sayısını arttırmanın bu durumda önemli faydalar sağlamadığı dikkat çekmektedir. Şekil 3, 500 epok ve 0.001 öğrenme oranı ile Model 1'in eğitim ve doğrulama doğruluğunu (a) ve kaybını (b) göstermektedir.

Model 1'in öğrenme oranı 0.0001'e ayarlandığında, model 300 epok sonrasında %80 doğruluk oranı ve 0,57 kayıpla elde eder, bu da bu öğrenme oranının Model 1 için alt-optimal olduğunu göstermiştir. Tersine, öğrenme oranı 0.01'e düşürmek, yaklaşık %50 doğruluk oranı ve 2 kayıp ile sonuçlanır, bu da bu öğrenme oranının Model 1 için uygun olmadığını gösterir.
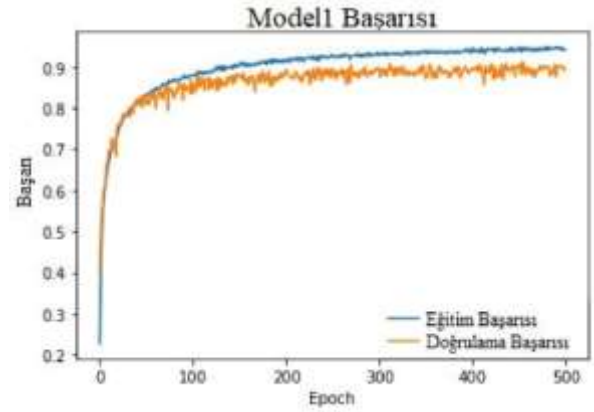
a
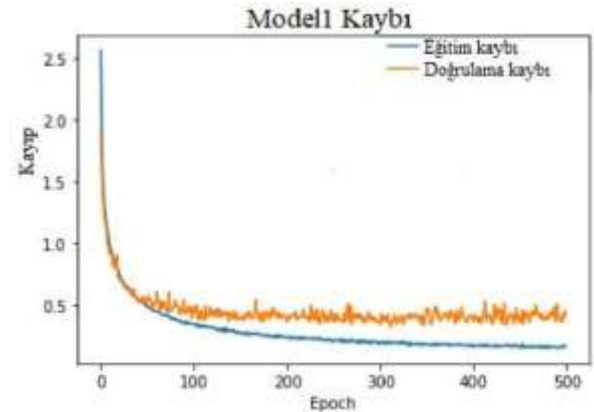
b

Şekil 3. Model 1'in eğitim ve doğrulama doğruluğu (başarısı) (a) ve kaybı (b).

3.2. Model 2

Bu yapılandırmada, tüm Düşme katmanları kullanıldığında, doğrulama doğruluğu eğitim doğruluğunu aşar, bu da potansiyel aşırı uydurmaya işaret eder. Şekil 4, 500 epok ve 0.001 öğrenme oranı ile Model 2'nin eğitim ve doğrulama doğruluğunu (a) ve kaybını (b) göstermektedir. Sonuç olarak, ilk ve ikinci Düşme katmanları kaldırıldığında, modelin performansında iyileşme gözlenmiştir. Adaptif öğrenme oranı optimizasyon algoritması olan Adam kullanılarak,

öğrenme oranı 0.001 olarak ayarlandığında ve sadece Yoğun (23) Öncesi son Düşme katmanının korunduğu durumda, Model 2 en iyi sonuçlarını vermiştir. 0,5 ve 0.25 Düşme oranlarıyla deney yapıldığında, 0,5 Düşme oranının en iyi sonucu verdiği görülmüştür. Öğrenme oranı 0.001 ve kayıp fonksiyonu olarak kategorik çapraz-entropi kullanılarak Adam optimizer ile Model 2 yaklaşık %97 doğruluk oranı ve 0.099 kayıp vermiştir.

Şekil 5, iki Düşme katmanı kaldırıldıktan sonra 500 epok ve 0.001 öğrenme oranı ile Model 2'nin eğitim ve doğrulama doğruluğunu (a) ve kaybını (b) göstermektedir. Özellikle, belirli Düşme katmanlarının kaldırılmasının ardından Model 2, Model 1'i geride bırakmıştır. Ayrıca, Model 2, istenen doğruluğa 100 epok içinde ulaşırken, Model 1'in yaklaşık 500 epok gerektirmektedir.
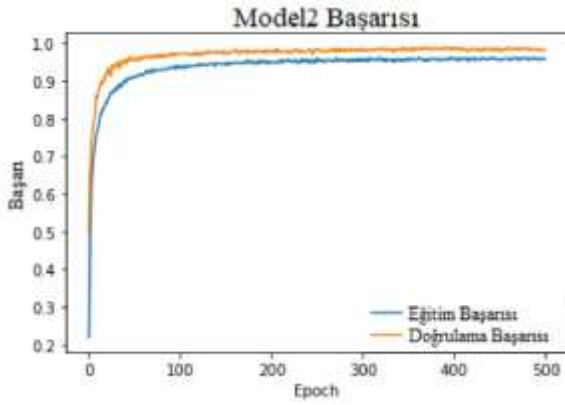
a
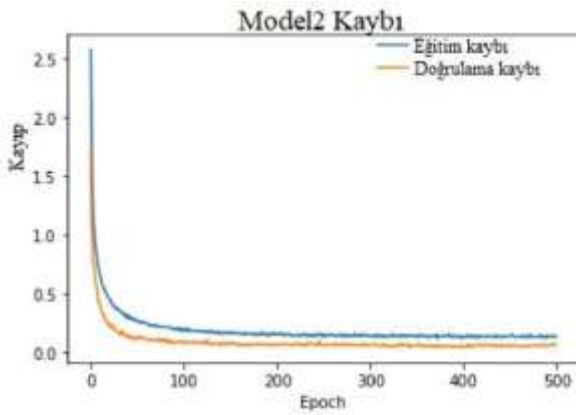
B

Şekil 4. Model 2'in (a) eğitim ve doğrulama doğruluğu (başarısı) ve (b) kaybı.
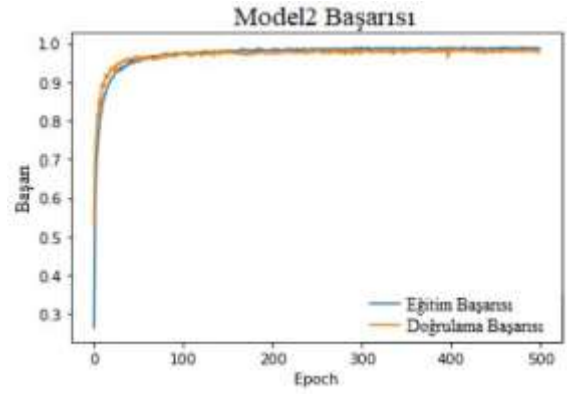
a
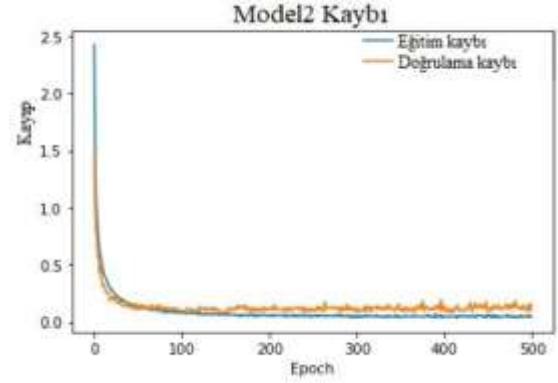
b

Şekil 5. Model 2 yapısından iki Dropout katmanı çıkarıldıktan sonra (a) eğitim ve doğrulama doğruluğu (başarısı) ve (b) kaybı.

3.3. Model 3

Model 3, girişte üç Conv2D katmanı kullanılması ve çıkış aşamasında bir Dropout katmanının dahil edilmesi nedeniyle üstün performans sergiler. Adam optimizer ve öğrenme oranı 0.001 olarak derlenen Model 3, çoklu sınıflandırma problemleri için uygun olan kategorik çapraz-entropiyi kayıp fonksiyonu olarak kullanır ve doğruluk üzerinden performansı değerlendirir. Bu koşullar altında Model 3, yaklaşık %98 doğruluk oranı ve 0.097 kayıp neticesini vermiştir. Şekil 6, Model 3 yapısının 500 epok ve 0.001 öğrenme oranı ile eğitim ve doğrulama doğruluğunu (a) ve kaybını (b) göstermektedir.

Model 3, performans açısından hem Model 1'i hem de Model 2'yi geçmektedir. Özellikle, Model 3, istenen doğruluğa sadece 80 epok sonunda ulaşırken, yaklaşık 500 epok gerektiren Model 1 ve daha düşük doğruluk elde etmek için yaklaşık 100 epok gerektiren Model 2'ye kıyasla verimlidir. Ayrıca, Adam optimizer kullanılarak 0.0001 öğrenme oranı ile yapılan deneyler, 200 epok sonrasında tatmin edici bir doğruluk sağlayamamış, bu da bu bağlamda 0.001 öğrenme oranının optimal bir seçim olduğunu yeniden doğrulamıştır.

a

b
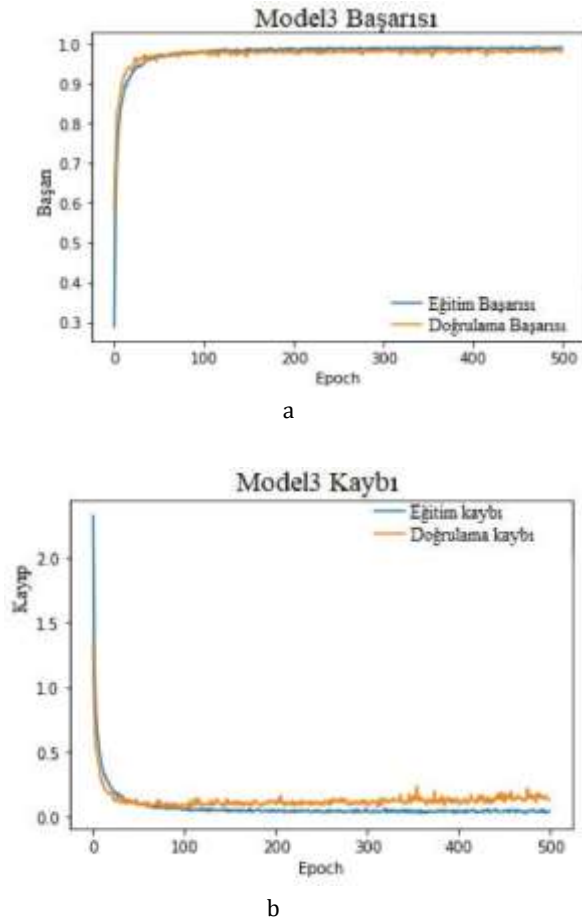
Şekil 6. Model 3 yapısının (a) eğitim ve doğrulama doğruluğu (başarısı) ve (b) kaybı.

Tablo 1, farklı koşullar altında eğitilen çeşitli sinir ağı modellerinin kapsamlı bir analizini sunmaktadır. Her modelin yapısını, epoch sayısını, optimizasyon edici fonksiyonunu, öğrenme oranını, kayıp fonksiyonunu ve elde edilen doğruluğu ayrıntılı olarak açıklamaktadır. Bu analiz, model performansını en üst düzeye çıkarmak için en uygun yapılandırmayı belirlemeyi amaçlamaktadır. Sonuçlar, model etkinliğini belirlemede optimizasyon fonksiyonu seçimi, öğrenme oranı ve eğitim süresinin kritik rolünü vurgulamaktadır. Model 1, artan epoch sayısı ve uygun öğrenme oranları ile kademeli olarak iyileşme göstermiş ve Adam optimize edici her durumda SGD'den daha iyi sonuçlar vermiştir. Model 2'nin başlangıçtaki aşırı uyum sorunu, dropout katmanlarının azaltılmasıyla etkili bir şekilde giderilmiş ve önemli bir doğruluk artışı sağlanmıştır. Model 3'ün daha az epoch ile üstün performansı, potansiyel olarak daha verimli bir mimari veya optimal hiperparametre ayarlarını göstermektedir. Sonuç olarak, bulgular, derin öğrenme modellerini optimize etmede hassas hiperparametre ayarlarının ve mimari yapının önemini göstermektedir. Farklı model yapıları arasındaki performans varyasyonlarında görüldüğü gibi, en kullanışlı yapıları belirlemek için tekrarlı deneyler ve iyileştirmeler gereklidir.

Tablo 2, işaret dili tanıma üzerine odaklanan çeşitli çalışmaların kapsamlı bir karşılaştırmasını sunmaktadır ve kullanılan işaret dili veri setleri, önerilen algoritmalar ve bunların doğruluk oranları detaylandırılmaktadır. Bu karşılaştırmalı çalışma ile farklı işaret dili veri setleri ve yaklaşımlar arasında algoritmik performanstaki eğilimleri belirlenmiştir. Analiz, Konvolüsyonel Sinir Ağlarının (CNN'ler) çeşitli işaret dili veri setleri ve türlerinde yüksek doğruluk oranlarına eriştiğini göstermektedir. Alfabe, kelime veya jestler için CNN kullanan çalışmalarda, doğruluk oranları %80.85 ile %98 arasında değişmektedir.

AlexNet ile farklı sınıflandırıcıları (KNN, SVM, Naive Bayes) birleştiren hibrit modellerin performansı hem alfabe hem de rakamları içeren veri setleri için kabul edilebilir seviyededir. Bu kategoride gözlemlenen en yüksek doğruluk oranı, AlexNet ile Naive Bayes'in birleştirilmesiyle elde edilen %97.92'dir. Önerilen CNN modelinin (Model3) %98 seviyesindeki doğruluk oranları mevcut en yüksek doğruluk oranları ile eşdeğerdir ve modelin Türk işaret dilini tanıma gücünü göstermektedir. Önerilen model işaret dili tanıma alanında rekabetçi bir yaklaşımdır.

4. Sonuç

İşitme engelliler için topluluk içinde iletişim aracı olarak işaret dili önemli bir rol oynar. Derin öğrenme teknolojisindeki ilerlemelerin kullanılması, işitme engelli bireylerle işitme engeli olmayanlar arasındaki iletişimi kolaylaştıran sistemlerin tasarlanmasında hayati öneme sahiptir. Bu araştırma yeni bir veri kümesi oluşturmuştur. Ardından, yeni oluşturulan veri kümesini işlemek için özel olarak tasarlanmış bir Evrişimli Sinir Ağı (CNN) modeli geliştirilmiştir. Bu makalede sunulan modeller, yeni veri kümesinin ortaya çıkardığı zorlukları ele almayı amaçlayan sonraki araştırma çabaları için temel bir çerçeve olarak kurgulanmıştır. Geniş parametre ayarlamaları ve model katmanlarında yapılan değişikliklerle, yaklaşık %98 doğruluk oranına sahip bir son model elde edilmiştir. İlerleyen çalışmalar, veri kümesini genişletme ve doğruluk oranlarını daha da artırmak için modeli iyileştirme üzerine odaklanacaktır.

Tablo 1. Farklı koşullar altında eğitilen çeşitli sinir ağı modellerinin kapsamlı bir analizi.

Yapı	Epok Sayısı	Optimizasyon Fonksiyonu	Öğrenme Oranı	Kayıp Fonksiyonu	Doğruluk
Model1	100	SGD	0.001	'categorical_crossentropy	45.62%
Model1	500	Adam	0.01	'categorical_crossentropy	56.54%
Model1	300	Adam	0.0001	'categorical_crossentropy	80%
Model1	100	Adam	0.001	'categorical_crossentropy	84.06%
Model1	300	Adam	0.001	'categorical_crossentropy	88%
Model1	500	Adam	0.001	'categorical_crossentropy	89.72%
Model2 (3 Dropout katmanı)			Aşırı Uyum (Overfitting)		
İki Dropout katmanı çıkarıldıktan sonra Model2	100	Adam	0.001	'categorical_crossentropy	97.53%
Model3	80	Adam	0.001	'categorical_crossentropy	98%

Tablo 2. işaret dili tanıma üzerine odaklanan çeşitli çalışmaların kapsamlı bir karşılaştırmalı analizi.

Kaynak	İşaret Dili Türü	Önerilen Algoritma	Doğruluk
Unutmaz ve ark., 2019,	9 TİD kelimesi	CNN	80.85%
		Karar Ağacı	53.83%
		Ağırlıklı KNN	61.40%
		Doğrusal SVM	71.47%
		Gauss SVM	49.95%
Sabeenian ve ark., 2020	MNIST AİD veri seti (alfabeler)	CNN	93%
Hurroo ve Walizad, 2020	10 AİD alfabesi	CNN	90%
Öztürk ve ark., 2021	TİD alfabeler	Faster R-CNN	88%
Shokoori ve ark.,2022	10 Pashto İşaret Dili alfabesi	CNN	98%
Shanmuga Priya ve ark., 2023	10 jest	CNN	90%
Addepalli ve ark., 2023	AİD (Alfabeler + rakamlar)	AlexNet + KNN	96.97%
		AlexNet + SVM	96.98%
		AlexNet + Naive Bayes	97.92%
Bizim Yapımız	TİD alfabeler	Model3-CNN	98%

Kaynaklar

Addepalli N, Pabolu RK, GaneshChennuru S, Vissampalli VL, Madhumati GL. 2023. Conversion of American Sign Language to text using deep learning for feature extraction and naive bayes for classification. In: IEEE 8th International Conference for Convergence in Technology (I2CT), April 07-09, Lonavla, India, pp: 1.

Alshehri S. 2023. The Relationship between Language and Identity. Int J Linguist Lit Transl, 6(7): 156-161.

Alzubaidi L, Zhang J, Humaidi AJ, Al-Dujaili A, Duan Y, Al-Shamma O, Santamaría J, Fadhel MA, Al-Amidie M, Farhan L. 2021. Review of deep learning: concepts CNN architectures

challenges applications future directions. J Big Data, 8(52): 1-74.

Anand K, Urolagin S, Mishra RK. 2021. How does hand gestures in videos impact social media engagement - Insights based on deep learning? Int J Inf Manag Data Insights, 1(2): 100036.

Arora S, Roy A. 2018. Recognition of sign language using image processing. Int J Bus Intell Data Min, 13(1-3): 163-176.

Bantupalli K, Xie Y. 2019. American Sign Language recognition using deep learning and computer vision. In: IEEE International Conference on Big Data, December 10-13, Seattle, WA, USA, pp: 4896.

Hurroo M, Walizad ME. 2020. Sign language recognition system using convolutional neural network and computer vision. Int J Eng Res Technol, 9(12): 59-64.

Jantunen T, Rousi R, Rainò P, Turunen M, MoeenValipoor M, García N. 2021. Is there any hope for developing automated translation technology for sign languages? In: Hämäläinen M, Partanen N, Alnajjar K. Editors. Multilingual Facilitation. University of Helsinki Rootroo, pp: 61-73.

Kaiming H, Xiangyu Z, Shaoqing R, Jian S. 2016. Deep residual learning for ımage recognition. In: IEEE Conference on Computer Vision and Pattern Recognition, June 27-30, Las Vegas, NV, USA, pp: 770.

Karaca MF, Bayır Ş. 2018. Türk işaret dili incelemesi: İletişim ve dil bilgisi. Ulus Eğit Akad Derg, 2(2): 35-58.

Katılmış Z, Karakuzu C. 2020. Recognition of two-handed posture finger turkish sign language alphabet. In: 5th International Conference on Computer Science and Engineering (UBMK), September 09-11, Diyarbakir, Türkiye, pp: 5.

Kaya F, Tuncer AF, Yildiz Ş. K. 2018. Detection of the turkish sign language alphabet with strain sensor based data glove. In: 26th IEEE Signal Processing and Communications Applications Conference SIU, May 02-05, Izmir, Turkey, pp: 1.

Khan SU, Haq IU, Khan N, Muhammad K, Hijji M, Baik SW. 2022. Learning to rank: An intelligent system for person reidentification. Int J Intell Syst, 37(9): 5924-5948.

Khan SU, Khan N, Ullah FUM, Kim MJ, Lee MY, Baik SW. 2023. Towards intelligent building energy management: AI-based framework for power consumption and generation forecasting. Energy Build, 279(2023): 112705.

Lu D, Yu Y, Liu H. 2016. Gesture recognition using data glove: An extreme learning machine method. In: 2016 IEEE International Conference on Robotics and Biomimetics (ROBIO), December 03-07, Qingdao, China, pp: 1349.

MacHiraju S, Urolagin S, Mishra RK, Sharma V. 2021. Face mask detection using keras opencv and tensorflow by ımplementing mobilenetv2. In: 2021 3rd International Conference on Advances in Computing Communication Control and Networking (ICAC3N), December 17-18, Greater Noida, India, pp: 1485.

Nguyen HBD, Do HN. 2019. Deep learning for American Sign Language fingerspelling recognition system. In: 2019 26th International Conference on Telecommunications (ICT), April 08-10, Hanoi, Vietnam, pp: 314.

Oktekin B. 2018. Development of Turkish sign language recognition application. MSc thesis, Near East University the Graduate School Of Applied Sciences, Nicosia, Turkish Republic of Northern Cyprus, pp: 71.

Öztürk A, Karatekin M, Saylar İA, Bardakci NB. 2021. Recognition of sign language letters using ımage processing and deep learning methods. J Intell Syst Theory Appl, 4(1): 17-23.

Qi J, Jiang G, Li G, Sun Y, Tao B. 2020. Surface EMG hand gesture recognition system based on PCA and GRNN. Neural Comput. Appl, 32(10): 6343-6351.

Sabeenian RS, SaiBharathwaj S, MohamedAadhil M. 2020. Sign language recognition using deep learning and computer vision. J Adv Res Dyn Control Syst, 12(5 Special Issue): 964-968.

Sadeddine K, Chelali ZF, Djeradi R, Djeradi A, BenAbderrahmane S. 2021. Recognition of user-dependent and independent static hand gestures: Application to sign language. J Vis Commun Image Represent, 79(March): 103193.

Sevli O, Kemaloğlu N. 2020. Turkish sign language digits classification with CNN using different optimizers. Int Adv Res Eng J, 4(3): 200-207.

ShanmugaPriya G, NitishaSree V, Magisha K, Pooviga S. 2023. Gesture recognition using convolutional neural network. In: 2023 Second International Conference on Advances in Computational Intelligence and Communication (ICACIC), December 07-08, Puducherry, India, pp: 1.

Shokoori AF, Shinwari M, Popal JA, Meena J. 2022. Sign language recognition and translation into pashto language alphabets. In: 6th International Conference on Computing Methodologies and Communication (ICCMC), March 29-31, Erode, India, pp: 1401.

Singh P, Krishn Mishra R, Urolagin S, Sharma V. 2021. Enhancing Security by ıdentifying facial check-in using deep convolutional neural network. In: 3rd International Conference on Advances in Computing Communication Control and Networking (ICAC3N), December 17-18, Greater Noida, India, pp: 1006.

Tan YS, Lim KM, Tee C, Lee CP, Low C. Y. 2021. Convolutional neural network with spatial pyramid pooling for hand gesture recognition. Neural Comput Appl, 33(10): 5339-5351.

Thomas J, Mcdonagh D. 2013. Shared language: Towards more effective communication. Australas Med J, 6(1): 46-54.

Toğaçar M, Cömert Z, Ergen B. 2021. Recognition of the digits in Turkish sign language using siamese neural networks. Dokuz Eylul Uni Fac Eng J Sci Eng, 23(68): 349-356.

Unutmaz B, Karaca A. C, Güllü M. K. 2019. Kinect iskelet ve evrişimsel sinir ağları ile Türkçe işaret dili tanıma. In: 2019 27th Signal Processing and Communications Applications Conference (SIU), April 24-26, Sivas, Türkiye, pp: 2.

Vijayalakshmi P, Aarthi M. 2016. Sign language to speech conversion. In: 2016 International Conference on Recent Trends in Information Technology (ICRTIT 2016), April 08-09, Chennai, India, pp: 1.

Yalçın M, Ilgaz S, Özkul G, KumbayYildiz Ş. 2018. Türkçe işaret dili alfabesi çevirici / Turkish sign language alphabet translator. In: 26th Signal Processing and Communications Applications Conference (SIU): May 02-05 Izmir, Türkiye, pp: 4.

Yıldız Z, Yıldız S, Bozyer S. 2018. İşitme engelli turizmi sessizturizm: dünya ve türkiye potansiyeline yönelik bir değerlendirme. Süleyman Demirel Üniv Vizyoner Derg, 9(20): 103-117.

Black Sea Journal of Engineering and Science

SÜT SIĞIRCILIĞI İŞLETMELERİNDE İŞLETME İÇİ KİRLİLİK VE TOPALLIK SKORU İLE SÜT VERİMİ ARASINDAKİ İLİŞKİ

Ahmet Refik ÖNAL[1]*, Rıdvan AYDIN[2]

[1]Tekirdağ Namık Kemal University, Faculty of Agriculture, Department of Animal Science, 59030, Tekirdağ, Türkiye
[2]Tekirdağ Namık Kemal University, Graduate School of Natural and Applied Sciences, Department of Animal Science, 59030, Tekirdag, Türkiye

Özet: Bu çalışmada ahır içi kirlilik durumu ile süt sığırlarında topallık arasındaki ilişki incelenmiştir. Bu amaçla, Balıkesir ilinde, 3000 baş kapasiteli modern süt sığırcılığı işletmesinde bulunan 778 baş Siyah Alaca sığırlarının topallık skorlaması, vücut kirliliği puanlaması 4 verim grubuna ayrılarak tespit edilmiş, ahır kirliliği, gezinti alan kirliliği ve sağım yolu kayganlığının topallığa olan etkisi araştırılmıştır. Ahır kirliliği, yataklık kirliliği ile gezinti alan kirliliği puanı sıyırıcıların düzenli çalışmasından dolayı 0 (temiz) puan, zemin kayganlığı ise yürüme yolunun kauçuk yataklık olmasından dolayı 0 (mükemmel) puan olarak tespit edilmiştir. Yapılan istatistik analizler sonucunda, 7 günlük süt veriminin topallıkla olan ilişkisinde, sadece 1. verim grubuyla istatistiki açıdan fark tespit edilmiştir (P<0,05). Sağılan gün sayısının topallık (1. ve 2. Verim grubu) ve kirlilik skorlarıyla olan ilişkisi arasında istatistiki açıdan önemli bulunmuştur (P<0,01; P<0,05; P<0,01). Çalışmada, laktasyon sayısının topallık skoru ile 305 günlük süt verimi arasında tüm verim gruplarında istatistik farklılık olmadığı, kirlilik skoru ile 305 günlük süt verimi arasında tüm verim gruplarında istatistik farklılık olmadığı tespit edilmiş (P>0,05). Çalışmada barınak iç koşullarının topallık üzerinde önemli etkisi bulunduğu tespit edilmiştir. Barınak iç koşullarından yataklık kirlilik durumu, gezinti alanlarındaki dışkı durumu, yetersiz havalandırma ve sağım yollarının kaygan olması gibi etkenler sürü içerisindeki topal hayvan sayısını etkilemektedir.

Anahtar kelimeler: Sığır vücut kirliliği, Topallık skorlaması, Ahır kirliliği, Zemin kayganlığı, Siyah alaca

The Relationship between Barn Cleanliness and Lameness Score and Milk Yield in Dairy Cattle Farms

Abstract: The relationship between indoor cleanliness score and lameness in dairy cattle was examined in this study. By this aim, the locomotion score of 778 main Holstein cattle, which has a total of 3000 heads modern dairy cattle operation, including 800 head milk, in Balıkesir province, body cleanliness score is determined by separating 4 yield groups, barn cleanliness, the feeding way cleanliness and the milking parlor way cleanliness has been investigated. The score of barn cleanliness, the feeding way cleanliness and the cleanliness score of the milking parlor way were found to be 0 (clear) points due to the regular stripper and greasiness of the ground found as 0 (excellent) points due to the rubber walking path. As a result of the statistical analyzes performed, the 7 day milk yield relation with locomotion score was found to statistically significant (P<0.05). Milking days relation between locomotion (only 1 and 2 yield groups) to pollution scores were found statistically significant difference (P<0.01; P<0.05; P<0.01). In the study, it was determined that there was no statistical difference between the lameness score of the number of lactations and 305-day milk yield in all yield groups, and that there was no statistical difference between the pollution score and 305-day milk yield in all yield groups (P>0.05). It was determined that the internal conditions of the barn had a significant effect on lameness. Among the internal conditions of the barn, factors such as bedding pollution, manure in walking areas, inadequate ventilation and slippery milking roads affect the number of lame animals in the herd.

Keywords: Cattle body hygiene, Locomotion score, Pollution of barn, Greasiness of ground, Holstein

1. Giriş

Hayvansal gıda talebini karşılamak ve endüstride meydana gelen gelişmeler ile birlikte hayvan yetiştiriciliği önemli bir endüstri haline dönüşmüş ve büyük kapasiteli endüstriye işletmelerin sayısı her geçen gün arttığı gözlenmektedir. Araştırıcılar, yetiştiricilerin topallığın yaygınlığı ve şiddetini çoğunlukla olduğundan daha düşük ekonomik kayıplara neden olduğunu düşündüklerinden, sürüde topallığın düzeyini azaltmak amacıyla sürü yönetimi, çevre ve besleme uygulamalarını değiştirmeleri konusunda yönlendirilmelerinin zor olduğunu bildirmişlerdir (Socha ve ark., 2002).

Siyah Alaca süt sığırlarında topallığın süt verimine etkisinin incelendiği bir çalışmada; 300 baş sağmal ineğe ait topallık verileri ve 305 günlük süt verimlerinin değerlendirildiği bildirilmiştir. Araştırıcılar sağlıklı ve topal olan hayvanlar arasında farklılığın; süt verimi, sütteki yağ ve protein oranları için sırasıyla 516,08 lt,

%0,16 ve %0,04 olarak hesaplandığını bildirmişlerdir (Toncho ve Konstantin, 2015). Akın (2008)'nın aktardığına göre ülkemizde farklı yıllarda ve bölgelerde yapılmış çalışmalarda ayak hastalıklarına rastlama oranlarının; Bursa yöresinde %44,07 (Seyrek ve ark. 2001), İstanbul ve Tekirdağ yöresinde %18,6 (Yücel 1982), Konya bölgesinde %68 (Yavru ve ark., 1992), Van yöresinde %26,31 (Alkan ve ark., 1993) düzeyindedir. Araştırıcı ayrıca topallık şikayeti olan 900 hayvandan 247 başının sürüden ayrıldığı ve bir ineğin bir laktasyonda ortalama 360 kg süt verim kaybına sebep olduğunu aktarmıştır (Green ve ark., 2002).

Yayla ve ark. (2012) Kars ve yöresinde sığırların bakım ve barındırma koşulları ile ayak hastalıkları arasındaki ilişkinin değerlendirilmesi isimli çalışmalarında; sığırlarda gebeliğin son aylarında ve laktasyonun ilk aylarında ayak hastalıklarının insidansının arttığı, gebelikte vücut ağırlığındaki artışın arka ayaklarda hastalık oluşumunda predispoze bir faktör olarak etki ettiğini bildirmişlerdir.

Burdur, Kırklareli ve Konya illerindeki süt sığırcılığı işletmelerinde ayak hastalıklarından kaynaklanan finansal kayıplar isimli çalışmada; her üç ilde ayak hastalıklarının ortalama görülme sıklığının %13,7, %13,4 ve %5,6 olarak hesaplandığını bildirmişlerdir. Çalışmada ayak hastalıkları; hafif, orta şiddetli ve şiddetli olarak sınıflandırmış ve bu sınıflandırmaya göre meydana gelen ekonomik kayıpların sırasıyla 271TL/vaka, 343TL/vaka, 509TL/vaka olduğu; tüm hastalık formlarının ortalaması için hesaplanan değerin 382TL/vaka olduğu bildirilmiştir. Üç ilin ortalaması olarak işletme başına ortalama ekonomik kaybın 865TL, bunun 589TL'sinin (%68) sakınabilir kayıplar oluşturduğunu bildirmişlerdir (Yalçın ve ark., 2010). Araştırıcılar ayak hastalıklarının süt sığırı işletmelerinde önemli ölçüde finansal kayıplara neden olduğu, ancak hastalık konusunda başarılı işletmelerin (insidens düzeyi hedef insidens seviyesinde olan işletmeler) söz konusu kayıpları önemli ölçüde azaltabildiğini bildirmişlerdir (Kossaibati ve ark., 1999; Göncü 2017).

2. Materyal ve Yöntem
2.1. Materyal
Çalışmada Balıkesir Bölgesinde halen üretime devam eden 3000 baş sağmal sığır kapasitesine sahip olan süt sığırı işletmesinin kendisi tarafından elde edilen veriler kullanılmıştır. Çalışma verileri Şubat 2016'da elde edilen verilerden yapılmıştır. Verilerde 778 süt sığırının topallık ve vücut kirlilik skorlamaları yapılmıştır. Verim düzeyleri (farklı padoklarda yetiştirilen) ve laktasyon sırasına göre hayvan sayılarının dağılımı Çizelge 1'de verilmiştir. Topallık skorlamaları hayvanlar sağıma giderken, vücut kirlilik skorlamaları ise sağımdan sonra hayvanlar yemlik kilit sistemine girdikten sonra yapılmıştır. Ayrıca zemin kaynaklık durumu (Grandin, 2008) ve Gezinti alanlarında (İşletme içi) gübre skoru yapılmıştır.
2.2. Skorlamalar
1. Topallık skoru: Topallık Skorlaması Sprecher

(1997)'te belirtilen ilkeler doğrultusunda yapılmıştır.

2. Hayvanların kirlilik skorlaması: Hayvan kirlilik skorunun belirlenmesinde beşli metot kullanılmıştır. Metot kapsamında hayvanlarda kirlenme derecesi üç farklı bölgede meme, alt bacak (ayak ve topuk), kalça ve karın bölgesi baz alınarak yapılmıştır (Reneau ve ark., 2005).

3. Zemin Kayganlık Skoru: Kayan ve düşen ineklerin sayısı kaydedilir (Aynı inek düşer veya birden fazla kayarsa o zaman tek bir olay olarak kaydedilir). Gözlem boyunca kayan ve düşen ineklerin toplam sayısı not edilerek aşağıdaki yönteme göre düşme ve kayma oranları hesaplanmıştır. Hesaplanan oranlara göre zemin kayganlık puanlamaları belirlenmiştir

Sürünün düşme oranı =(Düşen Hayvan Sayısı / Gözlemlenen Toplam Hayvan Sayısı) x 100
Sürünün kayma oranı =(Kayan Hayvan Sayısı / Gözlemlenen Toplam Hayvan Sayısı) x 100
Elde edilen oranlar kullanılarak zemin kayganlık skoru belirlenmiştir (Grandin, 2008).

4. Gezinti Alanlarında (İşletme içi) Gübre Skoru: Uygulamanın yapılabilmesi için üreticinin günlük ve düzenli olarak sıyırma ve temizlik işlemini yapması gerekir. Gübre yolunun ve dolayısıyla durakların temizliği inek verimini ve konforunu arttırmaktadır.

Çalışma başlangıcında gübre yolu boşaltılır ve hayvanlar avluya çıkarılır. Lastik çizmenin topuk derinliği ölçülür, ön taraftan 2 cm topuktan 4 cm olan bölgeleri kalemle işaretlenir. Ölçüm işlemi sıyırmadan 20 dakika önce ve sıyırmadan 20 dakika sonra yapılır. Sıyırmadan 20 dakika önce yapılan skorlamada, gübre yolunun bir ucundan diğer ucuna kadar yürünür. Çizmedeki genel gübre seviyesi belirlenerek puanlama yapılır. Sıyırma işleminden yaklaşık 20 dakika sonra aynı işlem tekrarlanır (Tablo 1).

Tablo 1. Gezinti alanlarında (işletme içi) gübre puanları

Kategori	Puan	Açıklama
Temiz	0	Çizme 0.5 cm düzeyinde kirlenmiş yada daha kuru
Az Kirli	1	Çizme 0.5-1 cm arasında kirlenmiş
Kirli	2	Çizme 1-3 cm arasında kirlenmiş
Çok Kirli	3	Çizme 3 cm den daha fazla kirlenmiş

2.3. İstatistik Analiz
Araştırma verilerinin değerlendirilmesinde tek yönlü varyans analiz yöntemi kullanılmıştır. Süt veriminin topallık skoru ve kirlilik skoruna göre dağılımları, ortalamaları ve varyans analizleri SPSS 10,0 paket programıyla (SPSS, 1999) yapılmıştır.

3. Bulgular ve Tartışma
305 günlük süt verimi 1, 2, 3 ve 4 verim gruplarına göre sırasıyla ortalama 8932,25±149,16 kg, 10601,01±213,76

kg, 10450,03±120,67 kg ve 10921,51±215,77 kg olarak bulunmuştur (Tablo 2). Verim düzeyleri bakımından topallık skorlarına göre grup ortalamaları arasındaki farklılığın belirlenmesi amacıyla yapılan varyans analizinde tüm gruplar arasında istatistik farklılık olmadığı belirlenmiştir (P>0.05). 1. Verim düzeyine ilişkin tanımlayıcılar istatistikler değerlendirildiğinde en yüksek ortalamanın (9629,89±1152,90 kg) 4 numaralı topallık skoruna sahip hayvanlar ve en düşük ortalamanın ise 1 numaralı topallık skoruna (8607,95±447,49 kg) sahip hayvanlarda olduğu gözlenmiştir. 1.verim düzeyinde topallık skoru 5 olan hayvan rastlanmamıştır. 2 verim düzeyinde ise en yüksek ortalamanın (12462,50±1049,75 kg) 5 numaralı topallık skoruna sahip hayvanlar ve en düşük ortalamanın ise 1 numaralı topallık skoruna (8604,00±726,52 kg) sahip hayvanlarda olduğu gözlenmiştir.

Üç verim düzeyindeki hayvanlara ait tanımlayıcı istatistikler değerlendirildiğinde en yüksek ortalamanın (11649,67±717,30 kg) 4 numaralı topallık skoruna sahip hayvanlar ve en düşük ortalamanın ise 1 numaralı topallık skoruna (9965,00±620,30 kg) sahip hayvanlarda olduğu gözlenmiştir. 4 verim düzeyi grubundaki hayvanlara ait tanımlayıcı istatistikler değerlendirildiğinde en yüksek ortalamanın (11080,40±390,99 kg) 3 numaralı topallık skoruna sahip hayvanlar ve en düşük ortalamanın ise 4 numaralı topallık skoruna (10212,75±1207,35 kg) sahip hayvanlarda olduğu gözlenmiştir. 4.verim düzeyinde

topallık skoru 5 olan hayvan tespit edilememiştir. Warnick ve ark. (2001) üç farklı sığırcılık işletmesinde yürüttüğü çalışmada süt verimindeki azalmayı sırasıyla 1,5 kg, 0,8 kg ve 0,5 kg olarak bildirmiştir. Çalışmamızda topallık düzeyinin artması ile birlikte süt veriminde düşüş gözlenmemiştir. Toncho ve Konstantin (2015) topal ve topal olmayan sağlıklı bir ineğin süt verimleri arasında 305 günlük laktasyon süt veriminde ortalama 516,08 lt fark olduğunu belirtmişlerdir. Hastalıktan dolayı hayvan refahında düşüş ve yem tüketimindeki azalıştan kaynaklandığı söylenebilir.

305 günlük süt verimi 1, 2, 3, ve 4. verim gruplarına göre sırasıyla ortalama 8932±149,164 kg, 10601,01±213,76 kg, 10450,03±120,67 kg ve 10921,51±215,77 kg olduğu gözlenmiştir (Tablo 3).

Verim düzeylerine göre kirlilik skoru grup ortalamaları arasındaki farklılığın belirlenmesi amacıyla yapılan variyans analizinde, tüm gruplar arasında istatistik farklılık olmadığı belirlenmiştir (P>0.05). 1. Verim düzeyine ilişkin tanımlayıcılar istatistikler değerlendirildiğinde en yüksek ortalamanın (9162,04±299,44 kg) 1 numaralı kirlilik skoruna sahip hayvanlarda ve en düşük ortalamanın ise 4 numaralı topallık skoruna (6873,50±1334,02 kg) sahip hayvanlarda olduğu gözlenmiştir. 2 verim düzeyinde ise en yüksek ortalamanın (10859,67±374,62 kg) 3 ve en düşük ortalamanın ise 1 numaralı kirlilik skoruna (10113,78±500,90 kg) sahip hayvanlarda olduğu gözlenmiştir.

Tablo 2. Verim düzeylerine göre topallık skoru ile ortalama 305 günlük süt verimi (kg) arasındaki ilişki

Verim Düzeyi	Topallık Skoru	n	Ortalama	Standart Sapma	Standart Hata	VK	Min.	Mak.	P
	1	21	8607,95	2050,68	447,49	24	5095	11543	
	2	107	9224,12	2053,31	198,50	22	4175	15372	
1	3	65	8459,97	1962,42	243,40	23	4729	14391	0,08
	4	9	9629,89	3458,72	1152,90	40	5136	16454	
	Genel	202	8932,25	2120,02	149,16	23	4175	16454	
	1	25	8604,00	3632,60	726,52	42	2093	15503	
	2	100	10113,02	3228,93	322,89	32	2224	17248	
2	3	88	11619,01	3049,12	325,03	26	3149	16180	0,25
	4	23	10674,65	3171,85	661,37	30	3215	15633	
	5	4	12462,50	2099,50	1049,75	17	10348	14272	
	Genel	240	10601,01	3311,56	213,76	31	2093	17248	
	1	10	9965,30	1961,58	620,30	20	6050	12899	
	2	148	10284,02	1886,70	155,08	18	4886	16453	
	3	67	10773,31	1749,23	213,70	16	5632	14938	0,09
3	4	9	11649,67	2151,90	717,30	18	7216	14251	
	5	7	10015,86	1718,03	649,35	17	7122	12041	
	Genel	241	10450,03	1873,39	120,67	17	4886	16453	
	1	13	10821,77	1826,94	506,70	17	8048	13856	
	2	54	10927,56	2261,64	307,77	21	5821	15189	
4	3	24	11080,04	1915,47	390,99	17	6500	14649	0,90
	4	4	10212,75	2414,71	1207,35	24	7802	12577	
	Genel	95	10921,51	2103,11	215,77	19	5821	15189	

Tablo 3. Verim düzeyine göre kirlilik skoru ile ortalama 305 günlük süt verimi (kg) arasındaki ilişki

Verim Düzeyi	Kirlilik Skoru	n	Ortalama	Standart Sapma	Standart Hata	VK	Min.	Mak.	P
	1	47	9162,04	2052,86	299,44	24	4729	12698	
	2	92	8894,53	2054,95	214,24	25	4175	15372	
1	3	59	8947,59	2214,08	288,25	27	5095	16454	0,23
	4	4	6873,50	2668,04	1334,02	45	5095	10832	
	Genel	202	8932,25	2120,02	149,16	25	4175	16454	
	1	46	10113,78	3397,28	500,90	34	3277	17248	
	2	110	10632,56	3233,66	308,31	30	2093	16155	
2	3	79	10859,67	3329,71	374,62	31	2906	16180	0,68
	4	5	10302,40	4480,44	2003,71	43	3215	15375	
	Genel	240	10601,01	3311,56	213,76	31	2093	17248	
	1	56	10674,34	1671,06	223,30	16	6633	14498	
	2	126	10339,97	1859,04	165,61	18	4886	14699	
3	3	57	10471,68	2094,66	277,44	20	5586	16453	0,74
	4	2	10486,50	2575,99	1821,50	25	8665	12308	
	Genel	241	10450,03	1873,39	120,67	18	4886	16453	
	1	21	10952,19	2105,69	459,50	19	6213	14508	
	2	47	11051,47	1882,22	274,55	17	6510	14649	
4	3	25	10684,72	2214,38	442,87	21	6500	14138	0,90
	4	2	10505,00	6624,17	4684,00	63	5821	15189	
	Genel	95	10921,51	2103,11	215,77	19	5821	15189	

Greenough ve ark. (1997) döl veriminde azalmanın topallıktan kaynaklanan ekonomik kayıplara sebep olan ana nedenlerden biri olduğunu bildirmiştir. Melendez ve ark. (2003) topal ve topal olmayan inekler arasında ilk tohumlamada gebelik oranı, yumurtalık kisti oranı ve genel gebelik oranı bakımından önemli düzeyde (P≤0.05) farklılık bulunduğunu bildirmişlerdir. Araştırıcılar topal ineklerin ilk tohumlamada gebelik oranının (%59) ve genel gebelik oranından %8,2 daha düşük olduğunu, yumurtalık kisti oranının da % 125 daha yüksek olduğunu bildirmişlerdir. Collick ve ark. (1989) topal ineklerde buzağılama ile ilk tohumlama arası sürenin 4 gün, servis periyodunun da 14 gün daha uzun olduğunu, ilk tohumlamada gebe kalma oranının topal ineklerde %46, topal olmayanlarda ise %56 düzeyinde gerçekleştiğini bildirmişlerdir. Araştırıcılar ayrıca ayıklama oranını topal ineklerde %16, topal olmayanlarda ise %5 düzeyinde bulduklarını belirtmişlerdir. Boelling ve Pollot (1998) sığırlarda topallığın hayvanın refahını etkileyen ve karlılığı azaltan önemli bir faktör olduğunu bildirmiştir. Bergsten ve Petterson (1992) işletme içi kirlilik ile tırnak sağlığı arasındaki yüksek bir ilişki olduğunu bildirmişlerdir. Nigel (2000) topallığın kış aylarında %24,8 ve bahar ile yaz aylarında %21,8 oranında görüldüğünü ayrıca hijyen ve topallık arasında yüksek oranda ilişki olduğunu, ıslak gübre ve kirli ahır içi şartlarında barınan hayvanlarda topallık ihtimalinin yüksek olduğunu bildirmiştir.

4. Sonuç

Araştırmanın sonuçları değerlendirildiğinde verim düzeylerine göre; topallık skoru ve kirlilik skoru ile 305 günlük verimi arasında istatistik farklılık olmadığı belirlenmiştir.

Sığırlarda topallık hayvan refahını etkileyen ve karlılığı azaltan en önemli faktörlerden biridir. Barınak iç koşullarının topallık üzerinde önemli etkisi bulunmaktadır. Barınak iç koşullarından yataklık kirlilik durumu, gezinti alanlarındaki dışkı durumu, yetersiz havalandırma ve sağım yollarının kaygan olması gibi etkenler sürü içerisindeki topal hayvan sayısını etkilemektedir.

Topallığın erken dönemde belirlenmesi topallıkla mücadelede özel önem arz etmektedir. Erken dönemde tespit edilen topallıklarla mücadele ileri ki dönemde meydana gelecek topallıktan kaynaklanan ekonomik kayıpların önlenmesine yardımcı olmaktadır.

Katkı Oranı Beyanı

Yazar(lar)ın katkı yüzdesi aşağıda verilmiştir. Tüm yazarlar makaleyi incelemiş ve onaylamıştır.

	A.R.Ö.	R.A.
K	50	50
T	70	30
Y	80	20
VTI	10	90
VAY	80	20
KT	20	80
YZ	50	50
KI	70	30
GR	80	20
PY	40	60

K= kavram, T= tasarım, Y= yönetim, VTI= veri toplama ve/veya işleme, VAY= veri analizi ve/veya yorumlama, KT= kaynak tarama, YZ= Yazım, KI= kritik inceleme, GR= gönderim ve revizyon, PY= proje yönetimi.

Çatışma Beyanı

Yazarlar bu çalışmada hiçbir çıkar ilişkisi olmadığını beyan etmektedirler.

Etik Onay Beyanı

Bu araştırmada hayvanlar ve insanlar üzerinde herhangi bir çalışma yapılmadığı için etik kurul onayı alınmamıştır.

Destek ve Teşekkür Beyan

Bu çalışma, Rıdvan Aydın'ın yüksek lisans tezinden üretilmiştir.

Kaynaklar

Akın İ. 2008. The relationship between the histological quality of the newly formed hoof tissue and the levels of trace elements in blood serum and hoof tissues during the recovery period of some hoof diseases in dairy cows. PhD Thesis, Uludağ University, Institute of Health Sciences, Bursa, Türkiye, pp: 88.

Alkan İ, Boynukara B, Genççelep M. 1993. Van ve yöresinde sığır ayak hastalıklarının yayılışı, nedenleri ve sağaltımı üzerine bir araştırma. YYÜ Vet Fak Derg, 4(1-2): 87-95.

Bergsten C, Pettersson B. 1992. The cleanliness of cows tied in stalls and the health of their hooves as influenced by the use of electric trainers. Prevent Vet Medic, 13(4): 229-238.

Boelling D, Pollott GE. 1998. Locomotion, lameness, hoof and leg traits in cattle. I. Phenotypic ınfluences and relationships. Livest Prod Sci, 54: 193-203.

Collick DW, Ward WR, Dobson H. 1989. Associations between types of lameness and fertility. Vet Record, 125(5): 103-106.

Göncü S. 2017. Süt sığırcılığı işletmelerinde topallık. URL= http://www.muratgorgulu.com.tr/altekran.asp?id=117 (erişim tarihi: 10 Aralık 2016).

Grandin T. 2008. Cattle transport guidelines for meat packers, feedlots, and ranches. URL= http://www.grandin.com/meat.association.institute.html (erişim tarihi: 20 Haziran 2016).

Green L, Hedges VD, Schukken YH, Blowey RW, Packington AJ. 2002. Hazirhe impact of clinical lameness on the milk yield of dairy cows. J Dairy Sci, 85: 2250-2256.

Greenough PR, Weaver AD, Brom DM, Esslemont RJ, Galİndo FA. 1997. Basic concepts of bovine lameness. In: Greenough PR, Weaver ED and Weaver AD ed., Lameness ın cattle. W.B. Saunders Company, Philadelphia, US, pp: 3-13.

Kossaibati MA, Esslemont RJ, Watson C. 1999. The Costs of Lameness in Dairy Herds. The National Lameness Conference, MDC, March 10-12, Stoneleigh, Coventry, US, pp: 40.

Melendez P, Bartolome J, Archbald LF, Donovan A. 2003. The association between lameness, ovarian cysts and fertility in lactating dairy cows. Theriogenology, 59: 927-937.

Nigel BC. 2000. The Impact of Freestall Barn Design on Lameness and Mastitis in Wisconsin, https://www.vetmed.wisc.edu/dms/fapm/publicats/proceeds/Freestalls_and_health.pdf

Reneau JK, Seykora AJ, Heins BJ, Endres MI, Farnsworth RJ, Bey RF. 2005. Association between hygiene scores and somatic cell scoresin dairy cattle. J Am Vet Med A, 227(8): 1297-1301.

Seyrek D, Gül NY, Çeçen G, Kanık S, Sağlık Y, Tan H, Salcı H, Çelimli N, Görgül OS. 2001. Bursa yöresinde sığırlarda karşılaşılan ayak hastalıklarının değerlendirilmesi: 249 olgu (1996-2001). II. Ulusal Buiatri Kongresi, 1-4 Eylül, Bursa, Türkiye, pp: 65-66.

Socha MT, Tomlinson DJ, Rapp CJ, Johnson AB. 2002. Lameness: diagnosis and impact on reproduction. 2002 Hoof Health Conf, Columbus, Ohio, US. Pp: 16-19.

Sprecher DJ, Hostetler DE, Kaneene JB. 1997. A lameness scoring system that uses posture and gait to predict dairy cattle reproductive performance. Theriogenology, 47: 1179-1187.

SPSS Inc. 1999. SPSS for Windows. Release 10.0.5 Standard Version. SPSS Inc. Headquarters, 233 S. Wacker Drive, 11th Floor Chicago, IL 60606.

Toncho P, Konstantin S. 2015. Effect of lameness on milk production traits in Holstein-Friesian dairy cows. Vet Med Zoot, 2015: 70-92.

Warnick LD, Janssen D, Guard CL, Gröhn YT. 2001. The effect of lameness on milk production in dairy cows. J. Dairy Sci. 84: 1988-1997.

Yalçın C, Sarıözkan S, Yıldız AŞ, Günlü A. 2010. Burdur, Kırklareli ve Konya illerindeki süt sığırcılığı işletmelerinde ayak hastalıklarından kaynaklanan finansal kayıplar. Ankara Üniv Vet Fak Derg, 57: 99-104.

Yavru N, Elma B, Koç Y, Erer H, Özkan K, İzci C, Kaya Z. 1992. Konya bölgesinde sığır topallıklarına neden olan ayak hastalıkları üzerine radyolojik ve histopatolojik incelemeler. SÜ Vet Fak Derg, 8(1): 3-8.

Yayla S, Aksoy Ö, Kılıç E. 2012. Kars ve yöresinde sığırların bakım ve barındırma koşulları ile ayak hastalıkları arasındaki ilişkinin değerlendirilmesi. Harran Üniv Vet Fak Derg, 1: 22-27.

Yücel R. 1982. İstanbul ve Tekirdağ bölgesindeki sığırlarda görülen ayak hastalıklarının toplu değerlendirilmesi. İÜ Vet Fak Derg, 8(1): 47-61.

DÖNER KANAT IHA MODELLENMESİ VE DENETİMİ: BİR KONTROL TASARIM UYGULAMASI

Erol DUYMAZ¹*, Abdullah Ersan OĞUZ²

¹*Ostim Teknik Üniversitesi, Mühendislik Fakültesi, Yapay Zekâ Mühendisliği Bölümü, 06374, Ankara, Türkiye*
²*Mudanya Üniversitesi, Mühendislik Mimarlık ve Tasarım Fakültesi, EE Mühendisliği Bölümü, 16940, Bursa, Türkiye*

Özet: İnsansız Hava Araçlarının (İHA) kullanımı konusunda son yıllarda çok büyük gelişmeler kaydedilmiş olup İHA'ları artık yalnız askeri ve endüstriyel uygulamalarda değil eğitimden lojistiğe oradan görsel sanatlara kadar her alanda görmek mümkündür. Öte yandan ülkemizde genel olarak mühendislik fakültelerinde elektrik-elektronik, mekatronik, kontrol mühendisliği bölümlerinde kontrol teorisi uygulamaları için deneysel platform sorunları zaman zaman göze çarpmaktadır. Bu çalışmada, lisans eğitimlerinde kontrol tasarımı uygulaması için bir İHA modellemesi ve denetimi yaklaşımı önerilmiştir. İHA modellemesi benzetim ortamında gerçekleştirilmiş, PD (Oransal-Türevsel) kontrol uygulaması ise benzetim ortamı ve örnek bir platform üzerinden gerçekleştirilmiştir. Teorik tartışmalardan sonra önerilen İHA sistem denetiminin hem benzetim ortamlarında hem de deneysel ortamlarda düşük maliyetli bir kontrol tasarım uygulama aracı olarak kullanılmasının mümkün olduğu görülmüştür.

Anahtar kelimeler: İHA denetimi, Sistem modelleme, Kontrolör tasarımı, Deneysel eğitim uygulaması

Rotary Wing UAV Modeling and Control: A Control Design Application

Abstract: The great progress has been made in the use of Unmanned Aerial Vehicles (UAVs) in recent years, and it is now possible to see UAVs not only in military and industrial applications but also in every field, from education to logistics and visual arts. On the other hand, experimental platform problems for control theory applications in electrical-electronics, mechatronics and control engineering departments in engineering faculties are occasionally noticeable from time to time. In this study, a UAV modeling and control approach is proposed for control design application in undergraduate engineering education. UAV modeling was carried out in a simulation environment, and PD (Proportional-Derivative) control application was carried out on a sample platform along with simulation experiments. After theoretical discussions, it has been seen that it is possible to use the proposed UAV system control as a low-cost control design application tool in both simulation and experimental environments.

Keywords: UAV control, System modeling, Controller design, Experimental training application

1. Giriş

Son yıllarda büyük oranda yaygınlaşan İHA'ların tasarımı konusunda artık çok sayıda kolay erişilebilir bilgi ve uygulama mevcuttur. Yeni dönem çalışmaları amaca uygun olarak daha düşük maliyetle daha uzun süre operasyon yapabilen, görev performansı yüksek İHA tasarımları üzerine yoğunlaşmıştır.

Diğer taraftan mühendislik fakültelerine elektrik, elektronik, bilgisayar, makine ve havacılık-uzay gibi birçok bölümde temel derslerden olan otomatik kontrol, geri beslemeli sistemler, kontrol teorisi, kontrol sistem tasarımı, modern kontrol vb. derslerin uygulamaları için deneysel teçhizat temini temel sorunlardandır.

Bu çalışmada, lisans eğitimlerinde kontrol tasarımı uygulaması kapsamında doğrusal olmayan bir modele sahip olan İHA'nın denetimi için kontrolör sistemleri tasarlanmış ve başarımları basamak tepkileri ile verilen yönergeleri/yörüngeleri takip etme yeteneklerinden gözlenmiştir. Tasarlanan denetleyicilerin performansı

bozucu bir etkiyi geri çevirme (robustness), sistem kararlılığını sürdürebilme ve gürültü altındaki davranışları gelecek çalışmalar arasında planlanmıştır. Benzetim sonuçları, uygulamanın eğitim yardımcısı olarak doğrusal yöntemler ile denetlenebilirliği ve klasik kontrol parametreleri gibi faktörlerin kontrol üzerindeki etkilerini göstermiştir.

Teorik tartışmalar ile birlikte hem benzetim hem de deneysel ortamlarda düşük maliyetli kontrol tasarım uygulaması olarak bir İHA denetim sistemi önerilmiştir. Araştırmamıza ilişkin ayrıntılar sonuç bölümünde sunulmuş olmakla birlikte İHA'nın matematiksel modeli, kontrol yöntemi matematik ve formülasyonları, benzetim sonuçları ile bir durum çalışması olarak kontrol tasarım dersi uygulamasına çalışma içerisinde yer verilmiştir.

Her alanda yaygınlaşmaları sonrası İHA'lar hakkındaki araştırma sayıları da son dönemde oldukça artmıştır. Akış aerodinamiğinden yapısal tasarıma, rota planlamasından uçuş kontrolüne, uçuş süresinden sürü

operasyonlarla ile ilgili çalışmalara kadar birçok alanda İHA araştırması görmek mümkündür.

Bu çalışmalardan bazılarında yapısal tasarım araştırmacıları gövde üzerinde akış incelemelerinde bulunmuşlardır. Yanıktepe ve ark. (2016) delta kanat modeli üzerinde oluşan yakın yüzey akış yapısı ve aerodinamik karakteristiklerini, boya görüntüleme, üç boyutlu Stereoskopik Parçacık Görüntüleme Tekniği (Stereo PIV) ve aerodinamik kuvvet ölçümleri kullanılarak araştırmışlardır. Yanıktepe ve Donald (2004) çalışmalarında yüksek görüntü yoğunluklu parçacık görüntü hız ölçümü tekniği kullanarak düşük süpürme açısına sahip delta kanatlardaki akış yapısını ve özellikle girdap bozulması ile durma fenomenlerinin meydana geldiği çapraz akış düzlemlerini incelemiş, kanattaki buffet (dengesiz/düzensiz titreşim-çalkantı) yüklemesinin bu fenomenlerin önemli kaynakları olduğunu göstermişlerdir. Yanıktepe ve Donald (2005) diğer çalışmalarında ise elmas ve lambda planformlarında anlık ve ortalama akış yapısını aynı ölçüm tekniği ile incelemiştir. Yapısal özellikleri; akış çizgisi topolojisinin desenleri, uzay-zaman görüntülemesinden elde edilen rms hız dalgalanması ve hız spektrumlarının görüntüleri ile birlikte yorumlamışlardır.

Diğer bir gruptaki araştırmalarda, Durmuş ve Duymaz (2023) İHA'ların uzaktan algılama ve görüntüleme alanında kullanımını araştırmış, Duymaz ve ark. (2020) İHA'larda GPS olmayan durumlarda seyrüsefer için EZKH (Eş-zamanlı Konum Belirleme ve Haritalama) çözümlü yeni bir durum tahmin aracı olarak parçacık akış filtresi yöntemini incelemişlerdir. Dinamik ortamda otonom İHA uçuşu için Oguz ve Duymaz (2016) yapay potansiyel alan tabanlı yeni bir yaklaşım önermişlerdir.

Tosun (2024) uçuş kontrolü için farklı yöntemleri karşılaştırmıştır. Doğrusal uçuş kontrol yöntemlerinden PID ve LQR denetleyicileri ile doğrusal olmayan yöntemlerden geri beslemeli doğrusallaştırma yöntemi, kayan kipli kontrol yöntemi ve geri adımlamalı kontrol yöntemlerini uçuş yörünge kontrolünde kullanmış, her iki tip (doğrusal-doğrusal olmayan) kontrol yaklaşımının quadrotor davranışında etkisini incelemiştir.

Oktay ve Özen (2021) çalışmalarında dört rotorlu İHA ile aynı faydalı yük kapasitesi ve aynı uçuş süresine sahip şekil değiştirebilen İHA sistem tasarımı ve PID (oransal integral türev) kontrolünü gerçekleştirmişlerdir. Hava aracının üzerinde bulundurduğu MEMS ve engel algılama sensörleri sayesinde dört rotorlunun kolları arasındaki kesişim açısını değiştirecek aktüatörün enerjilendirilmesi ile açı azaltılarak kapalı ortamda engellerden sakınması ve seyrine devam edebilmesi amaçlanmış, hava aracının seyir halinde şekil değiştirmesi neticesinde meydana gelen konfigürasyon değişikliğinin uçuş karakteristiğine olan etkileri de çalışmada incelenmiştir.

Elmas ve Alkan (2023) ise İHA tasarımında performans özelliklerini çıkarmak için "eCalc" programı kullanılmıştır. eCalc ile elde edilen sonuçlar MATLAB uygulamalarından elde edilen sonuçlarla karşılaştırılarak, bir İHA alt sistemleri için gerekli donanım ve yazılım mimarileri geliştirilerek uygulamada kullanılacak İHA tasarımı gerçekleştirilmiştir.

Çalışmamızda, yazında geçen diğer araştırmalardan farklı olarak, benzetim ve deney ortamlarında düşük maliyetli bir kontrol tasarım uygulaması ortaya konmaktadır. Eğitim yardımcısı olarak tasarlanan İHA denetim sisteminin doğrusal yöntemler ile denetlenebilirliği ve klasik kontrol parametreleri gibi faktörlerin kontrol üzerindeki etkileri de burada araştırılmıştır.

2. Materyal ve Yöntem

Döner kanatlı bir İHA sistemi, ana gövde eksenine bağlı 4 motordan oluşmakta olup sistemin hareket kontrolü motor pervane dönülerinin bağımsız olarak değiştirilmesiyle sağlanır (Şekil 1). Değişen pervane dönüleri, sistemde tork ve momentler oluşturur (Xu ve Ozguner, 2006)
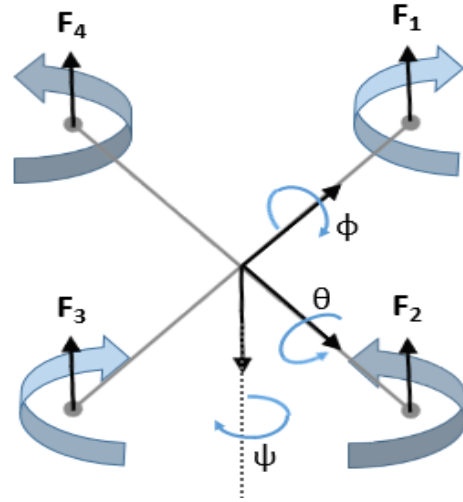
Şekil 1. Döner kanatlı İHA hareket kontrol sistemi.

2.1. Sistem Modeli

Döner kanatlı bir İHA sistemi modeli bu bölüm sonunda verilecek olup alt bileşenler şöyledir:

Eşitlik 1'de R, gövde düzleminden hareket düzlemine dönüşüm içeren Euler Rotasyon Matrisini (Directional Cosine Matrix) temsil eder. Gövde düzleminden hareket düzlemine açısal hız dönüşümlerinin yönelimler cinsinden ifadesi ise eşitlik 2 ve 3 ile verildiği gibidir (Bouabdallah ve Siegwart, 2007).

$$R = R_B^N = R_z(\psi).R_y(\theta).R_x(\phi) = \begin{bmatrix} \cos\theta\cos\psi & \sin\phi\sin\theta\cos\psi - \cos\phi\sin\psi & \cos\phi\sin\theta\cos\psi + \sin\phi\sin\psi \\ \cos\theta\sin\psi & \sin\phi\sin\theta\sin\psi + \cos\phi\cos\psi & \cos\phi\sin\theta\sin\psi - \sin\phi\cos\psi \\ -\sin\theta & \sin\phi\cos\theta & \cos\theta\cos\phi \end{bmatrix} \quad (1)$$

$$\begin{bmatrix} p \\ q \\ r \end{bmatrix} = T \begin{bmatrix} \dot{\phi} \\ \dot{\theta} \\ \dot{\psi} \end{bmatrix} = I \begin{bmatrix} \dot{\phi} \\ 0 \\ 0 \end{bmatrix} + R_x(\phi)^T \begin{bmatrix} 0 \\ \dot{\theta} \\ 0 \end{bmatrix} + R_x(\phi)^T R_y(\theta)^T \begin{bmatrix} 0 \\ 0 \\ \dot{\psi} \end{bmatrix} = \begin{bmatrix} 1 & 0 & -\sin\theta \\ 0 & \cos\phi & \sin\phi\cos\theta \\ 0 & -\sin\phi & \cos\phi\cos\theta \end{bmatrix} \begin{bmatrix} \dot{\phi} \\ \dot{\theta} \\ \dot{\psi} \end{bmatrix} \tag{2}$$

$$\begin{bmatrix} \dot{\phi} \\ \dot{\theta} \\ \dot{\psi} \end{bmatrix} = T^{-1} \begin{bmatrix} p \\ q \\ r \end{bmatrix} = \begin{bmatrix} 1 & \sin\phi\tan\theta & \cos\phi\tan\theta \\ 0 & \cos\phi & -\sin\phi \\ 0 & \dfrac{\sin\phi}{\cos\theta} & \dfrac{\cos\phi}{\cos\theta} \end{bmatrix} \begin{bmatrix} p \\ q \\ r \end{bmatrix} \tag{3}$$

Sistem dinamiği için kullanılan kuvvet denklemi eşitlik 4'de sunulmuştur (Runcharoon ve Srichatrapimuk, 2013):

$$\begin{bmatrix} \ddot{x} \\ \ddot{y} \\ \ddot{z} \end{bmatrix} = R \frac{1}{m} \left[\begin{bmatrix} 0 \\ 0 \\ -(F_1 + F_2 + F_3 + F_4) \end{bmatrix} + \begin{bmatrix} 0 \\ 0 \\ g \end{bmatrix} \right] = \begin{bmatrix} (\cos\phi\sin\theta\cos\psi + \sin\phi\sin\psi)\dfrac{-U_1}{m} \\ (\cos\phi\sin\theta\sin\psi - \sin\phi\cos\psi)\dfrac{-U_1}{m} \\ g - \cos\theta\cos\phi\dfrac{U_1}{m} \end{bmatrix} \tag{4}$$

Sisteme ait dönel dinamikler (momentler) ise eşitlik 5, 6 ve 7'de sunulduğu gibidir:

$$\begin{aligned}
M_{xb} &= l(-F_2 + F_4) = l(U_2), \\
M_{yb} &= l(F_1 - F_3) = l(U_3), \\
M_{zb} &= d(-Q_1 + Q_2 - Q_3 + Q_4) = d(U_4), \\
M_{gx} &= j\dot{\theta}\Omega, \\
M_{gy} &= -j\dot{\phi}\Omega, \\
M_{gz} &= j\dot{\Omega}
\end{aligned} \tag{5}$$

Motor pervane dönülerine ait ilişki ise eşitlik 6 ve 7'deki gibi olur;

$$\Omega = \Omega_1 - \Omega_2 + \Omega_3 - \Omega_4 \tag{6}$$

$$\begin{bmatrix} I_x \ddot{\phi} \\ I_y \ddot{\theta} \\ I_z \ddot{\psi} \end{bmatrix} = \begin{bmatrix} M_{xb} + M_{gx} + (I_x + I_y - I_z)\dot{\theta}\dot{\psi} \\ M_{yb} + M_{gy} + (-I_x - I_y + I_z)\dot{\phi}\dot{\psi} \\ M_{zb} + M_{gz} + (I_x - I_y + I_z)\dot{\phi}\dot{\theta} \end{bmatrix} = \begin{bmatrix} l(U_2) + j\dot{\theta}\Omega + (I_x + I_y - I_z)\dot{\theta}\dot{\psi} \\ l(U_3) - j\dot{\phi}\Omega + (-I_x - I_y + I_z)\dot{\phi}\dot{\psi} \\ (U_4) + j\dot{\Omega} + (I_x - I_y + I_z)\dot{\phi}\dot{\theta} \end{bmatrix} \tag{7}$$

U_1, U_2, U_3, U_4 giriş/kontrol sinyallerinin denklem ifadeleri eşitlik 8'de sunulmuştur (Rodríguez ve ark., 2014):

$$\begin{bmatrix} U_1 \\ U_2 \\ U_3 \\ U_4 \end{bmatrix} = \begin{bmatrix} k & k & k & k \\ 0 & -k & 0 & k \\ k & 0 & -k & 0 \\ d & -d & -d & d \end{bmatrix} \begin{bmatrix} \Omega_1 \\ \Omega_2 \\ \Omega_3 \\ \Omega_4 \end{bmatrix} \tag{8}$$

Sonuç olarak durum-uzay modelinde kullanılan durum denklemi aşağıda eşitlik 9 ve 10'da verilmiştir:

$$x = [x \quad \dot{x} \quad y \quad \dot{y} \quad z \quad \dot{z} \quad \phi \quad \dot{\phi} \quad \theta \quad \dot{\theta} \quad \psi \quad \dot{\psi}]^T \tag{9}$$

$$\begin{bmatrix} \dot{x} \\ \ddot{x} \\ \dot{y} \\ \ddot{y} \\ \dot{z} \\ \ddot{z} \\ \dot{\phi} \\ \ddot{\phi} \\ \dot{\theta} \\ \ddot{\theta} \\ \dot{\psi} \\ \ddot{\psi} \end{bmatrix} = \begin{bmatrix} \dot{x} \\ (\cos\phi\sin\theta\cos\psi + \sin\phi\sin\psi)\dfrac{-U_1}{m} \\ \dot{y} \\ (\cos\phi\sin\theta\sin\psi - \sin\phi\cos\psi)\dfrac{-U_1}{m} \\ \dot{z} \\ g - \cos\theta\cos\phi\dfrac{U_1}{m} \\ \dot{\phi} \\ lU_2 + j\dot{\theta}\Omega + (I_x + I_y - I_z)\dot{\theta}\dot{\psi} \\ \dot{\theta} \\ lU_3 - j\dot{\phi}\Omega + (-I_x - I_y + I_z)\dot{\phi}\dot{\psi} \\ \dot{\psi} \\ U_4 + j\dot{\Omega} + (I_x - I_y + I_z)\dot{\phi}\dot{\theta} \end{bmatrix} \tag{10}$$

Döner kanatlı İHA'nın mekanik tasarımı ve eylemsizlik moment hesaplamaları Solidworks ortamında gerçekleştirilmiştir (Şekil 2).
Bu bölümde kullanılan ve döner kanatlı İHA sistem (Şekil 2) modelini tanımlayan sabitler ise Tablo 1'de verildiği gibidir (Swarup, 2014).
Burada verilen eşitliklerle tanımlanan döner kanatlı İHA sistem modellemesinin Matlab benzetim ortamında gerçeklenmesinden sonra Bölüm 2.2'de belirtilen denetim yaklaşımları uygulanmıştır.
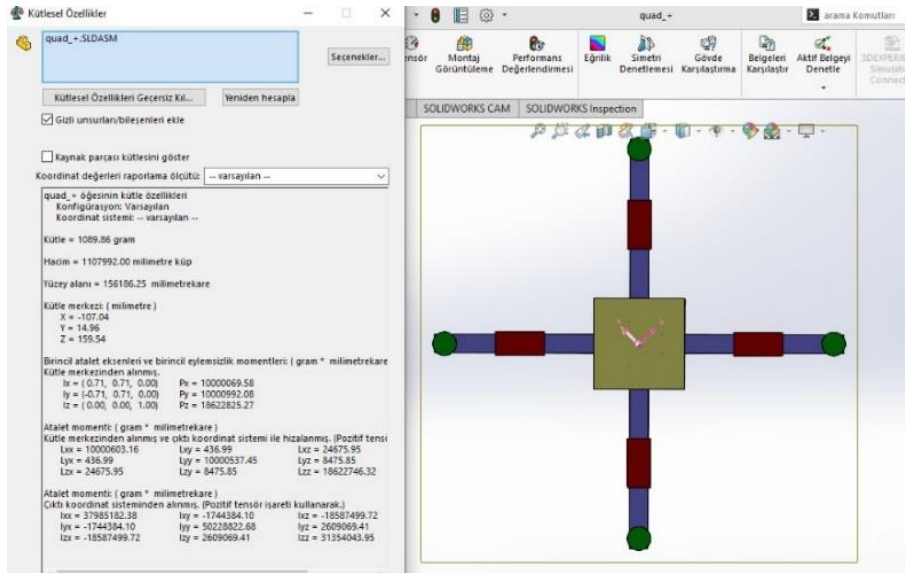
Şekil 2. Döner kanatlı İHA tasarımı benzetim modeli.

Tablo 1. Döner kanatlı İHA sistemi model sabitleri

Sembol	Sabit (Değişken)	Değer (Büyüklük)
Ix	X ekseni etrafındaki İHA atalet momenti	Ix = $10{,}65*10^{-3}$
Iy	Y ekseni etrafındaki İHA atalet momenti	Iy = $10{,}65*10^{-3}$
Iz	Z ekseni etrafındaki İHA atalet momenti	Iz = $21{,}2*10^{-3}$
J	Pervane ekseni etrafındaki toplam dönme atalet momenti	J = $6{,}5*10^{-5}$
k	İtme faktörü	k = $3{,}13*10^{-5}$
d	Sürükleme faktörü	d = $7{,}5*10^{-7}$
l	İHA'nın merkezine olan uzaklık	l = 0,21
m	İHA'nın kg cinsinden kütlesi	m = 0,784
g	Yerçekimi ivmesi	g = 9,81

B

2.2. Sistem Kontrolü

PID (oransal-integral-türevsel) denetleyiciler en yaygın doğrusal kontrol yaklaşımlarından olup Cp-Ci-Cd katsayıları sistemde yükselme zamanı (rise time), aşım (overshoot), kararlı-hal hatası (steady-state error) üzerinde etkilere sahiptir. (Rooh ve ark., 2015)

Çalışmamızda döner kanatlı bir İHA sisteminin platform kontrolünde PID denetleyici kullanımı öngörülmüş olup, önerilen yaklaşımın eğitim yardımcısı olarak kullanımı kapsamında durum çalışması olarak (case study) PD denetimi ele alınmıştır.

Yukarıda Eşitlik (10) ile verilen durum denklemlerinin kısmi türevleri alınarak havada askıda kaldığı denge durumunda doğrusallaştırma yapılır ise elde edilen jakobiyen matrisleri kullanılarak kontrolör parametreleri bulunur.

Burada denge noktası (x_0,u_0) etrafında systemin Taylor serisi açılımı eşitlik 11'de verilmiştir (Runcharoon ve Srichatrapimuk, 2013):0

$$f(x,u) \cong f(x_0,u_0) + \frac{\partial f}{\partial x}\bigg|(x - x_0)_{x=x_0}$$
$$+ \frac{\partial f}{\partial u}\bigg|(u - u_0)_{u=u_0} \qquad (11)$$
$$+ \cdots \text{diğer terimler}$$

Sistem doğrusallaştırma (linearization) başka bir çalışma konusu olduğundan burada ayrıntılarına yer verilmemiş olup ilgili kontrolör parametreleri aşağıda verilen Tablo 2 ile detaylandırılmıştır.

Tablo 2. Kontrolör parametreleri

	Cp	Cd
x	2,28	1,07
y	1,289	1,065
z	2,96	25
ϕ	0,0842	0,23
θ	0,25	0,90
ψ	0,0163	0,2837

Döner kanatlı İHA sistemi için tasarlanan PD (oransal-türevsel) kontrolör benzetim modeli ve örnek uygulama platformu Şekil 3'te verilmiştir. Konum ve yönelim denetim/kontrol performansı Bölüm 3'de belirtilen birim basamak tepkileri ile değerlendirilmiştir.
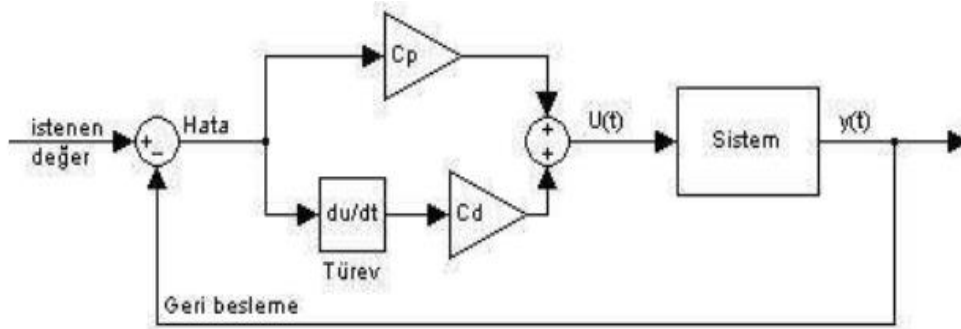
Şekil 3. Döner kanatlı İHA sistemi (üstte) ve kontrolör benzetim modeli (altta).

3. Bulgular

Döner kanatlı İHA sistemi için tasarlanan kontrolör birim basamak tepkileri Şekil 4-7'de verildiği gibi elde edilmiştir.

Denetim için teorik tartışmalardan sonra oransal (P) ve türevsel (D) kontrol parametrelerinin sistem üzerindeki etkisi benzetim ortamında değerlendirilebilmekte ve örnek platform üzerinde uygulanabilmektedir. Böylece lisans eğitimlerinde kontrol tasarımı uygulaması için etkin bir yardımcı elde edilmektedir.

Burada önerilen yapıda, İHA sisteminin X,Y,Z konumları için birim basamak tepkileri Şekil 4 ve 5 'de ve dönme (roll), yunuslama (pitch), süpürme (yaw) yönelim açıları için birim basamak tepkileri ise Şekil 5 ve 6 'da sunulmuştur.

Kontrol katsayılarına bağlı sonuçların yükselme zamanı (rise time), aşım (overshoot), kararlı-hal hatası (steady-state error) gibi parametreler üzerindeki etkileri benzetim ortamında test edildikten sonra örnek platformda (Şekil 3) uygulanmaktadır.

İHA sisteminin benzetim ortamında kontrol komutları ile X ve Y eksenlerindeki hareketleri ve araç seyrüsefer güzergahının 2 eksendeki gösterimi ise Şekil 7 ile sunulmuştur.

Döner kanatlı İHA sistemi için tasarlanan PD kontrolörün deneysel platform üzerinde gerçek zamanlı uygulamaları ve Donanım içeren Simülasyon (Hardware in the Loop) detayları bu sınırlı çalışma içerisine dahil edilmemiştir. Bununla birlikte sistemin deneysel ve benzetim çalışmalarında eğitim yardımcısı olarak kullanılabileceği değerlendirilmektedir.
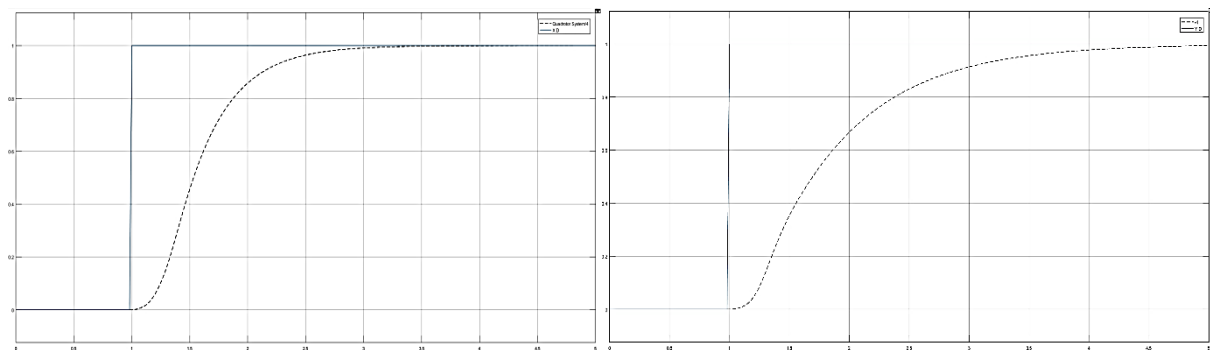
Şekil 4. İHA sisteminin X konum (solda) ve Y konum (sağda) birim basamak tepkileri.
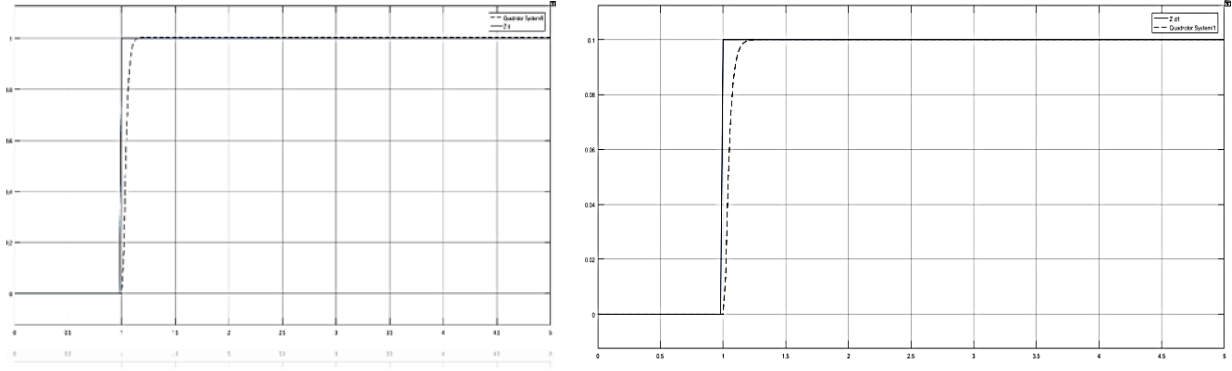
Şekil 5. İHA sisteminin Z konum (solda) ve Roll (solda) birim basamak tepkileri.
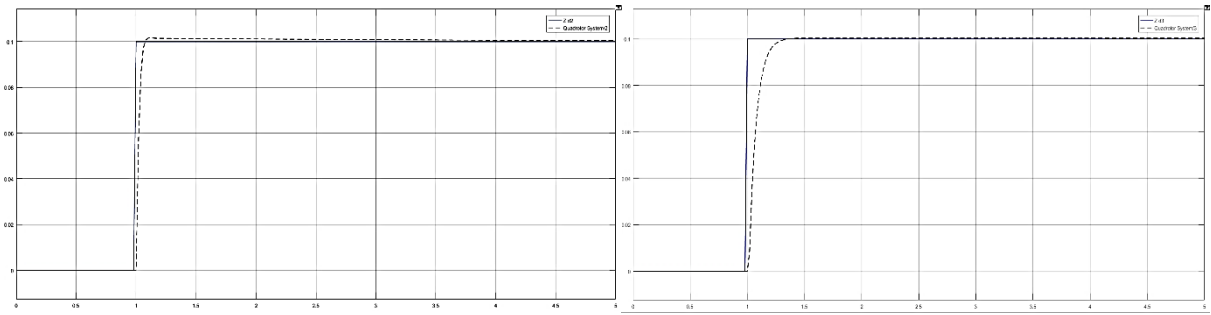
Şekil 6. İHA sisteminin Pitch (solda) ve Yaw (solda) birim basamak tepkileri.
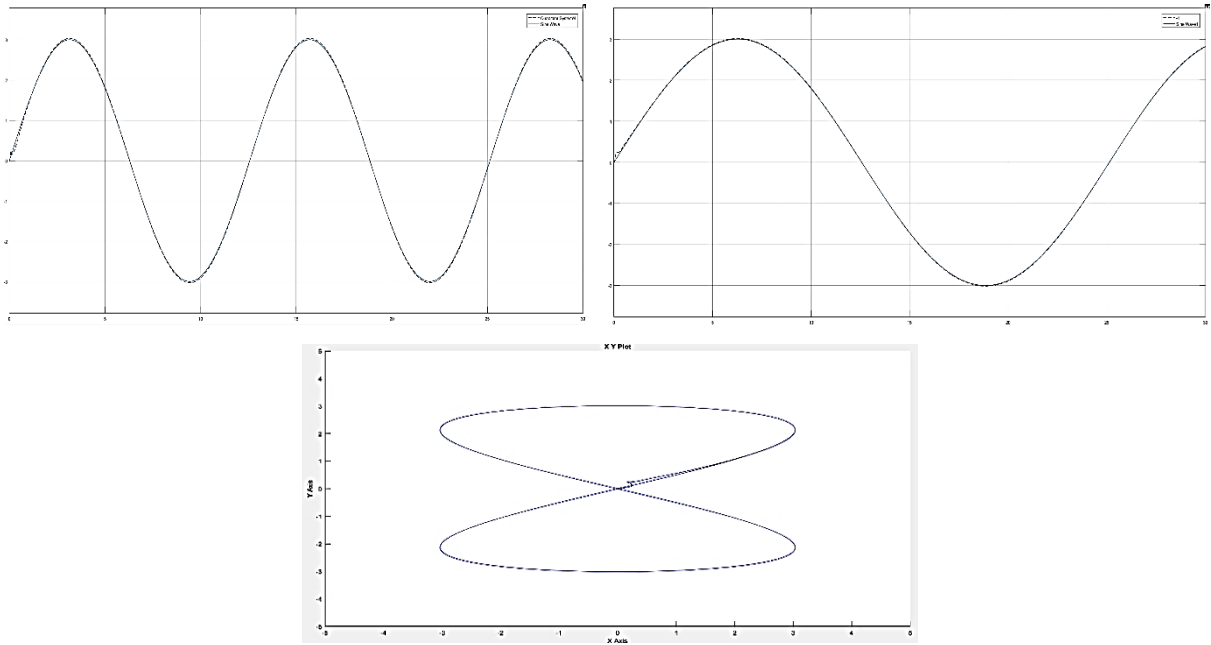
Şekil 7. Benzetim ortamında kontrol komutları ile İHA sisteminin X (solda), Y (sağda) eksenlerindeki hareketleri ve güzergahın 2 eksendeki gösterimi (aşağıda).

Çalışmamızın amacı kontrol tasarım eğitimleri için bir uygulama platformu önermek olduğundan kontrol tasarım performansını ölçmek hedeflenmemiş ve kontrol komutlarını izleme doğrulukları ile ilgili metriklere burda yer verilmemiştir. Durum çalışmalarımızda oransal-türevsel (Cp-Cd) kontrol katsayılarının sistemde yükselme zamanı (rise time), aşım (overshoot), kararlı-hal hatası (steady-state error) üzerinde etkileri görsel olarak incelenmiştir. Yazında taradığımız Oktay ve Özen (2021) ve Elmas ve Alkan (2023) gibi çalışmalarla karşılaştırıldığında yukarıdaki senaryolarda aldığımız kontrol performans değerlerinin ise genel olarak başarılı olduğu görülmektedir. İlerleyen çalışmalarda Donanım içeren Simülasyon (Hardware in the Loop- HiL) sistemli kontrolör tasarım özel olarak amaçlandığında doğruluklar ile ilgili metriklere detaylı yer verilmesi ve bunların da eğitim yardımcısı olarak kullanılması planlanmıştır.

4. Tartışma ve Sonuç

İHA'lar üzerinde bir kullanıcı taşımaya gerek duymayan yerden ve önceden programlanmış ve sisteme yüklenmiş bir uçuş rotasına göre görev yapan araçlar olarak günümüzde sivil ve askeri birçok görevde yaygın olarak kullanılmaktadır (Nguyen ve ark., 2020).

Bu makalede İHA'nın temel yapısı ile benzer sistemlerin kontrolü ve kontrol sistemlerinin test edilmesini sağlayacak deney düzeneğinin araştırılması amaçlanmıştır.

Lisans eğitimlerinde kontrol tasarımı uygulaması kapsamında doğrusal olmayan modele sahip olan bir İHA'nın denetimi için tasarlanan kontrolörlerin başarımları basamak tepkilerinden ve verilen yönergeleri/yörüngeleri takip etme yeteneklerinden gözlenmiştir. Benzetim sonuçları, doğrusal yöntemler ile sistem denetlenebilirliğini ve klasik kontrol katsayıları gibi faktörlerin denetim üzerindeki etkilerini içeren uygulamanın eğitim yardımcısı olarak kullanılabileceğini göstermiştir.

Yaklaşımın benzetim ortamına ilave olarak deneysel ortam kullanan düşük maliyetli bir kontrol tasarım uygulaması olarak sistem denetimi eğitimlerinde kullanılmasının mümkün olduğunu gösteren araştırmamıza ilişkin diğer ayrıntılar çalışmamızda sunulmuştur. İHA matematiksel modeli, kontrol yöntemi, matematik ve formülasyonları gibi teorik tartışmalar ile birlikte benzetim sonuçları ve durum çalışması olarak kontrol tasarım dersi uygulamasına da araştırma içerisinde yer verilmiştir.

Laboratuvar ortamında kontrol deney setinden elde edilen sonuçların benzer yapıda bir kontrolör kullanılarak serbest uçuş yapabilecek sistemlerle çeşitli bilimsel yarışma ve çalışmaları hedeflemek için motivasyon sağlayabileceği de değerlendirilmiştir.

Tasarlanan denetleyicilerin performansı bozucu bir etkiyi geri çevirme (robustness), sistem kararlılığını sürdürebilme ve gürültü altındaki davranışları gelecek çalışmalar arasında planlanmıştır.

Gelecek çalışmalarda ayrıca laboratuvar ortamında geliştirilen IHA üzerinde mikro-kontroller kullanılarak farklı denetleyicilerin gerçek zamanlı olarak Donanım içeren Simülasyon (Hardware in the Loop- HiL) sistemine uyarlanması ile ilgili detayların raporlanması amaçlanmıştır.

Kaynaklar

Bouabdallah S, Siegwart R. 2007. Full control of a quadrotor. Proceedings of the 2007 IEEE/RSJ International Conf. on Intelligent Robots and Systems, October 29, San Diego, California, US, pp: 153-158.

Canpolat Tosun D. 2024. Bir quadrotorun yörünge takibinde doğrusal ve doğrusal olmayan kontrol yöntemlerinin performans değerlendirmesi. Politeknik Derg, https://doi.org/10.2339/politeknik.1219648

Durmuş A, Duymaz E. 2023. Use of unmanned aerial vehicles for ımaging and remote sensing. In: Karakoc, T.H., Özbek, E. (eds) Unmanned Aerial Vehicle Design and Technology. Sustainable Aviation. Springer, Cham, the Netherland, https://doi.org/10.1007/978-3-031-45321-2_11

Duymaz E, Oğuz AE, Temeltaş H. 2020. Exact flow of particles using for state estimations in unmanned aerial systems` navigation. PLoS ONE,000 15(4): e0231412. https://doi.org/10.1371/journal.pone.0231412

Elmas EE, Alkan M. 2023. Bir insansız hava aracı sisteminin tasarımı, benzetimi ve gerçekleştirilmesi. Politeknik Derg, 26(2): 929-940. https://doi.org/10.2339/politeknik.1037319

Nguyen T, Quyen V, Nguyen V, Le M, Tran T. 2020. Control Algorithms for UAVs: A Comprehensive Survey, EAI Endorsed Trans Ind Netw Intell Syst, 7: 23-29. https://doi.org/10.4108/eai.18-5-2020.164586

Oguz AE, Duymaz E. 2016. Artificial potantial field based autonomus UAV fligh in dynamic environment. 16th AIAA Aviation Technology, Integration, and Operations Conference, Jun, June 13-17, Washington DC, US, pp: 1-9. https://doi.org/10.2514/6.2016-3454

Oktay T, Özen E. 2021. Döner kanatlı insansız hava aracının sistem tasarımı ve kontrolü. Avrupa Bil Teknol Derg, 27: 318-324. https://doi.org/10.31590/ejosat.957056

Rodríguez WE, Ibarra R, Romero G, Lara D. 2014. Comparison of

controllers for a UAV type quadrotor: Feedback control by Bessel´s Polynomials and LQR with Kalman Filter. Appl Mech Mater, 555: 40-48.

Rooh A, Li A, Shahab B. 2015. A review of quadrotor UAV: Control methodologies and performance evaluation. IJAAC, 10(2): 87-103. https://doi.org/10.10.1504/IJAAC.2016.076453

Runcharoon K, Srichatrapimuk V. 2013. Sliding mode control of quadrotor. The International Conference on Technological Advances in Electrical, Electronics and Computer Engineering TAEECE, May 9-11, Konya, Türkiye, pp: 552-557.

Swarup SA. 2014. Comparison of quadrotor performance using backstepping and sliding mode control - semantic scholar. The International Conference on Circuits, Systems and Control, November 21-22, Bangalore, India, pp: 7982-7986.

Xu R, Ozguner U. 2006. Sliding mode control of a quadrotor helicopter. The 45th IEEE Conference on Decision and Control, December 13-15, San Diego, CA, US, pp: 4957-4962.

Yanıktepe B, Donald R. 2004. Flow structure on a delta wing of low sweep angle. AIAA J, 42(3): 513-523, https://doi.org/10.2514/1.1207.

Yanıktepe B, Donald R. 2005. Flow structure on diamond and lambda planforms trailing edge region. AIAA J, 43(7): 1490-1500, https://doi.org/10.2514/1.7618.

Yanıktepe B, Özalp C, Canpolat Ç. 2016- Aerodynamics and flow characteristics of X-45 delta wing planform, KSU. J Eng Sci, 19(1): 1-10, https://doi.org/10.17780/ksujes.86852.

IMPROVING LEAD TIME THROUGH LEAN MANUFACTURING

Ülge TAŞ[1]*

[1]Aksaray University, Department of Industrial Engineering, 68100, Aksaray, Türkiye

Abstract: Lean manufacturing is a well-established methodology aimed at optimizing production by eliminating waste, enabling industries to thrive in a globally competitive environment. This paper presents a case study of a well-known automotive manufacturing industry focusing on the axle process. This article demonstrates how the Value Stream Mapping (VSM) methodology was used in the axle process to reduce lead time by producing quality products with a reduction in non-value-added activities. The current state of the axle process was mapped using industry data from the past six months. Significant improvements were realized following the successful implementation of VSM, including a reduction in the lead time from 89.50 hours to 50.55 hours. The new state map was also created after implementing the improvements. The results illustrated that the VSM increased the effectiveness of the axle process by 56.48%.

Keywords: Lean principle, Process improvement, VSM, Waste

1. Introduction

The automotive industry plays a considerable role in manufacturing and assembly and immensely impacts various aspects of production (Yousaf et al., 2023). Industrialization is increasing as technology advances; however, rejection or rework remains a significant concern for the automotive sector. Lean manufacturing tackles these concerns through a continuous improvement system that integrates material and information flows within an industry. The goal is to identify and eliminate waste that negatively affects lead time, material costs, product quality, and other production factors (Jimenez et al., 2019). VSM is one of the most effective lean tools industries use to find and eliminate waste to reduce product costs, improving quality and efficiency (Atigre et al., 2017; Banica and Belu, 2019; Duggan, 2002). VSM is employed to enhance the flow of materials and information on the shop floor and to eliminate seven types of waste, including transportation, excess inventory, waiting time, unnecessary motion, overproduction, over-processing, and defects, as identified in manufacturing industries (Saboo et al., 2014).

The axle in a vehicle is a crucial part of the drivetrain system, located at the rear end. It supports the axle, differential, and axle shafts, and is essential for bearing the vehicle's weight, transmitting power to the rear wheels, and providing a mounting point for the rear suspension. The protective structure encloses and supports the rear axle and its associated components, serving several important functions. The axle transmits power from the differential to the rear wheels, propelling the vehicle forward (Guleria et al., 2022; Ranjan et al., 2023).

Reviewing the literature, it is clear that VSM is a methodology used to reduce waste in most lean research publications. According to Rahani and Ashraf (2012), a significant amount of time spent in the production system is usually non-value-added. They also reported on the effectiveness of VSM in identifying hidden wastage and improving productivity. Belokar et al. (2012) reported that VSM is a highly useful tool for identifying and eliminating waste in a cycle, fostering a culture of lean practices. Rohani and Zahraee (2015) implemented VSM in the manufacturing industry's production line, reducing lead time from 8.5 days to 6 days. Romero and Arce (2017) found that implementing VSM can enhance the visibility of the value stream and boost manufacturer performance. Deshkar et al. (2018) used VSM in plastic bag manufacturing, reducing cycle time from 46 min to 26.6 min. Narke and Jayadeva (2020) implemented VSM, reducing setup time by a fixture and saving 336 hours per year. Operator fatigue was also significantly reduced. Guleria et al. (2022) claimed that the rejection rate in the rear axle process was reduced from 10.4% to 3.20% after implementing Lean Six Sigma. Badhotiya et al. (2023) with the new map show a possibility of a 62.65% reduction in total transportation time in the equipment industry.

VSM is a valuable tool for improving industry efficiency. However, many industries and literature do not frequently use VSM due to a lack of awareness compared to other lean tools. This field lacks sufficient case studies, making this study original. Previous research has not adequately addressed VSM as a case study, resulting in inadequate case studies. This study is uncommon in

filling this gap in the field. To contribute to the relevant literature and industry, this article presents a case study of the axle manufacturing industry. It discusses how the assembly line created a new status by reducing the lead time of the axle process through waste elimination. Hence, this article aims the VSM methodology was used in the axle process to reduce lead time by producing quality products with a reduction in non-value-added activities.

2. Materials and Methods

An established automotive manufacturing company has been selected to study and implement VSM. This company is a global player in the production of passenger cars, trucks, and buses worldwide. It operates in three shifts and has a workforce of 2,000+ manpower. Like other companies in the industry, this company has faced challenges related to long lead times in axles. The VSM methodology was selected to identify and eliminate waste in the axle production process.

The research was based on actual data and outlined the

steps used in the VSM process. It analyzed improvement steps taken based on data and waste elimination by a team of managers, engineers, and a researcher. Data was collected from the axle assembly line, which included 6 processes pre-assembly, LPH assembly, cable assembly, balance shaft assembly, cast console assembly, and tightening.

The stages of the case study can be summarized as the selection of the bottleneck, drawing the current state map, analysis, and creating a new state map.

3. Case Study and Discussion

This case study was carried out in an automotive manufacturing company. Axles are supplied and disassembled from the supplier in quantities of 462 pieces per week. Current status, 77 units of axles, each consisting of 6 processes (pre-assembly, LPH assembly, cable assembly, balance shaft assembly, cast console assembly, and tightening) are produced per day. Sample axle types and axle displays in vehicles are shown in Figure 1.

Figure 1. Sample axle types and axle displays in vehicles.

Following the assembly of each axle, one axle is installed on every vehicle. Annually, approximately 28,000 vehicles are produced.

VSM was selected to find and eliminate the wastage in the axle process. VSM is followed in the following steps i.e.;

- Selection of bottleneck: The VSM applies to a bottleneck in the axle process in this study. Accordingly, the product axle with the maximum lead time was selected for the study.
- Current state map: The state map was created using

six months of historical data on axle products. The case study was conducted as a historical document review to compile the necessary data for the current situation analysis. Current status problems included; (a) forklift transfers in internal logistics; (b) over-processing; (c) over-manpower; (d) over-waiting time; (e) unnecessary motion; and (f) decreased inventory level. VSM's current status, from the supplier to the customer, and the problems were illustrated with universal symbols in Figure 2.
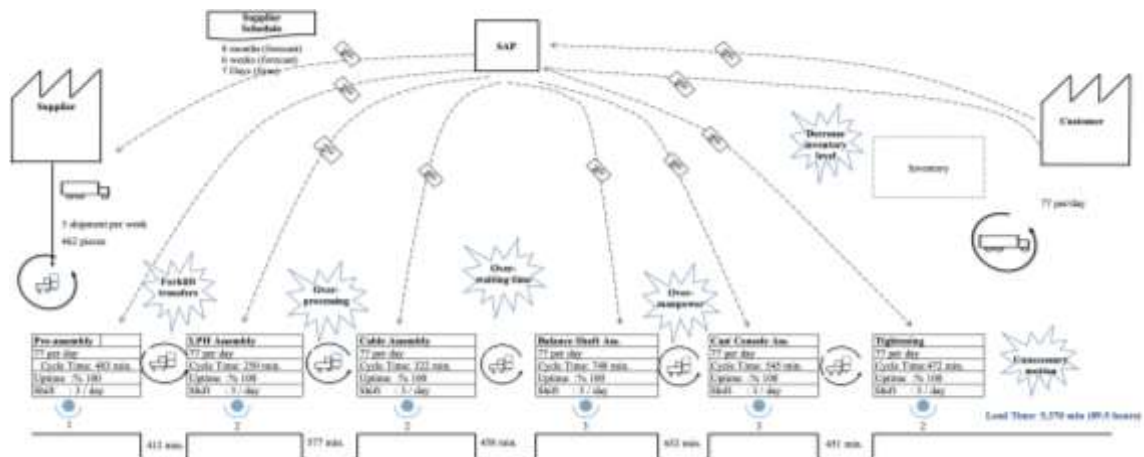
Figure 2. Current state map.

In VSM's current status, the delivery time from the supplier to the customer is 89.50 hours. During production, each vehicle has at least one axle mounted after its front assembly. The axle is a crucial component of the vehicle, and all vehicles complete their final assembly and come off the line on their wheels. Currently, 77 units of axles, each consisting of 6 processes including pre-assembly, are produced per day.

- Analyze: Forklift transfers in internal logistics, over-processing, over-manpower, over-waiting time, unnecessary motion, and decreased inventory level were the six major sources of waste identified after the current state map. To improve axle assembly, the decision was made to replace forklifts with unmanned vehicles or energy-saving wheelbarrows for material transportation. LPH assembly and Cable assembly processes were combined, streamlining the assembly into a single process. The number of operators has been reduced by combining processes, reducing forklifts, and reducing cycle times. With the use of Automated Guided Vehicle (AGV) and wheelbarrows and the decrease in the number of operators, waiting times have decreased. Finally, unnecessary motions have been eliminated by reducing the number of operators and forklift activities.

- New state map: A new state map was created to show the improved net lead time of the axle process. The VSM new state map represented demonstrating the enhanced optimal state of the processes in Figure 3.
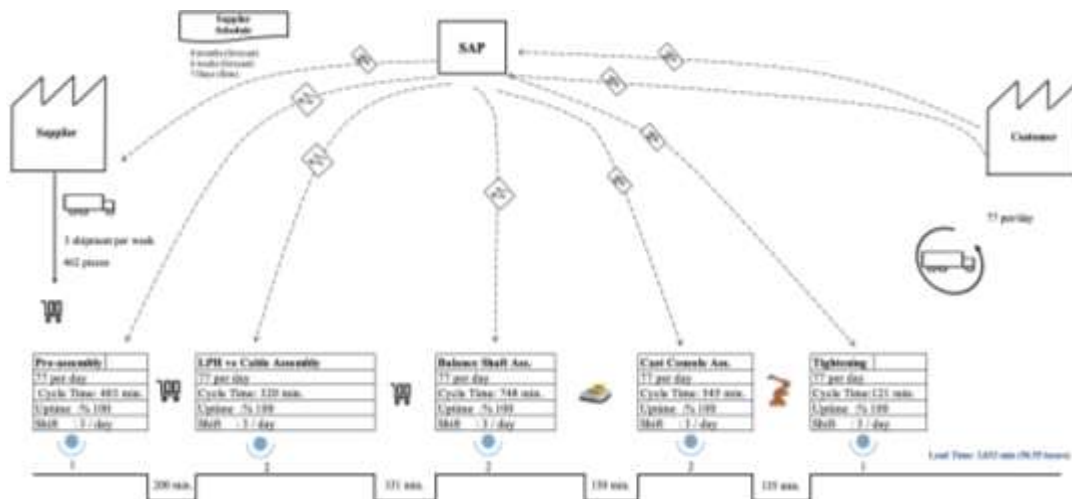
Figure 3. New state map.

The contribution of the VSM was to identify the wastages of the current status and to improve the new status. VSM's new status, the lead time from the supplier to the customer is 50.55 hours. The new status was applied to identify the ways to improve the axle process improvements using the VSM while achieving the operational excellence. According to new status, the improvements were identified as follows;

a) Forklift transfers in internal logistics: In order to improve the axle assembly process, the decision was made to replace forklifts with AGVs and energy-saving wheelbarrows for material transportation. The cycle time has been reduced by replacing the currently used forklifts with AGVs and wheelbarrows. While 6 forklift operators are in their current status working, in this way, the number of wheelbarrow operators has reduced to 3. AGVs are capable of reducing the cost of forklifts and their operators and can operate 24 hours a day, 7 days a week, without any operator supervision.

b) Over-processing: After analyzing the current situation, it has been decided to combine LPH and cable assembly into a single process to enhance cycle time and operator efficiency. By merging the LPH and cable assembly processes, the cycle time has been reduced from 572 minutes in the current status to 320 minutes in the new status.

c) Over-manpower: The current status, while 13 operators are working in the process, the number of operators has been reduced to 8 with the reduction of non-value-added activities.

d) Over-waiting time: Waiting times have been eliminated as cycle times decreased from 2,820 minutes to 2,217 minutes due to process mergers, reduced transportation times, and a decrease in the number of operators.

e) Unnecessary motion: Unnecessary motions have been eliminated by reducing the number of operators and forklift activities, it was decreased from 2,550 minutes to 816 minutes.

f) Decreased inventory level: After completing the final process, it was removed out an area of approximately 720 m^2 by removing the safety stock of 8 vehicles and shipping them directly to the customer from the production line. As a result, non-value-added movements have decreased, and it has saved space in the area.

The application of VSM to evaluate the expected effects in the lead time process resulted in improvements as follows. Table 1 illustrates the comparison between the current and new situations.

Findings from this case study show that with the application of VSM methodologies, significant improvements were achieved in the axle processes from the entrance warehouse to the customers. The success of

the VSM application depends on the results of the case study. Based on the improvements in VSM, the lead time, which was 89.50 hours in the current situation, has been reduced to 50.55 hours in the new situation, resulting in a reduction of approximately 56.48%. In the new status, the cycle time has been dramatically reduced compared to the current status.

Table 1. VSM improvements

Waste	Current Status	Future Status
Transfers in internal logistics	6 forklifts	3 wheelbarrows, 2 AGVs
Over-processing	6 process	5 process
Over-manpower	13 operator	8 operator
Over-waiting time	2820 min.	2217 min.
Unnecessary motion	2,550 min.	816 min.
Decreased inventory level	8 vehicle	0
Total	5370 min.	3033 min.
	89.50 hours	50.55 hours
Improvements	56.48%	

4. Conclusion

VSM is a crucial tool in lean manufacturing, and it has been applied in the automotive industry to analyze the axle manufacturing process in a specific case study. This article focuses on how the VSM methodology was used to optimize the axle process, aiming to reduce lead time, eliminate non-value-added activities, and ensure the production of high-quality products.

Upon analyzing the current state map, it became evident that non-value-added time, such as transportation and waiting time, could be significantly reduced to enhance productivity. After conducting a detailed analysis of the current state map and consulting with team members and operators, changes were implemented to improve the process. As a result of the successful implementation of VSM, the lead time was reduced from 89.50 hours to 50.55 hours. This led to a considerable reduction in operator fatigue and successfully achieved the goal of increasing lead time efficiency. A new status map was created to reflect the implemented improvements. The results demonstrated that the VSM improved process effectiveness by 56.48% in the axle manufacturing process. This improvement resulted in reduced internal logistics, decreased over-processing, over-manpower, over-waiting time, unnecessary motion, and a decreased in inventory levels through process enhancements.

Author Contributions

The percentage of the author(s) contributions is presented below. The author reviewed and approved the final version of the manuscript.

	Ü.T.
C	100
D	100
S	100
DCP	100
DAI	100
L	100
W	100
CR	100
SR	100

C=Concept, D= design, S= supervision, DCP= data collection and/or processing, DAI= data analysis and/or interpretation, L= literature search, W= writing, CR= critical review, SR= submission and revision.

Conflict of Interest

The author declared that there is no conflict of interest.

Ethical Consideration

Ethics committee approval was not required for this study because of there was no study on animals or humans.

References

Atigre PS, Shah AP, Patil VR. 2017. Application of 8D methodology for minimizing the defects in manufacturing process: A case study. IJERT, 6(09): 123-126.

Badhotiya GK, Chauhan AS, Yadav A, Kushwaha P, Singh Y. 2023. Application of value stream mapping for waste elimination: A case of construction equipment industry. In AIP Conference Proceedings, August 6-7, Dehradun, India, pp: 21.

Banica CF, Belu N. 2019. Application of 8D methodology an effective problem solving tool in automotive industry. Sci Bull Automotive Series, XXV(29): 1-7.

Belokar RM, Kumar V, Kharb SS. 2012. An application of value stream mapping in automotive industry: A case study. IJITEE, 1(2): 152-157.

Deshkar A, Kamle S, Giri J, Korde V. 2018. Design and evaluation of a lean manufacturing framework using value stream mapping (VSM) for a plastic bag manufacturing unit. Mater Today Proc, 5(2): 7668-7677.

Duggan KJ. 2002. Creating mixed model in value streams. Productivity Press, New York, US.

Guleria P, Pathania A, Sharma S, Sá JC. 2022. Lean six-sigma implementation in an automobile axle manufacturing industry: A case study. Mater Today Proc, 50: 1739-1746.

Jimenez G, Santos G, Sá JC, Ricardo S, Pulido J, Pizarro A, Hernández H. 2019. Improvement of productivity and quality in the value chain through lean manufacturing – a case study. Procedia Manuf, 41: 882-889.

Narke MM, Jayadeva CT. 2020. Value stream mapping: Effective lean tool for SMEs. Mater Today Proc, 24: 1263-1272.

Rahani AR, Al-Ashraf M. 2012. Production flow analysis through value stream mapping: A lean manufacturing process case study. Procedia Eng, 41: 1727-1734.

Ranjan A, Mutra RR, Kirty Y, Srinivas J, Norhisham M, Reddy DM. 2023. Study and failure analysis of non-drive automotive rear axle of heavy commercial vehicle. Int J Heavy Veh Syst, 30(1): 1-16.

Rohani JM, Zahraee SM. 2015. Production line analysis via value stream mapping: A lean manufacturing process of color industry. Procedia Manuf, 2: 6-10.

Romero LF, Arce A. 2017. Applying value stream mapping in manufacturing: A systematic literature review. IFAC Pap OnLine, 50(1): 1075-1086.

Saboo A, Garza-Reyes JA, Er A, Kumar V. 2014. A VSM improvement-based approach for lean operations in an Indian manufacturing SME. IJLER, 1(1): 41-58.

Yousaf MU, Aized T, Shabbir A, Ahmad M, Nabi HZ. 2023. Automobile rear axle housing design and production process improvement using FMEA. Eng Fail Anal, 154: 107649.

PARAMETRIC OPTIMIZATION OF STRUCTURAL FRAME DESIGN FOR HIGH PAYLOAD HEXACOPTER

Osman ÖZTÜRK[1]*

[1]*Konya Technical University, Faculty of Engineering and Natural Sciences, Department of Mechanical Engineering, 42250, Konya, Türkiye*

Abstract: For drones, the use of which has been increasing recently for load carrying, lightweight drone frame design is significant for increased flight time and payload capacity. Drones are produced in different configurations with three, four, or six rotors, and in different sizes depending on the purpose of use. While agility is more important in three and four rotor drone applications, six-rotor and relatively large-bodied drones are preferred in cases such as load carrying. When the body structure has to be large, lightening the design becomes very critical. Lightweight designs can be achieved by two commonly used methods for structural optimization: topology optimization and parametric optimization. Topology optimization is an advanced method that can significantly reduce weight but is expensive and time-consuming. Parametric optimization is a more practical approach to conventional manufacturing methods and was used in this study. This study aims to first simplify the hexacopter frame model and define key geometric parameters for mass-decreasing optimization. Finite element analysis simulations were used to evaluate the strength and deformation of the frame under various design scenarios. The results showed that parametric optimization successfully reduced the weight of the hexacopter frame while maintaining structural integrity. The maximum Von Mises stress was found as approximately one quarter of the yield strength of the frame material. The maximum total deformation was achieved below 0.3 mm, and deformation under 1 mm is considered safe in the literature. As a result, the optimized design offers a lighter drone structure in line with conventional manufacturing methods, providing better flight time and payload capacity while maintaining cost effectiveness. In future studies, comparisons can be made based on this study by performing weight optimizations suitable for current methods such as topology optimization or generative design. The cost factor and the availability of existing production lines should be taken into consideration when comparing the mentioned methods with parametric optimization.

Keywords: Parametric optimization, Hexacopter, Drone design, Finite element analysis

1. Introduction

Unmanned Aerial Vehicles (UAVs), also commonly known as drones, are a type of aircraft that does not require a human pilot onboard to operate. They are controlled remotely or autonomously using pre-programmed flight plans and onboard sensors. UAVs encompass a wide range of vehicles with varying sizes, capabilities, and applications. The two main categories of UAVs are fixed-wing UAVs and rotary-wing UAVs. The fixed-wing UAVs generate lift similar to traditional planes and are suitable for long-range missions (Fahlstrom et al., 2022). On the other hand, rotary wing UAVs utilize multiple rotors to generate lift and achieve vertical takeoff and landing capabilities. Two of the most common rotary-wing UAV types are hexacopters and quadcopters.

Hexacopters, also known as hexadrones, are a type of multirotor drone with six rotors. Compared to quadcopters (four rotors), hexacopters offer several advantages that make them increasingly popular across various sectors. First of all, with six rotors, even if one of the six rotors fails, the remaining five can provide enough thrust to maintain stability and allow for a controlled landing. Therefore, hexacopters are ideal for critical missions where reliability is crucial. The additional rotors translate to more lifting power, enabling hexacopters to carry heavier payloads than quadcopters. Increased payload enables the user to lift larger cameras, sensors, or delivery packages. The maximum takeoff weight is significantly higher for hexacopters compared to all other types of UAVs (Ramesh and Jeyan, 2022). The efficient lift distribution across six rotors translates to better energy efficiency, resulting in longer flight times than quadcopters with similar battery capacities. In conclusion, hexacopters are revolutionizing the drone industry with their decent stability, high payload capacity, and longer flight times. Because of these advantages, hexacopters are used in many sectors such as aerial photography and videography, search and rescue operations, agriculture, and delivery services (Elouarouar and Medromi, 2022).

The lightweight design of the hexacopter body is very significant for maximizing the flight performance of the

drone (Wu et al., 2021). Because the weight of the hexacopter frame impacts three concepts: flight time, payload capacity, and maneuverability. The relationship between lightweight design and these three concepts will be explained respectively because lowering the weight impacts these concepts positively or negatively. It is a known fact that there is a direct correlation between flight time and lightweight design. Every gram shaved off translates to less energy required to hover or fly. This allows the drone to stay in the air for longer on a single battery charge. Lighter weight translates to less strain on the motors, allowing them to operate more efficiently. This translates to increased battery life as less energy is wasted, overcoming the drone's weight. Although lightweight design offers a benefit, it also has less capacity to carry additional weight. Therefore, an optimization is required to achieve the best balance between weight and payload capacity for the intended application. For instance, the designer of a photography drone might prioritize stability and flight time for capturing smooth aerial footage, while a delivery drone might prioritize payload capacity to carry heavier packages. Also, maneuverability can be affected by the lightness. A lighter drone has less inertia, requiring less effort to change direction or perform maneuvers. This translates to increased agility and responsiveness, allowing for sharper turns, faster acceleration, and smoother overall flight control. This is crucial for drone races or aerial video capturing for high-speed motorsports.

Up to this point, the importance of lightweight design for vehicles such as drones has been emphasized. For this very reason, optimizing the structural parts of drones in terms of weight and strength is significant. Topology optimization, an advanced method, is currently used to reduce weight and material in the structural design of a drone. However, the costs of structural parts obtained through topology optimization are high, mainly when metallic materials are used. In some cases, it is not even possible to access metal additive manufacturing devices. Considering both these disadvantages and the existing traditional production methods in the industry, the parametric optimization method is lower in terms of material and labor costs. Parametric optimization is based on converting certain dimensions of easily machined geometries, such as holes or slots, into parameters on the structure whose weight is desired to be reduced. Optimizing these parametric dimensions to provide appropriate strength is possible with Computer Aided Engineering (CAE) software. In studies comparing topology optimization and parametric optimization, low labor cost and rapid production are shown as the advantages of parametric optimization. Removing the support parts of the parts produced with topology optimization by secondary operations is a more costly and time-consuming process than parametric optimization (Hassani et al., 2021).

There are various studies in the literature regarding the structural frame design of multicopters. Ismail et al. (2020) studied the design and development of the structural frame and propeller parts for a hexacopter intended to carry heavy loads. HEX-6X, one of the multicopter configurations, was used, and the frame material was Al 6061-T6 Grade, which is a lightweight option for UAV applications (Anweiler and Piwowarski, 2017). Using finite element simulations, a multicopter that is safe regarding equivalent stress and total deformation was designed to carry a 20 kg payload where each rotor has been designed to provide 3.4 kg thrust force. Aswath and Raj (2021) studied the design process of a payload hexacopter. Simulation of the multicopter arm is made by the researchers to obtain the safety of the structure in the design process. Maximum deformation is found as 8 mm where the material of the arm is plastic. Kumar et al. (2021) investigated different types of multicopter frame designs for four different materials. As a result, it has been seen that "X" or "+" type body frames using fiber-reinforced composite materials are suitable for quadcopter design. Wu et al. (2021) performed finite element simulations to obtain a sound multicopter design where the propeller and foldable arm are optimized for best performance. Certain airfoil design is proposed for better thrust force. Carbon fiber reinforced composite material for the foldable multicopter frame is also found as an alternative to the mostly used aluminum alloy. Shelare et al. (2023) performed both theoretical and numerical studies to design a hexacopter with a bottle hanger to carry a maximum 7500 g load. The results of the simulations indicate maximum 1 mm displacement for a safe multicopter design. Azhagan et al. (2023) used a generative design approach to find the best alternative body frame and structural arm for a hexacopter. In generative design, Artificial Intelligence (AI) algorithms are used to generate a great number of design alternatives. This design approach is only useful for applications where additive manufacturing is available because the final designs are organically shaped (Radakovic, 2021). Using nonlinear analysis, Sharma and Selvakumar (2018) examined a drone's structure. They increased the drone's weight until it reached the failure point. Sundararaj et al. (2021) conducted modal and structural analyses on various drone frames. The simulation yielded the maximum allowable stress, strain displacement, and frequency values. They discovered that although producing short armed rectangular frames is difficult, they indicate higher strength. MohamedZain et al. (2022) conducted a series of simulations to determine the weight of the drone components, considering allowable stress and displacement. Sreeramoju and Rao (2023) Using Autodesk Fusion 360 software, the frame is modeled in this work with regard to its durability and stress analysis. Its materials, ranging from metal to plastic, are compared, and the design is shape-optimized to achieve the goal. There are many studies in the literature that deal with the weight-

reducing optimization of the drone frame (Yemle et al., 2019; Urdea, 2021; Tura and Zaharia, 2023). All of the researchers above performed their studies mostly in the last five years. Therefore, the optimization of the drone frame has recently become a very popular topic because the use of drones is increasing very rapidly today. In addition, the geometry of the frame is particularly important because it needs to be high strength enough but also have a lower mass. The motivation of this study is to propose an approach to the optimization problem of the high payload hexacopter frame design. With the proposed approach, hollow-like geometries that can be parametrized in the hexacopter frame can be designed and these cavities can be brought to their optimum dimensions with the help of numerical simulations. In addition, the motivation for using parametric optimization instead of topology optimization is to achieve a design optimization suitable for drone frame structures that can be machined on existing CNC machines due to the cost advantage.

In this study, the frame and arm of a payload hexacopter are simplified and redesigned for parametric optimization. SolidWorks Simulation and Design Study modules are used for parametric optimization. The design process is divided into two phases to prevent excessive design scenarios. Two types of hollow geometries are defined for each phase. The optimal result has been achieved by user selection to ensure both low weight and high strength.

2. Materials and Methods

2.1. Material

The aerospace, defense, and automotive industries frequently utilize aluminum 6061-T6, owing to its excellent mechanical qualities, strong corrosion resistance, and exceptional weldability (Namlu et al., 2019). In this paper, Al 6061-T6 was preferred in this study due to its lightness and the exceptional properties described above. Additionally, this material has very good machinability, allowing for a clean surface finish

(Najiha et al., 2015). The material properties of aluminum alloy is given in Table 1. These values were obtained from the material database of SolidWorks.

Table 1. The mechanical and physical properties of Al 6061 T6

Property	Value	Unit
Elastic Modulus	69	GPa
Poisson's Ratio	0.33	-
Tensile Strength	310	MPa
Yield Strength	275	MPa
Mass Density	2700	kg/m^3
Hardening Factor	0.85	-

2.2. CAD Modeling and Simplification of Hexacopter

The structural components of a hexacopter with a high-payload were redesigned and optimized in the present study. There are various types of configurations for multicopters and the most used ones are called; Quad+, Quad X, Tri, Y4, Hex 6, Hex 6 X, and Hex 6 Y shaped (Anweiler and Piwowarski, 2017). These configurations, as well as the one presented in this study, are given in Figure 1. Two main differences exist in these configurations; the shape of the frame and propeller rotation. Propeller rotations are designed to ensure the stability of the drone. In this study, a Hex 6 Y-shaped hexacopter design was preferred. The hexacopter model called "Multirotor Drone with Payload Carrying" was obtained from GrabCAD Library with permission from the designer. Since the structural body of the hexacopter was to be optimized, the two frames and propeller arm had been isolated from the main assembly, as in Figure 2. To proceed with the parametric optimization, the frames and arm were simplified to determine the design parameters. The simplified and isolated components are given in Figure 3. The simplification process is essential because the original design is suitable for additive manufacturing, while this study depends highly on the design for conventional manufacturing methods.
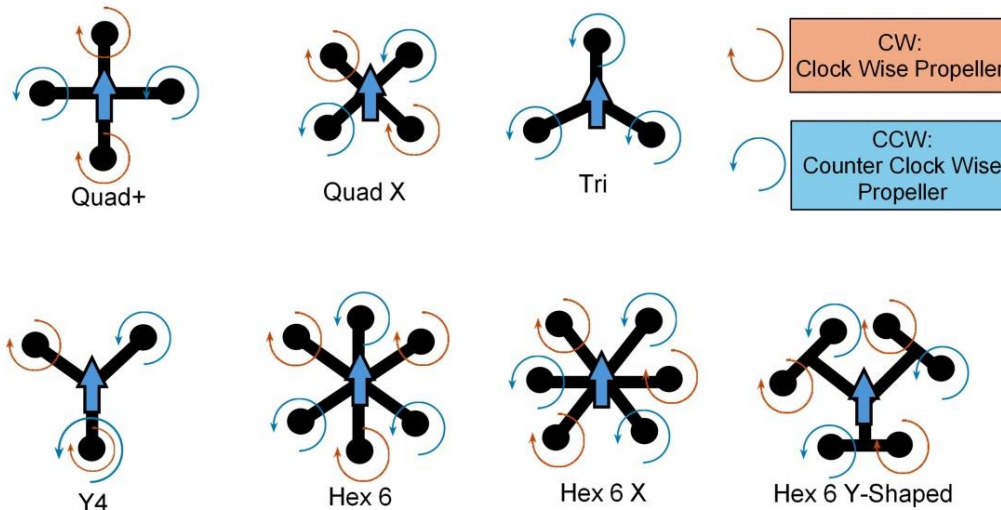
Figure 1. Configurations of multicopter body (Anweiler and Piwowarski, 2017).
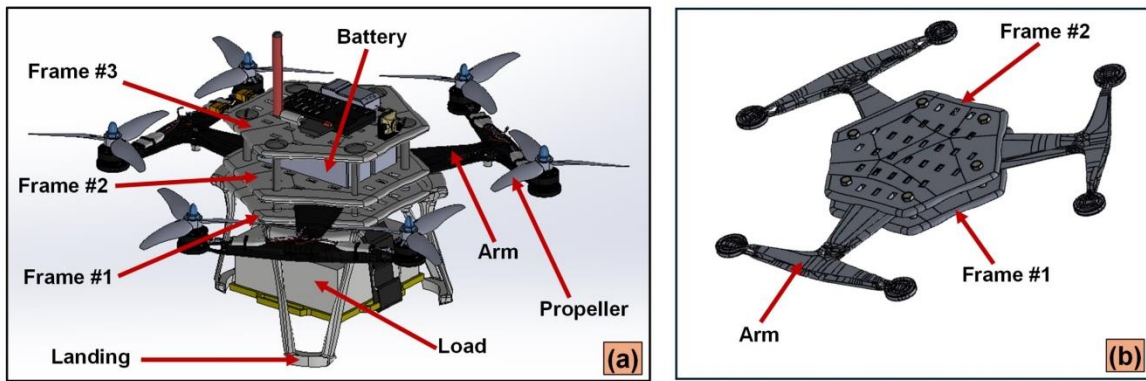
Figure 2. (a) Design of the high-payload carrying hexacopter, (b) isolated frames and propeller arm.
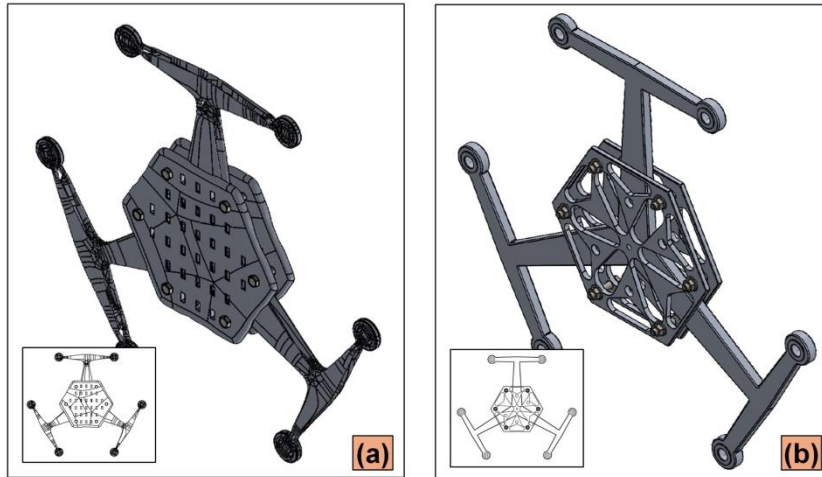
Figure 3. (a) Original design of the frame and propeller arm of the hexacopter, (b) Simplified design of the frame and propeller arm of the hexacopter.
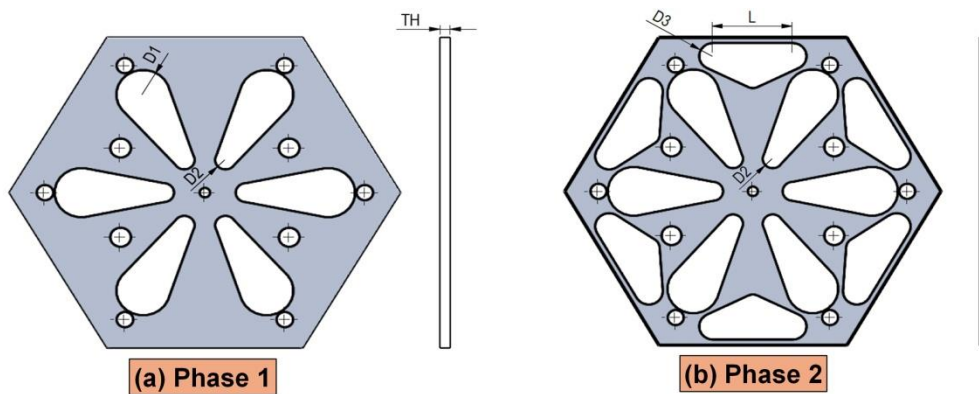
Figure 4. (a) 1st phase of the optimization and corresponding parameters (D1, D2 and TH), (b) 2nd phase of the optimization and corresponding parameters (D3 and L).

For the parametric optimization of the hexacopter drone, five different dimensions were defined as variable parameters of the design space. Since the design study depends on the number of parameters and levels, the optimization process was divided into two phases. The first phase consists of three parameters such as; D1 (first radius of slot), D2 (second radius of the slot), and TH (thickness of the frame). After optimizing parameters of the first phase, the second phase was performed. The parameters of the second phase are D3 (twin radii of the slot) and L (distance between slot origins). The phases

and corresponding parameters of the frame are given in Figure 4. The parameter levels and design table are given in Table 1. There are 27 and 9 design scenarios in 1st phase and 2nd phase of the parametric optimization, respectively.

2.3. Finite Element Simulation

After the optimization parameters were determined, the finite element model was established. The frames are fixed at the bolt connection surfaces. The external forces are defined as the following constraints of the hexacopter:

- the thrust force of each propeller (3.5 kgf),
- the payload at the bottom (20 kgf),
- and weight of the Frame #3 and other electronic components.

In Figure 5, defined forces are demonstrated. The thrust force for each propeller was determined as 34.3 N (3.5 kgf) which is in agreement with the literature considering the high payload. The payload was defined as 219 N. The actual load was 196 N (20 kgf) and the remaining was the landing component, Frame #3 and other electronic components are given in Figure 2 previously in this study.

The materials were also defined as Al 6061-T6 Grade for Frame #1, Frame #2 and the propeller arm. Al 6061-T6 Grade is a commonly used multicopter structure material due to its high strength/weight ratio. The connection components were defined as 1045 steel. Thus, the software could calculate the overall weight of the isolated parts. When forces and materials were defined, the curvature type mesh was generated in SolidWorks Simulation.

A mesh sensitivity analysis was conducted to examine how simulation results change with mesh element size. In a mesh sensitivity analysis, convergence occurs when the numerical solution obtained with one grid size or configuration is not significantly different from another (Abdulsalam, 2021). This means that an acceptable level of accuracy has been attained, and further refinement is not required. The sensitivity analysis was made according to the gradual change of the maximum element size between 32 mm and 8 mm. Figure 6 shows the variation in mesh distribution between the extreme points of this gradualness, which ranges from coarse to fine.
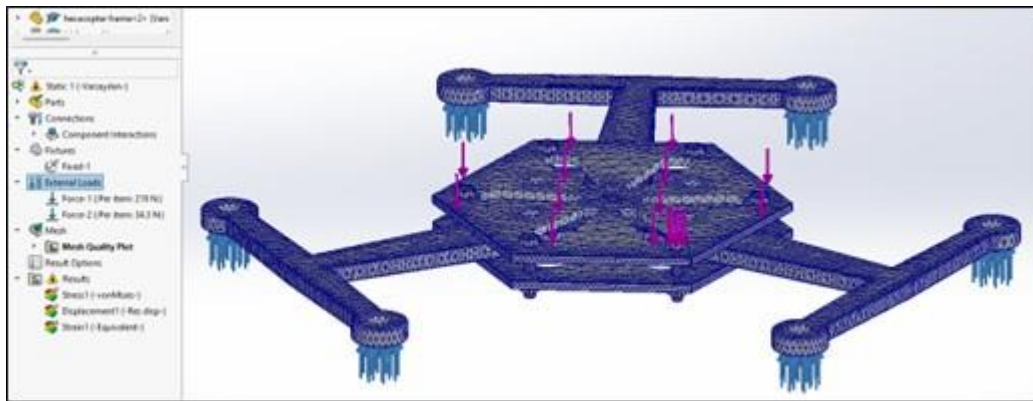
Figure 5. Defining external loads and generating mesh in SolidWorks simulation.
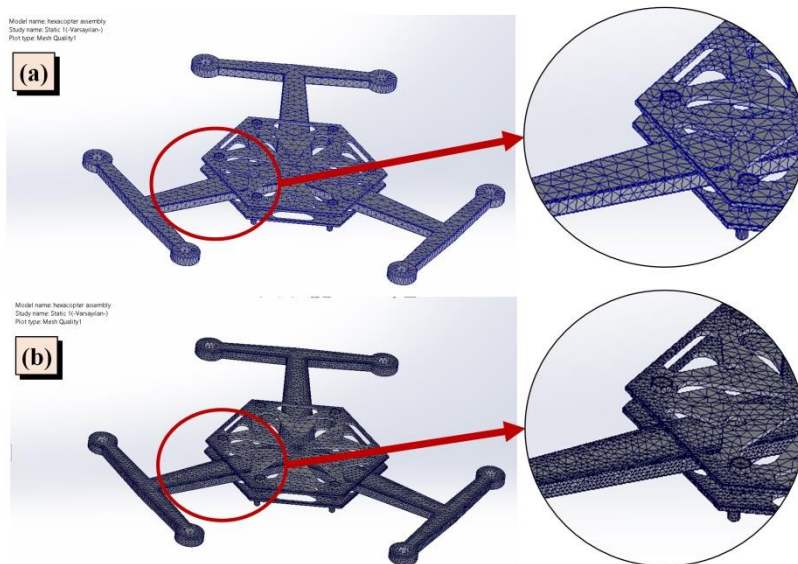
Figure 6. (a) Coarse and (b) fine meshing of hexacopter sub-assembly.

3. Results and Discussion

3.1. Mesh Sensitivity Analysis

The results of the mesh sensitivity analysis are given in Table 2. As can be seen from the Table, the maximum stress of the resultant did not significantly change after 14 mm of element size. Therefore, in this study, fine meshing, which is between 9 mm and 14 mm, was preferred. The visualization of the Table 2 is given in Figure 7. In this figure, the convergence was clear, and a 9 mm element size was chosen for the simulations. Further decreasing the mesh size was not allowed in the educational version of SolidWorks Simulation.

Table 2. The results of the mesh sensitivity analysis

Mesh Density	Max. Element Size (mm)	Max. Von Mises Stress (MPa)	Maximum Deformation (mm)	Max. Equivalent Strain
Coarse	32	49.84	0.3045	$3.625 \cdot 10^{-4}$
↑	29	53.57	0.3059	$3.349 \cdot 10^{-4}$
↑	26	54.62	0.3053	$3.484 \cdot 10^{-4}$
↑	23	56.22	0.3028	$2.731 \cdot 10^{-4}$
↑	20	58.86	0.2997	$2.916 \cdot 10^{-4}$
↓	17	61.94	0.3046	$3.179 \cdot 10^{-4}$
↓	11	61.98	0.3041	$3.301 \cdot 10^{-4}$
↓	14	62.22	0.3044	$2.558 \cdot 10^{-4}$
Fine	9	63.10	0.3158	$3.875 \cdot 10^{-4}$
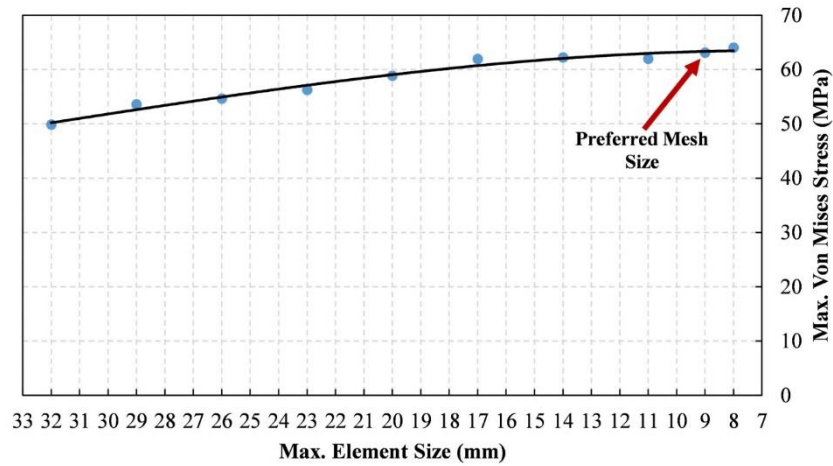
Figure 7. Result of the mesh sensitivity analysis.
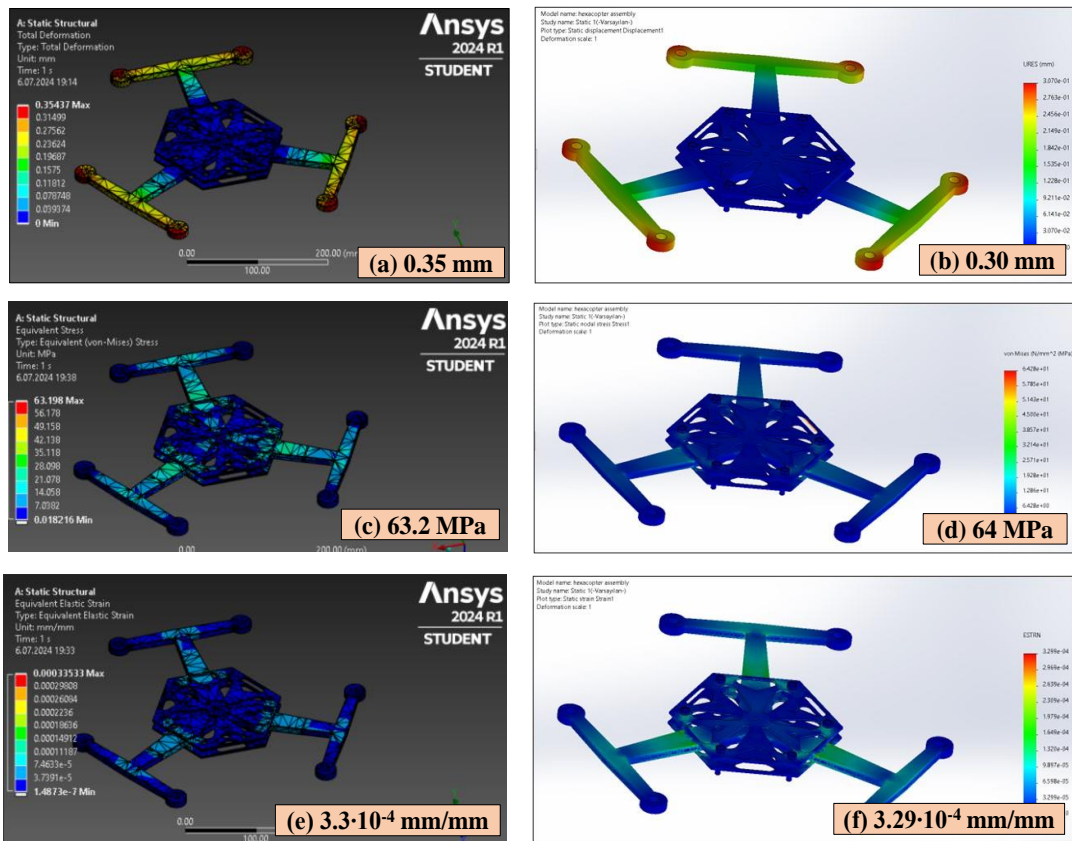
Figure 8. The comparison between total deformation for (a) ANSYS Mechanical and (b) SolidWorks Simulation; between Von Mises stress for (c) ANSYS Mechanical and (d) SolidWorks Simulation; between equivalent strain for (e) ANSYS Mechanical and (f) SolidWorks Simulation.

3.2. Sofware Reliability Assessment

In this study, SolidWorks Simulation software was chosen for linear static analyses. When performing linear static analyzes in which Hooke's law of elasticity is valid, SolidWorks Simulation is used because the analysis time is faster than other software (Tyflopoulos and Steinert, 2022). However, software such as ANSYS Mechanical, where simulation parameters are more flexible and tunable, can be perceived as more reliable. Therefore, to test the reliability of SolidWorks Simulation software, linear static analyses were performed with both software with the same parameters. According to the results, the maximum Von Mises stresses were obtained as 63.2 MPa and 64 MPa for ANSYS and SolidWorks Simulation, respectively. The equivalent elastic strain was obtained as $3.3 \cdot 10^{-4}$ and $3.29 \cdot 10^{-4}$ in the same order. Finally, the total deformation was obtained as 0.35 mm and 0.30 mm in the same order. When the results were examined, it was seen that there was a maximum of 2% difference between the stress and strain values. The total deformation was also consistent with each other with a maximum error of 15%. As a result, SolidWorks Simulation was used in the continuation of the study due to its advantages such as shorter analysis time. The results of the two software are given in Figure 8 to clearly observe the differences.

3.3. 1st Phase of Parametric Optimization

The results of the 1st phase of parametric optimization are given in Table 3. The maximum deformation was below 0.3 mm which was acceptable when compared to 1 mm deformation of the hexacopter arm in the literature (Shelare et al., 2023). The maximum Von Mises stress was found to be approximately 52 MPa, indicating a safe drone design, considering the yield strength of the Al 6061-T6 is 275 MPa. The Von Mises stress, equivalent strain, and total deformation results are given in Figure 9, Figure 10, and Figure 11, respectively.

To determine the optimal design scenario, the mass of the sub-assembly (mass of the frame-arm assembly) was sorted in ascending order. Sorted data is visualized in Figure 12. It is clear from Figure 12 that the optimal design scenario can be chosen as simulation no. 3. Because simulation no. 3 is below the average mass and indicates the minimum equivalent strain in that region. The optimal simulation was chosen by the user-driven optimization approach because the minimizing weight approach does not consider changes in equivalent strain.

Table 3. Result table for 1st phase parametric optimization. The optimal design scenario is highlighted

No.	D1 (mm)	D2 (mm)	TH (mm)	Max. Deformation (mm)	Mass (g)	Eq. Strain
1	R10	R5	5	0.26	1215	$2.57 \cdot 10^{-4}$
2	R10	R5	4	0.27	1117	$2.71 \cdot 10^{-4}$
3	R10	R5	3	0.28	1020	$2.58 \cdot 10^{-4}$
4	R10	R7	5	0.26	1175	$2.70 \cdot 10^{-4}$
5	R10	R7	4	0.27	1102	$2.67 \cdot 10^{-4}$
6	R10	R7	3	0.28	1009	$2.62 \cdot 10^{-4}$
7	R10	R9	5	0.26	1175	$2.60 \cdot 10^{-4}$
8	R10	R9	4	0.27	1086	$2.61 \cdot 10^{-4}$
9	R10	R9	3	0.28	997	$2.62 \cdot 10^{-4}$
10	R12.5	R5	5	0.26	1183	$2.60 \cdot 10^{-4}$
11	R12.5	R5	4	0.27	1092	$2.72 \cdot 10^{-4}$
12	R12.5	R5	3	0.29	1002	$2.69 \cdot 10^{-4}$
13	R12.5	R7	5	0.26	1165	$2.62 \cdot 10^{-4}$
14	R12.5	R7	4	0.28	1078	$2.53 \cdot 10^{-4}$
15	R12.5	R7	3	0.29	990	$2.73 \cdot 10^{-4}$
16	R12.5	R9	5	0.26	1144	$2.50 \cdot 10^{-4}$
17	R12.5	R9	4	0.27	1061	$2.68 \cdot 10^{-4}$
18	R12.5	R9	3	0.29	978	$2.62 \cdot 10^{-4}$
19	R15	R5	5	0.27	1149	$2.70 \cdot 10^{-4}$
20	R15	R5	4	0.28	1065	$3.08 \cdot 10^{-4}$
21	R15	R5	3	0.29	981	$2.61 \cdot 10^{-4}$
22	R15	R7	5	0.27	1131	$2.59 \cdot 10^{-4}$
23	R15	R7	4	0.28	1051	$2.76 \cdot 10^{-4}$
24	R15	R7	3	0.29	970	$2.62 \cdot 10^{-4}$
25	R15	R9	5	0.27	1110	$3.41 \cdot 10^{-4}$
26	R15	R9	4	0.28	1034	$2.78 \cdot 10^{-4}$
27	R15	R9	3	0.29	958	$2.64 \cdot 10^{-4}$
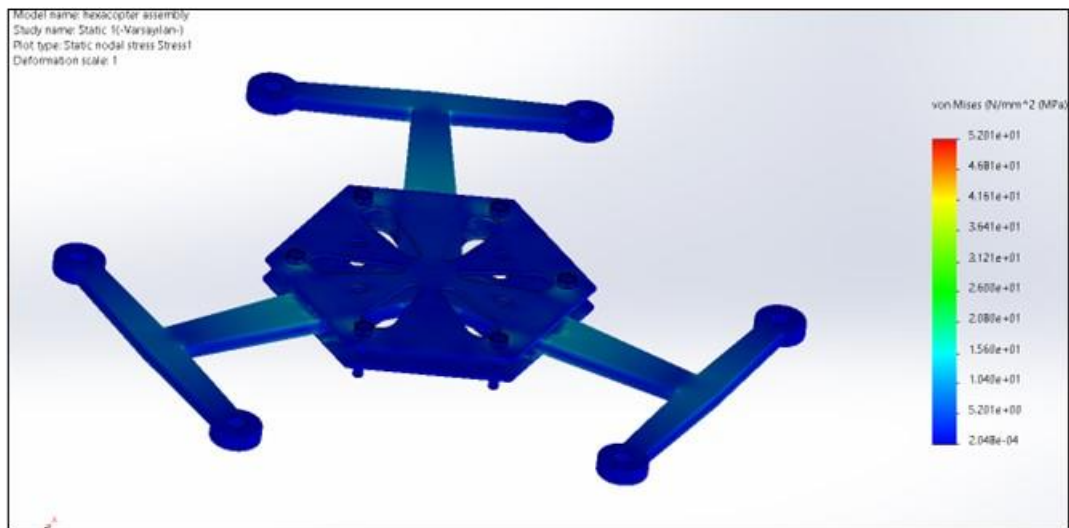
Figure 9. Von Mises stress results for the optimal solution in 1st phase.
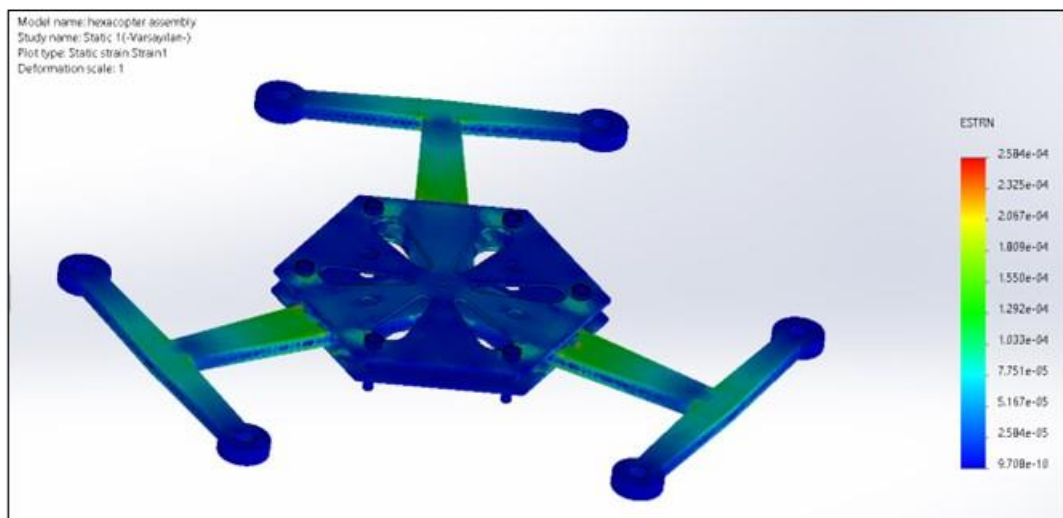
Figure 10. Equivalent strain results for the optimal solution in 1st phase.
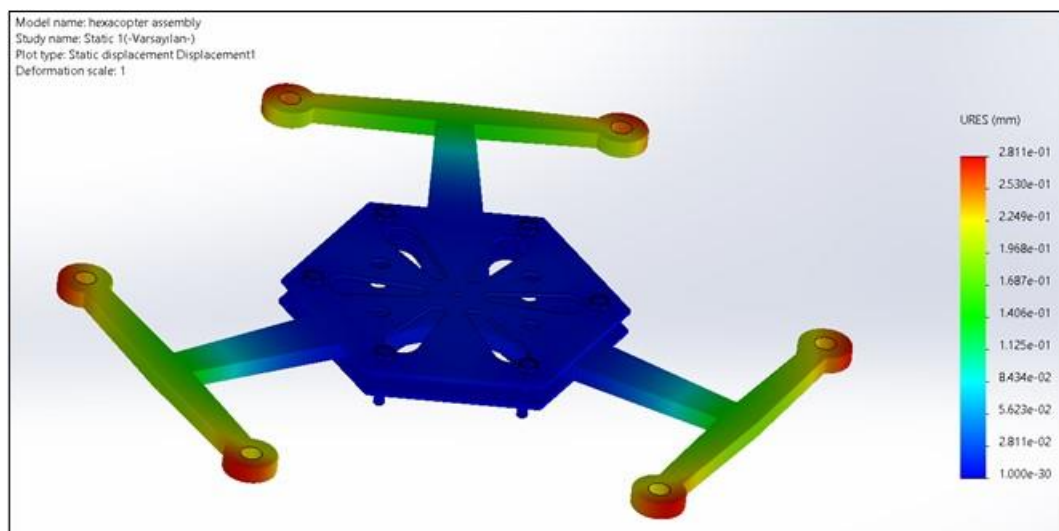
Figure 11. Total deformation results for the optimal solution in 1st phase.
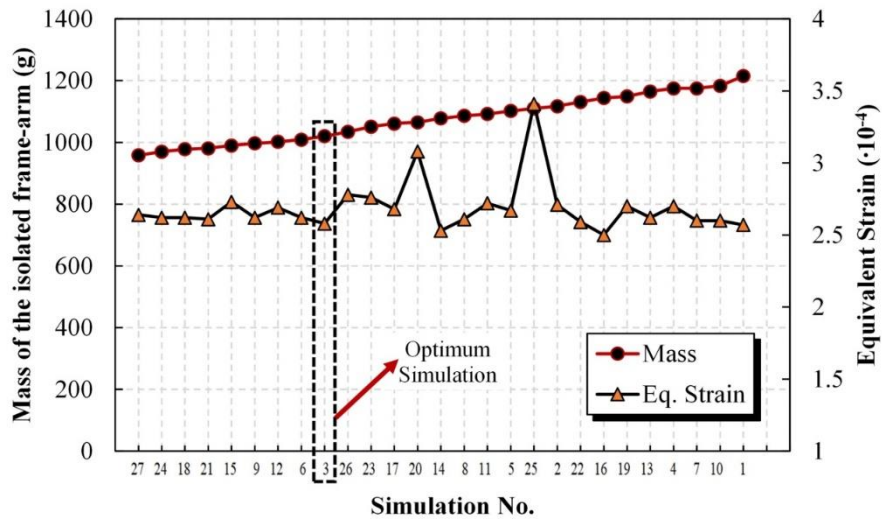
Figure 12. 1st phase graph of mass-equivalent strain where the mass of the frame-arm assembly was sorted in ascending order.

Table 4. Result table for 2nd phase parametric optimization. The optimal design scenario is highlighted

No.	D3 (mm)	L (mm)	Max. Deformation (mm)	Mass (gr)	Eq. Strain
1	R5	20	0.29	976	$2.93 \cdot 10^{-4}$
2	R5	30	0.30	962	$3.29 \cdot 10^{-4}$
3	R5	40	0.32	947	$4.13 \cdot 10^{-4}$
4	R6	20	0.29	970	$3.22 \cdot 10^{-4}$
5	R6	30	0.30	954	$3.53 \cdot 10^{-4}$
6	R6	40	0.33	938	$3.36 \cdot 10^{-4}$
7	R7	20	0.30	963	$3.39 \cdot 10^{-4}$
8	R7	30	0.30	946	$3.29 \cdot 10^{-4}$
9	R7	40	0.35	929	$4.81 \cdot 10^{-4}$

3.4. 2nd Phase of Parametric Optimization

The results of the 2nd phase of parametric optimization are given in Table 4. Similarly, the maximum deformation was nearly 0.3 mm. The maximum Von Mises stress was found approximately 64 MPa, indicating a safe drone design considering the yield strength of the Al 6061-T6 is 275 MPa. The Von Mises stress, equivalent strain, and total deformation results are given in Figure 13, Figure 14, and Figure 15 respectively. A similar user-driven optimization approach leads the designer to choose the optimal simulation as simulation no. 8 as shown in Figure 16. The parameters corresponding to these optimum simulations will lead to the parameter set that will give the optimum result.

As a result, the first and second optimization processes are summarized in Figure 17 where the highest, lowest, and optimal parameters are given. Using parametric optimization, basic hollow geometries on the hexacopter frame are optimized for low weight and high strength. The most important result of this study was the weight reduction of the hexacopter, where the weights of the battery, motors, propellers, and payload are assumed to be constant. Considering the design in Figure 3b, a weight reduction was achieved with the optimized design compared to the fully filled frame. According to the numerical analysis results, the mass information of the sub-assembly in Figure 3b was taken from the SolidWorks mass properties option. Accordingly, based on alternative situations where the frame thickness is 3 mm, 4 mm, and 5 mm; the total mass of the sub-assembly was reduced by 15 %, 18 %, and 20 % respectively. If the change in mass is examined, the mass of the sub-assembly using the 3 mm thick frame design decreased from 1108 g to 946 g; the 4 mm thick one decreased from 1235 g to 1019 g; and the 5 mm thick one decreased from 1361 g to 1092 g. Since the flight time increases as the thrust to mass ratio increases as stated in the previous studies, mass reduction will increase the flight time of the hexacopter in this study (Pollet et al., 2022). In literature, the studies mostly focus on the optimal configuration of multicopters, instead of focusing on the mass reduction of the frame. For instance, in a study conducted by Shelare et al. (2023), the mass optimization of the payload in a hexacopter design by numerical simulations has been investigated. They carried out analyzes at six different payload values while keeping the hexacopter frame weight constant. Based on the maximum stress values obtained in the analysis, they found that the maximum weight that could be used would be 7.5 kg. In this study, unlike the previously mentioned study, the load was assumed to be constant, and the drone frame design was optimized, resulting in a mass reduction of up

to 20 % in the frame design of the drone.

In future studies, it is possible to improve the optimization process, the same hexacopter body can be improved by both parametric and topology optimization for comparison. There are studies in the literature comparing both optimization methods. In one of these studies, three methods which are topology optimization, parametric optimization and simultaneous parametric topology optimizations were compared (Tyflopoulos and Steinert, 2020).
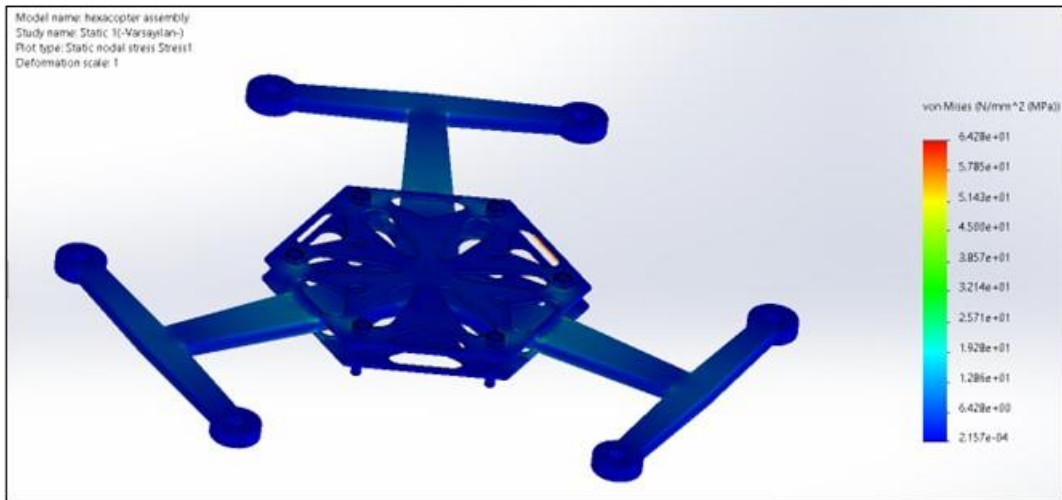
Figure 13. Von Mises stress results for the optimal solution in 2nd phase.
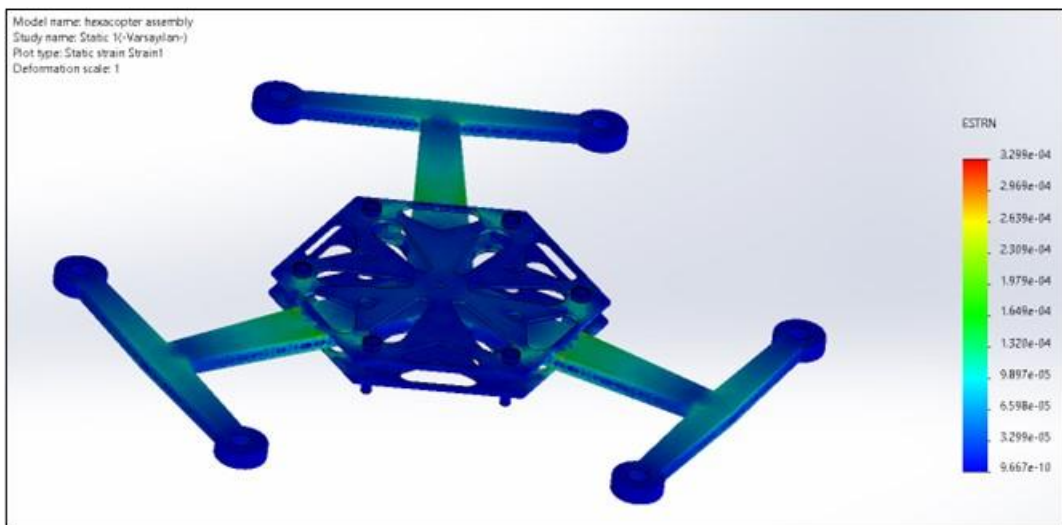
Figure 14. Equivalent strain results for the optimal solution in 2nd phase.
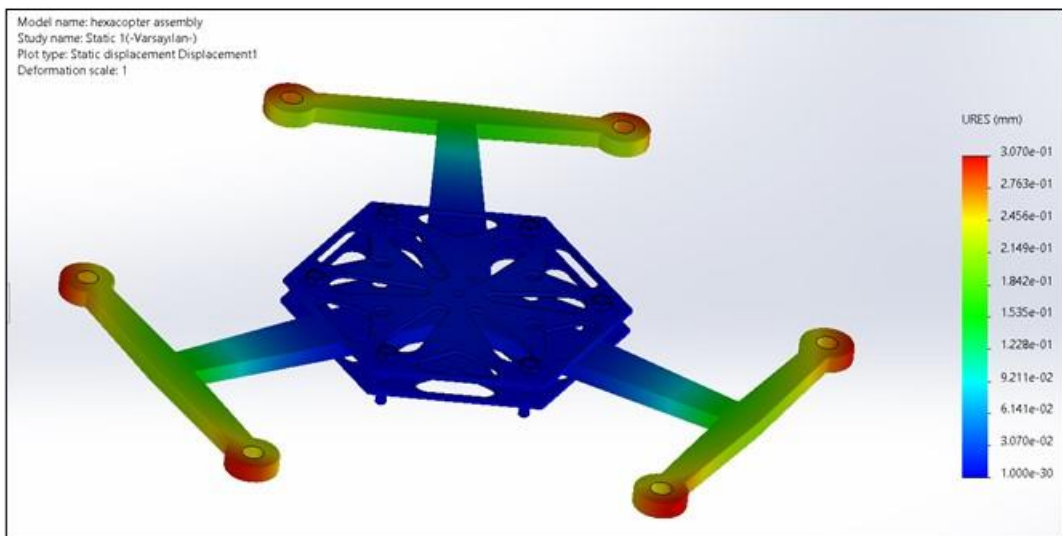
Figure 15. Total deformation results for the optimal solution in 2nd phase.
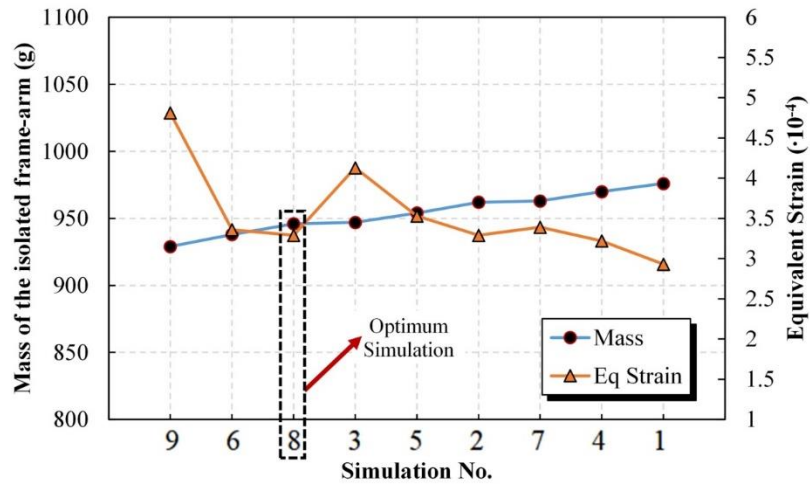
Figure 16. 2nd phase graph of mass-equivalent strain where the mass of the frame-arm assembly was sorted in ascending order.
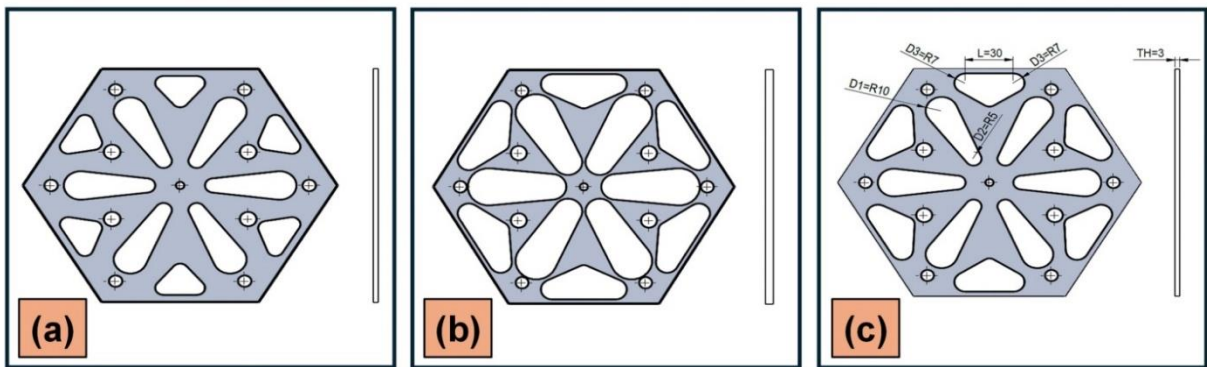
Figure 17. (a) Minimum parameter levels for both 1st phase and 2nd phase, (b) Maximum parameter levels for both 1st phase and 2nd phase, (c) Optimal parameter levels for both 1st phase and 2nd phase with optimal dimensions.

According to the results of the study, the third alternative method, which is simultaneous, was found to be the most efficient optimization method. Therefore, although they are quite different in terms of cost and optimization time, topology optimization and parametric optimization can be seen as methods that positively affect each other in calculations such as mass reduction.

4. Conclusion

A parametric optimization via design study for the essential structural parts of a high payload hexacopter drone was presented. The main load-carrying parts of the hexacopter were isolated and simplified. The payload was 20 kgf, and each propeller had 3.5 kgf lifting capability. The material of the components was Al 6061-T6, primarily used for drone structures. The parametric optimization was performed in two stages. In the first stage, both frames are updated with a slot geometry to decrease the total mass of the drone body. In the second stage, mass was reduced even further. The maximum Von Mises stress was found to be 64 MPa, and the design is safe since the stress was nearly one-quarter of the yield strength. The maximum deformation was also below 0.3 mm with optimal parameters. As a result, a lighter hexacopter structure is achieved by using a design

approach suitable for conventional machining methods. Further studies can be conducted by generating the G-codes using computer-aided manufacturing (CAM) software. This allows a cost comparison between the drone frame made by additive manufacturing and the one designed to be machined using conventional methods for a similar size.

Author Contributions

The percentage of the author(s) contributions is presented below. The author reviewed and approved the final version of the manuscript.

	O.Ö.
C	100
D	100
S	100
DCP	100
DAI	100
L	100
W	100
CR	100
SR	100

C=Concept, D= design, S= supervision, DCP= data collection and/or processing, DAI= data analysis and/or interpretation, L= literature search, W= writing, CR= critical review, SR= submission and revision.

Conflict of Interest

The author declared that there is no conflict of interest.

Ethical Consideration

Ethics committee approval was not required for this study because of there was no study on animals or humans.

Acknowledgements

References

Abdulsalam H. 2021. Mesh sensitivity assessment on 2D and 3D elastic finite element analysis on a compact tension specimen geometry using ABAQUS/CAE software. IOP Conf Ser Earth Environ Sci, 730(1): 012032.

Anweiler S, Piwowarski D. 2017. Multicopter platform prototype for environmental monitoring. J Clean Prod, 155: 204-211.

Aswath M, Raj SJ. 2021. Hexacopter design for carrying a payload for warehouse applications. IOP Conf Ser Mater Sci Eng, 1012(1): 012025.

Azhagan MT, Shanmugam R, Khan S, Lata S. 2023. Design optimization of hexacopter frame using generative design and additive manufacturing. ASME Int Mech Eng Cong Expo, 87608: V003T03A048.

Elouarouar S, Medromi H. 2022. Hexacopter drones overview. 2nd International Conference on Innovative Research in Applied Science, Engineering and Technology, March 3-4, Meknes, Morocco, pp: 1-7.

Fahlstrom PG, Gleason TJ, Sadraey MH. 2022. Introduction to UAV systems. John Wiley & Sons, New York, US, pp: 276.

Hassani V, Mehrabi HA, Ibrahim Z, Ituarte IF. 2021. A Comparison between parametric structural optimization methods and software-based topology optimization of a rectangular sample under tensile load for additive manufacturing processes. Int J Appl Eng Res Appl, 11(2): 37-58.

Ismail KB, Rahim AHA, Zawawi F. 2020. Design and development of heavy-lift hexacopter for heavy payload. J

Transp Eng, 2020: 53-63.

Kumar VA, Sivaguru M, Janaki BR, Eswar KS, Kiran P, Vijayanandh R. 2021. Structural optimization of frame of the multi-rotor unmanned aerial vehicle through computational structural analysis. J Phys Conf, 1849(1): 012004.

MohamedZain AO, Chua H, Yap K, Uthayasurian P, Jiehan T. 2022. Novel drone design using an optimization software with 3D model, simulation, and fabrication in drone systems research. Drones, 6(4): 97.

Najiha MS, Rahman MM, Kadirgama K. 2015. Machining performance of aluminum alloy 6061-T6 on surface finish using minimum quantity lubrication. Int J Automot Mech Eng, 11: 2699.

Namlu RH, Yılmaz OD, Kilic SE, Cetin B. 2019. Investigating the effect of cutting conditions on machining performance of Al 6061-T6 alloy. 10th Int. Congr. Machining, November 7-9, Antalya, Türkiye, pp: 293-304.

Pollet F, Delbecq S, Budinger M, Moschetta JM, Liscouët J. 2022. A common framework for the design optimization of fixed-wing, multicopter and VTOL UAV configurations. 33rd Congress of the International Council of the Aeronautical Sciences, September 4-9, Stockholm, Sweden, pp: 1-18.

Radakovic D. 2021. Bridging nature-art-engineering with generative design. In Experimental and Computational Investigations in Engineering: Proceedings of the International Conference of Experimental and Numerical Investigations and New Technologies, CNNTech 2020. Springer International Publishing, pp: 326-343.

Ramesh PS, Jeyan JML. 2022. Comparative analysis of fixed-wing, rotary-wing and hybrid mini unmanned aircraft systems (UAS) from the applications perspective. INCAS Bull, 14(1): 137-151.

Sharma P, Selvakumar A. 2018. Conceptual design and non-linear analysis of triphibian drone. Procedia Comput Sci, 133: 448-455.

Shelare S, Belkhode P, Nikam KC, Yelamasetti B, Gajbhiye T. 2023. A payload based detail study on design and simulation of hexacopter drone. Int J Interact Des Manuf, 2023: 1-18.

Sreeramoju S, Rao MS. 2023. Design and analysis of quad copter chassis using shape optimization technique. Int J Res Appl Sci Eng Technol, 11(3): 1569-1575.

Sundararaj S, Dharsan K, Ganeshraman J, Rajarajeswari D. 2021. Structural and modal analysis of hybrid low altitude self-sustainable surveillance drone technology frame. Mater Today Proc, 37: 409-418.

Țura DM, Zaharia SM. 2023. Design, additive manufacturing and testing of a quadcopter drone. Land Forces Acad, 28(3): 245-254.

Tyflopoulos E, Steinert M. 2020. Topology and parametric optimization-based design processes for lightweight structures. Appl Sci, 10(13): 4496.

Tyflopoulos E, Steinert M. 2022. A comparative study of the application of different commercial software for topology optimization. Appl Sci, 12(2): 611.

Urdea M. 2021. Stress and vibration analysis of a drone. IOP Conf Ser Mater Sci Eng, 1009(1): 012059.

Wu YT, Qin Z, Eizad A, Lyu SK. 2021. Numerical investigation of the mechanical component design of a hexacopter drone for real-time fine dust monitoring. J Mech Sci Technol, 35: 3101-3111.

Yemle S, Durgude Y, Kondhalkar G, Pol K. 2019. Design & analysis of multi-frame for octo & quad copter drones. Int Res J Eng Technol, 6(06): 2395-0056.

COMPARATIVE ANALYSIS OF LSTM AND ARIMA MODELS IN STOCK PRICE PREDICTION: A TECHNOLOGY COMPANY EXAMPLE

Yasin KIRELLİ[1]*

[1]*Kutahya Dumlupınar University, Management Information Systems, 43020, Kütahya, Türkiye*

Abstract: Stock price forecasting has been an important area of interest for economists and computer scientists. In addition to traditional statistical methods, advanced artificial intelligence techniques such as machine learning can stand out with their ability to process complex data sets and adapt to historical data. In recent years, hybrid models combining deep learning and time series methods have demonstrated superior performance in stock selection and portfolio optimization. This study comparatively analyses the performance of LSTM and ARIMA models in time series forecasting. In the study, the stock prices of Oracle company are predicted using two different models, LSTM and ARIMA. Model performance is evaluated using metrics like MSE, MAE, RMSE, and MAPE. Both models have been found to be successful in different metrics. The LSTM model has lower error values; meanwhile, the ARIMA model produced proportionally more accurate forecasts. The study concludes that given the potential offered by deep learning, models such as LSTM are essential for time series forecasting. The flexibility of deep learning allows the development of customized models for different data types and time series problems.

Keywords: LSTM, ARIMA, Time series, Stock price forecasting

1. Introduction

Stock market price prediction is a research topic not only for economists but also for computer scientists, which is why statistical methods and machine learning are used to build a prediction model. Considering 2019 data, the global stock market is known to be more than 85 trillion dollars. Investors can use simple statistical methods to predict price changes to increase their income, but these methods could be faster due to the high volume of transactions and rapid changes. Advanced artificial intelligence methods are often preferred and used (Gandhmal and Kumar, 2019; Shah et al., 2019; Kanavos et al., 2020; Nabipour et al., 2020). The ability of the methods to predict with a high degree of accuracy is an important constraint. Therefore, machine learning methods are widely preferred. The most frequently preferred methods are logistic regression, linear regression, support vector machines, and artificial neural networks. It provides the advantage of creating strong, stable models for multidimensional problems and adaptability to historical data (Lu et al., 2021). In general, the stock market has a structure that combines high risk and high return. In this regard, investors aim to achieve maximum gains through technical and fundamental analysis methods. Fundamental analysis generally derives insights by considering the balance sheet analysis of companies,

competitive advantages, or macroeconomic developments. In technical analysis, price inferences are carried out with the assistance of indicators such as Moving Average Convergence Divergence (MACD), Momentum, Stochastic Oscillator with Moving Averages (KDJ), Relative Strength Index (RSI), and Moving Average (MA) (Rouf et al., 2021). Stock exchanges, where financial transactions take place, are regulated by a set of rules of governments and institutions to protect investors and companies. Stock prices operate according to the principles of supply and demand, and performance indicators (KPIs) depend on the rise and fall of prices, as shown in Table 1 (Bustos and Pomares-Quimbaya, 2020; Nti et al., 2020; Sarvesh et al., 2021).

Forecasting models for stock prices have attracted increased attention in recent years. Due to the financial opportunity provided, several papers have recently been published that use deep learning and time series methods to produce robust forecasting results. With the increasing power of today's machines and the improvement of computational capability, better results are being achieved for challenging problems of such complexity (Agrawal et al., 2013; Strader et al., 2020; Kumbure et al., 2022; Sheng et al., 2022). Singh et al. (2023) proposes a hybrid CNN-LSTM model combining deep learning for stock selection and the mean-variance model for portfolio

optimization. Benchmarks on Indian stock market analysis show that the model outperforms single models and other compared strategies. The results suggest that the hybrid CNN-LSTM approach can be an effective tool in portfolio management (Singh et al., 2023). Choi et al. (2023) propose a new method called "Hybrid Information Mixing Module," using deep learning and news data to predict stock price movements. It aims to make more accurate predictions by combining price and text data features and modeling their multimodal interactions. The model is tested on a high volatility stock market simulation, successfully validated, and performs better than other methods (Choi et al., 2023). Jadhav et al. (2021) proposes a new model using GAN architecture to predict stock market prices. The model consists of a hybrid generator and MLP parser using Naive Bayes for sentiment analysis from financial news and LSTM for prediction. The system predicts stock values using financial data and performs sentiment analysis on financial news (Jadhav et al., 2021). Singh et al. (2022) proposed a new investment decision support system by comparing ARIMAX, Prophet, LSTM, and pairwise LSTM models using historical stock market data. The model aims to maximize profit and minimize loss by optimizing investment decisions during crises such as COVID-19 with 98.60% and 96.97% accuracy (Singh et al., 2022). Choy et al. (2021) compared various time series algorithms to predict stock market prices: ARIMA, LSTM, SARIMA, Holt Winter, and Prophet. The research has been conducted on Malaysia stock market data covering six different sectors. The results show that the ARIMA and LSTM models achieve lower error rates than the others. Moreover, ARIMA model is more successful than LSTM especially in trend forecasting. This study suggests that the ARIMA model may be suitable for short-term stock price forecasting (Choy et al., 2021; Singh et al., 2022). Sisodia et al. (2022) propose a Deep Learning (DL) based Long Short-Term Memory (LSTM) algorithm to predict stock

market price movements. The research develops a model using ten years of historical price information of the NIFTY 50 index from the National Stock Exchange of India (NSE) data. After normalization, the training and testing process is performed, and an accuracy rate of 83.88% is obtained. These results show that the proposed model has the potential to predict stock market price movements (Sisodia et al., 2022). Ruan et al. (2020) propose a new method to predict sudden stock price changes, especially during unexpected events such as COVID-19. The study uses ARIMA and LSTM models to forecast individual stocks and the entire market. In addition, social media data reflecting investor psychology are also integrated into the models. The 98% average forecast accuracy obtained using the 2016-2020 period data of 100 companies in the study provides promising results for improving existing forecasting methods (Ruan et al., 2020).

Table 1. Key performance indicators

Indicator Name	Indicator Description
Open	Opening price
Close	End-of-day closing price
Low	Intraday low price
High	Intraday high price
Volume	Total number of stocks traded during the trading session

Using the Web of Science (WOS) database, the methods that have been used in stock market forecasting searched between 2012 and 2024, and the word cloud is shown in Figure 1.a. and Figure 1.b. obtained. LSTM and ARIMA models, which are also the subject of this study, have been explicitly analyzed, and it is clear from Figure 1.a. and Figure 1.b that the LSTM deep learning approach is the subject of more research area than the ARIMA model.
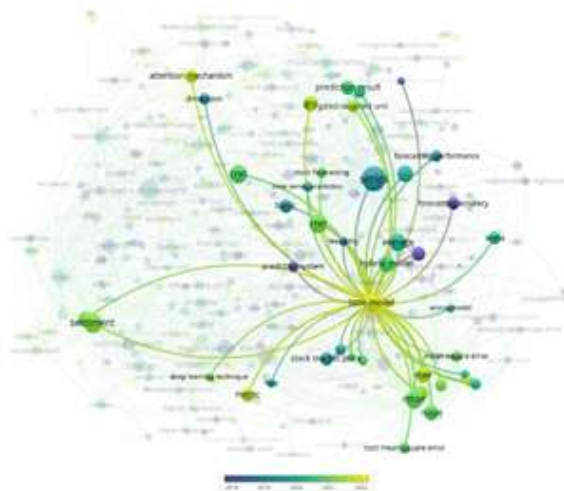
a. LSTM Bibliometric Analysis
b. Arima Bibliometric Analysis
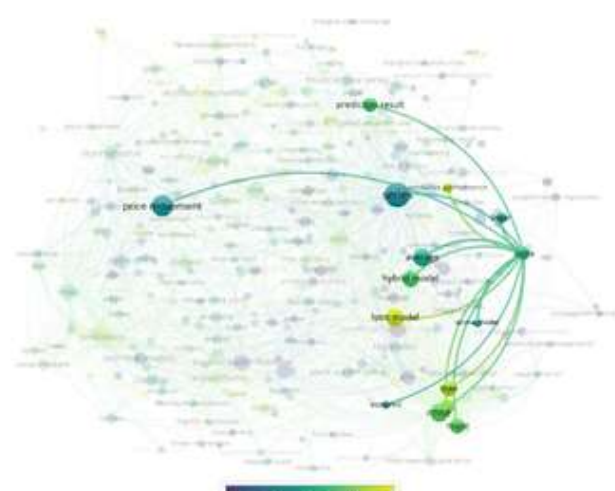
Figure 1. Bibliometric analysis of stock market forecasting methods.

2. Materials and Methods

This study constructs two models to forecast Oracle stock prices: LSTM and ARIMA. The objective is to evaluate these models' performance and ease of use and provide insights for financial analysts and investors. The background and basic principles of the LSTM and ARIMA models are explained in the first stage of the research. Then, both models are applied to daily data of Oracle stock prices, and their performance is compared using metrics such as MSE, MAE, RMSE, and MAPE. The results reveal the strengths and weaknesses of each model and demonstrate their success in predicting stock prices.

2.1. Long Short Term Memory (LSTM)

Long Short Term Memory (LSTM) networks are a specialized deep learning method, a Recurrent Neural Networks (RNN) sub-branch. It can store long-term dependencies and can maintain dependencies. Unlike RNNs, LSTM networks also store long-term dependencies, making them better suited to complex problems such as time series (Lipton et al., 2015; Sherstinsky, 2020; Van Houdt et al., 2020; Yang et al., 2020). In LSTM architecture, information is stored in cells, and the data's meaning can be interpreted according to the condition. An advantage of LSTMs is that they have a forget gate mechanism. Thus, it also solves the problem of gradient loss (Staudemeyer and Morris, 2019). This structure provides the advantage of giving successful results in time series or lengthy texts.

As shown in Figure 2, an LSTM network has three main structures: the forget gate, the input gate, and the output gate.
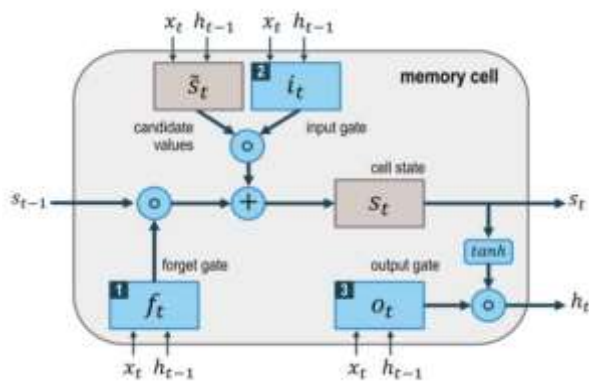
Figure 2. LSTM network.

The cell state stores past information and uses it for future prediction. The forget gate determines which information from the previous cell will be forgotten. The input gate decides which information is sent to the 'cell state'. The output gate decides which information from the 'cell state' will be output. According to equations 1-5, x_t is the input vector, h_t is the output vector, f_t is the forget vector, and c_t is the cell state vector. i_t and o_t are the input and output gates, respectively. W and b are the weights and bayes values (Ojo et al., 2019).

$$f_t = \sigma(W_f[h_{t-1}, x_t] + b_f) \tag{1}$$

$$i_t = \sigma(W_i[h_{t-1}, x_t] + b_i) \tag{2}$$

$$c_t = \tanh(W_c[h_{t-1}, x_t] + b_c) \tag{3}$$

$$o_t = sigma(W_o[h_{t-1}, x_t] + b_o) \tag{4}$$

$$h_t = sigma * \tanh(c_t) \tag{5}$$

2.2. Autocorrelated Integrated Moving Average (ARIMA)

Autocorrelated Integrated Moving Average (ARIMA) is a statistical model. It is used as a method for analyzing and forecasting time series. The ARIMA model consists of autocorrelation (AR), integration (I), and moving average (MA) (Khan and Alghulaiakh, 2020). Autocorrelation is the relationship between past and present data in a time series, and its effect is measured. Integration refers to stationarity in a time series. It is provided by taking the difference from the time series' previous values. Moving average refers to random variation in a time series. This method converts time series to stationary through differencing and is called a linear stochastic model. This is generally expressed as ARIMA(p,d,q) (Kontopoulou et al., 2023; Kumar and Vanajakshi, 2015). In the model, d refers to the degree of differencing, and p and d refer to the autoregressive and moving average, respectively.

2.3. Proposed Models and Implementations

2.3.1. Exploratory data analysis

In the study, Oracle Company, which is listed on the Nasdaq Stock Exchange, is analyzed. The Nasdaq Stock Exchange is a New York-based American Stock Exchange and is among the most active in volume. It is traded as the second most active area after the New York Stock Exchange (Oracle Corporation (ORCL), 2024) . The data set in the study has been obtained from the platform where the current trading prices of the companies listed on the Nasdaq official website are also available. The data set includes the opening and closing price, the highest and lowest price, and volume information of the symbol on a historical basis. The day-based closing price, which users mostly prefer, is evaluated in the training set. Table 2 shows a view of the data set derived for the prediction model.

Table 2. Dataset sample view

Date	Close/Last	Volume	Open	High	Low
01/29/2024	$113.75	7014424	$114.19	$114.59	$113.01
01/26/2024	$114.64	5541900	$114.64	$115.48	$114.2746
01/25/2024	$115.00	8877205	$114.89	$116.18	$114.35
01/24/2024	$114.31	11702700	$113.42	$115.42	$113.33
01/23/2024	$111.83	9185921	$110.29	$112.68	$109.56

2.3.2. LSTM model implementation

The analysis has been performed with a total of 2516 sample data for ten years between February 2014 and February 2024 of the company considered in the study. As shown in Figure 3, the company's time series is visualized according to the closing price and date values. The last year's data (after 2023) is divided into test data (10%), and up until 2023, it is divided into training data. In the first part of the study, the proposed LSTM and ARIMA models are used for forecasting in the second part. The last section gives the forecasting performance comparisons of the two models. This study evaluates the prediction results with the proposed LSTM model; Python programming language version 3.10 is preferred. The model has been designed with the TensorFlow deep learning library. According to the proposed model, the training and test data have been normalized with the Min-Max scaler method in the pre-processing step, and accordingly, the data have been scaled between 0-1. The model and hyperparameters are shown in Table 3.

The loss value of the model result is close to zero, and the validation loss value range is observed in the range of 0 - 0.002. The time series graph comparing the prediction values generated according to the proposed model and the actual values of the test set is shown in Figure 4.

Figure 3. Time series by training and test data.

Table 3. Model and hyperparameter values

Hyperarametres	Values	Model		
Scaling	Min-Max Scaler	Model: "sequential"		
		Layer (type)	Output Shape	Param
Optimiser	Adam	==		
		lstm (LSTM)	(None, 100, 50)	10400
Epoch	100	_____		
		lstm_1 (LSTM)	(None, 100, 50)	20200
Batch Size	64	_____		
		lstm_2 (LSTM)	(None, 50)	20200
		_____		
		dense (Dense)	(None, 1)	51
		Total params: 50,851		
		Trainable params: 50,851		

Figure 4. LSTM Model test set and prediction values comparison time series plot.

2.3.3. ARIMA model implementation

As the second method created in the study, the ARIMA model aims to observe the forecasting performance by dividing the data set into training and test data sets at the same rate. According to the Akaike Information Criterion (AIC) criterion, in the stepwise search for the best ARIMA model, the lowest AIC value has been obtained with the ARIMA (0, 1, 1) model, as shown in Table 4. According to this model, past values (p=0) do not directly affect current values. It is assumed that the data are initially non-stationary (d=1) and have a moving average (q=1).

According to Figure 5, the time series is distributed between -8 and 11. Most of the residuals are concentrated around 0, suggesting that the model consistently fits the data. The residuals appear randomly distributed on the horizontal axis, concluding that the model has no autoregressive error. It is observed that the ARIMA (0, 1, 1) model is generally compatible with the time series data. As a result of the model training, the time series and forecast region evaluation graph of the 277-day test data from 2023 is observed, as shown in Figure 6.
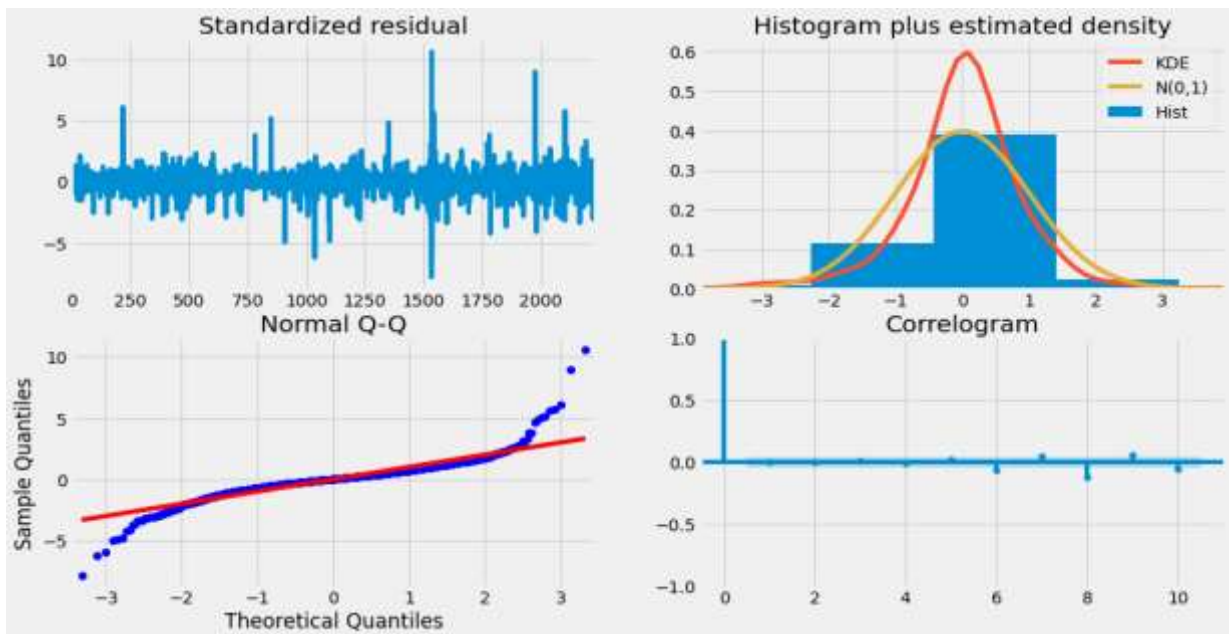
Figure 5. Standardised residual graph of data.
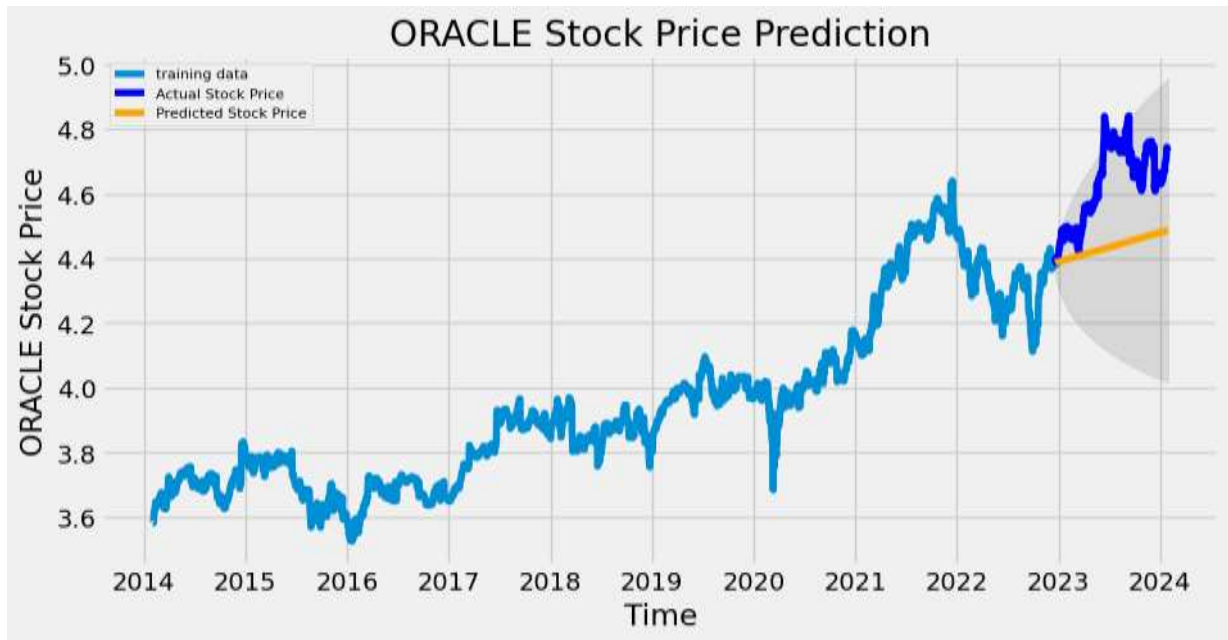
Figure 6. ARIMA model prediction.

Tablo 4. Stepwise search to minimize AIC

ARIMA(0,1,0)	AIC = -12070.156
ARIMA(1,1,0)	AIC = -12099.264
ARIMA(0,1,1)	AIC = -12099.390
ARIMA(0,1,0)	AIC = -12071.055
ARIMA(1,1,1)	AIC = -12097.461
ARIMA(0,1,2)	AIC = -12097.461
ARIMA(1,1,2)	AIC = -12095.459
ARIMA(0,1,1)	AIC = -12099.961
ARIMA(1,1,1)	AIC = -12098.046
ARIMA(0,1,2)	AIC = -12098.049
ARIMA(1,1,0)	AIC = -12099.874
ARIMA(1,1,2)	AIC = -12096.046

3. Results and Discussion

Different metrics can be used to evaluate the performance of time series forecasting models, the most common of which are:

Mean Squared Error (MSE): Expressed as the mean squared error, it is the average sum of squares between the predicted ($\hat{y}$) and actual (y_i) values as equation 6.

$$MSE = \frac{1}{N}\sum_{i=1}^{N}(y_i - \hat{y})^2 \tag{6}$$

Mean Absolute Error (MAE): Refers to the mean of the absolute value between the predicted actual values as equation 7.

$$MAE = \frac{1}{N}\sum_{i=1}^{N}|y_i - \hat{y}| \tag{7}$$

Root Mean Squared Error (RMSE): The square root of the root mean squared error is a better representation of the scale of the amount of error as equation 8.

$$RMSE = \sqrt{\frac{1}{N}\sum_{i=1}^{N}(y_i - \hat{y})^2} \tag{8}$$

Mean Absolute Percentage Error (MAPE) Refers to the mean absolute percentage between the predicted and actual values as equation 9.

$$MAPE = \frac{1}{N}\sum_{i=1}^{N}\frac{|y_i - \hat{y}_i|}{y_i} \tag{9}$$

The comparison of metric values for the two models included in the study is observed in Table 5.

Table 5. LSTM and ARIMA model performance metrics

	MSE	MAE	RMSE	MAPE
LSTM Model	0.0374	0.1700	0.1936	0.1855
ARIMA Model	0.0488	0.1968	0.2211	0.0419

According to the comparative result metrics, both models have low MSE values, which supports the consistency of the models. The LSTM model has a lower MAE value than the ARIMA model, which means that the LSTM model makes less error on average. The results show that the LSTM model tends to produce estimates with less error and variation than the ARIMA model. The study compares the performance of LSTM and ARIMA models in time

series forecasting. The findings show that both models stand out in specific metrics. The choice of model depends on the prioritized metrics and the dataset's characteristics. The LSTM model generally produces fewer error and variation forecasts than the ARIMA model. In contrast, the ARIMA model tends to produce proportionally more accurate forecasts. The results of this study have important implications for investors. Deep learning models such as LSTM, improve decision-making processes for investors by reducing errors in price prediction. Such strategic approaches are also an indicator for ensuring risk management. Advanced forecasting models also provide portfolio optimization, conscious decision-making capabilities and competitive advantage for investors. Given the potential offered by deep learning, models such as the LSTM are essential for future time series forecasting. Future research could focus on comparing the performance of LSTM and ARIMA models on different data sets and combining them into a hybrid model. Developing advanced models for time series forecasting is also an essential area of research. Consequently, it is inferred that both LSTM and ARIMA models are practical tools for time series forecasting based on the literature. The flexibility of deep learning allows the development of customized models for different data types and time series problems.

Author Contributions

The percentage of the author(s) contributions is presented below. The author reviewed and approved the final version of the manuscript.

	Y.K.
C	100
D	100
S	100
DCP	100
DAI	100
L	100
W	100
CR	100
SR	100
PM	100

C=Concept, D= design, S= supervision, DCP= data collection and/or processing, DAI= data analysis and/or interpretation, L= literature search, W= writing, CR= critical review, SR= submission and revision, PM= project management.

Conflict of Interest

The author declared that there is no conflict of interest.

Ethical Consideration

Ethics committee approval was not required for this study because of there was no study on animals or humans.

References

Agrawal JG, Chourasia V, Mittra A. 2013. State-of-the-art in stock prediction techniques. Int J Adv Res Electr Electron Instrum Eng, 2(4): 1360-1366.

Bustos O, Quimbaya A. 2020. Stock market movement forecast: A systematic review. Expert Syst Appl, 156: 113464.

Choi J, Yoo S, Zhou X, Kim Y. 2023. Hybrid information mixing module for stock movement prediction. IEEE Access, 11: 28781-28790.

Choy YT, Hoo MH, Khor KC. 2021. Price prediction using time-series algorithms for stocks listed on Bursa Malaysia. In: 2nd International Conference on Artificial Intelligence and Data Sciences, 8-9 September, Piscataway, New Jersey, USA, pp: 1-5.

Gandhmal DP, Kumar K. 2019. Systematic analysis and review of stock market prediction techniques. Comput Sci Rev, 34: 100190.

Jadhav R, Sinha S, Wattamwar S, Kosamkar P. 2021. Leveraging Market Sentiment for Stock Price Prediction using GAN. In: 2nd Global Conference for Advancement in Technology, 01-03 October, 2021, Bangalore, India, pp: 1-6.

Kanavos A, Vonitsanos G, Mohasseb A, Mylonas P. 2020. An entropy-based evaluation for sentiment analysis of stock market prices using Twitter data. In: 15th International Workshop on Semantic and Social Media Adaptation and Personalization, 29-30 October Zakynthos, Greece, pp: 1-7.

Khan S, Alghulaiakh H. 2020. ARIMA model for accurate time series stocks forecasting. Int J Adv Comput Sci Appl, 11(7).

Kontopoulou V, Panagopoulos AD, Kakkos I, Matsopoulos GK. 2023. A review of ARIMA vs. machine learning approaches for time series forecasting in data driven networks. Future Int, 15(8): 255.

Kumar SV, Vanajakshi L. 2015. Short-term traffic flow prediction using seasonal ARIMA model with limited input data. Eur Transp Res Rev, 7: 1-9.

Kumbure MM, Lohrmann C, Luukka P, Porras J. 2022. Machine learning techniques and data for stock market forecasting: A literature review. Expert Syst Appl, 197: 116659.

Lipton ZC, Kale DC, Elkan C, Wetzel R. 2015. Learning to diagnose with LSTM recurrent neural networks. ArXiv, 2015: 1511.

Lu W, Ge W, Li R, Yang L. 2021. A Comparative Study on the Individual Stock Price Prediction with the Application of Neural Network Models. In: International Conference on Computer Engineering and Artificial Intelligence, 27-29 August, Shanghai, China, pp: 235-238.

Nabipour M, Nayyeri P, Jabani H, Mosavi A, Salwana E. 2020. Deep learning for stock market prediction. Entropy, 22(8): 840.

Nti IK, Adekoya AF, Weyori BA. 2020. A systematic review of fundamental and technical analysis of stock market predictions. Artif Intell Rev, 53(4): 3007-3057.

Ojo SO, Owolawi PA, Mphahlele M, Adisa JA. 2019. Stock market behaviour prediction using stacked LSTM networks. In: International Multidisciplinary Information Technology and Engineering Conference, 21-22 November, Vanderbijlpark, South Africa, pp: 1-5.

Oracle Corporation Stock Historical Prices & Data Yahoo Finance. URL: https://finance.yahoo.com/quote/ORCL/history (accessed date: January 29, 2024).

Rouf N, Malik MB, Arif T, Sharma S, Singh S, Aich S, Kim HC. 2021. Stock market prediction using machine learning techniques: a decade survey on methodologies, recent developments, and future directions. Electronics, 10(21): 2717.

Ruan J, Wu W, Luo J. 2020. Stock Price Prediction Under

Anomalous Circumstances. In: IEEE International Conference on Big Data, pp: 4787-4794.

Sarvesh S, Sidharth RV, Vaishnav V, Thangakumar J, Sathyalakshmi S. 2021. A hybrid model for stock price prediction using machine learning techniques with CNN. In: 5th International Conference on Information Systems and Computer Networks, pp: 1-6.

Shah D, Isah H, Zulkernine F. 2019. Stock market analysis: A review and taxonomy of prediction techniques. Int J Financ Stud, 7(2): 26.

Sheng Y, Fu K, Wang L. 2022. A PCA-LSTM Model for Stock Index Forecasting: A Case Study in Shanghai Composite Index. In: 7th International Conference on Cloud Computing and Big Data Analytics, pp: 412-417.

Sherstinsky A. 2020. Fundamentals of recurrent neural network (RNN) and long short-term memory (LSTM) network. Physica D, 404: 132306.

Singh A, Bansal A, Nair A, Kaushal A. 2022. Predictive Analytics of Stock Market as a Time Series. In: 4th International Conference on Advances in Computing, Communication Control and Networking, pp: 770-777.

Singh P, Jha M, Sharaf M, El-Meligy MA, Gadekallu TR. 2023. Harnessing a Hybrid CNN-LSTM Model for Portfolio Performance: A Case Study on Stock Selection and Optimization. IEEE Access, 11: 104000-104015.

Sisodia PS, Gupta A, Kumar Y, Ameta GK. 2022. Stock market analysis and prediction for NIFTY50 using LSTM Deep Learning Approach. In: 2nd international conference on innovative practices in technology and management, pp: 156-161.

Staudemeyer RC, Morris ER. 2019. Understanding LSTM a tutorial into long short-term memory recurrent neural networks, ArXiv, 2019: 1909.

Strader TJ, Rozycki JJ, Root TH, Huang YHJ. 2020. Machine learning stock market prediction studies: review and research directions. J Int Technol Inf Manage, 28(4): 63-83.

Van Houdt G, Mosquera C, Nápoles G. 2020. A review on the long short-term memory model. Artif Intell Rev, 53(8): 5929-5955.

Yang S, Yu X, Zhou Y. 2020. Lstm and gru neural network performance comparison study: Taking yelp review dataset as an example. In: International workshop on electronic communication and artificial intelligence, pp: 98-101.

Black Sea Journal of Engineering and Science

PREPARATION AND IN VITRO CHARACTERIZATION OF CARBAMAZEPINE-LOADED CHITOSAN-COATED/UNCOATED PLGA AND ZEIN NANOPARTICLES

Afife Büşra UĞUR KAPLAN[1], Meltem ÇETİN[1]*

[1]*Atatürk University, Faculty of Pharmacy, Department of Pharmaceutical Technology, 25240, Erzurum, Türkiye*

Abstract: The aim of this study is to prepare CBZ-loaded chitosan (Ch)- coated/uncoated poly(lactic-co-glycolic acid) (PLGA) and Zein (using 20 mg or 40 mg Zein) nanoparticles (CBZ-PLGA-Zein-NPs or CBZ-PLGA-Zein-Ch-NPs) and to characterize (Particle size, PDI, zeta potential, percent encapsulation efficiency (EE%), FT-IR, DSC and XRD analyzes, and *in vitro* release study) them *in vitro*. These nanoparticles were prepared using a modified emulsification-solvent evaporation method. The particle sizes of CBZ-PLGA-Zein(20)-NPs, CBZ-PLGA-Zein(40)-NPs and CBZ-PLGA-Zein(20)-Ch-NPs were found to be about 222 nm, 245 nm and 221 nm, respectively. The PDI value of all NP formulations was below 0.3. This indicates a narrow particle size distribution. The EE% values of CBZ-PLGA-Zein(20)-NPs, CBZ-PLGA-Zein(40)-NPs and CBZ-PLGA-Zein(20)-Ch-NPs were determined as about 64%, 56% and 62%, respectively. The coating of the optimum formulation (containing 20 mg Zein) with chitosan did not lead to a significant difference in the particle size and EE% value of this formulation (P>0.05). A sustained release of CBZ from all prepared NPs formulations was achieved until 48th h. In conclusion, CBZ-PLGA-Zein(20 mg or 40 mg)-NPs and CBZ-PLGA-Zein(20 mg)-Ch-NPs were successfully prepared and characterized *in vitro*.

Keywords: Epilepsy, Chitosan, Nanoparticles, PLGA, Zein

*Corresponding author: Atatürk University, Faculty of Pharmacy, Department of Pharmaceutical Technology, 25240, Erzurum, Türkiye
E mail: melcetin@atauni.edu.tr (M. ÇETİN)
Afife Büsra UĞUR KAPLAN   https://orcid.org/0000-0003-2222-8789
Meltem ÇETİN   https://orcid.org/0000-0003-4009-2432

1. Introduction

Epilepsy, which is a heterogeneous disorder characterized by epileptic syndromes, variable prognosis and diverse etiologies, affects around 65 million people worldwide and has many causes, each reflecting underlying brain dysfunction. Epileptic seizures, defined as the temporary occurrence of signs and/or symptoms caused by excessive and abnormal or synchronous neuronal brain activity, are quite common and often result in bodily injuries such as burns, fractures, and concussions (Stafstrom and Carmant, 2015; Kanner and Bicchi, 2022; Manole et al, 2023). Types of epilepsy are classified as generalized, focal (these are the most common), combined focal and generalized and unknown (Devinsky et al., 2018; Sarmast et al., 2020; Kanner and Bicchi, 2022). Surgery, vagus nerve stimulation, a special diet (ketogenic diet) and the use of antiseizure drugs are treatment approaches for epilepsy (Green et al., 2020). Epileptic seizures require long-term use of anti-seizure drugs due to their recurring nature. However, long-term exposure of the central nervous system to these drugs leads to adverse effects such as impairment of liver and kidney functions, psychiatric problems and cognitive impairment. In addition, pharmacotherapy has limited efficacy due to blood-brain barrier, untimely medication

and drug-resistant epilepsy (Wu et al., 2022). In drug-resistant epilepsy, seizures persist despite the use (at effective daily doses) of at least two syndrome-adapted antiseizure medications, and its prevalence is approximately 30% (Guery and Rheims, 2021). With appropriate use of antiseizure drugs, seizure control is achieved in approximately 70% of cases (Ulamek-Koziol et al., 2019; WHO, 2024).

Carbamazepine (CBZ), used for epilepsy management and treatment, is a sodium channel blocker that inhibits action potential generation and causes a decrease in synaptic transmission. It is also approved for use in the treatment of trigeminal neuralgia and acute manic and mixed episodes (associated with bipolar *I* disorder*) (*Lo, 2014; Maan et al., 2024)*.* CBZ is a Class II (Biopharmaceutics Classification System) drug with high permeability and low solubility. Therefore, its low solubility in water and dissolution rate are the determining factors for its oral bioavailability (Uzunović et al., 2010). Moreover, it is metabolized in the liver and cytochrome P450 3A4 is the main isoform responsible for CBZ-10,11-epoxide metabolite formation (Pearce et al., 2008; Maan et al., 2024). The most common side effects associated with CBZ use are dizziness, vomiting, nausea, ataxia and drowsiness. Rarely, it causes a few

serious skin reactions (Maan et al., 2024). In the literature, nano-sized drug delivery systems have been prepared to increase the solubility of CBZ, enhance its therapeutic efficacy, and reduce their potential adverse effects (Scioli Montoto et al., 2018; Zybina et al., 2018; Qushawy et al., 2019; Kandilli et al., 2020; Ugur Kaplan et. al., 2023).

Our aim was to prepare CBZ-loaded chitosan-uncoated/coated poly(lactic-*co*-glycolic) acid (PLGA) and Zein (Z) nanoparticles (CBZ-PLGA-Zein-NPs or CBZ-PLGA-Zein-Ch-NPs) and to characterize them *in vitro*. To our knowledge, this is the first study on CBZ-loaded PLGA+Zein NPs or PLGA+Zein+Ch NPs. PLGA is an FDA-approved, biocompatible and biodegradable copolymer widely used in the preparation of polymeric nanoparticles due to its low immunogenicity, minimal toxicity, and safety profile (Swider et al., 2018; Kandilli et al., 2020). Zein, the main protein found in corn, belongs to the prolamin protein class and is commercially available. It is soluble in water-glycols or water-alcohol mixture. Due to its biocompatibility, biodegradability and high coating capacity, this biopolymer has been used in the preparation of drug delivery systems (Pascoli et al., 2018; André de Almeida Campos et al., 2023).

2. Materials and Methods

2.1. Materials

CBZ was a gift from Biofarma İlaç San. Tic. A.Ş. (Türkiye). PLGA (50:50, Resomer RG 502 H, Ave. Mw 7000-17000 Da) and chitosan (low molecular weight; 50000-190000 Da) were bought from Sigma-Aldrich (Germany) and Sigma-Aldrich (Iceland), respectively. Zein and poly (vinyl alcohol) (PVA; Mw 30000-70000 Da) were obtained from Sigma-Aldrich (USA). All other materials used were analytical grade.

2.2. Preparation of Chitosan-Uncoated/Coated PLGA+Zein NPs

The uncoated PLGA-Zein NPs [CBZ-PLGA-Z(20)-NPs or CBZ-PLGA-Z(40)-NPs] were prepared by a modified emulsification-solvent evaporation method. Briefly, PLGA (80 mg) and CBZ (40 mg) were dissolved in dichloromethane (DCM). Also, Zein (20 mg or 40 mg) [PLGA:Zein ratio (4:1 and 2:1 w/w); Zein:CBZ ratio (1:1 and 1:2 w/w)] was dissolved in DCM:ethanol (1:1, v/v). The solution of PLGA and CBZ was added to the Zein solution under a magnetic stirrer (500 rpm, 15 min) to obtain an organic phase. The organic phase was added dropwise into the aqueous solution of PVA (3%, w/v)

when stirring using an Ultraturrax T10 at 25000 rpm for 5 min (IKA, Germany). Then, it was sonicated using an ultrasonic probe for 5 min (using 60% power; Sonoplus HD 2070, Bandelin Electronics, Germany). The NPs dispersion was centrifuged (12500 rpm, 40 min, 15 °C) after removing the organic solvent under reduced pressure. The NPs were freeze-dried for 24 h (Martin Christ, Alpha 1-2 LD Plus, Germany).

Blank PLGA-Zein NPs [B-PLGA-Z(20)-NPs or B-PLGA-Z(40)-NPs] were also prepared using the same procedure without CBZ.

In addition, chitosan-coated blank or CBZ-loaded PLGA-Zein NPs [B-PLGA-Z(20)-Ch-NPs or CBZ-PLGA-Z(20)-Ch-NPs] were prepared by the above-mentioned procedure until the centrifugation step. Before centrifugation step, 0.1% (w/v) chitosan solution in 1% (v/v) aqueous acetic acid was added to the aqueous dispersion of the blank or CBZ-loaded PLGA-Zein NPs prepared using 20 mg of Zein (chitosan solution:PLGA-Zein NPs suspension, 1:2 v/v) and shaken in a water bath shaker (horizontal, 50 rpm) for 30 min at room temperature. Centrifugation and lyophilization steps were then performed as described above.

2.3. Characterization of Chitosan-Uncoated/Coated PLGA+Zein NPs

The morphological analysis of NPs was carried out using TEM (Hitachi HighTech HT7700, Japan). The images of the NPs were obtained at an accelerating voltage at 120 kV after being placed on a copper grid and dried at room temperature for 24 h. "Zetasizer Nano ZSP (Malvern Ins. Ltd, UK)" was used to measure the particle size (PS) of NPs (at a scattering angle of 173°) as well as the zeta potential (ZP) values of these formulations. The formulations were diluted (20-fold) before the measurements.

The CBZ content in the prepared NPs was determined as follows: 20 mL DCM:ethanol (1:1, v/v) mixture was added to the lyophilized NPs (20 mg) and kept in an ultrasonic bath for 15 min. Then, the mixture was stirred on a magnetic stirrer for 3 h and filtered (PTFE membrane filter; 0.45 μm). The CBZ content in the samples was determined using a validated HPLC method (Kandilli et al. 2018). The percentage of encapsulation efficiency (EE%) and percent drug loading (DL%) were calculated (Kandilli et al., 2020).

Also, the DCS, FT-IR and XRD analyzes were performed for NPs formulations. The conditions of these analyzes are given in Table 1.

Table 1. The conditions of DSC, FT-IR and XRD analyzes

Analysis	Device	Conditions
DSC	Differential Scanning Calorimetry (Hitachi STA 7300, Japan)	25–250 °C; 10 °C/min; a constant flow of nitrogen gas (200 mL/min)
FT-IR	Fourier Transform Infrared Spectroscopy (Shimadzu IRSpirit-T, Japan)	4000-400 cm^{-1}
XRD	PANalytical Empyrean diffractometer (Netherlands)	CuKα radiation (λ 1.5406 Å); 0.5° divergence slit; 2θ range of 10-90°

2.3.1. *In vitro* release studies

The release studies were performed in phosphate buffer (PB, pH 6.8) or HCl (pH 1.2) using the dialysis bag method. NPs were dispersed in 1 mL of release medium, and the dispersion was placed in a dialysis bag (MWCO 14000 Da; Sigma-Aldrich). The dialysis bags were immersed in the release media (50 mL) in the vials in a water bath shaker (horizontal, 50 rpm, 37±0.5 °C). Samples (1 mL) were withdrawn at selected time points, and 1 mL of release medium was added to maintain the "Sink Condition". The samples were filtered (PVDF membrane filter; 0.45 μm), and CBZ contents of the samples were analyzed by the HPLC method validated in our study (Kandilli et al. 2018).

3. Results and Discussion

The TEM images of NPs showed that almost spherical NPs were prepared (Figure 1). While the particle size values of NPs with 20 mg of Zein were smaller than 229 nm, the particle size values of NPs with 40 mg of Zein were smaller than 252 nm. The PDI value of all NP formulations was below 0.3, indicating a narrow particle size distribution. The EE% values of PLGA-NPs with Zein (20 mg or 40 mg) were about 64% and 56%, respectively (Table 2). The DL% values calculated for these formulations are given in Table 2. Considering the particle size, EE% and DL% values, PLGA NPs with 20 mg Zein were selected for coating with chitosan. Then, PLGA-Zein-Ch NPs were prepared by coating PLGA-Z(20)-NP with chitosan (mentioned in methods). There was no significant difference between the particle sizes of the CBZ-containing PLGA-Zein-NP formulations and their respective blank-NP formulations (P>0.05). However, increasing the amount of zein in the formulation (from 20 mg to 40 mg) caused a significant increase in NPs particle sizes (P<0.05) (Table 2). Moreover, the addition of chitosan to the formulation containing 20 mg Zein did not cause a significant change in particle sizes of NPs (P>0.05, Table 2).

In this study, ZP measurement was also carried out. ZP specifies the NP'surface charge and is important for predicting the physical stability of NPs dispersions. In our study, negative zeta potential values were obtained for PLGA- Zein (20 mg or 40 mg) NPs (absolute value less than or equal to approximately 12 mV; Table 2) due to the presence of terminal carboxylic groups in PLGA, the PVA adsorption on the surface of particles, and the rearrangement of Zein (Mura et al., 2011; Gagliardi et al., 2021).
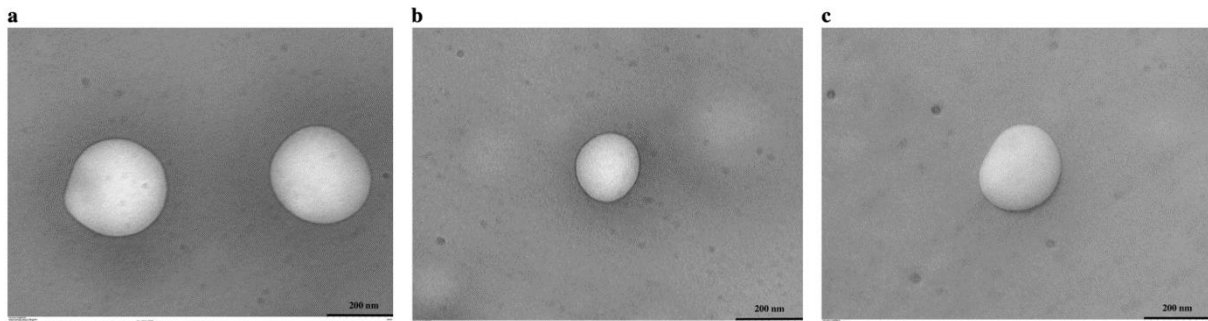
Figure 1. The TEM images of CBZ-PLGA-Z(20)-NP (a), CBZ-PLGA-Z(40)-NP (b) and CBZ-PLGA-Z(20)-Ch-NP (c). [CBZ: Carbamazepine; Ch: Chitosan; NP: nanoparticle, PLGA: poly(lactic-*co*-glycolic) acid; Z: Zein; CBZ-PLGA-Z(20)-NP: CBZ-loaded PLGA-Zein nanoparticles with 20 mg Zein; CBZ-PLGA-Z(40)-NP: CBZ-loaded PLGA-Zein nanoparticles with 40 mg Zein; CBZ-PLGA-Z(20)-Ch-NP: Chitosan-coated CBZ-loaded PLGA-Zein nanoparticles with 20 mg Zein].

Table 2. The particle size, PDI, zeta potential, EE (%) and DL (%) values for Blank- NPs and CBZ-loaded NPs

Formulation	Particle Size (nm) (n=9; X±SD)	PDI (n=9; X±SD)	Zeta Potential (mV) (n=9; X±SD)	EE% (n=6; X±SD)	DL% (n=6; X±SD)
B-PLGA-Z(20)-NP	227.91±9.87[a]	0.19±0.05	-12.11±1.45		
CBZ-PLGA-Z(20)-NP	222.06±14.20[b]	0.14±0.03	-8.51±1.36	63.96±2.08[c]	21.79±0.69
B-PLGA-Z(40)-NP	250.82±7.50[a]	0.21±0.01	-12.10±2.11		
CBZ-PLGA-Z(40)-NP	244.62±5.57[b]	0.18±0.03	-6.86±1.41	56.35±1.93[c]	16.32±0.50
B-PLGA-Z(20)-Ch-NP	226.20±11.40	0.20±0.02	39.98±2.63		
CBZ-PLGA-Z(20)-Ch-NP	221.46±6.12	0.19±0.02	37.69±5.89	62.28±3.09	21.33±0.63

[a]= P<0.05 between B-PLGA-Z(20)-NPs and B-PLGA-Z(40)-NPs; [b and c]= P<0.05 between CBZ-PLGA-Z(20)-NPs and CBZ-PLGA-Z(40)-NPs. [B= blank; CBZ= carbamazepine; Ch= chitosan; NP= nanoparticle, PLGA= poly(lactic-*co*-glycolic) acid; SD= standard deviation; X= mean; Z= zein; B-PLGA-Z(20)-NP= blank PLGA-Zein nanoparticles with 20 mg Zein; B-PLGA-Z(40)-NP= blank PLGA-Zein nanoparticles with 40 mg Zein; CBZ-PLGA-Z(20)-NP= CBZ-loaded PLGA-Zein nanoparticles with 20 mg Zein; CBZ-PLGA-Z(40)-NP= CBZ-loaded PLGA-Zein nanoparticles with 40 mg Zein; B-PLGA-Z(20)-Ch-NP= chitosan-coated blank-PLGA-Zein nanoparticles with 20 mg Zein; CBZ-PLGA-Z(20)-Ch-NP= chitosan-coated CBZ-loaded PLGA-Zein nanoparticles with 20 mg Zein].

Colloidal drug carriers with ZP values between -10 mV and +10 mV are considered neutral (Clogston and Patri, 2011). In addition, we found that PLGA-Zein (20 mg)-Ch NP formulations had positive zeta potential values (greater than 30 mV; Table 2) due to the adsorption of chitosan, a cationic polymer, on the surface of PLGA-Zein NPs (Pauluk et al., 2019; Dandamudi et al., 2021). The dispersions of NPs with ZP values of ≤ -30 mV or $\geq +30$ mV are considered to have sufficient physical stability (Clogston and Patri, 2011; Ugur Kaplan et al., 2023). We carried out DSC and FT-IR analysis to determine whether there was an interaction between CBZ and other components in the NP formulation. Figure 2 shows the FT-IR spectra recorded for CBZ and blank- and CBZ-loaded NPs. CBZ's FT-IR spectrum showed the characteristic peaks that we detailed in our previous

study (Kandilli et al., 2020). Additionally, it can be seen in Figure 2 that the FT-IR spectra of blank-NPs and the corresponding CBZ-loaded NPs are similar. Furthermore, Figure 3 shows DSC thermograms obtained for CBZ and blank- and CBZ-loaded NPs. DSC analysis is also used to evaluate of active substances in the formulations. The endothermic peaks seen at 171.5 °C and 191.3 °C (as distinct) in the DSC thermogram obtained for CBZ were not observed in the DSC thermograms of CBZ-loaded NPs formulations. This supports the result obtained by FT-IR analysis. Ma et al. (2020) reported that the DSC thermogram of CBZ-form III showed two endothermic peaks at 175 °C (related to its melting point) and 192 °C. It also stated that the endothermic peak related to its melting point was observed at 192 °C in the thermogram of CBZ-form I (Ma et al. 2020).
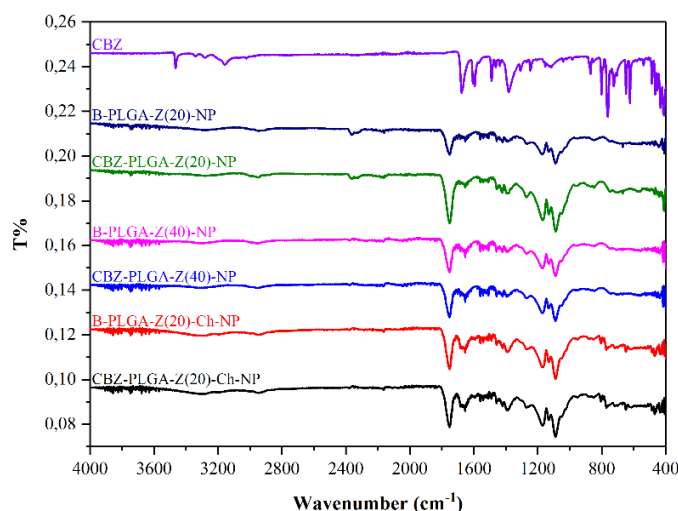
Figure 2. FT-IR spectra of free CBZ and all NP formulations [B= blank; CBZ= carbamazepine; Ch= chitosan; NP= nanoparticle, PLGA= poly(lactic-*co*-glycolic) acid; Z= zein; B-PLGA-Z(20)-NP= blank PLGA-Zein nanoparticles with 20 mg Zein; B-PLGA-Z(40)-NP= blank PLGA-Zein nanoparticles with 40 mg Zein; CBZ-PLGA-Z(20)-NP= CBZ-loaded PLGA-Zein nanoparticles with 20 mg Zein; CBZ-PLGA-Z(40)-NP= CBZ-loaded PLGA-Zein nanoparticles with 40 mg Zein; B-PLGA-Z(20)-Ch-NP= chitosan-coated blank-PLGA-Zein nanoparticles with 20 mg Zein; CBZ-PLGA-Z(20)-Ch-NP= chitosan-coated CBZ-loaded PLGA-Zein nanoparticles with 20 mg Zein].
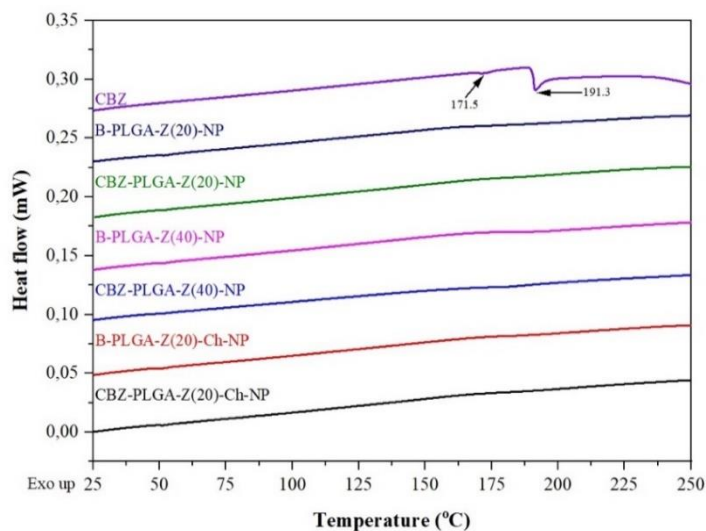
Figure 3. DSC thermograms of free CBZ and all NP formulations (Abbreviations used for the samples are as in Figure 2). In addition, XRD patterns of free CBZ, blank- and CBZ-loaded nanoparticles were recorded (Figure 4). In the

XRD patterns of free CBZ, there are several distinct diffraction peaks at 13.2°, 15.4°, 16.0°, 19.6°, 25.1°, and 27.7°, 30.9°, 32.2° (related to CBZ form III), indicating its crystalline character. Similar XRD patterns for CBZ were obtained in previous studies (Wang et al., 2012; Caliandro et al., 2013; Pinto et al., 2014; Krstić et al., 2015). However, in the XRD patterns of CBZ-loaded NPs, several peaks related to CBZ appeared but in much less intensity. This supports the result obtained by DSC analysis and shows that CBZ is successfully entrapped within the prepared NPs.

EE% and DL% values calculated for the formulations are given in Table 2. A significant decrease (P<0.05) was observed in the EE% and DL% values by increasing the amount of zein in the formulation (from 20 mg to 40 mg). However, it was determined that the addition of chitosan to the formulation with Zein (20 mg) did not cause a significant change in the EE% and DL% values (P>0.05). Many factors (solubility of the active substance, the affinity of active substance to polymer, manufacturing process, etc.) have an impact on the EE (%). Therefore, the different physicochemical properties of the polymers with different chemical structures affect the entrapment/encapsulation process (Valo et al., 2009). In our study, increasing the amount of Zein in the formulation may have negatively affected the PLGA-CBZ interaction.

Liu et al. (2021) developed docosahexaenoic acid-loaded zein nanoparticles or Zein+PLGA nanoparticles. The EE (%) values obtained for docosahexaenoic acid-loaded nanoparticles prepared using PLGA+Zein were higher than the EE (%) values determined for nanoparticles prepared using Zein alone. Additionally, increasing the Zein:docosahexaenoic acid ratio from 10:1 to 50:1 in the formulation did not cause a significant change in the EE (%) values obtained for Zein+PLGA nanoparticles. It has been reported that PLGA can support the entrapment of docosahexaenoic acid, which is a hydrophobic polyunsaturated fatty and hardly soluble in water, into Zein + PLGA nanoparticles and allows to obtain increased EE% values (Liu et al., 2021).

In vitro release studies were carried out in the different release media (HCl pH 1.2 and PB pH 6.8). The release profiles of CBZ from the prepared NPs are given in Figure 5. While the CBZ release from PLGA NPs containing 20 mg or 40 mg Zein and PLGA-Zein-Ch NPs in the HCl (pH 1.2) release medium in the first hour was approximately 17%, 20% and 16%, respectively; in the PB (pH 6.8) release medium, it was approximately 15%, 20% and 14%, respectively. It indicates a burst drug release. Furthermore, at 48 h, CBZ release from PLGA NPs containing 20 mg or 40 mg Zein and PLGA-Zein-Ch NPs was determined to be approximately 100% for the three NP formulations (in HCl release medium) and 99%, 100% and 98% (in PB release medium), respectively (Figure 5). These results indicate that the pH of the release medium, the amount of Zein in the formulation, or the chitosan coating do not have a significant effect on the CBZ release from NPs. As a result, the release profiles of all NPs formulations showed that a pH-independent and sustained-CBZ release up to 48 h in both release media was achieved. In addition, PLGA nanoparticles exhibit a biphasic release pattern with an initial burst release of the active substance followed by sustained release (Kandilli et al. 2020; Sakhi et al., 2022).
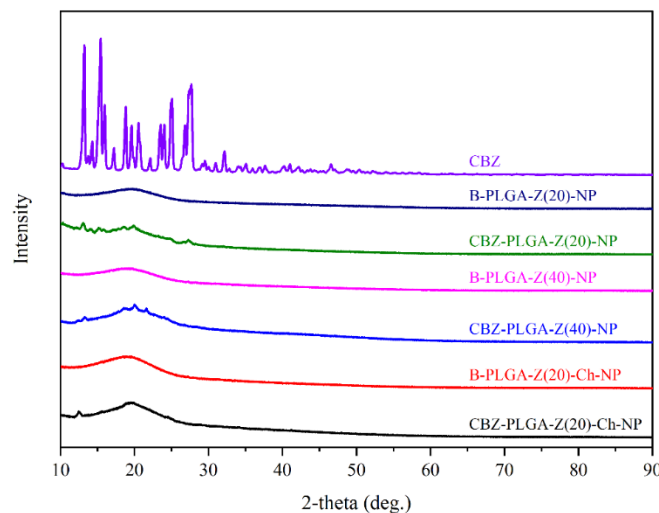
Figure 4. X-ray patterns of free CBZ and all NP formulations [B= blank; CBZ= carbamazepine; Ch= chitosan; NP= nanoparticle, PLGA= poly(lactic-*co*-glycolic) acid; Z= zein; B-PLGA-Z(20)-NP= blank PLGA-Zein nanoparticles with 20 mg Zein; B-PLGA-Z(40)-NP= blank PLGA-Zein nanoparticles with 40 mg Zein; CBZ-PLGA-Z(20)-NP= CBZ-loaded PLGA-Zein nanoparticles with 20 mg Zein; CBZ-PLGA-Z(40)-NP= CBZ-loaded PLGA-Zein nanoparticles with 40 mg Zein; B-PLGA-Z(20)-Ch-NP= chitosan-coated blank-PLGA-Zein nanoparticles with 20 mg Zein; CBZ-PLGA-Z(20)-Ch-NP= chitosan-coated CBZ-loaded PLGA-Zein nanoparticles with 20 mg Zein].
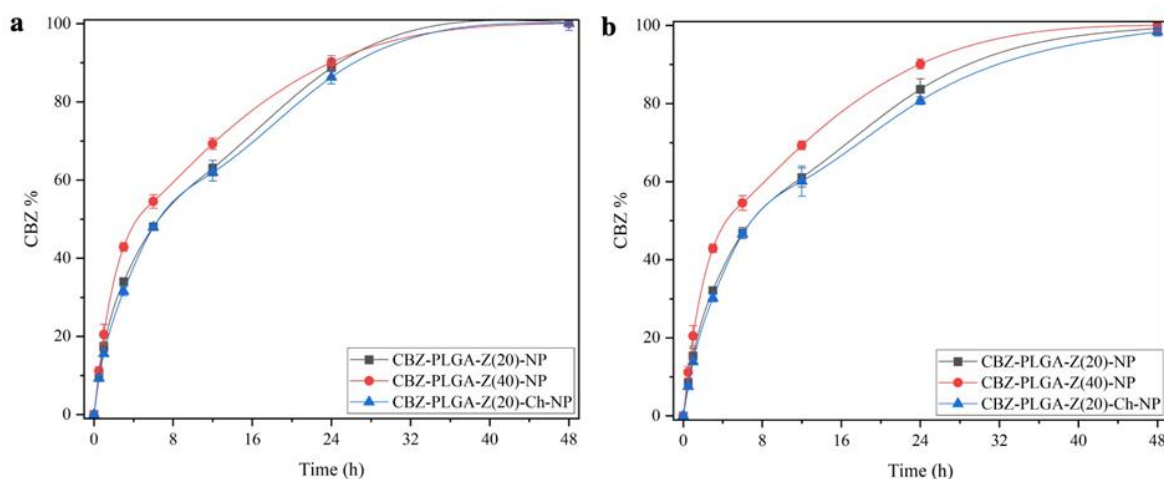
Figure 5. In vitro release profiles of CBZ-PLGA-Z(20)-NP, CBZ-PLGA-Z(40)-NP and CBZ-PLGA-Z(20)-Ch-NP at HCl pH 1.2 (a) and PB pH 6.8 (b) (X±SD; n=3) [CBZ= carbamazepine; Ch= chitosan; NP= nanoparticle, PLGA= poly(lactic-*co*-glycolic) acid; Z= Zein; CBZ-PLGA-Z(20)-NP= CBZ-loaded PLGA-Zein nanoparticles with 20 mg Zein; CBZ-PLGA-Z(40)-NP= CBZ-loaded PLGA-Zein nanoparticles with 40 mg Zein; CBZ-PLGA-Z(20)-Ch-NP= Chitosan-coated CBZ-loaded PLGA-Zein nanoparticles with 20 mg Zein].

Kandilli et al. (2020) developed CBZ and levetiracetam-loaded NPs. They performed an *in vitro* release study in pH 7.4-PB medium using a dialysis bag (cutoff MW 14,000 Da) method. It was observed that approximately 40% and 90% of CBZ were released from NPs within 3 h and 48 h, respectively. The release profile showed that an initial burst CBZ release was followed by sustained CBZ release (Kandilli et al., 2020).

Besides, Zybina et al. (2018) prepared the CBZ-loaded PLGA nanoparticles via high pressure homogenization followed by solvent evaporation. An in vitro release study was carried out by resuspending the lyophilized NPs in PBS (pH 7.4), diluting this suspension 25-fold with PBS, and then incubating at 37 °C under continuous shaking. They reported that about 90% of CBZ was released from NPs after 1 h of incubation (Zybina et al., 2018).

4. Conclusion

CBZ-loaded PLGA NPs with Zein (20 mg or 40 mg) and CBZ-loaded PLGA-Zein (20 mg)-Ch-NPs were successfully prepared and characterized. Compared to the NP formulation with 40 mg Zein (PLGA:Zein, 2:1 w/w and Zein:CBZ, 1:1 w/w), the NP formulation with 20 mg Zein (PLGA:Zein 4:1 w/w and Zein :CBZ 1:2 w/w) had a smaller average particle size and also a higher encapsulation efficiency value. Furthermore, the coating of the optimum formulation (containing 20 mg Zein) with chitosan did not lead to a significant difference in the particle size and EE (%) value of this formulation. However, chitosan coating allowed obtaining a zeta potential value above +30 mV, which is a suitable value for the physical stability of a colloidal dispersion. The positive zeta potential values indicate that the NPs were successfully coated with chitosan. A sustained release of CBZ from all prepared NPs formulations was achieved until 48th h.

Author Contributions

The percentage of the author(s) contributions is presented below. All authors reviewed and approved the final version of the manuscript.

	A.B.U.K.	M.Ç.
C		100
D	50	50
S		100
DCP	100	
DAI	50	50
L	50	50
W	50	50
CR	50	50
SR	50	50
PM	50	50
FA	50	50

C=Concept, D= design, S= supervision, DCP= data collection and/or processing, DAI= data analysis and/or interpretation, L= literature search, W= writing, CR= critical review, SR= submission and revision, PM= project management, FA= funding acquisition.

Conflict of Interest

The authors declared that there is no conflict of interest.

Ethical Consideration

Ethics committee approval was not required for this study because of there was no study on animals or humans.

References

André de Almeida Campos L, Francisco Silva Neto A, Cecília Souza Noronha M, Ferreira de Lima M, Macário Ferro Cavalcanti I, Stela Santos-Magalhães N. 2023. Zein nanoparticles for drug delivery: Preparation methods and biological applications. Int J Pharm, 635: 122754. https://doi.org/10.1016/j.ijpharm.2023.122754

Caliandro R, Di Profio G, Nicolotti O. 2013. Multivariate analysis of quaternary carbamazepine-saccharin mixtures by X-ray diffraction and infrared spectroscopy. J Pharm Biomed Anal, 78-79: 269-279. https://doi.org/10.1016/j.jpba.2013.01.042

Clogston JD, Patri AK. Zeta potential measurement. 2011. Methods Mol Biol, 697: 63-70. https://doi.org/10.1007/978-1-60327-198-1_6

Dandamudi M, McLoughlin P, Behl G, Rani S, Coffey L, Chauhan A. 2021. Chitosan-coated PLGA nanoparticles encapsulating triamcinolone acetonide as a potential candidate for sustained ocular drug delivery. Pharmaceutics, 13(10): 1590. https://doi.org/10.3390/pharmaceutics13101590

Devinsky O, Vezzani A, O'Brien TJ, Jette N, Scheffer IE, de Curtis M. 2018. Epilepsy. Nat Rev Dis Primers, 4(1): 1-24. https://doi.org/10.1038/nrdp.2018.24

Gagliardi A, Paolino D, Costa N, Fresta M, Cosco D. 2021. Zein-vs PLGA-based nanoparticles containing rutin: A comparative investigation. Mater Sci Eng C Mater Biol Appl, 118: 111538. https://doi.org/10.1016/j.msec.2020.111538

Green SF, Nguyen P, Kaalund-Hansen K, Rajakulendran S, Murphy E. 2020. Effectiveness, retention, and safety of modified ketogenic diet in adults with epilepsy at a tertiary-care centre in the UK. J Neurol, 267(4): 1171-1178. https://doi.org/10.1007/s00415-019-09658-6

Guery D, Rheims S. 2021. Clinical management of drug resistant epilepsy: A review on current strategies. Neuropsychiatr Dis Treat, 17: 2229-2242. https://doi.org/10.2147/NDT.S256699

Kandilli B, Uğur AB, Çetin M, Miloğlu FD. 2018. A simple HPLC-UV method for simultaneous determination of levetiracetam and carbamazepine. HUJPHARM, 38(2): 58-64.

Kandilli B, Ugur Kaplan AB, Cetin M, Taspinar N, Ertugrul MS, Aydin IC, et al. 2020 Carbamazepine and levetiracetam-loaded PLGA nanoparticles prepared by nanoprecipitation method: in vitro and in vivo studies. Drug Dev Ind Pharm, 46(7): 1063-1072. https://doi.org/10.1080/03639045.2020.1769127

Kanner AM, Bicchi MM. 2022. Antiseizure medications for adults with epilepsy: A review. JAMA, 327(13): 1269-1281. https://doi.org/10.1001/jama.2022.3880

Krstić M, Popović M, Dobričić V, Ibrić S. 2015. Influence of solid drug delivery system formulation on poorly water-soluble drug dissolution and permeability. Molecules, 20(8): 14684-98. https://doi.org/10.3390/molecules200814684

Liu E, Su Z, Yang C, Ji Y, Liu B, Meng X. 2021. Fabrication, characterization and properties of DHA-loaded nanoparticles based on zein and PLGA. Food Chem, 360: 129957. https://doi.org/10.1016/j.foodchem.2021.129957

Lo JCY. 2014. Carbamazepine. In: Wexler P, editor. Encyclopedia of Toxicology (Third Edition). Academic Press, Oxford, UK, pp: 665-667.

Ma X, Müller F, Huang S, Lowinger M, Liu X, Schooler R, et al. 2020. Influence of carbamazepine dihydrate on the preparation of amorphous solid dispersions by hot melt extrusion. Pharmaceutics, 12(4): 379. https://doi.org/10.3390/pharmaceutics12040379

Maan JS, Duong T vi H, Saadabadi A. Carbamazepine. 2024. URL: http: //www.ncbi.nlm.nih.gov/books/NBK482455/ (accessed 26 February 2024).

Manole AM, Sirbu CA, Mititelu MR, Vasiliu O, Lorusso L, Sirbu OM. 2023. State of the art and challenges in epilepsy—A narrative review. J Pers Med, 13(4): 623. https://doi.org/10.3390/jpm13040623

Mura S, Hillaireau H, Nicolas J, Le Droumaguet B, Gueutin C, Zanna S. 2011. Influence of surface charge on the potential toxicity of PLGA nanoparticles towards Calu-3 cells. Int J Nanomedicine, 6: 2591-2605. https://doi.org/10.2147/IJN.S24552

Pascoli M, de Lima R, Fraceto LF. 2018. Zein nanoparticles and strategies to improve colloidal stability: A mini-review. Front Chem, 6: 6. https://doi.org/10.3389/fchem.2018.00006

Pauluk D, Padilha AK, Khalil NM, Mainardes RM. 2019. Chitosan-coated zein nanoparticles for oral delivery of resveratrol: Formation, characterization, stability, mucoadhesive properties and antioxidant activity. Food Hydrocolloids, 94: 411-417. https://doi.org/10.1016/j.foodhyd.2019.03.042

Pearce RE, Lu W, Wang Y, Uetrecht JP, Correia MA, Leeder JS. 2008. Pathways of carbamazepine bioactivation in vitro. III. The role of human cytochrome P450 enzymes in the formation of 2,3-dihydroxycarbamazepine. Drug Metab Dispos, 36(8): 1637-1649. https://doi.org/10.1124/dmd.107.019562

Pinto MAL, Ambrozini B, Ferreira APG, Cavalheiro ÉTG. 2014. Thermoanalytical studies of carbamazepine: hydration/dehydration, thermal decomposition, and solid phase transitions. Braz J Pharm Sci, 50(4): 877-884.

Qushawy M, Prabahar K, Abd-Alhaseeb M, Swidan S, Nasr A. 2019. Preparation and evaluation of carbamazepine solid lipid nanoparticle for alleviating seizure activity in pentylenetetrazole-kindled mice. Molecules, 24(21): 3971. https://doi.org/10.3390/molecules24213971

Sakhi M, Khan A, Iqbal Z, Khan I, Raza A, Ullah A. 2022. Design and characterization of paclitaxel-loaded polymeric nanoparticles decorated with trastuzumab for the effective treatment of breast cancer. Front Pharmacol, 13: 855294. https://doi.org/10.3389/fphar.2022.855294"

Sarmast ST, Abdullahi AM, Jahan N. 2020. Current classification of seizures and epilepsies: Scope, limitations and recommendations for future action. Cureus, 12(9): e10549. https://doi.org/10.7759/cureus.10549.

Scioli Montoto S, Sbaraglini ML, Talevi A, Couyoupetrou M, Di Ianni M, Pesce GO. 2018. Carbamazepine-loaded solid lipid nanoparticles and nanostructured lipid carriers: Physicochemical characterization and in vitro/in vivo evaluation. Colloids Surf B Biointerfaces, 167: 73-81. https://doi.org/10.1016/j.colsurfb.2018.03.052

Stafstrom CE, Carmant L. 2015. Seizures and epilepsy: An overview for neuroscientists. Cold Spring Harb Perspect Med, 5(6): a022426. https://doi.org/10.1101/cshperspect.a022426

Swider E, Koshkina O, Tel J, Cruz LJ, de Vries IJM, Srinivas M. 2018. Customizing poly(lactic-co-glycolic acid) particles for biomedical applications. Acta Biomater, 73: 38-51. https://doi.org/10.1016/j.actbio.2018.04.006

Ugur Kaplan AB, Cetin M, Bayram C, Yildirim S, Taghizadehghalehjoughi A, Hacimuftuoglu A. 2023. In vivo evaluation of nanoemulsion formulations for metformin and repaglinide alone and combination. J Pharm Sci, 112(5): 1411-1426. https://doi.org/10.1016/j.xphs.2023.01.008

Ułamek-Kozioł M, Czuczwar SJ, Januszewski S, Pluta R. 2019. Ketogenic Diet and Epilepsy. Nutrients, 11(10): 2510. https://doi.org/10.3390/nu11102510

Uzunović A, Vranić E, Hadziedić S. 2010. Impairment of the in vitro release of carbamazepine from tablets. Bosn J Basic Med Sci, 10(3): 234-238. https://doi.org/10.17305/bjbms.2010.2693

Valo H, Peltonen L, Vehviläinen S, Karjalainen M, Kostiainen R, Laaksonen T. 2009. Electrospray encapsulation of hydrophilic and hydrophobic drugs in poly(l-lactic acid)

nanoparticles. Small, 5(15): 1791-1798. https://doi.org/10.1002/smll.200801907

Wang Z, Chen B, Quan G, Li F, Wu Q, Dian L. 2012. Increasing the oral bioavailability of poorly water-soluble carbamazepine using immediate-release pellets supported on SBA-15 mesoporous silica. Int J Nanomedicine, 7: 5807-5818. https://doi.org/10.2147/IJN.S37650

WHO. 2024. Epilepsy. URL: https://www.who.int/news-room/fact-sheets/detail/epilepsy (accessed 26 February 2024).

Wu D, Fei F, Zhang Q, Wang X, Gong Y, Chen X. 2022. Nanoengineered on-demand drug delivery system improves efficacy of pharmacotherapy for epilepsy. Sci Adv, 8(2): eabm3381. https://doi.org/10.1126/sciadv.abm3381

Zybina A, Anshakova A, Malinovskaya J, Melnikov P, Baklaushev V, Chekhonin V. 2018. Nanoparticle-based delivery of carbamazepine: A promising approach for the treatment of refractory epilepsy. Int J Pharm, 547(1): 10-23. https://doi.org/10.1016/j.ijpharm.2018.05.023

Black Sea Journal of Engineering and Science

METAKAOLİN KULLANILARAK KUM BİR ZEMİNE YAPILAN ZEMİN ISLAHININ RİJİT KAPLAMA KALINLIĞINA VE MALİYETİNE ETKİLERİNİN ARAŞTIRILMASI

Tacettin GEÇKİL[1], Talha SARICI[1], Bahadır KARABAŞ[1]*

[1]İnönü University, Faculty of Engineering, Department of Civil Engineering, 44280, Malatya, Türkiye

Özet: Bu çalışmada, metakaolin kullanılarak stabilize edilen yol taban zemininin, üzerine tasarlanan rijit bir yolun tabaka kalınlığına ve yapım maliyetine etkileri incelenmiştir. İlk olarak, zemin sınıflandırma deneyleri ile zemin sınıfı tespit edilmiş ve zemin özelliklerinin belirlenmesi amacıyla bazı laboratuvar deneyleri yapılmıştır. Daha sonra, zemine ağırlıkça %3, %6, %9, %12 ve %15 metakaolin ilave edilerek hazırlanan zemin numunelerine standart proktor deneyi uygulanmıştır. Ardından, 28 gün boyunca kür süresine tabi tutulan ve farklı oranlarda metakaolin kullanılarak hazırlanan numunelere serbest basınç deneyi yapılmıştır. Deneyler sonucunda, en yüksek dayanım %12 oranında metakaolin içeren karışım numunelerinde elde edilmiştir. Daha sonra, katkısız ve %12 oranında metakaolin katkılı numunelere 28 gün kür süresinin ardından, uygulanan Kaliforniya taşıma gücü oranı deneyi neticesinde, dayanımın %227,56 arttığı tespit edilmiştir. Deneysel çalışmalardan sonra, Amerikan Devlet Karayolları ve Ulaştırma Birliği (AASHTO) tarafından önerilen rijit yol üstyapı tasarım esaslarına göre üstyapı tabaka kalınlığı ve maliyeti araştırılmıştır. Hesaplamalar neticesinde, %12 oranında metakaolin ile iyileştirilen yol taban zemininin, rijit üstyapı tabaka kalınlığını %29,17 oranında ve maliyeti %2,68 oranında düşürdüğü tespit edilmiştir.

Anahtar kelimeler: Kötü derecelenmiş kum, Zemin ıslahı, Metakaolin, Ulaştırma geotekniği

Investigation of the Effects of Soil Improvement in Sandy Soil Using Metakaolin on Rigid Pavement Thickness and Cost

Abstract: In this study, the effects of subgrade soil improved by the usage of metakaolin on the layer thickness and construction cost of a rigid road designed on it were investigated. First, soil classification tests were conducted to determine the soil class, and several laboratory tests were performed to identify soil properties. Then, standard proctor tests were applied to soil samples prepared by adding 3%, 6%, 9%, 12%, and 15% metakaolin by weight. Subsequently, unconfined compressive strength tests were conducted on the samples prepared with different proportions of metakaolin after a curing period of 28 days. As a result of the tests, the highest strength was obtained in samples containing 12% metakaolin. Then, after 28 days of curing, the California bearing ratio test was applied to the samples prepared without additives and with 12% metakaolin, resulting in a 227.56% increase in strength value. After the experimental studies, pavement layer thickness and cost were investigated according to the rigid pavement design guidelines recommended by the American Association of State Highways and Transportation (AASHTO). As a result of the calculations, it was determined that the subgrade improved with 12% metakaolin reduced the rigid pavement layer thickness by 29.17% and the cost by 2.68%.

Keywords: Poorly graded sand, Soil stabilization, Metakaolin, Transportation geotechnics

1. Giriş

Ulaşım ihtiyacının karşılanmasında yaygın olarak kullanılan karasal ulaşım yapılarının dizayn ve yapım safhasında göz önüne alınan kriterlerin başında zemin durumu, trafik, bölgesel ve ekonomik faktörler yer almaktadır. Bölgesel ve ekonomik gerekliliklerin karşılanması maksadıyla belirlenen karayolları güzergahlarında yapılan zemin etütleri neticesinde tespit edilen zemin özellikleri, karayolu tasarımlarının emniyet ve ekonomik kısıtlar göz önüne alınarak hayata geçirilmesinde büyük önem arz etmektedir. Özellikle

taşıma gücü zayıf zeminlere sahip güzergahlarda yapılması planlanan stabilizasyon faaliyetleri, tasarımların ekonomik ve güvenli şekilde uygulanmasının önemli bir parçasıdır (Uzuner, 2016; Tunç, 2002). Günümüzde stabilizasyon uygulamalarında kireç, çimento ve bitüm gibi malzemelerin (Tunç, 2007) yanında, alternatif malzemeler ile zeminlerin taşıma gücünün arttırılmasına yönelik çalışmalar vasıtasıyla (Demir ve Sarıcı, 2017; Sarıcı, 2014; Ok ve ark., 2021; Sarıcı ve ark., 2022) tasarımların daha güvenli, ekonomik ve çevreye saygılı bir şekilde inşa edilmesine katkıda

sağlayacağı düşünülmektedir. Kumar ve Sharma (2004) tarafından, uçucu külün farklı oranlarda (%5, %10, %15, %20) karıştırılmasıyla elde edilen numunelerin plastisite, kompaksiyon ve dayanım özellikleri araştırılmıştır. Kompaksiyon testlerine göre, uçucu kül oranı arttıkça plastik limit ve maksimum kuru yoğunluk değerleri yükselirken, optimum su içeriği ve likit limit değerleri düşüş göstermiştir. Uçucu kül oranının artmasıyla, karışımların serbest basınç dayanımının arttığını belirtmişlerdir. Jauberthie ve ark. (2010), nehir siltlerinin çimento ve kireç ile stabilizasyonunu araştırmışlardır. Hem kireç hem de çimento ile yapılan iyileştirmeler sonucunda Kaliforniya taşıma oranı (KTO) ve serbest basınç dayanımı değerlerinde artış gözlemlemişlerdir. Öksüz ve Yıldız (2006), kumlu zemine %5 oranında sabit çimento ve %0, %5, %10, %15, %20 oranlarında değişen miktarlarda uçucu kül ekleyerek deneysel çalışmalar yapmışlardır. Uçucu külün doğal zemin numunesine eklenmesiyle, serbest basınç dayanımı değerlerinde %100 ile %500 arasında artış tespit etmişlerdir. Geçkil ve ark. (2021a), killi kum bir zemini atık araç lastiklerinden üretilen siyah karbon (SK) ile stabilizasyonu yönelik araştırmalar yapmışlardır. Deneyler neticesinde %10 oranında SK kullanılmasıyla, 1, 7 ve 28 gün kür sürelerinden sonra KTO değerlerinde kür sırasına göre 1,28 kat, 1,77 kat ve 2,87 kat artış gözlemlemişlerdir. Kulanthaivel ve ark. (2023), killi zeminin stabilizasyonuna yönelik kireç ve atık yumurta kabuğu tozu ile araştırma yapmışlardır. %9 kireç ve %12 atık yumurta kabuğu tozu karışımı kombinasyonu ile en yüksek mukavemet değerini elde etmişlerdir. Sarıcı (2019), yüksek fırın cürufu (YFC) ve uçucu kül kullanarak inşaat yıkıntısı atıklarını granül dolgu olarak kullanılabilirliğini araştırdığı çalışmada, %20 YFC ilavesinin en yüksek dayanım değerini sağladığını tespit etmiştir. Bu katkı oranında, serbest basınç mukavemeti ve KTO değerlerine göre, 7 gün kür sonunda 14,72 kat, 28 gün kür sonunda ise 25 kat maksimum artış görmüştür. Çınar (2024) 07 Şubat 2023'de meydana gelen Kahramanmaraş depremi akabinde meydana gelen gaz beton (GB) atıklarının, killi kumlu zemini iyileştirilmesine yönelik %5, %10, %15, %20 oranlarında ve %10 sabit Afşin Elbistan yüksek fırın cürufu (AEC) oranı ile karışımlar hazırlamıştır. Araştırması neticesinde, %10 AEC ve %15 GB atığı kullanılmasının en iyi güçlendirilmeyi sağladığını belirtmiştir.

Kaolin kilinin saflaştırılmasıyla elde edilen, amorf bir yapıya sahip ve beyaz renkli metakaolinin, stabilizasyon malzemesi olarak çeşitli zemin tiplerinin iyileştirilmesine yönelik çalışmalarda (Ayyappan ve ark., 2017; Reddy ve ark., 2018; Abdulkareem ve Abbas, 2021; Wassie ve Demir, 2024) kullanıldığı ve başarılı olunduğu görülmektedir. Bu çalışmalardan Ayyappan ve ark. (2017) killi bir zeminde farklı oranlarda metakaolin ile yapılan çalışmalarda kohezyon ve mukavemet parametrelerinin iyileştirilmesinde etkili olduğunu belirlemişlerdir. Reddy ve ark. (2018), siyah pamuklu zeminin (black cotton soil) stabilizasyonunu uçucu kül,

metakaolin ve bunların karışımları ile test etmişlerdir. Deney sonuçlarında, %9 oranında uçucu kül, %12 oranında metakaolin ve %8 oranında uçucu kül + %6 oranında metakaolin eklenerek en yüksek mukavemet değerlerinin elde edildiğini göstermişlerdir. Abdulkareem ve Abbas (2021) laterit zemini iyileştirmek amacıyla metakaolin kullanım potansiyelini araştırmışlardır. Yapılan serbest basınç ve Kaliforniya Taşıma Oranı (CBR) neticesinde, metakaolin içeriğinin artmasıyla zeminin mühendislik özelliklerinde genel bir iyileşme meydana geldiği, en iyileşmenin % 30 metakaolin içeren karışımdan elde edildiğini tespit etmişlerdir. Wassie ve Demir (2024), yüksek plastisiteli inorganik silt üzerinde çimento ve metakaolin ile yapılan stabilizasyon deneylerinde %8 çimento ve %3 metakaolin ilavesinde en iyi serbest basınç değerlerine ulaşıldığını, ayrıca kesme mukavemeti parametrelerinde önemli bir artış meydana geldiğini tespit etmişlerdir.

Bu araştırma kapsamında yapılan literatür incelemesi neticesinde; kum bir yol taban zemininin metakaolin ile stabilize edilmesinin rijit üst yapı tasarımına etkilerine yönelik herhangi bir çalışmaya ulaşılamamıştır. Bu amaçla kum zemin metakaolin ile stabilizasyon edildikten sonra tabaka kalınlıkları hesaplanarak ve maliyet analizi yapılarak incelenmiştir. Bunun için öncelikle zeminin fiziksel özellikleri elek analizi, hidrometre, kıvam limitleri ve piknometre gibi deney yöntemleriyle belirlenmiştir. Ardından, kum zemine ağırlıkça %3, %6, %9, %12 ve %15 metakaolin katılarak stabilize karışımlar hazırlanmıştır. Katkısız ve katkılı zemin örneklerine standart proktor deneyi, serbest basınç deneyi ve KTO deneyleri uygulanmıştır. Rijit yol üst yapı kalınlığı tasarımı AASHTO (1993) yöntemiyle gerçekleştirilmiş ve tasarım tabaka maliyetleri hesaplanmıştır.

2. Materyal ve Yöntem
2.1. Zemin Örneği
Çalışma kapsamında, Malatya Yazıhan İlçesi Eğribük Mahallesinden zemin örneği temin edilmiştir. Zemin örneğinin özelliklerini tespit için ASTM D422-63 ve ASTM C136/C136M standartlarına göre elek analizi ile hidrometre deneyi yapılmış ve zeminin dane çapı dağılımı tespit edilmiştir. Zeminin dane çapı dağılım eğrisi Şekil 1'de verilmiştir.

Akabinde, ASTM D4318'e göre zemin örneğinin kıvam limitleri belirlenmiştir. Daha sonra, ASTM D824 standardına göre özgül ağırlığın tespiti için piknometre deneyi gerçekleştirilmiştir. Ardından, zeminin maksimum kuru yoğunluğu (ρ_{kmax}) ve optimum su içeriği (ω_{opt}) ASTM D698 esaslarında standart proktor deneyi ile tespit edilmiştir. Uygulanan deneyler sonucunda kullanılan zeminin "kötü derecelenmiş kum" (SP) ve AASHTO sınıflandırma yöntemine göre "A-3" zemin sınıfına ait olduğu tespit edilmiştir. Tablo 1'de deneyler ile belirlenen zemin özellikleri ve Şekil 2'de zemin numunesinin fotoğrafı sunulmuştur.
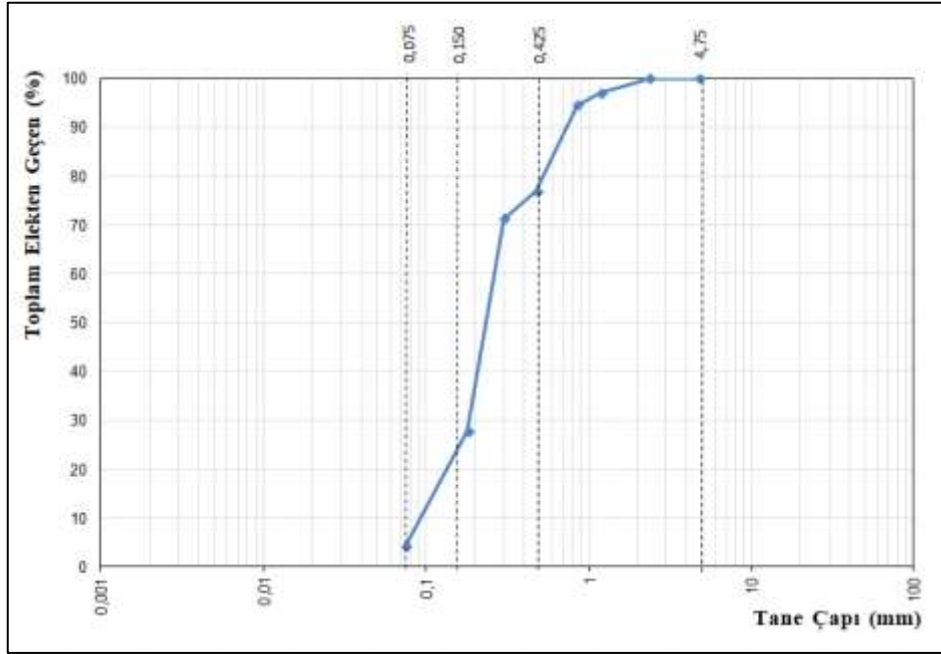
Şekil 1. Dane çapı dağılımı eğrisi.

Tablo 1. Zemin numunesinin belirlenen özellikleri

Değişken Adı	Simge	Birim	Değeri	Standartlar
Maksimum kuru yoğunluğu	ρ_{kmax}	g/cm^3	1,685	ASTM D698
Tane yoğunluğu	ρ_s	g/cm^3	2,669	ASTM D824
Likit limit	ω_L	%	-	ASTM D4318
Plastik limit	ω_p	%	-	ASTM D4318
Plastisite İndisi	PI	%	NP	ASTM D4318
Optimum su içeriği	ω_{opt}	%	18,5	ASTM D698
Sınıflandırma (Birleştirilmiş Zemin Sınıfı)	-	-	SP	ASTM D2487

Şekil 2. Zemin numunesi.

Kaolin kilinin suyunu kaybettiği dehidrolizasyon sıcaklığı ise 500°C ve 800°C arasındadır. Dehidrolizasyon ardından oluşan sıcaklıkta, kaolinit yapısını korur ve meydana gelen bu ürüne metakaolin denir. Metakaolinin temel bileşenleri SiO_2 ve Al_2O_3'tür. Bunun yanı sıra, Fe_2O_3, Na_2O ve K_2O gibi elementler az miktarda bulunur. Metakaolinin katkı malzemesi olarak kullanılması, özellikle SiO_2 ve Al_2O_3 içeriğine dayanmaktadır. Metakaolinin genellikle amorf veya az kristalli SiO_2 gibi bileşikleri daha çok ticari amaçlar için kullanılan ürünlerde yer almaktadır (Nebioğulları, 2010; Karahan, 2011). Deneysel çalışmalarda kullanılan metakaolin'in kimyasal özellikleri Tablo 2'de ve numune örneği ise Şekil 3'te gösterilmiştir.

2.2 Metakaolin

Metakaolinin genel kimyasal bileşimi $Al_2Si_2O_5(OH)_4$ şeklindedir ve kaolin kilinin saflaştırılmasıyla elde edilmektedir. Ayrıca amorf bir yapıya sahiptir ve beyaz renklidir. Üretim sürecinde, kil mineralleri yaklaşık 100-200°C sıcaklıkta içeriğinde bulunan suyu kaybeder.

Tablo 2. Metakaolinin kimyasal özellikleri

Kimyasal Formülü	$Al_2Si_2O_5(OH)_4$
Renk	Beyaz
Al_2O_3	% 43,11
SiO_2	% 56,68
K_2O	% 0,30
CaO	% 0,30
SO_3	% 0,0006
Fe_2O_3	% 1,38
MgO	% 0,30
Na_2O	% 0,62
Kızdırma Kaybı (KK)	% 1,40

Şekil 3. Metakaolin numunesi görüntüsü.

2.3. Standart Proktor ve Serbest Basınç Deneyleri
Standart proktor deneyi, su ile mekanik gereçler kullanılmasıyla havanın atılarak zemin numunesinin ρ_{kmax} ve ω_{opt} belirlenmesine dayanır. Söz konusu deney ASTM D698 standardına uygun olarak gerçekleştirilir. Kullanılan kalıp boyutları yaklaşık 105 mm çapında ve 115,5 mm yüksekliğindedir. İstenen su oranlarıyla yoğrulan örnekler kalıba yerleştirilir ve 2,5 kg ağırlığındaki tokmak ile vurularak (25 defa) sıkıştırılma işlemi gerçekleştirilir. 3 aşamada serilme süreci yapılır, son katmandan sonra üstü düzeltilir ve kütlesi belirlenir. Bu aşamalar, değişik oranlarda su içeriklerinde 5 kez tekrarlanır ve her birinde su içeriği ile kuru yoğunluğu hesaplanır. Belirlenen veriler doğrultusunda kompaksiyon eğrisi oluşturulur ve ρ_{kmax} ile ω_{opt} belirlenir (Yılmaz ve ark., 2017).

Serbest basınç deneyi, hazırlanan numunelere belirli kür sürelerinin ardından dayanımlarının belirlenmesi amacıyla ASTM D2166 standardına uygun olarak gerçekleştirilir. Uygulama esnasında, zemin numunesi etüvde 24 saat boyunca 105°C'de kurutulur. Kullanılacak kalıbın boyutları (çap 38 mm ve boy 76 mm) deney başlamadan önce ölçülerek kontrol edilir. Önceden hesaplanan miktarlarda su ilave edilerek hazırlanan örnekler, kalıba 4 aşamada serilir. Her tabakadan sonra çekiçle 10 defa vurularak sıkıştırılır. Sıkıştırma işlemi tamamlandıktan sonra numune kalıptan çıkarılır. Belirlenen kür süresince oda sıcaklığında bekletilir ve beklenen kür süresi sonrası örnekler cihaza yerleştirilir. Birim boy kısalması %0,5 ve %2 arasında (dakikada) olmalıdır. Deney süresi 10 dakikayı geçmemelidir. Deney sonrasında şekil değişimleri ve deformasyonlar gözlemlenerek numunelerin dayanım değerleri belirlenir (Orhan, 2013).

Bu çalışmada, serbest basınç deneyi, zemin ve karışım numunelerine 28 günlük kür süresinin ardından ASTM D2166 standardına uygun olarak gerçekleştirilmiştir. Deney numuneleri ρ_{kmax} ve ω_{opt} değerlerinde olacak şekilde hazırlanmıştır. Şekil 4'te serbest basınç deneyinin uygulama aşamaları gösterilmektedir.

Şekil 4. Serbest Basınç Deneyine ait Uygulama Aşamaları

2.4 Kaliforniya Taşıma Gücü Oranı Deneyi
Kaliforniya taşıma gücü oranı (KTO) deneyi, ρ_{kmax} ile ω_{opt} değerlerine göre hazırlanan numunelere, planlanan kür süresinin ardından, 1,27 mm/dk hızla yaklaşık 1935 mm² alanlı pistonun zemine itilmesi ile dayanımının belirlenmesine dayanır. ASTM D1883-13 göre uygulanmaktadır. KTO değeri, zeminin belirli penetrasyon (2,5 mm ile 5 mm) değerlerinde tatbik

edilen yükün standart kırma taş örneğine, aynı derinlikte batması için tatbik edilen yüke orantılanmasıyla hesaplanır. Deneyin uygulanmasında, kullanılacak kalıbın boyutları ölçülür ve kaydedilir. Akabinde, zemin örneği 24 saat süre ile 105°C'de bırakılır. ρ_{kmax} ile ω_{opt} değerinde numune hazırlanır. Karışım KTO kalıbına 3 safhada ve her tabakada tokmakla 56 defa vurularak sıkıştırılır.

Sıkıştırma işlemi tamamlanınca numune bulunan kalıp tartılır. Numuneler belirlenen kür süresinden sonra deney cihazına yerleştirilir. Deney neticesinde KTO değerleri penetrasyonun 2,5 ile 5 mm değerleri için belirlenir (Yılmaz ve ark., 2017). Şekil 5'te KTO deney aşamaları görülmektedir.

Şekil 5. Kaliforniya taşıma oranı deneyi uygulama aşamaları

2.5 Rijit Üst Yapı Tasarımı
Rijit üst yapı tasarımı, yol taban zemini üzerine çimento esaslı dizayn edilen beton bir plaka olarak yapılandırılır. Tasarım aşamasında, dizayn ömrü, tabaka kalınlıkları, trafik yoğunluğu, yöresel faktörler, ekonomik ve zemin koşulları gibi çeşitli unsurlar dikkate alınır. Analiz süresi boyunca kaplama üzerinden geçen yoğun trafik yüklerinin neden olabileceği büyük deformasyonlara karşı dayanıklı olacak beton ve tabaka kalınlıklarının belirlenmesi önem taşımaktadır (AASHTO, 1993; KGM, 2019). Şekil 6, rijit üstyapıdaki tabakaları göstermektedir.
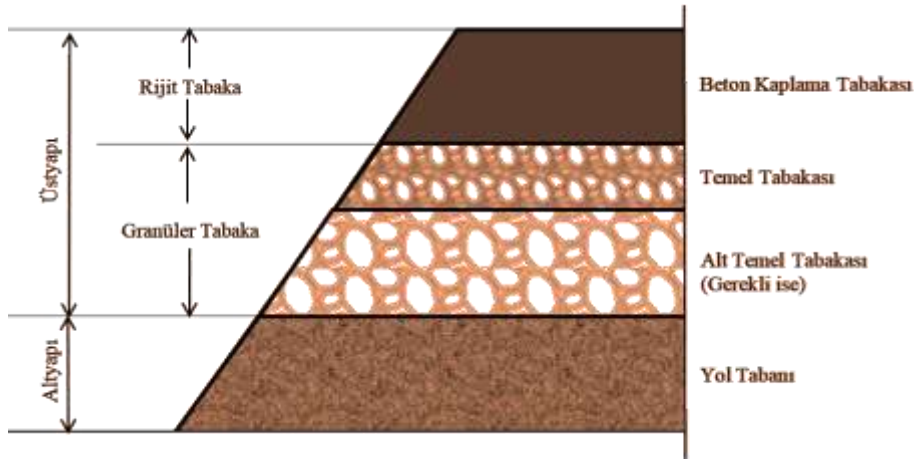
Şekil 6. Rijit Üstyapı Kesit Görünümü (Kök, 2019; Geçkil ve ark., 2021b)

AASHTO (1993) tasarım rehberine göre eşitlik 1 yardımı ile rijit üstyapı tabaka kalınlıkları hesaplanmaktadır (AASHTO, 1993).

$$\log_{10}(T8,2) = ZR.S0 + 7,35.\log_{10}(d+1) - 0,06 + \frac{\log_{10}[\frac{\Delta PSI}{4.2-1.5}]}{1 + \frac{1,624.10^7}{(d+1)^{8,46}}} + (4,22 - 0,32.Pt).\log_{10}[\frac{S'c.Cd(d^{0,75}-1,132)}{215,63.J[d^{0,75}\frac{18,42}{(Ec/k)^{0,25}}]}] \qquad 1$$

Burada;
$T_{8.2}$: Proje trafiğinin eşdeğer standart dingil yükü tekrar sayısı (8,2ton),
Z_R: Standart sapma,
S_o: Performans ve trafik öngörüsünün bileşik standart hatası,
d: Beton kaplama kalınlığı rijit üstyapı (inç),
ΔPSI: Toplam hizmet kabiliyeti kaybı,
J: Yük transfer katsayısı,
P_0: Başlangıç hizmet kabiliyeti indeksi,

C: Drenaj katsayısı,

P_t: Nihai hizmet yeteneği indeksini gösterir,

S'_c: Betonun kopma modülü (Eğilmede çekme mukavemeti) (psi),

k: Yatak katsayısı (pci),

E_c: Betonun elastisite modülü (psi) değerini göstermektedir.

Bu çalışmada, MK ile yapılan stabilizasyonun rijit üstyapı üzerindeki etkilerini belirlemek maksadıyla tasarım optimum karışım oranı dikkate alınarak yapılmıştır.

3. Bulgular ve Tartışma

Yol taban zemininin metakaolin ile stabilizasyonunun rijit yol üst yapı etkisinin araştırıldığı bu çalışmada, uygulanan deneyler ve rijit üst yapı tasarımı sonuçları aşağıdaki başlıklarda sunulmuştur.

3.1. Standart Proktor Deneyi Bulguları

Katkısız zemin (SAF) ile ağırlıkça %3, %6, %9, %12 ve %15 metakaolin (MK) katkılı örneklere standart proktor deneyi uygulanmıştır. Deney neticesinde belirlenen ω (%) ve ρ_k (g/cm³) sonuçlarına göre Şekil 7'de çizilen kompaksiyon eğrileri verilmiştir. Belirlenen ω_{opt} ile ρ_{kmax} sonuçları Tablo 3'te verilmiştir.
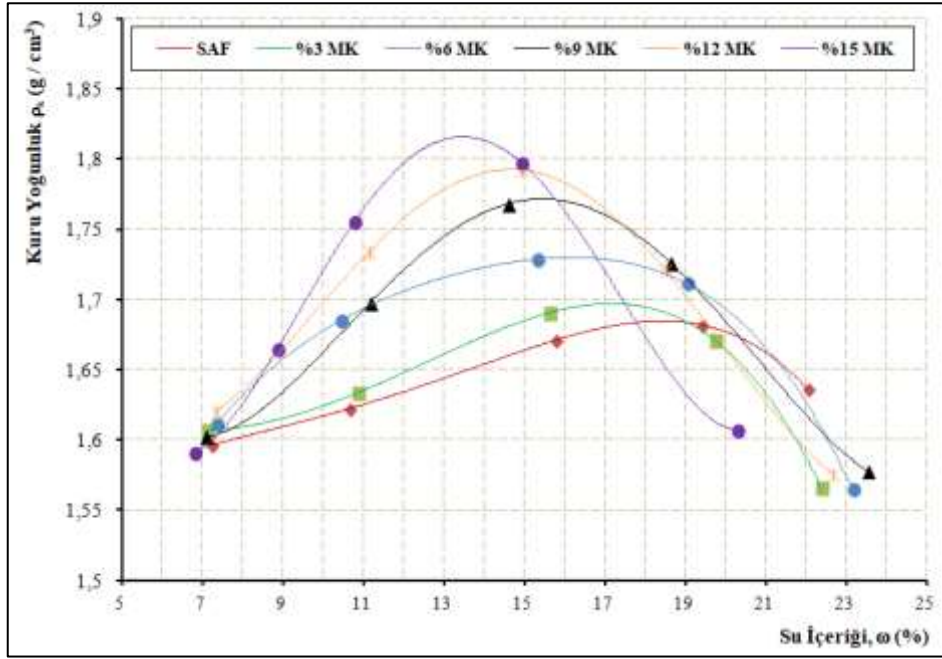
Şekil 7. Standart proktor deneyine ait kompaksiyon eğrileri.

Tablo 3. katkısız zemin ve metakaolin katkılı zeminin standart proktor deneyi sonuçları

Test Numunesi	ρ_{kmax} (g/cm³)	ω_{opt} (%)
SAF	1,685	18,50
%3 MK	1,697	17,20
%6 MK	1,730	16,30
%9MK	1,772	15,50
%12MK	1,792	14,60
%15MK	1,813	13,70

Proktor deneyi sonuçlarında, hazırlanan karışımlarda MK oranının artmasıyla ω_{opt} değerinin azaldığı, ρ_{kmax} değerinin arttığı gözlemlenmiştir. Bu bulguların, literatür (Ghida, 2022) ile uyumlu olduğu görülmüştür. MK'nın zemin numunesinden daha ince dane yapısına sahip olması nedeniyle filler (dolgu) etkisi gösterdiği bu durumun ρ_{kmax} değerini arttırdığı düşünülmektedir. Ayrıca uygulanan deneylerde MK oranı artıkça, ω_{opt} azalmasının, literatürde (Chakkor, 2021) MK'nın daha az suya ihtiyaç duyan amorf bir morfolojiye sahip olduğu görüşüyle uyumlu olduğu görülmektedir.

3.2. Serbest Basınç Deney Bulguları

Katkısız zemin (SAF) ile ağırlıkça %3, %6, %9, %12 ve %15 MK'lı örnekler, belirlenen ω_{opt} ile ρ_{kmax} verileri dikkate alınarak hazırlanmıştır. Örneklere, oda sıcaklığındaki 28 günlük kür süresi sonrası serbest basınç deneyi uygulanmıştır. Deneylerin 10 dakikayı aşmadığı gözlemlenmiştir. Katkısız zemin ve MK katkılı numunelerin eksenel gerilme (q) ile birim şekil değiştirme (ε) sonuçları grafiklerle Şekil 8'de, serbest basınç mukavemeti (q_u) ve serbest basınç mukavemetinin oluştuğu andaki birim şekil değiştirme (ε_u) değerleri Tablo 4'te verilmiştir.
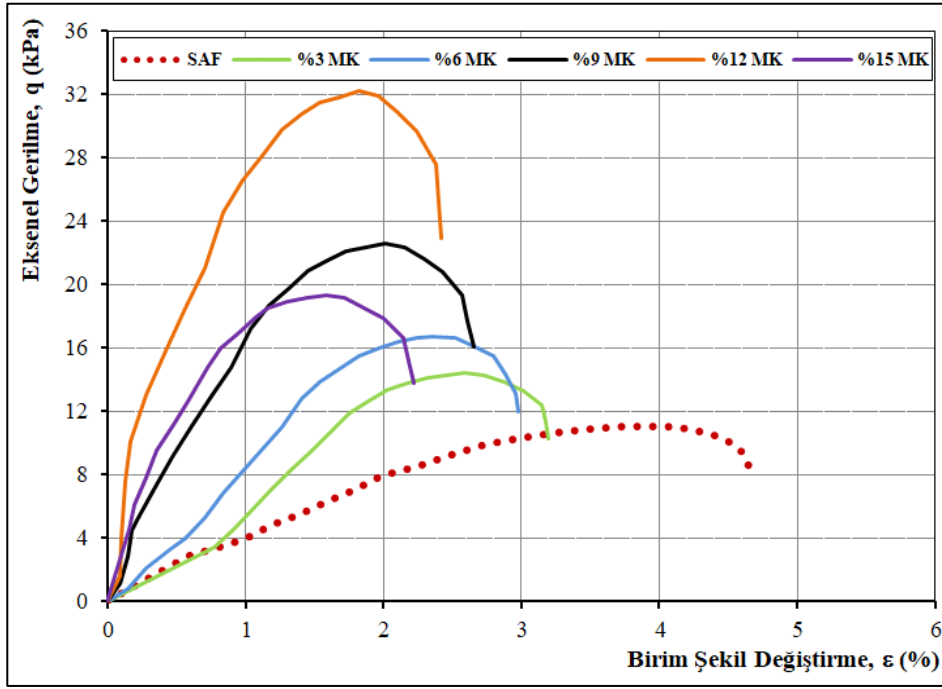
Şekil 8. 28 günlük kür sonrası katkısız ve metakaolin katkılı numunelerin q-ε grafiği.

Tablo 4. 28 günlük kür sonrası katkısız ve metakaolin katkılı q_u-ε_u verileri

Test Numunesi	q_u (kPa)	ε_u (%)
SAF	11,03	3,98
%3 MK	14,40	2,59
%6 MK	16,67	2,35
%9 MK	22,57	2,01
%12 MK	32,17	1,82
%15 MK	19,33	1,58

Serbest basınç deneyi sonuçlarında, MK'lı numunelerin katkısız zeminin serbest basınç dayanımından daha fazla olduğu görülmüştür. MK katkısının zeminin dayanımını artırdığı ve bu sonuçların literatürle (Reddy ve ark., 2018; Abdulkareem ve Abbas, 2021; Ayyappan ve ark., 2017) uyumlu olduğu tespit edilmiştir. MK ilavesi yapılan tüm numunelerin serbest basınç dayanımlarının katkısız zemine göre daha yüksek olduğu gözlemlenmiştir. %3, %6, %9, %12 ve %15 oranlarında metakaolin ilavesiyle hazırlanan karışımlarda, mukavemet değerinde en iyi artış %12 MK oranında görülmüş ve katkısız zemine göre 2,92 kat artış olduğu hesaplanmıştır. Literatürde (Siddique ve Kalus, 2009; Badogiannis ve ark., 2004; Khatib ve Hibber, 2005), kalsine edilme sürecinde metakaolindeki alüminyum ve silisin kristal yapılarının bozulduğu, amorf yapılı ve yüksek puzolanik özelliklere sahip bir ürün ortaya çıktığı, ayrıca metakaolinin ince yapısının, boşlukları doldurarak filler etkisi ile mekanik özellikleri iyileştirdiği belirtilmektedir. Çalışmamızda hazırlanan karışımlarda metakaolinin puzolanik özellik gösterdiği ve filler etkisiyle mekanik özellikleri artırdığı düşünülmektedir. Ancak, metakaolin miktarının artışının

belirli bir oranın üzerine çıkmasının yararlı olmadığı ve fazla katkı malzemesinin reaksiyona giremediği, bu nedenle karışımların dayanımını yeterince artıramadığı düşünülmektedir. MK miktarının artışıyla birlikte birim şekil değiştirmenin azaldığı ve bu durumun MK'nın numunelerin sertliğini artırmasıyla (rijitleştirme etkisi) ilişkili olduğu değerlendirilmektedir. Elde edilen sonuçlar, literatürde (Uzuner, 2014) belirtilen yumuşak zeminlerin sert zeminlere kıyasla daha fazla deformasyona uğradığı görüşüyle örtüşmektedir.

3.3. Kaliforniya Taşıma Gücü Oranı Deney Bulguları
KTO deneyi yapılmasına yönelik serbest basınç deney sonuçlarından elde edilen ağırlıkça %12 MK sonucu esas alınarak, katkısız zemin (SAF) ve %12 MK ilaveli karışım numuneleri hazırlanmıştır. Numuneler ω_{opt} ve ρ_{kmax} esas alınarak hazırlanmıştır. Numunelere 28 günlük kür süresinin ardından KTO deneyi uygulanmıştır. KTO deneyleri sonucunda 28 günlük kür süresi sonunda tespit edilen yük-deplasman grafiği Şekil 9'da ve KTO değerleri ise Tablo 5'te verilmiştir.
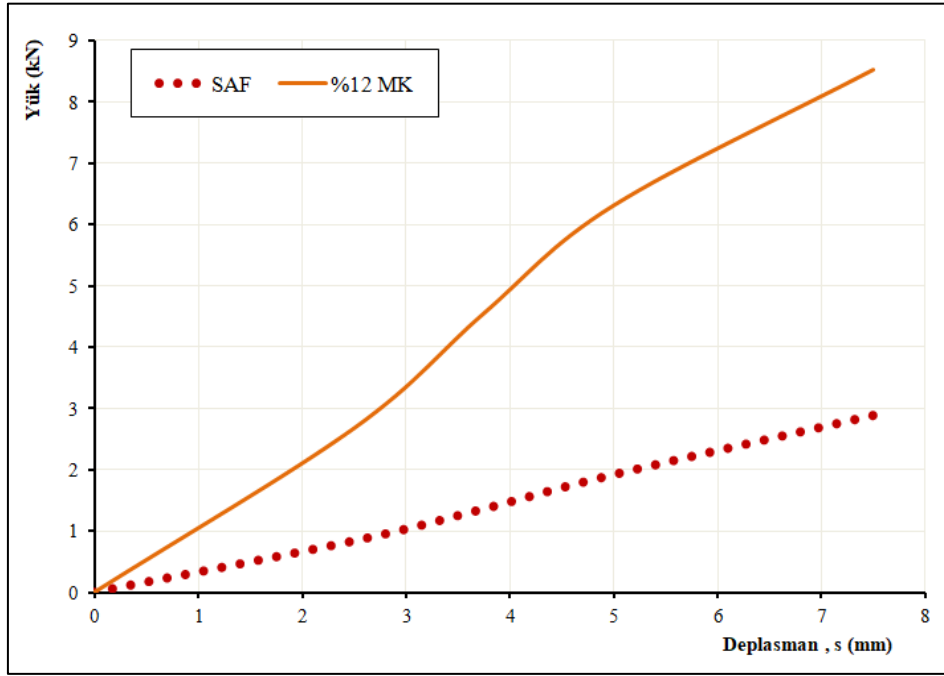
Şekil 9. 28 günlük kür ardından katkısız ve metakaolin katkılı numunelerin yük-deplasman ilişkisi.

Tablo 5. 28 günlük kür ardından katkısız ve metakaolin katkılı numunelerinin test sonuçları

Test Numunesi	2,5 mm için KTO Değeri, (%)	5 mm için KTO Değeri, (%)
SAF	6,36	9,65
%12 MK	20,20	31,61

KTO deneyi sonuçları incelendiğinde, 28 günlük kür süresinin ardından KTO deneyine uygulanan numunelerde, 2,5 ile 5 mm deplasman için elde edilen KTO değerleri katkısız zemin için sırasıyla %6,36 ve %9,65; %12 MK ilaveli zemin için ise %20,20 ve %31,61 olarak bulunmuştur. KTO değerinin, MK katkılı örneklerde 2,5 ile 5 mm penetrasyon için katkısız zemin numunelerine göre sırasıyla %217,61 ve %227,56 oranında arttığı belirlenmiştir. MK'lı karışımların KTO değerinin katkısız numuneden daha yüksek olduğu bu durumun literatürde (Onyelowe ve ark., 2023; Umar ve ark., 2022; Attah ve ark., 2009) MK katkılı zeminlerin taşıma gücünü iyileştirdiği görüşü ile örtüştüğü belirlenmiştir.

3.4. Rijit Üst Yapısı Tasarımı Yapılması

AASHTO 1993'te belirtilen kurallara uygun olarak, rijit üst yapı tasarımı esaslarına göre, 28 günlük kür süresinin ardından elde edilen katkısız zemin ve %12 MK ilaveli zemin KTO değerleri kullanılarak dizayn yapılmıştır. Dizaynda, derzli donatısız rijit yol kaplama kalınlığı incelenmiştir. Bu etüt yapılırken yolun;

- Proje analiz süresinin 30 yıl olduğu,
- 2 x 2 = 4 şeritli devlet yolu,
- Trafiğin ilk sene için günlük kamyon 1355 adet treyler, 498 adet, otobüs 1298 adet, otomobil 10500 adet, minibüs 960 adet olduğu varsayılarak, 8,2 ton

eşdeğer standart tek dingil yükü tekrar sayısı 130.000.000 olarak değerlendirilmiştir.
- Güvenilirlik oranı R=% 99,9 olarak alınmıştır.
- Hesaplanan rijit üstyapı tabaka kalınlığı, temel veya alt temelin var olduğu esas hesaplanmıştır.

Rijit üst yapı tasarımı için en yüksek KTO değerleri baz alınarak katkısız zemin için %9,65 ve %12 MK ilaveli karışım için %31,61 kullanılmıştır. Hesaplamalarda Tablo 6'daki parametreler kullanılmıştır.

Tablo 6. Rijit üstyapı hesabında kullanılan parametreler

Parametreler	Seçilen Değer
Proje trafiğinin eşdeğer standart tek dingil yükü tekerrür sayısı, $T_{8,2}$	130.000.000
Portland çimentolu betonun kopma modülü (psi)	660
Drenaj katsayısı, Cd	1
Betonun elastisite modülü, Ec (C 35/45)	4.786.244
Yolun ilk servis kabiliyeti, P_0	4,5
Trafik tahmini ve peformans tahmininin bileşik standart hatası, S_0	0,35
Yolun son servis kabiliyeti, Pt	2,5
Servis kabiliyeti indeksi, ΔPSI	2
Yük transfer katsayısı, J	2,7
Güvenilirliğin standart normal sapması, Z_R (Devlet yolu R=%99,9)	-3,090

Hesaplamalarda ilk adım olarak, yol taban zemininin yatak katsayısı (k) ve esneklik modülü (M_R) belirlenmiştir. M_R hesaplanmasına yönelik, 2024 yılı Ocak ayında AASHTO tarafından yayımlanan mekanik-ampirik teknik revizyonları içeren kaplama tasarım kılavuzu 3. baskısında (MEPDG-3) yer alan, zemine ait M_R (psi) = 2555 (KTO)$^{0.64}$ korelasyonu (AASHTO, 2024) ve k = M_R / 19,4 korelasyonu (AASHTO, 1993) mevcuttur. M_R ve k değerlerinin belirlenmesinde söz konusu korelasyon kullanılmıştır.

Katkısız zemin için MR ve k değeri 10.902 psi (75183127 Pa) ve 561,94 hesaplanmıştır. %12 MK'lı karışım için M_R ve k değeri 23.296 psi (160661042 Pa) ve 1200,82 hesaplanmıştır. Bu veriler ve Tablo 6'daki değerler kullanılarak denklem (1) yardımı ile C 35/45 beton sınıfı için katkısız zeminin plak kalınlığı (d) 18,76 inç uygulama esas alınarak 48 cm, %12 MK katkılı zemin için ise 13,38 inç uygulama esas alınarak 34 cm seçilmiştir. Bu sonuçlara göre, %12 MK içeren karışımlar için tabaka kalınlığının katkısız zemine göre 14 cm azalarak yaklaşık %29,17 oranında azaldığı belirlenmiştir.

3.5. Rijit Üstyapının Ekonomik Analizi

MK ile stabilize edilmiş yol tabanının karayolu rijit üstyapı maliyetine etkisi, Karayolları Genel Müdürlüğü şartlarına göre değerlendirilmiştir. Çevre ve Şehircilik Bakanlığı'nın 2024 yılı birim fiyat cetvellerine (ÇSB, 2024) göre, C 35/45 basınç sınıfındaki betonun birim alan (m²) maliyeti hesaplanmıştır. Analiz ve maliyet hesaplamalarına göre, katkısız zemin için rijit yol üstyapısının birim maliyeti 1364,28 TL/m², %12 MK katkılı zemin için ise 966,55 TL/m² olarak belirlenmiş ve bu bilgiler Tablo 7'de sunulmuştur.

Tablo 7. Katkısız ve %12 MK katkılı zeminler için tabaka birim maliyetleri

Poz no	Tanım	Birim	Birim Fiyat (TL)	m² /cm Maliyeti (TL)	Hesaplanan Tab.Kal. (cm)	m² Maliyeti (TL)
15.150.1007 (Katkısız)	Beton Santralinde Üretilen veya Satın Alınan ve Beton Pompasıyla Basılan, C 35/45 Basınç Dayanım Sınıfında Beton Dökülmesi (Beton Nakli Dâhil)	m³	2842,8	28,43	48	1364,28
15.150.1007 (%12 MK)		m³	2842,8	28,43	34	966,55

Ayrıca, %12 MK ile yol tabanın 20 cm kalınlığında stabilize edilmesindeki analizde; malzemenin taşınması, traktör riperi ile zeminin kabartılması, traktör buldozeri ile stabilizatör malzeme dağıtılması, greyder ile serme ve karıştırma, arazöz ile sulama, titreşimli silindirle ve lastik tekerlekli silindir ile sıkıştırma yapılması esas alınarak 361,49 TL/m² alınmıştır. MK'nın ton bazında şantiye mahalline teslim fiyatı göz önüne alınmıştır. Tablo 8'de stabilizasyonun m² birim maliyetleri verilmiştir. Ayrıca, katkısız zemin ile %12 MK katılarak iyileştirilen zeminler göz önüne alınarak Şekil 10'da %12MK ilave edilmiş ve edilmemiş durumda beton tabaka ve zemin stabilizasyon maliyetleri görülmektedir.

Hesaplanan tabaka maliyetleri değerlendirildiğinde, yapım maliyetinde %2,68 oranında bir azalma görülmüştür. Yapılan hesaplamalarda, 20 metre genişliğindeki ve 1000 metre uzunluğundaki bir yolda, %12 MK ile iyileştirilmiş bir yol tabanıyla 730.040,00 TL maliyet azaltılarak tasarruf sağlanacaktır. Bu kapsamda, karayolu ağının uzunluğu dikkate alındığında, zemin stabilizasyonu sayesinde rijit kaplama yapılması durumunda önemli kazanç sağlanacağı değerlendirilmektedir.

Tablo 8. %12 MK katkılı zemin için stabilizasyon birim maliyetleri

Poz no	Tanım	Birim	Birim Fiyat (TL)	Maliyet (TL) m² /cm	Maliyet (TL) m²
KGM 03.507	Traktör ripperin bir saatlik ücreti	saat	2083,73	0,0208	0,42
KGM 03.511	Traktör Buldozerin 1 saatlik ücreti	saat	1946,93	0,0876	1,75
KGM/15.140	Makina ile serme ve karıştırma (Greyder ile)	m³	13,95	0,1395	2,79
KGM/15.047	Arazöz ile sulama	ton	104,79	0,1048	2,10
KGM/15.052/3	Titreşimli silindirle sıkıştırma yapılması	saat	1221,53	0,1222	2,44
KGM/15.058/1	Lastik tekerlekli silindir ile sıkıştırma yapılması	saat	891,94	0,0892	1,78
Piyasa	%12 MK Temini Nakliye Dahil	kg	9,12	17,5104	350,21
				Toplam:	361,49
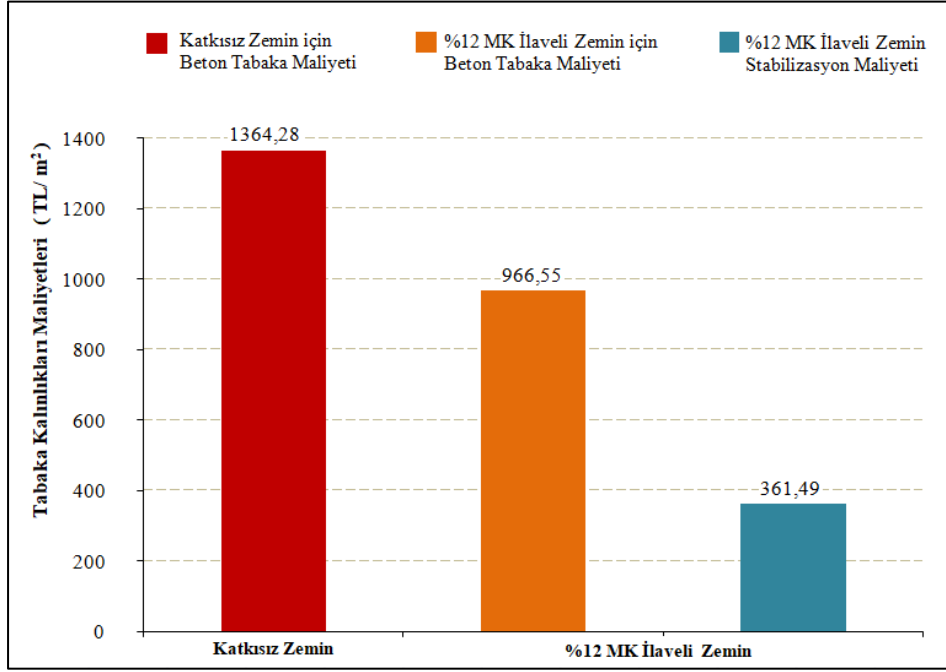
Şekil 10. %12MK ilave edilmiş ve edilmemiş durumda beton tabaka ve zemin stabilizasyon maliyetleri.

4. Sonuç ve Öneriler

Bu araştırmada, kötü derecelenmiş kum bir yol tabanın metakaolin ile iyileştirilmesinin rijit yol üst yapısı kalınlığı ile maliyeti üzerindeki etkileri incelenmiştir. Bu çalışmanın sonuçları aşağıda özetlenmiştir.

Standart proktor deneyi sonuçlarında; MK oranının artmasıyla ω_{opt} değerinin azaldığı, ρ_{kmax} değerinin ise arttığı, bu durumun MK'nın filler (dolgu) etkisi gösterdiği ve zemin numunesinden daha az su emme kapasitesine sahip olmasının etkili olduğu düşünülmektedir.

MK miktarının artmasıyla numunelerin sertliğini arttığı bu nedenle birim şekil değiştirmenin azaldığı değerlendirilmiştir.

Serbest basınç deneyi neticelerinde, MK ile iyileştirilen zeminlerde 28 günlük kür sonunda en büyük mukavemet değerinin ağırlıkça %12 MK'lı numunede belirlenmiştir. Katkısız zemine göre mukavemet değerinin 2,92 kat arttığı belirlenmiştir.

KTO deney sonuçlarında ise %12 MK katkılı zeminlerin 28 günlük kür süresi sonundaki 2,5 ile 5 mm penetrasyon için KTO değerleri, katkısız zemin numunelerine göre sırasıyla %217,61 ve %227,56 oranında arttığı belirlenmiştir. Bu artışın MK katkılı zeminlerin taşıma gücünü iyileştirdiğini göstermektedir.

KTO ve serbest basınç deney sonuçlarından, metakaolinin puzolanik özellik gösterdiği ve filler etkisi meydana getirerek mekanik özellikleri iyileştirdiği değerlendirilmektedir.

Yol üst yapısı tasarım sonuçlarında ise, %12 MK içeren stabilize zeminler için tasarlanan rijit üstyapı kalınlığında %29,17 oranında azalma olduğu, bu durumun MK'nın taşıma gücüne olumlu etkisinden kaynaklandığını göstermektedir.

Maliyet analizi sonuçlarında ise, %12 MK katkılı stabilize zeminlerin üstyapı maliyetlerinin, katkısız zemine kıyasla %2,68 oranında azaldığı belirlenmiştir. Bu hesaplamalar ışığında, 20 metre genişliğindeki ve 1000 metre uzunluğundaki bölünmüş bir yolda, %12 MK ile yol taban zemininin stabilizasyonu durumunda rijit üstyapı maliyetinde 730.040,00 TL maliyet azaltılarak tasarruf sağlanabilecektir.

Sonuç olarak, metakaolinin yol taban zemininin iyileştirilmesinde kullanılmasının, zeminin taşıma kapasitesini arttırılmasını sağlayacağı, rijit üst yapı tabaka kalınlığını ve maliyetini düşüreceği belirlenmiştir. Böylelikle rijit üst yapı yapımında kullanılan malzeme miktarının azaltılması ile, özellikle beton imalatında kullanılan çimento ve agreganın üretimi, taşınması ve uygulanmasında meydana gelen CO_2 salımı başta olmak üzere çevreye verilen zararın azaltılacağı ve böylelikle çevrenin korunmasına katkı sağlanacağı düşünülmektedir. Ayrıca, MK'nın proje bazında temin miktarının artmasıyla ve karayolu projelerinin uzunlukları da dikkate alınarak, MK'nın daha ekonomik olarak tedarik edilerek projelerin maliyetinin daha da azaltılabileceği değerlendirilmektedir.

Kaynaklar

AASHTO. 1993. Guide for design of pavement structures. American Association of State Highway and Transportation Officials, Washington, DC, USA, pp: N1.

AASHTO. 2024. Mechanistic-Empirical Pavement Design Guide, 3rd Edition (MEPDG-3), American Association of State Highway and Transportation Officials, Washington, DC, USA, pp: 128.

Abdulkareem SA, Abbas JM. 2021. Effect of adding metakaolin based geopolymer to improve soft clay under different conditions. Earth Environ Sci, 856: 012011-8.

Attah IC, Jonah CA, Etim RK, Ogarekpe NM. 2019. Modelling and predicting CBR values of lateritic soil treated with metakaolin for road material. ARPN J Engin Applied Sci, 14(20): 3609-3618.

Ayyappan A, Palanikumar S, Kumar D, Vinoth M. 2017. Influence of geopolymers in the stabilization of clay soil. Inter J Emerging Technol Engin Res, 5: 108-120.

Badogiannis E, Papadakis VG, Chaniotakis E, Tsivilis S. 2004. Exploitation of poor Greek kaolins: strength development of metakaolin concrete and evaluation by means of k-value. Cement Concrete Res, 34: 1035-1041.

Chakkor O. 2021. Kırmızı çamur ve metakaolin tabanlı geopolimer harçların mekanik ve durabilite özelliklerinin incelenmesi. Doktora Tezi, İstanbul Aydın Üniversitesi, Lisansüstü Eğitim Enstitüsü, İstanbul, Türkiye, pp: 138.

Çınar M. 2024. Kahramanmaraş depremi sonrası oluşan gaz beton atıkları ile stabilize edilmiş killi kum zeminin geoteknik özelliklerinin araştırılması. DUJE, 15: 269-275.

Çevre ve Şehircilik Bakanlığı Birim Fiyatları. 2024. URL: https://webdosya.csb.gov.tr/db/yfk/icerikler/1--2024-birim-fiyatlar-20240123142524.pdf. (erişim tarihi: 24 Mayıs 2024).

Demir A, Sarıcı T. 2017. Bearing capacity of footing supported by geogrid encased stone columns on soft soil. Geomechan Engin, 12(3): 417-439.

Geçkil T, Sarıcı T, Karabaş B. 2021a. Siyah karbon ile stabilize edilen taban zeminin yol esnek üst yapı maliyetine etkisi. Avrupa Bilim Teknol Derg, (23): 222-235.

Geçkil T, Sarıcı T, Karabaş B. 2021b. Siyah Karbon Stabilizasyonlu Zeminin Rijit Kaplama Kalınlığı ve Maliyetine Etkileri. El-Cezerî J Sci Engin, 8(3): 1372-1384.

Ghida A. 2022. Efects of incorporation of cement and metakaolin on the mechanical properties of poorly graded sand. Arabian J Geosci, 15(24): 1777.

Jauberthie R, Rendell F, Rangeard D, Molez L. 2010. Stabilisation of estuarine silt with lime and/or cement. Applied Clay Sci, 50: 395-400.

Karahan O. 2011. Metakaolin ve silis dumanı içeren harçların aşınma direncinin karşılaştırılması. Bilimsel Araştırma Projesi, Kesin Sonuç Raporu, Erciyes Üniversitesi Bilimsel Araştırma Projeleri Birimi, Kayseri, Türkiye, ss: 68.

KGM. 2019. Karayolları beton yol üstyapılar projelendirme rehberi. T.C. Ulaştırma Bakanlığı Karayolları Genel Müdürlüğü Teknik Araştırma Dairesi Başkanlığı Üstyapı Şubesi Müdürlüğü, Ankara, Türkiye, ss: 53.

Khatib JM, Hibbert JJ. 2005. Selected Engin properties of concrete incorporating slag and metakaolin. Construct Build Mater, 19: 460-472.

Kök BV. 2019. Karayolu Mühendisliği ve Tasarımı, Nobel Akademik Yayıncılık Ankara, ss:192.

Kumar BRP ve Sharma RS. 2004. Effect of fly ash on engineering properties of expansive soils. J Geotec Geoenviron Engin, 130(7): 764-767.

Kulanthaivel P, Harikaran M, Gokulakannan S, Vinodhkumar A. 2023. Eco-friendly soil stabilization: a combined approach using lime and waste eggshell powder. Global NEST J, 25(7): 120-130.

Nebioğulları MA. 2010. Metakaolin, yüksek fırın cürufu ve uçucu kül katkısının beton hidratasyon sıcaklığına etkisi. Yüksek Lisans Tezi, Niğde Üniversitesi Fen Bilimleri Enstitüsü, Niğde, Türkiye, ss: 130.

Ok B, Demir A, Sarıcı T, Ovalı M. 2021. Geosentetiklerle güçlendirilmiş karayolu temellerinin plaka yükleme deneyi ile değerlendirilmesi. Pamukkale Üniv Müh Bilim Derg, 27(6): 718-728.

Onyelowe KC, Ebid AM, Kontoni DN, Onukwugha ER. 2023. Effect of metakaolin and ashcrete blend on the mechanical properties of lateritic soil for sustainable subgrade and subbase construction. Multiscale Multidiscip Modeling, Experi Design, 7(2): 1197-1208.

Orhan M. 2013. Zemin mekaniği laboratuvar deneyleri. Gazi Kitabevi, Ankara, Türkiye, ss: 156.

Öksüz K, Yıldız AA. 2006. Uçucu külün zemin stabilizasyonunda kullanımı. Yüksek Lisans Tezi, Çukurova Üniversitesi, Fen Bilimleri Enstitüsü, Adana, Türkiye, ss: 146.

Reddy DS, Kowshik K, Kishor MJ, Durga RV, Kumar VP. 2018. Enhancement of soil properties by using fly ash and metakaolin, Inter J Innov Technol Explor Engin (IJITEE), 8(2): 1-6.

Sarıcı T. 2019. Puzolan ile güçlendirilmiş inşaat ve yıkıntı atıklarının granüler dolgu olarak kullanılabilirliğinin değerlendirilmesi. FBE, Doktora Tezi, İnönü Üniversitesi, Fen Bilimleri Enstitüsü, Malatya, Türkiye, ss: 335.

Sarıcı T. 2014. Geosentetik ile güçlendirilmiş taş kolonların taşıma kapasitesinin analizi. Yüksek Lisans Tezi, İnönü Üniversitesi, Fen Bilimleri Enstitüsü, Malatya, Türkiye, ss: 134.

Sarıcı T, Ok B, Mert A, Çömez Ş. 2022. The resilient modulus of hybrid construction and demolition wastes reinforced by a geogrid, Acta Geotech Sloven, 19(2022/2): 2-14.

Siddique R, Kalus J. 2009. Influence of metakaolin on the properties of mortar and concrete: a review, Applied Clay Science, 43, 392-400.

Tunç A. 2002. Yol mühendisliğinde geoteknik ve uygulmaları. Nobel Yayınevi, Ankara, Türkiye, ss: 912.

Tunç A. 2007. Yol malzemeleri ve uygulamaları. Nobel Yayınevi, Ankara, Türkiye, ss: 840.

Umar SY, Yero SA, Muhammed A, Abdulkarim II. 2022. Effect of metakaolin on strength properties of lateritic soil intended for use as road construction material. Path Sci: Inter Electron Sci J, 8: 2.

Uzuner BA. 2016. Temel mühendisliğine giriş. Derya Kitabevi, Trabzon, Türkiye, ss: 409.

Uzuner BA. 2014. Temel zemin mekaniği. Derya Kitabevi, Trabzon, Türkiye, ss: 734.

Wassie TA, Demir G. 2024. Mechanical strength and microstructure of soft soil stabilized with cement, lime, and metakaolin-based geopolymer stabilizers. Adv Civil Engin, 2024: 6613742.

Yılmaz I, Yıldıran M, Keskin İ. 2017. Zemin mekaniği laboratuvar deneyleri ve çözümlü problemler. Seçkin Kitabevi, Ankara, Türkiye, ss: 288.

OPTIMIZING RESOURCE ALLOCATION IN THE BLACK SEA TR83 AREA OF TÜRKİYE: ADVANCING TOWARDS AN INDUSTRIAL CIRCULAR ECONOMY

Mohammad Safayat HOSSAIN[1]*, Nada A. A. JARADAT[1], Bilge AYDIN ER[1], Yüksel ARDALI[1]

[1]*Ondokuz Mayıs University, Faculty of Engineering, Department of Environmental Engineering, 55200, Samsun, Türkiye*

Abstract: The TR83 region in Türkiye is recognized as one of the leading industrial centers of the Black Sea region with its efficient use of resources and wide range of activities. In the project carried out jointly by the University and the Central Black Sea Development Agency, the potential for optimizing resource use in the industrial sector of the region was evaluated to demonstrate circular economy applicability. Research was conducted to determine the current situation in the sector and to draw up a road map for the future. These surveys followed by a comprehensive field survey, where the data was processed and analyzed with the guidance of experts. Additionally, a Data SWOT Analysis was undertaken. In the research, the responses of companies in Amasya, Çorum, Samsun and Tokat provinces were analyzed. The findings highlighted the importance of implementing resource efficient approaches in the industrial sector. The proposed measures advocate the adoption of resource-efficient goods and the implementation of a circular economy strategy. The study also aims to identify requirements for environmentally friendly design and promote the use of best practices in industrial sectors and highlighted the need for a synchronized effort to achieve a future that is both ecologically sustainable and resource-optimized in the TR83 region.

Keywords: Circular economy, Economic potential, Environmental sustainability, Industrial infrastructure TR83 region, Resource efficiency

*Corresponding author: Ondokuz Mayıs University, Faculty of Engineering, Department of Environmental Engineering, 55200, Samsun, Türkiye	
E mail: safayathossain076@gmail.com (M. S. HOSSAIN)	
Mohammad Safayat HOSSAIN https://orcid.org/0000-0002-0152-8806	**Received:** January 15, 2024
Nada A. A. JARADAT https://orcid.org/0009-0001-1473-7439	**Accepted:** August 09, 2024
Bilge AYDIN ER https://orcid.org/0000-0002-6546-0089	**Published:** September 15, 2024
Yüksel ARDALI https://orcid.org/0000-0003-1648-951X	

1. Introduction

The exponential growth of the worldwide population and economic prosperity has caused a substantial increase in living standards and needs, leading to the exhaustion of resources (Weterings et al., 2013). Enhancing resource efficiency is essential for mitigating environmental deterioration and facilitating affluence for a burgeoning population. Implementing policies and activities aimed at enhancing resource efficiency might effectively decrease global resource extraction while also stimulating economic activity (Nong et al., 2023). Recycling is crucial for optimizing resource efficiency by maximizing the use of materials and products (Schmidt, 2010). Resource efficiency, defined as the capacity to utilize resources in a manner that minimizes waste and optimizes productivity, is of utmost importance for achieving sustainable development and enhancing economic competitiveness (Worrell and Reuter, 2014). Implementing policies and activities aimed at enhancing resource efficiency might effectively decrease worldwide resource extraction and greenhouse gas emissions, while simultaneously stimulating economic activity (Nong et al., 2023). The Rural Development strategy of the

European Union is crucial in attaining resource efficiency goals (Herrmann, 2018). The results emphasize the significance of resource efficiency in tackling environmental issues and advancing sustainable development. The imperative to enhance resource efficiency considering diminishing natural resources and environmental deterioration is an urgent concern (Horodetska et al., 2022). The development of industrial strategies that prioritize the use of best available techniques and secondary resources can accomplish this objective (Skobelev, 2021). It is essential to identify and implement technologies, products, and strategies that have a high potential for resource efficiency (Rohn et al., 2011). Optimizing energy utilization in production is crucial for minimizing resource use and waste (Ross, 1992). However, a lack of knowledge, potential approaches, limited financial accessibility, and poor human capabilities prevent businesses from adopting resource-efficient and environmentally friendly production methods (Vorfolomeiev and Vorfolomeev, 2019). To tackle these difficulties, organizations should prioritize the economical and effective utilization of resources and energy during manufacturing, which may

lead to cost savings and enhance competitiveness (Nong et al., 2023). Moreover, the notion of highly efficient factories that maximize their influence on the surrounding environment might serve as a crucial approach for competitive and sustainable production (Lentes et al., 2016). Andriushchenko (2022) devised a strategic plan for overseeing the region's capacity for innovation, whereas Konash and Nasr (2022) underscored the significance of comprehending the intricate interplay of technology, economics, and society. Reaney et al. (2023) emphasized the necessity of a well-established infrastructure and specialized skills for the advancing information systems and business process management settings. Integrating with local government to guarantee resource efficiency is of paramount importance for a growing nation since it promotes a circular economy model (Hossain et al., 2023). Finally, Motte et al. (2022) emphasized the importance of technological variables and professional competence in attaining effective administration in public management. These studies offer vital insights that contribute to the growth of the region. Several two research have been carried out to meet the demand for technological progress and higher rates of employment in the TR83 Region Market. "Several studies have been conducted to meet the demand for technological advancement and increased employment rates in the TR83 Region market. It has been determined that there has been no study on resource efficiency needs analysis in the region, and the first resource efficiency needs analysis report specific to the region has been prepared by filling this gap with this study.

1.1. Literature Review

Map of Türkiye and TR83 Region in the Black Sea in Türkiye was given in Figure 1.

Resource efficiency in industry is a crucial element of sustainable development, offering the possibility of substantial cost reductions (Nong et al., 2023). This notion has had significant historical significance and currently plays a crucial role in the shift towards a circular economy (Schmidt et al., 2019, Van and Fadeeva, 2020). Nevertheless, there is a dearth of agreement over the methodology for quantifying resource efficiency, resulting in many divergent methodologies and techniques (Sfez et al., 2017). This emphasizes the necessity for standardized assessment techniques to

guarantee comparability and suitability of resource efficiency computations in the industrial sector. Studies on resource efficiency measures have discovered several elements that influence their adoption, such as market circumstances (Delmas and Pekovic, 2015). Although the use of natural resources is increasing, there has been insufficient action taken to reduce their usage. This emphasizes the importance of implementing effective solutions to increase resource efficiency (Rohn et al., 2014). Frohling et al. (2012) introduced a method that uses material flow analysis to improve resource efficiency in production and recycling networks. This approach emphasizes the investigation of both technological and economic factors, as well as ecological considerations. A comprehensive enhancement plan has been established for the European metal mechanic industry, encompassing a decision-making toolkit to pinpoint opportunities for conserving resources (Blume et al., 2017). These studies emphasize the significance of resource efficiency measures in tackling environmental and economic concerns. Several metrics have been created to assess the effectiveness of resource utilization in different sectors (Ingaramo et al., 2009) presented eco-efficiency indicators for water and wastewater management in the sugar cane sector, whereas (Henriques and Catarino, 2017) suggested the sustainable value indicator for enhancing energy efficiency in wastewater treatment facilities. A study conducted by Wang et al. (2017) examined the interconnection between water, energy, and emissions in China's steel sector. It emphasized the possibility of employing technology-driven approaches to decrease resource consumption and emissions. Oliveira-Esquerre et al. (2009) introduced a system for managing water and wastewater in the petrochemical sector. In that study, it highlights the significance of process variability in attaining efficiency. These studies highlight the need to use indicators particular to each business and the possibility of making resource efficiency gains through technology. Various studies have emphasized the potential advantages of investing in resource efficiency in the industrial sector. Jollands and Hirsch (2018) highlight the importance of financial infrastructure and project finance in motivating such investments, especially in developing economies.
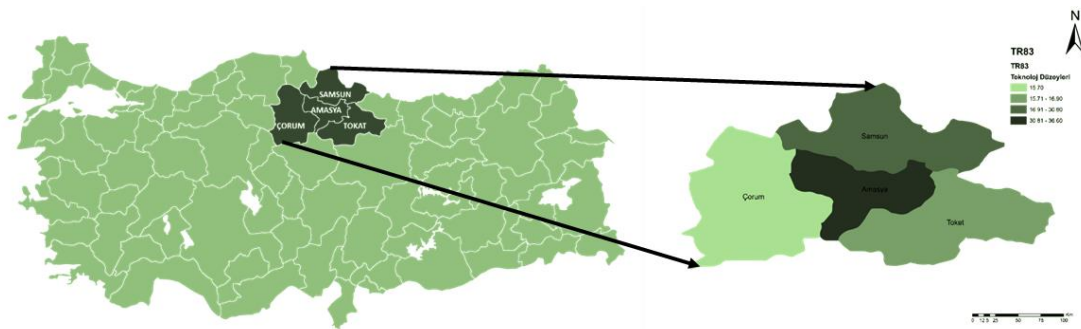
Figure 1. Map of Türkiye and TR83 region in the Black Sea in Türkiye.

Domenech and Bahn-Walkowiak (2019) presents concrete illustrations of resource-efficient technology and goods, whereas Bassi et al. (2012) emphasizes the beneficial effects of investing in energy, water, and waste efficiency within the industrial sector. Ozbugday et al. (2020) provide more evidence that resource efficiency investments have a beneficial impact on the growth performance of European small and medium-sized enterprises (SMEs). These studies highlight the potential of resource efficiency initiatives to provide environmental and economic advantages in the sector. Various studies have examined the impact of rules and self-regulation on the promotion of environmentally friendly industries. Hillary and Thorsen (1999) discovered that neither of the methods had achieved complete success in this aspect, although (Tukker, 2015) emphasized the global potential of cleaner manufacturing. In his study, (Maio et al., 2017) specifically examined China's endeavours efforts in this field, with a special emphasis on the development and execution of policies related to cleaner industrial systems. These studies emphasize the significance of both domestic and global legal matters in promoting resource efficiency and environmentally friendly industries. The European Union (EU) has been leading the way in advocating for resource efficiency and the circular economy, specifically emphasizing cleaner manufacturing and industrial symbiosis. Cainelli et al. (2017) emphasize that environmental policy has a crucial role in promoting the adoption of eco-innovations focused on resource efficiency. Meanwhile, Camilleri (2020) underscores the importance of sustainable production and consumption behaviours within the circular economy. Van Berkel and Fadeeva (2020) emphasize the advantages for businesses and the whole economy that come from resource efficiency and circularity. Ewijk (2018) examines the economic benefits, obstacles, and policies associated with these ideas. These studies emphasize the significance of resource efficiency in the European Union's attempts to shift towards a circular economy. Resource efficiency, especially within the framework of the circular economy, is a crucial catalyst for achieving both economic and environmental advantages (Muller, 2012). This is emphasized by the necessity for an efficiency revolution aimed at diminishing consumption and generating competitive advantages (Bilgen and Sarıkaya, 2016). Optimizing energy use is essential, since a comprehensive strategy for meeting future energy needs should prioritize the adoption of energy-efficient technologies to minimize environmental harm and enhance economic benefits (Hanley et al., 2006). Nevertheless, the effects of a stimulus aimed at improving energy efficiency on both the economy and the environment are intricate, since it may lead to unforeseen outcomes such as heightened energy usage and pollution (Hepbasli and Ozalp, 2003). Several studies have investigated the level of resource efficiency in the industrial sector of Türkiye. But TR83

was behind it. Hepbasli and Ozalp (2003) and Utlu and Hepbasli (2007) emphasize the significance of energy efficiency, with Utlu and Hepbasli (2007) especially examining the energy utilization efficiencies in different subsectors. Ozbilen et al. (2019) expands upon this discourse by examining the forecast of resource-efficient capacity within the Turkish manufacturing sector, highlighting the importance of implementing cleaner production practices. Onut et al. (2008) adds to this discourse by assessing the optimal energy sources for the industrial sector using the analytic network approach. These studies emphasize the importance of resource efficiency in the Turkish industrial sector and offer useful insights for future studies and policy development. An extensive literature review has been carried out to emphasize the importance of requirement analysis in business, specifically in relation to resource efficiency (Lieder, 2014). The original data has been gathered from much scientific research, reports, news stories, and other sources. The survey and expert integration have generated secondary data. Moreover, the study has highlighted the necessity of using a methodical assessment strategy to measure resource efficiency and cost effectiveness in production systems, especially in small and medium-sized companies (Lieder, 2014). The results of this study are anticipated to have a favorable influence on the cost-benefit ratio within each industry, as they establish a foundation for the formulation of resource-efficient strategies and pricing policies (Shmygol et al., 2023).

2. Materials and Methods

An exhaustive examination of resource efficiency in the TR83 region was carried out in three stages. In TR83 Region a total of 76 company, 6553 personal, and 103 industrial area has been surveyed. The initial stage encompassed the distribution of information, a comprehensive examination of existing literature, and a survey. Subsequently, the second stage entailed gathering expert perspectives and evaluating the efficacy of available resources. The concluding stage involved conducting interviews and engaging in field research, specifically emphasizing the SWOT analysis and on-site consultations. This study highlighted the significant influence of resource efficiency on both the economy and the environment.

2.1. Field Survey
2.1.1. Annexe-I
This study examined the aspects of waste, water, wastewater, energy, and emissions inside the organized industrial zones (OIZ's) of the TR83 region. The questionnaire was converted into a set of 57 questions that pertain to these specific subjects. Participants were instructed to select either "positive", "negative" or "uncertain" in response to each subject matter in the current and forthcoming periods. The responses were gathered in a manner that allows for statistical reporting. The OIZ administration was thereafter requested to

prioritize three needs from the listed ones to address the most important needs within the region and provinces. The sufficiency percentages for each need were compared to assess their respective influence.

2.1.2. Annexe-II

This part specifically addressed the utilization of raw materials, the optimization of resource efficiency, and the management of waste. The analysis encompassed the evaluation of labor force proficiency and employment, selection, and utilization of raw materials, as well as their management, water and energy consumption and their management, and waste management. The questionnaire also encompassed inquiries regarding the augmentation of capacity, research, and development (R&D), innovation, efficiency studies, and future endeavours of enterprises operating within the OIZ.

2.2. SWOT Analysis

The sustainability and adoption level of resource efficiency studies in these developer OIZs were evaluated with SWOT analysis.

2.3. Expert Integration

The TR83 Region Resource Efficiency Needs Analysis emphasized the need for collaboration, skill development, and environmentally friendly production techniques (Ardali, 2020). The findings align with Comtois, 2007 which underscored the imperative of integrating sustainable development methods in the maritime transportation industry. Boden et al. (2016) emphasized the importance of stakeholder gatherings and mutual learning to implement in the regional smart specialization programs. Welfens et al. (2017) and Jaegersberg et al. (2007) highlighted the significance of sustainable development, environmentally friendly production, and inventive approaches in eco-industrial networks and regional supply chains. Collective data that backs the integration of experts and the focus on collaboration, enhancement of skills, and adoption of sustainable manufacturing methods in the TR83 Region.

2.4. Data Analysis

A remarkable guidance has been discovered that provides both value and quantity, enabling every sector to ascertain the precise actions required to enhance their resource efficiency in waste, wastewater, energy, and emissions. This course of action was identified after the completion of data collection, with the purpose of generating the demand for the resource efficiency sector in the TR83 region. Several software programs, such as SPSS, were employed to do the study, and the findings were transformed into percentages to enhance understanding. Charts and tables can be useful for diagram-based analysis in specific situations, facilitating people's understanding of numerical issues.

3. Results and Discussion

In Annex-I, research has been conducted to evaluate the resource efficiency potential and structure of the region in the TR83 region for the purpose of cooperation. The survey covered corporate organizations from different sectors, especially companies that make significant contributions to the economy, exhibit high employment rates and actively conduct research and development activities. According to the survey, some companies in the region had 100% foreign capital, while some had domestic capital. Businesses utilized varying levels of workforce, utilized energy, natural gas and water services, and handled waste management efficiently. They established quality control systems, monitored the inputs and outputs of production, and were aware of developing technology. 60% of companies collaborated with universities or research centers and received government funding for research and development. Many businesses have committed to increasing their workforce without making formal agreements with stakeholders.

Table 1 presents a concise overview of the results pertaining to waste management, water and wastewater management, energy consumption, and knowledge of emissions among the participants. Concerning waste management, most participants had information regarding the specific sort of waste generated and the corresponding costs involved. Most participants additionally protect storage sites from external influences. Regarding water and wastewater management, a considerable number of people have information regarding their monthly water usage, upkeep, sanitation, and methods for disposing of sludge in their personal treatment facilities. Nevertheless, a significant proportion of individuals lack awareness in these areas. Concerning energy consumption, most participants demonstrate awareness of their monthly energy usage and express a desire to install motion sensor lighting systems. Regarding emission awareness, most participants have information about the sources of emissions but lack understanding of how emissions are categorized and measured. Certain participants do not possess adequate infrastructure for controlling and managing air pollution emissions. In Annex-II, the TR83 area has implemented initiatives to foster competitive manufacturing and expedite productivity and industrial development. A collaborative resource efficiency assessment study was done with Central Black Sea Development Agency - Ondokuz Mayıs University to analyze the potential for resource efficiency and enhance the organizational framework of enterprises in the TR83 region. The poll focused on organizations that make significant contributions to the economy, maintain a high level of employment, and actively participate in research and development projects. The survey had 45 inquiries pertaining to general information, sector-specific information, raw materials, resource utilization, and waste production. The assessment questions encompassed a range of areas, including general metrics and uses, workforce excellence and employment, resource choice, water and energy usage and control, wastewater and solid waste control, waste gas control, and research and development, innovation, and productivity investigations.

Table 1. Summary of the Annex-I, survey report

Parameter	Findings
Waste	1. Most participants had knowledge regarding the specific type of waste that is produced inside their respective companies. 2. A substantial proportion (59.1%) of participants possess awareness regarding the monthly expenses associated with waste removal, storage, and treatment in their respective businesses. 3. A significant majority (72.7%) of participants indicated that both product and waste storage locations are safeguarded against external influences. 4. A minority (9.1%) of participants reported that storage facilities lack protection. 5. A fraction (18.2%) of participants expressed no discernible viewpoint or knowledge on the posed inquiries.
Water and Wastewater	1. 68.2% of individuals possess knowledge regarding their monthly water consumption. 2. 27.3% of individuals lack awareness of their monthly water usage. 3. 4.5% of individuals are completely unaware of their monthly water consumption. 4. 27.3% of individuals are well-informed about maintenance, cleaning, and sludge disposal procedures if they possess their own treatment facility. 5. 45.4% of individuals lack information regarding maintenance, cleaning, and sludge disposal for their personal treatment facility. 6. 27.3% of individuals possess knowledge about maintenance, cleaning, and sludge disposal for their personal treatment facility. 7. Most respondents answered "no" to both questions.
Energy	1. Approximately 77.3% of the participants are aware of the exact amount of energy they consume monthly. 2. 13.6% of participants are unaware of their monthly energy consumption. 3. According to the survey, a significant majority of participants, specifically 86.4%, hold the belief that the walls are not enclosed and are adorned with various colors. 4. 13.6% of participants hold the belief that the walls are not open and adorned with colors. 5. Approximately 59.1% of the participants either currently utilize or have intentions to install a motion sensor lighting system. 6. A total of 27.3% of the participants either do not use or have no intention of installing a motion sensor lighting system. 7. A total of 13.6% of the interviewees expressed uncertainty over the utilization or installation of a motion sensor lighting system.
Emission	1. Most participants, namely 59.1%, were aware of the origins of both direct and indirect emissions that affect water, soil, and air within their organization. 2. Out of the participants, 18.2% responded negatively when asked if they were aware of the sources of emissions. 3. A total of 22.7% of participants expressed neutrality towards the issue. 4. Half of the participants expressed interest in the categorization and volume of emissions. 5. A total of 31.8% of participants exhibited a lack of awareness regarding the physical and chemical properties, as well as the amount, of emissions. 6. 18.2% of participants expressed neutrality towards the subject. 7. A total of 36.4% of the participants possessed an appropriate outlet system and monitoring equipment to regulate the release of air pollution from the boiler room. 8. 36.4% of participants lacked an appropriate infrastructure for an outlet system or monitoring equipment. 9. 27.2% of participants expressed neutrality towards the subject.

In the study assessed and visually displayed the responses provided by the businesses based in the provinces of Amasya, Corum, Samsun, and Tokat. Table 2 illustrates the prevalence and viability of key criteria throughout several provinces. Samsun has the biggest proportion of enterprises, accounting for 42.8% of the total. Amasya follows with 28.6% and Corum with 14.3%. With a workforce and employment ratio of 37.3%,

Samsun leads Corum by 31.4%. With a rate of 34.5%, Amasya has the highest feasibility for selecting, using, and managing the raw materials, while Tokat comes in second with a rate of 26.4%. Corum comes in second with 18.2% of water management applications, while Samsun has 36.4%. Like this, Samsun has the highest percentage of energy consumption and management applications 37.2% with Corum coming in second at 14.7%. Samsun has the greatest proportion of wastewater management with 38.7%, while Corum follows with 12.9%. Samsun has the biggest proportion of solid waste handling with 36.4%, while Corum follows with 12.1%. Regarding waste gas management, Samsun has the biggest proportion, accounting for 35.5%, while Corum follows closely with 15.4%.

Figure 2 illustrates the resource efficiency potential of the TR83 region, focusing on the specific regions of Amasya, Corum, Samsun, and Tokat. The data offers information on several elements that contribute to resource efficiency in these locations. Amasya has a significant potential of 36% in terms of technological levels, whereas Corum demonstrates a comparatively lower potential of 16% for implementing these technologies. Amasya and Samsun have higher employment rates, with Amasya at 36% and Samsun at 29%. Regarding industrial symbiosis relations, Amasya and Corum each had a 50% share, while Tokat and Samsun both had a 50% share. Interestingly, Tokat had a significant and astounding 33% share of industrial symbiosis ties, which is comparatively higher than other indicators. Amasya and Samsun provided a more favorable atmosphere inside the innovation ecosystem compared to the other two.

In Figure 3, it illustrates the sequential resource efficiency financing process that industries in the TR83 area of Türkiye might use. The figure is partitioned into four distinct portions, each corresponding to a separate geographical region: Amasya, Corum, Samsun, and Tokat. The figure provides data on the levels of technology, the job market, the relationships of industrial symbiosis, and the innovation ecosystem in each region. The percentages for each aspect are further supplied, offering a distinct picture of the resource efficiency potential in these areas. To achieve resource efficiency, it is necessary to have a thorough grasp of the possible advantages and tactics for putting it into practice. The TR83 region acknowledges the importance of cooperation and assistance in assisting enterprises in efficiently implementing resource efficiency.

Table 2. Summary of Annex-II, survey report

Parameters	Amasya (%)	Corum (%)	Samsun (%)	Tokat (%)
Distributions of Businesses	28.6	14.3	42.8	14.3
Distribution of Workforce and Employment	37.3	13.7	31.4	17.6
Feasibility of Raw Material Selection, Use and Management	34.5	14.6	34.5	26.4
Applicability of Water Management	36.4	18.2	30.9	14.5
Energy Consumption and Management Applicability	37.8	14.7	32.8	14.7
Wastewater Management	38.7	12.9	32.2	16.2
Solid Waste Management	36.4	12.1	33.7	18.2
Waste Gas Management	35.5	15.4	33.1	16
R&D, Innovation and Efficiency Studies	31.3	16.8	37.7	14.2
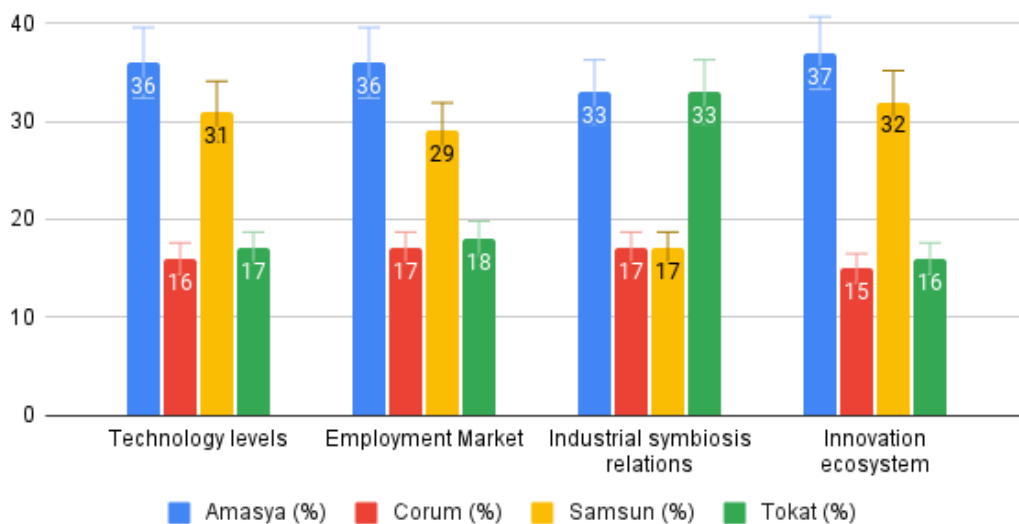
Figure 2. Resource efficiency potential of the TR83 region Black Sea in Türkiye.
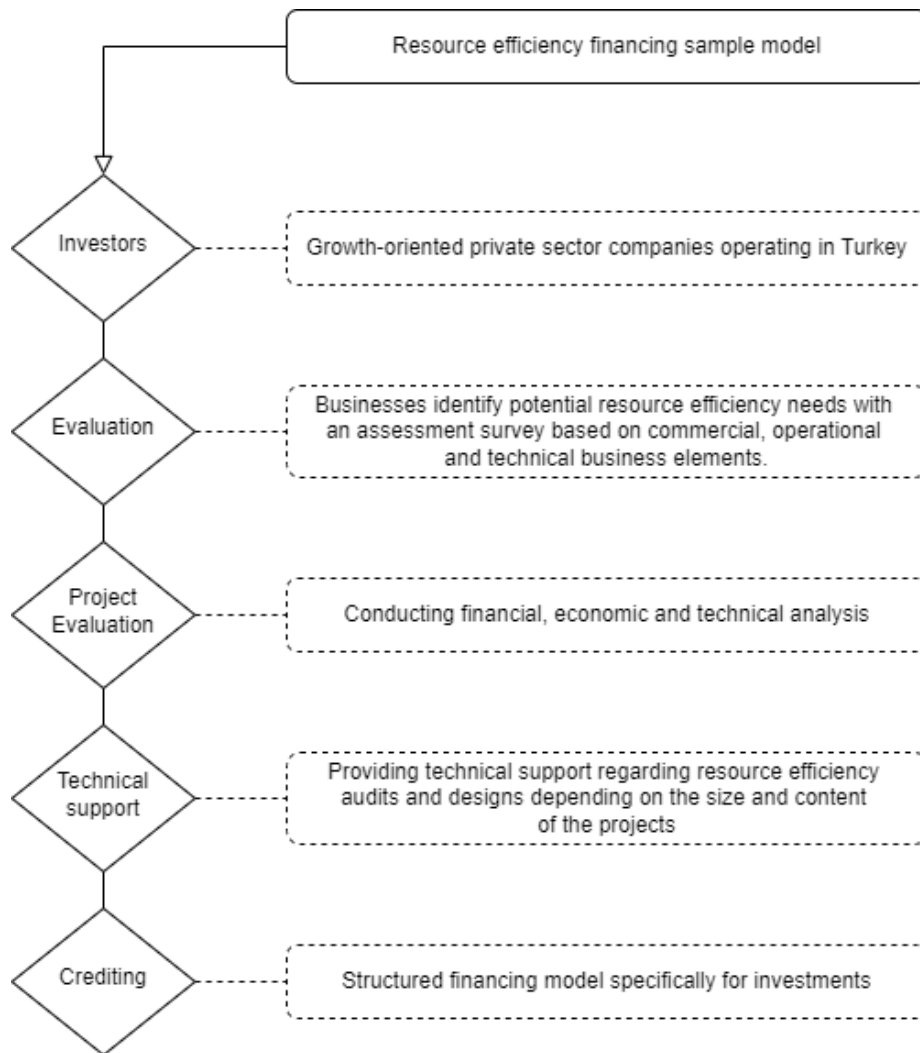
Figure 3. Resource efficiency financing sample model for TR83 region Black Sea in Türkiye.

By fulfilling these requirements, companies can achieve cost reductions, higher environmental sustainability, increased competitiveness, and a range of other advantages. Among the nine indicators, Samsun and Amasya exhibit superior performance compared to Tokat and Corum. Hence, to enhance the present situation in Tokat and Corum, they might emulate the practices of Samsun and Amasya and establish a partnership with their respective local industrial authorities. In summary, the resource efficiency assessment study of the TR83 region emphasizes the significance of implementing resource-efficient practices in the industrial sector. It highlights the capacity of enterprises to attain economic prosperity while also safeguarding the environment and fostering sustainable development. By implementing strategic planning, providing education, and fostering collaboration, the area can establish a production environment that is both more efficient and sustainable.

3.1. SWOT Analysis

This study provides a brief overview of the sensitivities and conditions related to waste management, water and wastewater management, energy use and emission awareness (Table 3). The information provided covers container use, segregation processes, transformations of hazardous waste, storage conditions for both products and waste materials, impacts of water consumption, impacts of energy consumption and sensitivity to emissions. The issues that attracted our attention in this study are summarized in Table 4.

The data analysis uncovers discrepancies in average values pertaining to several facets of waste management and sensitivity in TR83 region (Ardali, 2020). These discrepancies reflect disparities in customs and sensitivities among urban areas. Areas requiring enhancement encompass waste management, utilization of raw materials, methodologies for product packaging, utilization of equipment, prevention and cleansing of chemical waste, provision of an appropriate working environment for staff, and storage conditions for both products and waste. There is potential for improvement in sensitivities to emissions. Still, the data shows that scenarios for reducing waste and reusing it, breaking down and changing the condition of hazardous wastes, water consumption sensitivities, and energy consumption sensitivities have higher average values. This suggests that good practices should be used in these areas.

Table 3. Summary of SWOT analysis in TR83 region in the Black Sea in Türkiye

Strengths	• The urban staging plan exhibits a favorable combination of universities, natural resources, and economic capability. • Authority and impact on decision-making • A city located on a port that connects with Central Anatolia • Policies that promote the relationship between universities and industries • The presence of a trained workforce that is eager to work in the region • Adoption of policies that promote sustainable development • Active involvement in research and plans related to resource efficiency
Weakness	• Inadequate sample size and unclear source • Ambiguous techniques and legislation • Insufficient collaboration and lack of a standardized technique for comparison • Limited accessibility to resource efficiency tools • Insufficient knowledge and absence of technological adaptability in optimizing resource efficiency. • Lack of meaningful standards for improving resource efficiency • Slow implementation of legislative measures and political reform • Disparity in the assessment of resource efficiency and the comparison of outcomes • The lack of promptness in decision-making procedures at the national level
Opportunities	• Gathering and organizing data; constructing and enhancing databases • Legislation and governmental tactics • Potential for investment • Facilitating cooperation between institutions and businesses • Enhancing recognition of respective capabilities • Embracing and advocating for the adoption of change and the implementation of the circular economy. • Conducting training sessions for newly hired individuals in the field of KV vehicle development • Enlisting the participation of local governments • Undertaking research to foster cooperation with nearby universities; optimizing the use of incentive possibilities • Increasing acknowledgment of sustainable economic development and the circular economy
Threats	• Expensive operations without incentives or strategic assistance • Limited influence of small and medium-sized businesses • Reluctance to adapt production methods • Depletion of trained labor • Insufficient investment in human resources • Elaborate procedure for transitioning applications • Insufficient pool of skilled persons • Lack of strategic assistance and uniform procurement terminology • Failure to adhere to universities without supported mechanisms • Limited understanding of the benefits of industrial collaboration • Incapacity to keep a highly qualified workforce

Table 4. Compressional value table in TR83 on different indicators

Parameters (%)	Amasya		Corum		Samsun		Tokat	
	Mean	StdDev	Mean	StdDev	Mean	StdDev	Mean	StdDev
Knowledge level about waste	6.00	-	4.67	2.30	5.21	0.89	5.33	1.15
Knowledge level about raw material usage	5.00	1.41	5.00	1.00	4.29	1.49	3.33	1.15
Waste reduction and reuse situations	17.00	-	14.33	1.76	16.71	3.04	13.00	6.92
Product packaging methods	5.00	1.41	3.67	1.52	4.14	1.29	4.33	0.57
Knowledge level about equipment usage	3.50	2.12	4.67	1.15	4.57	1.39	4.33	1.52
Prevention and cleaning of chemical wastes	5.00	1.41	4.33	1.52	4.93	0.99	4.67	1.15
Suitable working environment for employees	5.00	1.41	5.67	0.57	5.29	0.91	4.67	1.15
Sensitivities shown in container use	4.00	2.82	5.00	1.00	4.64	1.64	4.00	-
Decomposition and changing states of hazardous wastes	5.00	2.82	7.67	1.15	7.14	1.61	8.67	0.57
Product and waste storage situations	6.00	-	5.33	1.15	4.43	1.39	5.33	1.15
Water consumption sensitivities	24.00	2.82	23.33	5.77	22.43	4.34	24.00	7.21
Energy consumption sensitivities	38.50	9.19	40.33	3.05	36.14	5.77	37.67	6.11
Sensitivities to emissions	17.00	5.65	12.33	2.51	13.64	3.91	14.00	6.24

Table 5. TR83 region, according to the field research results, the industries in the region approaches

	Activities has been done (%)	Opportunities can be created (%)
Develops and implements new business and/or production processes,	69	31
Makes significant improvements to existing business and/or production processes and implements them,	71	29
Implemented new marketing/service delivery methods,	59	41
Developing new products/services and introducing them to the market/use,	60	40
Making significant improvements in existing products/services and bringing them to market/use,	69	31
Makes significant changes in the design or packaging of its products. services,	50	50
Conducts studies on environmental protection, energy efficiency, and/or use of renewable energy resources,	53	47
It has been determined that organizational changes have been made to increase corporate efficiency and effectiveness and reduce costs.	69	31

3.2. Environmental, Economic, and Social Benefit Analysis

Integrating sustainable practices in organizations can result in substantial environmental, economic, and social benefits (Chan et al., 2022). Implementing these practices can mitigate pollution, enhance manufacturing efficiency, and enhance an organization's reputation, among other advantages. Nevertheless, the significance of environmental management in manufacturing strategy differs among companies (Crowe and Brennan, 2005). According to Jafari (2017) environmental practices that focus on internal operations and socially sustainable practices have the greatest influence on both environmental and financial performance. The organization's attitude toward understanding and pursuing community requirements, the methodical identification and control of sustainability, and the consideration of staff needs all have an impact on the execution of sustainability initiatives (Fonseca, 2015). Based on an in-depth analysis of the data, this study suggests that the TR83 region may successfully adopt circular economy strategies by carefully adhering to industry-specific procedures. Moreover, by recognizing TR83 as an Economic Potential Zone (Ardali, 2020), the implementation of joint endeavours to adopt circular economy techniques might result in significant advantages. Although several indicators have displayed promising signals due to the adopted measures, it is essential to focus on improving the speed at which the establishment is being carried out, since it is currently below the desired levels. Several chances are waiting to be utilized, given the unexplored potential that exists. By

accelerating the rate of implementation, TR83 can generate several possibilities and promote a more enduring and robust economic environment.

Table 5 presents a concise overview of the activities and possibilities associated with the enhancement and advancement of business in the TR83 region. Based on the findings of the field research, industries in the region have undertaken many initiatives to improve their operations. These activities encompass the creation and execution of novel business and production procedures, substantial enhancements to current procedures, the implementation of innovative marketing and service delivery approaches, the development and introduction of fresh products or services to the market, and substantial modifications to product or service design or packaging. In addition, enterprises in the area have undertaken research on environmental conservation, energy conservation, and the use of sustainable energy sources. Organizational adjustments have been implemented to enhance business efficiency and effectiveness while also decreasing expenses.

According to the World Business Council for Sustainable Development (WBCSD), sustainable production and consumption contribute to environmental quality through the efficient production and use of natural resources, waste minimization, and optimization of products and services. The sustainable production approach is a production strategy that not only provides environmental benefits but also economic returns. The

widespread adoption of resource efficiency practices, which can be considered a prerequisite for sustainable production, is highly important and effective. However, when resource efficiency practices remain within the boundaries of a firm, these practices can only enhance environmental performance to a certain extent. Therefore, to achieve further gains, a comprehensive regional approach that goes beyond the boundaries of individual firms and often facilitates inter-company and inter-sectoral collaboration is crucial for amplifying the multiplier effect of resource efficiency practices. Efficient and sustainable use of raw materials, energy and water, reducing the impact on the environment and increasing competitiveness by producing more value by using fewer inputs, will contribute to the sustainability of production and therefore the economy, awareness has been raised among the regional producers. Today, when the importance of resource efficiency has become clearer, the development and effective implementation of policies, strategies and actions in this field has emerged as a necessity in Türkiye. Investments in resource efficiency practices enhance the environmental performance of industrial organizations, positively influencing their economic performance and corporate prestige, contributing to growth, and increasing productivity. Resource efficiency will contribute greatly not only to sustainability and environmental improvement, but also economically.

Table 6. Proposals for enhancing resource efficiency in the TR83 region based on the discovered results

Strategic consumption markets allow for the use of products produced with resource efficiency can be directed.

Requests from public institutions should be supportive of resource efficiency must be provided.

Awareness should be raised - training should be provided. Welding-related communication and training process It should become a part of daily life.

Awareness campaigns should be carried out.

Explain the requirements and benefits of resource efficiency with best practice examples

Visualization is necessary to initiate learning processes. Entry of products into the market should be supported.

In accordance with the eco-design directive, the standards have improved the average mass market products. It should be directed towards resource efficiency.

New region-specific resource efficiency requirements should be included.

A study on appropriate clustering in Organized Industrial Zones and industries. Integrated programs should be planned in these areas.

Resource efficiency scales should be developed in industries and existing scales should be adapted according to industry branches.

For resource efficiency, the current burden of the industry will be alleviated through support, incentives and grants.

New production-consumption approaches should be adopted.

Resource efficiency will be effective in solving existing problems in the TR83 region.

4. Conclusion

In conclusion, the study identified a wide range of strategies that can be implemented to increase resource efficiency in the TR83 region. These initiatives span many sectors and methodologies. The proposed measures, which include promoting the use of resource-efficient goods, establishing environmentally friendly design standards, and implementing comprehensive programs

in industrial areas, highlight the complex and diverse aspects of resource efficiency. This research highlights the possible circular economic and environmental advantages of investing in resource efficiency, particularly in optimizing the use of natural resources such as raw materials, electricity and water. Although there are obstacles and hurdles, the article puts a positive perspective on the joint efforts of the European Union

and Türkiye to gradually adopt resource efficiency programs. Solving the current problems and utilizing the significant potential for resource-efficient practices in the TR83 region will create a positive chance for economic growth and making significant contributions to the protection of the global climate. While the concept of resource efficiency and circular economy in the region is associated only with energy, awareness of the need to manage raw material, water, energy and chemical inputs has been created. In addition, the importance of waste, wastewater and waste emission control as outputs was also emphasized. By providing a significant data accumulation for green production, it has become important in determining the road map for the future. In summary, the article supports the idea of a deliberate and coordinated effort to achieve a future that is both sustainable and efficient in the use of resources in the TR83 region. With the approach of "doing more using less resources" to achieve the goal of sustainable production in our region; The aim is to raise awareness about the potential economic gains as well as the environmental benefits that resource efficiency practices will provide to institutions and companies, to encourage industrial enterprises in the region to use resources efficiently by creating good practice examples, and to disseminate industrial symbiosis practices. To implement green industrial practices in industries in the region.

Author Contributions

The percentage of the author(s) contributions is presented below. All authors reviewed and approved the final version of the manuscript.

	M.S.H.	N.A.A.J.	B.A.E.	Y.A.
C	25	25	20	30
D	25		25	50
S			30	70
DCP		50	50	
DAI	25	25	25	25
L	70	30		
W	50	30	10	10
CR	30	10	10	50
SR	100			
PM			30	70
FA			30	70

C=Concept, D= design, S= supervision, DCP= data collection and/or processing, DAI= data analysis and/or interpretation, L= literature search, W= writing, CR= critical review, SR= submission and revision, PM= project management, FA= funding acquisition.

Conflict of Interest
The authors declared that there is no conflict of interest.

Ethical Consideration
Ethics committee approval was not required for this study because of there was no study on animals or humans.

References

Andriushchenko M. 2022. Towards understanding sharpness-aware minimization. URL= https://proceedings.mlr.press/v162/andriushchenko22a.html (accessed date: January 17, 2023).

Ardali Y. 2020. TR83 Region resource efficiency needs analysis project, Ministry of Trade and Industry-Central Black Sea Agency. URL= https://www.kalkinmakutuphanesi.gov.tr/dokuman/tr83-bolgesi-kaynak-verimliligi-ihtiyac-analizi-raporu/1911 (accessed date: January 17, 2023).

Bassi AM, Tan Z, Mbi A. 2012. Estimating the impact of investing in a resource efficient, resilient global energy-intensive manufacturing industry. Technol Forecast Soc Change, 79(1): 69-84. https://doi.org/10.1016/j.techfore.2011.05.011

Bilgen S, Sarıkaya İ. 2016. Contribution of efficient energy use on economy, environment, and sustainability. Energy Sour Part B: Econ Plan Policy, 11(12): 1166-1172. https://doi.org/10.1080/15567249.2016.1177622

Blume S, Kurle D, Herrmann C, Thiede S. 2017. Toolbox for increasing resource efficiency in the European metal mechanic sector. Procedia CIRP, 61: 40-45. https://doi.org/10.1016/j.procir.2016.11.247

Boden M, Santos P, Haegeman K, Marinelli E, Valero S. 2016. Implementing RIS3 in the region of eastern Macedonia and thrace: Towards a RIS3 tool box. URL= https://www.semanticscholar.org/paper/Implementing-RIS3-in-the-Region-of-Eastern-and-a-Boden-Santos/3ab39020ec7252923b57dafb278b845076eb1913?utm_source=direct_link (accessed date: January 17, 2023).

Cainelli G, Amato A, Mazzanti M. 2017. Resource efficiency, Environmental policy and Eco-innovations for a circular economy: Evidence from EU firms. Soc Sci Res Network, 2017: 24. https://doi.org/10.2139/ssrn.3070397

Camilleri MA. 2020. European environment policy for the circular economy: Implications for business and industry stakeholders. Sust Devel, 28(6): 1804-1812. https://doi.org/10.1002/sd.2113

Chan SS, Ng TF, Hassan MS, Ying CK, Tan ML, Radzi SFM, Assi RA. 2022. Integrating environmental protection and sustainable waste practices among the communities in higher education institutions: case study in a Malaysian university. Front Environ Sci, 10: 886060. https://doi.org/10.3389/fenvs.2022.886060

Comtois C. 2007. Restructuring the maritime transportation industry: Global Overview of Sustainable development Practices. URL= https://www.semanticscholar.org/paper/Restructuring-the-Maritime-Transportation-Industry%3A-Comtois-Slack/2f55bb39e0170475c8ebae06bb2077b4d947a67f?utm_source=direct_link (accessed date: January 17, 2023).

Crowe D, Brennan L. 2005. Environmental considerations within manufacturing strategy: an international study. Busin Strat Environ, 16(4): 266-289. https://doi.org/10.1002/bse.482

Delmas MA, Pekovic S. 2015. Resource efficiency Strategies and market conditions. Long Range Plan, 48(2): 80-94.

https://doi.org/10.1016/j.lrp.2013.08.014

Domenech T, Bahn WB. 2019. Transition towards a resource efficient circular economy in Europe: policy lessons from the EU and the member States. Ecol Econ, 155: 7-19. https://doi.org/10.1016/j.ecolecon.2017.11.001

Ewijk S. 2018. Resource efficiency and the circular economy Concepts, economic benefits, barriers, and policies. URL= https://www.semanticscholar.org/paper/Resource-efficiency-and-the-circular-economy-and-Ewijk/555047b07c40505740aba1455a0485d657d4120c?utm_source=direct_link (accessed date: January 17, 2023).

Fonseca L. 2015. Strategic Drivers for Implementing Sustainability Programs in Portuguese organizations-let's listen to Aristotle: From triple to quadruple bottom line. Sustainability: J Record, 8(3): 136-142. https://doi.org/10.1089/sus.2015.29004

Frohling M, Schwaderer F, Bartusch H, Schultmann F. 2012. A material flow-based approach to enhance resource efficiency in production and recycling networks. J Indust Ecol, 17(1): 5-19. https://doi.org/10.1111/j.1530-9290.2012.00502.x

Hanley N, McGregor P, Swales J, Turner K. 2006. The impact of a stimulus to energy efficiency on the economy and the environment: A regional computable general equilibrium analysis. Renew Energy, 31(2): 161-171. https://doi.org/10.1016/j.renene.2005.08.023

Henriques J, Catarino J. 2017. Sustainable value - An energy efficiency indicator in wastewater treatment plants. J Cleaner Prod, 142: 323-330. https://doi.org/10.1016/j.jclepro.2016.03.173

Hepbasli A, Ozalp N. 2003. Development of energy efficiency and management implementation in the Turkish industrial sector. Energy Convers Manag, 44(2): 231-249. https://doi.org/10.1016/s0196-8904(02)00051-1

Herrmann C. 2018. Resource efficiency. Springer eBooks, pp: 1-2. https://doi.org/10.1007/978-3-642-35950-7_6613-4

Hillary R, Thorsen N. 1999. Regulatory and self-regulatory measures as routes to promote cleaner production. J Cleaner Prod, 7(1): 1-11. https://doi.org/10.1016/s09596526(98)00030-4

Horodetska T, Zaichenko K, Ivashchenko A. 2022. Increasing the efficiency of using resources as a factor of environmental business activity. Ekonomika Finansi Pravo, 7: 9-13. https://doi.org/10.37634/efp.2022.7.2

Hossain MS, Jaradat NAA, Turan NG. 2023. Circular economy approach in municipal solid waste management for developing countries: case study of Bangladesh (1st ed., Vol. 1). Bilsel. https://bilselkongreleri.com/

Ingaramo A, Heluane H, Colombo M, Cesca MR. 2009. Water and wastewater ecoefficiency indicators for the sugar cane industry. J Cleaner Prod, 17(4): 487-495. https://doi.org/10.1016/j.jclepro.2008.08.018

Jaegersberg G, Ure J, Lloyd A. 2007. Trans-Regional Supply Chain Research Network: Developing innovation strategies within and between regional oil and gas clusters. Springer eBooks, pp: 801-808. https://doi.org/10.1007/978-1-84628-976-7_88

Jafari M. 2017. Assessing the Impact of Sustainable Practices on Organizational Performance. Environmental Science, Business. URL= https://spectrum.library.concordia.ca/id/eprint/982617/1/Jafari_MSc_F2017.pdf (accessed date: December 23, 2023).

Jollands N, Hirsch P. 2018. Mobilising finance for resource efficiency investments. Springer eBooks. pp: 211-225. https://doi.org/10.1007/978-3-319-78867-8_10

Konash A, Nasr N. 2022. The circular economy and resource use

reduction: A case study of long-term resource efficiency measures in a medium manufacturing company. Cleaner Prod Lett, 3: 100025. https://doi.org/10.1016/j.clpl.2022.100025

Lentes J, Mandel J, Schließmann U, Blach R, Hertwig M, Kuhlmann T. 2016. Competitive and sustainable manufacturing by means of ultra-efficient factories in urban surroundings. Int J Prod Res, 55(2): 480-491. https://doi.org/10.1080/00207543.2016.1189106

Lieder M. 2014. Integrated evaluation of resource efficiency and cost effectiveness in production systems. URL= https://www.semanticscholar.org/paper/Integrated-evaluation-of-resource-efficiency-and-in-Lieder/1ac0665d97434b13224051527b4ab7d16d41c4e7?utm_source=direct_link (accessed date: December 23, 2023).

Motte J, Nachtergaele P, Mahmoud M, Vleeming H, Thybaut JW, Poissonnier J, Dewulf J. 2022. Developing circularity, renewability and efficiency indicators for sustainable resource management: Propanol production as a showcase. J Cleaner Prod, 379: 134843. https://doi.org/10.1016/j.jclepro.2022.134843

Muller M. 2012. Increased resource efficiency: the key issue for ecology and the economy. In: Angrick, M., Burger, A., Lehmann, H. (eds) Factor X. Eco-Efficiency in Industry and Science, vol 30. Springer, Dordrecht, the Netherlands, pp: 19-29. https://doi.org/10.1007/978-94-007-5712-7_2

Nong D, Schandl H, Lu Y, Verikios G. 2023. Resource efficiency and climate change policies to support West Asia's move towards sustainability: A computable general equilibrium analysis of material flows. J Cleaner Prod, 421: 138458. https://doi.org/10.1016/j.jclepro.2023.138458

Oliveira-Esquerre KP, Kiperstok A, Kalid R, Sales EA, Teixeira LC, Pires VM. 2009. Water and wastewater management in a petrochemical raw material industry. Comput Aided Chem Eng, 27: 1047-1052. https://doi.org/10.1016/s1570-7946(09)70395-5

Onut S, Tuzkaya UR, Saadet N. 2008. Multiple criteria evaluation of current energy resources for Turkish manufacturing industry. Energy Convers Manag, 49(6): 1480-1492. https://doi.org/10.1016/j.enconman.2007.12.026

Ozbilen SK, Rende K, Kilicaslan Y, Onder ZK, Onder G, Tongur U, Tosun C, Durmus O, Atalay N, Keskin BA, Donmez N, Aras G. 2019. Prediction of the resource-efficient potential of Turkish manufacturing industry: a country-based study. Clean Technol Environ Policy, 21(5): 1013-1037. https://doi.org/10.1007/s10098-019-01689-x

Ozbugday FC, Fındık D, Metin-Ozcan K, Başçi S. 2020. Resource efficiency investments and firm performance: Evidence from European SMEs. J Cleaner Prod, 252: 119824. https://doi.org/10.1016/j.jclepro.2019.119824

Reaney IM, Walsh B, Vilarinho PM. 2023. Resource efficiency and energy efficiency (REEE) in the Portuguese ceramic industry: Towards net zero carbon production. Open Ceramics, 15: 100390. https://doi.org/10.1016/j.oceram.2023.100390

Rohn H, Lettenmeier M, Pastewski N. 2011. Identification of Technologies, products and strategies with high resource efficiency potential: Results of a cooperative selection process. In: Bleischwitz, R., Welfens, P., Zhang, Z. (eds) International Economics of Resource Efficiency. Physica-Verlag HD, pp: 335-347. https://doi.org/10.1007/978-3-7908-2601-2_16

Rohn H, Pastewski N, Lettenmeier M, Wiesen K, Bienge K. 2014. Resource efficiency potential of selected technologies, products and strategies. Sci Total Environ, 473-474: 32-35. https://doi.org/10.1016/j.scitotenv.2013.11.024

Ross MH. 1992. Efficient energy use in manufacturing. National Acad Sci USA, 89(3): 827-831. https://doi.org/10.1073/pnas.89.3.827

Schmidt M, Spieth H, Haubach C, Kuhne C. 2019. Resource efficiency in industrial society. Springer eBooks, pp: 2-25. https://doi.org/10.1007/978-3-662-56745-6_1

Schmidt M. 2010. Approaches towards the efficient use of resources in the industry. Chem Eng Technol, 33(4): 552-558. https://doi.org/10.1002/ceat.201000043

Sfez S, Dewulf J, De Soete W, Schaubroeck T, Mathieux F, Kralisch D, De Meester S. 2017. Toward a Framework for Resource Efficiency Evaluation in Industry: Recommendations for research and innovation projects. Resources, 6(1): 5. https://doi.org/10.3390/resources6010005

Shmygol N, Luczka W, Khvostina IM, Chyba Z, Galtsova O. 2023. Resource efficiency and pricing policy of industries the sustainable development context. IOP Conf Series, 1150(1): 012003. https://doi.org/10.1088/1755-1315/1150/1/012003

Skobelev D. 2021. Industrial policy of increasing resource efficiency and the achievement of the sustainable development goals. J New Econ, 21(4): 153-173. https://doi.org/10.29141/2658-5081-2020-21-4-8

Tukker A. 2015. Product services for a resource-efficient and circular economy - a review. J Cleaner Prod, 97: 76-91. https://doi.org/10.1016/j.jclepro.2013.11.049

Utlu Z, Hepbasli A. 2007. A review and assessment of the energy utilization efficiency in the Turkish industrial sector using energy and exergy analysis method. Renew Sust Energy Rev, 11(7): 1438-1459. https://doi.org/10.1016/j.rser.2005.11.006

Van BR, Fadeeva Z. 2020. Role of industries in resource efficiency and circular economy. Springer eBooks, pp: 171-183. https://doi.org/10.1007/978-981-15-1620-7_20

Vorfolomeiev A, Vorfolomeev AV. 2019. Implementation of resource efficient and cleaner production options at Ukrainian enterprises. Acta Innovat, 30: 68-75. https://doi.org/10.32933/actainnovations.30.7

Wang C, Wang R, Hertwich EG, Liu Y. 2017. A technology-based analysis of the waterenergy-emission nexus of China's steel industry. Resour Conservat Recycl, 124: 116-128. https://doi.org/10.1016/j.resconrec.2017.04.014

Welfens PJJ, Bleischwitz R, Geng Y. 2017. Resource efficiency, circular economy and sustainability dynamics in China and OECD countries. Int Econ Econ Policy, 14(3): 377-382. https://doi.org/10.1007/s10368-017-0388-0

Weterings R, Bastein A, Tukker A, Rademaker J, De RM. 2013. Resources for our Future. Amsterdam University Press, Amsterdam, the Netherlands, pp: 200. https://doi.org/10.2307/j.ctt6wp6zb

Worrell E, Reuter M. 2014. Recycling. Elsevier eBooks, pp: 3-8. https://doi.org/10.1016/b978-0-12-396459-5.00001-5

NOVEL AND LOW-COST TECHNIQUES FOR EXTENDING THE ETCH CAPABILITIES OF AN INDUCTIVELY COUPLED PLASMA ETCH TOOL THAT HAS CLAMP FINGERS FOR CLAMPING 4-INCH DIAMETER WAFERS

Mehmet YILMAZ[1]*

[1]*Bilkent University, National Nanotechnology Research Center (UNAM), 06800, Ankara, Türkiye*

Abstract: Widening the processing capabilities of an inductively coupled plasma (ICP) etch tool by "preventing wafer breakage" during processing of wafers, or by gaining the capability to do "through-wafer silicon etch" are important challenges that may need to be resolved with very limited resources. Resolving the undesired wafer breakage issues caused during processing of wafers is important to reduce the manufacturing costs, and increase production yield. Furthermore, considering the high prices of the state-of-the-art wafer processing tools, it is also important to prevent wafer breakage by using low-cost approaches especially if the resources for purchasing state-of-the-art processing equipment are not available. Two novel methods (method #1, and method #2) are developed to prevent wafer breakage and allow through-wafer silicon etching. With method #1, an aluminium alloy ring (AAR) and an o-ring are employed to obtain uniform load distribution (instead of point loads) on the required outer region on the surface of a wafer, and to minimize or completely remove the bending moment that may be formed on the possible cross-sections of the entire wafer, during clamping of the wafer. With method #2, through-wafer silicon etching is made possible by simultaneous application of method #1 and addition of a helium cooling gas (HCG) leakage blocking dicing tape at the back side of the wafer that is under processing for through-wafer etching. By using the explained methods, wafer breakage during ICP etch processing is eliminated, and through-wafer silicon etching is made possible. From the other side, the effective wafer area that can be used for processing is reduced by 48%. Novel and capability enabling 2 different techniques that are extremely low-cost compared to purchasing a state-of-the-art ICP etch tool are presented to extend the processing capabilities of an ICP etch tool for deep silicon etching (method #1), and through-wafer silicon etching (method #2).

Keywords: Low-cost, Inductively coupled plasma (ICP), Wafer breakage, Wafer breakage prevention, Wafer breakage-free, Through-wafer silicon etch

1. Introduction

Prices of state-of-the-art inductively coupled plasma (ICP) etch tools for deep reactive ion etching (DRIE) of silicon wafer at research laboratories may easily start from 1 million USD, and go up to 1.5 million USD or even more per tool, depending on the purchased technical capabilities of the tool (SPTS, 2024), (Plasma-Therm, 2024), (Oxford Instruments, 2024), (Corial, 2024), (Sentech, 2024). However, such large amounts of money may not be easily obtained or may not be immediately available for purchasing state of the art plasma etch tools for deep reactive ion etching (DRIE) processing needs of cleanroom users. Instead, to satisfy some of the critical needs (such as wafer breakage prevention or through wafer silicon etching) of ICP etch tool users, novel techniques that are very low-cost, may be developed for a very small fraction of the total price of state-of-the-art plasma etch tools.

Over the years, wafer breakage has been identified as a critical problem that has taken attention of engineers and scientists to find solutions to prevent wafer breakage to decrease manufacturing costs, and increase production rates (McLaughlin and Willoughby, 1987), (Chen et al., 2010), (Brun and Melkote, 2009), (Chowdhury et al., 2020), (Zhou et al., 2015), (Chen et al., 2007), (Liu et al., 2022), (Saffar et al., 2015). Causes of the wafer breakage can be classified under three major branches such as:

1. Wafer breakage during manufacturing of the wafers (Wafer World Inc., 2021), (Silyb Wafer Services Inc., 2023), (Chen et al., 2010), (Liu et al., 2022),

2. Wafer breakage during transportation and handling of the wafers (Wafer World Inc., 2021), (Silyb Wafer Services Inc., 2023), (Brun and Melkote, 2009), (Chowdhury et al., 2020), (Saffar et al., 2015),

3. Wafer breakage during processing of the wafers in the relevant processing equipment (Chowdhury et al., 2020).

According to (Chowdhury et al., 2020), to minimize wafer

breakage inside a dry etch tool, "clamping force adjustment and chuck curvature control" should be optimized. Furthermore, considering that "wafer clamping" at the beginning of a process or "wafer clamping" during processing a wafer can be considered as "wafer handling", appropriate wafer handling approaches presented in (Brun and Melkote, 2009), and (Saffar et al., 2015), may be used to minimize wafer breakage events. For example, both (Brun and Melkote, 2009), and (Saffar et al., 2015), suggest that, the wafers should be handled such that the propagation of cracks or initiation of cracks should be avoided to prevent the wafers from breakage. In order to minimize crack propagation or crack initiation, it is important to minimize the stresses or stress concentrations on the wafers. This research paper aimed to minimize stresses or stress concentrations on wafers to prevent undesired crack propagation or crack initiation.

According to the available literature, there are at least three different approaches to handle a wafer during etch processing. These three approaches are listed below:

1. Using electrostatic chucks to clamp the wafers (Bonfim et al., 1993), (Izyumov, 2009),
2. Using carrier wafers to adapt the wafer under process to the clamping conditions of the etch equipment (Noori et al., 2024), and (Meyer et al., 2022),
3. As in the etch tool used in this research study, wafers can be clamped by using symmetrically arranged clamping fingers.

One of the silicon wafers that has been processed with the original wafer clamping system of the etch tool used in this study is shown in Figure 1. As can be seen in Figure, the wafer is broken during the etch processing of the wafer. Based on the experimental studies performed in this research, two optimization opportunities on the design of the original wafer clamping system of the etch tool are identified that cause wafer breakage as the depth of the features etched into silicon become deeper and deeper:

1. Point loads from equally separated 8 points (clamping fingers) are applied on the wafer. Such point loads (clamping fingers) cause stress concentrations that cause wafer breakage especially after sufficient amount of depth of silicon is etched,
2. Due to the location of the applied point loads (i.e. misaligned from the top of the "bottom o-ring (helium cooling gas (HCG) gasket)"), bending moments are formed on the wafer. These bending moments cause wafer breakage especially after sufficient amount of depth of silicon is etched.
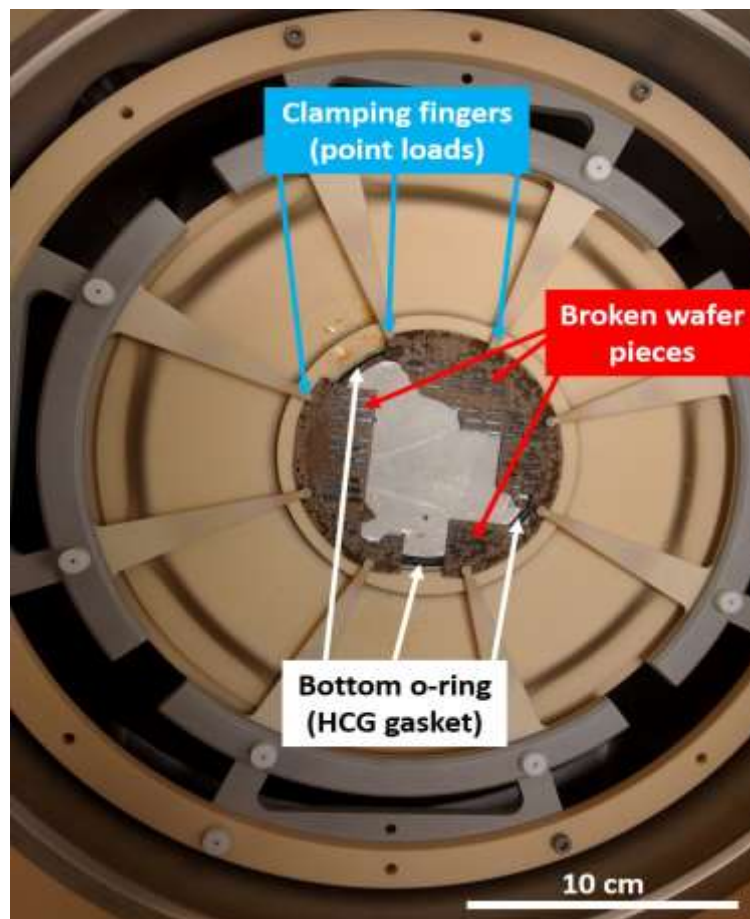
Figure 1. Top-down view of the inner side of the ICP etching tool process chamber that has a broken wafer. For the demonstration of the possible issues, broken wafer pieces are still clamped under the 8 clamping fingers (8 point loads) of the ICP etch tool. (HCG: helium cooling gas to cool the wafer from the back side of the wafer).

To achieve "breakage-free" wafer production approaches (explained in method #1), two modifications has been done to:

1. Uniformly distribute the clamping force that is applied on the designated region of a wafer,
2. Minimize or completely remove the bending moment that is applied on the wafer.

In this research article, two novel techniques that are aiming two different improvements to significantly extend the "without wafer breakage" processing capabilities of an inductively coupled plasma (ICP) deep silicon etch tool are presented. The first novel method is about preventing wafer breakage during "deep silicon" etching (deeper than 50 microns) using the inductively coupled plasma (ICP) tool that has 8 clamping fingers to clamp a 4-inch diameter silicon wafer during ICP etch processing. The second novel method is about achieving "through-wafer" silicon etching using the same ICP tool with 8 clamping fingers. In other words, this research paper demonstrates development of 2 novel techniques to be able to perform deep silicon etching (method #1), and through-wafer silicon etching (method #2) using wafer scale microfabrication approaches, without causing breakage of the wafers.

2. Materials and Methods

2.1. Materials

2.1.1. Silicon wafers (substrates)

4-inch diameter single crystal silicon wafers with the standard crystallographic orientations and at least 500 +/- 25 micrometers wafer thickness are tested for deep silicon etching (method #1) and through-wafer silicon etching (method #2). Silicon wafers that are thinner than 500 +/- 25 micrometers may also be used with these two novel methods. However, thinner wafers have not been studied extensively while the results for silicon wafers that are at least 500 +/- 25 micrometers thick are very repeatable with the ICP etch processing tool available at our cleanroom facilities.

2.1.2. Aluminium alloy ring (AAR) with an o-ring channel for uniform load distribution

Main purpose of using an aluminium alloy ring (AAR) (Figure 2) with an o-ring between the 8 clamping fingers and the wafer is to provide a mechanical element that is sufficiently rigid, that can easily receive a set of point loads coming from the 8 clamping fingers of the ICP etching tool (Figure 2 for the 8 clamping fingers that are capable of applying point load only), can easily distribute these 8 point loads as uniformly distributed load, and transfer the uniformly distributed load to the wafer with minimal bending moment on the wafer. The minimal bending moment application on the wafer would be satisfied by making sure that the bottom o-ring (HCG gasket) below the wafer is well aligned with the o-ring that is between the AAR and the top side of the wafer. This way, the wafer would be clamped on the bottom o-ring (gasket) (Figure 1) surface of the helium cooling gas (HCG) chamber with uniformly distributed force rather than the point loads applied directly by the clamping

fingers of the ICP tool. Furthermore, because the o-ring above the wafer, and the bottom o-ring (gasket) below the wafer are well aligned, there would be minimized or no bending moment on the wafer. Furthermore, due to formation of native alumina (Al_2O_3) on the outer surface of the aluminium alloy materials when aluminium alloy surface is exposed to oxygen (Nabavi et al., 2023) in the air, the aluminium alloy ring becomes very selective to plasma etch processes that have only SF_6, or SF_6 and O_2 gas plasma that may be used in deep etching of silicon wafers.

2.1.3. Circular cross-section o-ring to prevent scratches on the silicon wafer (substrate) surface

To make sure that there is no direct hard contact between the AAR surface and the silicon wafer (or the photoresist on the silicon wafer) surface, it is planned to have a circular cross-section o-ring material (NBR 70 SHORE) to provide soft contact between the aluminium alloy ring, and the wafer. To safely position the circular cross-section o-ring (NBR 70 SHORE), a channel is manufactured into the aluminium alloy ring that is facing the plasma exposed side of the silicon wafer and well aligned with the bottom o-ring (HCG gasket) to minimize the bending moment on the wafer while the wafer is clamped during plasma processing (Please see Figure 3 for the position of the o-ring with respect to the aluminium alloy ring and wafer surface). Hence, the purpose of the circular cross-section o-ring is twofold: First, to eliminate the possibility of direct hard contact between the AAR and the wafer surface, and second, to align the distributed force with the bottom o-ring such that the bending moment on the clamped wafer is minimized.

2.1.4. Dicing tape at the back side of the wafer to prevent the helium cooling gas (HCG) from entering into the ICP process chamber

In this study, a type of dicing tape (ADWILL D-841) that is UV light sensitive and that has very strong adhesion properties before being exposed to UV light, and very weak adhesion properties after being exposed to UV light, is successfully used to prevent the helium cooling gas (HCG) from entering into the plasma process chamber (PPC) once there is a micro opening though the thickness of the wafer during through-wafer silicon etching.

According to the representative cross-sectional geometry of the ICP etching tool as shown in Figure 1 at (Yang et al., 2006), to keep the temperature of the wafer at constant temperature when the wafer is under plasma processing conditions, the wafer needs to be cooled with HCG that is continuously cooling the wafer from the back side (i.e. the side of the wafer that is not exposed to the plasma processing) of the wafer. As long as the wafer does not have any "etched holes or channels through the entire wafer thickness", between the cooling side below the wafer and the plasma processing chamber side above the wafer, the wafer under plasma processing conditions is safely cooled while the entrance of the HCG leakage into the plasma chamber is also prevented.
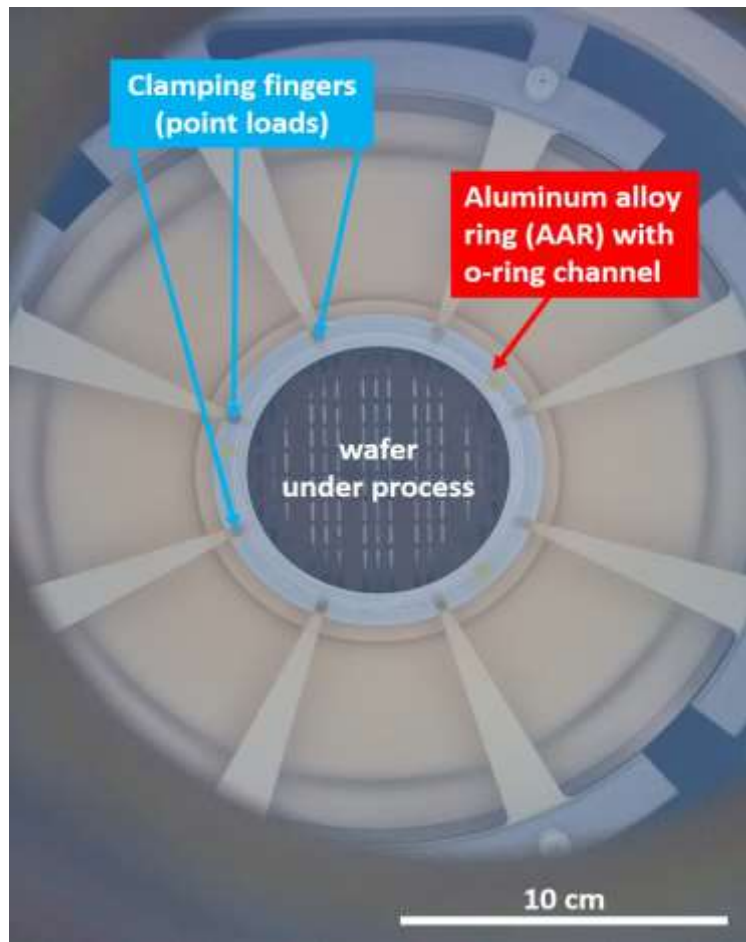
Figure 2. Aluminium alloy ring (AAR) with an o-ring channel. The o-ring channel (not visible in this view) is between the top surface of the wafer and back side of the AAR. O-ring channel is well aligned with the bottom o-ring (HCG gasket) shown in Figure. Well alignment between the o-ring channel and the bottom o-ring is important to minimize bending moment formation on the silicon wafer.
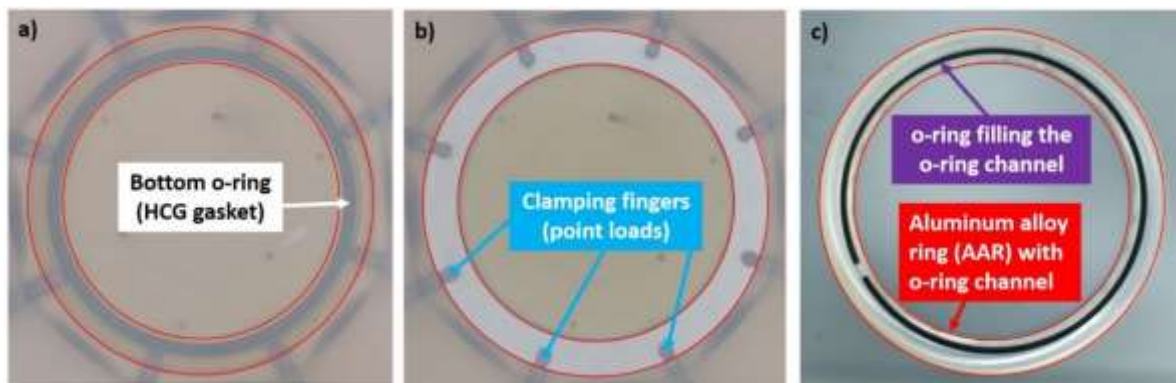
Figure 1. Aluminium alloy ring (AAR), and circular cross-section o-ring. The red colored circles in each image show the boundaries of AAR. a) To be able to see the position of the bottom o-ring (HCG gasket) with respect to the wafer and AAR, a transparent glass wafer is clamped with the 8 fingers of the ICP tool. b) AAR and the o-ring in the o-ring channel are positioned above the Pyrex glass wafer and below the 8 clamping fingers to uniformly distribute the point loads applied by the clamping fingers. c) At the back side of the AAR there is an o-ring channel for positioning of a circular cross-section o-ring.

However, after sufficient amount of plasma processing time of the silicon wafer, once a small through hole or a small through channel between the plasma processed (i.e. front) side and helium gas cooled (i.e. back) side of the wafer are not separated with a thickness of silicon material (Please see Figure 4 for the partially etched through wafer holes), the cooling gas can easily leak into the plasma process chamber and significantly affect the process conditions in an undesired way, if this gas leakage is not prevented. To prevent the passage of HCG

into the PPC, or to prevent the process chamber pressure from changing due to the small through holes or small through channels between the front side and back side of the wafer, a layer of material that can block the cooling gas from entering the plasma processing chamber may be prepared at the back side of the wafer. This layer of material must be strong enough to resist rupture of the layer of material. Furthermore, the layer of material must also be a reasonable conductor of heat (i.e. must have

reasonably good thermal conductivity to allow the cooling of the wafer while the layer of material prevents the passage of HCG into the PPC). Good candidates for such purpose would be types of dicing tapes that can be safely removed from the wafer, after the completion of the through silicon wafer etching process. Hence, UV light sensitive dicing tapes such as ADWILL D-841 are good candidates for HCG leakage prevention.
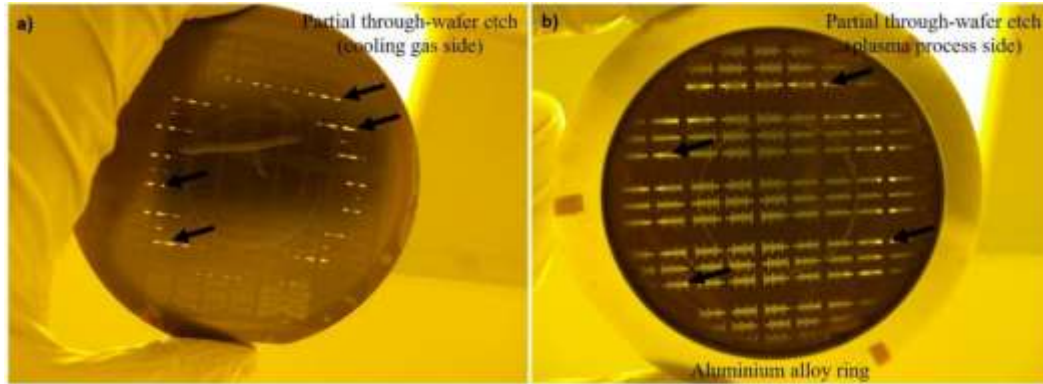
Figure 2. Partially completed though-wafer silicon etch. Black arrows show several of the fully etched locations. a) View from the cooling gas side (back side) of the wafer. This side of the wafer is covered with a dicing tape (UV sensitive ADWILL D-841) to prevent HCG from entering the PPC side. b) View from the PPC side (front side) of the wafer. This side of the wafer has patterned photoresist that is used to etch the plasma exposed silicon surface. AAR that is proposed in Section 2.1.2., is used to obtain minimized bending moment and uniformly distributed force on the edges of the wafer to prevent the breakage of the wafer.

2.1.5. Photoresist and HMDS for photolithography

Before plasma etching, for patterning of the silicon wafers various types of photoresists may be used. For example, for shallow depth silicon etching, AZ 5214E photoresist may be used, while for deep silicon etching or through wafer silicon etch processes, AZ 4562 photoresist may be used. Here it is important to emphasize that before spinning the photoresist, an adhesion layer between wafer and photoresist material, such as HMDS (hexamethyldisilazane), must be used to enhance the adhesion between photoresist and substrate surface.

2.2. Methods

2.2.1. Dimension determination and manufacturing of the aluminium alloy ring (AAR) with a channel for circular cross-section o-ring

The dimension determination approach for the dimensions of the AAR is based on the known diameter dimension of the silicon wafers that are used during the plasma etching process. It is well known that silicon wafers that are used in our research studies with the ICP etch tool in our cleanroom laboratory are either 4-inch diameter or 10 cm diameter. This wafer diameter information is used to calculate and obtain the rest of the dimensions for the AAR and the o-ring channel.

For clarity, Figure 5 a), b), and c) show the unedited versions of the images that are edited in Figure 5 d), e), and f). In Figure 5, red colored circles in d), e), and f) show the inner diameter and outer diameter on the AAR.

In Figure 5, yellow colored circles in d), e), and f) show the inner diameter and outer diameter on the o-ring channel where the circular cross-section o-ring is planned to be assembled.

Starting from the diameter dimension (10 cm diameter) of a silicon wafer, the inner diameter and outer diameter of the AAR are calculated based on dimension scaling to calculate the dimensions given below:

1. Outer diameter of the AAR piece: 100 mm
2. Inner diameter of the AAR piece: 80 mm
3. Thickness of the AAR piece: 2.5 mm

Similarly, starting from the diameter dimension of a silicon wafer, the inner diameter and outer diameter of the o-ring channel inside the AAR are calculated based on dimension scaling to calculate the dimensions given below:

1. Outer diameter of o-ring between wafer and AAR piece: 88 mm
2. Inner diameter of o-ring between wafer and AAR piece: 84 mm
3. Depth of the o-ring channel: 1.3 mm

While determining the dimensions of the o-ring channel, it is paid attention to make sure that o-ring channel inside the AAR is well aligned with the bottom o-ring (gasket) that is used to seal the HCG from entering into the plasma processing chamber (Please see Figure 3 to remember where the bottom o-ring is located). To minimize the costs, it is also paid attention to make sure that the o-ring channel inside the AAR is easy to fill with

a commercially available circular cross-section o-ring which would not require customized o-ring material manufacturing. Furthermore, based on the careful measurements done of the ICP etch tool (i.e. maximum allowable wafer thickness inside the ICP process chamber is 9 mm) it is calculated that a thickness of 2.5

mm for the thickness of the AAR is sufficient to obtain uniformly distributed force distribution that is coming from the 8 point loads that are normally applied directly on the wafer surface by the alumina clamping fingers of the ICP etch tool.
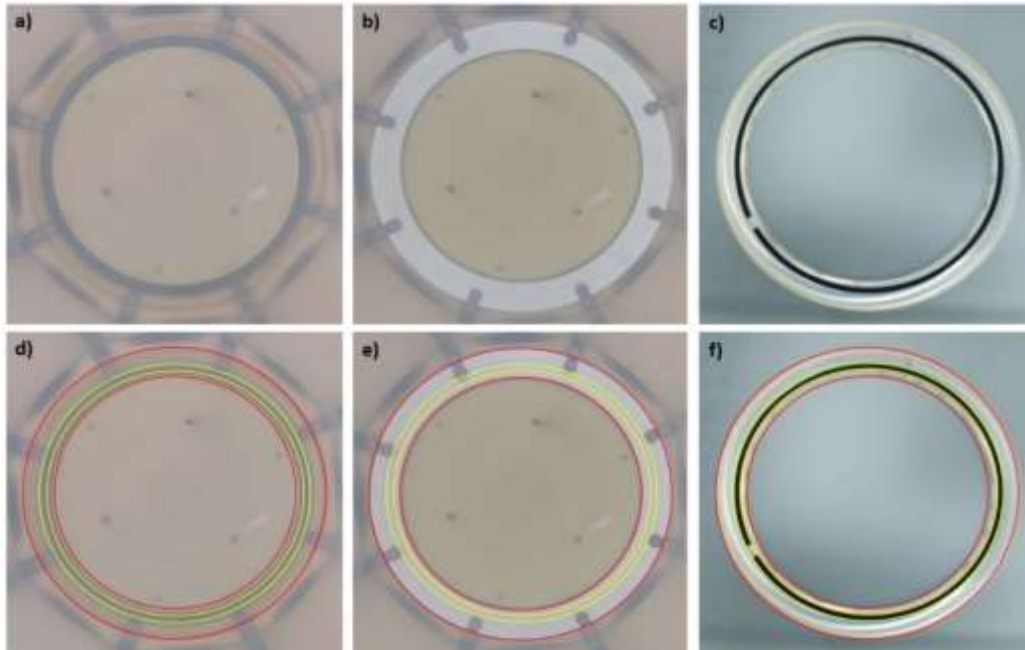
Figure 5. Description of the method used for the determination of the dimensions for the AAR, and o-ring channel. Sub figures a), b), and c) show the unedited versions of sub figures shown in d), e, and f). Red colored circles in sub figures d), e), and f) show the inner diameter and outer diameter on the AAR. Yellow colored circles in d), e), and f) show the inner diameter and outer diameter on the o-ring channel.

2.2.2. Integrating the aluminium alloy ring (AAR), circular cross-section o-ring, wafer (substrate), and dicing tape

After the preparation of the AAR with the o-ring channel, circular cross-section o-ring, wafer, and dicing tape, initially the dicing tape and the wafer are attached to each other. To attach the dicing tape to the back side of the wafer, well known protocols for the assembly of wafer and dicing tape are followed. After the assembly of wafer and dicing tape, the AAR with o-ring channel and circular cross-section o-ring are assembled as well. Next, these two assembled pairs are assembled to each other by aligning the AAR and the wafer till a good contact between the o-ring (NBR 70 SHORE) and the wafer is done. Finally, to keep the assembled components together, Kapton tape pieces are used to connect the top side of the AAR and bottom side of the wafer that has the dicing tape (Please see Figure 6 for the components assembled with Kapton tape pieces).

The o-ring (NBR 70 SHORE) with circular cross-section that is normally used for sealing purposes is used as a cushioning (i.e. spring and damper) material between the hard surfaces of the o-ring channel inside the AAR, and photoresist coated silicon wafer surface to prevent direct mechanical contact between the AAR and the photoresist coated silicon wafer surface. The o-ring inside the o-ring channel is also well aligned with the bottom o-ring (HCG

gasket) to make sure that the bending moment on the clamped wafer is minimized to prevent wafer breakage. In addition, because of the manufacturing technology differences between the AAR and the very high precision manufacturing of a wafer compared to CNC milling, the o-ring is expected to help with uniform force balancing between the silicon wafer surface and the o-ring contact surface.

Furthermore, as stated before, to make sure that AAR and wafer do not move (i.e. slide) relative to each other, hence to prevent sliding of the AAR and the o-ring on the photoresist coated wafer surface, Kapton tape pieces that do not affect the plasma etch process are used to fix the AAR relative to the wafer edges (Figure 6).

Because of the manufacturing processes used for the manufacturing of the AAR and the o-ring channel at the AAR (i.e. regular CNC milling), it is assumed that there may be microscale aluminium alloy chips at the edges or milled surfaces of the AAR due to chip formation (i.e. chipping) during CNC milling. These chips are manually removed by medium grade sand paper processing of the sharp edges and surfaces of the AAR. Then, to remove any dust particles originating from sand paper processing, the AAR is washed multiple times in acetone and DI water while the AAR is kept inside a sonication bath.
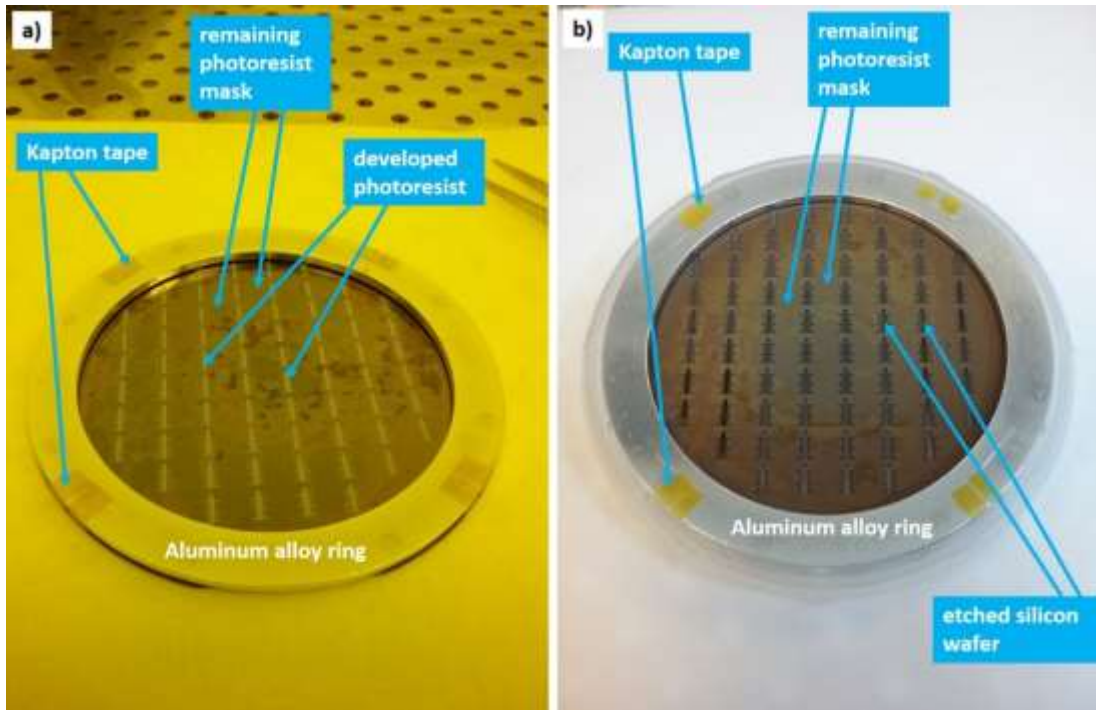
Figure 6. Aluminium alloy ring prevents wafer breakage during deep etch of silicon wafers. a) Using Kapton tape, the wafer, o-ring, and AAR are assembled together to prevent wafer breakage during deep silicon etching. b) Features that are significantly deeper than 50 micrometers are etched into the silicon wafer.
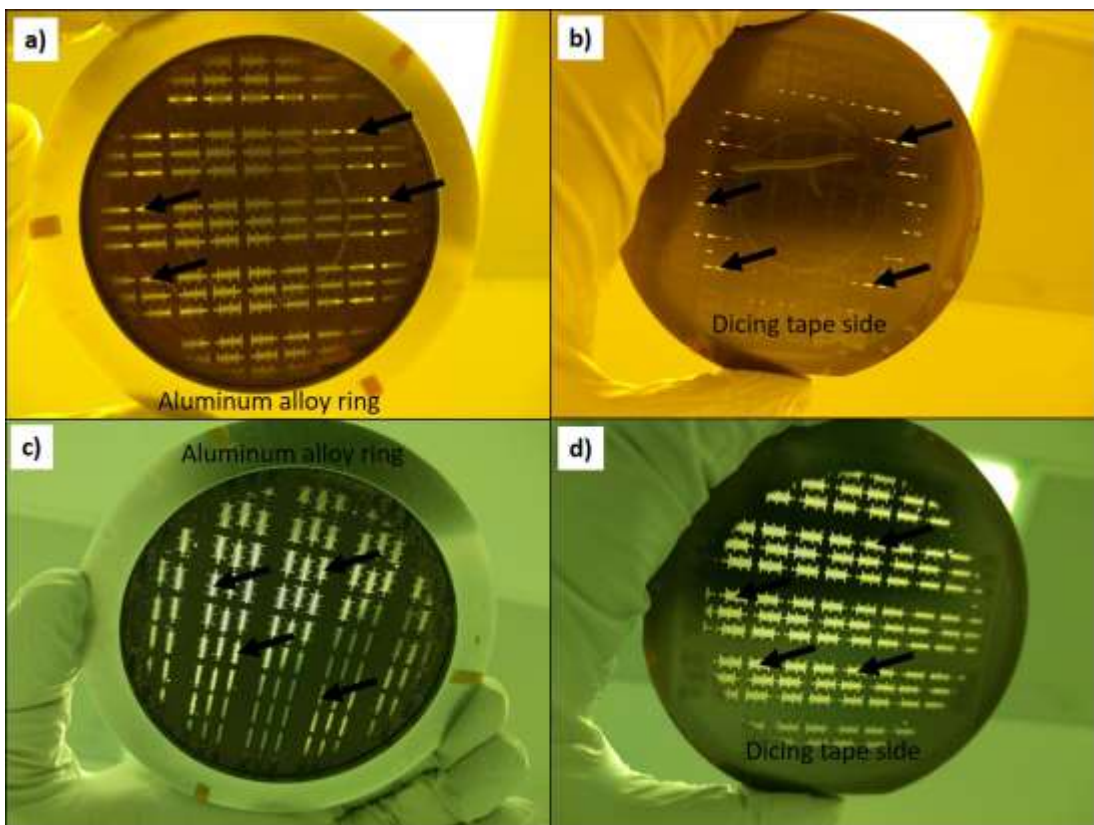
Figure 7. Demonstration of through-wafer silicon etch using the AAR to prevent wafer breakage and UV sensitive dicing tape to prevent HCG entrance into the process chamber side. a) black arrows show the through-wafer etched regions from the aluminium alloy side of the wafer at an early phase of the through-wafer etch process, b) black arrows show the through-wafer etched regions from the dicing tape side of the wafer, c) black arrows show the through-wafer etched regions from the aluminium alloy side of the wafer, d) black arrows show the through-wafer etched regions from the dicing tape side of the wafer.

3. Results

3.1. Applicability of the Aluminium Alloy Ring (AAR) for the Prevention of Wafer Breakage

Method #1 is successfully used to etch more than 50 micrometers deep or deeper features into silicon wafer as shown in Figure 6. With method #1, a rigid AAR that may significantly reduce the stress concentrations coming from individual clamping fingers is proposed. This way, the 8 clamping fingers from above are in direct contact with the AAR, and then the AAR is initially in contact with the o-ring and then the o-ring made from NBR 70 to prevent scratch formation and minimize bending moment is in contact with the wafer that needs to be etched.

Because the strength (i.e. bending stiffness) of a silicon wafer that is at least 500 +/- 25 micrometers thick is sufficient to withstand the point loads that are applied by the 8 clamping fingers of the original equipment manufacturer of the ICP tool, usage of the aluminium alloy ring may not be required for shallow silicon etching of about 50 micrometer deep features. However, silicon wafers with features that are etched deeper than 50 micrometer into the silicon wafers may need the usage of the aluminium alloy ring to prevent local stress formation at the sharp corners of the etched geometries on the surface and inside the wafer. Furthermore, when the etched features become deeper and deeper, the features etched into silicon start behaving as concentrated stress raiser regions. Furthermore, the 8 clamping fingers of the etch tool also behave as point-load stress inducers because the clamping force on the silicon wafer is not sufficiently uniformly distributed when only the 8 clamping fingers are used to clamp the wafers. Hence, when the stress inducers in the etched silicon wafers are combined with the point loads from the 8 clamping fingers, the wafers break prematurely inside the ICP chamber (Figure 1) hindering the completion of the microfabrication of the wafers with deep silicon etched features.

3.2. Applicability of the Combination of Aluminium Alloy Ring (AAR) and Back Side Dicing Tape for Prevention of Wafer Breakage and Allowing Through Wafer Etch At the Same Time

Method #2 is successfully used to etch through the thickness of a silicon wafer as shown in Figure 7. With method #2, different than what is proposed in method #1, addition of a layer of dicing tape is proposed to prevent HCG to enter into the PPC after there are features that are etched through the wafer.

While using method #2, 8 clamping fingers from above are in direct contact with the AAR, and then the AAR is initially in contact with the o-ring and then the o-ring made from NBR 70 is in contact with the wafer that needs to be etched. Additionally, the back side of the silicon wafer is coated with the dicing tape (ADWILL D-841) that prevents HCG from entering into the PPC after there are features that are etched through the wafer.

4. Discussion

As can be seen from the obtained results, the proposed methods that prevent wafer breakage (method #1, and method #2), and allow through-wafer etch (method #2) are very useful to extend the capabilities of an ICP tool if the resources to purchase a state-of-the-art equipment do not exist. Although, wafer breakage is prevented by adapting an AAR, using the AAR brings a limitation to be aware of: Normally, the wafer is 4-inch in diameter and this is the total workable area of a wafer if the capabilities of an ICP etch tool allows. However, because AAR also behaves as a mask during etching process, it is important to understand that not all the surface area of the wafer will be exposed to ICP etch process after adapting the AAR to the ICP etch process. Hence, there is a reduction in the total workable area of a 4-inch diameter wafer. In other words, the regions that are under the AAR would not be expected to have functional process results. According to the geometry of the AAR, the workable area of a 4-inch diameter wafer is reduced by 48%. Nevertheless, even if there is 48% reduction in the workable area of a 4-inch diameter wafer, by using the AAR, the process is safely completed on the silicon wafers to obtain the needed results or progress with the rest of the processes. So, rather than looking this 48% reduction in workable area, the researchers should be focused on available 52% workable area to obtain good process results. This 48% reduction in workable area may be unacceptable if the expected goal from the ICP tool is to increase throughput for high profit production studies. In such case, the ICP tool could be replaced with a state-of-the-art ICP etch tool that will cost extremely significant amount of money compared to the amount of money consumed to be able to use 52% workable area of a 4-inch diameter wafer with the already available ICP etch tool.

After the completion of a process that is using only AAR and o-ring (method #1) to have deep, but not through-wafer etch, features patterned into silicon wafer, AAR and o-ring are easily separated (disassembled) from the processed silicon wafer. From the other side, after the completion of a process that has the dicing tape at the back side of the wafer, it is important to do UV light exposure on the UV light sensitive dicing tape (ADWILL D-841) to be able to easily peel the dicing tape from the back side of the wafer. No wet etching process, or no other plasma processing is needed for the removal of the UV light exposed dicing tape. Simple mechanical peeling after UV light exposure is sufficient for the removal of the dicing tape from the wafer. If only mechanical peeling is not possible for reasons that may be related with the limitations of the wafer or the microfabrication process, the dicing tape may also be removed with oxygen plasma processing without exposing the wafer to wet processing conditions (A manuscript is in preparation about explaining the details of this process).

For applications where through wafer etch is performed, instead of using dicing tape types for the prevention of

HCG leakage into the PPC, a "carrier wafer" may be used instead of a dicing tape. However, using a "carrier wafer" may not be as effective as using a dicing tape unless good thermal contact between the "carrier wafer" and the wafer under through-wafer etching is satisfied. Hence, using dicing tape is advantageous compared to working with a "carrier wafer" that may serve the same purpose of preventing the leakage of HCG from the cooling chamber into the PPC.

Finite element modelling (FEM) may be done for more precise calculations. However, FEM modelling was not needed and was not performed for this study after observing that the encountered wafer breakage problems are resolved even without performing FEM modelling for the aluminium alloy ring, and o-ring structure that are used for uniform distribution of the point loads that are applied by the 8 clamping fingers of the ICP etching equipment.

5. Conclusion

Novel and capability enabling 2 different techniques that are extremely low-cost compared to purchasing a state-of-the-art ICP etch tool are presented to extend the processing capabilities of the ICP etch tool for deep silicon etching (method #1), and through wafer silicon etching (method #2).

These novel methods can be used, or adapted for use, with confidence on the ICP etch tools that have wafer clamping fingers to fix the position of wafers. Major advantages of the presented methods are:

1. to prevent wafer breakage by preventing crack initiation or crack propagation,

2. to enable process chamber cleanliness of ICP etch tools,

3. to allow using the already available process equipment without making significant money investment for a new process tool.

Conflict of Interest

The author declared that there is no conflict of interest.

Ethical Consideration

Ethics committee approval was not required for this study because of there was no study on animals or humans.

References

Bonfim MJC, Swart JW, Velasco CEM, Okura JH, Verdonck PB. 1993. A low frequency remote plasma rapid thermal CVD system with face down electrostatic clamp wafer holder. In: Spring Meeting of the Materials Research Society, Symposium on Rapid Thermal and Integrated Processing II, April 12-15, San Francisco, CA, USA, 303: 407–412.

Brun XF, Melkote SN. 2009. Analysis of stresses and breakage of crystalline silicon wafers during handling and transport. Sol Energy Mater Sol Cells, 93 (8): 1238-1247.

Chen P-Y, Chen SL, Tsai MH, Jing MH, Lin T-C. 2007. Investigation of wafer strength in 12 inch bare wafer for prevent wafer breakage. In: Proceedings of IEEE Conference on Electron Devices and Solid-State Circuits, December 20-22, Tainan, Taiwan, pp: 545-548.

Chen P-Y, Tsai MH, Yeh WK, Jing MH, Chang Y. 2010. Relationship between wafer fracture reduction and controlling during the edge manufacturing process. Microelectron Eng, 87 (10): 1809-1815.

Chowdhury S, Wu Y, Shen L, McCarthy L, Parikh P, Rhodes D, Hosoda T, Kotani Y, Imanishi K, Asai Y, Ogino T, Kiuchi K. 2020. 5000+Wafers of 650 V highly reliable GaN HEMTs on Si substrates: wafer breakage and backside contamination results. In: 31st Annual SEMI Advanced Semiconductor Manufacturing Conference (ASMC), August 24-26, Saratoga Springs, NY, USA, pp: 3.

Corial. 2024. Deep reactive ion etching (DRIE). URL: https://corial.plasmatherm.com/en/technologies/drie-deep-reactive-ion-etching (accessed date: July, 09, 2024).

Izyumov M. 2009. An electrostatic clamp with temperature stabilization of semiconductor wafers under plasma treatment. Instrum Exp Tech, 52: 886-887.

Liu T, Su Y, Ge P. 2022. Breakage ratio of silicon wafer during fixed diamond wire sawing. Micromachines, 13(11): 1-13.

McLaughlin JC, Willoughby AFW. 1987. Fracture of silicon wafers. J Cryst Growth, 85(1-2): 83-90.

Meyer T, Petit-Etienne C, Pargon E. 2022. Influence of the carrier wafer during GaN etching in Cl_2 plasma. J Vac Sci Technol A, 40: 023202.

Nabavi R, Sarraf S, Soltanieh M. 2023. Optimization of hard anodizing process parameters on 6061-T6 aluminum alloy using response surface methodology. J Mater Eng Perform, 2023: 1-14. https://doi.org/10.1007/s11665-023-08717-4.

Noori Y, Skandalos I, Yan X, Zhelev N, Hou Y, Gardes F. 2024. Wafer bonding for processing small wafers in large wafer facilities. IEEE Trans Compon Pack Manuf Technol, 14 (2): 342-348.

Oxford Instruments. 2024. Inductively coupled plasma etching (ICP RIE). URL: https://plasma.oxinst.com/technology/icp-etching (accessed date: July, 09, 2024).

Plasma-Therm. 2024. Inductively coupled plasma (ICP) technology for etching high etch rates, process flexibility and reduced ion bombardment. URL: https://www.plasmatherm.com/process/etch/icp/ (accessed date: July, 09, 2024).

Saffar S, Gouttebroze S, Zhang ZL. 2015. Stress and fracture analyses of solar silicon wafers during suction process and handling. J Sol Energy Eng Trans-ASME, 137(3): 031010.

Sentech. 2024. Plasma etching. URL: https://www.sentech.com/products/plasma-process-technology/plasma-etching/ (accessed date: July, 09, 2024).

Silyb Wafer Services, Inc. 2023. What are the main causes of silicon wafer breakage? URL: https://www.silybwafers.com/what-are-the-main-causes-of-silicon-wafer-breakage (accessed date: July, 09, 2024).

SPTS. 2024. Plasma etch. URL: https://www.spts.com/categories/plasma-etch (accessed date: July, 09, 2024).

Wafer World Inc. 2021. Top causes of silicon wafer breakage. URL: https://www.waferworld.com/post/top-causes-of-silicon-wafer-breakage (accessed date: July, 09, 2024).

Yang Y-J, Kuo W-C, Fan K-C. 2006. Single-run single-mask inductively-coupled-plasma reactive-ion-etching process for fabricating suspended high-aspect-ratio microstructures. Jpn J Appl Phys, 45(1A): 305-310.

Zhou L, Qin F, Sun J, Chen P, Yu H, Wang Z, Tang L. 2015. Fracture strength of silicon wafer after different wafer treatment methods. In: 16th International Conference on Electronic Packaging Technology (ICEPT), August 11-14, Changsha, China, pp: 871-874.

ENERGY CONVERSION BY HELICAL HYDROKINETIC TURBINE IN A PIPE

Mehmet Salih TÜRKER¹*, Mehmet İshak YÜCE²

¹*Ankara Yıldırım Beyazit University, Faculty of Engineering and Natural Sciences, Department of Civil Engineering, 6010, Ankara, Türkiye*

²*Gaziantep University, Faculty Engineering, Department of Civil Engineering, 27470, Gaziantep, Türkiye*

Abstract: Hydrokinetic turbines are mechanisms designed for the purpose of utilizing the kinetic energy present in the movement of water bodies like rivers, tidal currents, or ocean currents, and transforming it into electrical power. These turbines' function based on a principle akin to that of wind turbines; however, they are positioned underwater to harness the energy of the water flow. This study focuses on the fundamentals of hydrokinetic turbines and presents existing research. Additionally, simulations have been conducted to observe how the hydrokinetic turbine responds hydrodynamically inside a pipe. A three-bladed vertical-axis helical hydrokinetic turbine was installed within a circular conduit and subjected to analysis under varying flow conditions. The k-ω SST turbulence model was employed in the analyses. The results indicated that increasing the turbine's angular velocity initially raises the torque and the power coefficient until a peak is reached, after which the power coefficient decreases. The highest power coefficient was observed at a flow velocity of 2 m/s. Moreover, consistent with previous studies, the hydrokinetic turbine within the pipe surpassed the Betz limit.

Keywords: Hydrokinetic energy, Pipe hydropower, Helical turbine, Vertical axis turbine, Current energy devices

1. Introduction

Renewable energy is energy that is generated from natural and replenishable sources such as sunlight, geothermal heat, wind, water, and biomass. For the last decades, renewable and sustainable energy conversion systems have been under investigation by many researchers. Since the most prevalent energy source is fossil fuel, therefore increasing energy demand, environmentally hazardous effects, and high prices of fossil fuel have demanded to find new, healthy, renewable, and sustainable energy sources. Renewable energy sources generate more economical energy in comparison with fossil and nuclear energy sources (OECD/IEA, 2024). The management planning and prioritization of energy resources should be decided well (Kantoglu and Argun, 2022). This issue is important in terms of commissioning different energy sources from day to day (such as aquifer thermal energy), for future energy consumption and meeting demand (Ertuğrul et al., 2018). Hydropower energy sources are the most utilized one, with 53.6 %, among renewable energy sources (Cuming et al., 2015). The reasons for this are reliability, availability, cost, and payback period of hydroelectricity.

Water, which covers about 70% of the Earth's surface, contains significant potential energy in the form of flowing water, ocean currents, and waves. This energy can be harnessed for various applications, highlighting the vast potential of water as an energy source. Hydropower, or hydroelectric power, is primarily generated by constructing dams to store the flowing water of rivers or streams. However, dam projects are extensive and costly, with substantial environmental impacts, including local climatic variations, and inundation of agricultural land, historical sites, and residential areas.

On the other hand, scientists and experts have been investigating clean and environmentally friendly alternative energy sources that demand lower investment costs and shorter installation times. (Al-Dabbagh, 2017). Through examining the historical evolution of hydropower, research and development have attained unprecedented levels. These endeavors encompass a broad spectrum of technical concepts and diverse application areas, indicating that hydrokinetic technologies could emerge as a successful alternative energy source in the future (Khan et al., 2009).

Kinetic energy has the potential to be transformed into power through the utilization of hydrokinetic turbines, which are alternatively referred to as low-head turbines. These turbines require minimal civil work and minimal environmental impact (Muratoglu, 2014). Unlike dams, hydrokinetic systems do not require water storage, making them a cost-effective and environmentally acceptable energy solution (Rajaonary,2016).

Hydrokinetic turbines, categorized as small-scale

turbines concerning energy generation, have the potential to be installed in numerous units to enhance power generation, akin to wind turbine arrays (Muratoglu, 2014). Recently, some turbines have been utilized for urban applications, generating power for domestic, agricultural, and industrial districts (Casini, 2015). Studies regarding hydrokinetic turbines frequently reference the principles of wind turbine technology due to the analogous operational characteristics shared between the two systems, with distinctions primarily arising from the nature of the fluid involved. Hydrokinetic systems are commonly composed of a propeller equipped with blades that undergo rotational motion along either a horizontal or vertical axis. Water movement produces drag and lift forces that drive the rotational motion of the blades (Al-Dabbagh, 2017).

Horizontal-axis turbines are defined by an axis parallel to the fluid-flow and are equipped with propeller-type rotors, commonly referred to as axial flow turbines. These turbines are frequently used in tidal energy converters and operate similarly to wind turbines in terms of their fundamental principles and design configuration. Conversely, vertical-axis turbines have a rotating shaft perpendicular to the flow. Hydrokinetic turbines are employed in various water flows, including rivers, tidal flows, and ocean currents. Recently, tubular turbines placed within pipes have also been introduced, as depicted in Figure 1. These in-pipe hydro systems can generate electricity under diverse pressure and flow conditions. They can be installed in pipes made of materials such as steel, ductile iron, and concrete, and are not affected by weather conditions (Casini, 2015).
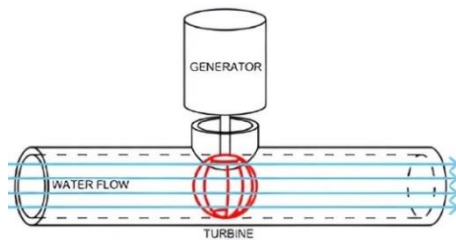
Figure 1. Placed hydrokinetic turbine in pipe.

Hydrokinetic turbines are important not just for generating energy, but also for managing water networks efficiently. By integrating these turbines into the system, the pressure within water networks can be optimized through a monitoring system powered by the turbine. This optimization helps prolong the service life of the pipes (Casini, 2015).

In this study, the hydrokinetic turbines were evaluated and reviewed. Furthermore, an example of a numerical study, which is related to a hydrokinetic turbine in a pipe, was investigated.

2. Background of Hydrokinetic Turbines

Mainly two types of hydrokinetic turbines exist in the application. They are horizontal and vertical axis turbines. Horizontal axis turbines have propeller-type rotors and an axis parallel to fluid flow. These turbines are known as axial flow turbines. These turbines, resembling wind turbines in concept and design, are commonly employed in tidal energy converters. A turbine's shaft is vertical when perpendicular to flow, called vertical axis turbine. Besides their application in river flows, tidal flows, and ocean currents, there is also a relatively new concept known as tubular turbines, which are installed within pipes.

Hydrokinetic power has come from the ancient Near East in the 3rd century BC with water mills, which are utilized for grain grinding. Because watermills drive mechanical operation with water motion. However, this technology is under development, especially in the last decades, and it is an emerging source of renewable energy.

Moreover, the Archimedean screw, which is an ancient invention (287-212 BC), can be categorized as hydrokinetic power because screw turbine uses the principle of the Archimedean screw. Schleicher et al. (2014) developed a unique Archimedean spiral rotor for a micro-hydro turbine. The maximum efficiency was obtained numerically at 72%, aligning well with experimental results, which ranged from 68.2% to 74.5% (Schleicher, 2014).

Furthermore, hydrokinetic systems can be economically competitive with fossil fuels and other energy sources. According to Güney and Kaygusuz (2010), the cost of generation ranges from \$4.8 to \$10.8 per kilowatt, but this amount can be reduced through further research and development (Güney and Kaygusuz, 2010).

The conversion system has a minimum environmental impact in comparison with other systems. Because there is no need for any huge construction work. Also, the system does not need to be set like a dam to create the head difference. Hydrokinetic turbines, unlike traditional dams, don't significantly alter water flow because they harness the kinetic energy of natural water currents rather than impeding or redirecting them. Therefore, the flow path of the water remains constant after placing the turbine in a river. Moreover, climate change is not observed due to the hydrokinetic conversion systems.

The blades of the hydrokinetic turbine can be helical or straight in shape. Al-Dabbagh and Yuce (2018) conducted a study indicating that the efficiency of a helical turbine outperforms that of a straight-blade turbine when both are of the same size and operate under identical conditions (Figure 2).

The tip speed ratio often denoted as TSR, represents the ratio between the rotational velocity of the rotor tips and the velocity of the free stream flow. Helical turbines have a promising future technology, if necessary, investigations are performed.
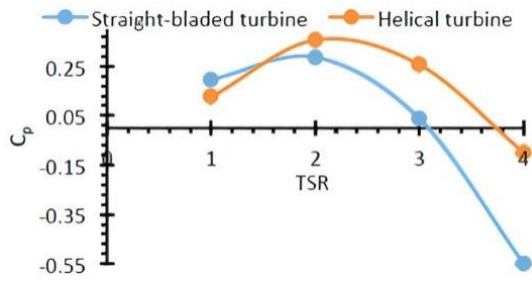
Figure 2. Power coefficient- tip sped ratio graph (Al-Dabbbagh and Yuce, 2018).

Two types of turbines are utilized for the hydrokinetic energy conversion systems. Horizontal and vertical axis turbines differentiate them according to their rotating axis. Vertical axis turbines offer advantages such as simple design, minimal tool requirements, and reduced noise. Vertical axis turbines have certain advantages such as simpler design, reduced tool requirements, and lower noise levels. However, they are plagued by issues like low starting torque, torque ripple, and lower efficiency. In contrast, horizontal turbines offer benefits stemming from the extensive knowledge base established through wind turbine technology, along with enhanced performance and the potential for further improvement with the use of ducts and similar components. (Khan et al., 2009).

Vibration is a serious problem for the turbines. However, some studies indicated that, this problem can be solved by flexible blades. Zeiner-Gundersen, 2015 investigated a vertical-axis turbine with flexible blades as shown in Figure 3. The study was done on a river in Norway and the power coefficient was as 0.37 for the flow velocity is 0.79 m/s case (Zeiner-Gundersen, 2015).
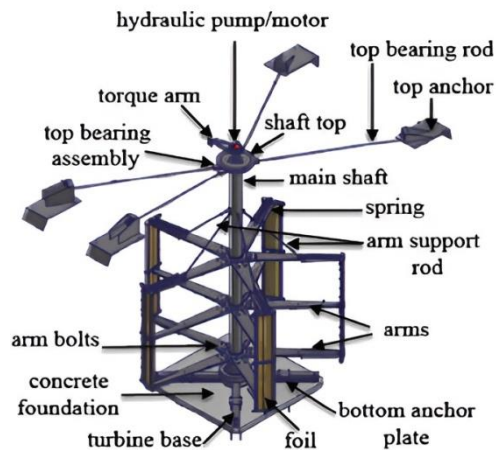
Figure 3. Components of turbine with flexible blades (Zeiner-Gundersen, 2015).

The hydrokinetic turbine provides a great opportunity for rural areas. Electricity can be generated as off-grid in rural areas by the turbines. Case studies were done in some regions of the world and they were edited by Anyi and Kirke (2010). In the study, they investigated case studies, which are done in Africa, Australia, South America, and the UK. The best efficiency for each study

was 0.12, 0.50, 0.25, and 0.27 respectively as shown in Table 1. Generally, the main problem was debris and sedimentation for the open channel domain, because, sand, silt and other waste materials in the river cause damage and low efficiency for the turbines. Otherwise, high efficiency was observed due to the placed duct around the turbine (Anyi and Kirke, 2010).

Table 1. Characteristics of case studies reviewed by Anyi and Kirke (2010)

Study Region	Rotor diameter (m)	Flow velocity (m/s)	Overall efficiency (%)
Africa	1.8	1.5	12
South America	0.8	—	50
Australia	2	1.1	25
UK	2.75	1.25	27

According to investigations, augmented turbines provide more energy due to the increasing flow velocity of the fluid. There exists Betz law, which limits the efficiency of the turbine for bare turbines. The law expresses that, the efficiency of traditional open turbines can't exceed the %59 efficient rate. However, this law does not apply to the ducted or augmented turbines. Therefore, more power efficiency can be obtained with ducted turbines, although it is more expensive (Khan et al., 2009).

Wind turbine technology experiences stated that an augmented wind turbine creates sub-atmospheric pressure, so more air passes through the blade plane (Phillips et al., 1999). Moreover, a wind turbine with augmentation produces approximately four times more power compared to a standard turbine of the same size. (Fletcher, 1980).

Usually, the hydrokinetic turbine studies are based on the wind turbine approach. Nunes et al. (2019) completed the development of a diffuser-enhanced propeller hydrokinetic turbine (Nunes et al., 2019). A wind turbine approach is implemented in the study. The study showed that different kinds of diffusers increase the efficiency of the turbines as shown in Table 2.

Table 2. Results of Shrouded Turbines (Nunes et al., 2019).

Configuration	Power Coefficient	Tip Speed Ratio
Free Runner	0.39	1.4
Diffuser S1223	0.58	2.0
Diffuser Lens CII	0.70	2.3

Shahsavarifard et al. (2015) investigated the impact of a shroud on a horizontal hydrokinetic turbine. An experiment conducted at the University of Manitoba involved testing a 19.8 cm diameter turbine in a water channel. The study evaluated two shroud designs, comparing power and thrust curves between shrouded

and unshrouded turbines across their performance range. Results indicated that the power coefficient surpassed 91% without the use of a shroud (Shahsavarifard et al., 2015).

Pudur et al. (2022) revealed that a two-blade Savonius rotor stands out as the most efficient for harvesting hydrokinetic energy compared to three and four-blade variants. With the aid of a suitable gear system, power extraction from free-flowing rivers is feasible. In the study, observation indicated that the two-blade rotor experiences minimal balancing issues due to high water turbulence, whereas the four-blade rotor rotates smoother compared to the three-blade variant. Moreover, theoretical analysis also supports these findings, suggesting that an increase in the number of blades leads to a decrease in turbine revolution. However, practical experimentation revealed discrepancies between theoretical predictions and observed behavior, particularly attributed to the significant jerking effect in the two-blade system caused by the substantial distance between subsequent blades. They concluded that the experiment serves to validate the theoretical concepts (Pudur et al., 2022).

3. Hydrokinetic Turbine in Pipe

Recently, the adoption of hydrokinetic turbines installed within pipes has gained popularity due to their higher efficiency compared to bare turbines. Additionally, these systems can replace Pressure Reducing Valves (PRVs) to generate power instead of dissipating energy. The enclosed nature of the pipe system offers advantages such as predictability and protection from external factors like debris and fish.

Water loss in the water supply network is the main problem for the municipalities. To prevent water loss, some devices are needed such as a flow meter, data logger, pressure-reducing valve...etc. Therefore, energy supply is important for these systems. Hydro Spin Company installed a turbine into the pipe to supply energy for the measurement devices to observe the water losses in the water distribution network (Hydro Spin, 2017).

Pressure-reducing valves (PRV) are designed to decrease the water pressure to the desirable level for safety downstream. PRV breaks the pressure on the water distribution networks, which are utilized in residential, industrial ... etc. As a summary, excessive energy in the systems is broken by PRV. However, excess pressure can be turned into energy by integrating a hydrokinetic turbine into the system. With present technology, at least the need of one hundred homes of electricity can be supplied in this way. Turbine can be placed in a pipe, especially a gravitational water network system. Onedia and Thorn Run reservoirs had PRV in the network. In 2012, the Rentricity Company installed an energy-producing turbine system onto the existing infrastructure, resulting in an annual generation of 131.4

MWh.

Hong Kong Polytechnic University, together with Sino Group and Arup, initiated a groundbreaking research endeavor focusing on in-building hydropower. The objective was to harness untapped water head in pipelines. The first installation was implemented at the Olympian City 2 shopping mall, powering the elevator lighting system. This initiative is projected to save approximately 700 kg of carbon dioxide emissions annually, equivalent to the environmental benefit of around 30 trees.

Chen et al. (2013) conducted a study on hydrokinetic turbines placed within pipes, focusing on a vertical axis turbine designed for monitoring water supply networks. The turbine, featuring a 100 mm pipeline, aimed to maximize energy generation with a water velocity of 1.5 m/s and an estimated water head drop of 5 m. Through 20 simulations and experiments, they achieved a power generation of 88.2 W using a hollow turbine with an eye-shaped block, as illustrated in Figure 4 (Chen et al., 2013).

Drag type turbine design	Max power (W)	Head drop (m)
1st gen: 5-blade solid turbine (∅86 mm) + vertical half block	0	0
1st gen: 5-blade solid turbine (∅92 mm) + 80% short slanted block	12.0	N/A
2nd gen: 6-blade solid turbine (∅92 mm) + 90% slanted eye shaped block	32.2	5.82
3rd gen: 12-blade (∅92 mm) hollow turbine + 90% slanted eye-shaped block	88.2	4.85

Figure 4. Testing results of turbine (Chen et al., 2013).

Turbine material has effects on the turbine performance. Oladosu and Koya (2018) studied how turbines in water pipes could generate electricity. The study conducted turbine models and simulations implemented in water distribution network pipes to generate electricity using lift-based turbines. They found that the available power depended on factors such as the density of the turbine material, discharge, and pipe diameter. In their study, a stainless-steel turbine achieved a power output of 1080 W in a 250 mm diameter pipe, while an aluminum turbine reached a peak power value of 1663 W (Oladosu and Koya, 2018).

A water supply and distribution system's inline tubular propeller was the subject of an experimental study by Samora et al. (2016). The 85 mm diameter type was tested and optimized for flows between 5 and 50 m³/h, removing heads that were less than 7.5 mWc. The optimal efficiency points, approximately 63.75%, were attained with a head of 0.34 bar and a flow rate of 15.95 m³/h. Furthermore, it was determined that the highest

power output of 328 W could be obtained at a rotational speed of 1500 rpm. With an efficiency of 60%, the study indicates that the turbine has room for improvement given the positive and satisfactory results (Samora et al., 2016).

Bizhanpour et al. (2023) investigated the performance of vertical-axis in-pipe turbines equipped with different types of deflectors across various operational conditions to identify the optimal deflector geometry for harnessing energy from urban water supplies. The research combines numerical simulations, validated by experimental tests. The study primarily aims to enhance turbine performance under off-design conditions by utilizing deflectors, commonly employed to direct flow towards turbine blades effectively. Five different deflector geometries have been investigated and the study numerically assessed their impact on the efficiency of an in-pipe Savonius turbine across varying flow rates. Results indicated that a dynamic guide vane deflector, capable of adjusting its position dynamically at different flow rates, significantly enhanced performance outside the optimal design point. Furthermore, a novel systematic design procedure was proposed for such deflectors within the constraints of small-scale pipes. Numerical simulations were validated against experimental data from the provided test rig, ensuring accuracy (Bizhanpour et al., 2023).

Kumar and Sarkar (2023) employed a spherical-shaped Darrieus hydrokinetic turbine (SDHKT) within the pipeline. Six distinct SDHKT models were devised by altering diameters, solidity, and blade number. In the study, performance assessment was conducted through experimental and numerical analyses under varying pipe flow conditions. As a result, turbine performance exhibited enhancement with an increased blockage ratio. Also, pressure drop across the turbines escalated with a rising Tip Speed Ratio (TSR) and increased pipe flow (Kumar and Sarkar, 2023).

4. Material and Methods

Several non-dimensional parameters are essential for evaluating the performance of hydrokinetic turbines, as they significantly influence their overall efficiency. These parameters include aspect ratio, tip speed ratio, lift and drag forces, solidity, and overall efficiency.

4.1. Tip Speed Ratio

One important metric in hydrokinetic turbines is the tip speed ratio (TSR), which is represented by λ and is the ratio of the rotational velocity of the rotor tips to the flow's free stream velocity. It plays a key role in determining the optimal angular velocity range of the turbine for generating maximum power. The relationship between turbine performance and TSR is often depicted graphically using the Cp-TSR curve. The TSR value can be calculated using equation 1.

$$\lambda = \frac{\omega R}{v_\infty} \tag{1}$$

(ω) is the angular velocity, (R) is the radius, and (v) is the flow velocity in the equation. According to Gorlov (1998), in order to produce more torque and avoid cavitations for a three-bladed helical turbine, the TSR value should be between 2-2.2 (Zingman, 2007).

The power coefficient usually increases as the tip speed ratio (TSR) goes up, but only to a certain point. After reaching this point, if the TSR keeps rising, the power coefficient starts to drop. This increase begins at the cut-in speed, where the best TSR value is found. When the cut-off speed, or stall point, is reached, the fluid inside the turbine starts to separate, causing the performance to decrease.

4.2. Solidity

The solidity, expressed as the ratio of chord length to turbine circumference, is calculated using equation 2.

$$\Sigma = \frac{c \, x \, n}{2\pi R} \tag{2}$$

where (n) is the number of blades, (c) is the chord length, (R) is the turbine radius, and (σ) indicates the solidity of the turbine. Increasing solidity affects turbine performance and rotational speed by raising flow resistance. The turbine functions as a barrier, impeding water flow and preventing the production of electricity, when the angular velocity is greater than the flow velocity. Thus, the number of blades must be carefully selected to optimize turbine performance during the design process. Higher solidity values result in increased torque and reduced TSR, leading to poorer turbine performance. This relationship between torque coefficient and TSR is illustrated in Figure 5.
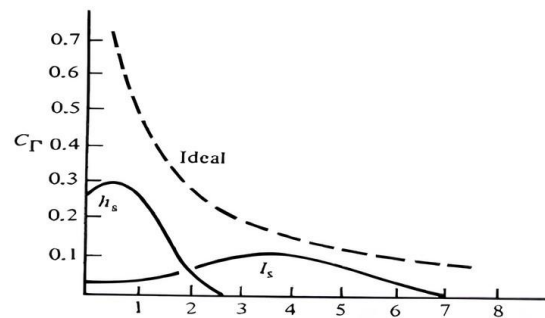
Figure 5. Torque coefficient – TSR relationship (Al-Dabbagh, 2017).

4.3 Lift and Drag Effects

Lift and drag forces are key factors in determining the performance of turbine blades. These forces result from changes in velocity and pressure, as well as variations in viscosity. Hydrodynamic loads are influenced by factors such as velocity, density, frontal areas, and the size and orientation of the body (Çengel and Cimbala 2006). Figure 6 illustrates the forces acting on the hydrofoil section of the turbine.

The drag force, aligned with the flow direction, arises from factors such as viscous effects, friction, and pressure distribution disparities across the hydrofoil section. The drag force is influenced by both surface friction and pressure drag coefficients acting on the turbine.

Conversely, the lift force is generated by variations in pressure between the upper and lower surfaces of the hydrofoil. The camber induces higher fluid velocities on the upper surface, resulting in lower pressure compared to the lower surface. This pressure differential gives rise to lift forces, directed perpendicular to the chord line.
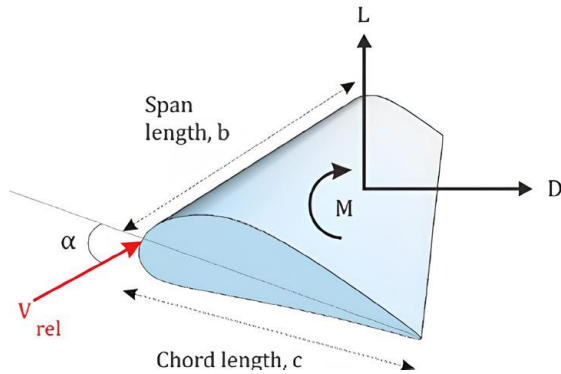
Figure 6. Forces on the hydrofoil (Muratoglu, 2014).

4.4. Aspect ratio

The aspect ratio, AR, reflects the overall dimensions of the turbine's axial length. It's computed by dividing the blade height by the rotor radius (D = 2R), as depicted in Figure 7 (equation 3), primarily relevant for vertical axis turbines. (D'Ambrosio and Medaglia, 2010; Brusca et al., 2014).
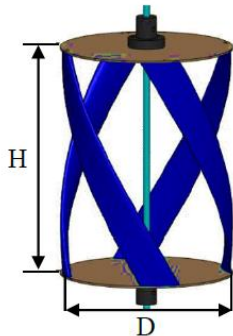
Figure 7. Aspect ratio of vertical turbine.

$$AR = \frac{H}{R} \tag{3}$$

It can also be defined as the ratio between the chord length of the hydrofoil to the blade length for Darrieus and Gorlov turbines, where the general design consists of blades with a hydrofoil cross-sectional shape (equation 4) (Al-Dabbagh, 2017).

$$AR_B = \frac{L}{c} \tag{4}$$

where (c) is the chord length of the hydrofoil (m), L is the blade length (m).

The aspect ratio is a critical factor in determining the torque and performance coefficient of the turbine. Typically, higher aspect ratios lead to increased power coefficients. However, exceeding a certain limit can lead to blade deflection and vibration issues. Moreover, limitations on the aspect ratio are imposed by installation constraints and the size of the domain where

the turbine will be placed (Al-Dabbagh, 2017).

4.5. Power Coefficient (Cp)

The performance of the turbine is characterized by the efficiency or performance coefficient, a dimensionless parameter calculated using the following equations 5, 6 and 7.

$$P_t = T\,\omega \tag{5}$$

$$P_w = 0.5\rho A v^3 \tag{6}$$

$$C_p = \frac{P_t}{P_w} = \frac{T\omega}{0.5\rho A v^3} \tag{7}$$

where:
C_p: efficiency
P_t: output power.
P_w: available energy in water.
T: Torque (N-m).
ω: angular velocity of the turbine (rad/s).
ρ: density of water (kg/m3).
A: frontal cross-sectional area of turbine (m2).
v: fluid velocity (m/s).

4.6. The Betz Limit

The Betz limit represents the maximum theoretical power coefficient achievable by a hydrokinetic turbine. At the Betz limit, theoretical efficiency is roughly 59.3%. Figure 8 shows the tip speed ratio versus power coefficient for a variety of turbine designs and their respective Betz limitations.
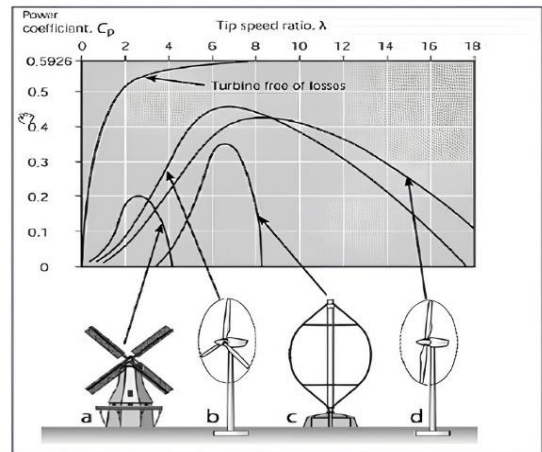
Figure 8. Power coefficient and betz limit of turbines (D'Ambrosio and Medaglia, 2010).

The Betz limit typically applies to free streams without constraints. However, studies have shown that the Betz limit can be surpassed when turbines are positioned within a pipe or duct. For instance, an inline tubular propeller for a water supply system was studied by Samora et al., and they were able to attain a maximum efficiency of 63.75% (Samora et al., 2016).

5. Case Study

This part presents a simulation of the flow field and uses ANSYS FLUENT 17.1 to evaluate a hydrokinetic turbine example, a Gorlov type 3-bladed hydrokinetic turbine. This chapter also provides an explanation of the

simulation steps.

5.1. Turbine Geometry

The turbine blades exhibit quasi-rotation around their vertical axis, as depicted in Figure 9. This turbine is categorized as a vertical axis type, characterized by a rotating vertical shaft submerged in water. To reduce the complexity and duration of the analysis, the shaft and support components are omitted. These components are not expected to significantly impact the flow characteristics; thus, their exclusion does not alter the analysis results.
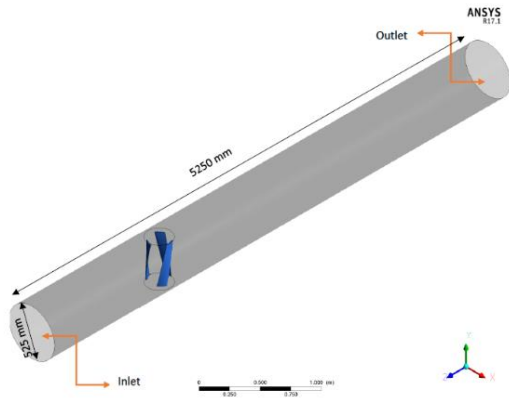
Figure 9. Isometric view of the pipe.

As indicated in Table 3, the turbine is mounted in a pipe that has a diameter of 525 mm and a length of 5250 mm. It has three blades that are designed by the NACA 4415 airfoil. It is placed close to the inlet to gauge its effect on the flow.

Table 3. Turbine properties

Dimension	Length (mm)
Height	450
Width	219
Diameter of Turbine	219
Diameter of Pipe	525
Length of Pipe	5250

5.2. Numerical simulation

The complete domain and geometry are assigned to the numerical simulation once it has been meshing. First, the physical and hydrodynamic parameters are provided as Table 4 illustrates. The density of the fluid is 998.2 kg/m³ (water) at 20 °C temperature.

Table 4. Fluid Properties

Property	Value
Density	998.2 kg/m³
Viscosity	0.001003Kg/m-s
Temperature	20 °C

The pressure-based absolute solver is utilized, appropriate for low-speed and incompressible flow conditions, in contrast to the density-based solver, which is applied to high-speed and compressible flows. The k-ω SST (Shear Stress Transport) model is selected as the turbulence model for this study. Throughout the various simulation scenarios, all these parameters (pressure-based and k-ω SST) were maintained as constants.

6. Results and Discussion

In the simulations, different flow velocities of 1 m/s, 1.5 m/s, and 2 m/s are analyzed. While selecting the flow velocities, studies in the literature and water velocities used in existing water distribution networks were taken into account. The results are consistent across these different flow velocities. Detailed visual outputs, including velocity contours, pressure contours, and velocity streamlines, are presented for each case at maximum efficiency and TSR values. Other parameters, such as pipe diameter and turbine location, are kept constant. The computational fluid dynamics (CFD) analysis demonstrates significant advantages in terms of time and cost over experimental studies.

6.1. Distribution of Velocity Contour

The depiction of velocity distribution within the pipe is presented via contour plots, illustrated in Figure 10. The direction of flow proceeds from right to left. Three different cases were analyzed for inlet velocities of 1 m/s, 1.5 m/s, and 2 m/s. The outlines delineate a notable enhancement in the flow velocity within the turbine section for each scenario. Upon the inlet flow velocity reaching 1 m/s, a surge to approximately 3.5 m/s was evident within the turbine section. This escalation remained uniform throughout all three scenarios. After traversing the turbine section, the flow velocity commenced reverting to its initial condition. The most elevated velocity outlines were identified surrounding the turbine blades, with no-slip conditions being observed at the pipe boundaries (Turker, 2019).
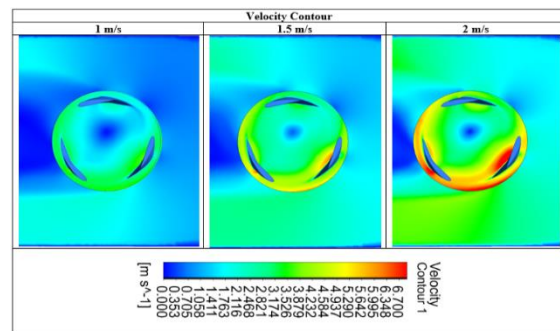
Figure 10. Velocity contours.

6.2. Pressure Contours Distribution

The pressure distribution is illustrated through contour plots in Figures 11 and 12. Figure 11 shows the pressure contours for the entire domain, while Figure 12 focuses on the pressure distribution around the blades. The flow direction is from right to left in both figures. The pressure at the tip of the blades increases with the flow velocity, indicating the impact of the flow dynamics on the turbine blades (Turker, 2019).
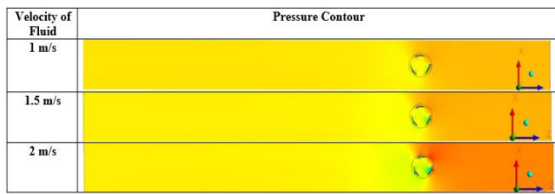
Figure 11. Pressure contours.
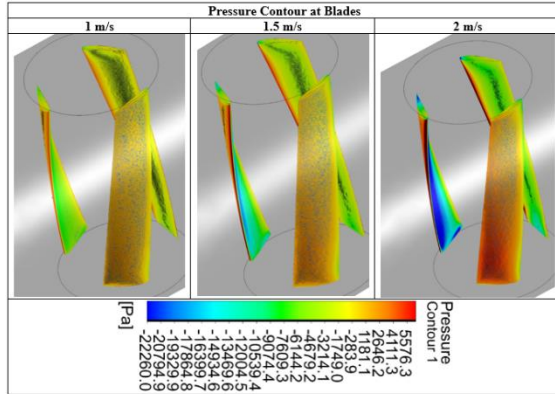
Figure 12. Pressure contours at blades.

6.3. Distribution of Velocity Vectors

The vector distribution for each case is depicted in Figure 13, clearly demonstrating the turbine's rotation on its vertical axis driven by the vector movements. Additionally, velocity streamlines are presented in Figures 14 through 16. As the flow velocity increases from 1 m/s to 2 m/s, the rotation speed of the turbine correspondingly increases, thereby enhancing the generated power. The streamlines indicate a significant velocity increase around the turbine with rising flow velocity (Turker, 2019).
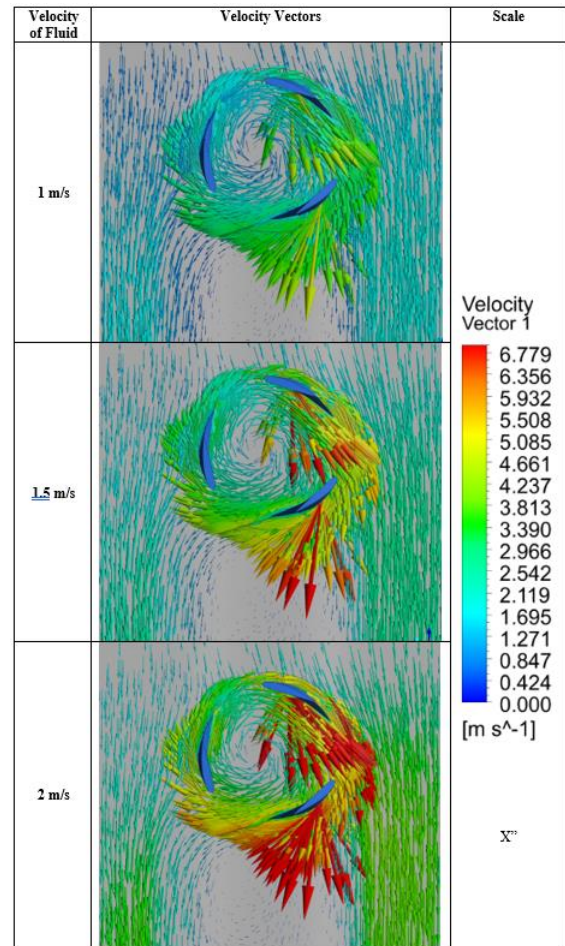
Figure 13. Velocity vectors for different flow velocity cases.
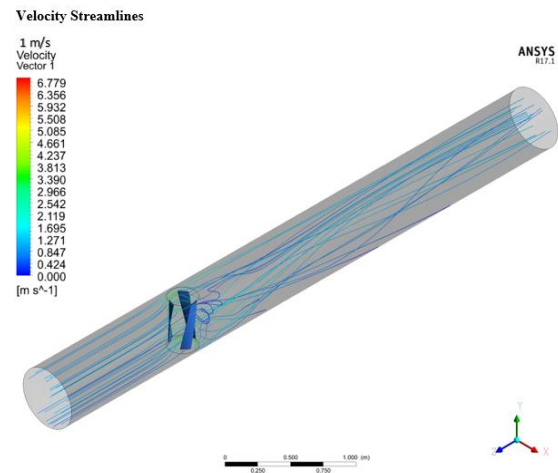
Figure 14. Streamlines for the case of 1 m/s.
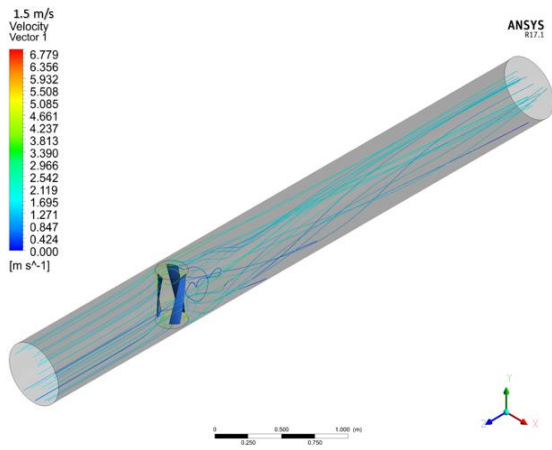
Figure 15. Streamlines for the case of 1.5 m/s.
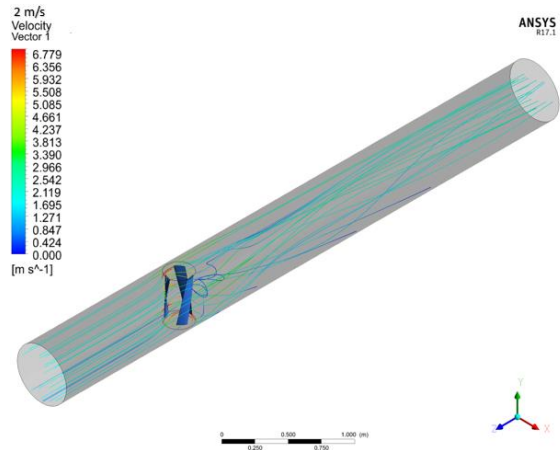
Figure 16. Streamlines for the case of 2 m/s.

6.4. Results of the simulations

The vertical hydrokinetic turbine of the helical (Gorlov) type was examined at various flow rates. Using a particular formula, the power coefficient (Cp) was determined as the turbine power to potential power ratio. The best power coefficients were 0.69 at 1 m/s, 0.71 at 1.5 m/s, and 0.75 at 2 m/s flow velocities, according to the results, which are shown in Table 5. It was found that up to a certain angular velocity, power coefficients and torques both rose; beyond that, they started to decline. This decrease happens because the rotating turbine begins to act like a thick wall at greater angular velocities, impeding flow and decreasing efficiency (Turker, 2019).

Table 5. Power coefficient for various flow velocities (Turker, 2019)

Flow Velocity (m/s)	TSR	W (rad/s)	T (N.m)	Potential Power	Turbine Power	Cp
1.00	0.50	4.57	0.40	49.19	1.80	0.04
1.00	1.00	9.13	1.54	49.19	14.03	0.29
1.00	1.50	13.70	2.47	49.19	33.78	0.687
1.00	2.00	18.26	1.87	49.19	34.13	0.694
1.00	2.50	22.83	0.69	49.19	15.78	0.32
1.00	3.00	27.40	-0.43	49.19	-11.80	-0.24
1.50	0.50	6.85	0.94	166.00	6.41	0.04
1.50	1.00	13.70	3.71	166.00	50.76	0.31
1.50	1.50	20.55	5.67	166.00	116.53	0.70
1.50	2.00	27.40	4.28	166.00	117.34	0.71
1.50	2.50	34.25	1.60	166.00	54.96	0.33
1.50	3.00	41.10	-0.93	166.00	-38.05	-0.23
2.00	0.50	8.73	1.65	393.49	14.38	0.04
2.00	1.00	17.47	5.51	393.49	96.16	0.24
2.00	1.50	26.20	10.25	393.49	268.64	0.68
2.00	2.00	34.93	8.47	393.49	295.77	0.75
2.00	2.50	43.67	3.99	393.49	174.18	0.44
2.00	3.00	52.40	-0.51	393.49	-26.57	-0.07

The graphs made the turbine's response to rising angular velocity easier to see. Figure 17 displays the graphs of the tip speed ratio (TSR) vs power coefficient (Cp). The graph indicates that the power coefficient started to decline when it reached its highest value. The maximum power coefficient recorded was 0.75 at a 2 m/s flow rate (Turker, 2019).

The best efficiencies are obtained at tip speed ratios (TSR) of 2, as shown in Figure 17. At a fluid velocity of 2 m/s, a maximum efficiency of roughly 0.75 is recorded. The power coefficient starts to decline at this point (TSR = 2), suggesting that the turbine behaves more like a solid barrier after a certain angular velocity (Turker, 2019).
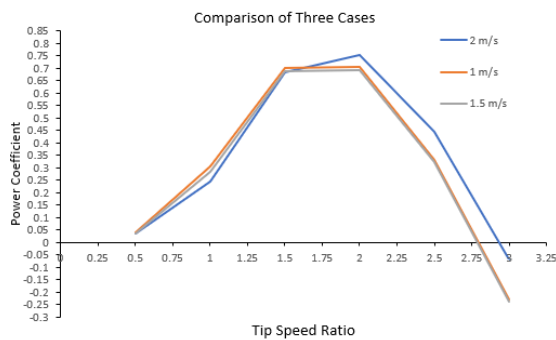
Figure 17. Comparison of the Cp - TSR graphs.

7. Conclusion

Hydrokinetic energy harnesses water's kinetic energy for electricity generation. It's sustainable and eco-friendly but less efficient than conventional hydropower, requiring further improvement.

In this study, hydrokinetic turbines were reviewed in different aspects. Various studies and case studies were presented. In addition, some parameters have an impact on the design of the turbines. Additionally, this study stands out from previous hydrokinetic turbine research by focusing on a helical (Gorlov) type vertical axis turbine installed within a pipe, simulated using ANSYS FLUENT CFD software. Vertical axis turbines offer advantages over horizontal axis counterparts, including independence from the current direction, easier generator placement, stacking capability, and self-starting without the need for pitching mechanisms. Moreover, turbines installed in pipes offer predictability advantages over those in open channels, as the flow can be controlled and unaffected by external factors such as debris, climate change, or flow regime variations.

Three distinct velocity scenarios were simulated involving a turbine within a fully developed circular pipe flow. The computational fluid dynamics (CFD) simulations employed the Reynold-Averaged Navier Stokes equations, with the k-ω SST turbulence model applied uniformly across all scenarios.

Visualizations including velocity and pressure contours, velocity vectors, and velocity streamlines were generated. Additionally, results were summarized in tables and graphs. The maximum efficiency of 0.75 was achieved at a flow speed of 2 m/s with a tip speed ratio of 2. This study sheds light on hydrokinetic turbine performance, particularly within pipes, and highlights the potential to surpass the Betz limit in pipe-based systems. It also provides insights into using CFD simulations to optimize hydrokinetic turbine efficiency.

Additionally, the hydrokinetic turbine system can serve dual purposes in water distribution systems by acting as a pressure reducing valve (PRV) while simultaneously generating electricity. Pressure management is a critical concern for municipalities, and turbines offer a solution by reducing pressure and preventing leakage. Moreover, the enclosed nature of the turbine within the pipe minimizes its impact on aquatic life, addressing environmental concerns.

As a result, hydrokinetic turbine technology holds promise for the future, offering potential benefits in renewable energy generation and water management. However, further advancements are necessary to enhance its efficiency and expand its applicability in various settings. Continued research and development efforts are crucial to unlock the full potential of this technology and address existing challenges.

Author Contributions

The percentage of the author(s) contributions is presented below. The author reviewed and approved the final version of the manuscript.

	M.S.T	M.İ.Y
C	35	65
D	60	40
S	40	60
DCP	60	40
DAI	50	50
L	60	40
W	70	30
CR	40	60
SR	60	40
PM	40	60
FA	50	50

C=Concept, D= design, S= supervision, DCP= data collection and/or processing, DAI= data analysis and/or interpretation, L= literature search, W= writing, CR= critical review, SR= submission and revision, PM= project management, FA= funding acquisition.

Conflict of Interest

The authors declared that there is no conflict of interest.

Ethical Consideration

Ethics committee approval was not required for this study because of there was no study on animals or humans.

References

Al-Dabbagh MA, Yuce MI. 2018. Simulation and comparison of helical and straight-bladed hydrokinetic turbines. Int J Renew Ener Res, 8(1): 514-519.

Al-Dabbagh MA. 2017. Simulation of Helical hydrokinetic turbines in river flows. PhD Thesis, Gazinatep University, Institute of Science, Gaziantep, Türkiye, pp: 167.

Anyi M, Kirke B. 2010. Evaluation of small axial flow hydrokinetic turbines for remote communities. Ener Sustain Devel, 14: 110-116.

Bizhanpour A, Hasanzadeh N, Najafi AF, Magagnato F. 2023. Investigation of different deflector geometry and mechanism effect on the performance of an in-pipe hydro Savonius turbine. Appl Ener, 350: 121697.

Brusca S, Lanzafame R, Messina M. 2014. Design of a vertical-axis wind turbine: how the aspect ratio affects the turbine's performance. Int J Ener Environ Eng, 5: 333-340.

Casini M. 2015. Harvesting energy from in-pipe hydro systems at urban and building scale. Int J Smart Grid Clean Ener, 72: 00196. https://doi.org/10.12720/sgce.4.4.316-327

Çengel YA, Cimbala JM. 2006. Fluid mechanics fundamentals and applications, Ebook. McGraw Hill, New York, US, pp: 1005.

Chen J, Yang HX, Liu CP, Lau CH, Lo M. 2013. A novel vertical axis water turbine for power generation from water pipelines. Energy, 54: 184-193. https://doi.org/10.1016/j.energy.2013.01.064

Cuming V, Mills L, Strahan D, Boyle R, Stopforth K, Latimer S, Becker L. 2015. Global trends in renewable energy investment 2015. https://www.fs-unep-centre.org/wp-content/uploads/2019/11/Global_Trends_Report_2015.pdf (accessed date: May 11, 2023).

D'Ambrosio M, Medaglia M. 2010. Vertical axis wind turbines: History, technology and applications. Polytechnic International Press, Montreal, Quebec, Canada, pp: 152.

Ertuğrul NA, BağcI ZH, Ertuğrul ÖL. 2018. Aquifer thermal energy storage systems: Basic concepts and general design methods. Turkish J Eng, 2(2): 38-48.

Fletcher CAJ. 1980. Diffuser-augmented wind turbine analysis. Institution of Engineers, Vienna, Australia, pp: 435-438.

Gorlov A. 1998. Development of the helical reaction hydraulic turbine. Final technical report, July 1, 1996--June 30, 1998 (No. DOE/EE/15669-T1). Northeastern University, Boston, MA, USA, pp: 124.

Güney MS, Kaygusuz K. 2010. Hydrokinetic energy conversion systems: A technology status review. Renew Sustain Energy Rev, 14(9): 2996-3004.

Hydro Spin. 2017. https://www.h-spin.com/ (accessed date: May 10 2024)

Kantoglu B, Argun ID. 2022. Evaulation of renewable energy source alternatives prioritization. Turkish J Eng, 7(1): 1-8.

Khan MJ, Bhuyan G, Iqbal MT, Quaicoe JE. 2009. Hydrokinetic energy conversion systems and assessment of horizontal and vertical axis turbines for river and tidal applications: A technology status review. Appl Ener, 86: 1823–1835. https://doi.org/10.1016/j.apenergy.2009.02.017

Kumar R, Sarkar S. 2023. Performance analysis of spherical-shaped Darrieus hydrokinetic turbine for an in-pipe hydropower system. Ener Conver Manag, 294: 117600.

Muratoglu A. 2014. Design and simulation of a riverine hydrokinetic turbine. PhD Thesis, Gazinatep University, Institute of Science, Gaziantep, Türkiye, pp: 238.

Nunes MM, Mendes RCF, Oliveira TF, Brasil Junior ACP. 2019. An experimental study on the diffuser-enhanced propeller hydrokinetic turbines. Renew Ener, 133: 840-848. https://doi.org/10.1016/j.renene.2018.10.056

OECD/IEA. 2024. https://www.iea.org/ (accessed date: May 10, 2024).

Oladosu TL, Koya OA. 2018. Numerical analysis of lift-based in-pipe turbine for predicting hydropower harnessing potential in selected water distribution networks for waterlines optimization. Eng Sci Technol Int J, 21: 672-678.

Phillips DG, Richards PJ, Mallinson GD. 1999. Computaional modelling of diffuser design for a diffuser augmented wind turbine. Phoenics J Comput Fluid Dynam Appl, 12: 158-172.

Pudur R, Rajak MK, Zafar S. 2022. Analysis of savonius rotor with multiple blades for hydrokinetic application. Springer, Singapore, pp: 623-634.

Rajaonary TT. 2016. Design and optimization of a hydrokineic turbine with CFD. MSc Thesis, Gazinatep University, Institute of Science, Gaziantep,Türkiye, pp: 99.

Samora I, Hasmatuchi V, Minch-Alligni C, Franca MJ, Schleiss AJ, Ramos HM. 2016. Experimental characterization of a five blade tubular propeller turbine for pipe inline installation. Renew Ener, 95: 356-366.

Schleicher W, Ma H, Riglin J, Kraybill Z, Wei W, Klein R, Oztekin A. 2014. Characteristics of a micro-hydro turbine. J Renew Sustain Ener, 6: 013119. https://doi.org/10.1063/1.4862986

Shahsavarifard M, Bibeau EL, Chatoorgoon V. 2015. Effect of shroud on the performance of horizontal axis hydrokinetic turbines. Ocean Eng, 96: 215-225.

Turker MS. 2019. Design of a hydrokinetic turbine in a pipe. MSc Thesis, Gaziantep University, Institute of Science, Gaziantep, Türkiye, pp: 80.

Zeiner-Gundersen DH. 2015. A novel flexible foil vertical axis turbine for river, ocean, and tidal applications. Appl Ener, 151: 60-66. https://doi.org/10.1016/j.apenergy.2015.04.005

Zingman AAO. 2007. Optimization of a Savonius rotor vertical-axis wind turbine for use in water pumping systems in rural honduras. PhD Theis, Massachusetts Institute of Technology, Massachusetts, USA, pp: 163.

THE EFFECT OF JACKET AREA ON THE BEHAVIOR OF REPAIRED/STRENGTHENED REINFORCED CONCRETE COLUMNS

Yağmur KOPRAMAN[1]*, Hüsnü CAN[2]

[1]Gazi University, Faculty of Technology, Department of Civil Engineering, 06560, Ankara, Türkiye
[2]Gazi University, Faculty of Engineering, Department of Civil Engineering, 06570, Ankara, Türkiye

Abstract: Jacketing is the most popular method for strengthening reinforced concrete columns under axial loading. This repair and strengthening technique is widely used not only in Türkiye but also in other technologically developed countries. In this study, the effectiveness of this method is investigated experimentally, by testing two test parameters which are column section geometry and jacket thickness. The specimens were enlarged on all four sides to understand how the thickness of the jacket layer affects the behavior of the column. Using the experimental data, load versus deformation curves were plotted for each test specimen. The parameters (strength, rigidity, ductility, and energy dissipation capacity) that determine the behaviour of the reinforced column were then analyzed. At the end of this study, the effects of column section geometry and jacket thickness on the jacketing method are discussed, providing valuable preliminary data for future experimental studies.

Keywords: Strengthening, Repair, Jacketing, Axial load, Reinforced concrete, Column

*Corresponding author: Gazi University, Faculty of Technology, Civil Engineering Department, 06560, Ankara, Türkiye
E mail: yagmur@gazi.edu.tr (Y. KOPRAMAN)
Yağmur KOPRAMAN   https://orcid.org/0000-0001-9552-3039
Hüsnü CAN   https://orcid.org/0000-0003-4202-875X

Cite as: Kopraman Y, Can H, 2024. The effect of jacket area on the behavior of repaired/strengthened reinforced concrete columns. BSJ Eng Sci, 7(5): 928-938.

1. Introduction

Since the repair and strengthening of reinforced concrete columns is a widely used technique, many studies have been found in the literature on the effectiveness of jacketing technique, which is one of the strengthening methods, and the effects of jacketing on behavior and strength. In a master's thesis by Aksan (1988), the effectiveness of different types of jacketing was investigated only in terms of axial load-carrying capacity. For this purpose, a series of experiments consisting of five test specimens were carried out. Four of them reflect various types of jacketing in terms of application conditions, while the fifth is a monolithic reference specimen with the same cross-section, properties and reinforcement as the jacketed columns in order to determine the effectiveness of different jacketing methods. Although 70-80% of the strength of the monolithic specimen was reached with the repair jacketing in the unloaded condition, the repair jacketing in the loaded condition did not exhibit the same performance and this repair jacketing could only reach 50% of the strength of the monolithic specimen and only the jacketing was loaded. The ductility, energy consumption and similarly stiffness of the repaired members are less than the monolithic and reinforced members both under load and unloaded conditions. In

addition, excessive deformations were observed in the repaired specimens as a result of reloading.

Suleiman (1991) experimentally investigated the behavior of jacketed or strengthened reinforced concrete columns under axial load and single curvature bending. Three of the five specimens were tested under uniform load or reversible load and then these members were jacketed and retested. According to the jacketing, the repair and strengthening jacketing was named as repair and strengthening jacketing depending on the damage in the lean test specimen. In addition to these specimens, two monolithic reference specimens were also tested. It was shown that the reinforced jacketed specimens behaved as well as the monolithic reference specimen under both monotonic and reversible loads. In the case of the repaired jacketed members, both stiffness and strength were observed to be smaller than the monolithic reference member.

Yanarateş (1990) investigated the repair and strengthening of axially loaded columns under eccentric loading in an experimental study. Repair of columns damaged under axial load by jacketing was carried out under unloaded conditions after the load was removed. It was concluded that the use of Expanding Metal Mesh (EMM) as wrapping reinforcement was not an effective solution for the columns that were retested after repair. Yumak (1991) was observed that jacketed columns

anchored with epoxy and mechanical methods exhibited good behavior. In the case of discontinuous longitudinal reinforcement; the results obtained were not very reassuring. Can (1995a) concluded that the stirrup used as wrapping reinforcement during jacketing is highly effective in the success of the jacketing, and if possible, a strong and closed stirrup surrounding the entire column by stripping the rust allowances on the back face of the column will increase the success of the jacketing. Can (1995b) found that 92% of the monolithic section capacity could be achieved with reinforcement jacketing on four sides of the columns and 88% with repair jacketing. However, the columns jacketed on four faces (repaired and strengthened) exhibited a successful behavior in terms of strength, stiffness and ductility in general. In columns jacketed on three sides, 90% of the monolithic section capacity could be reached with the strengthening jacket and 82% with the repair jacket. Although the stiffness and ductility of the repaired and strengthened columns are close to the monolithic column, a certain reduction in energy consumption is observed. The strength of the reinforced column jacketed from two adjacent faces was 89% of the monolithic column and 86% of the repaired column. Although the ductility and energy consumption of the jacketed columns (retrofit and repair) were lower compared to the monolithic column, these specimens exhibited a good behavior in terms of stiffness. In the whole experimental study, the adjacent two-face and three-face jacketed columns exhibited lower values in terms of strength and ductility compared to the four-face jacketed columns.

Demirel et al. (1995) determined that the z-shaped bars connecting the additional longitudinal reinforcement of the jacketing and the existing longitudinal reinforcement, the spacing of these bars, and the way they are welded have a significant effect on the strength and behavior. Cısdık (1998) tested the usability of fretted jacketing for repair and strengthening of columns under axial loads. The research was carried out on two different types of columns with fretted and circular ribs. As a result of the experiments, it was found that in both types of columns, the bare column bearing strength increased by at least 60-80% with jacketing and the initial brittle behavior became ductile. The load-unit deformation curves of the columns were drawn with the data obtained and as a result of the evaluations, it was concluded that fretted jacketing can be safely used in the repair and strengthening of reinforced concrete columns.

After jacketing, strengthening/repair with steel, CFRP and TRM has been intensively studied in the strengthening/repair literature for the last 10 years. Structural specimens were strengthened by jacketing in the nineties and then by bonding steel plates to the tensile and shear surfaces with adhesives and bolts. This method has been used for many years, but it has been abandoned over time due to reasons such as the need for skilled workmanship and changing the architectural appearance of the building, the need to protect the steel specimens against effects such as corrosion and fire, the added steel reinforcement specimens changing the structural dynamics characteristics due to their weight and installation difficulties. Fiber-reinforced polymer fabrics (FRP), which are produced from composite materials, have become a widely preferred alternative to reinforcement with steel strips due to their high mechanical strength values, easy application due to their light weight, ease of installation, properties that do not change the dynamic characteristics since they do not add additional weight to the structure and high resistance to environmental effects. FRP reinforcement has been the most preferred construction material for strengthening structures for the last 20 years (Ozbakkaloglu et al., 2013; Ghoroubi et al., 2020; Mercimek et al., 2021; Mercimek et al., 2023; Türer et al., 2023). Epoxy material with organic structure was used to form a cohesive zone between the FRP and the surface to which the FRP was applied. However, (a) poor resistance to fire (Triantafillou and Thanasis, 2006), (b) inapplicability on wet or damp surfaces (Bournas and Thanasis, 2007), (c) lack of ability to replace the coating layer (Francisco et al., 2012) (d) classification as a hazardous material during disposal, (e) high cost of FTEK techniques (Francisco et al., 2012), (f) permeability: insufficient vapor permeability and the use of organic resins can cause damage to concrete (Triantafillou and Thanasis, 2006). Considering these negativities, the widespread use of TTH through scientific research has been recognized as a remarkable progress in the field of structural reinforcement (Triantafillou and Thanasis, 2006; Bournas and Thanasis, 2007). TTH is a composite building material consisting of a cement-based inorganic mortar with textiles made of different materials (steel, carbon, basalt, glass, etc.). Textiles used as reinforcement of the composite material typically consist of strands of fibers oriented perpendicular to each other (bi-directional). Considering that the mortar is produced and applied by conventional methods, it was realized that TTH has some advantages over FTEK. These advantages are; (a) low cost, (b) resistance to high temperatures, (c) applicability to concrete, reinforced concrete and masonry surfaces, (d) applicability to wet surfaces, (e) low thermal transmittance and (f) high bearing strength. Considering these advantages, researchers have widely increased the use of TTH in the development of retrofit/repair details in the last 10 years (Mercimek, 2023; Mercimek et al., 2022; Mercimek et al., 2024).

After the February 6, 2023 Kahramanmaraş earthquakes, retrofitting projects were prepared for many buildings in the earthquake zone. It was observed that many engineers who prepared these projects strengthened the moderately damaged structures by jacketing the columns and adding shear walls. Although it is a subject that has been researched since the early nineties, some deficiencies have been identified at many critical points. A thesis study was conducted by Kopraman (2003) on the subject. In this study, based on Kopramans (2003),

aimed to investigate the behavior of columns with enlarged cross sections by jacketing method. During the application of this method, a reinforced concrete jacket was formed by placing additional longitudinal reinforcement at all four corners of the existing column and the same wrapping reinforcement as the plain column reinforcement along the column and the column cross section was enlarged in three different ratios. The column cross sections were selected so that these ratios were similar for both rectangular and square columns. For the two different types of column geometries, the characteristic ratios of Acj/Acc=0.8 for the narrow type mantle, Acj/Acc=1.0 for the normal type mantle and Acj/Acc=1.8 for the wide type mantle were tried to be achieved. At the end of the experiment, these ratios were found to be sufficient to give meaningful results in terms of purposeful behavior.

2. Materials and Method

The specifications of the experimental specimens are presented in Table 1. Since three different mantle areas were determined, three lean columns were fabricated for each cross-section. However, jacketing parameters were not tested for columns with square cross-sections in the repair group experiments. The main reason for this is that the jacketing method has been applied on square and circular section specimens more than rectangular section columns (Cısdık, 1998; Ünsal 1998). For this reason, jacketing was applied only to rectangular columns for the repair group. In the retrofitting group experiments, square and rectangular columns were tested as a complete set.

In addition to these test specimens, two monolithic (single cast) specimens, one with square and one with rectangular cross-section, with normal type jacketing, were manufactured. The monolithic members were included in the scope of the experiments to provide a reference for the specimens. Fourteen experimental specimens were tested within the scope of these experiments. The schematic view and donate plans of the specimens are shown in Figure 1. Some images of the production stages of the experimental specimens are shared in Figure 2.

Care was taken to ensure that the concrete used in the test specimens was easy to place in the mold and had high strength. In order to repeat these properties in different castings, a mixture ratio that was found suitable for the casting of the experimental specimens was used as a standard. For this reason, different mixtures were made and broken after 28 days of strength. As a result, it was decided to use two mixtures with different workability properties. During the concreting of the specimens, at least seven cylinder samples were taken from each concrete mix. The cylinder specimens were of standard dimensions, 150 mm in diameter and 300 mm in height. The specimens were subjected to the same vibration as the test specimen and placed in the formwork. However, they were kept in the same place and condition as the specimens in order to ensure that the specimen strengths were representative of the specimen strengths. The concrete compressive strengths of the specimens are given in Table 2.

Table 1. Experimental groups, names and cross-sectional properties of specimens

Specimen		Column Section		Jacketed Column		Cross-section geometry	Acj / Acc
		Dimension (mm)	h/b	Dimension (mm)	h/b		
Strengthened Specimens	S1	120x120	1.00	170x170	1.00	Square	1.01
	S2	120x120	1.00	160x160	1.00	Square	0.78
	S3	120x120	1.00	200x200	1.00	Square	1.78
	S4	90x160	1.78	140x210	1.54	Rectangle	1.04
	S5	90x160	1.78	130x200	1.50	Rectangle	0.81
	S6	90x160	1.78	170x240	1.41	Rectangle	1.83
Damaged Specimens	B4	90x160	1.78	---	---	Rectangle	---
	B5	90x160	1.78	---	---	Rectangle	---
	B6	90x160	1.78	---	---	Rectangle	---
Repaired Specimens	R4	90x160	1.78	140x210	1.54	Rectangle	1.04
	R5	90x160	1.78	130x200	1.50	Rectangle	0.81
	R6	90x160	1.78	170x240	1.41	Rectangle	1.83
Reference Specimens	M1	---	---	170x170	1.00	Square	1.01
	M4	---	---	140x210	1.50	Rectangle	1.04

Table 2. Compressive strength of concrete material

Specimen	Column (MPa)	Jacket (MPa)
S1,S2,S3	18.8	23.9
S4,S5,S6	19.4	23.9
R4, R5, R6	18.8	18.9
M1,M4	23.0	---
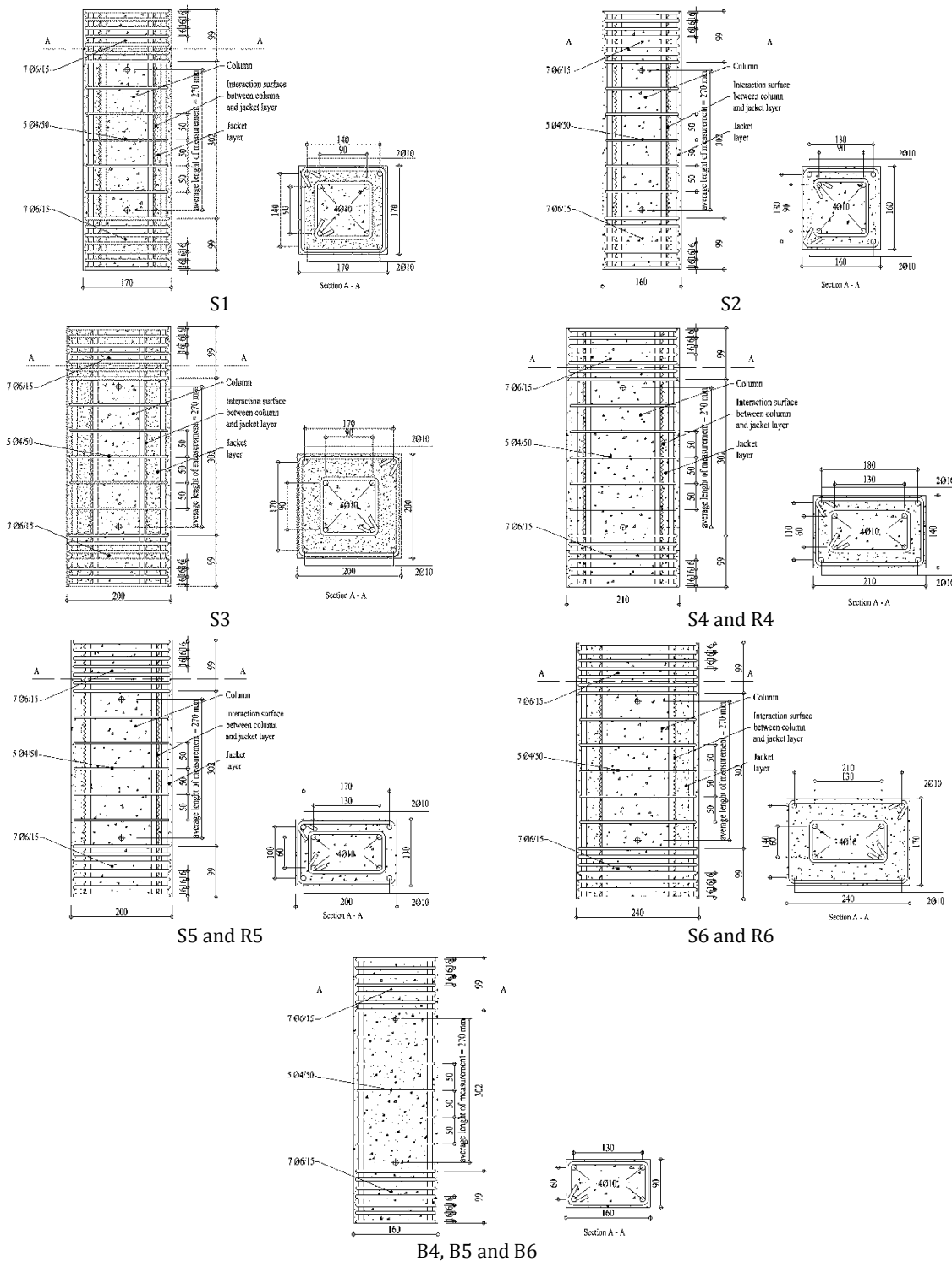
Figure 1. Dimensions and reinforcement detail of specimens

Steel reinforcement with flat surface was used in all experimental specimens. In the construction of the experimental specimens, Ø10 was used as longitudinal reinforcement. Ø4 reinforcement was used in the middle region of the column and Ø6 reinforcement was used in the end regions of the column.

The same reinforcements were used in all of the specimens. A sufficient number of samples were taken from these reinforcements and their average yield strengths were determined. The yield strengths of the reinforcements are given in Table 3.

Table 3. Yield strength of the reinforcements used in the experiments

Diameter (mm)	Yield Strength (MPa)
ϕ 4	450
ϕ 6	362
ϕ 10	365

(a)

(b)

(c)

(d)

(e)

(f)
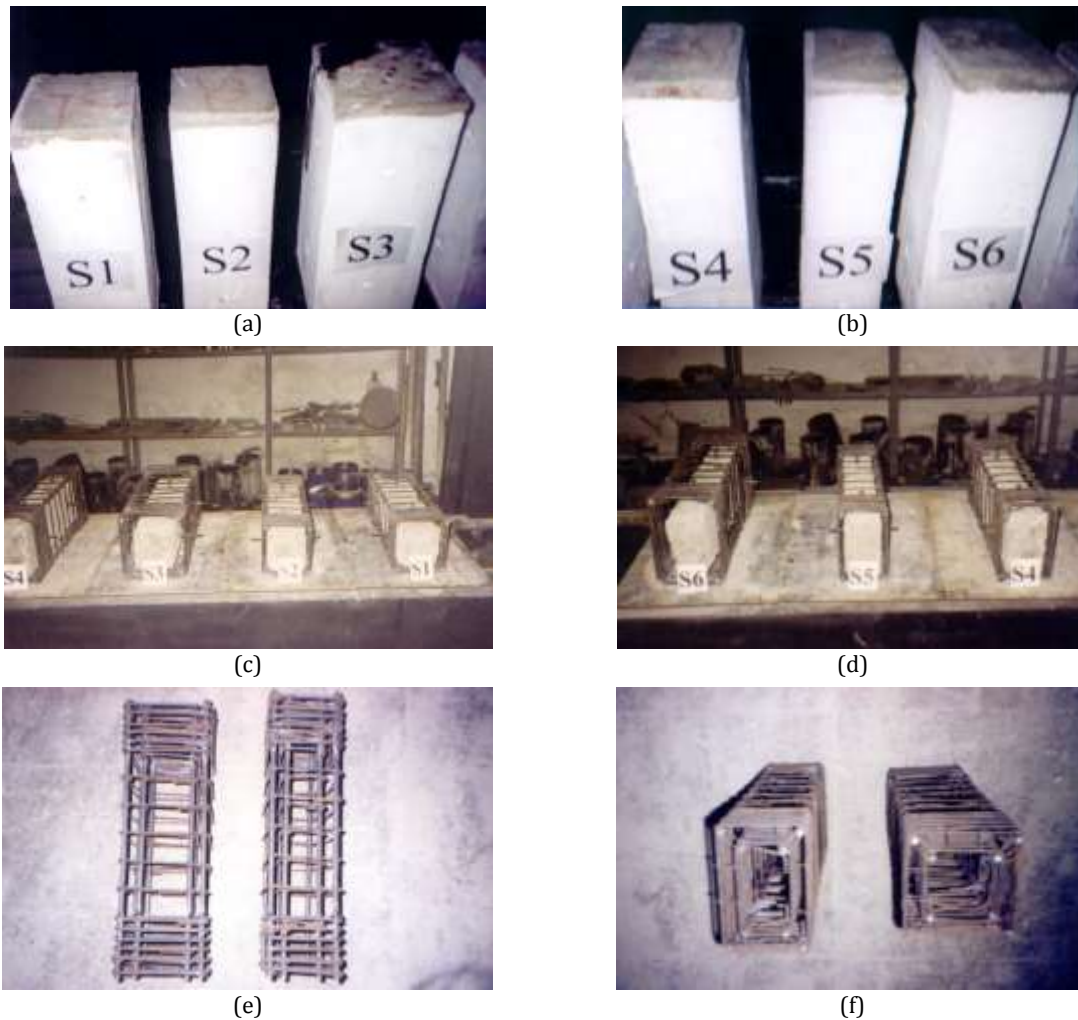
Figure 2. Production process of specimens

The experimental setup is shown in Figure 3. The loading frame, which is the main specimen of the setup, is 2 m high. During the experiment, a load of 2000 kN was applied to the specimens with a hydraulic jack. The loading was tried to be done at constant speed. The applied load was transmitted to the scanner-reader with a load meter with a pressure capacity of 2000 kN and recorded on the computer. Displacement records were taken from 4 displacement meters over the experimental specimens.
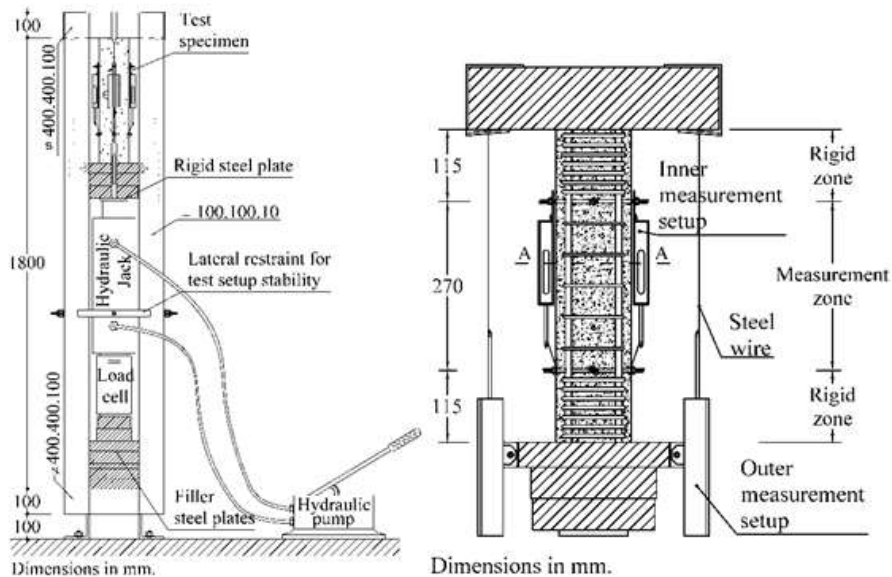
Figure 3. Experiment and measurement setup.

3. Results

The load-displacement graphs of the specimens are shown in Figure 4. In drawing the load-unit deformation relationship of the specimens, the deformation readings on the four faces were averaged and interpretations were made accordingly.   The damage distribution of the specimens is given in Figure 5. Since the concretes of all the test specimens could not be prepared simultaneously, the experiments were carried out on specimens with concretes of different strengths. For this reason, the load-unit deformation relationships of the specimens were first rearranged according to a common concrete strength (fc=20 MPa) and all test results were evaluated based on these curves. In this evaluation, strength, strength degradation, energy dissipation capacity, ductility and stiffness were considered as the determining parameters of the specimen behavior. In order to determine the success of the method, firstly, the reinforced and repaired specimens were compared with a cast (monolithic) specimen.
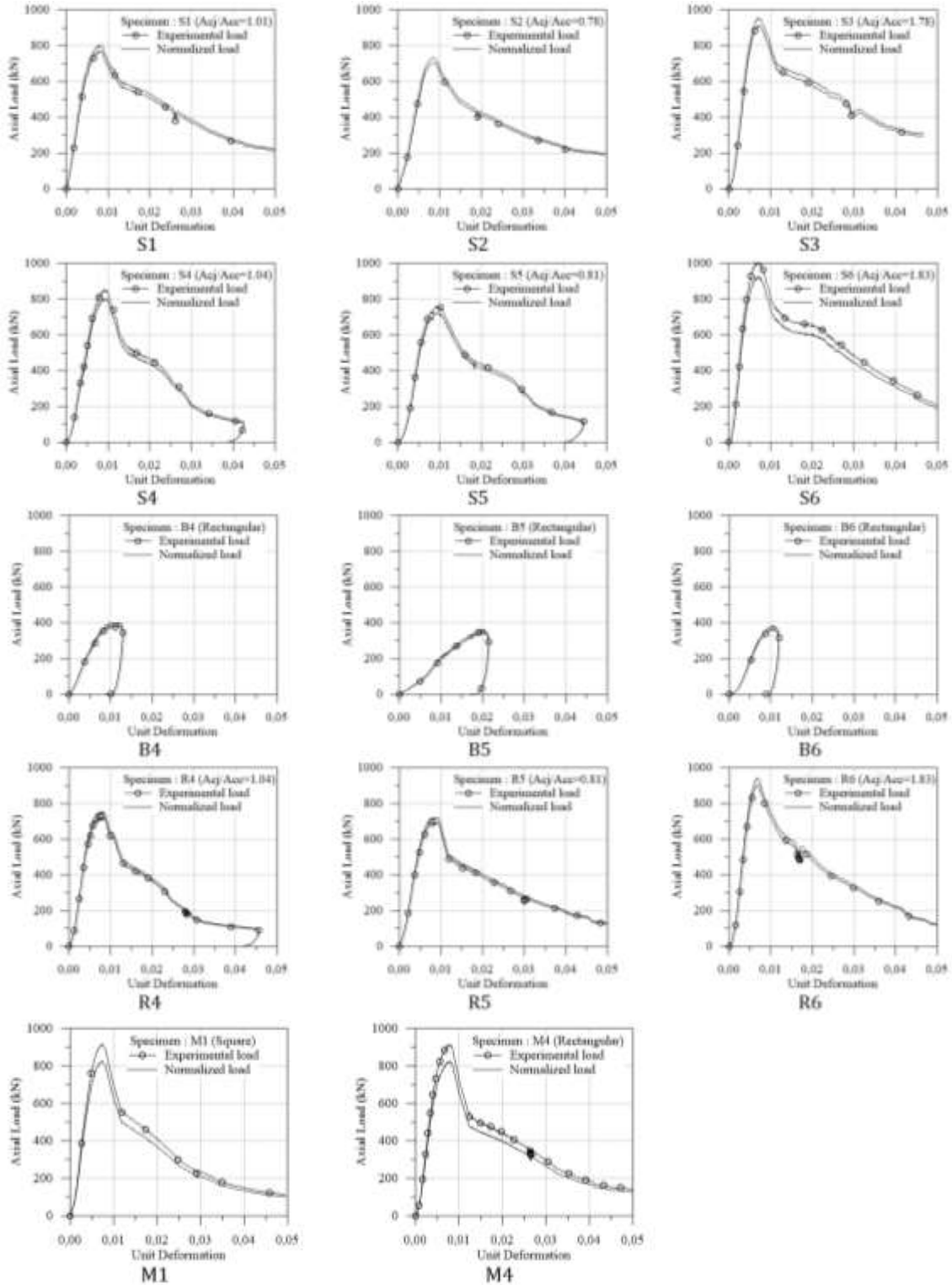
Figure 4. Load-displacement graphs

Figure 5. Damage distribution of specimens after test

The S1 specimen did not show any damage until the 429 kN axial load level, but after this point, damage effects started to be seen in the member with whitewash blistering starting from the south face. At 630 kN load, 2.83 mm axial deformation occurred in the specimen and crushing was observed in the upper and lower rigid zones outside the measurement zone on the west face. This crushing proceeded directly into the measurement zone of the specimen. When the specimen deformed by 4.31 mm in response to an axial load of 768 kN, a sudden collapse occurred inside the measurement zone.

In the S2 specimen, whitewash blistering at the stirrup line occurred under a deformation of 2.14 mm against 377 kN. Crushing first occurred in the upper rigid zone outside the measurement zone on the east face under an axial force of 594 kN. When 705 kN and 4.19 mm

deformation was read, the specimen started to lose strength. Buckling of the longitudinal reinforcement started after the peak point was exceeded and the reinforcement at the south-east corner buckled at 395 kN and then the reinforcement at the south-west corner buckled.

In the S3 test specimen, the swelling at the stirrups started when the axial load was at 585 kN. After the swellings occurred at the stirrups on all faces, crushing started at the corners of the rigid region of the specimen when the load increased to 686 kN. Crushing, which first started outside the south-east measurement zone, was observed outside the upper and lower measurement zone at the north-west corner at 882 kN. After the bearing capacity peak of 919 kN and 3.00 mm was exceeded, the shear plane did not draw its direction

precisely within the measurement zone until the deformation point of 802 kN and 3.93 mm, and was observed as local dents. After this point, it was observed that the shear plane made an angle of 600 with the horizontal when viewed from the north, and the crushing zone, which started outside the measurement zone on the west face, descended into the measurement zone on the same face and then proceeded towards the lower boundary of the measurement zone on the east face. It was observed that the reinforcement at the south-west and south-east corners buckled under a displacement of 10.67 mm and an axial load of 553 kN.

Although there was a deformation of 5.09 mm and an axial load of 815 kN in the S4 test specimen, there was no crushing progression within the measurement zone. While the specimen with 5.84 mm deformation under 846 kN load exceeded this peak, the crushes formed in the shell concrete and generally in the lower rigid zone rapidly progressed into the measurement zone. The experiment was terminated with a deformation of 20 mm in the S5 test specimen. No stirrup opening or rupture was observed in the mantle and lean sections. However, the ups and downs seen in the load-deformation curve of the specimen are thought to be caused by the roughness of the loading plane. This uneven plane was flattened with the effect of the load and lost its negative effect when it exceeded the peak point of the specimen. S6 member was subjected to 40 mm axial deformation. The failure was caused by the shear plane starting from the upper region on the north face, moving downwards and making an angle of 45o with the horizontal. The vertical cracks formed during the experiment indicate that concentric loading was applied more successfully in this experiment compared to the other experiments.

Care was taken to avoid excessive damage to the B4 test specimen. The longitudinal reinforcements have ejected the shell concrete. However, none of them reached the buckling level. The experiment was terminated according to the behaviour of the specimen. At the end of the experiment, the total deformation of the member was 5.81 mm for an axial load of 267 kN. In the B5 specimen, the total deformation of the member was recorded as 10.07 mm when it reached the axial load level of 272 kN, which is the bearing capacity. The reason for the excessive axial deformation in this specimen is the early

damage to the corners of the rigid zones. For this reason, the axial force value carried by the specimen remained at a low level. Experimental specimen B6 reached a bearing capacity of 288 kN at an axial deformation level of 4.80 mm. The specimen behaved quite well, allowing similar loading effects to be observed on all four faces. However, in this specimen, the behavior of the member was also affected by the early crushing at the top and bottom of the rigid zone. As a result of the observations, no buckling of the longitudinal reinforcement was observed. The experiment was terminated when the specimen deformed by 5.30 mm against 242 kN.

The R4 specimen suddenly exceeded the peak point of 725 kN and the center region was crushed at the same time on all four faces. Its reinforcement buckled under a deformation of 9.14 mm and an axial force of 438 kN, all of which were within the measurement zone. It was observed that a stirrup was broken under a displacement of 18.22 mm and a load of 187 kN. At the end of the experiment, 30 mm deformation was applied to the specimen. The R5 specimen exceeded the peak value under 694 kN and 3.29 mm deformation and suddenly crushed and collapsed. Crushing first started outside the measurement zone. However, when 538 kN and 5.52 mm displacement was read, the crushing was effective within the measurement zone. It was understood that 5 stirrups were broken during the axial force values of 187.2 kN, 110 kN, 82.9 kN, 73.9 kN and 73.3 kN respectively. The specimen was deformed by 30 mm during the experiment. There was no visible damage to the R6 specimen until the axial load value of 493 kN. As the load increased to 675 kN, crushing was observed outside the measurement zone. The first crushed area is the upper forehead of the specimen. This was followed by crushing of the upper and lower regions of one corner as the load increased to 797 kN. Under 4.05 mm deformation and 903 kN axial force, the specimen exceeded the peak point and collapsed due to sudden crushing inside the measurement zone.

The axial load strengths of the specimens are given in Table 4. The axial stiffnesses of the specimens were obtained from the slope of the output arms of the load-unit deformation curves of the experimental specimens. The ratios of axial stiffnesses diagonally between the specimens are given in Table 5.

Table 4. Experimental results

| Spec. | Axial load and Unit deformations | | | | | | | | Ratios | | | |
| | Yield Point | | | Peak Capacity | | | Ductility Limit | | $\frac{N_{oN}}{N_{yN}}$ | $\frac{(\varepsilon_{co})_i}{(\varepsilon_{cy})_i}$ | $\frac{(\varepsilon_{0.85})_o}{(\varepsilon_{cy})_o}$ | $\frac{(\varepsilon_{0.85})_o}{(\varepsilon_{co})_o}$ |
	$N_{yN}{}^*$	$(\varepsilon_{cy})_i$	$(\varepsilon_{cy})_o$	$N_{oN}{}^*$	$(\varepsilon_{co})_i$	$(\varepsilon_{co})_o$	$N_{0.85N}{}^*$	$(\varepsilon_{0.85})_o$				
S1	647	0.0015	0.0047	807	0.0035	0.0083	686	0.0106	1.25	2.27	2.26	1.28
S2	617	0.0016	0.0058	735	0.0028	0.0085	625	0.0110	1.19	1.74	1.89	1.30
S3	776	0.0011	0.0048	961	0.0021	0.0070	817	0.0099	1.24	2.01	2.06	1.41
S4	648	0.0013	0.0061	806	0.0021	0.0094	685	0.0114	1.24	1.53	1.88	1.22
S5	583	0.0013	0.0061	725	0.0023	0.0093	616	0.0126	1.24	1.79	2.07	1.36
S6	745	0.0014	0.0043	927	0.0024	0.0070	788	0.0096	1.25	1.71	2.23	1.36
R4	600	0.0014	0.0047	756	0.0023	0.0078	643	0.0100	1.26	1.66	2.14	1.28
R5	568	0.0015	0.0050	723	0.0030	0.0089	614	0.0106	1.27	2.00	2.11	1.19
R6	780	0.0009	0.0048	944	0.0019	0.0068	802	0.0091	1.21	2.00	1.87	1.32
M1	688	0.0010	0.0047	828	0.0023	0.0075	704	0.0091	1.20	2.39	1.92	1.22
M4	663	0.0015	0.0046	825	0.0028	0.0074	701	0.0096	1.24	1.85	2.07	1.29

*Load values is in kN.4

Table 5. Comparative stiffness table of specimens with respect to each other

	S1	S2	S3	S4	S5	S6	R4	R5	R6	M1	M4
S1	1.00	1.01	2.01	1.21	1.19	1.26	1.17	0.96	1.62	1.74	1.26
S2		1.00	1.99	1.20	1.18	1.25	1.15	0.95	1.61	1.72	1.25
S3			1.00	0.60	0.59	0.63	0.58	0.48	0.81	0.87	0.63
S4				1.00	0.98	1.04	0.96	0.79	1.34	1.43	1.04
S5					1.00	1.06	0.98	0.81	1.36	1.46	1.06
S6						1.00	0.92	0.76	1.29	1.38	1.00
R4		Undefined Region					1.00	0.83	1.39	1.49	1.08
R5								1.00	1.69	1.81	1.31
R6									1.00	1.07	0.78
M.										1.00	0.73
M.											1.00

The unit deformation at the moment when the load-unit deformation curves of the experimental specimens were reduced to 85% of the maximum strength on the descending arm of the load-unit deformation curves was taken as the maximum unit deformation, and the specimen ductility was obtained from the ratio of this unit deformation to the unit deformation at yield. Accordingly, the ductility ratios obtained from the external measurement devices are presented in Table 6. In general, the specimens were not ductile enough. However, as it is known, excessive ductility is not expected in reinforced concrete columns subjected to concentric loading. Therefore, it is already known that this inadequacy in ductility is a behaviour of concentrically loaded reinforced concrete columns rather than the repair/strengthening method applied.

Table 6. Comparison of ductility ratios of specimens.

	S1	S2	S3	S4	S5	S6	R4	R5	R6	M1	M4
S1	1.00	0.99	0.87	1.06	0.89	0.97	0.88	0.97	1.04	0.90	0.97
S2		1.00	0.88	1.07	0.90	0.98	0.89	0.98	1.05	0.91	0.98
S3			1.00	1.21	1.01	1.10	1.00	1.11	1.19	1.03	1.11
S4				1.00	0.84	0.91	0.83	0.92	0.99	0.85	0.92
S5					1.00	1.09	0.99	1.09	1.18	1.01	1.09
S6						1.00	0.91	1.00	1.08	0.93	1.00
R4		Undefined Region					1.00	1.10	1.19	1.02	1.10
R5								1.00	1.08	0.93	1.00
R6									1.00	0.86	0.93
M.										1.00	1.08
M.											1.00

4. Conclusion

In this experimental study, the behavior of jacketed or reinforced rectangular columns (h/b=1.80 before jacketing and h/b=1.50 after jacketing) under monotonic axial loads was investigated. All members were jacketed in the unloaded condition. In addition, jacketing was applied after the deformations on the damaged member were reversed in repair and resurrection cases. As a result of the experiments, the following conclusions were reached by analyzing the parameters such as strength, stiffness, ductility and energy consumption obtained from the specimens.

• No difference was observed between the behavior of the new column obtained as a result of the repair/strengthening of rectangular section columns by jacketing and the repair/strengthening of square section columns by jacketing in previous studies and it was observed that both columns behaved the same.

• Although there was a 100% increase in cross-section and reinforcement, only the strength of the reinforced specimen reached 100% of the monolithic specimen strength. In the repaired members, 95% of the monolithic member strength was reached on average.

• The axial stiffness of all specimens was lower than the monolithic specimen stiffness. The reinforced specimen reached 90% of the monolithic specimen stiffness. In the repaired specimens, this ratio was around 60% to 70%.

• When the specimen ductility was compared with the monolithic column, the reinforced specimen ductility reached 80% of the monolithic column ductility. On the other hand, the repaired specimens could only reach 50~60% of the monolithic specimen ductility. In general, all specimens, including the monolithic, failed to show sufficient ductility with a behavior typical of reinforced concrete columns subjected to concentric loading.

• Although less than the monolithic specimen, the difference was very small and all specimens had sufficient energy dissipation capacity The findings and their implications should be discussed in the broadest context possible. Future research directions may also be highlighted.

• Even under laboratory conditions, where meticulous work is required, ensuring the sufficient success of the jacketing application necessitates rigorous supervision and should be entrusted to experienced personnel to achieve the desired quality and performance.

• The strength reduction observed at the tail end of the experimental load-strain curves for monolithic, strengthened, repaired, and retrofitted elements, at approximately 0.03 strain, is around 60%.

Author Contributions

The percentages of the author(s) contributions are presented below. All authors reviewed and approved the final version of the manuscript.

	Y.K.	H.C.
C	0	100
D	10	90
S	0	100
DCP	100	0
DAI	40	60
L	60	40
W	90	10
CR	50	50
SR	100	0
PM	50	50
FA	50	50

C=Concept, D= design, S= supervision, DCP= data collection and/or processing, DAI= data analysis and/or interpretation, L= literature search, W= writing, CR= critical review, SR= submission and revision, PM= project management, FA= funding acquisition.

Conflict of Interest

The authors declared that there is no conflict of interest.

References

Aksan B. 1988. Jacketed column behaviour under axial load alone. MSc Thesis, Civil Engineering, Middle East Technical University, Ankara, Türkiye, pp: 123.

Bournas DA, Thanasis CT. 2007. Textile-reinforced mortar versus fiber reinforced polymer confinement in reinforced concrete columns. ACI Struct J, 104(6): 740-748.

Can H. 1995a. Betonarme kolonların komşu iki yüzden manto ile onarımı ve güçlendirilmesi. TMMO Teknik Derg, 6(1): 51.

Can H. 1995b. İki, üç ve dört yüzünden mantolanmış kolonların eksenel yük altında davranışı. TMMO Teknik Dergi, 6(4): 38.

Cısdık M. 1998. Fretli manto ile onarılmış/güçlendirilmiş betonarme kolonların (spiralli ve dairesel etriyeli) eksenel yük altındaki davranışı. Yüksek Lisans Tezi, Gazi Üniversitesi, Ankara, Türkiye, ss: 147.

Demirel, Y, Can, H, Tankut, T. 1995, Onarılmış betonarme kolon davranışı ve dayanımı. TÜBİTAK, İnşaat Teknolojileri Araştırma Grubu, Proje No. INTAG 512, Ankara, Türkiye, ss: 178.

Francisco J, Basalo DCY, Matta F, Nanni A. 2012. Fiber reinforced cement-based composite system for concrete confinement. Construct Buil Mater, 32: 55–65.

Ghoroubi R, Mercimek Ö, Özdemir A, Anil Ö. 2020. Experimental investigation of damaged square short RC columns with low slenderness retrofitted by CFRP strips under axial load. Struct, 28: 170-180.

Kopraman Y. 2003. Onarılmış ve güçlendirilmiş betonarme kolonlarda manto alanının davranışa etkisi. Yüksek Lisans Tezi, Fen Bilimleri Enstitüsü, Gazi Üniversitesi, Ankara, Türkiye, 170.

Mercimek O, Anil O, Ghoroubi R, Sakin S, Yilmaz T. 2021. Experimental and numerical investigation of RC column strengthening with CFRP strips subjected to low-velocity

impact load. Struct Engin Mechan, 79(6): 749-765.

Mercimek Ö, Çelik A, Ghoroubi R, Özgür A. 2024. Retrofitting of squat RC column by using TRM strip under axial load. Struct, 60: 105909.

Mercimek Ö, Ghoroubi R, Anil Ö, Çakmak C, Özdemir A, Kopraman Y. 2023. Strength, ductility, and energy dissipation capacity of RC column strengthened with CFRP strip under axial load. Mechan Based Design Struct Machin, 51(2): 961-979.

Mercimek Ö, Ghoroubi R, Özdemir A, Anıl Ö, Baran M. 2022. Punching behaviour of two-way RC slabs having different multiple opening locations and sizes strengthened with TRM. Struct, 42: 531-549.

Mercimek Ö. 2023. Experimental and analytical investigation of the effects of anchor types and strip shapes on shear-deficient reinforced concrete beams strengthened with TRM versus FRP. Inter J Civil Engin, 21(12): 1927-1950.

Ozbakkaloglu T, Lim JC, Vincent T. 2013. FRP-confined concrete in circular sections: Review and assessment of stress–strain models. Engin Struct, 49: 1068-1088.

Suleiman R. 1991. Repair and strengthening of reinforced concrete columns. PhD Thesis, Civil Engineering, Middle East Technical University, Ankara, pp: 143.

Triantafillou T, Thanasis L. 2006. Concrete confinement with textile reinforced mortar jackets. ACI Struct J, 103(1): 28-37.

Türer A, Mercimek Ö, Anıl Ö, Erbaş Y. 2023. Experimental and numerical investigation of punching behavior of two-way RC slab with different opening locations and sizes strengthened with CFRP strip. Struct, 49: 918-942.

Ünsal F. 1998. Betonarme kolonların (kare ve fretli) eksenel yük altında fretli manto ile onarımı ve güçlendirilmesi. Yüksek Lisans Tezi, Gazi Üniversitesi, Ankara, Türkiye, pp: 92.

Yanarateş, M.S. 1990. Use of expandable metals as shear/confinement reinforcement in concrete members, phase 1, axially loaded columns. MSc Thesis, Civil Engineering, Middle East Technical University, Ankara, Türkiye, pp: 73.

Yumak Y. 1991. Effects of bar development methods on jacketed column behavior. MSc Thesis, Civil Engineering, Middle East Technical University, Ankara, Türkiye, pp: 48.

Black Sea Journal of Engineering and Science

COMPRESSIVE STRENGTH ANALYSIS OF ADDITIVELY MANUFACTURED ZIRCONIA HONEYCOMB SANDWICH CERAMIC PARTS WITH DIFFERENT CELLULAR STRUCTURES

Betül KAFKASLIOĞLU YILDIZ[1]*, Elif IŞIK[1], Ali Suat YILDIZ[2]

[1]*Sivas University of Science and Technology, Department of Metallurgical and Materials Engineering, 58000, Sivas, Türkiye*
[2]*Sivas University of Science and Technology, Department of Mechanical Engineering, 58000, Sivas, Türkiye*

Abstract: In this study, ZrO_2 honeycomb sandwich structures with different cellular geometry were manufactured by SLA 3D-printing technology to analyze the compressive strength behaviour. After the printing procedure, the samples were sintered at 1450 °C for 2h. Among the samples with different cellular geometry, ZrO_2 parts with circular cells were superior to that of square and triangular honeycomb structures and 1867±320 MPa compressive strength was obtained for this structure. The stress distributions in honeycomb structures were investigated using the COMSOL Multiphysics® for exposing the effect of cellular geometry on compressive strength. While more uniform stress distributions were seen on the inner wall of the circular honeycomb sample, the cellular structure of the square and triangle honeycomb samples mostly displayed compressive stress concentration on the joints of the honeycomb structure. Also, according to Rankine failure criterion, the parts with square cellular geometries were found to be more prone to failure. The highest specific compressive strength was obtained for the ZrO_2 parts with circular cellular geometry. These findings demonstrated that the ZrO_2 honeycomb sandwich structures with circular cellular geometry produced using SLA ceramic 3D-printing technology may be a suitable material to utilize in lightweight structural designs.

Keywords: ZrO_2, SLA, Honeycomb sandwich, Compressive strength

*Corresponding author: Sivas University of Science and Technology, Department of Metallurgical and Materials Engineering, 58000, Sivas, Türkiye
E mail: bkyildiz@sivas.edu.tr (B. KAFKASLIOĞLU YILDIZ)
Betül KAFKASLIOĞLU YILDIZ   https://orcid.org/0000-0002-6527-2918
Elif IŞIK   https://orcid.org/0000-0001-8289-9512
Ali Suat YILDIZ   https://orcid.org/0000-0001-6914-5222

1. Introduction

Advanced ceramics are in demand for a variety of engineering applications because of their superior mechanical and physical qualities (Schwentenwein et al., 2014; Chen et al., 2019). Zirconia (ZrO_2) is one of the most attractive high tech ceramics because of its mechanical characteristics and broad variety of uses such as energy, biomedical, aerospace, mechatronics etc. (Chang et al., 2022; Wang et al., 2023). ZrO_2 ceramics have also high hardness, outstanding wear resistance and thermal stability properties (Manicone et al., 2007; Wang et al., 2023). Nevertheless, complexly shaped ZrO_2 parts are challenging to fabricate due to brittle character, high hardness and wear resistance of the material. Additive manufacturing (AM) offers the potential to manufacture intricately formed ZrO_2 parts. AM, often known as 3D printing technology is utilized to build intricate three-dimensional objects layer by layer using metals, polymers, and ceramics (Buchanan and Gardner, 2019; Zhou et al., 2020; Shen et al., 2021). Since it is very difficult to fabricate ceramic objects with complicated shapes using traditional production methods, ceramic 3D printing technology is one of the most promising and demanding approaches to this problem. Several

techniques, including stereolithography (SLA), selective laser melting/sintering (SLM, SLS), and digital light processing (DLP), are available for 3D printing. Among these technologies, the use of SLA in 3D printing has garnered significant interest for producing ceramics with intricate and complicated architectures because of the highest level of accuracy that ensures industrial quality results from the SLA production process (Lu et al., 2021; Shen et al., 2021; Yu et al., 2023; Wang et al., 2023).

Sandwich structures are becoming increasingly common in lightweight design for high-performance applications, particularly in the automotive, and aerospace industries. Because of its periodic structure and customizable anisotropic qualities, honeycomb offers greater control over features as core of sandwich structures (Haldar et al., 2016; Wang et al., 2019). Honeycomb structures can achieve improved material efficiency if they can be built for particular loading circumstances due to their periodicity and anisotropy. In a wide range of industries, including architectural, automotive, railway, aircraft, satellites, electronic communications, nanofabrication, and medical implants, honeycomb materials have been well-developed and widely employed (Zhang et al., 2015; Qi et al., 2021; Shirvani et al., 2023).

The use of honeycomb ceramic sandwich structures (CSSs), which are often made out of solid ceramic face-sheets and a lightweight ceramic honeycomb core, has gained popularity in recent years. Due to high stiffness and strength to weight ratios and low thermal expansion coefficient, honeycomb CSSs are also being studied as a potential promotional material for example for the next generation of spacecraft thermal protection systems (Srikanth et al., 2017; Hu and Wang, 2021). The utilisation of SLA has emerged as the primary method for producing intricately formed porous ceramics (Chen et al., 2023). This technology has enabled the creation of several porous complex shapes, including micro-lattices, honeycombs, micro-scale trusses (Shen et al., 2021; Xu et al., 2023). In this respect, the investigation of the compressive strength of ZrO_2 sandwich honeycomb structures prepared via SLA printing technology for structural applications, has been the research subject of this study. Because ceramic sophisticated materials and structures are brittle by nature and strength is a key consideration. Compression strength properties were analyzed for lattice ceramic structures prepared by 3D printing in various studies (Fabris et al., 2019; Mamatha et al., 2020; Mei et al., 2021). However, experimental evaluation of compressive strength of ceramic honeycomb structures is very rare (Mamatha et al., 2020). It is important to examine the mechanical behavior and performance of ceramic honeycombs, especially sandwich honeycomb structures, under compressive load and their suitability for structural applications after they are produced with a 3D printer for a functional ceramic material as ZrO_2. Based on this, this paper proposed to prepare various ZrO_2 honeycomb sandwiches with different cellular structures (square, triangle, circle) by SLA technology, and these structures were obtained by pressureless sintering.

2. Materials and Methods

3 mol% Y_2O_3 stabilized ZrO_2 (YSZ) cylinders were printed by a ceramic 3D-printer (C100 Easy Lab, 3DCERAM, France) for mechanical testing using proprietary ceramic-filled photosensitive resin formulation (3DMIX ZR3-E02) on the SLA 3D printer. The size of the cylinders was determined considering ASTM C-1424 standard for compressive strength test in 6.35 mm diameter and 12.1 mm height. The CAD models of the parts prepared for printing are presented in Figure 1. The designed honeycomb cellular structures comprise lower and upper face-sheets (height of each: 0.3 mm) with a honeycomb core (height: 11.5 mm). Details of the hole diameters and cell dimensions of all samples can be seen in Figure 2.a in addition to Figure 1. Both the dimensions of cells and holes and thickness of lower and upper face-sheets were determined considering Kafkaslıoğlu Yıldız et al. (2024) study. The scale factor values given by the supplier were considered to ensure dimensional accuracy after sintering. The printing process operates a 405 nm UV laser to cure the slurry layer-by-layer. The laser power was adjusted to 120 mW, and the layer thickness was set to 50 μm during the printing process at room temperature. First, a metal blade is used to evenly spread the ZrO_2 slurry on the magnetic paper on the working platform. Then, the laser head scans linearly to cure the ceramic slurry in accordance with the cross-sectional shape of the layer that is now in place. The working platform descends to construct another layer after the first layer has formed. Until the entire ZrO_2 component is created, this process is repeated. Fifteen green samples were prepared for each cellular structure. The samples on printing table after the printing process are seen in Figure 2.b.

Following the printing process, the remaining uncured slurry was removed from the green bodies by thoroughly cleaning them with Ceracleaner and compressed air. Debinding is required to remove the organic materials from the green bodies following the 3D printing process. Debinding was carried out in multiple stages up to 615 °C in nitrogen atmosphere using the supplier's thermal cycle. The brown bodies were sintered by heating to 1150 °C at 3.0 °C/min, then proceeding to 1450 °C at 2.0 °C/min by holding 2 h in air in a box furnace (Protherm MOS-B 170/4, Alserteknik, Türkiye).
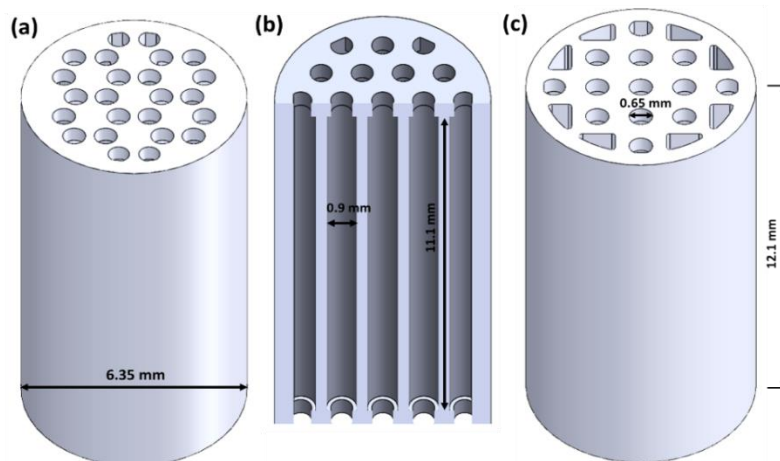
Figure 1. CAD models of the parts before printing process for the samples with a) triangular, b) circular, c) square cellular geometry.
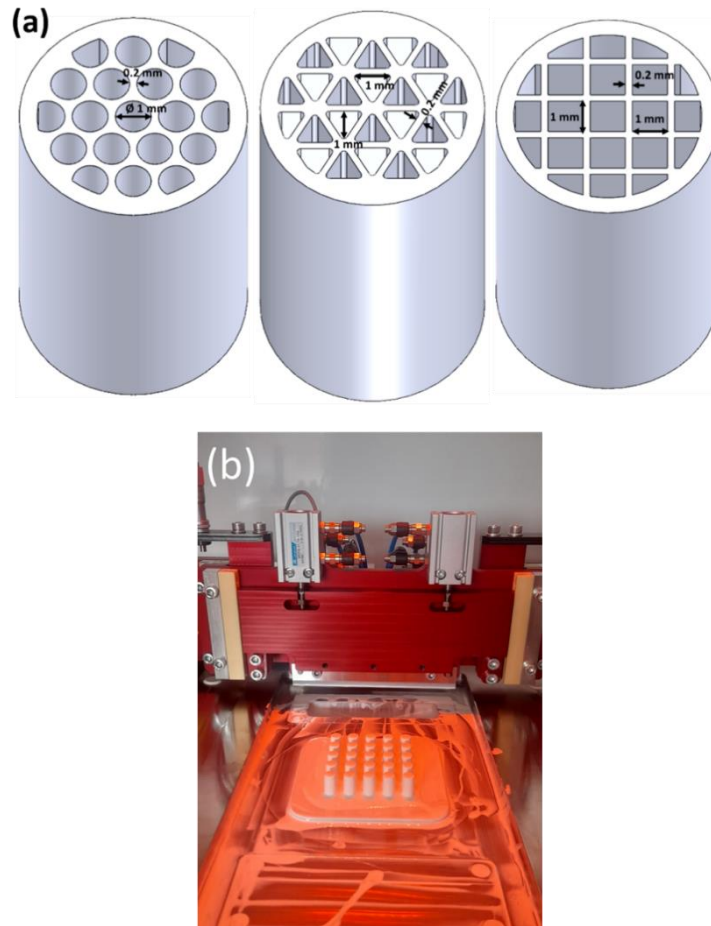
Figure 2. a) Detailed cell dimensions of the parts, b) the samples on printing table after 3D-printing.

From mass and sizes, the bulk density of the sintered ceramic bars was calculated using a volumetric method. The volume values were calculated based on the sample dimensions measured with a caliper. The bulk density to theoretical density ratio of YSZ (6.10 g/cm³) was used to calculate the relative density values. The compressive strength tests of all the ceramic structures were performed by an electronic universal testing machine (Shimadzu AGS-X) equipped with a 50 kN load cell at a loading speed of 0.2 mm/min and the load-displacement curves were recorded until the samples failed at room temperature. To reduce friction, oil (oleic acid) was applied to the surfaces of the samples in contact with the device. Fifteen samples were tested for every cellular structure. The compressive strength of the samples was calculated using the formula given in equation 1 (Mei et al., 2021):

$$\sigma_c = \frac{P}{S} \qquad (1)$$

where σ_c, P, and S are the compressive strength, maximum load, and cross-sectional area of a honeycomb, respectively. In addition, the stress distributions created by compression loads were examined using the software COMSOL Multiphysics® in order to explain the strength difference caused by the cellular geometry of the honeycomb structures.

3. Results and Discussion

After the sintering process, the relative densities were 57.0±0.3, 65.6±0.5, and 64.2±0.5 for the honeycomb sandwich samples with square, triangular, and circular cellular geometries, respectively. This difference between the relative density values was related to the difference in the hollow spaces of the samples with different cellular geometry. This was also evident from their average mass. The average mass of the samples were 1.32, 1.52, 1.50 g for square, triangular and circular cellular geometry, respectively. The cross-sections of the samples were also observed on an optical microscope after sintering as given in Figure 3. The samples could be obtained in almost the designed dimensions (both internal and external dimensions) after printing and sintering. Since the shrinkage ratios of the samples were different in X (1.27), Y (1.26), and Z (1.31) axis, there was a difference of 0.1 mm in the designed cell diameters for every geometry and a difference of 0.1 mm in the distance between two cells for the sample with a circular cell geometry.

Figure 4 shows the result of the compressive strength tests for the honeycomb sandwich samples with different cellular structure. As can be seen, the highest average strength was obtained for the honeycomb sandwich structure with circular cellular geometry as 1867±320 MPa. It is well known fact that the advanced ceramics are

inherently brittle materials, therefore mechanical properties like compressive strength can vary considerably. Beside material inhomogeneity such as porosity and the presence of microcracks, the ceramic 3D printing process itself can introduce inconsistencies and small defects can cause considerable variations in compressive strength (Huang et al., 2023). While calculating the compressive strength values, solid cross-sectional areas were taken into account. Examinations and calculations were carried out on the core structure regions (11.5 mm) as the upper and lower face-sheets were very thin (0.3 mm). The solid cross-sectional areas were calculated using an optical microscope image of the samples by Image J. The solid area values were 18.28, 21.64, and 20.17 mm^2 for the samples with square, triangular and circular cellular geometry, respectively. The highest compressive strength was not obtained for the triangular cellular geometry, which had the highest solid cross-sectional area. The difference between the compressive strength values of the samples was mostly related to stress concentrations depending on the cellular geometry.

To better interpret the effect of cellular geometry on compressive strength, the stress distributions in honeycomb structures were investigated using solid mechanics module with a linear elastic material of COMSOL Multiphysics®. The Young's modulus, density, and Poisson ratio of the specimen were set to 188 GPa, 6.10 g/cm^3, and 0.3, respectively. Then the model was meshed using a physics-controlled mesh with a Free Tetrahedral with fine size element. The number of degrees of freedom is changing from 742266 to 2049480. The first principal stress distribution in the 1 mm above the bottom closing surface is shown in the Figure 5. When the analysis results were compared, cellular structure of square and triangle honeycomb sample mostly exhibited compressive stress concentration on the junctions of the honeycomb structure, while more uniform stress distributions were observed on the inner wall of the circular honeycomb sample. This finding was also in agreement with the compressive strength values given in Figure 4.
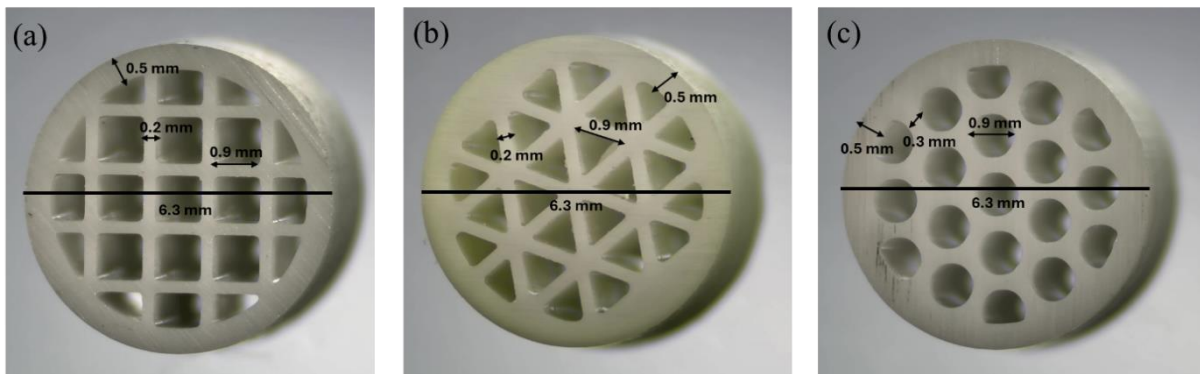
Figure 3. Optical microscope images of the cross-sections of honeycomb samples with a) square, b) triangular, and c) circular cellular geometry.
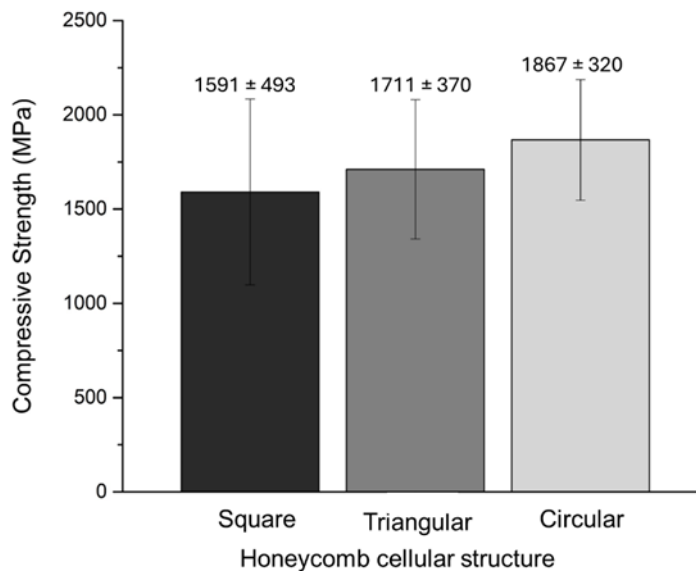
Figure 4. Compressive strength of the honeycomb sandwich ZrO$_2$ samples with different cellular structure.
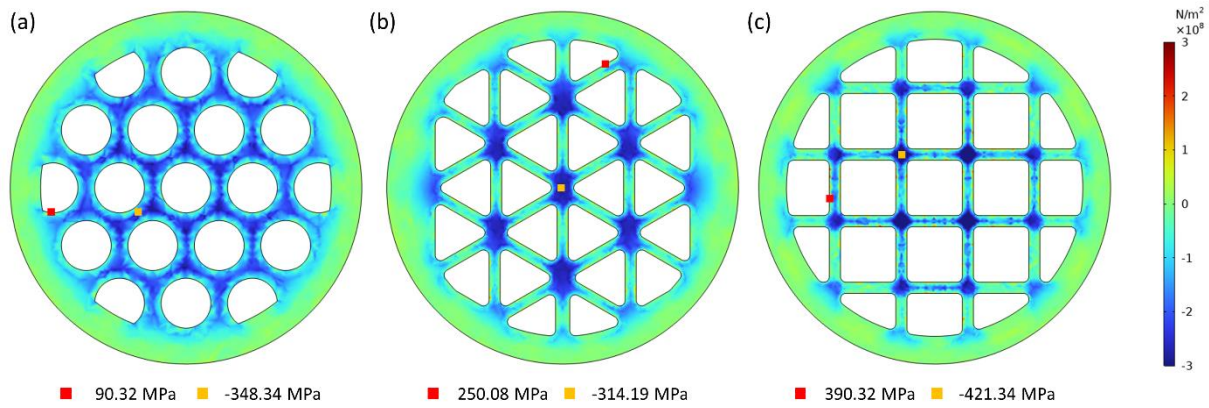
Figure 5. First principal stress state of the samples with a) circular, b) triangular, and c) square cellular structure.
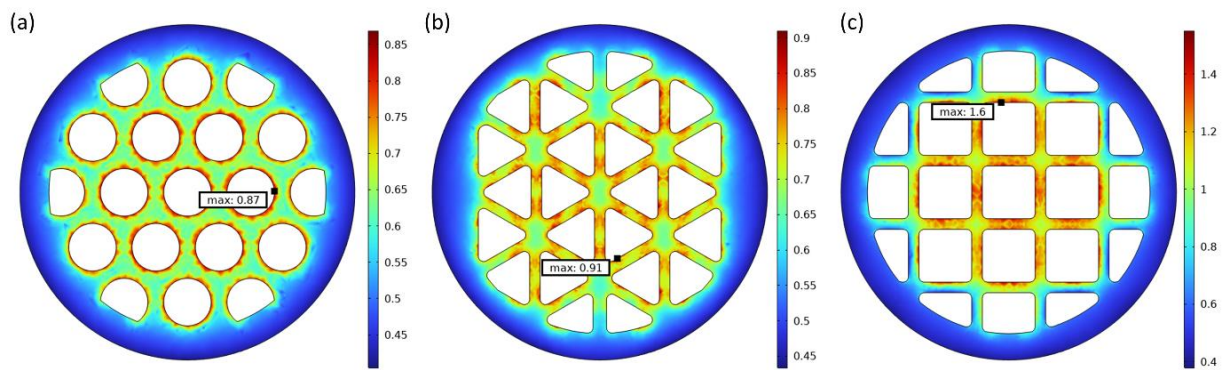
Figure 6. Failure index of honeycomb structures with different cellular geometries.

The compressive strength of the material was defined as 2500 MPa and the geometries were checked for the risk of failure according to the Rankine criterion (maximum normal stress criterion). Here, values greater than 1 on the cross-sectional area can cause crack propagation. Under a force of 29 kN, the Rankine failure index values were calculated for volume average as 0.559, 0.601, and 0.701 for circular, triangular and square cellular geometries, respectively. It can be inferred that the samples with triangle cellular geometry exhibited a 7.5% lower strength than their circular geometry counterparts. This finding was also in agreement with the compressive strength values showed in Figure 5 as 8.35%. Also, the distribution of the Rankine failure criterion across the cross-section were checked for the risk of failure. When the distribution of the Rankine failure criterion across the cross-section of 1 mm below the top surface, where the compressive force was applied, as presented in Figure 6, the parts with square cellular geometries were found to be more prone to failure. The lower strength of the honeycomb structures can be attributed to the stress concentration inner wall for the triangle and square core geometries.

After expressing the strength difference of the samples depending on the cellular geometry, it is necessary to examine the specific strength relationship, which is important for honeycomb sandwich structures (Xue et al., 2022). The material's resistance to compressive loads in relation to its density is measured by its specific compressive strength. A high specific compressive strength guarantees that honeycomb sandwich ceramics, which are frequently employed in structural applications where weight is a crucial consideration, can support significant loads while maintaining their lightweight nature. Maintaining the structural integrity of parts and structures depends on this attribute. The lightweight nature of ceramic materials for honeycomb sandwich construction is one of its main benefits. Lightweight structures can be built with high specific compressive strength without sacrificing strength or durability. This is especially helpful in the automotive, marine, and aerospace industries as lighter vehicles can result in better load capacity, fuel economy, and performance. The highest specific compressive strength was obtained for the ZrO_2 parts with circular cellular geometry while the other structures were nearly same specific strength level as shown in Figure 7. Ultimately, this study showed that ZrO_2 honeycomb sandwich structure with circular cellular geometry produced using SLA technology is an appropriate choice to use in such materials for lightweight structural designs.
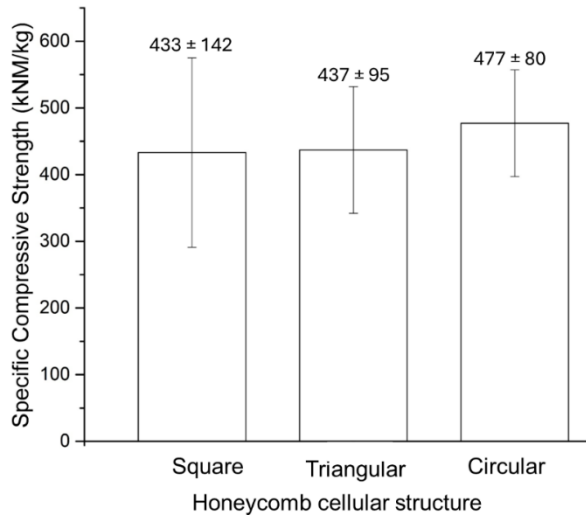
Figure 7. Specific compressive strength values of honeycomb sandwich samples with different cellular geometry.

4. Conclusion

SLA 3D-printing technology was used to prepare ZrO_2 honeycomb sandwich structures with different cellular geometry. The compressive strength of the parts was investigated experimentally and effect of cellular geometry on strength was analyzed by finite element analysis. The highest compressive strength values were attained for the samples with circular cellular geometry as 1867±320 MPa due to stress concentration difference with the other cellular geometries; square and triangular. Also, it was found that square cellular geometries were found to be more prone to failure compared to other structures according to the Rankine failure criterion. When the specific compressive strength examination of the samples was carried out, it was seen that the ZrO_2 honeycomb sandwich samples, which also have circular geometry, was the most suitable design that can be recommended for lightweight structural applications with the highest specific strength.

Author Contributions

The percentage of the author(s) contributions is presented below. All authors reviewed and approved the final version of the manuscript.

	B.K.Y.	E.I.	A.S.Y.
C	50	10	40
D	50	10	40
S	100		
DCP	40	40	20
DAI	40	40	20
L	50	10	40
W	60	10	30
CR	60	10	30
SR	100		
PM	100		
FA	100		

C=Concept, D= design, S= supervision, DCP= data collection and/or processing, DAI= data analysis and/or interpretation, L= literature search, W= writing, CR= critical review, SR= submission and revision, PM= project management, FA= funding acquisition.

Conflict of Interest

The authors declared that there is no conflict of interest.

Ethical Consideration

Ethics committee approval was not required for this study because of there was no study on animals or humans.

References

Buchanan C, Gardner L. 2019. Metal 3D printing in construction: A review of methods, research, applications, opportunities and challenges. Eng Struct, 180: 332-348.

Chang J, Zou B, Wang X, Yu Y, Chen Q, Zhang G. 2022. Preparation, characterization and coloring mechanism of 3D printed colorful ZrO2 ceramics parts. Mater Today Commun, 33: 104935.

Chen J, Su R, Zhai X, Wang Y, Gao X, Zhang X, Zhang Y, Zhang Y, Liu S, He R. 2023. Improving the accuracy of stereolithography 3D printed Al2O3 microcomponents by adding photoabsorber: Fundamentals and experiments. JMR&T, 27: 757-766.

Chen Z, Li Z, Li J, Liu C, Lao C, Fu Y, Liu C, Li Y, Wang P, He Y. 2019. 3D printing of ceramics: a review. J Eur Ceram Soc, 39: 661-687.

Fabris D, Mesquita-Guimarães J, Pinto P, Souza JCM, Fredel MC, Silvab FS, Henriques B. 2019. Mechanical properties of zirconia periodic open cellular structures, Ceram Int, 45: 15799-15806.

Haldar AK, Zhou J, Guan Z. 2016. Energy absorbing characteristics of the composite contoured-core sandwich

panels. Mater Today Commun, (8): 156-164.

Hu JS, Wang BL. 2021. Crack growth behavior and thermal shock resistance of ceramic sandwich structures with an auxetic honeycomb core. Compos Struct, 260: 113256.

Huang Z, Liu LY, Yuan J, Guo H, Wang H, Ye P, Du Z, Zhao Y, Zhang H, Gan CL. 2023. Stereolithography 3D printing of Si3N4 cellular ceramics with ultrahigh strength by using highly viscous paste. Ceram Int, 49: 6984-6995.

Kafkaslıoğlu Yıldız B, Yıldız AS, Kul M, Tür YK, Işık E, Duran C, Yılmaz H. 2024. Mechanical properties of 3D-printed Al2O3 honeycomb sandwich structures prepared using the SLA method with different core geometries. Ceram Int, 50: 2901-2908.

Lu J, Dong P, Zhao Y, Zhao Y, Zeng Y. 2021. 3D printing of TPMS structural ZnO ceramics with good mechanical properties. Ceram Int, 47: 12897-12905.

Mamatha S, Biswas P, Das D, Johnson R. 2020. 3D printing of cordierite honeycomb structures and evaluation of compressive strength under quasi-static condition. Int J Appl Ceram Technol, 17: 211-216.

Manicone PF, Iommetti PR, Raffaelli L. 2007. An overview of zirconia ceramics: basic properties and clinical applications. J Dent, 35(11): 819-826.

Mei H, Tan Y, Huang W, Chang P, Fan Y, Cheng L. 2021. Structure design influencing the mechanical performance of 3D printing porous ceramics. Ceram Int, 47: 8389-8397.

Qi C, Jiang F, Yang S. 2021. Advanced honeycomb designs for improving mechanical properties:A review, Compos B Eng, 227: 109393.

Schwentenwein M, Schneider P, Homa J. 2014. Lithography-based ceramic manufacturing: a novel technique for additive manufacturing of high-performance ceramics. Adv Sci Technol, 88: 60-64.

Shen M, Qin W, Xing B, Zhao W, Gao S, Sun Y, Jiao T, Zhao Z. 2021. Mechanical properties of 3D printed ceramic cellular materials with triply periodic minimal surface architectures. J Eur Ceram Soc, 41: 1481-1489.

Shirvani SMN, Gholami M, Afrasiab H, Talookolaei RAJ. 2023. Optimal design of a composite sandwich panel with a hexagonal honeycomb core for aerospace applications. Iranian J Sci Technol Trans Mech Eng, 47: 557-568.

Srikanth O, Khivsara SD, Aswathi R, Madhusoodana CD, Das RN, Dutta VSP. 2017. Numerical and experimental evaluation of ceramic honeycombs for thermal energy storage. Trans Ind Ceram Soc, 76(2): 102-107.

Wang L, Yao L, Tang W, Dou R. 2023. Effect of Fe2O3 doping on color and mechanical properties of dental 3Y-TZP ceramics fabricated by stereolithography-based additive manufacturing. Ceram Int, 49: 12105-12115.

Wang Z, Lia Z, Xiong W. 2019. Numerical study on three-point bending behavior of honeycomb sandwich with ceramic tile, Compos B Eng, 167: 63-70.

Xu H, Li S, Liu R, Bao C, Mu M, Wang K. 2023. Fabrication of alumina ceramics with high flexural strength using stereolithography. IJAMT, 128: 2983-2994.

Xue D, He L, Tan S, Li Y, Xue P, Yang X. 2022. Study on compression characteristics of honeycomb sandwich structure with multistage carbon fiber reinforced composites. Polym Compos, 43: 6252-6264.

Yu X, Wang Z, Wang Y, Yu Z, Zhao Y, Zhao J. 2023. Optimization, formation, and evolution of the photoinduced curing gradients and in-situ lamellar gaps in additive manufacturing of ZrO2 ceramics: From curing to sintering behaviors. J Eur Ceram Soc, 43: 6279-6295.

Zhang Q, Yang X, Li P, Huang G, Feng S, Shen C, Han B, Zhang X, Jin F, Xu F, Lu TJ. 2015. Bioinspired engineering of honeycomb structure – Using nature to inspire human innovation. Prog Mater Sci, 74: 332-400.

Zhou LY, Fu J, He Y. 2020. A review of 3D printing technologies for soft polymer materials. Adv Funct Mater, 30(28): 2000187.

Black Sea Journal of Engineering and Science

OPTIMIZATION OF WOOD-BASED BIRCH PLYWOOD CO₂ LASER ENGRAVING PROCESS PARAMETERS WITH TAGUCHI METHOD

Mehmet GÜNEŞ[1]*, Çağatay ERSİN[2]

[1]Çankırı Karatekin University, Department of Design, 18100, Çankırı, Türkiye
[2]Çankırı Karatekin University, Department of Electronics and Automation, 18100, Çankırı, Türkiye

Abstract: In this study, the optimization of the parameters used in the engraving process of wooden birch plywood material with a CO₂ laser machine was investigated using the Taguchi method. An industrial laser machine with a 150W glass tube was used during the experimental examination process. There are basic factors affecting the engraving process of wooden surfaces such as laser power (P), engraving speed (S) and laser head parts (F). The engraving depth (D) and engraving width formed on the surface during the engraving process are the main factors that determine the aesthetics of the product. Taguchi L25 orthogonal array was used in the experiments to determine and optimize the highly important parameters. The optimum combination of parameters in the laser engraving process was then evaluated. The research results showed that the effect of P and S factors played a leading role, and the F parameter had a small effect on the depth of wood scraping. Optimization results found that F:5, S:100 and P:30 gave the best engraving depth optimization, while F:6, S:300 and P:10 gave the lowest engraving depth optimization result.

Keywords: Taguchi method, parameter optimisation, CO₂ laser, wood carving, birch plywood

*Corresponding author: Çankırı Karatekin University, Department of Design, 18100, Çankırı, Türkiye
E mail: mehmetgunes@karatekin.edu.tr (M. GÜNEŞ)
Mehmet GÜNEŞ 🆔 https://orcid.org/0000-0002-1222-7590
Çağatay ERSİN 🆔 https://orcid.org/0000-0001-5018-9313

1. Introduction

Wood is one of the most abundant materials in nature and has superior properties compared to other building materials (Oğurlu, 2024). Wood is a renewable material with low density, low thermal conductivity, high mechanical strength, easy workability and good aesthetic appearance. (Kurt and Can, 2021). Medium density fiberboard and plywood are generally used in wood laser engraving. Birch plywood used in laser engraving is made by bonding birch veneers in single layers with opposite grain directions. Plywood obtained from birch wood has high quality, high resistance properties and sufficient hardness. However, high-quality birch veneers are used on visible surfaces in furniture, interior decoration panels, handicrafts and various special places (Çakıroğlu et al., 2018).

Laser cutting, which is frequently used in wood processing, creates high-cutting quality and smooth cutting surfaces unlike other thermal cutting methods. In these aspects, laser cutting is superior to other methods (Uzungörür, 2015). Laser light for marking, engraving, and surface cleaning in wood processing (Uzungörür, 2015, Kúdela et al., 2020) primary wood processing in automated systems (McMillin et al., 1984) and MDF (medium density fibreboard) cutting (Eltawahni et al., 2011) for the production of decorative and ornamental items. Laser machines are widely used in the furniture

industry, decoration and ornaments production. However, to obtain a quality result with the laser cutting method, it is not enough to select the laser cutting machine suitable for the material to be cut. (Yaka et al., 2011). In addition to machine selection, cutting parameters such as cutting speed and gas pressure should also be determined appropriately. It is important to determine the cutting parameters correctly to complete the cutting process with minimum thermal damage (Uzungörür, 2015). Since laser machines do not contain cutting elements, they do not produce chips and dust, so they are more advantageous than other cutting methods. (Aniszewska et al., 2020). In CO₂-powered laser devices, high electrical voltage is applied to the carbon dioxide gas to cut. In addition, nitrogen and helium gas can be added to carbon dioxide gas to further increase efficiency. With the ease of obtaining the laser beam in this way, increases in application areas have been seen. The biggest reason for production with laser cutting is to minimise production error and to provide automation (Tunç, 2015).

In the cutting of plywood material with a CO₂ laser; it has been stated that focal length (Tayal et al., 1994), cutting speed (Gabdrakhmanov et al., 2019), laser power, laser gas and air pressure have an effect on the cutting (Çavdar and Tanrısever, 2013). Many studies have been carried out on the effects of beam power, polarisation, optical directions of the lens, and position of the focal point, gas

spray support system, workpiece thickness, material density and moisture content in laser wood processing (Barnekov et al., 1986). Also, the effect of laser power cutting speed and the number of rings per year on the notch width at the top and bottom grades of the cutting notch (Kubovský et al., 2020) laser engraving properties of some wood and wood-based composite materials (Teivonen, 2016) current research has also been carried out.

When cutting wood with a CO_2 laser, optimization of parameters related mainly to laser performance and cutting speed is important. These parameters have significant effects on production efficiency and cutting quality (Ružiak et al., 2022). The factors affecting the laser cutting of wood can be divided into three groups; these are the characteristics of the radiation beam, laser power (P), cutting speed (V), focal point position, annual ring number, moisture content and density of the wood (Sinn et al., 2020).

This study aimed to investigate the best combination of laser engraving factors for birch plywood surfaces using ANOVA analysis of variance with L25 orthogonal Taguchi sequence design. In wood laser engraving, the width and depth of the engraving determine the light and dark tones of the resulting image. As the laser radiation power increases, the carving width and depth also increase. For example, when carving an image into wood, a shallow depth will cause the image to appear blurred and out of focus if the surface area increases. The findings of the study show that the effect parameters can be optimised to guarantee high-quality wood carving with the desired carving width and depth as well as the capacity to adapt to complex designs.

2. Materials and Methods
2.1. Taguchi Method
The Taguchi method is a powerful statistical approach often used for product and process optimisation that plays an important role in quality engineering. This method was developed by Japanese engineer and statistician Genichi Taguchi (Roy, 2010). The Taguchi method is an experimental analysis technique used to improve the quality and reduce the costs of product or process designs. The basic philosophy of the Taguchi method is to minimise variation in product or process performance due to the influence of uncontrollable factors (noise factors) (Phadke, 1995). This approach uses a strategy called "parameter design" to determine optimal levels of controllable elements. This makes the product or process performance more resilient to disruptive factors. One of the most important features of this method is the use of orthogonal arrays. By using orthogonal arrays, maximum information can be obtained with minimum experimentation (Taguchi et al., 2004). This saves a lot of time and costs. In addition, the Taguchi method optimises both average power and power variation simultaneously through signal-to-noise ratio (S/N) analysis. The application of the Taguchi

method generally involves the following steps: Defining the problem, determining the control factors and control levels, selecting the appropriate orthogonal array, performing the experiment, analysing the data and determining the optimum conditions, and finally performing verification experiments. (Mehat and Kamaruddin, 2012, Güneş et al., 2024, Gökçe and Ersin, 2020, Nguyen et al., 2022). This method has wide applications in technical and industrial applications. In particular, effective results can be obtained in areas such as production process optimisation, product design, material selection and quality control (Shuster, 2007). Optimising the parameters of the CO_2 laser engraving process using the Taguchi method provides the opportunity to systematically analyse and optimise this complex process. This approach makes it possible to identify the important parameters in the laser engraving process and the optimum combination of these parameters. During the studies, the measured responses are converted into appropriate S/N ratios using three general classes "Highest is better in equation 1", " Lowest is better in equation 2" and "nominal is best in equation 3". The following equations are used to calculate S/N ratios for various quality attributes as follows.

$$\text{Highest best} \frac{S}{N} = -10\log(\frac{1}{n}\sum_{i=1}^{n}\frac{1}{y_i^2}) \quad (1)$$

$$\text{Lowest best} \frac{S}{N} = -10\log(\frac{1}{n}\sum_{i=1}^{n} y_i^2) \quad (2)$$

$$\text{Nominal best} \frac{S}{N} = 10\log(\frac{\bar{y}}{S_y^2}) \quad (3)$$

2.2. Experimental Study
In the study, five 100x80x3 mm birch plywood test pieces were prepared for obtaining measurement data by laser cutting machine. The physical properties of the birch plywood used in the engraving process such as equilibrium moisture content, full dry density and air dry density are given in Table 1.

Table 1. Physical properties of birch plywood

Physical Properties		
Equilibrium Humidity (%)	Full dry density (gr/cm³)	Air dry density (gr/cm³)
12.48	0.460	0.487

Lasersoft software of Triumph Company was used for the laser machine in the processing of the parts. The laser machine cutting head distance on these parts was adjusted to 3, 4, 5, 6 and 7 mm. The laser machine cutting speed was applied at five different speeds of 100, 150, 200, 250 and 300 mm/sec and the power of the 150-watt tube was applied at 10%, 15%, 20%, 25% and 30%. With these processing parameters, the scraping height occurring in the material was measured and how much change in which parameter was determined. The milling parameters used are shown in Table 2 for power, speed and focal distance. Using the L25 orthogonal array, a Taguchi experimental design was applied to the data obtained from the tests to determine the effect of each

independent input parameter on the dependent parameters. The independent variables are laser power 10 W - 30 W, engraving speed 100 mm/sec - 300 mm/sec, and focal distance 3 - 7 mm.

Table 2. Scraping parameters

Parameters		Power (%W)	Speed (mm/s)	Focus distance (mm)
		P	S	F
Symbol	1	10	100	3
	2	15	150	4
	3	20	200	5
	4	25	250	6
	5	30	300	7

The wood engraving process was carried out with a 3-axis industrial CO_2 laser machine with 150W power. The laser cutting machine where the engraving process was carried out is shown in Figure 1.

Figure 1. CO_2 laser machine used in the engraving process.

3. Results and Discussion

Plywood samples made of 3 mm birch (*Betula pendula*) wood were engraved with a CO_2 laser cutting device at different parameters. A total of 25 experiments were carried out to determine the scraping depth (D) values using Taguchi L25 orthogonal array. With the determined parameters, the milling process was carried out on the wood samples as shown in Figure 2.
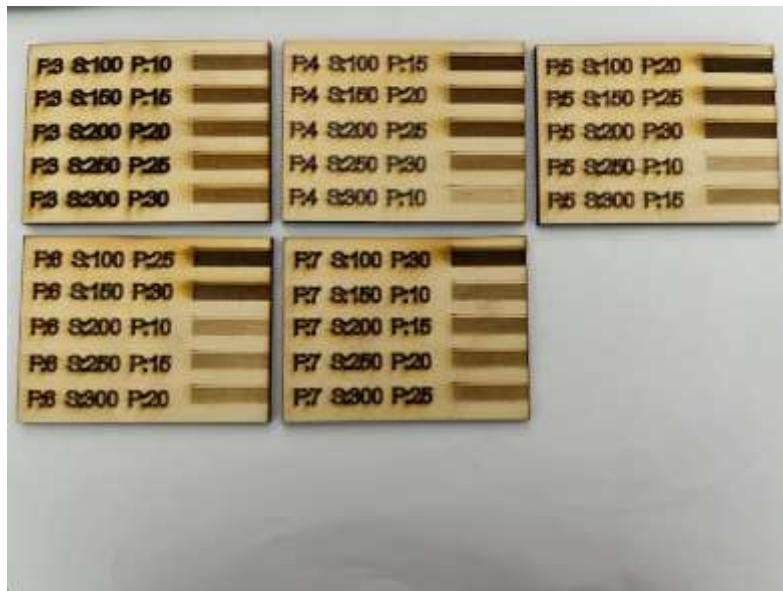
Figure 2. Processed birch plywood material.

Taguchi method was applied to determine the effect of all input parameters on the output parameters with the selected L25 orthogonal array. Preliminary engraving tests were performed to determine the range of input parameter values. For the 150 W laser, the power parameters were set between 10%-50%, 100-300 mm/s for the engraving speed and 3-7 mm for the laser head focal length.

A total of 25 engraving operations were performed to determine the engraving depth (D) values using Taguchi L25 orthogonal test setup. With the determined power, speed and focal height parameters, scraping was performed on plywood samples as shown in Figure 2 and analysed by connecting to the computer in the digital microscope shown in Figure 3.

Thanks to the 220X digital zoom feature, the microscope showed the scraping depth (D) and width in Figure 4. The images taken from the microscope were transferred to the computer and recorded from the appropriate parts of the samples by indicating the process dimensions on the image.

Figure 3. Digital microscope.

Figure 4. Wood plywood milling depth (D) and determined milling width.

Figure 5 shows the engraving process on wood birch plywood samples using a digital microscope. In order to measure the test results consistently on the samples, the engraving process was carried out with a width of 5 mm with a precision of 0.001. The experimental samples created with the L25 taguchi sequence and the measurement data obtained from these samples are shown in Table 3. Taguchi orthogonal L25 array ANOVA analysis of variance was performed to evaluate the basic parameters affecting the depth of scraping process on the wood plywood surface. The basic parameters and the most influential parameters were analysed using Taguchi-based SN ratio.

According to the results of ANOVA analysis of variance in Table 4, it is understood that firstly the laser power is the most effective parameter in the engraving depth process and then the engraving speed is the effective parameter.

Since P>0.05, the focal length of the laser cutting head was found to have the least effect on the engraving depth.
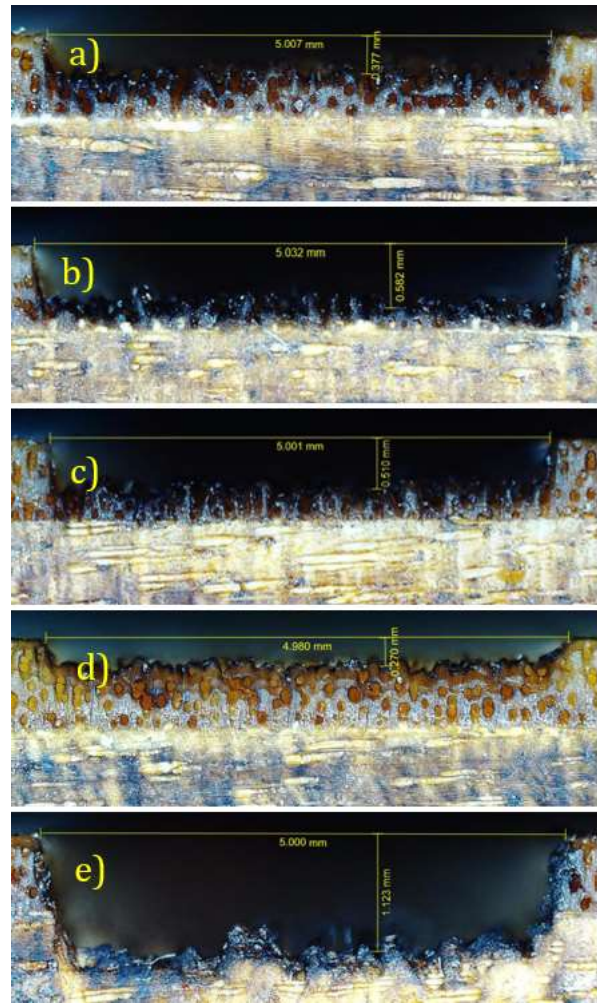
Figure 5. a) F:3-S:200-P:20, b) F:4-S:100-P:15, c) F:5-S:150-P:25, d) F:6-S:300-P:20, e) F:7-S:100-P:30.

Table 3. Measurement results obtained from the experimental study

Experiment No	Independent variable parameters			Dependent Variable
	P (%W)	S (mm/s)	F (mm)	Depth (mm) H
1	1	1	1	0.223
2	1	2	2	0.463
3	1	3	3	0.377
4	1	4	4	0.389
5	1	5	5	0.341
6	2	1	2	0.582
7	2	2	3	0.517
8	2	3	4	0.510
9	2	4	5	0.413
10	2	5	1	0.083
11	3	1	3	0.761
12	3	2	4	0.649
13	3	3	5	0.664
14	3	4	1	0.092
15	3	5	2	0.199
16	4	1	4	0.778
17	4	2	5	0.741
18	4	3	1	0.107
19	4	4	2	0.211
20	4	5	3	0.270
21	5	1	5	1.123
22	5	2	1	0.139
23	5	3	2	0.280
24	5	4	3	0.333
25	5	5	4	0.353

Table 4. ANOVA variance analysis results

Source	DF	Seq SS	Contribution	Adj SS	Adj MS	F-Value	P-Value
Focus	4	0.03580	2.25%	0.03	0.008	0.99	0.450
Speed	4	0.64557	40.56%	0.64	0.161	17.85	0.000
Power	4	0.80171	50.37%	0.801	0.200	22.17	0.000
Error	12	0.10848	6.82%	0.108	0.009		
Total	24	1.59156	100%				

3.1. Effect of process parameters on milling depth

When the analysis of variance in Table 5 and the Mean of S/N ratios in Figure 6 are analysed, it is understood that the laser head focal distance is not an effective parameter in the engraving depth. It was found that at low power and high speed, the engraving depth was low, while at high power and low processing speed, the engraving depth was high.

Table 5. Response table for signal-to-noise ratios

Level	Focus	Speed	Power
1	-9.148	-4.256	-18.386
2	-9.116	-7.183	-9.997
3	-8.886	-9.670	-7.500
4	-9.817	-11.934	-5.806
5	-9.157	-13.081	-4.436
Delta	0.930	8.825	13.950
Rank	3	2	1

Figure 6. Effect of laser cutting parameters on the scraping depth (SN ratios).

Surface Plot of Depth vs Power; Speed
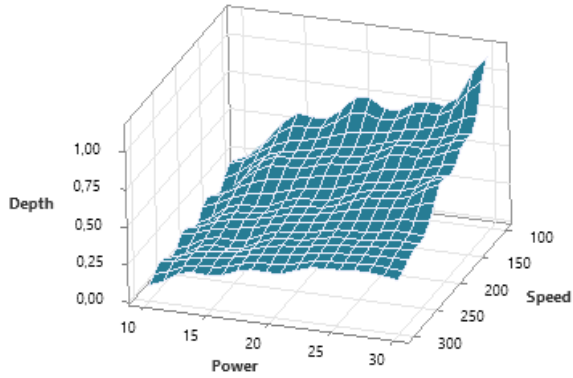
Figure 7. Graph of speed and power affecting milling depth (D).

According to the surface plot graph in Figure 7, when the laser power is increased and the feed rate is decreased, the depth of engraving increases. According to the graph, it is understood that the choice of high power and low speed has an increasing effect on the scraping depth. Low power and high speed should be preferred when the depth is desired to be at the minimum level.

Surface Plot of Depth vs Speed; Focus
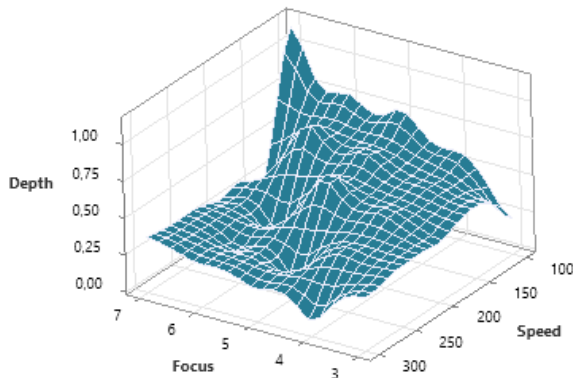
Figure 8. Focus and velocity graph affecting the scraping depth (D).

When the surface plot graph in Figure 8 is analysed, it can be seen that when the focal height is partially increased and the feed rate is decreased, the milling depth increases. According to the graph, it is understood that the average focal height and low-speed preference affect the milling depth in an increasing direction. It is understood that low focal length and high speed should be preferred when the depth is desired to be at the minimum level.

When the surface plot graph in Figure 9 is analysed, it shows similar changes to Figure 8. When the laser power and focal height are increased, the engraving depth increases. According to the graph, it is understood that high power and focal height have an increasing effect on the engraving depth. Low power should be preferred when the depth is desired to be at the minimum level.

Surface Plot of Depth vs Power; Focus
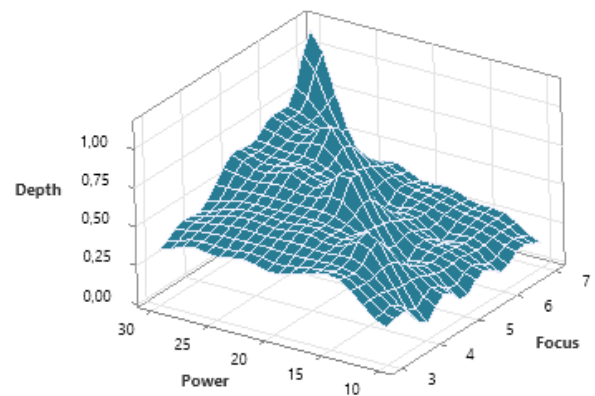
Figure 9. Graph of speed and power affecting milling depth (D).

According to the L25 Taguchi octogonal array highest is best S/N optimisation results, and the highest optimisation scraping result according to F:5, S:100, P:30 data is given in Figure 10 (a). The example of the lowest optimisation according to F:6, S:300, and P:10 data is also shown in Figure 10 (b).
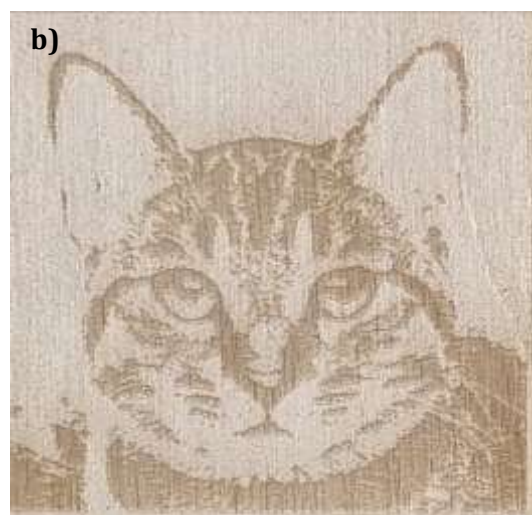
Figure 10. Highest optimised milling result.

4. Conclision

There are many parameters affecting the engraving quality in wood laser engraving processes. The most effective of these parameters are the focal length of the laser head to the material, laser cutting speed and laser engraving power. In this study, the effect of which of the factors affecting the engraving quality of the glass tube CO_2 laser cutting device with 150 W power on the engraving quality was investigated and carried out experimentally. In order to reduce the number of experiments, the optimisation process was performed using the L25 Taguchi orthogonal array. ANOVA analysis of variance was performed on the S/N data and it was determined that the most effective parameters were laser engraving speed and laser power. It was found that the focal length of the laser head to the material was not an effective factor compared to other parameters. Among the parameters used in the engraving process on wood birch plywood, it has been determined by experimental studies that low engraving speed and high engraving power give the best result and high speed and low power give the lowest engraving result. In addition, it was determined that more aesthetic images were created by increasing the scraping depth.

Author Contributions

The percentage of the author(s) contributions is presented below. All authors reviewed and approved the final version of the manuscript.

	M.G.	Ç.E.
D	70	30
S	50	50
DCP	70	30
DAI	60	40
L	40	60
W	50	50
SR	60	40

D= design, S= supervision, DCP= data collection and/or processing, DAI= data analysis and/or interpretation, L= literature search, W= writing, SR= submission and revision.

Conflict of Interest

The authors declared that there is no conflict of interest.

Ethical Approval Statement

Since no studies were conducted on animals or humans in this study, ethics committee approval was not received.

References

Aniszewska M, Maciak A, Zychowicz W, Zowczak W, Mühlke T, Christoph B, Lamrini S, Sujecki S. 2020. Infrared laser application to wood cutting. Mat, 13(22): 5222.

Barnekov V, McMillin C, Huber H. 1986. Factors influencing laser cutting of wood. For Prod J, 1: 36.

Çakıroğlu EO, Aydın İ, Demir A. 2018. Comparison of mechanical properties of contractplanks produced from birch and local beech tombs imported from coastal countries to the Black Sea. J Black Sea Res Inst, 4(6): 353-359.

Çavdar K, Tanrısever T. 2013. Laser cutting of different materials. J Uludag Univ Fac Eng, 18(2): 79-99.

Eltawahni H, Olabi AG, Benyounis K. 2011. Investigating the CO_2 laser cutting parameters of MDF wood composite material. Opt Laser Technol, 43(3): 648-659.

Gabdrakhmanov A, Bobrishev A, Shafigullin L. 2019. Application of the laser cutting of wood-containing materials in construction. In IOP Conference Series: Mat Sci Eng. IOP Publishing. 481(1): 12-45.

Gökçe H. Ersin Ç. 2020. Investigation of the loudness and vibrations occurred during the drilling of custom 450 stainless steel in terms of cutting parameters. Elect Lett Sci Eng, 16(2): 171-183.

Güneş M, Ersin Ç, Altunok M. 2024. Effect of climate and wood type on elastic modulus of heat-treated wood and its optimisation by the Taguchi method. BioRes, 19(2): 3138-3148.

Kubovský I, Krišťák Ľ, Suja J, Gajtanska M, Igaz R, Ružiak I, Réh R. 2020. Optimization of parameters for the cutting of wood-based materials by a CO_2 laser. Appl Sci, 10(22), 8113.

Kúdela J, Kubovský I, Andrejko M. 2020. Surface properties of beech wood after CO_2 laser engraving. Coat, 10(1): 76-77.

Kurt R, Can A. 2021. Optimisation of the effect of accelerated weathering conditions on wood surfaces via the Taguchi method. BioRes, 16(1): 1642.

McMillin CW, Conners RW, Huber HA. 1984. ALPS-a potential new automated lumber processing system. For Prod J, 34(1): 13-20.

Mehat NM. Kamaruddin S. 2012. Quality control and design optimisation of plastic product using Taguchi method: a comprehensive review. Int J Plast Tech, 16: 194-209.

Nguyen V, Altarazi F, Tran T. 2022. Optimisation of process parameters for laser cutting process of stainless steel 304: a comparative analysis and estimation with Taguchi method and response surface methodology. Math Probl Eng, 1: 1-14.

Oğurlu İ. 2024. Doğal-Ekolojik üç yapi malzemesi taş-kerpiç–ahşap için sürdürebilirlik analiz modeli. Avr Bilim Tekno Der, 53: 150-167.

Phadke MS. 1995. Quality engineering using robust design. USA, Prentice Hall PTR, USA, 1st ed., pp: 1-250.

Roy R.K. 2010. A primer on the Taguchi method. Society of manufacturing engineers, USA, 2nd ed., pp: 1-10.

Ružiak I, Igaz R, Kubovský I, Gajtanska M, Jankech A. 2022. Prediction of the effect of CO_2 laser cutting conditions on spruce wood cut characteristics using an artificial neural network. Appl Sci, 12(22): 11355.

Shuster JJ. 2007. Design and analysis of experiments. Top Bios, 404: 235-259

Sinn G, Chuchała D, Orlowski KA, Taube P. 2020. Cutting model parameters from frame sawing of natural and impregnated Scots pine (Pinus sylvestris L.). Eur J Wood Wood Prod, 78(6): 777-784.

Taguchi G, Chowdhury S, Wu Y. 2004. Taguchi's quality engineering handbook. Wiley, New Jersey, USA. 1st ed., pp: 100-125.

Tayal M, Barnekov V, Mukherjee K. 1994. Focal point location in laser machining of thick hard wood. J Mater Sci Lett, 13(9): 44-646.

Teivonen A. 2016. Laser surgery system. Lahti University of Applied Sciences Degree Programme in Materials Engineering Spring, Lahti, Finland, pp: 23-35.

Tunç M. 2015. Investigation of the effects of cutting parameters

on surface roughness in CO_2 laser cutting machines, MSc Thesis, Karabuk University Institute of Science and Technology, Karabuk, 15-17.

Uzungörür M, 2015. Inconel 718 sac malzemelerin lazer ile kesilmesinde işlem parametrelerinin etkilerinin araştırılması. Yüksek Lisans Tezi, Eskişehir Osmangazi Üniversitesi, Fen Bilimleri Enstitüsü, Eskişehir, Türkiye, ss: 61-63

Yaka H, Akkuş H, Uğur L. 2016. Optimisation of the effect of cutting parameters on surface roughness in turning of AISI 1040 steel by Taguchi method. Celal Bayar Univ J Sci, 12(2): 283-288.

ANALYSIS OF CYBER ATTACKS USING HONEYPOT

Hakan Can ALTUNAY¹*

¹*Ondokuz Mayıs University, Çarsamba Chamber of Commerce Vocational School, Department of Computer Technologies, 55200, Samsun, Türkiye*

Abstract: In the cybersecurity world, the concept of a honeypot is generally referred to as trap systems that have real system behaviors, intentionally leave a security gap, and aim to collect information about cybercriminals who want to access them. It is a computer system that sets itself as a target to attract cyberattacks like bait. It is used to imitate a target such as cyberattackers and to learn about attack attempts, ways of working, or to distract them from other targets. In this study, a VoIP-based honeypot was used to determine the profiles of cyberattacks and attackers. A network environment was created using a low-interaction honeypot to analyze the behavior of cyberattackers and identify the services frequently preferred by these individuals. The honeypot in the network environment was monitored for a period of 90 days. 105,308 events were collected regarding protocols such as Telnet, SIP, SSH, SMB, and HTTP. There was no complex malware attack on the observed system. The service that was most attacked was determined to be Telnet. It was determined that many attacks occurred from the same IP address, indicating that automatic scanning tools were used. According to the results obtained, the proposed method performed a detailed analysis of the services from which cyberattacks came and the behaviors of the people who carried out these attacks. In addition, the highest level of understanding of user interaction was achieved thanks to the VoIP-based honeypot.

Keywords: Honeypot, Cyberattack, SIP, SMB, SSH

1. Introduction

Sending voice, video or messages over IP (Internet Protocol) is called Voice Over Internet Protocol (VoIP). Since it works over the internet or computer networks, it is usually cheaper, sometimes free (Wang et al., 2005). For this reason, it is one of the most preferred telecommunication communication methods today. Gateway devices are used to convert analog lines to VoIP (Franco et al., 2021). VoIP converts voice information into digital signals that travel over the internet. If you are calling a regular phone number using broadband service, the signal is converted to a regular phone signal before reaching the destination (Rashid et al., 2024). All of this is done through a broadband internet connection instead of a regular or analog phone line (Spahn et al., 2023). The hardware required to make this possible is a broadband high-speed internet connection (Zhu et al., 2024). This problem can be solved with a computer, adapter or a phone manufactured for this purpose. While some VoIP services support the use of your regular phones connected to a VoIP adapter, others only work on a computer or a special VoIP phone (Srinivasa et al., 2022). When examining the types of fraud on VoIP, hackers and fraudsters first try to take over the VoIP system and then earn income by calling high-priced places. Therefore, in this study, it is suggested to establish a honeypot system to test the security in the systems and detect the attacks

or hijacking methods (Djap et al., 2021).

Attacks on a network can be detected using honeypots. In traps using honeypots, critical data is given the impression that it is stored in a computer on the network. In fact, this computer forms the basis of the honeypot trap. (Bartwal et al., 2022). This structure, designed using honeypots, collects information about the methods of cyberattackers and is used to detect attacks and monitor activity (Bringer et al., 2012). They mimic the behavior of real systems and are isolated from the host system (Conti et al., 2022).
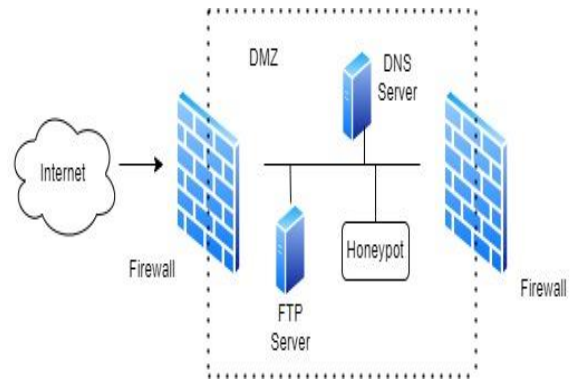
Figure 1. Location of honeypot in the network .

Honeypots are divided into three groups. They are called low-interaction, high-interaction, and pure honeypots

(Dai et al., 2021). Low-interaction honeypots focus on imitating services such as remote authentication services and file transfer services (Akiyama et al., 2018). Their main advantage is that they consume relatively fewer resources than high-interaction honeypots and are easier to install. Their disadvantage is that the service they emulate is limited to detecting security vulnerabilities only (Abdulqadder et al., 2023). High-interaction honeypots, unlike low-interaction, emulate multiple services at the same time (Javadpour et al., 2024). The advantage of high-interaction honeypots is that since there are many services for attack, it can be more convincing that the honeypot is a real system (Lanka et al., 2024). However, implementing and maintaining such honeypots is more difficult. Pure honeypots are systems where the activities of attackers are monitored and recorded (Ackerman, 2020). No special software is required in these systems and the task is performed using normal systems (Altunay et al., 2024). However, expert knowledge is needed to prevent these systems from causing security vulnerabilities in the network (Adiou et al., 2022).

In this study, experiments were conducted to determine attacks and attackers using data obtained from the honeypot environment. Statistical data about attacks and attackers, such as time, region, service type, attack content, attack type, frequency, and attack origin region and attacker fingerprint were analyzed, and how cyber attackers implement certain types of attacks was explained. In addition, when attack packets from different countries were examined in the study, it was seen that they generally perform the same types of attacks. The malware loaded into the honey trap was analyzed to understand how the attacks were carried out. The results obtained from the malware will help to prevent attacks or minimize their impact by classifying the packets coming over the network.

The general structure of the study is as follows. In Section II, a literature review on VoIP honeypot solutions was conducted, and the related studies were explained in detail. In Section III, information about the established honeypot environment was provided. In Section IV, the results obtained in the experimental study were shared. In the last section, the obtained values were discussed and future planned studies were mentioned.

2. Related works

Initially, the idea of honeypots was explained by Lance Spitzner, who evolved honeypots into honeypot networks (Spitzner, 2003). In 1998, a honeypot software called Cybercop Sting was prepared. It is also known as Decoy Server. Decoy Server could simulate services such as Telnet and SMTP (Østvang and Houmb, 2019). Although it had a very limited usage and logging ability, it was very useful in analyzing attacker attacks. There are studies in the literature that suggest using honeypot systems to capture malicious traffic in VoIP systems. Carmo et al. (2011), built a SIP (Session Initation

Protocol) specific honeypot system called Artemisa and created a collection of attack traces. However, in networks using Session Initiation Protocol (SIP), different methods are applied to detect attacks other than SPIT (Spam over Internet Telephony). Attacks on this protocol, which initiates and manages interactive user sessions including voice, video, instant messaging and other multimedia sessions, are increasing day by day. In order to analyze the attacker's behavior and capture the original attack traffic, it is important that the attackers do not realize that they have accessed the honeypot. Provos and Holz describe how attackers can detect that they are inside a honeypot, especially in virtualized environments (Provos and Holz, 2007). However, since virtualization is currently used in production systems, it is not a definitive proof of a honeypot. A simple statistical analysis of VoIP attacks on virtualized low-interaction honeypot environments is given by Valli (2010).

Nassar et al. (2007) proposed an IDS to detect cyberattacks on the SIP protocol. The focus of this intrusion detection system is on a honeypot. In the study, attacks were prevented by using a honeypot with a low level of interaction. Script-based operation in service implementation and relational interpretation of situations in managing security events are the limitations of the honeypot.

In order to be able to examine and interpret the work performed by the attacker in detail, it is necessary to have information about details such as protocol, service, status and port information. It is important to have a more general view of the attack behavior. Another study proposed a honey trap-based model that deploys predefined software images and stores attack information in a database (Safarik et al., 2013). Dionaea is used as a database in the proposed model. In the evaluation part of the model, the obtained data is transmitted to a central server and detailed analysis is performed. The most significant disadvantage of the model suggested in the study is its high resource usage. In addition, the installation and maintenance of the hardware on which it will operate at remote points also requires time and cost. Gruber et al., (2011) analyzed real-world attacks obtained from honeypot solutions and revealed the current security status of VoIP systems.

Hoffstadt et al., (2012) recorded 47.5 million SIP messages in the customized SIP honeypot system they established and examined the collected data with statistical packet analysis.

3. Proposed Model

In order to investigate the behavioral analysis of the attackers, data must be collected reliably. In case the server where the honeypot is installed is compromised by the attacker in any way, the data must be transferred to another reliable server. The attacker must not be able to access the previous monitoring logs in any way. In this way, the privacy and personal information of the

attackers are also protected. In this study, some data was used to sample the attacks. In particular, the password that the attackers try most often, or the determination of the most used password in the data set can be given as an example. During the experimental study, the entire data set was used, and some information was filtered. The data collected from the servers where the honeypot was running was stored in a database on another server. MySQL database was used in the study. The data in the database was analyzed in detail using SQL queries. Code fragments written in Python were also used during the analysis process. In order to determine whether the incoming requests are from automatic scanning systems or real user behavior, the time of the incoming requests, access time, frequency, repetition, IP addresses, and the attempted passwords and commands were evaluated as parameters.

There are different approaches to design honeypot systems. Each of these approaches focuses on different attack scenarios. However, hybrid models are required to obtain the attacker profile, penetration models and attack behavior. In hybrid models, the material and moral damages that the attacker can cause can be revealed in advance by in-depth analysis of the attacker's behavior. The honeypot environment shown in Figure 1 was designed for both general security analysis and to collect and analyze attacks against VoIP systems. This heterogeneous infrastructure connected to the Internet allows to catching different attackers and get a broad perspective on the VoIP security status. In the simulation environment, all packets from the other side are recorded for statistical analysis, and malware and commands used for the attack are extracted and stored through deep analysis of the packets. In the test environment we prepared, a simulated service environment that can respond to all message types and status flows specified in the RFC standard document was created. Known attack scenarios such as identity theft, call dropping, and interception were modeled and constructed in the test environment. In order to perform fraudulent activities, an open SIP trunk service has been integrated to the internet and easy-to-guess passwords have been assigned to sections such as the web interface, SIP trunk management console, and PBX telnet/SSH services. A unique identification method has been applied to correlate data across different honeypot software and locations. A summary value has been obtained by combining IP, time, protocol, and message type information within each request. The basic components of our honeypot environment and the applications used to collect data are as follows.

Firewall is used to minimize the impact of cyberattacks by detecting abnormal situations on the network. Attacks such as demanding high fees for any service or fee fraud against users can also be detected by the firewall. (Agarwal, 2022). HoneyDrive, a virtual machine image that contains pre-installed and configured honeypot services for many services, is used. All important honeypot related software is included in HoneyDrive. In addition, many scripts and utilities such as Kippo-Graph, HoneydViz, DionaeaFR, an ELK are available in HoneyDrive to analyze, enhance and visualize data. In addition, there are almost 90 malware analysis, forensics and network monitoring tools. Asterisk IP PBX, an open source Internet Telephone PBX infrastructure based on Linux, is used. Finally, Flowroute SIP Trunk Service Management, a paid software, is used. Calls are made through this service via Asterisk.

4. Results

In order to identify security threats in the global VoIP system compromise phases and to obtain information about active attackers, findings obtained from different components of the honeypot solution and their correlations are presented. Therefore, normalization, classification and analysis processes were performed to compare the collected data. In order to provide a better understanding of the collected data, a statistic is presented in Table 1. Although it is not appropriate to compare the numbers directly, it gives an idea about the results of the following analyses. The honeypot system provides a wider target IP address range. In addition, all SIP requests are collected with the honeypot. The results show that the source of the attacks is similar.

Table 1. Number and types of data collected.

Types of Data	Number of data collected
Number of Urls	194
Number of IPs	29375
Number of collections	106781

No complex malware attack was observed in the honeypot system we observed. However, as seen in Figure 2, attacks were carried out via different services, especially Telnet port 23. Attacks via SIP port are in second place. It is also seen that more than one attack was carried out using the same IP address. This situation shows us that automatic scanning and attack tools are being used. Attackers use self-concealment methods such as Tor and VPN. In this way, they gain access from different countries. In password attacks, the combination of admin/123456 and admin/admin was tried. Another striking point is that when the commands used in password attempts and SSH sessions are examined, it is seen that IoT devices are also used for this purpose.

The network using the honeypot was attacked 4 times via the SSH service and operating system commands were run. However, although there was a lot of VoIP message traffic, no full conversation was made and no fraud was committed. After the attackers took over the service, they created new users, viewed the content of files containing passwords, and set up programs to include them in the botnet network, while a serious increase in computing applications aimed at generating bitcoins has recently been observed.
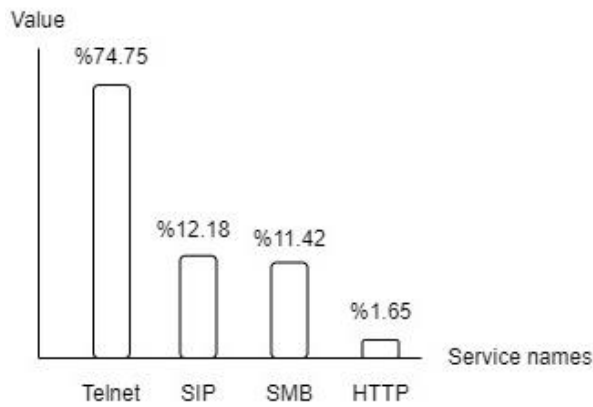
Figure 2. Attack rates on services.

In the attack attempts made for the services, only 1.67 percent of successful access was achieved and in only 48 percent of these accesses, the attacker ended the session without performing any action. It was evaluated that the biggest factor in this situation was the fact that the attempts were made with automatic tools and the attacker gave up because it was a low-interaction honeypot. In password attempts, the attackers tried known information such as team, city, date of birth, with different variations. There were no methods such as not repeating the same password or waiting for a while between attempts that could lock the account. When the time spent in the attack cases was examined, it was observed that the most time was spent trying the password and then searching for valuable information on the machine.

Our honeypot system collected 765 malware samples. The most common type is the Conficker malware. The results show that the attackers perform a comprehensive IP scan and use a wide IP range when performing SIP-based VoIP attacks. When we examine the sources of the detected IP addresses, as seen in Figure 3, the attackers mostly come from Russia, India, China, Spain, the USA, and Germany.
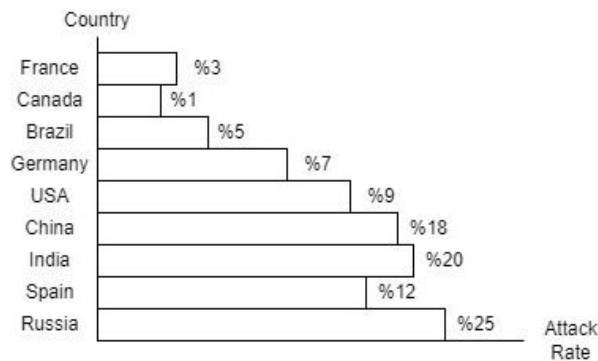
Figure 3. Distribution of attacks by country.

In order to understand the attack behaviors on the VoIP side and to recognize the tools they use, the SIP User Agent devices used were examined. The User-Agent information, which is a parameter within the SIP protocol, can be expressed as introducing itself with a text. Attackers come to the system by introducing themselves in this way. Attackers introduce themselves in this way and come to the system. They have carried out many attacks using the User Agent in a four-week period. The "Asterisk PBX" and "friendly-scanner" agents were preferred as User Agents. This situation shows that the attackers are trying to hide their VoIP attacks. Because instead of the commonly used attack tools, they have developed new tools and carried out SIP-based VoIP attacks. In order to carry out the fraudulent activity, the attacker first scans SIP-based VoIP devices with SIP OPTION messages using the User Agent. Then, they perform a Registration Hijacking attack on the devices they find with SIP REGISTER and INVITE messages. The striking point here is that messages directed to the same target are seen from the same IP address using different User-Agents.

5. Discussion and Conclusion

This article shares the results of a flexible and low-interaction honeypot system that was established to examine attacks on VoIP systems and the behavior of attackers. Honeypots are useful solutions for capturing information, generating alarms, attracting attackers, and trapping them. Thanks to honeypot environments, it is possible to obtain statistical analyses such as what type of attacks, how often they occur and from which country. For example, the tools used by attackers, the identification of new types of attacks, the collection of malware samples, help us discover future defense methods against unknown attacks. In addition, honeypots are preferred as an effective method to monitor the behavior of hackers and increase the effectiveness of developed security tools.

The results obtained from the honeypot system show that hackers use different methods and try to infiltrate in this way. Our future research aims to detect new malware families and zero-day attacks. It is planned to establish a high-level honeypot environment and create live traffic with critical services and transfer copied data from real interactions to the environment. In this way, all the behaviors and reactions of the attackers will be recorded, and more detailed analyses will be performed. As the number of detected attacks increases, precise analyses that can further improve VoIP security protection mechanisms will be possible.

Author Contributions

The percentages of the author contributions are presented below. The author reviewed and approved the final version of the manuscript.

	H.C.A.
C	100
D	100
S	100
DCP	100
DAI	100
L	100
W	100
CR	100
SR	100
PM	100
FA	100

C=Concept, D= design, S= supervision, DCP= data collection and/or processing, DAI= data analysis and/or interpretation, L= literature search, W= writing, CR= critical review, SR= submission and revision, PM= project management, FA= funding acquisition.

Conflict of Interest

The author declared that there is no conflict of interest.

Ethical Consideration

Ethics committee approval was not required for this study because of there was no study on animals or humans.

References

Abdulqadder IH, Zou D, Aziz IT. 2023. The dag blockchain: a secure edge assisted honeypot for attack detection and multi-controller based load balancing in sdn 5g. Future Gener Comput Syst, 141: 339-354.

Ackerman P. 2020. Modern cybersecurity practices: exploring and implementing agile cybersecurity frameworks and strategies for your organization. BPB Publications, Delhi, India, pp: 243.

Adiou ML, Benzaïd C, Taleb T. 2022. Topotrust: a blockchain-based trustless and secure topology discovery in sdns. International Wireless Communications and Mobile Computing (IWCMC), May 30- June 03, Dubrovnik, Croatia, pp: 1107–1112.

Agarwal Y. 2022. Apache Log4j Logging Framework and Its Vulnerability. MSc Thesis, Metropolia University of Applied Sciences, Department of Information Technology, Metropolia, Finland, pp: 67.

Akiyama M, Yagi T, Hariu T, Kadobayashi Y. 2018. Honeycirculator: distributing credential honeytoken for introspection of web-based attack cycle. Int J Info Secur, 17(2): 135-151.

Altunay HC, Albayrak Z, Çakmak M. 2024. Autoencoder-based intrusion detection in critical infrastructures. Curr Trends Comput, 2(1): 1-12.

Bartwal U, Mukhopadhyay S, Negi R, Shukla S. 2022. Security orchestration, automation, and response engine for deployment of behavioural honeypots. IEEE Conference on

Dependable and Secure Computing (DSC), June 22-24, Edinburgh, UK, pp: 1-8.

Bringer ML, Chelmecki CA, Fujinoki H. 2012. A survey: Recent advances and future trends in honeypot research. Int J Comput Network Info Secur, 4(10): 63.

Carmo R, Nassar M, Festor O. 2011. Artemisa: an open-source honeypot back-end to support security in VoIP domains. 12th IFIP/IEEE International Symposium on Integrated Network Management, May 23-27, Dublin, Ireland, pp: 361-368.

Conti M, Trolese F, Turrin F. 2022. Icspot: A high-interaction honeypot for industrial control systems. International Symposium on Networks, Computers and Communications (ISNCC), July 19-22, Shenzhen, China, pp: 1-4.

Dai B, Zhang Z, Wang L, Liu Y. 2021. APT Attack heuristic induction honeypot platform based on snort and open flow. International Conference on Smart Computing and Communication, December 29-31, New York, US, pp: 340-351.

Djap R, Lim C, Silaen KE, Yusuf A. 2021. Xb-pot: Revealing honeypot-based attacker's behaviors. 9th International Conference on Information and Communication Technology (ICoICT), August 3-5, Virtual, pp: 550-555.

Franco J, Aris A, Canberk B, Uluagac A S. 2021. A survey of honeypots and honeynets for internet of things, industrial internet of things, and cyber-physical systems. IEEE Commun Surv Tutor, 23(4): 2351-2383.

Gruber M, Fankhauser F, Taber S, Schanes C, Grechenig T. 2011. Security status of VoIP based on the observation of real-world attacks on a honeynet, IEEE International Conference on Privacy, Security, Risk and Trust, October 9-11, Boston, US, pp: 1041-1047.

Hoffstadt D, Marold AE, Rathgeb E. 2012. Analysis of SIP-based threats using a VoIP honeynet system. IEEE 11th International Conference on Trust, Security and Privacy in Computing and Communications, June 25-27, Liverpool, UK, pp: 541-548.

Javadpour A, Ja'fari F, Taleb T, Shojafar M, Benzaïd C. 2024. A comprehensive survey on cyber deception techniques to improve honeypot performance. Comput Secur, 140: 103792.

Lanka P, Gupta K, Varol C. 2024. Intelligent threat detection—AI-driven analysis of honeypot data to counter cyber threats. Electronics, 13(13): 2465.

Nassar M, Niccolini, S, State R, Ewald T. 2007. Holistic VoIP intrusion detection and prevention system. The 1st International Conference on Principles, Systems and Applications of IP Telecommunications, July 19-20, New York, US, pp: 1-9.

Østvang ME, Houmb SH. 2019. Honeypot technology in a business perspective. Ring, M., Wunderlich, S., Grüdl, D., Landes, D., & Hotho, A. (2017). A toolset for intrusion and insider threat detection. Data Analyt Decis Sup Cybersecur, 2019: 3-31.

Provos N, Holz T. 2007. Virtual honeypots: From botnet tracking to intrusion detection, Addison-Wesley Professional, Boston, US, pp: 440.

Rashid SZU, Haq A, Hasan ST, Furhad MH, Ahmed M, Ullah AB. 2024. Faking smart industry: exploring cyber-threat landscape deploying cloud-based honeypot. Wireless Networks, 30(5): 4527-4541.

Safarik J, Voznak M, Rezac F, Partila P, Tomala K. 2013. Automatic analysis of attack data from distributed honeypot network. Mobile Multimedia/Image Process Secur Appl, 2013: 8755.

Spahn N, Hanke N, Holz T, Kruegel C, Vigna G. 2023. Container Orchestration Honeypot: Observing Attacks in the Wild. 26th

International Symposium on Research in Attacks, Intrusions and Defenses, October 16-18, Hong Kong, pp: 381-396.

Spitzner L. 2003. The honeynet project: Trapping the hackers. Secur Privacy Magaz, 1(2): 15-23.

Srinivasa S, Pedersen MJ, Vasilomanolakis E. 2022. Interaction matters: a comprehensive analysis and a dataset of hybrid IoT/OT honeypots. 38th Annual Computer Security Applications Conference, December 5-9, New York, US, pp: 742-755.

Valli C. 2010. An analysis of malfeasant activity directed at a VoIP honeypot. The 8th Australian Digital Forensics Conference, November 30, Perth, Australia, pp: 168-174.

Wang W, Liew SC, Li VO. 2005. Solutions to performance problems in VoIP over a 802.11 wireless LAN. IEEE Transact Vehicular Technol, 54(1): 366-384.

Zhu H, Liu M, Chen B, Che X, Cheng P, Deng R. 2024. HoneyJudge: A PLC Honeypot Identification Framework Based on Device Memory Testing. IEEE Transact Info Forens Secur, 19: 6028-6043.

PERFORMANCE COMPARISON OF SUPERVISED MACHINE LEARNING METHODS IN CLASSIFYING CELESTIAL OBJECTS

Maide Feyza ER[1]*, Turgay Tugay BİLGİN[2]

[1]Bandirma Onyedi Eylul University, Faculty of Engineering and Natural Sciences, Department of Software Engineering, 10200, Balıkesir, Türkiye
[2]Bursa Technical University, Faculty of Engineering and Natural Sciences, Department of Computer Engineering, 16350, Bursa, Türkiye

Abstract: In recent times, astronomy has entered a new era with rapidly growing data sources and advanced observation techniques. The construction of powerful telescopes has enabled the collection of spectral data from millions of celestial objects. However, the increasing number and variety of data have made it challenging to categorize these celestial objects. This study employs machine learning methods to address the fundamental problem of classifying stars, galaxies, and quasars in astronomy. The dataset underwent detailed preprocessing to identify effective features for classification. KNIME Analytics Platform was used for data analysis and visualization, facilitating rapid and efficient data analysis through its drag-and-drop interface. Among the machine learning methods used in our study—Decision Trees, Random Forest, and Naive Bayes—the highest accuracy rate of 97.86% was achieved with the Random Forest model. Notably, despite its lower overall performance compared to other models, the Naive Bayes classifier exhibited superior performance in distinguishing the STAR class, which is one of the study's interesting findings. Future studies aim to enhance model accuracy by using larger and more diverse datasets and exploring different machine learning algorithms. Additionally, the impact of deep learning methods on classification performance will be investigated.

Keywords: Machine learning, Classification, Decision tree, Naive Bayes, Random forest

1. Introduction

Nowadays, astronomy has entered a new era with rapidly growing data sources and advanced observation techniques. With the construction of more powerful telescopes, spectral data from millions of celestial objects are being collected. Additionally, it is anticipated that the volume of data generated by next-generation telescopes will significantly increase in the future (Hughes et al., 2022). Consequently, it is becoming increasingly difficult for astronomers to manually examine and label the ever-growing astronomical data. In situations where large quantities of data are available, as well as detailed data, distinguishing the source type is time-consuming and often impractical. Therefore, understanding this vast amount of data and conducting large-scale analyses to classify galactic and extragalactic sources has become a challenging task. For such large datasets, machine learning methods have emerged as useful and valuable tools for analyzing and classifying data.

Machine learning provides powerful tools for extracting meaningful information from large and complex datasets, enabling more precise and efficient classification. Consequently, in recent years, the use of machine learning methods in the classification of quasars, stars, and galaxies has become increasingly widespread.

Machine learning methods perform well in identifying and characterizing different types of galactic objects through techniques such as modeling large datasets and feature extraction.

Quasars, stars, and galaxies are fundamental building blocks of the universe, and accurately classifying these cosmic objects is crucial for astronomical research. Quasars are highly luminous active galactic nuclei (Hughes et al., 2022). The identification of quasars emerged following the detection of radio emissions from star-like sources with high redshift values (Clarke et al., 2020). Even with larger optical telescopes at their disposal, astronomers find it extremely difficult to distinguish between a star and a quasar since both appear as bright points of light. Machine learning methods are particularly advantageous in this domain due to their potential to overcome the limitations of human vision and traditional techniques.

Machine learning algorithms can recognize complex patterns in large datasets and classify these objects with high accuracy. These algorithms process spectral features, brightness variations, and other astronomical data to distinguish subtle differences between quasars, stars, and galaxies. Additionally, machine learning provides astronomers with more precise and rapid

classification capabilities. In this context, a study by Omat et al. (2022) highlighted the importance of feature engineering techniques in classifying galaxies, stars, and quasars using machine learning methods. By employing machine learning methods such as Decision Trees, K-Nearest Neighbors, Multinomial Logistic Regression, Naive Bayes Classifier, Support Vector Classification, and Random Forest, their study found that Random Forest performed best with an accuracy of 98%. Furthermore, Random Forest was found to correctly classify all instances labeled as stars in the dataset.

Mehta et al. (2022) conducted a study on a dataset consisting of 100,000 observations, investigating the classification of stellar features into Galaxy and Star categories using machine learning algorithms. The study aimed to explore the effectiveness of various machine learning algorithms, including K-Nearest Neighbors, Support Vector Classifier, Random Forest, Logistic Regression, Decision Tree, and Naive Bayes, in classifying stars based on their spectral features. The findings revealed that the Support Vector Classifier demonstrated the highest accuracy among the tested models, highlighting its effectiveness in star classification, while the Decision Tree model showed the lowest accuracy.

In their study, Kumar and Gharat (2023) presented a novel approach to classify stars as binary or exoplanet candidates using deep learning techniques. The proposed model is designed to accept two different types of inputs to enhance both accuracy and generalization. One input layer receives pre-computed statistical features, while the other input layer takes time series data from light curves. The proposed method demonstrated a strong performance with a test accuracy of 81.17%.

Haghighi (2023) examined various machine learning algorithms, including Linear Regression, Logistic Regression, Naive Bayes, SVM, Decision Trees, and Neural Networks. Some of the proposed models were applied to a dataset consisting of variable and non-variable stars from the SDSS Survey Stripe 82. The findings showed that Decision Trees provided the best accuracy and F1 score.

In their study, Huichaqueo and Orrego (2022) presented a machine learning-based method for the automatic spectral classification of stars using data from the SDSS database. They developed a Random Forest model to extract the spectral class of observed stars, training the model considering three data usage scenarios: the use of original data, undersampling, and oversampling techniques. Their study found that the model trained with augmented data outperformed the other scenarios. Furthermore, experimental results showed that the combinatorial use of data as an input model contributed to the improvement of prediction scores across all data usage scenarios (Huichaqueo and Orrego, 2022).

In his study, Brice (2019) utilized standard classification methods such as K-Nearest Neighbors, Random Forest, and Support Vector Machine to automatically classify spectra using data from the SDSS. The study focused on reducing the high dimensionality of stellar spectrum data through Feature Selection methods, including Chi-Square and Fisher score, as well as incorporating domain-specific astronomical knowledge to enable classification in a lower-dimensional space. The research highlighted the potential of machine learning to automate the classification of stellar spectra, offering a more efficient alternative to traditional, observation-based methods, which can be time-consuming.

Lastly, Savyanavar et al. (2023) compared the performance of traditional machine learning classifiers with a proposed CNN model to classify star and galaxy images. Their study aimed to improve classification accuracy by leveraging the feature extraction capabilities of CNNs in star-galaxy classification. They proposed a novel CNN architecture consisting of three sub-blocks for feature extraction, enhancement, and noise reduction. While traditional machine learning algorithms achieved a maximum accuracy of 78%, the proposed CNN model outperformed them, achieving an accuracy of 92.44% on the star-galaxy dataset.

The similarity of quasars to both galaxies and stars makes their differentiation challenging. Therefore, this study aims to classify stars, galaxies, and quasars based on their spectral features and to determine which classifier performs better for this problem. Decision Trees, Random Forest, and Naive Bayes classifiers were employed for this purpose, and performance metrics were evaluated.

The classification of galactic objects using machine learning methods is a well-studied topic in the literature. However, determining which classifier performs better in classifying specific classes such as quasars, stars, and galaxies is the focus of this study. The KNIME Analytics Platform was employed for data analysis, visualization, and classification in the study. Its user-friendly drag-and-drop interface facilitates rapid and effective analysis of data, requiring minimal technical expertise.

2. Materials and Methods

The dataset used in the study aims to classify stars, galaxies, and quasars based on their spectral features. The data, comprising a total of 100,000 space observations, was obtained by the Sloan Digital Sky Survey (SDSS) and is available on the Kaggle website under the title 'Stellar Classification Dataset - SDSS17' (Fedesoriano, 2022). Each data point consists of 17 feature columns and one class column that categorizes the data into stars, galaxies, or quasars. The names and descriptions of the features are provided in Table 1.

The analysis, model training, performance evaluation, graphs, and visual figures in the study were conducted using the KNIME Analytics Platform. The KNIME Analytics Platform is an open-source software that enables accessing, analyzing, and visualizing data without any coding requirements. KNIME provides a visual programming environment with an intuitive interface that integrates various technologies (Fillbrunn et al., 2017).

Table 1. Attributes and descriptions of the dataset.

Attribute	Description
obj_ID	Unique value that identifies the object
alpha	Right ascension angle
delta	Deviation angle
u	Ultraviolet filter in the photometric system
g	Green filter in the photometric system
r	Red filter in the photometric system
i	Near infrared filter in photometric system
z	Infrared filter in photometric system
run_id	Run Number used to identify the specific scan
rereun_id	Rerun number to indicate how the image was processed
cam_col	Camera column that defines the scan line within the study
field_id	Field number to identify the field
spec_obj_id	Unique identification used for optical spectroscopic objects
class	Object class
redshift	Redshift value depending on the increase in wavelength
plate	License plate ID that identifies each license plate in SDSS
mjd	Modified Julian Date used to indicate when a particular piece of SDSS data was received
fiber_id	Fiber ID, which identifies the fiber directing light to the focal plane in each observation

In KNIME, a workflow is constructed with nodes. Data is passed between nodes through connections throughout the workflow. Each node can perform various tasks such as reading and writing files, transforming data, training models, or generating visuals. Depending on their tasks, nodes have specific settings that can be configured in their configuration dialogs.

2.1. Dataset Overview

The KNIME Data Explorer node was used to examine the dataset broadly and to observe the characteristics of its attributes. The Data Explorer node provides a variety of options to interactively view the properties of input data through a table. It was checked from the resulting table whether there were any missing, empty, or NaN (Not-a-Number) values in the dataset, and none of these values were found.

The table also displayed the statistical properties of numerical columns, including their minimum, maximum, mean, standard deviation, and variance. Upon inspection, notably high standard deviation and variance values for certain attributes (especially u, g, and z) provided a significant indication that outliers might be present.

Another important clue for identifying outliers is provided by the histogram of the attribute, which visually represents the frequency of values in the dataset. The histogram graph was obtained using the Statistics node in KNIME. Similar to the Data Explorer node, the

Statistics node displays statistical properties but produces histogram graphs in a less complex and more easily readable format compared to the Data Explorer node. Therefore, histogram graphs were obtained using the Statistics node.

Upon examining the histogram graphs of all attributes in the dataset, it was observed that the attributes u, g, z, field_ID, and redshift contain outliers. Additionally, the attribute rerun_ID was found to have the same value for all records. The histogram graphs of these attributes are provided in Figure 1.
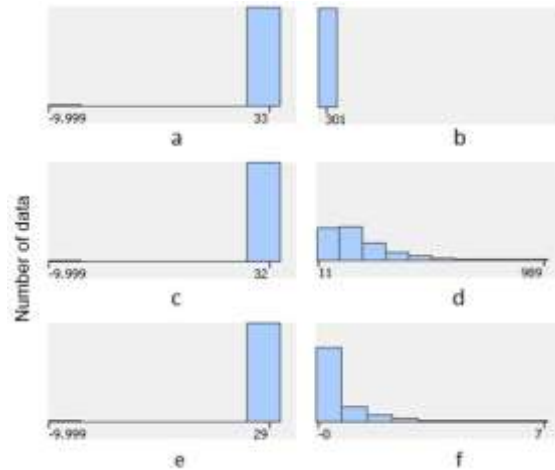
Figure 1. Histogram graphs of u (a), rerun_ID (b), g (c), field_ID (d), z (e) and redshift (f) attributes obtained with the Statistics node.

Standard deviation, variance, or histogram alone are not sufficient to accurately identify outliers in all attributes. For a more detailed analysis, KNIME's Box Plot node was used. Box Plot node; Displays statistical parameters such as minimum, lower quartile, median, upper quartile and maximum. The Box Plot node provides a quick overview of the outliers of a dataset.

Box Plot graphics were examined for all attributes of the data set and it was seen that in addition to the u, g, z, field_ID and redshift attributes, the r and i attributes also had outliers. An example graphic for this is given in Figure 2 for the r and i attributes.

In addition to missing and outlier values, another important issue to check in the data set is whether class labels are distributed fairly. The chart in which the number of data according to classes is obtained using KNIME's Bar Chart node is given in Figure 3. When the graph is examined, it is seen that the class labels are unevenly distributed.
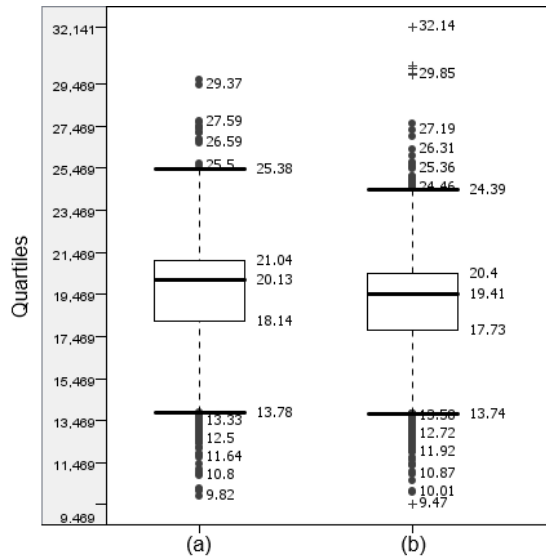
Figure 2. Representation of r and i attributes with box plot.

When the data set is examined with KNIME's visualization tools; It was determined that there were outliers for some attributes and class labels were unevenly distributed. The methods used in the study to overcome these problems are explained in detail under the heading of Data Preprocessing.
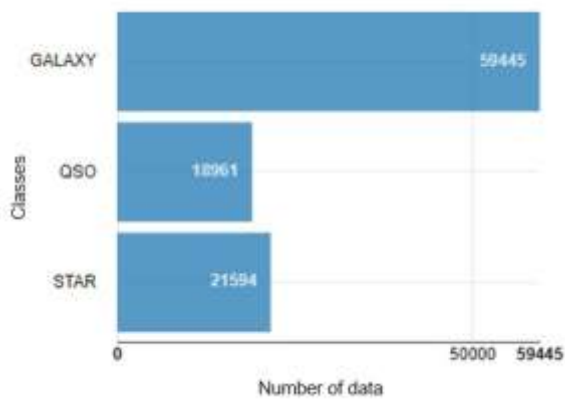
Figure 3. Number of data by classes.

2.2. Data Preprocessing
KNIME's Numeric Outliers node was used to remove outliers in the data set. The Numeric Outliers node detects and processes outliers separately for each of the selected columns via the interquartile range (IQR).
KNIME's Numeric Outliers node first calculates the IQR value to detect outliers of a particular column. IQR calculation is as in equation 1. The formula used to calculate whether an entry is an outlier, such that the interquartile distance factor k≥0, is given in equation 2. Accordingly, if the R value falls outside its calculated range, it is marked as an outlier.

$$IQR = Q_3 - Q_1 \tag{1}$$
$$R = [Q_1 - k(IQR),\ Q_3 + k(IQR)] \tag{2}$$

In the study, $k = 1.5$ value was used for the Numeric Outliers node, and the configuration of the node was made to convert these values into missing data when outlier treatment was found.
After applying the Numeric Outliers node to the dataset, the outliers turned into missing data. KNIME's Missing Value node was used to fill in the missing data. The configuration of the Missing Value node has been set to use the Linear Interpolation method to fill in the missing data. Linear Interpolation is a mathematical technique used to estimate the value between two known data points on a line. This method assumes a linear relationship between data points. The formula of Linear Interpolation is as in equation 3. Where y_1 and y_2 are two known points, x_1 and x_2 are the x-coordinates of the known points, y is the estimated value between y_1 and y_2.

$$y = y_1 + \frac{(y_2 - y_1) \times (x - x_1)}{x_2 - x_1} \tag{3}$$

After filling in the missing data, KNIME's SMOTE node was used to eliminate the imbalance in class labels. SMOTE is a technique based on the k-Nearest Neighbor (kNN) algorithm. Creates new synthetic samples using sampling data from the minority class. These synthetic samples increase the representation of the minority class in the dataset while considering the immediate neighbors of existing samples, thus reducing class imbalance (Li et al., 2021). The graph showing the number of data in the classes after sampling the minority class with SMOTE is given in Figure 4.
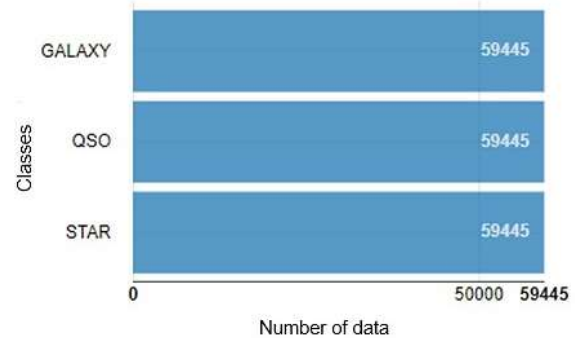
Figure 4. Data distribution according to classes after sampling with SMOTE.

2.3. Feature Selection
After the data preprocessing phase, feature selection was made. Feature selection reveals which features are more important and add valuable information in training the classifier. In addition to revealing the features that distinguish classes from each other, it also enables the removal of features that are not decisive in classification, thus training the model faster. For this purpose, two different feature selection methods were used in the study. The first of these is correlation analysis.
Correlation analysis is a method used to understand the relationship between variables and evaluate the connection between data. Correlation measures the direction and strength of the relationship between two

variables, whether positive or negative.

KNIME's Linear Correlation node was used to perform correlation analysis of the features in the data set. This node calculates the correlation coefficient for each selected pair of columns. Which correlation measure to apply depends on the type of variables. The Linear Correlation node uses the Pearson Correlation Coefficient method for numerical data and Pearson's Chi Square Test for nominal data.

Since all values in the data set, except the class attribute, consist of numerical variables, the Pearson correlation coefficient method was used. The linear correlation analysis graph of the attributes in the relevant data set is given in Figure 5. Accordingly, the value of the measurement varies between -1 (strong negative correlation) and +1 (strong positive correlation). A value of 0 indicates that there is no linear correlation.
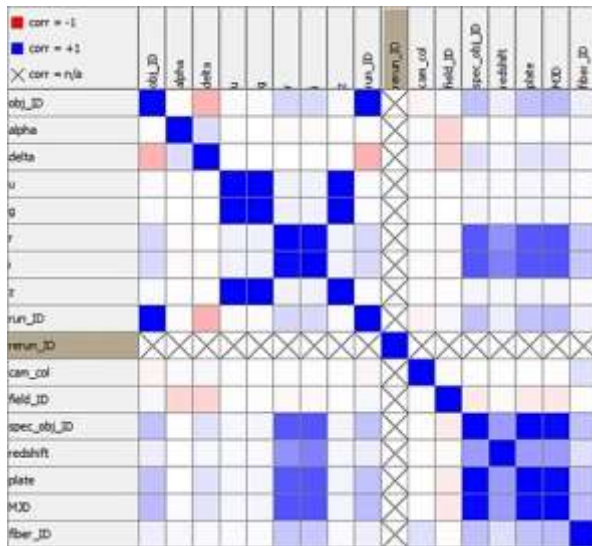
Figure 5. Linear correlation analysis graph of attributes in the data set.

When the linear correlation analysis given in Figure 5 is examined, it is seen that the rerun_ID attribute is not related to other attributes. It can be seen that the u, g and z attributes have a positive correlation with each other. While spec_obj_ID, plate, and MJD have a strong positive correlation with each other, the positive correlation with the redshift attribute is relatively weak. Likewise, it is seen that these attributes have a positive correlation, albeit weak, with the r and i attributes.

When the correlation analysis was examined, it was seen that the rerun_ID attribute was not positively or negatively correlated with other attributes in the data set. However, it was observed from the histogram of the attribute in Figure 1 that it gave the same value for all records. Based on these analyses, it is understood that the attribute does not play a decisive role in the formation of classes. Therefore, the rerun_ID attribute is removed from the data set as it will not help in model training.

Another method used for feature selection is Kernel Density Estimation (KDE). It was used to reveal at which

values the attributes were concentrated.

Kernel Density Estimation is given in equation 4. Accordingly, $K(x)$ is called the Kernel function. The kernel function is symmetrical, like the Gaussian distribution, it increases as it gets closer to the data point and decreases as it gets further away. KDE basically applies the Kernel function to each X_i in the sample, with X_i being the data point. Thus, each data point represents X_i as small density bumps and then sums all these small bumps to get the final density estimate (Chen, 2018).

$$\widehat{p_n}(x) = \frac{1}{nh}\sum_{i=1}^{n} K\left(\frac{X_i - x}{h}\right) \qquad (4)$$

where h>0 in the equation, it is the bandwidth that controls the amount of smoothing. Bandwidth h plays an important role in the quality of KDE. When the bandwidth h is very small, the density curve has a very wavy and convoluted structure. On the other hand, when h is very large, fusion of the bumps occurs. This excessive smoothing causes important values to be hidden (Chen, 2018). Therefore, choosing the right bandwidth is extremely important.

Kernel Density Estimation was used in the study to reveal at what values the attributes in the data set concentrated or differed on a class basis. KNIME's 1D Kernel Density Plot node was used for this. Gaussian was chosen as the kernel estimation method. To select the appropriate bandwidth, the configuration of the node was made to use the Silverman Approach, which is the most practical and easiest to calculate method, considering the size of the data set. Kernel Density Estimation graphs of the features drawn with KNIME's 1D Kernel Density Plot node are given in Figure 6, Figure 7 and Figure 8.

When the graphs in Figure 6 and Figure 7 are examined, it is seen that some values of the attributes are effective in determining the classes. When Figure 6(f), Figure 7(a) and Figure 7(d) are examined, where the MJD, *plate* and *spec_obj_ID* attributes are given in the KDE graph according to classes, respectively, it is seen that the attributes have values that clearly distinguish all three classes. It has been observed that the attributes *g* and *i* in Figure 6(d) and Figure 6(e) and the *r* and *u* attributes in Figure 7(b) and Figure 7(e) clearly stand out in determining the QSO class.

The *alpha* features in Figure 6(a) and *delta* in Figure 6(b) are not as prominent as other features in reflecting the characteristics of the classes. However, for some values of the attributes, it has values that slightly distinguish the GALAXY and QSO classes.
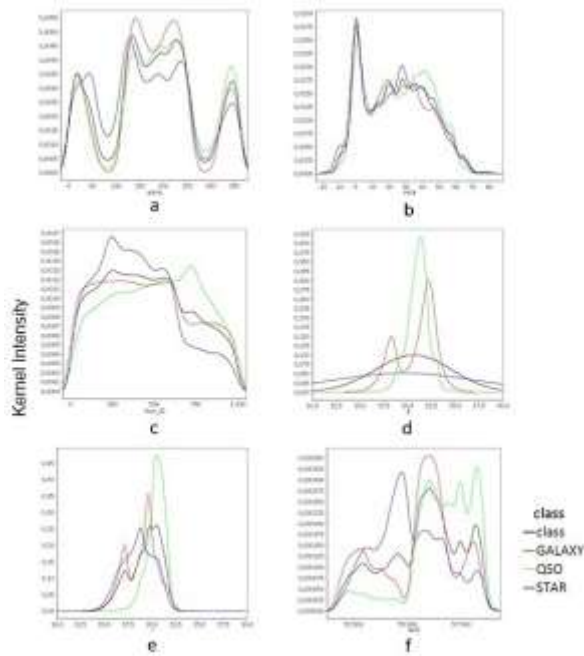
Figure 6. Kernel Density Estimation graphs of alpha (a), delta (b), fiber_ID (c), g (d), i (e) and MJD (f) attributes.
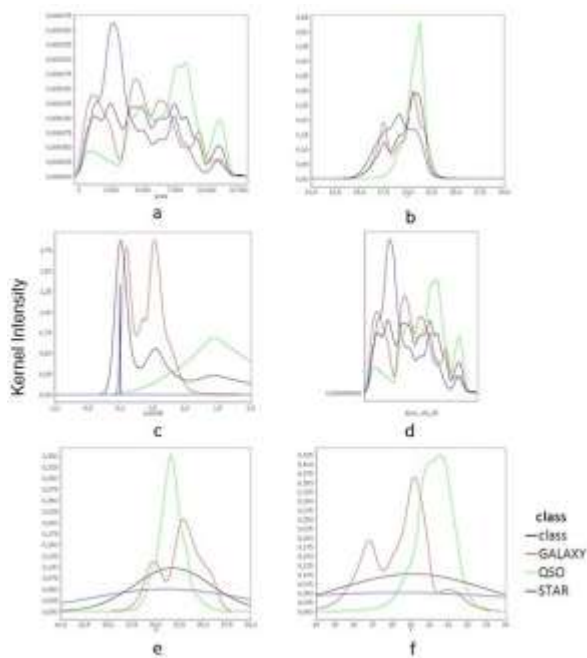
Figure 7. Kernel Density Estimation graphs of plate (a), r (b), redshift (c), spec_obj_ID (d), u (e) and z(f) attributes.

On the other hand, when the KDE graphs in Figure 8 are examined, it is seen that the attributes do not contain values that distinguish the classes. For almost all values, the distribution showed approximately the same characteristic. Therefore, since these features will not contribute to determining classes, they are removed from the data set before model training.
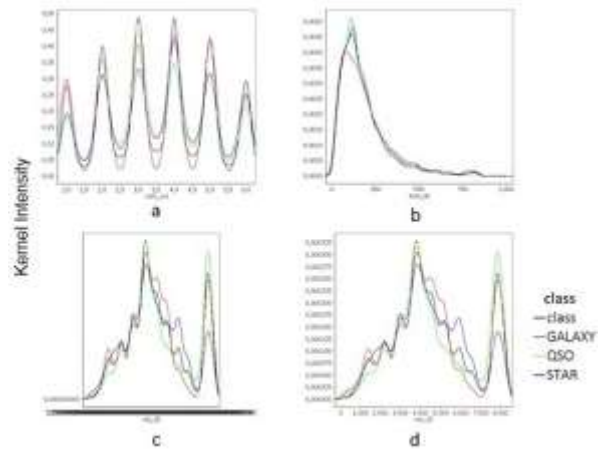
Figure 8. Kernel Density Estimation graphs of cam_col (a), field_ID (b), obj_ID (c) and run_ID (d) attributes.

2.4. Classifier Selection and Model Training

In the study, three different machine learning methods were used for model training. These; Decision Trees, Random Forest and Naive Bayes.

When the characteristics of the data set are taken into account, Random Forest, Decision Trees and Naive Bayes appear to be good machine learning methods. Naive Bayes works under the assumption that the characteristics of the data set are independent and generally performs well on small or medium-sized data sets. When there are independent features in your data set, Naive Bayes will evaluate this situation better and perform well. Random Forest and Decision Trees can work better on large data sets. Because these algorithms can capture the variations and relationships in the data set more effectively.

However, Naive Bayes is quite advantageous in terms of the transparency and simplicity of the model. In Decision Trees, it is quite interpretable because it clearly shows which feature makes which decision at each step.

Finally, in terms of the complexity of the algorithm, Naive Bayes is a relatively simpler algorithm and requires less computational power, which is advantageous especially when fast results are needed. Random Forest and Decision Trees require hyperparameter adjustment, which can increase the performance of the model.

2.4.1. Decision trees

Decision trees are an effective method used in the field of machine learning and data mining to solve classification and regression problems. Decision trees are basically a tree-structured classifier consisting of a root node, branches, internal nodes and leaf nodes in a hierarchical manner. It is a structure where internal nodes represent features of a dataset, branches represent decision rules, and each leaf node represents the outcome (Thomas et al., 2020). This hierarchical structure of decision trees is given in Figure 9.

Decision trees divide the data set into smaller subsets and determine a decision rule in each split. Each rule is based on a specific feature of the data set. With these rules, data points are classified or predicted by following

different paths in the branches of the tree. It uses the divide and conquer strategy by performing greedy search to determine the most suitable split points within a tree (Thomas et al., 2020). It provides a graphical representation of all possible solutions to a problem based on given conditions. It stands out as a simple, understandable and high-performance model. Decision trees have a wide range of usage as they provide successful results in large data sets and complex problems.
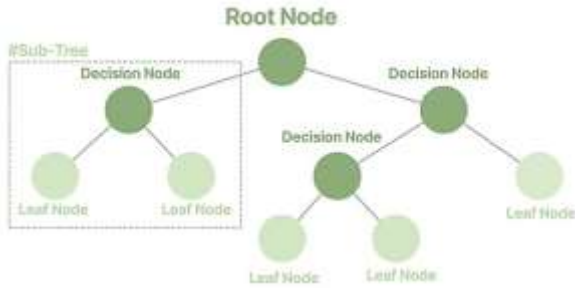
Figure 9. Hierarchical tree structure of decision trees.

2.4.2. Random Forest

Random forests are an ensemble learning method formed by combining multiple decision trees (Mouchel-Vallon and Hodzic, 2023). Each tree is trained using random samples of the dataset and runs independently on different subsets. This way, each tree makes its own prediction and combines its results to get majority votes for the average. This reduces overlearning and increases overall reliability (Mouchel-Vallon and Hodzic, 2023). An example random forest representation is given in Figure 10.
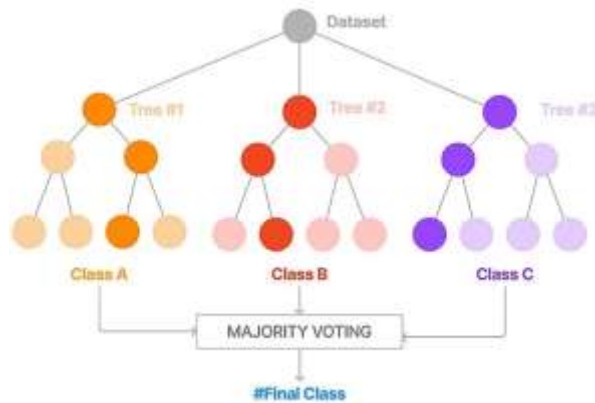
Figure 10. An example representation of the random forest structure consisting of a combination of decision trees.

The building blocks of the random forest algorithm are decision trees. The main difference between decision tree and random forest algorithm is that in random forest, the creation of root nodes and the separation of nodes are done randomly. While decision trees are trained using the entire dataset, random forests use random samples of the dataset in training each tree. This sampling process allows each tree to operate independently on different subsets.

Random forests can produce more stable and generalizing results because they consist of multiple trees. They also reduce overlearning and are better able to handle noise in the dataset. Random forests can operate at high speed on large data sets and provide high performance in classification and regression problems. Therefore, random forests have a wide range of applications.

2.4.3. Naive Bayes

Naive Bayes is a probability-based algorithm used to solve classification problems in the field of machine learning. Basically, it is based on the principle of Bayes theorem (Ramana, 2022). Naive Bayes is called "naive" because it assumes that the features observed in the classification process are independent of each other. This assumption means that each feature is evaluated independently without affecting the class.

Naive Bayes enables the classification of a new sample based on a predetermined class label. The classification process is based on calculating the probability of each class. After determining the relationship of the attributes in the data set with the class label, classification is made using Bayes' theorem. This theorem uses the probability of the class and the probabilities of the properties being observed in the given class to calculate the probability that the data point at which the properties are observed belongs to a class. Bayes' theorem is given in equation 5.

$$p(A|B) = \frac{p(A).p(B|A)}{p(B)} \tag{5}$$

In the equation, P(A) represents the probability of event A occurring and P(B) represents the probability of event B occurring. P(A|B) represents the probability of event A occurring if event B occurs, and P(B|A) represents the probability of event B occurring if event A occurs.

Naive Bayes is an algorithm that is often used successfully in areas such as spam filtering and text classification. Because it can provide effective results in large data sets with its simple structure and fast calculation ability (Ramana, 2022). However, the assumption that all features are independent is usually not valid in real life. Therefore, it may achieve low accuracy in cases where there are strong dependencies between features.

2.4.4. Building models with KNIME

80% of the data set was used for training and 20% for testing. KNIME's Partitioning node was used to divide the data set. This node divides the input table into two row-wise sections. The two sections it separates are delivered to two output ports. Learner nodes are connected to the output where 80% of the data is transmitted, and Predictor nodes are connected to the output where 20% of the data is transmitted. The classifiers used for model training in the study and the KNIME workflow diagram are given in Figure 11.
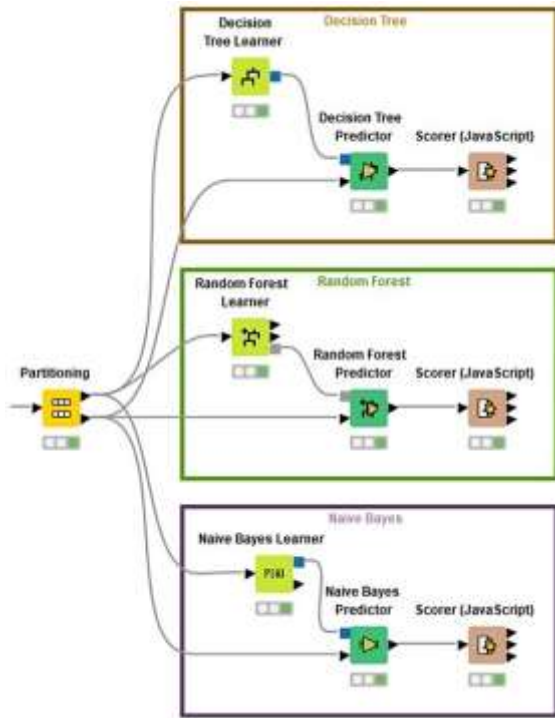
Figure 11. Classifiers used in model training and KNIME workflow diagram.

KNIME's Decision Tree Learner and Decision Tree Predictor nodes were used to build the Decision Trees model. The Decision Tree Learner node creates a decision tree in main memory for classification. The target attribute must be nominal. Other attributes used to make decisions can be nominal or numerical. Numerical splits are always binary, dividing the domain into two parts at a given split point. The algorithm provides two quality measures for the division calculation; Gini index and earnings rate. Additionally, a post pruning method is available to reduce tree size and increase prediction accuracy. The Decision Tree Predictor node was used to predict the class value of the model.

KNIME's Random Forest Learner and Random Forest Predictor nodes were used to build the Random Forest model. The Random Forest model created with Random Forest Learner consists of a selected number of decision trees. Each decision tree model is built with a different set of records, and a randomly chosen set of columns is used for each split within a tree. Rowsets for each decision tree are created by bootstrapping and have the same size as the original input table. The feature set for an individual split in a decision tree is determined by randomly selecting sqrt(m) features from the available features, where m is the total number of learning columns. The output model identifies a random forest and passes it to the Random Forest Predictor node for prediction.

KNIME's Naive Bayes Learner and Naive Bayes Predictor nodes were used to establish the Naive Bayes model. The Naive Bayes Learner node creates a Bayesian model from the given training data. Calculates the number of rows

per attribute value per class for nominal attributes and the Gaussian distribution for numeric attributes. The created model can be used as the Naive Bayes Predictor node to predict the class membership of unclassified data.

Models were trained with the three different classifiers described above. Performance outputs were obtained with KNIME's Scorer node, which was connected to the output of the Predictor node of the models. The Scorer node uses performance metrics such as accuracy, error, sensitivity, precision, specificity and F-measure to measure the performance of models and presents the results in an interactive table. The values obtained with the Scorer node are given in the Findings section and the results are discussed.

2.5. Performance Evaluation of Models

Machine learning performance metrics are measures used to evaluate how well a machine learning model works. These metrics help evaluate how accurate the model's predictions are, misclassification rates, the model's ability to generalize, and other performance characteristics. In the study, accuracy, error, sensitivity, precision, specificity and F1-measure metrics were used to evaluate the performance of the models along with the complexity matrix.

2.5.1. Complexity Matrix

A complexity matrix is a table used to evaluate the classification performance of a machine learning model. The complexity matrix helps analyze the model's accuracy and error types by comparing predicted class labels with actual class labels.

The complexity matrix consists of four main components: true positive, false positive, false negative and true negative. True Positive (TP) is the number of samples that are actually positive that are correctly predicted as positive. False Positive (FP) is the number of samples in which samples that are actually negative are wrongly predicted as positive. False alarm situations are examples of FP. False Negative (FN) is the number of samples in which samples that were actually positive were incorrectly predicted as negative, while true negative (TN) is the number of samples that were actually negative were correctly predicted as negative. The complexity matrix contains the numerical values of these four components and allows to analyze the performance of the model in detail. This matrix can be used to calculate various performance metrics.

2.5.2. Performance Metrics

Table 2. Performance metrics, descriptions and formula used to measure the performance of the model (Erickson and Kitamura, 2021)

Metric	Description	Formula
Accuracy	It represents the proportion of samples that the model predicted correctly.	$\dfrac{(TP + TN)}{(TP + FP + FN + TN)}$
Sensitivity	It indicates how many of the truly positive samples were correctly detected.	$\dfrac{TP}{(TP + FN)}$
Precision	It refers to the ratio of samples predicted to be positive to samples that are actually positive.	$\dfrac{TP}{(TP + FP)}$
Specificity	It is a performance metric that measures a model's ability to correctly predict negative examples that are actually negative in classification problems	$\dfrac{TN}{(TN + FP)}$
F1-Score	It is the harmonic average of sensitivity and sensitivity metrics. It is used to achieve a balance between precision and sensitivity in unbalanced data sets.	$\dfrac{2TP}{(2TP + FP + FN)}$

3. Results and Discussion

Results from performance metrics were obtained by connecting the Scorer node to the output of the Predictor nodes of the models. Therefore, model performances were compared only on test data.

Complexity matrices obtained from Decision Tree, Random Forest and Naive Bayes models are given in Table 3, Table 4 and Table 5, respectively.

Table 3. Complexity matrix of the Decision Tree model

		Predicted		
		GALAXY	QSO	STAR
Actual	GALAXY	11464	404	21
	QSO	499	11389	1
	STAR	24	0	11865

Table 4. Complexity matrix of the Random Forest model

		Predicted		
		GALAXY	QSO	STAR
Actual	GALAXY	11536	232	121
	QSO	406	11482	1
	STAR	3	0	11886

Table 5. Complexity matrix of the Naive Bayes model

		Predicted		
		GALAXY	QSO	STAR
Actual	GALAXY	8740	2975	174
	QSO	1233	10654	2
	STAR	0	0	11889

When the complexity matrices given in Table 3, Table 4 and Table 5 are examined, it is seen that the number of False Positives and False Negatives for GALAXY and QSO classes is high in all three models. The models show the same tendency to misclassify and repeat certain errors. This indicates that the GALAXY and QSO classes are more difficult to recognize accurately and the characteristics of these classes may be more ambiguous than the STAR class.

Performance values of the models are given in Table 6. Accuracy values for Decision Trees, Random Forest and Naive Bayes models were obtained as 97.34%, 97.86% and 87.71%, respectively, while loss values were found to be 2.66%, 2.14% and 12.29%, respectively. These results show that the Random Forest method has the highest accuracy rate. Although Decision Trees and Naive Bayes algorithms have also achieved high accuracy values, it is clear that Random Forest provides superior performance.

When the sensitivity, precision and specificity values of the GALAXY and QSO classes, which are most similar to each other, are examined, it is seen that the Random Forest model obtains higher values than Decision Trees. However, the Naive Bayes model, which is weaker than other classifiers, achieved the highest sensitivity value by correctly predicting all true positive examples in the STAR class.

It is seen that the STAR class has the highest sensitivity, sharpness, specificity and f1-measure values in all three classifiers. The fact that the star class has the highest values in all four metrics shows that the model is more successful than other classes in correctly classifying stars. Additionally, this shows that the features of the star class are more distinct and distinctive than other classes, so the classifiers learn the star class better.

In terms of F1-measure, very high values for all class labels are seen especially in the Random Forest model and Decision Trees. This shows that the models generally exhibit a balanced performance. These findings show that the Random Forest model can perform effective classification on this data set and performs well.

Table 6. Results obtained from the performance metrics of the models

Classification Method	Accuracy	Loss	Classes	Sensitivity	Precision	Specificity	F1-measure
			GALAXY	96.43%	95.64%	97.80%	96.03%
Decision Trees	97.34%	2.66%	QSO	95.79%	96.57%	98.30%	96.18%
			STAR	99.80%	99.81%	99.91%	99.81%
			GALAXY	97.03%	96.58%	98.28%	96.80%
Random Forest	97.86%	2.14%	QSO	96.58%	98.02%	99.02%	97.29%
			STAR	99.97%	98.98%	99.49%	99.48%
			GALAXY	73.51%	87.64%	94.81%	79.96%
Naive Bayes	87.71%	12.29%	QSO	89.61%	78.17%	87.49%	83.50%
			STAR	100%	98.54%	99.26%	99.27%

4. Conclusion

Within the scope of this study, we evaluated the performance of three different machine learning algorithms: Decision Trees, Random Forest and Naive Bayes to classify GALAXY, QSO and STAR classes. Our study was carried out on the K-NIME platform. The results obtained show that all three algorithms exhibit superior performance in classifying the STAR class. Decision Trees and Random Forest models attracted attention with their high accuracy (97.34% and 97.86%) and low error rates (2.66% and 2.14%). Similarly, in the study of Omat et al. (2022) Random Forest showed the best performance with an accuracy rate of 98%. Especially for the STAR class, the sensitivity, precision, specificity and F1-measure values of these models were found to be almost perfect. Haghighi (2023), who tested various classifiers, showed that Decision Trees provided the best accuracy and F1 score.

Although the Naive Bayes algorithm had lower overall accuracy than the other two models (87.71%), it still showed high performance in the STAR class. However, one of the interesting results of the study is that the Naive Bayes classifier can distinguish the STAR class in the best way. As a result, it has been observed that the STAR class can be successfully classified by all algorithms thanks to its distinct and distinctive features, but more advanced and complex models (such as Random Forest) give better results in separating the GALAXY and QSO classes. While the study helps us understand which algorithm will perform better on a given data set, the findings highlight the importance of choosing the right algorithm in classification problems. At the same time, these findings provide important clues in the selection of machine learning algorithms used in classifying astronomical objects.

In future studies, it is aimed to increase classification performance by using larger data sets and more complex models. Improvements can be added to make the model better recognize and distinguish GALAXY and QSO classes. Different analysis techniques can be applied to reveal the superior ability of the Naive Bayes classifier in determining the STAR class. A more comprehensive comparison can be made using different data sets and algorithm parameters, and more detailed results can be obtained by examining different metrics.

Author Contributions

The percentage of the authors contributions is presented below. All authors reviewed and approved the final version of the manuscript.

	M.F.E.	T.T.B.
C	70	30
D	70	30
S	40	60
DCP	40	60
DAI	50	50
L	50	50
W	70	30
CR	40	60
SR	80	20

C=Concept, D= design, S= supervision, DCP= data collection and/or processing, DAI= data analysis and/or interpretation, L= literature search, W= writing, CR= critical review, SR= submission and revision.

Conflict of Interest

The authors declared that there is no conflict of interest.

Ethical Consideration

Ethics committee approval was not required for this study because of there was no study on animals or humans.

References

Brice MJ. 2019. Classification of stars from redshifted stellar spectra utilizing machine learning. MSc Thesis, Central Washington University, Computational Science, Washington,

US, pp: 73.

Chen YC. 2018. Lecture 6: Density Estimation: Histogram and Kernel Density Estimator. URL= http://faculty.washington.edu/yenchic/18W_425/Lec6_hist_KDE.pdf (accessed date: May 10, 2024).

Clarke AO, Scaife AMM, Greenhalgh R, Griguta V. 2020. Identifying galaxies, quasars, and stars with machine learning: A new catalogue of classifications for 111 million SDSS sources without spectra. Astronomy Astrophys, 639: A84.

Erickson BJ, Kitamura F. 2021. Magician's corner: 9. Performance metrics for machine learning models. Radiol Artif Intel, 3(3): e200126.

Fedesoriano. 2022. Stellar Classification Dataset-SDSS17. URL= https://www.kaggle.com/fedesoriano/stellar-classification-dataset-sdss17 (accessed date: May 15, 2024).

Fillbrunn A, Dietz C, Pfeuffer J, Rahn R, Landrum GA, Berthold MR. 2017. KNIME for reproducible cross-domain analysis of life science data. J Biotechnol, 261: 149-156.

Haghighi MHZ. 2023. Analyzing astronomical data with machine learning techniques. arXiv Preprint, arXiv: 2302.11573.

Hughes AC, Bailer-Jones CA, Jamal S. 2022. Quasar and galaxy classification using Gaia EDR3 and CatWise2020. Astronomy Astrophys, 668: A99.

Huichaqueo MO, Orrego RM. 2022. Automatic spectral classification of stars using machine learning: An approach based on the use of unbalanced data. Machine Learn Appl, 9(4): 01-16.

Kumar A, Gharat S. 2023. Star cassification: A deep learning approach for ıdentifying binary and exoplanet stars. arXiv Preprint, arXiv: 2301.13115.

Li J, Zhu Q, Wu Q, Zhang Z, Gong Y, He Z, Zhu F. 2021. SMOTE-NaN-DE: Addressing the noisy and borderline examples problem in imbalanced classification by natural neighbors and differential evolution. Know Based Syst, 223: 107056.

Mehta T, Bhuta N, Shinde S. 2022. Experimental analysis of stellar classification by using different machine learning algorithms. 2022 International Conference on Industry 4.0 Technology (I4Tech), September 23-24, Pune, India, pp: 1-8.

Mouchel-Vallon C, Hodzic A. 2023. Toward emulating an explicit organic chemistry mechanism with random forest models. J Geophys Res Atmospheres, 128(10): e2022JD038227.

Omat D, Otey J, Al-Mousa A. 2022. Stellar objects classification using supervised machine learning techniques. International Arab Conference on Information Technology (ACIT), November 22-24, Abu Dhabi, United Arab Emirates, pp: 1-8.

Ramana PV. 2022. Naïve Bayes to machine learning approach for structural dynamic complications. ASPS Conf Proc, 1(4): 1283-1291.

Savyanavar AS, Mhala N, Sutar SH. 2023. Star-galaxy classification using machine learning algorithms and deep learning. Int J Info Technol Secur, 15(2): 87-96.

Thomas T, Vijayaraghavan P, Emmanuel A, Thomas S, Vijayaraghavan TP, Emmanuel S. 2020. Applications of decision trees. Machine Learn Appr Cyber Secur Analyt, 2020: 157-184.

PYALLFFS: AN OPEN-SOURCE LIBRARY FOR ALL FILTER FEATURE SELECTION METHODS

Tohid YOUSEFI[1]*, Özlem VARLIKLAR[1]

[1]*Dokuz Eylul University, Faculty of Engineering, Department of Computer Engineering, 35160, Izmir, Türkiye*

Abstract: Feature selection is a significant data mining and machine learning technique that enhances model performance by identifying important features within a dataset, reducing the risk of overfitting while aiding the model in making faster and more accurate predictions. Pyallffs is a Python library developed to optimize the feature selection process, offering rich content and low dependency requirements. With 19 different filtering methods, pyallffs assists in analyzing dataset features to determine the most relevant ones. Users can apply custom filtering methods to their datasets using pyallffs, thereby achieving faster and more effective results in data analytics and machine learning projects. The source codes, supplementary materials, and guidance is publicly available on GitHub: https://github.com/tohid-yousefi/pyallffs.

Keywords: Feature selection, Filter methods, Feature selection library, Open-source library, Python software

*Sorumlu yazar (Corresponding author): Dokuz Eylul University, Faculty of Engineering, Department of Computer Engineering, 35160, Izmir, Türkiye	
E mail: tohid.yousefi@ogr.deu.edu.tr (T. YOUSEFI)	
Tohid YOUSEFI https://orcid.org/0000-0003-4288-8194	**Received:** April 09, 2024
Özlem VARLIKLAR https://orcid.org/0000-0001-6415-0698	**Accepted:** September 03, 2024
	Published: September 15, 2024

1. Introduction

Optimizing model performance and efficiency in machine learning relies heavily on feature selection, where the most relevant attributes are chosen for model building. This process streamlines the model, reducing computational complexity and enhancing its ability to generalize to new data by focusing solely on essential features. However, in high-dimensional datasets, the growing number of features can pose challenges, such as the curse of dimensionality (Miao and Niu, 2016; Shardlow, 2016). This phenomenon can lead to overly complex models, increasing the risk of overfitting and diminishing their generalization capabilities. Thus, effective feature selection techniques are vital to address these challenges and ensure the reliability and robustness of machine learning models, particularly in the face of increasing data dimensionality (Kalousis et al., 2007).

Feature selection plays a fundamental role in the realms of machine learning and data analytics, aiming to enhance model performance and diminish unnecessary noise within datasets. This process is carried out through various methods, including filter (Chandrashekar and Sahin, 2014), wrapper (Kohavi and John, 1997), embedded (Zheng and Casari, 2018), ensemble (Opitz and Maclin, 1999), and hybrid methods (Kabir et al., 2010). In this study, we will specifically delve into filter methods. Filter methods assist in identifying the most significant features within a dataset by analyzing their relationships and impact on the target variable. These methods examine the independence between features and select the most suitable ones, thereby improving model performance while mitigating the risk of overfitting. Consequently, filter methods play a pivotal role in the feature selection process (Yousefi and Varlıklar, 2024).

Filter methods are integral to feature selection in machine learning, focusing on identifying the most relevant attributes within a dataset based on intrinsic characteristics (Yousefi and Aktaş, 2024). The pyallffs library, developed for this purpose, offers a comprehensive array of filtering techniques, facilitating seamless integration and exploration of various methods. With pyallffs, researchers and practitioners can efficiently pinpoint the most influential features within datasets, enhancing the accuracy and robustness of machine learning models.

This paper makes the following key contributions:

1. Novel Integration of Filter Methods: We introduce the *pyallffs* library, which consolidates multiple filtering techniques into a single, accessible platform, enabling researchers to efficiently apply and compare different methods.

2. Empirical Evaluation: Through rigorous testing on diverse datasets, we demonstrate the effectiveness of filter methods in improving model accuracy and robustness, particularly in high-dimensional data environments.

3. Comprehensive Analysis: The paper provides a detailed examination of the impact of various filter methods on model performance, offering valuable insights into their strengths and limitations.

The structure of this paper is organized as follows: The *Materials and Methods* section details the feature

selection process, with a particular focus on filter feature selection methods. It also describes the datasets used in the study and provides information on the implementation and usage of the *pyallffs* library. Following this, the *Results* section presents the outcomes of our experiments, highlighting the effectiveness of the selected methods. Finally, the *Conclusion and Future Work* section summarizes the key findings and discusses potential directions for further research.

2. Materials and Methods

Figure 1. Feature selection process.

2.2. Filter Methods
The filter feature selection method (Chandrashekar and Sahin, 2014) is a technique used to identify the most important features in a dataset. This method aims to select the most suitable features by analyzing relationships between features and how they affect the target variable. As depicted in Figure 2, filter methods help improve model performance by reducing the dataset's dimensionality. These methods typically use metrics that evaluate the importance of features, such as statistical measures. Filter methods reduce model complexity, prevent overfitting, and enhance the model's generalization ability. Therefore, the filter feature selection method plays a significant role in data analytics and machine learning projects (Yousefi and Varlıklar, 2024).

Filter methods are paramount in feature selection, serving to enhance model performance by identifying relevant attributes within datasets. However, given the plethora of techniques utilized within filter methods and the absence of a unified tool for their simultaneous application, a library addressing this need has been developed in this study. This library, namely pyallffs, is a versatile toolkit boasting 19 distinct filter feature selection methods. With pyallffs, researchers and practitioners can effortlessly navigate through various filtering techniques, as depicted in Figure 3, facilitating efficient and informed feature selection processes tailored to their specific dataset needs.

2.2.1. Fisher score
The Fisher Score (Gu et al., 2012), employed in binary classification scenarios, assesses the discriminative capability of a feature across two classes. It quantifies this by computing the ratio of squared mean differences

2.1. Feature Selection
Feature selection is an important part of machine learning and data analysis. It helps to pick out the most useful features while leaving out the ones that don't matter much. This process, shown in Figure 1, makes models better by focusing on the most important features and making them easier to understand. It also helps to prevent problems like overfitting and makes models more accurate. By choosing features carefully, people who work with data can make better models and understand their data better. So, feature selection is a big help in analyzing data and making good decisions (Yousefi and Varlıklar, 2024).

between feature values for each class to the sum of variances within each class. A higher Fisher Score suggests a more pronounced discrimination between classes, rendering the feature more significant. The Fisher Score formula can be expressed as in equation 1:

$$Fisher\_score(f_i) = \frac{\sum_{j=1}^{c} n_j (\mu_{i,j} - \mu_i)^2}{\sum_{j=1}^{c} n_j \sigma(i,j)^2} \quad (1)$$

Here, n_j, μ_i, $\mu_{i,j}$, and $\sigma(i,j)^2$ respectively denote the number of samples in class j, the mean value of feature f_i, the mean value of feature f_i for samples in class j, and the variance value of feature f_i for samples in class j. This feature selection method is commonly employed for binary classification purposes (Gu et al., 2012).

2.2.2. T-score
The fundamental concept behind the T-score (Carey and Delaney, 2010) is to assess whether a feature can statistically differentiate between the means of two classes by calculating the ratio between the mean difference and the variance of the two classes. Generally, the higher the t-score, the more significant the feature (Faulkner, 2005). The T-score relies on the t-value, which is among the most commonly used filter methods. As mentioned earlier, a relationship score is computed for each class using the sample size, mean, and standard deviation values of features, and features with high scores are added to the subset in the t-score method (Budak and Taşabat, 2016). The T-Score formula can be expressed as in equation 2 (Chandrashekar and Sahin, 2014):

$$TScore(f_i) = \frac{|\mu_1 - \mu_2|}{\sqrt{\frac{\sigma_1^2}{n_1} + \frac{\sigma_2^2}{n_2}}} \quad (2)$$

Here, μ_1 and μ_2 are the mean feature values for samples

from the first and second classes, respectively, while σ_1^2 and σ_2^2 represent the corresponding standard deviation values, and n_1 and n_2 denote the number of samples from these two classes (Chandrashekar and Sahin, 2014).
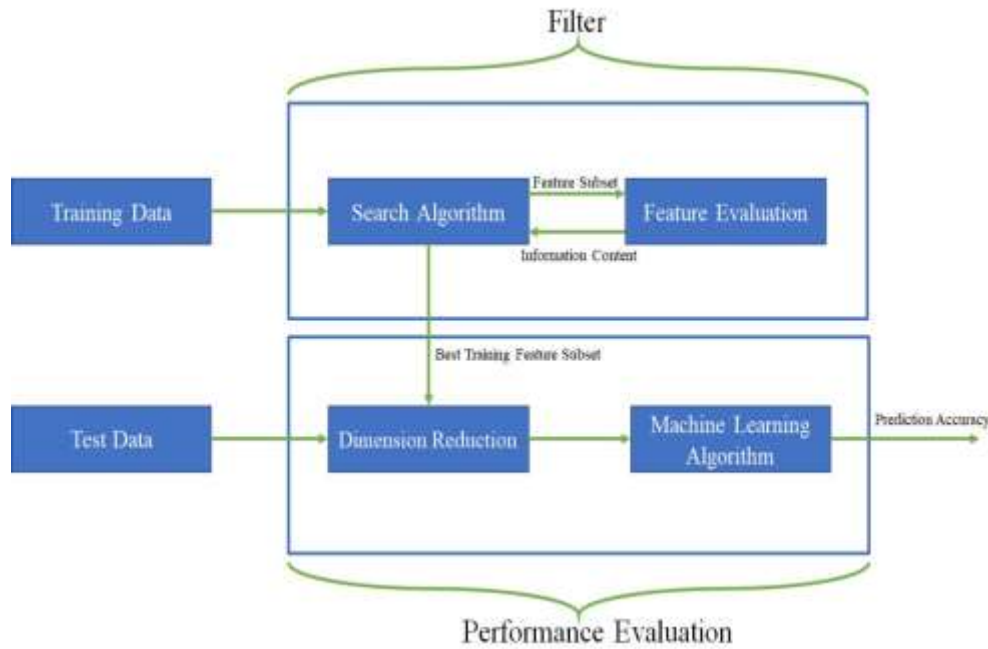
Figure 2. The general framework of filter method

Figure 3. All filter feature selection methods.

2.2.3. Welch's T-statistic

Welch's t-statistic (Welch, 1947) is a technique used in feature selection to spot differences between groups of features. It calculates variations in group means, within-group variances, and sample sizes. Unlike the standard t-test, Welch's method is more reliable when group sizes and variances differ. It offers a flexible approach to evaluating how features stand out across groups by normalizing mean differences. The Welch's t-statistic formula can be expressed as in equation 3:

$$Welch'sTstatistic(f_i) = \frac{|\mu_1 - \mu_2|}{\sqrt{\frac{(\sigma_1^2)^2}{n_1} + \frac{(\sigma_2^2)^2}{n_2}}} \qquad (3)$$

Here, μ_1 and μ_2 are the mean feature values for samples from the first and second classes, respectively, while σ_1^2 and σ_2^2 represent the corresponding variances values, and n_1 and n_2 denote the number of samples from these two classes (Delacre et al., 2017).

2.2.4. Chi-squared

The chi-square (Kass, 1980) statistic serves as a

technique for feature selection, primarily assessing the association between features and the target variable, particularly in classification tasks involving categorical features. It determines whether a feature is independent of the target variable by measuring the strength of their relationship. This test evaluates the independence hypothesis between two categorical variables through the ratio of squared differences between observed and expected frequencies, thereby gauging the existence of a relationship between them. The mathematical formula of chi-square statistic is as in equation 4 (Witten and Frank, 2002):

$$ChiSquared(f_i) = \sum \frac{(O_i - E_i)^2}{E_i} \tag{4}$$

Here, O_i stands for observed frequency, indicating the actual occurrence frequencies of category combinations within the dataset, while E_i represents expected frequency, depicting the frequencies expected under the assumption of independence between the two variables (Ugoni and Walker, 1995). The chi-square statistic calculates the sum of the squared differences between observed and expected frequencies for category combinations, serving as a measure of the relationship between the feature and the target variable. A high chi-square value indicates a robust relationship, whereas a low value suggests a weaker association between the two variables (Bryant and Satorra, 2012).

2.2.5. Information gain

Information gain, also known as Kullback-Leibler (Kullback and Leibler, 1951) divergence, is a measure of the entropy gained through operations performed on a dataset or random variable (Cover, 1999). Entropy represents the level of variation in data; lower entropy indicates less variation and stronger relationships. Higher information gain signifies greater importance of a feature. It operates independently across all features and is based on their information gain (Hall and Smith, 1998). The information gain of a feature denotes the difference between previous uncertainty and expected subsequent uncertainty. Information gain is highest for classes with equal probability, indicating lowest uncertainty. Shannon entropy is commonly used as a measure of uncertainty (Shannon, 1948). The mathematical formula of information gain is as in equation 5:

$$H(X) = -\sum_{x_i \in X} P(x_i) \, log\big(P(x_i)\big)$$
$$H(X|Y) = \sum_{y_i \in Y} P(y_i) \sum_{x_i \in X} P(x_i|y_i) \, log\big(P(x_i|y_i)\big) \tag{5}$$
$$Information\ Gain\ (X, Y) = H(X) - H(X|Y)$$

Here, Information Gain (X, Y) denotes the information gain between dataset X and feature Y. H(X) signifies the entropy of dataset X, which equals zero when the dataset is entirely homogeneous. H(X|Y) represents the conditional entropy of dataset X given feature Y. It assesses the homogeneity of the dataset following its division based on feature values.

2.2.6. Gain ratio

Gain Ratio is a feature selection criterion utilized to gauge the importance of features in the feature selection process. As a variant of Information Gain, it offers a normalized perspective, considering the intrinsic information content of a split. It assesses the homogeneity of subsets formed by feature splitting while also factoring in the number of values the feature can assume. This metric aims to address the bias towards features with a large number of unique values, which often exhibit higher Information Gain, by normalizing it with the split information (Witten et al., 2005). The Gain Ratio is typically calculated as in equation 6 (Novaković, 2016):

$$GainRatio(X) = \frac{Information\ Gain\ (X)}{Split\ Information\ (X)} \tag{6}$$

Here, Information Gain (X) denotes the information gain attributed to feature X, while Split Information (X) quantifies the information generated by splitting based on feature X. Split Information is determined by the cardinality of feature values; higher unique values lead to diminished Split Information, consequently elevating the Gain Ratio, thus ensuring a more equitable metric for feature selection across diverse feature sets (Novaković, 2016; Priyadarsini et al., 2011).

2.2.7. Symmetric uncertainty coefficient

The Symmetric Uncertainty Coefficient is a method devised to overcome the drawbacks of information gain by dividing the entropies of X and Y (Dash and Liu, 2003). It assesses the suitability of features in relation to the target class, with higher values indicating greater importance. Symmetric Uncertainty Coefficient can be calculated using the formula in equation 7 (Hernández-Torruco et al., 2014):

$$SUC(X, Y) = \frac{2 * Information\ Gain\ (X, Y)}{H\ (X) + H(Y)} \tag{7}$$

Here, $SUC(X, Y)$ denotes the Symmetric Uncertainty Coefficient between variables X and Y, while $Information\ Gain\ (X, Y)$ measures the information gain between them, with $H\ (X)$ and $H(Y)$ representing their respective entropies (Ali and Shahzad, 2012). Similar to gain ratio, this method also ranges between 0 and 1. When the symmetric uncertainty coefficient equals 1, it indicates that one feature completely predicts the other, whereas a value of 0 signifies no relationship between X and , Y (Mani and Kalpana, 2016).

2.2.8. Relief score

Relief, proposed by Kira and Rendell (Kira and Rendell, 1992), is a widely used classic filter method for classification problems, functioning as a multivariate feature selection technique. It operates by randomly selecting instances from the data and then finding the nearest neighbors from the same and opposite classes, updating relevance scores for each feature based on these comparisons (Hall and Holmes, 2000). In other words, Relief measures the relevance of features by comparing the value of the current feature for instances classified as the same and different classes (Esmael et al., 2012). Its strengths lie in its independence from intuitive scans,

efficient operation in low-degree polynomial time, and applicability to binary and continuous data, and resilience to noisy data and feature interactions. However, it fails to distinguish among redundant features, thus potentially misleading the algorithm with a limited number of training instances (Lun Gaoa et al., 2013). Relief score can be calculated using the formula in equation 8 (Miao and Niu, 2016; Nilsson, 2007):

$$Relief\_Score = \frac{1}{2} \sum_{j=1}^{l} d\big(X(j,i) - X(NM(j),i)\big)$$
$$- d\big(X(j,i) - X(NH(j),i)\big) \quad (8)$$

Here, NM(j) and NH(j)indicate the nearest data instances to x_j with the same class label and a different class label, respectively. Typically, d is set as the Euclidean distance metric(Miao and Niu, 2016; Nilsson, 2007).

2.2.9. Relief-F score
Relief-F (Kononenko, 1994) is an extension of the original Relief algorithm. Whereas the original Relief operates by randomly selecting an instance from the data and then finding the nearest neighbors from the same and opposite classes, Relief-F extends its capabilities to handle multi-class problems and offers increased robustness against missing and noisy data (Arauzo-Azofra et al., 2004; Urbanowicz et al., 2018). This method is universally applicable, has low error rates, accounts for feature interactions, and can capture local dependencies overlooked by other methods. The core idea of this approach is to select features capable of distinguishing examples originating from different classes (Kononenko, 1994; Vora and Yang, 2017). Relief-F calculates its score using the formula in equation 9 (Kononenko, 1994):

$$ReliefF(f_i)$$
$$= \frac{1}{c} \sum_{j=1}^{l} \left(-\frac{1}{m_j} \sum_{x_r \in NH(j)} d\big(X(j,i) - X(r,i)\big) \right.$$
$$\left. + \sum_{y \neq y_j} \frac{1}{h_{jy}} \frac{P(y)}{1 - P(y)} \sum_{x_r \in NM(j,y)} d\big(X(j,i) - X(r,i)\big) \right) \quad (9)$$

Here, NH(j) and NM(j,y) denote the nearest data instances to x_j with the same class and a different class y, respectively, with sizes h_{jy} and m_j. P(y) represents the proportion of examples with class label y (Vora and Yang, 2017).

2.2.10. mRMR
The Minimum Redundancy Maximum Relevance (mRMR) score, proposed by Ding ad Peng in 2005 (Ding and Peng, 2005), is a filter-based and supervised feature selection method. It selects features by minimizing redundancy among them while maximizing relevance, aiming to reduce feature redundancy and maximize feature relevance (Chandra and Gupta, 2011; Radovic et al., 2017). Additionally, this method utilizes the mutual information criterion as a fitness measure across different datasets (Ding and Peng, 2005; Bolón-Canedo et al., 2014). The mRMR score can be calculated using the formula in equation 10 (Ding and Peng, 2005):

$$w = \frac{1}{|S|^2} \sum_{i,j} c(i,j)$$
$$V_F = \frac{1}{|S|} \sum_{i \in S} F(i,h) \quad (10)$$

Here, S represents a set of features, $|S|$ denotes the number of features in S, $c(i,j)$ represents the correlation between features i and j, h is the target, and $F(i,h)$ is the F-statistic. The Minimum Redundancy Maximum Relevance (mRMR) method is one of several feature selection techniques applicable in both classification and regression tasks. It has been observed to perform particularly well in high-dimensional datasets where the number of features is significantly larger than the number of samples (Ding and Peng, 2005; Peng and Fan, 2015).

2.2.11. Absolute Pearson correlation coefficients
Feature selection based on correlation involves assessing the connection between a feature and either the target variable or other features, indicating the strength of their relationship. The correlation coefficient, often measured using the Pearson correlation coefficient, quantifies this relationship between two variables. With values ranging from -1 to 1, a coefficient close to 1 signifies a positive linear relationship, while a coefficient near -1 suggests a negative linear relationship. Conversely, a coefficient close to 0 indicates no linear relationship between the variables. The Pearson correlation coefficient can be calculated using the formula in equation 11 (Sedgwick, 2012):

$$pearson\_correlation\_coefficients(r)$$
$$= \frac{\sum_{i=1}^{n}(x_i - \overline{x})(y_i - \overline{y})}{\sigma_x \sigma_y} \quad (11)$$

Here, $\overline{x}$ and $\overline{y}$ represent the means, while σ_x and σ_y denote the standard deviations of x_i and y_i, respectively (Goswami and Chakrabarti, 2014).

2.2.12. Maximum likelihood feature selection
Maximum likelihood feature selection (Suzuki et al., 2008) is a multivariate and supervised feature selection method that prioritizes variables based on the measure of input-target dependency. Estimators utilize maximum likelihood mutual information to measure the dependency between input and target. This method is a density estimation-based mutual information estimator. The density ratio of this method is calculated using the formula in equation 12 (Ding and Peng, 2005; Suzuki et al., 2008; Suzuki Ding and Peng, 2009):

$$w(x,y) = \frac{P_{xy}(x,y)}{P_x(x)P_y(y)} \quad (12)$$

Here, $P_{xy}(x,y)$ denotes the joint density of X and Y, while $P_x(x)$ and $P_y(y)$ represent the densities of X and Y, respectively. Maximum likelihood feature selection is a method employed for both classification and regression problems (Suzuki et al., 2008).

2.2.13. Least squares feature selection
Least Squares Feature Selection is a method utilized to enhance model accuracy or effectively explain the target variable by selecting features from a dataset. It employs a linear regression model to gauge feature importance,

utilizing the least squares method within this framework. Practically, it involves estimating coefficients in the linear regression model and evaluating their absolute magnitudes to determine feature importance. Features are prioritized or ranked based on the absolute values of their coefficients, providing insights into their significance in the model. Mathematically, this technique is represented by estimating coefficients in the linear regression model and examining their absolute values to ascertain feature importance. The least squares feature selection can be calculated using the formula in equation 13 (Xiang et al., 2012):

$$\hat{\beta} = (X^T X)^{-1} X^T y \tag{13}$$

Here, $\hat{\beta}$ denotes the estimated parameter vector of the model, X represents the data matrix, and y is the vector of the target variable.

2.2.14. Laplacian feature selection score

The Laplacian feature selection score (He et al., 2005) is fundamentally based on Laplacian eigenmaps (Belkin and Niyogi, 2001) and locality preservation forces (He and Niyogi, 2003); moreover, this method is a graph-based, unsupervised, and univariate feature selection algorithm that ranks features according to their locality preservation forces (Von Luxburg, 2007). In the Laplacian algorithm, features are evaluated independently; therefore, this algorithm cannot assess feature redundancy (Liu et al., 2010). The Laplacian score of a feature can be calculated using the formulas in equation 14 (He et al., 2005):

$$Lap(f_i) = \frac{\tilde{f}_i' L f_i'}{\tilde{f}_i' D f_i'}$$

$$f_i = f_i - \frac{f_i' D 1}{1' D 1} 1 \quad , 1 = [1,1,\ldots,1]'$$

$$D(i,j) = \sum_{j=1}^{n} S(i,j) \tag{14}$$

$$S(i,j) = \frac{e^{-\|x_i - x_j\|^2}}{t}$$

$$Laplacian\_matrix(L) = D - S$$

It is well-known that constructing the Laplacian graph is computationally expensive, particularly when the number of features is high (He et al., 2005) .

2.2.15. Mutual information

Mutual Information was initially proposed by Shannon in 1948 (Shannon, 1948). This method is a univariate and supervised feature weighting technique. Moreover, it calculates the mutual information between each feature and the target class label, then ranks the features accordingly and selects the best ones. In other words, this method quantifies the amount of information that two random variables convey about each other. Additionally, it has a symmetric structure $I(X;Y) = I(Y;X)$ and can detect nonlinear relationships between variables. Hence, it has become a very popular criterion (Battiti, 1994; François et al., 2007). The reason is that mutual information, unlike other methods, does not only handle linear dependencies (Doquire and Verleysen, 2011). The mutual information method has been successfully adopted in filter feature selection methods to assess both

the relevance of a subset of features in predicting the target variable and their redundancy with respect to other variables (Beraha et al., 2019). Mutual information can be calculated using the formula in equation 15 (Cover, 1999):

$$Mutual\_Information(X,Y)$$
$$= \sum_{x} \sum_{y} p(x,y) \log \frac{p(x,y)}{p(x) * p(y)} \tag{15}$$

Here, X and Y represent two random features or variables, with $p(x)$ and $p(y)$ being the probability density functions and $p(x,y)$ the joint probability density function (Kannan and Ramaraj, 2010; Vergara and Estévez, 2014). Mutual Information is a fundamental method for evaluating how much information is associated between two features. It is defined as the difference between the sum of marginal entropies and the joint entropy. For completely independent objects, mutual information is always zero (Singh et al., 2014). A prediction or classification model aims to reduce uncertainty in the output, the dependent variable. As mentioned above, it is a good criterion for assessing the relevance of a set of features, a simplified prediction model. Naturally, it measures the uncertainty of the output due to knowledge of the inputs (Rossi et al., 2006).

2.2.16. Euclidean distance

The Euclidean Distance is a widely employed metric for gauging the similarity or dissimilarity between features, denoting the straight-line distance between two points within the feature space. This distance measure finds extensive application in various machine learning and data mining algorithms to quantify the distance or similarity between features (Suebsing and Hiransakolwong, 2009). The mathematical expression for the Euclidean Distance between two points is given by the formula in equation 16 (Ladha and Deepa, 2011):

$$Euclidean\_Distance(x,y) = \sqrt{\sum_{i=1}^{n} (x_i - y_i)^2} \tag{16}$$

Here, x and y are feature vectors, x_i and y_i represent the $i-th$ components of vectors x and y, respectively, and n is the dimensionality of the feature vectors (i.e., the number of features). A smaller Euclidean Distance suggests similarity between two vectors, whereas a larger Euclidean Distance suggests dissimilarity. This metric is especially valuable for assessing the proximity or separation of clusters or data points within the feature space (Ladha and Deepa, 2011).

2.2.17. Cramer's V test

The chi-square test is a widely recognized method employed to examine associations between variables, demonstrating efficacy in the domain of feature selection (Lu and Weng, 2007). However, its sensitivity to sample size is a well-documented limitation. To address this issue, researchers often turn to Cramer's V test, a prominent nominal technique used to quantify the strength of relationships between variables. Notably, Cramer's V is advantageous as it remains unaffected by sample size variations, making it particularly valuable in scenarios where statistical significance in chi-square

results may be attributed to large sample sizes rather than genuine associations between variables. As such, Cramer's V test serves as a reliable tool for assessing the degree of relationship between target and predictor variables. The calculation of Cramer's V value is determined by the formula in equation 17 (Martínez Casasnovas et al., 2008):

$$V = \sqrt{\frac{x^2}{N * (k-1)}} \qquad (17)$$

Here, Cramer's V value is derived from the chi-square (x^2) statistic and is calculated based on the total number of observations (N) and the number of categories (k) in the features. This value ranges between 0 and 1, where a higher value signifies a stronger relationship between the categorical variables. In feature selection, features exhibiting higher Cramer's V values are generally deemed more significant and prioritized over others (Martínez Casasnovas et al., 2008).

2.2.18. Markov blanket filter

The concept of the Markov Blanket, originating from Pearl's seminal work in 1988 (Pearl, 1988), serves as a fundamental component in probabilistic graphical modeling. The Markov Blanket Filter, an essential tool for feature selection, identifies a subset of variables crucial for maintaining the conditional independence of a target variable within a probabilistic framework. For a variable X_i, its Markov blanket includes directly connected variables that influence or are influenced by X_i, encompassing both parents and children nodes within a graphical model. This blanket, defined as $MB(X_i)$, plays a pivotal role in Bayesian networks and graphical models by encapsulating the minimal set of variables needed to predict X_i given all others in the network (Tsamardinos et al., 2003; Tsamardinos et al., 2003). The mathematical definition of the Markov blanket for the variable X_i, is expressed as in equation 18:

$$MB(X_i) = Pa(X_i) \cup Ch(X_i) \cup Pa(Ch(X_i)) \qquad (18)$$

Here, the Markov blanket $MB(X_i)$ of X_i comprises its parents $Pa(X_i)$, its children $Ch(X_i)$, and the parents of its children $Pa(Ch(X_i))$. This concept is instrumental in depicting the independence relationships within Bayesian networks and serves as a tool in feature selection methodologies (Koller and Sahami, 1996; Shen et al., 2008).

2.2.19. Kruskal-Wallis test

The Kruskal-Wallis test is a supervised, univariate, non-parametric feature selection method that assesses whether two or more classes have equal medians and provides a corresponding value. In essence, this method is a cost-effective and straightforward feature selection technique with lower computational overhead. A value close to zero indicates discriminatory power of the feature, effectively selecting features containing discriminatory information while discarding others. Similar to other statistical tests, the Kruskal-Wallis test computes a test statistic and compares it with a critical value to determine significance (Saeys et al., 2007; Ali Khan et al., 2014). The formula used to apply the Kruskal-Wallis test is as in equation 19 (Naik and Rangwala, 2016):

$$kruskal\_wallis = (N - 1)\frac{\sum_{i=1}^{L} n_i(\bar{r}_i - \bar{r})^2}{\sum_{i=1}^{L}\sum_{j=1}^{n_i} n_i(r_{ij} - \bar{r})^2} \qquad (19)$$

Here, n_i represents the number of examples in class i, r_{ij} denotes the ranking of example j in class i, and $\bar{r}$ indicates the average ranking across all examples.

2.3. Dataset

In this study, we utilized the breast cancer dataset to evaluate the performance of the pyallffs library we developed. The dataset consists of 30 features associated with breast cancer, excluding identifiers and diagnosis labels. These features are employed to forecast the occurrence of breast cancer in individuals. You can freely access the dataset on Kaggle using the following link: https://www.kaggle.com/datasets/yasserh/breast-cancer-dataset.

2.4. How to Use pyallffs Library?

In this study, we introduce the pyallffs library, which provides a convenient way to apply 19 different feature selection methods to your datasets for rapid identification of the most important features. This library is designed to streamline the process of feature selection by offering a comprehensive suite of methods that can be easily adapted to various datasets. By leveraging pyallffs, researchers and data scientists can efficiently identify critical features for predictive modeling and analysis.

To access the codes and utilize the functionalities of the pyallffs library, you can install the library using the command "pip install pyallffs". After installation, you can import all the mentioned methods into your workflow using "from pyallffs import *". Once imported, you can instantiate an object of interest from the available methods and feed your dataset into it. The library will then generate graphical outputs showcasing the most important features based on the chosen method.

For further information and to access the library's source code, please visit the following links:

https://pypi.org/project/pyallffs/

https://github.com/tohid-yousefi/pyallffs

https://www.kaggle.com/tohidyousefi/pyallffs

3. Results and Discussion

In our study, we applied our developed pyallffs library to perform feature selection using all filter methods on the breast cancer dataset, reducing the feature set from 30 to 10 features. We conducted predictive modeling using the random forest algorithm based on this reduced feature set. Additionally, we compared this approach to using all features without feature selection. The results, as depicted in Table 1 and Figure 4, demonstrate that employing our library for feature selection led to improved predictive performance compared to using the entire set of features. This outcome underscores the effectiveness of our pyallffs library in enhancing predictive accuracy through efficient feature selection, contributing to more robust and reliable modeling outcomes in breast cancer prediction.

Table 1. Metrics of all filter feature selection methods using pyallffs library

Feature Selection Methods	Accuracy	Precision	Recall	F1 Score	ROC AUC
Kruskal Wallis	0.982	1.000	0.953	0.976	0.977
Laplacian Score	0.982	0.977	0.977	0.977	0.981
Fisher Score	0.974	0.976	0.953	0.965	0.970
T-Score	0.974	0.976	0.953	0.965	0.970
Welch T-Score	0.974	0.976	0.953	0.965	0.970
Cramers V	0.965	0.976	0.930	0.952	0.958
Mutual Information	0.965	0.976	0.930	0.952	0.958
Without-Feature-Selection	0.965	0.976	0.930	0.952	0.958
Symmetric Uncertainty Coefficient	0.965	1.000	0.907	0.951	0.953
Information Gain	0.965	0.976	0.930	0.952	0.958
mRMR	0.965	1.000	0.907	0.951	0.953
Pearson Correlation	0.956	0.952	0.930	0.941	0.951
Gain Ratio	0.956	0.975	0.907	0.940	0.946
Markov Blanket	0.956	0.952	0.930	0.941	0.951
Relief	0.947	0.930	0.930	0.930	0.944
Maximum Likelihood	0.947	0.951	0.907	0.929	0.939
Least-Squares	0.947	0.951	0.907	0.929	0.939
Euclidean Distance	0.947	0.951	0.907	0.929	0.939
Chi-Squared	0.947	0.951	0.907	0.929	0.939
Relief-F	0.930	0.889	0.930	0.909	0.930
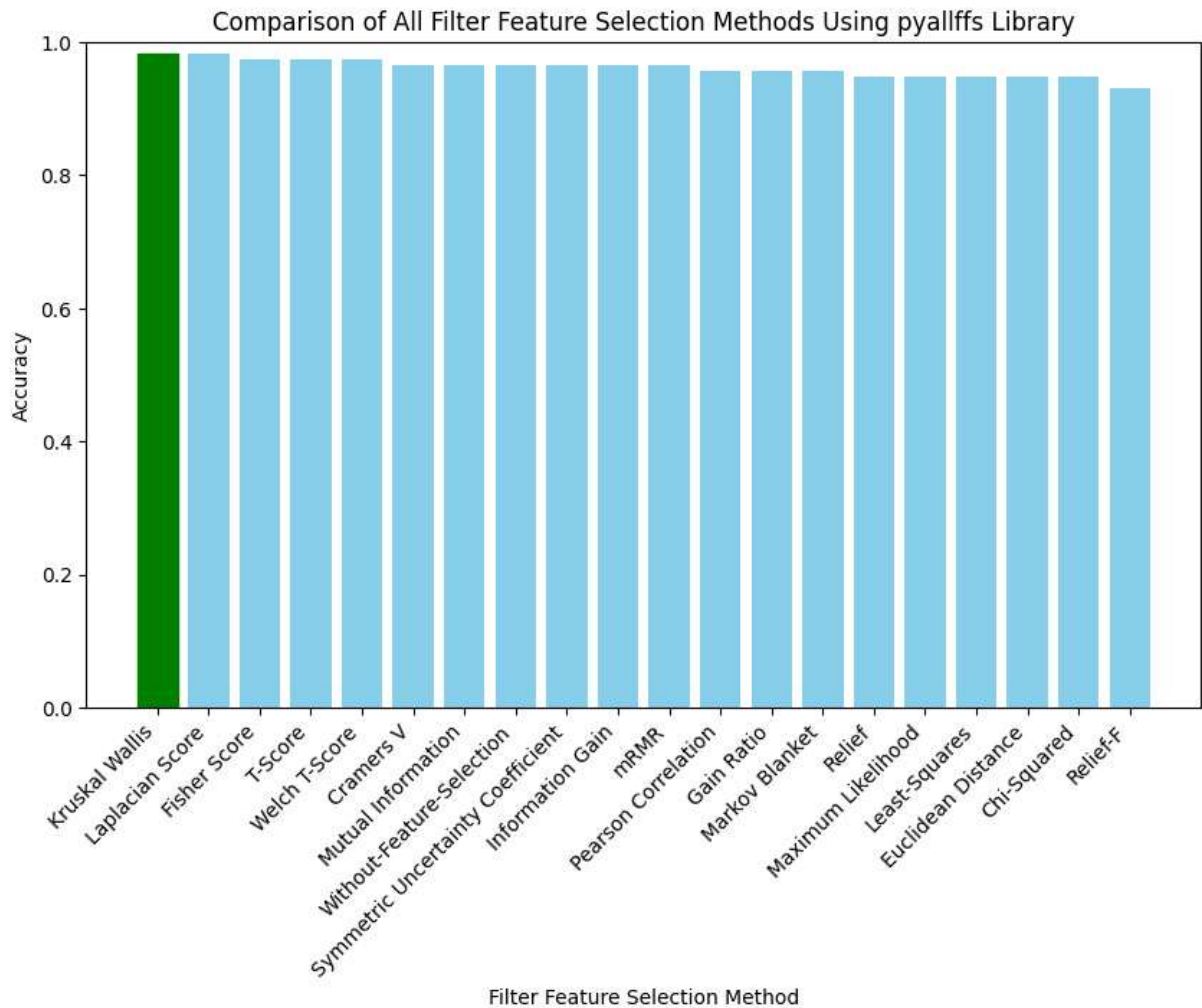
Figure 4. Comparison of all filter feature selection methods using PYALLFFS library.

In conclusion, our developed pyallffs library facilitated feature selection using all filter methods on the breast cancer dataset, followed by predictive modeling using the random forest algorithm. Comparing the performance of this approach with predictive modeling using all features without feature selection, our results clearly demonstrate superior predictive accuracy when leveraging the pyallffs library for feature selection. Therefore, we believe that the pyallffs library offers significant advantages to developers by consolidating all feature selection methods under a single framework, providing enhanced performance, and simplifying the process of model development and optimization in breast cancer prediction tasks. This consolidation not only improves efficiency but also supports more informed decision-making in machine learning workflows.

In the future, we plan to enhance the pyallffs library by integrating metaheuristic algorithms to optimize the parameters of feature selection methods, aiming to create a more comprehensive tool. Additionally, we intend to design a user-friendly interface and offer this library as a free product, making it accessible to a broader audience and further supporting the machine learning community.

Author Contributions

The percentage of the authors contributions is presented below. All authors reviewed and approved the final version of the manuscript.

	T.Y.	Ö.V.
C	100	100
D	100	
S		100
L	100	100
W	100	100
CR	100	100
SR	100	100
PM	100	100
FA	100	100

C=Concept, D= design, S= supervision, L= literature search, W= writing, CR= critical review, SR= submission and revision, PM= project management, FA= funding acquisition.

Conflict of Interest

The authors declared that there is no conflict of interest.

Ethical Consideration

Ethics committee approval was not required for this study because of there was no study on animals or humans.

References

Ali Khan S, Hussain A, Basit A, Akram S. 2014. Kruskal-Wallis-based computationally efficient feature selection for face recognition. Sci World J, 2014: 1-6.

Ali SI, Shahzad W. 2012. A feature subset selection method based on symmetric uncertainty and ant colony optimization. In: 2012 Inter Conference on Emerging Technologies, 8-9 October, 2012, Islamabad, Pakistan, pp: 1-6.

Arauzo-Azofra A, Benitez JM, Castro JL. 2004. A feature set measure based on relief. In: Proceedings of the fifth Inter conference on Recent Advances in Soft Computing, April 27-28, Copenhagen, Denmark pp: 104-109.

Battiti R. 1994. Using mutual information for selecting features in supervised neural net learning. IEEE Transact Neural Networks, 4: 537-550.

Belkin M, Niyogi P. 2001. Laplacian eigenmaps and spectral techniques for embedding and clustering. Adv Neural Inform Proces Systems, 2001: 14.

Beraha M, Metelli AM, Papini M, Tirinzoni A, Restelli M. 2019. Feature selection via mutual information: New theoretical insights. In: 2019 Inter Joint Conference on Neural Networks (IJCNN), 14-19 July 2019, Budapest, Hungary pp: 1-9.

Bolón-Canedo V, Sánchez-Marono N, Alonso-Betanzos A, Benítez JM, Herrera F. 2014. A review of microarray datasets and applied feature selection methods. Inform Sci, 282: 111-135.

Bryant FB, Satorra A. 2012. Principles and practice of scaled difference chi-square testing. Struct Equation Model: A Multidisciplin J, 3: 372-398.

Budak H, Taşabat SE. 2016. A modified t-score for feature selection. Anadolu Univ J Sci Technol A-Applied Sci Engin, 5: 845-852.

Carey JJ, Delaney MF. 2010. T-scores and Z-scores. Clinical Rev Bone Mineral Metabol, 8: 113-121.

Chandra B, Gupta M. 2011. An efficient statistical feature selection approach for classification of gene expression data. J Biomed Inform, 4: 529-535.

Chandrashekar G, Sahin F. 2014. A survey on feature selection methods. Comput Elect Engin, 1: 16-28.

Cover TM. 1999. Elements of information theory. John Wiley & Sons, London, UK, pp: 54.

Dash M, Liu H. 2003. Consistency-based search in feature selection. Artificial Intel, 1-2: 155-176.

Delacre M, Lakens D, Leys C. 2017. Why psychologists should by default use Welch's t-test instead of Student's t-test. Inter Rev Soc Psychol, 1: 92-101.

Ding C, Peng H. 2005. Minimum redundancy feature selection from microarray gene expression data. J Bioinform Comput Biol, 2: 185-205.

Doquire G, Verleysen M. 2011. Feature selection with mutual information for uncertain data. In: Data Warehousing and Knowledge Discovery: 13th Inter Conference, DaWaK 2011, Toulouse, France, August 29-September 2, pp: 330-341.

Esmael B, Arnaout A, Fruhwirth R, Thonhauser G. 2012. A statistical feature-based approach for operations recognition in drilling time series. Inter J Comput Inform Systems Industrial Manage Applicat, 4(6): 100-108.

Faulkner KG. 2005. The tale of the T-score: review and perspective. Osteoporosis Inter, 16, 347-352.

François D, Rossi F, Wertz V, Verleysen M. 2007. Resampling methods for parameter-free and robust feature selection with mutual information. Neurocomput, 70(7-9): 1276-1288.

Goswami S, Chakrabarti A. 2014. Feature selection: A practitioner view. Inter J Inform Technol Comput Sci (IJITCS), 6(11): 66

Gu Q, Li Z, Han J. 2012. Generalized fisher score for feature selection. arXiv preprint arXiv:1202.3725.

Hall MA, Holmes G. 2000. Benchmarking attribute selection techniques for data mining. IEEE Trans Knowl Data Eng, 15 (2003): 1437-1447.

Hall MA, Smith LA. 1998. Practical feature subset selection for machine learning. In: Computer Science Proceedings of the 21st Australasian Computer Science Conference ACSC'98, Perth, 4-6 February, Berlin, Germany, pp: 181-191.

He X, Cai D, Niyogi P. 2005. Laplacian score for feature selection.

Adv Neural Inform Proces Systems, 2005: 18.

He X, Niyogi P. 2003. Locality preserving projections. Adv Neural Inform Proces Systems, 2003: 16.

Hernández-Torruco J, Canul-Reich J, Frausto-Solís J, Méndez-Castillo JJ. 2014. Feature selection for better identification of subtypes of Guillain-Barré syndrome. Comput Math Methods Med, 2014: 432109.

Kabir MM, Islam MM, Murase K. 2010. A new wrapper feature selection approach using neural network. Neurocomput, 73(16-18): 3273-3283.

Kalousis A, Prados J, Hilario M. 2007. Stability of feature selection algorithms: a study on high-dimensional spaces. Knowledge Inform Systems, 12: 95-116.

Kannan SS, Ramaraj N. 2010. A novel hybrid feature selection via symmetrical uncertainty ranking based local memetic search algorithm. Knowledge-Based Systems, 23(6): 580-585.

Kass GV. 1980. An exploratory technique for investigating large quantities of categorical data. J Royal Stat Soc: Series C (Applied Stat), 29(2): 119-127.

Kira K, Rendell LA. 1992. The feature selection problem: Traditional methods and a new algorithm. In: Proceedings of the Tenth National Conference on Artificial intelligence, July 12–16, California, USA, pp: 129-134.

Kohavi R, John GH. 1997. Wrappers for feature subset selection. Artificial Intel, 97(1-2): 273-324.

Koller D, Sahami M. 1996. Toward optimal feature selection. In: ICML, 292.

Kononenko I. 1994. Estimating attributes: Analysis and extensions of RELIEF. In: European Conference on Machine Learning, April 6-8, Catania, Italy, pp:71-182.

Kraskov A, Stögbauer H, Grassberger P. 2004. Estimating mutual information. Physical Rev E, 69(6): 066138.

Kullback S, Leibler RA. 1951. On information and sufficiency. Annals Math Stat, 22(1): 79-86.

Ladha L, Deepa T. 2011. Feature selection methods and algorithms. Inter J Comput Sci Engin, 3(5): 1787-1797.

Liu H, Motoda H, Setiono R,Zhao Z. 2010. Feature selection: An ever evolving frontier in data mining. Feature Select Data Min, 2010: 4-13.

Lu D, Weng Q. 2007. A survey of image classification methods and techniques for improving classification performance. Inter J Remote Sensing, 28(5): 823-870.

Lun Gaoa TL, Yaob L, Wenb F. 2013. Research and application of data mining feature selection based on relief algorithm. Work, 2013: 515.

Mani K, Kalpana P. 2016. A review on filter based feature selection. Inter J Innov Res Computer Communicat Engin (IJIRCCE), pp: 2320-9801.

Martínez Casasnovas JA, Klaasse A, Nogués Navarro J, Ramos Martín MC. 2008. Comparison between land suitability and actual crop distribution in an irrigation district of the Ebro valley (Spain). Spanish J Agri Res, 6(4): 700-713.

Miao J, Niu L. 2016. A survey on feature selection. Procedia Comput Sci, 91: 919-926.

Naik A, Rangwala H. 2016. Embedding feature selection for large-scale hierarchical classification. In: 2016 IEEE Inter Conference on Big Data (Big Data), December 5-8, Washington DC, USA, pp: 1212-1221.

Nilsson R. 2007. Statistical feature selection: with applications in life science. Institutionen för fysik, kemi och biologi, Berlin, Germany, pp: 54.

Novaković J. 2016. Toward optimal feature selection using ranking methods and classification algorithms. Yugoslav J Operat Res, 21: 1.

Opitz D, Maclin R. 1999. Popular ensemble methods: An empirical study. J Artific Intel Res, 11: 169-198.

Pearl J. 1988. Probabilistic reasoning in intelligent systems: networks of plausible inference. Morgan kaufmann.

Peng H, Fan Y. 2015. Direct l_ (2, p)-Norm learning for feature selection. arXiv preprint arXiv: 1504.00430.

Priyadarsini RP, Valarmathi M, Sivakumari S. 2011. Gain ratio based feature selection method for privacy preservation. ICTACT J Soft Comput, 1(4): 201-205.

Radovic M, Ghalwash M, Filipovic N, Obradovic Z. 2017. Minimum redundancy maximum relevance feature selection approach for temporal gene expression data. BMC Bioinform, 18: 1-14.

Rossi F, Lendasse A, François D, Wertz V,Verleysen M. 2006. Mutual information for the selection of relevant variables in spectrometric nonlinear modelling. Chemometrics Intel Lab Systems, 80(2): 215-226.

Saeys Y, Inza I, Larranaga P. 2007. A review of feature selection techniques in bioinformatics. Bioinformatics, 23(19): 2507-2517.

Sedgwick P. 2012. Pearson's correlation coefficient. BMJ, 2012: 345.

Shannon CE. 1948. A mathematical theory of communication. Bell System Technic J, 27(3): 379-423.

Shardlow M. 2016. An analysis of feature selection techniques. J Univ Manchester, 2016: 1-7.

Shen J, Li L, Wong W-K. 2008. Markov Blanket Feature Selection for Support Vector Machines. AAAI, 2008: 696-701.

Singh B, Kushwaha N, Vyas OP. 2014. A feature subset selection technique for high dimensional data using symmetric uncertainty. J Data Analysis Inform Proces, 2(4): 95-105.

Suebsing A, Hiransakolwong N. 2009. Feature selection using euclidean distance and cosine similarity for intrusion detection model. In: 2009 First Asian Conference on Intelligent Information and Database Systems, April 1-3, Dong Hoi, Quang Binh, Vietnam, pp: 86-91.

Suzuki T, Sugiyama M, Sese J, Kanamori T. 2008. Approximating mutual information by maximum likelihood density ratio estimation. PMLR, 2008: 5-20.

Suzuki T, Sugiyama M, Tanaka T. 2009. Mutual information approximation via maximum likelihood estimation of density ratio. In: 2009 IEEE Inter Symposium on Information Theory, 28 June - 3 July, Seoul, Korea, pp: 463-467.

Tsamardinos I, Aliferis CF, Statnikov A. 2003. Time and sample efficient discovery of Markov blankets and direct causal relations. In: Proceedings of the ninth ACM SIGKDD Inter Conference on Knowledge Discovery and Data Mining, August 24-27, Washington, DC, USA, pp: 673-678.

Tsamardinos I, Aliferis CF, Statnikov AR, Statnikov E. 2003. Algorithms for large scale Markov blanket discovery. FLAIRS, 2003: 376-381.

Ugoni A, Walker BF. 1995. The Chi square test: an introduction. COMSIG Rev, 4(3): 61.

Urbanowicz RJ, Olson RS, Schmitt P, Meeker M, Moore JH. 2018. Benchmarking relief-based feature selection methods for bioinformatics data mining. J Biomed Inform, 85: 168-188

Vergara JR, Estévez PA. 2014. A review of feature selection methods based on mutual information. Neural Comput Applicat, 24, 175-186

Von Luxburg U. 2007. A tutorial on spectral clustering. Stat Comput, 17: 395-416.

Vora S, Yang H. 2017. A comprehensive study of eleven feature selection algorithms and their impact on text classification. In: 2017 Computing Conference, 18-20 July, Kensington, London, UK, pp: 440-449.

Welch BL. 1947. The generalization of 'STUDENT'S' problem when several different population varlances are involved.

Biometrika, 34(1-2): 28-35.

Witten IH, Frank E. 2002. Data mining: practical machine learning tools and techniques with Java implementations. Acm Sigmod Rec, 31(1): 76-77.

Witten IH, Frank E, Hall MA, Pal CJ, Data M. 2005. Practical machine learning tools and techniques. Data Mining, 2005: 403-413.

Xiang S, Nie F, Meng G, Pan C, Zhang C. 2012. Discriminative least squares regression for multiclass classification and feature selection. IEEE Transact Neural Networks Learn Systems, 23(11): 1738-1754.

Yousefi T, Aktaş ÖV. 2024. Predicting Customer Satisfaction with Hybrid Basic Filter-Based Feature Selection Method.

Yousefi T, Varlıklar Ö. 2024. Breast cancer prediction with hybrid filter-wrapper feature selection. Inter J Adv Nat Sci Engin Res, 8: 411-419.

Zheng A, Casari A. 2018. Feature engineering for machine learning: principles and techniques for data scientists. O'Reilly Media, London, UK, pp: 263.

IDENTIFICATION AND MOLECULAR CHARACTERIZATION OF A SERINE PROTEASE INHIBITOR GENE IN THE KHAPRA BEETLE *Trogoderma granarium*

Aslı DAĞERİ[1]*

[1]*Necmettin Erbakan University, Faculty of Science, Department of Molecular Biology and Genetics, 42090, Konya, Türkiye*

Abstract: Insect serine protease inhibitors (ISPIs) are essential for regulating various protease-mediated activities and play crucial roles in metabolism, metamorphosis, reproduction, and immunity. As a member of the ISPIs, serpins are recognized as the most essential protease inhibitor family in higher eukaryotes, encompassing a diverse array of biological functions. They are involved in the Toll pathway, the prophenoloxidase cascade, development, immunity, and reproduction in all insects. In this study, a serpin from the khapra beetle, *Trogoderma granarium* (Everts) (Coleoptera: Dermestideae) was identified and characterized using both transcriptomic and bioinformatics methodologies. The BGISEQ-500 platform was used to construct a cDNA library from *T. granarium*, which led to the identification and characterization of a novel Serine Protease Inhibitor gene (*TgSPI*). Sequence analysis confirmed TgSPI's classification within the serine protease inhibitor (SPI) superfamily. It has conserved features, including a Reactive Center Loop (RCL) close to the C-terminal end, which is essential for protease inhibition. Phylogenetic analysis and 3D structure modeling of TgSPI were performed using MEGA6 software and the Phyre2 Protein Fold Recognition Server, respectively. The phylogenetic analysis positioned TgSPI within a cluster of coleopteran insect SPIs (ISPIs), supporting its evolutionary lineage. Predicted tertiary structure modeling of TgSPI revealed similarity to conserpin in the latent state. This study provides foundational information on the evolutionary patterns and structural-functional aspects of TgSPI in the khapra beetle and highlights probable role of TgSPI as a promising target for further genetic and functional studies aimed at sustainable pest control strategies.

Keywords: Gene characterization, Insect serine protease inhibitor, Khapra beetle, Serpin

*Corresponding author: Necmettin Erbakan University, Faculty of Science, Department of Molecular Biology and Genetics, 42090, Konya, Türkiye
E mail: adageri@erbakan.edu.tr (A. DAĞERİ)
Aslı DAĞERİ   https://orcid.org/0000-0001-8564-9922

1. Introduction

Approximately one-third of all characterized proteolytic enzymes are classified as serine proteases, distinguished by the nucleophilic Serin residue at their active site (Hedstrom, 2002). Serine protease inhibitors (SPIs) are a superfamily of protease inhibitors essential for regulating various protease-mediated proteolysis activities in many organisms (Yang et al., 2017; Shakeel, 2021). These inhibitors play crucial roles in metabolism, metamorphosis, reproduction, and immunity (Yang et al., 2017; Li et al., 2022). Insect serine protease inhibitors (ISPIs) are categorized as canonical/non-canonical SPIs, α-macroglobulins, and serpins (Li et al., 2022).

Serpins are a superfamily of comparatively large proteins, generally 350–500 amino acids long with a molecular weight of 45–50 kDa, characterized by three β-sheets and seven to nine α-helices (Shakeel et al., 2019). They engage in a suicide inhibition mechanism within the Reactive Center Loop (RCL), leading to the irreversible and permanent inactivation of both the serpin and the protease (Meekins et al., 2017). Following cleavage between the P1 and P1' residues, the serpin experiences a swift conformational change, incorporating the N-terminal segment of the RCL into its core structure (Loebermann et al., 1984; Huntington et al., 2000). During this process, the protease, covalently attached to the RCL, is translocated, causing the distortion and inactivation of its active site; consequently, the resultant stable protease-serpin complex is then targeted for degradation (Stratikos and Gettins, 1999; Huntington and Carrell, 2001; Sanrattana et al., 2021).

Compared to higher mammals, insects possess a sophisticated innate immune system governed by continuous reaction cascades and developed through evolution to combat pathogen invasion. Serpins are crucial in modulating the proteolytic cascade, thereby enhancing the effectiveness of the insect's immune system when serine proteases are unnecessary (Liu et al., 2024). Distinct serpins have been identified and characterized from numerous insects, illustrating their critical roles in insect physiology. Shakeel (2021) reported that the fat body of *Helicoverpa armigera* (Lepidoptera: Noctuidae) is the primary expression site of serpin, with fluctuations observed during developmental stages. They also noted relatively high expression level during the prepupal stage, suggesting its prominent function at the wandering stage.

In another study, it was found that up-regulated serpin in *H. armigera* contributes to *Bacillus thuringiensis* (Bt) resistance by inhibiting trypsin and chymotrypsin activities (Zhang et al., 2022). Similarly, a Serpin from *Musca domestica* (Diptera: Muscidae) (MDSPI16) has been demonstrated to possess inhibitory activity against elastase and chymotrypsin (Tang et al., 2016). Furthermore, Serpin6 from *Bombyx mori* (Lepidoptera: Bombycidae) has been shown to regulate prophenoloxidase activity and the expression of antimicrobial proteins, suggesting its involvement in silkworm immune responses (Li et al., 2017).

The khapra beetle, *Trogoderma granarium* (Everts) (Coleoptera: Dermestideae) is a destructive quarantine pest that infests stored cereals and grain derivatives worldwide, particularly in South Asia and Africa, as well as in Mediterranean countries such as Türkiye and Cyprus (EPPO, 2024). It can enter long-term diapause, lasting up to eight years, which complicates management efforts. Furthermore, the development of insecticide resistance necessitates the exploration of alternative management methods. Specific genes expressed under various stress conditions, such as cold- and starvation-induced diapauses, have been reported to enhance the khapra beetle's tolerance, thereby identifying these genes as potential targets for pest management strategies (Dageri et al., 2023; Dageri, 2024).

To date, only a few serpin studies have been carried out in Coleoptera, such as *Tenebrio molitor* (Coleoptera: Tenebrionidae) and *Tribolium castaneum* (Coleoptera: Tenebrionidae) (Jiang et al., 2011), and no studies on any SPIs from *T. granarium* have been conducted yet. In *Tenebrio molitor*, 62 serine protease inhibitor (SPI) genes have been detected and classified into serpin, canonical SPI, and α-macroglobulins families, demonstrating roles in immunity, development, and digestion with stage-specific and tissue-specific expression patterns (Li et al., 2022). In the present study, a *serine protease inhibitor* gene (*TgSPI*) was identified from the cDNA library of the khapra beetle. Using various bioinformatics tools, the gene was characterized and found to belong to the serpin superfamily. Phylogenetic and tertiary structure analyses were conducted to provide a comprehensive understanding of this gene and its putative amino acid sequence.

2. Materials and Methods

2.1 RNA Isolation and cDNA Library Construction

RNA isolation was carried out from the khapra beetle using the NucleoZOL reagent (Machery-Nagel GmbH, Düren, Germany). The extracted RNA was evaluated using an Agilent 2100 Bioanalyzer instrument (Agilent Technologies Inc.) with the RNA6000 kit, which provided measurements of total RNA concentration, RNA integrity, 28S/18S ratios, and fragment length distribution. Transcriptome sequencing was conducted by Beijing Genomics Institute (BGI) China on a BGISEQ-500 platform sequencer following the manufacturer's instructions. Briefly, the sequencing process included mRNA

enrichment, RNA fragmentation and reverse transcription, end repair: "A" tailing and adaptor ligation, PCR amplification, denaturation and cyclization, sequencing on BGISEQ-500, sequencing reads filtering, *de novo* assembly and unigene functional annotation. Contigs were annotated via BLAST2Go suite (Conesa et al., 2005).

2.2. Bioinformatic Analysis

A full-length unigene cDNA encoding *serine protease inhibitor* gene (*TgSPI*) was detected from the transcriptome database of khapra beetle. BLASTX tool was used to search the similarity of *TgSPI* to other genes (https://blast.ncbi.nlm.nih.gov/Blast.cgi). To determine open reading frame of the nucleotide sequence of *TgSPI*, ORFFinder tool was utilized (https://www.ncbi.nlm.nih.gov/orffinder). The isoelectric point and molecular weight of the predicted protein were evaluted using pI/Mw tool (https://web.expasy.org/compute_pi/). SignalP-6.0 server was employed to detect predicted signal peptide (https://services.healthtech.dtu.dk/services/SignalP-6.0/). Putative phosphorylation residues were predicted using the NetPhos 3.1 server https://services.healthtech.dtu.dk/services/NetPhos-3.1/). Multiple sequence alignment of the ISPIs from different coleopteran insects was performed using Kalign (https://www.ebi.ac.uk/jdispatcher/msa/kalign) (Madeira et al., 2022). BoxShade tool was utilized to shade the conserved regions in amino acid sequences (https://junli.netlify.app/apps/boxshade/). Phyre2 was utilized to visualize the predicted secondary and tertiary protein structures (http://www.sbg.bio.ic.ac.uk/phyre2/html).

2.3. Phylogenetic Analysis

The evolutionary history was deduced using the Neighbor-Joining method (Saitou and Nei, 1987). The phylogenetic tree was drawn to scale in MEGA6 (Tamura et al., 2013), with branch lengths in the same units as the evolutionary distances used to infer it. The Poisson correction method (Zuckerkandl and Pauling, 1965) was used to calculate evolutionary distances, which were measured in the units of the number of amino acid substitutions per site. The positions including gaps and missing data were eliminated. The percentage of replicate trees is displayed next to branches (Felsenstein, 1985).

3. Results and Discussion

As members of the ISPI family, serpins are found in nearly all eukaryotes and are occasionally present in microorganisms such as fungi and bacteria (Irving et al., 2000). They play a crucial role in the innate immunity of insects (Liu et al., 2024). Thus far, the number of studied coleopteran serpins remains limited (Jiang et al., 2011). In this study, the full-length cDNA of the serine protease inhibitor gene (*TgSPI*) was identified for the first time from the cDNA library of the khapra beetle, containing a predicted ORF of 1910 nucleotides encoding 550 amino acids. *TgSPI* showed 59.30% nucleotide identity to *serine protease inhibitor 28Dc* from another coleopteran insect,

Zophobas morio (Coleoptera: Tenebrionidae). Predicted amino acid sequence of TgSPI has an approximate molecular weight of 61.23 and a pI of 8.75. It includes a signal peptide of 17 amino acid residues (MLLKVLIFLAFCGFLEG). The amino acid sequence of TgISP was analyzed, revealing the presence of putative phosphorylation sites. The sequence was found to include potential phosphorylated residues at tyrosine (Y), serine (S), and threonine (T) positions. This suggests that TgISP may undergo phosphorylation, which could play a significant role in its functional regulation and interaction within the cell. Identifying these putative sites provides valuable insight into the potential regulatory mechanisms governing TgISP activity and its involvement in cellular processes. Furthermore, the putative TgSPI possesses a domain belonging to the serine protease inhibitor (serpin) superfamily, confirming its classification within this superfamily (Figure 1).

Serpins are large proteins with conserved structures, consisting of three β-sheets and seven to nine α-helices, and include signature motifs such as a Reactive Center Loop (RCL) that attaches to the active protease site, as well as a predicted P1–P1' cleavage site (Shakeel, 2021). Following the P1-P1′ cleavage, the serpin goes through a substantial conformational shift caused by the insertion of the RCL into the central β-sheet A, leading to the inactivation of the protease through the distortion of its structure (Chamankhah et al., 2003). An RCL was found near the C-terminal end of the TgSPI, with the P1-P1′ residues being highly conserved among coleopteran species, including *T. granarium* (Figure 2). This conservation might suggest a vital functional role for the RCL in *T. granarium*, potentially related to its involvement in protease inhibition. Furthermore, the existence of these conserved structural elements in TgSPI not only verifies its classification as a serpin but also implies its probable significance in the physiology and immune response of *T. granarium*.

Figure 1. Deduced amino acid sequence of TgSPI. The predicted signal peptide is marked by an underscore. Serpin domain is shown in a blue box (66-544 residues). Putative phosphorylated tyrosine (Y), serine (S), and threonine (T) residues are indicated by blue-shaded frames.
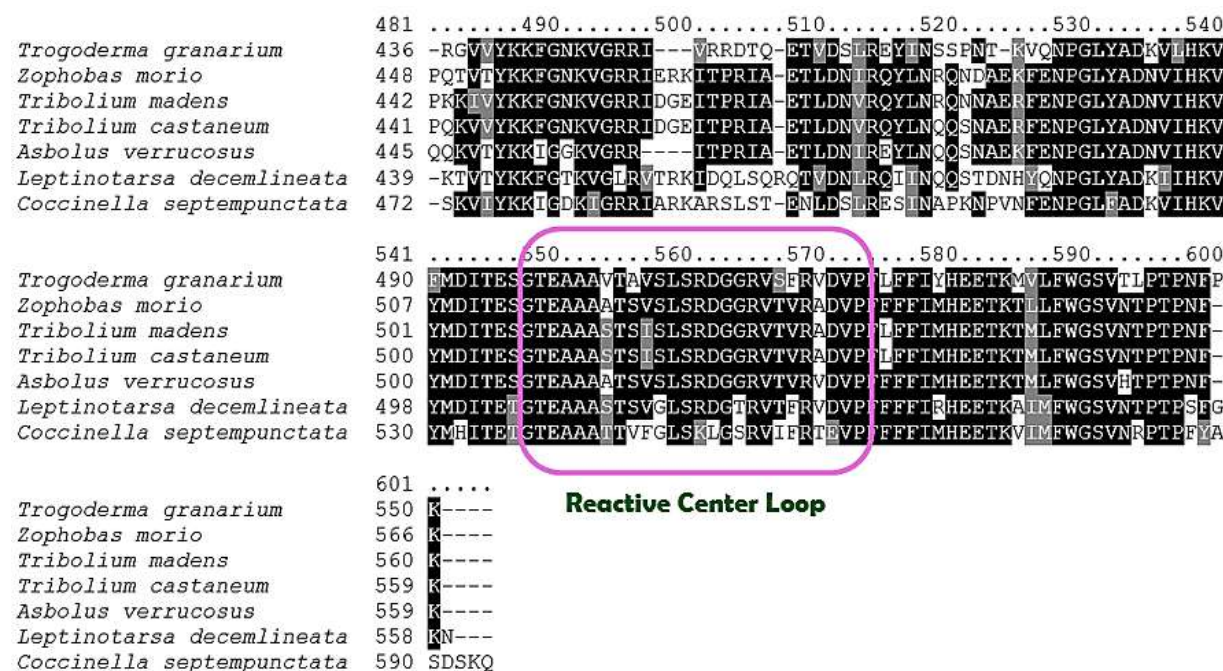
Figure 2. Multiple partial sequence alignment of the deduced amino acids of the coleopteran ISPIs, including TgSPI. The conserved Reactive Center Loop (RCL) was highlighted in a pink box.
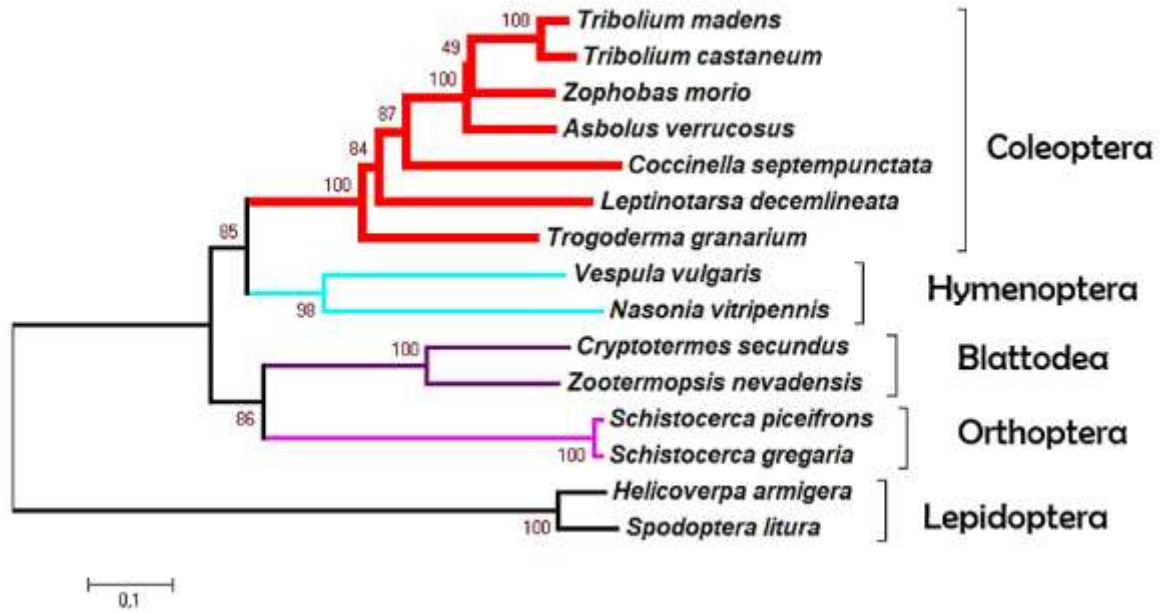
Figure 3. Phylogenetic tree of serine protease inhibitors from various insect species constructed using MEGA6. Each different order was indicated using different colors. GenBank Accession numbers of each species are as follow: *Tribolium madens* Serine protease inhibitor 28Dc XP_044254319.1; *Tribolium castaneum* Serine protease inhibitor 28Dc XP_008191787.1; *Zophobas morio* Serine protease inhibitor 28Dc XP_063914317.1; *Asbolus verrucosus* Serpin B12 RZC34043.1; *Coccinella septempunctata* Serine protease inhibitor 28Dc isoform X2 XP_044748515.1; *Leptinotarsa decemlineata* Serine protease inhibitor 28Dc-like XP_023026529.1; *Vespula vulgaris* Serine protease inhibitor 28Dc-like isoform X3 XP_050854871.1; *Nasonia vitripennis* Serine protease inhibitor 28Dc isoform X2 XP_001603946.3; *Cryptotermes secundus* Serine protease inhibitor 28Dc XP_023720181.1; *Zootermopsis nevadensis* Serine protease inhibitor 28Dc-like XP_021926289.1; *Schistocerca piceifrons* Serpin B6-like XP_047105853.1; *Schistocerca gregaria* Serpin B6-like XP_049854892.1; *Helicoverpa armigera* Serine protease inhibitor XP_021182965.2; *Spodoptera litura* Serine protease inhibitor-like XP_022837600.1.
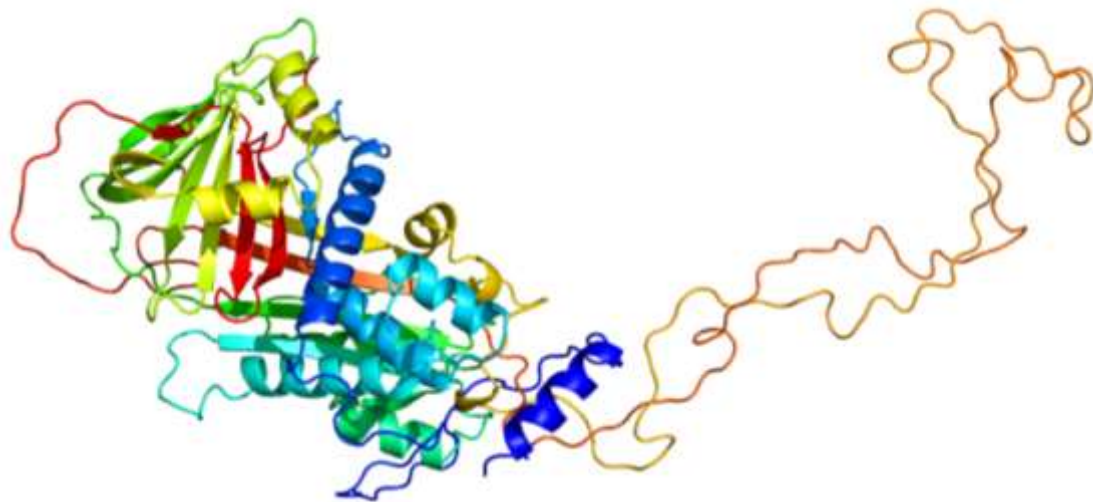
Figure 4. Predicted 3D formation of TgSPI.

The constructed phylogenetic tree of ISPIs consists of two main branches. One main branch comprises ISPIs from Lepidoptera, while the other contains ISPIs from Orthoptera, Blattodea, Hymenoptera, and Coleoptera, including the TgSPI. TgSPI clustered together with coleopteran ISPIs, indicating consistency with the BLAST result (Figure 3).

The tertiary structure of TgSPI was predicted using the "c5cdzyA_" model with 100% confidence and 66%

coverage (Figure 4). It showed highest identity to crystal structure of conserpin in the latent state with 37%.

Identifying and characterizing genes such as *TgSPI* is essential for pest management strategies. Saadati and Bandani (2011) found that incorporating serine protease inhibitors such as SBTI, TLCK, TPCK, and a combination of SBTI and TPCK into the diet of *Eurygaster integriceps* (Hemiptera: Scutelleridae) at concentrations of 1% and 4% of dietary protein resulted in notable detrimental

impacts on growth, development, and gut proteinases. This research highlighted the potential of these inhibitors as a pest management tool in *E. integriceps*, emphasizing the importance of understanding the functional roles of protease inhibitors in pest species. Han et al. (2014) identified and characterized three *serpins* in *Plutella xylostella* (Lepidoptera: Plutellidae), revealing their highest expression in the fat body and hemolymph of the 4th larval stage. They demonstrated that RNAi-mediated knockdown of these genes led to significantly lower expression levels and increased mortality and immune responses in the presence of destruxin A. In another study, knockdown of the *Spn5* gene by RNAi in *Drosophila melanogaster* (Diptera: Drosophilidae) resulted in a complete defect in wing unfolding and expansion in freshly eclosed mutant flies, despite not affecting early embryogenesis (Charron et al., 2008). These studies indicated the potential of genetic manipulation of *serpin* genes to enhance pest control strategies. Characterizing genes such as *TgSPI* can assist to discover novel targets for genetic manipulation, leading to the development of effective, sustainable pest control methods. This approach can not only reduce reliance on chemical pesticides but also minimize environmental impact by contributing to more sustainable agricultural practices. The limitations of this study include the absence of direct experimental validation of *TgSPI*'s functional role in *T. granarium*, such as through gene knockdown or overexpression studies, which would help confirm its involvement in protease inhibition and its impact on insect physiology. Additionally, the study does not account for environmental factors like diapause, temperature, humidity, or pathogen exposure that could influence *TgSPI* expression and function. These factors are essential for fully understanding the gene's role in the insect's immune response and its potential as a target for pest control strategies.

4. Conclusions

This study presents the first characterization, phylogenetic analysis, and predicted 3D structure of the putative TgSPI protein in *T. granarium*. This information could significantly contribute to understanding the evolutionary patterns of serpins in insects. Moreover, the *TgSPI* gene may emerge as a promising candidate for genetic control strategies such as Clustered Regularly Interspaced Short Palindromic Repeats (CRISPR) and RNA interference (RNAi). Further comprehensive studies are required to elucidate the mechanisms of action and regulatory pathways involving *TgSPI* in the physiology and immune response of *T. granarium*, potentially paving the way for novel pest management strategies.

References

Chamankhah M, Braun L, Visal-Shah S, O'Grady M, Baldwin D, Shi X, Hegedus DD. 2003. *Mamestra configurata* serpin-1 homologues: cloning, localization and developmental regulation. Insect Biochem Mol Biol, 33(3): 355-369.

Charron Y, Madani R, Combepine C, Gajdosik V, Hwu Y, Margaritondo G, Vassalli JD. 2008. The serpin Spn5 is essential for wing expansion in *Drosophila melanogaster*. Int J Dev Biol, 52(7): 933-942.

Conesa A, Götz S, García-Gómez JM, Terol J, Talón M, Robles M. 2005. Blast2GO: a universal tool for annotation, visualization and analysis in functional genomics research. Bioinformatics 21(18): 3674-3676. https://doi.org/10.1093/BIOINFORMATICS/BTI610

Dageri A, Kadir ML, Guz N, Ogreten A, Arshad M. 2023. The involvement of Antifreeze protein maxi-like and Cold-shock domain-containing protein genes in cold-induced larval diapause and cold-shock treatment of khapra beetle. J Stored Prod Res, 101: 102074.

Dageri A. 2024. Molecular characterization and expression analysis of six small heat shock protein genes in *Trogoderma granarium* during cold and starvation-induced larval diapause. J Stored Prod Res, 108: 102368.

EPPO. 2024. European and Mediterranean plant protection organization. EPPO global data base. *Trogoderma granarium*. URL=https://gd.eppo.int/taxon/TROGGA/distribution (accessed date: July 01, 2024).

Felsenstein J. 1985. Confidence limits on phylogenies: An approach using the bootstrap. Evolution 39: 783-791.

Han P, Fan J, Liu Y, Cuthbertson AG, Yan S, Qiu BL, Ren S. 2014. RNAi-mediated knockdown of serine protease inhibitor genes increases the mortality of *Plutella xylostella* challenged by destruxin A. PloS One, 9(5): e97863.

Hedstrom L. 2002. Serine protease mechanism and specificity.

Chem Rev, 102(12): 4501-4524.

Huntington JA, Read RJ, Carrell RW. 2000. Structure of a serpin–protease complex shows inhibition by deformation. Nature, 407(6806): 923-926.

Huntington JA, Carrell RW. 2001. The serpins: nature's molecular mousetraps. Sci Prog, 84(2): 125-136.

Irving JA, Pike RN, Lesk AM, Whisstock JC. 2000. Phylogeny of the serpin superfamily: implications of patterns of amino acid conservation for structure and function. Genome Res, 10(12): 1845-1864.

Jiang R, Zhang B, Kurokawa K, So YI, Kim EH, Hwang HO, Lee BL. 2011. 93-kDa twin-domain serine protease inhibitor (Serpin) has a regulatory function on the beetle Toll proteolytic signaling cascade. J Biol Chem, 286(40): 35087-35095.

Li B, Yu HZ, Ye CJ, Ma Y, Li X, Fan T, Xu JP. 2017. *Bombyx mori* Serpin6 regulates prophenoloxidase activity and the expression of antimicrobial proteins. Gene, 610: 64-70.

Li GY, Yang L, Xiao KR, Song QS, Stanley D, Wei SJ, Zhu JY. 2022. Characterization and expression profiling of serine protease inhibitors in the yellow mealworm *Tenebrio molitor*. Arch Insect Biochem Physiol, 111(3): e21948.

Liu T, Chu J, Wang Q, Wang Y, Zhang X, Liu D, Wang. 2024. Role of serpin-25 in prophenoloxidase activation and expression of antimicrobial peptide genes in the silkworm *Bombyx mori*. J Asia-Pac Entomol, 27(2): 102222.

Loebermann H, Tokuoka R, Deisenhofer J, Huber R. 1984. Human α1-proteinase inhibitor: crystal structure analysis of two crystal modifications, molecular model and preliminary analysis of the implications for function. J Mol Biol, 177(3): 531-557.

Madeira F, Pearce M, Tivey AR, Basutkar P, Lee J, Edbali O, Lopez R. 2022. Search and sequence analysis tools services from EMBL-EBI in 2022. Nucleic Acids Res, 50(W1): W276-W279.

Meekins DA, Kanost MR, Michel K. 2017, February. Serpins in arthropod biology. Sem Cell Devel Biol, 62: 105-119.

Saadati F. Bandani AR. 2011. Effects of serine protease inhibitors on growth and development and digestive serine proteinases of the Sunn pest, *Eurygaster integriceps*. J Insect Sci, 11(1): 72.

Saitou N, Nei M. 1987. The neighbor-joining method: A new method for reconstructing phylogenetic trees. Mol Biol Evol 4: 406-425.

Sanrattana W, Sefiane, T, Smits S, van Kleef ND, Fens MH, Lenting PJ, de Maat S. 2021. A reactive center loop–based prediction platform to enhance the design of therapeutic SERPINs. Proc Natl Acad Sci, 118(45): e2108458118.

Shakeel M, Xu X, De Mandal S, Jin F. 2019. Role of serine protease inhibitors in insect- host-pathogen interactions. Arch Insect Biochem Physiol, 102(3): 1-8. https://doi.org/10.1002/arch.21556

Shakeel M. 2021. Molecular identification, characterization, and expression analysis of a serine protease inhibitor gene from cotton bollworm, *Helicoverpa armigera* (Lepidoptera: Noctuidae). Braz J Biol, 81(3): 516-525.

Stratikos E, Gettins PG. 1999. Formation of the covalent serpin-proteinase complex involves translocation of the proteinase by more than 70 Å and full insertion of the reactive center loop into β-sheet A. Proc Natl Acad Sci, 96(9): 4808-4813.

Tamura K, Stecher G, Peterson D, Filipski A, Kumar S. 2013. MEGA6: Molecular Evolutionary Genetics Analysis version 6.0. Mol Biol Evol, 30: 2725-2729.

Tang Y, Wang Y, Pei Z, Li W, Zhang D, Liu L, Kong L, Liu S, Jiang X, Ma H. 2016. A serine protease inhibitor from *Musca domestica* larva exhibits inhibitory activity against elastase and chymotrypsin. Biotechnol Lett, 38(7): 1147-1153. https://doi.org/10.1007/s10529-016-2089-0

Yang L, Mei Y, Fang Q, Wang J, Yan Z, Song Q, Lin Z, Ye G. 2017. Identification and characterization of serine protease inhibitors in a parasitic wasp, *Pteromalus puparum*. Sci Rep, 7(1): 1-13. https://doi.org/10.1038/s41598-017-16000-5

Zhang C, Wei J, Naing ZL, Soe ET, Tang J, Liang G. 2022. Up-regulated serpin gene involved in Cry1Ac resistance in *Helicoverpa armigera*. Pestic Biochem Physiol, 188: 105269.

Zuckerkandl E, Pauling L. 1965. Evolutionary divergence and convergence in proteins. Edited in Evolving Genes and Proteins by V. Bryson and HJ. Vogel. Academic Press, New York, US, pp: 97-166.

BENT KAPAĞI ALTINDAN GEÇEN AKIMIN OLUŞTURDUĞU HİDROLİK SIÇRAMANIN KONUMUNUN DENEYSEL VE NÜMERİK OLARAK BELİRLENMESİ

Ali YILDIZ¹*

¹Konya Technical University, Faculty of Engineering and Natural Science, Department of Civil Engineering, 42250, Konya, Türkiye

Özet: Bent kapakları, rezervuardaki su seviyesini kontrol edilmesini ve kapasitenin üzerindeki fazla suyun belli bir debi ile kontrollü bir şekilde mansap tarafına aktarılmasını sağlarlar. Bir bent kapağının altından geçen akım, serbest veya batmış akım durumda olabilir. Serbest akım durumunda kapak altından sel rejimiyle çıkan akım, nehir rejimine geçişinde, kapak sonrasında bir hidrolik sıçrama meydana getirir. Oluşan hidrolik sıçramanın, etraftaki yapılara ve bulunduğu kanala zarar vermemesi için hidrolik sıçrama konumunun tam olarak bilinmesi gerekmektedir. Bu çalışmada dikdörtgen kesite sahip bir açık kanal sisteminde, hidrolik sıçrama oluşturmak için bent kapağı ve doğrusal savak kullanılmıştır. Oluşan hidrolik sıçramanın konumunun, debi ve kapak açıklığı ile değişimi incelenmiştir. Deneylerde iki farklı kapak açıklığı (e_1 =2,5 cm ve e_2 =5 cm) kullanılmış ve 34 farklı debi değeri için deneyler yapılmıştır. Hidrolik sıçrama konumunun kapak açıklığına bağlı olarak farklı oranlarda, debi ile lineer değişim gösterdiği görülmüştür. Ayrıca fiziksel deney düzeneklerinin, 2-boyutlu nümerik modelleri oluşturulmuş ve deneylerden elde edilen hidrolik sıçrama konumları ve akım derinlikleri, nümerik modeller ile karşılaştırılmıştır. Elde edilen sonuçlara göre nümerik model ile fiziksel model, e=2,5 cm kapak açıklığı için %92,22 ve e=5 cm kapak açıklığı için %95,69 oranında tutarlılık göstermişlerdir.

Anahtar kelimeler: Bent kapakları, Fluent, Hesaplamalı akışkanlar dinamiği, Serbest hidrolik sıçrama

Experimental and Numerical Investigation of the Position of Hydraulic Jump Formed by Flow Passing Under the Sluice Gate

Abstract: Sluice gates control the water level in the reservoir and transfer the excessive water above the reservoir capacity to the downstream side in a controlled manner with a certain discharge. The flow passing under a sluice gate can be in free or submerged flow conditions. In the case of free flow, when the flow regime is changed from subcritical to supercritical, hydraulic jump occurs after the gate. The location of the hydraulic jump must be known to prevent the damage caused by the hydraulic jump to hydraulic structures and the channel. In this study, a sluice gate and a linear weir were used to create a hydraulic jump in the rectangular open channel system. The relation of the position of the hydraulic jump with discharge and gate opening was examined. Two different gate openings (e_1 = 2.5 cm and e_2 = 5 cm) were used in the experiments and experiments were carried out for 34 different discharge values. It has been observed that the hydraulic jump position changes linearly with the discharge. In addition, 2-dimensional numerical models of the physical experimental setups were created, and the hydraulic jump positions and flow depths obtained from the experiments were compared with the numerical models. According to the results obtained from numerical model and physical model showed a consistency of 92.22% for e_1 = 2.5 cm gate opening and 95.69% for e_2 = 5 cm gate openings.

Keywords: Sluice gate, Fluent, Computational fluid dynamics , Free hydraulic jump

1. Giriş

Su insan, hayvan ve bitki yaşamı için önemli bir doğal kaynak olduğu için, suyun kullanımına ve yönetilmesine yönelik çalışmalar, insanlığın varoluşuyla birlikte başlamıştır. İnsan hayatı üzerinde büyük önem taşıyan suyun temininde ve kontrolünde barajlar ve hidrolik yapılar kullanılmaktadır. Suyun akışını geciktirerek, yönlendirerek ve önleyerek rezervuarlar ve göller oluşturan, farklı malzeme ve tiplerden oluşan büyük boyutlu engel yapıları baraj olarak adlandırılmaktadır. Barajlar ve su yapıları insanoğlu için çok önemli bir yere sahip olan suyun temini ve depolanması için kullanılmaktadır.

Baraj rezervuarındaki fazla su, dolusavaklar ile mansap tarafına güvenli ve kontrollü bir şekilde aktarılmalıdır. Enerji üreten barajlarda, en yüksek düşü yüksekliğini elde etmek için rezervuardaki su kotunun maksimum seviyede tutulması gerekmektedir. Seviyenin maksimum kotta tutulması gövde üzerine yerleştirilen bent kapakları ile sağlanabilmektedir. Bent kapakları altlarındaki net açıklığın değişmesi ile suyun dolusavak üzerinden kontrollü salınımı sağlanarak, yoğun yağış

sonrasında ani su baskınlarının mansap tarafına geçmesi engellenir. Serbest akım durumunda, bent kapağının altından sel rejiminde geçen akım, kapaktan sonra hidrolik sıçramaya neden olabilir.

Bent kapakları, açık kanallarda ve nehirlerde debiyi, akım derinliğini kontrol etmek ve su üzerinde yüzen nesneleri yakalamak için yaygın olarak kullanılır (Safranez, 1929). Kapak altından sel rejiminde gelen akım, dolusavak eteğinde ve nehrin mansap tarafında oyulmalara sebep olabilir, bu yüzden akımın nehir yatağına geçmeden enerjisinin kırılması gerekmektedir. Bu enerji kırınımını gerçekleştirmek için, dolusavakların uçlarına enerji kırıcı yapılar inşa edilir (Hager, 1992). Bu enerji kırıcı yapılar, akımın enerjisinin bir kısmının kırması için hidrolik sıçramanın oluşmasını sağlarlar ve suyun nehir rejiminde ($F_r<1$) mansap yatağına geçmesine izin verirler (Peterka, 1984). Hidrolik sıçrama oluşturmanın temel amacı enerjiyi kırılımını sağlamaktır. Bazı durumlarda, enerji kırınımını iyileştirmek amacıyla enerji kırıcı havuzların içerisine, bloklar, engeller ve eşikler yerleştirilir (Bradley ve Peterka, 1957). Hidrolik sıçramanın, sıçrama havuzlarının içindeki belirlenmiş bir alanda oluşturulması amaçlanır (Bakhmeteff ve Matzke, 1936). Enerji kırıcı havuzlar dışarısında oluşan kontrolsüz bir hidrolik sıçrama, nehir yatağı gibi hidrolik yapılar için tehlikeli olabilir (Cihan Aydın ve Ulu, 2017). Ayrıca, hidrolik sıçrama, suyun havalandırılması ve kimyasalların suya karıştırılması için de kullanılmaktadır. Hidrolik sıçramanın konumu (L), kırılan enerji miktarı (ΔE), sıçramadan önceki (y_1) ve sonraki (y_2) akım derinlikleri, hidrolik sıçrama hesabındaki en önemli parametrelerdir.

Hidrolik sıçrama ile ilgili ilk çalışmalarda araştırmacılar, hidrolik sıçramanın davranışını momentum denklemleriyle açıklanmaya çalışmışlardır (Bidone, 1819; Bélanger, 1828). Levy ve ark. (1927) yaptığı hidrolik sıçrama deneylerinde, hidrolik sıçrama esnasında oluşan enerji kaybını (ΔE) ve hidrolik sıçrama esnasında kimyasalların suya karışmasını incelemiştir. Rouse ve ark. (1959) hidrolik sıçramanın davranışını açıklamak için sıçrama esnasında oluşan ortalama hızları ve türbülansları deneysel ve teorik olarak incelemişlerdir. Silvester (1964) yatay dikdörtgen, üçgen, parabolik, dairesel ve yamuk kanallarda farklı Froude sayıları (F_r) için eşlenik derinlik, enerji kaybı oranı (%ΔE) ve sıçrama uzunluğu (L) için yarı ampirik analitik çözümler bulmuşlardır. Rajaratnam ve Subramanya (1968) pürüzsüz ve dikdörtgen kesitli açık kanallarda oluşturulan hidrolik sıçramalar için genelleştirilmiş bir su yüzeyi profili çıkarmışlardır. Hager ve Wanoschek (1987) üçgen kesitli kanaldaki hidrolik sıçramanın yüzey profilleri ve hız dağılımlarını belirlemiş ve sonuçlar dikdörtgen kesitli açık kanaldaki hidrolik sıçramalarla karşılaştırmışlardır. Araz ve Hanif (1991) düşük yatak eğimine sahip dikdörtgen bir kanalda oluşan hidrolik sıçramanın iki boyutlu sayısal modelini oluşturmak için Boussesq denklemlerini kullanmışlardır. Ead ve Rajaratnam (2002) farklı taban pürüzlülük değerlerine

sahip açık kanal üzerinde hidrolik sıçramaları deneysel olarak 4'ten 10'a kadar olan Froude sayıları (F_r) için incelemişlerdir. Habibzadeh ve ark. (2011) dikdörtgen bent kapakları altından geçen, batmış ve serbest akım durumlarında oluşan enerji kaybını (ΔE) hesaplamak için, teorik yöntemler kullanarak debi katsayısı (C_d) formülü çıkarmışlardır. Literatürde yapılan deneysel çalışmalar kullanılarak formülün doğruluğu test edilmiş ve debi katsayısından (C_d) elde edilen sonuçların deneysel veriler ile tutarlı sonuçlar verdiği görülmüştür. Bent kapaklarında oluşan enerji kaybı (ΔE) temel olarak kapağın geometrisinden etkilenmektedir. Cassan ve Belaud (2012) bent kapağı altından geçen akım üzerinde deneysel ve nümerik çalışmalar yapmışlardır. ANSYS-Fluent programı kullanılarak yapılan nümerik modeller 2 boyutlu olarak oluşturulmuş ve elde edilen analiz sonuçlarına göre k-ε RNG (Renormalization group) ve RMS (Reynolds Stress Model) türbülans modellerinin, standart k-ε ve k-ω türbülans modellerine göre daha iyi sonuç vermişlerdir. Gumus ve ark. (2016) dikdörtgen bir açık kanal üzerinde bent kapağı altından geçen akımın oluşturduğu batmış hidrolik sıçramayı deneysel ve nümerik olarak incelemişlerdir. Nümerik modelde 5 farklı türbülans modeli kullanılmış ve optimum doğrulukta sonuç elde etmek için farklı büyüklükteki meshler ile analizler yapılmıştır. Aydın ve Ulu (2017) bent kapaklarının mansap tarafına yerleştirilen dikdörtgen ve yarım daire şeklindeki taban engellerinin, batmış akım durumunda hıza olan etkilerini, nümerik ve deneysel olarak incelemişlerdir. Karami ve ark. (2020) bent kapağı altına yerleştirilen eşiğin şeklinin, yüksekliğinin ve konumunun, debi katsayısına (C_d) olan etkisini sayısal olarak araştırmışlardır. Kullanılan nümerik modeli doğrulamak için Akoz ve ark. (2009) tarafından yapılan deneyleri kullanmışlardır. Retsinis ve Papanicolaou (2020) 2,44 ile 5,38 arasında değişen Froude sayıları (F_r) için dikdörtgen kesitli bir açık kanalda oluşturulan hidrolik sıçramanın konumunu ve su yüzeyi profillerini, deneysel ve nümerik olarak modelleyip, sonuçlarını karşılaştırmışlardır. Daneshfaraz ve ark. (2021) serbest akım durumu için bent kapaklarını açık kanal sistemine dik eksenle 10, 20 ve 30 derece açı yapacak şekilde yerleştirerek, mansap tarafındaki oluşacak akımı FLOW-3D programını kullanarak nümerik olarak modellemişlerdir. Elde edilen hata oranlarına göre, RNG türbülans modeli, k-ε, k-ω ve LES (Large Eddy Simulation) türbülans modellerinden daha iyi sonuç vermiştir. Lazzarin ve ark (2023) barajlardaki kapak yıkılmalarının da sebepleri arasında bulunan geniş kapak açıklıkları (e) için deneysel ve nümerik çalışmalar yapmışlardır. Baraj yıkılmasını simüle etmek için, belirli bir kapak açıklığında (e) suyun, kapağın altından ani bir şekilde serbest bırakılmasıyla oluşan davranışı süreye bağlı olarak incelemişlerdir.

Bu çalışmada kapak altından geçen bir akımın oluşturduğu hidrolik sıçramanın debiye ve kapak açıklığına bağlı olarak değişen konumu incelenmiştir. 2 farklı kapak açıklığı (e_1=2,5 cm ve e_2=5 cm) ve toplamda

34 farklı debi değeri ile deneyler yapılmıştır. Değişen kapak açıklığının, hidrolik sıçramanın konumuna etkisini daha belirgin gözlemleyebilmek için, kapak açıklığı 2 kat olarak arttırılmıştır. Her kapak açıklığı (e) için, artan debi (Q) değerine bağlı olarak hidrolik sıçramanın mansaptaki konumu belirlenmiştir. Bütün debi (Q) değerleri için, nümerik modeller oluşturulmuş ve memba su seviyesi (H), sıçramadan önceki su derinliği (y1) ve hidrolik sıçramanın konumu (L) bakımından nümerik ve fiziksel modellerin sonuçları birbirleriyle karşılaştırılarak tartışılmıştır.
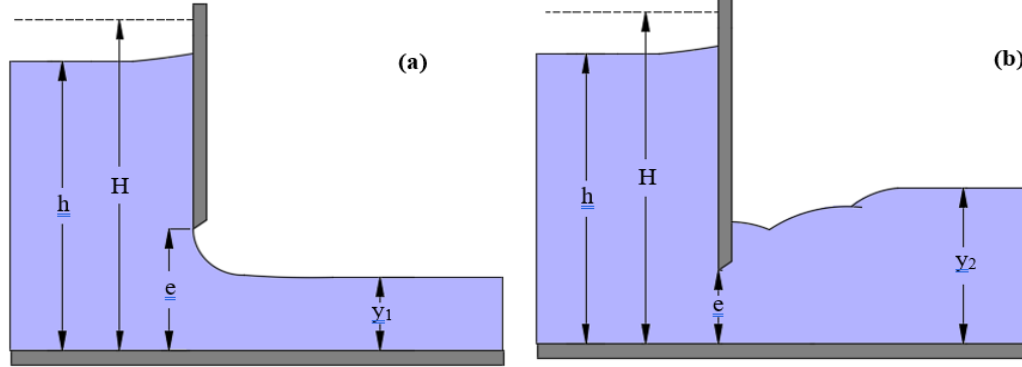
Şekil 1. Bent kapağının altında geçen serbest (a) ve batmış (b) akım durumları.

2. Materyal ve Yöntem

2.1. Bent kapakları ve hidrolik sıçrama

Kontrollü dolu savaklar genellikle bir bent kapağı vasıtasıyla kontrol edilirler. Bent kapaklarına, karşıdan bakıldığında, dikdörtgen kesitinde bir taban açıklığı sağlarlar. Bent kapakları, haznedeki suyun maksimum seviyede tutar ve gerektiği zaman hazneden suyu mansap tarafına tahliye ederler. Ayrıca bent kapağı, yüzen cisimlerin, buzun, sürüntü maddelerinin tutulması ve taşkın debisinin mansap tarafına geçmesini engellemek amacıyla da kullanılırlar. Bent kapaklarının altındaki açıklığa (e) ve memba tarafındaki su seviyesine bağlı olarak, altından geçen debi miktarı değişmektedir. Bir bent kapağının altından geçen akım iki durumda olabilir. Bunlar;

1-Serbest akım durumu: Kapağın altından geçen akım, sel rejiminde ve atmosfere açıktır (Şekil 1(a)). Akımın derinliği (y1) kapak açıklığından (e) daha küçüktür. Mansap tarafındaki akım, nehir rejimindeyse, kapaktan uzakta hidrolik sıçrama meydana gelebilir ve enerji kırınımı (ΔE, yük kaybı) gerçekleşir.

2-Batmış akım durumu: Akımın neden olduğu hidrolik sıçrama, bent kapağının bitişiğinde oluşur. Akımın derinliği (y2) kapak açıklığından (e) daha fazladır ve kapağın altından geçen akım atmosfere açık değildir (Şekil 1(b)). Hidrolik sıçrama oluşmaz fakat yüksek türbülanslar ve geri akış etkilerinden dolayı yük kaybı meydana gelir. Bent kapağındaki serbest ve batmış akım durumları Şekil 1'de gösterilmiştir. Kapak arkasındaki toplam memba su yükü (H), piyezometrik derinlik (h) ve hız yükünü ($V^2/2 \times g$) toplamına eşittir. (H=h+ $V^2/2 \times g$)

Bent kapağının altından geçen akımın debisi aşağıdaki eşitlik (1) ile belirlenir. Kapak altından geçen debi:

$$Q = C_d * e * b * \sqrt{2 * g * y_1} \tag{1}$$

Burada;

Q	: Debi (m³/sn)
C_d	: Debi katsayısı
e	: Kapak altındaki açıklık (m)
b	: Kapak genişliği (m)
y1	: Mansap su yüksekliği (batmış akım için y2) (m)
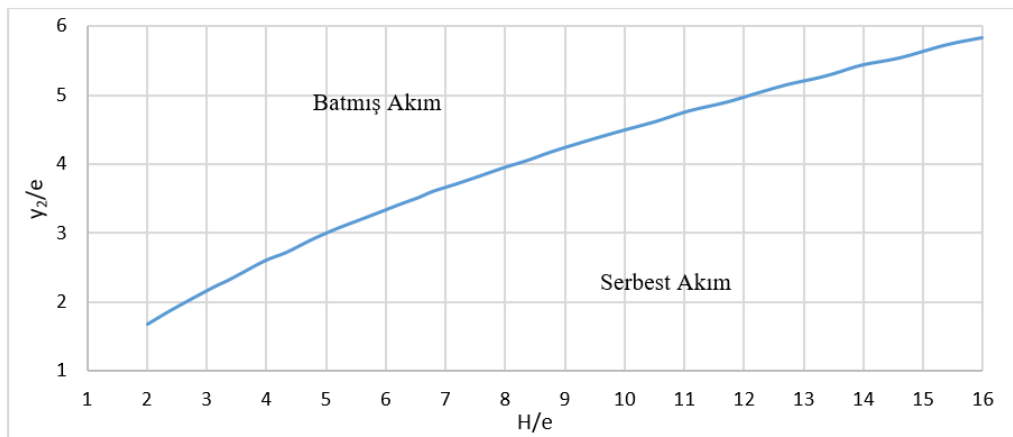
Şekil 2. Kapak altından geçen akımın batmış veya serbest akımda olma durumlarının H/e ve y2/e oranlarına bağlı olarak belirlenmesi (Rajaratnam ve Subramanya, 1968).

Bir kapak altından geçen akımın, serbest veya batmış olma durumu memba ve mansap su seviyelerine bağlı olarak Şekil 2' den belirlenebilmektedir. H/e ve y_2/e oranlarına bağlı olarak elde edilen değerin, eğrinin üstünde ve altında kalmasına bağlı olarak akımın batmış veya serbest akım durumunda olacağı belirlenir.

Serbest akım durumda debi katsayısı (C_d), memba su seviyesi (H) ve kapak açıklığına (e) bağlı iken batmış akım durumunda ise debi katsayısı (C_d) mansap su seviyesi (y_2) ve kapak açıklığına (e) bağlıdır. Ayrıca serbest akım durumda debi katsayısı (C_d) değerleri tek bir eğri üzerinden okunurken, batmış akım durumunda batmışlık derecesine bağlı olarak debi katsayısı (C_d) farklı eğrilerden okunur. Debi katsayısının (C_d), H/e ve y_2/e oranına bağlı olarak değişimi Şekil 3'te gösterilmiştir.
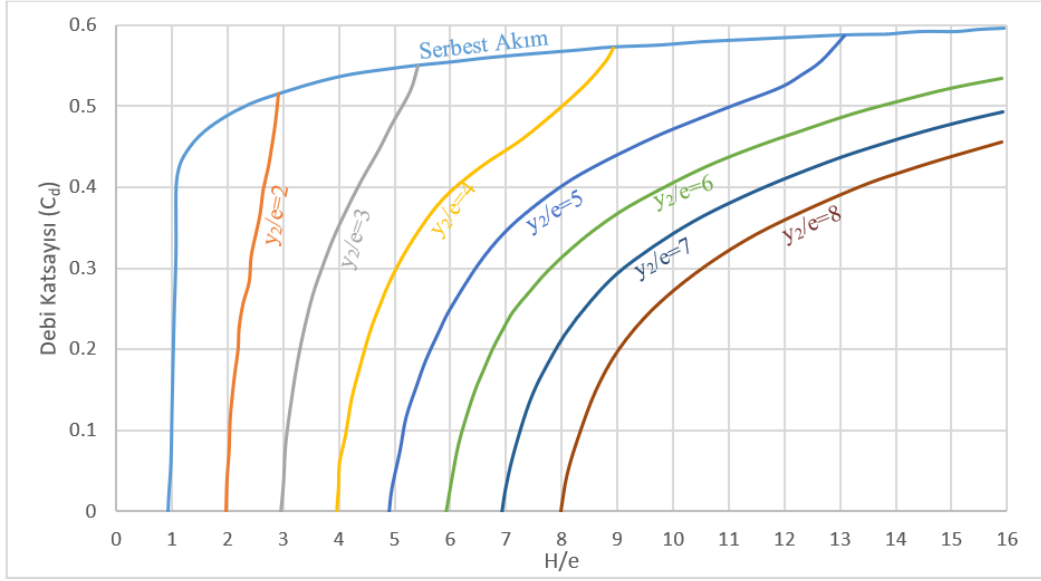
Şekil 3. Bent kapağı altından geçen batmış ve serbest akım durumlarına göre H/e ve y_2/e oranlarına bağlı olarak debi katsayısının (C_d) belirlenmesi (Swamee, 1992).

Açık kanaldaki bir akımın derinliği kısa bir mesafede önemli bir ölçüde değişiyorsa buna hızlı değişen akım (HDA) ve uzun bir mesafede daha yavaş bir değişim gösteriyorsa yavaş değişen akım (YDA) olmak üzere ikiye ayrılmaktadır. Hidrolik sıçrama hızlı değişen akım olarak (HDA) sınıflandırılır ve akımın sel rejiminden (Fr≥1), nehir rejimine (Fr≤1) geçerken türbülansa girmesiyle meydana gelir (Şekil 4). Açık kanallarda akımın rejimi Froude sayısının büyüklüğüne bağlı olarak belirlenmektedir. Froude sayısı atalet kuvvetlerinin, yer çekimi kuvvetlerine oranından hesaplanmaktadır ve $F_r = V/\sqrt{g*y}$ şeklinde formülüze edilmektedir. Burada, V hızı, g yerçekimi ivmesini ve y hidrolik derinliği ifade etmektedir. Atalet kuvvetleri, yer çekimi kuvvetlerinden büyük olduğu durumda Fr>1 olmaktadır ve bu sel rejimi olarak adlandırılır. Atalet kuvvetlerinin, yer çekimi kuvvetlerinden küçük olduğu durumda ise Fr<1 olmaktadır ve nehir rejimi olarak adlandırılmaktadır. Hidrolik sıçrama, akımın durumuna bağlı olarak, batmış ve serbest olmak üzere iki şekilde gerçekleşir (Kubrak ve ark., 2020).
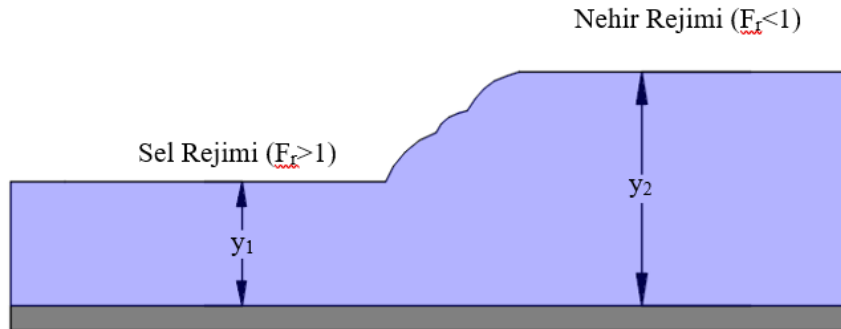
Şekil 4. Hidrolik sıçramanın genel şeması.

Hidrolik sıçrama açık kanallarda kontrolsüz olarak meydana geldiğinde büyük tehlike oluşturur çünkü, sıçrama esnasında büyük kuvvetler oluşur ve akımın derinliği bir anda artış gösterir. Kontrollü bir hidrolik sıçrama suyun havalanması ve enerji kırılımı (yük kaybı) açısından faydalıdır. Batmış hidrolik sıçramalarda, akımın sel ve nehir kısımlarının tam olarak belirlenememesinin yanında kırılacak enerji miktarı da

serbest sıçramada kullanılan formüllerle hesaplanamamaktadır. Batmış hidrolik sıçramaların hesapları genellikle deneysel ve nümerik çalışmalarla yapılmaktadır. Dolusavaklardan gelen yüksek enerjili akım nehir yatağında erozyona neden olabilir. Güçlü türbülanslar akarsu yatağının malzemesine zarar verip aşınmalara sebep olabilir. Dolusavaktan sel rejiminde gelen akımın kontrollü bir hidrolik sıçramaya maruz bırakılması, akımın enerjisini azaltacak ve suyun taşınması daha kolay ve güvenli olacaktır. Hidrolik sıçramadan önceki (y_1) ve sonraki akım derinliği (y_2) ve oluşan enerji kaybı (ΔE) eşitlik 2 ve 3 ile hesaplanmaktadır.

$$y_2 = \frac{y_1}{2} * (\sqrt{1 + 8 * Fr_1^2} - 1) \qquad (2)$$

$$\Delta E = \frac{(y_1 + y_2)^3}{4 * y_1 * y_2} \qquad (3)$$

Burada; y_1 hidrolik sıçramadan önceki akım derinliği, y_2 hidrolik sıçramadan sonraki akım derinliği, Fr_1 sel rejimindeki Froude sayısı ve ΔH hidrolik sıçramada kaybolan enerji miktarıdır.

2.2. Fiziksel Deney Düzeneği

Hidrolik yapıların tasarım aşamasında suyun davranışını gözlemlemek ve karşılaşılabilecek sorunları önceden belirlemek için laboratuvar ortamında ölçekli fiziksel modeller oluşturulur. Bu yüzden bir hidrolik yapıda, gerçekleşmesi beklenen hidrolik sıçramanın laboratuvar ortamında oluşturulacak ölçekli deney düzenekleri ile model testlerinin yapılması gerekmektedir. Bu çalışmada,

bent kapağı altından geçen bir akımın debiye ve kapak açıklığına bağlı olarak değişen konumunu incelmek için bir açık kanal sistemi üzerinde deneyler yapılmıştır (Şekil 5). Fiziksel deney düzeneklerinin hazırlandığı açık kanal sistemi 6,5 m uzunluğunda, 0,5 m derinliğinde ve 0,6 m genişliğindedir. Açık kanal sisteminin duvarları ve tabanı 1,2 cm kalınlığında lamine edilmiş temperli camdan yapılmıştır. Açık kanal sisteminin taban eğimi %0.007'dir. Açık kanalındaki akım, 1. hazneye su getiren boru sistemine bağlanmış iki adet pompa ile sağlanmaktadır. Pompaların boruya vereceği debi büyüklüğü, pompaların yönetildiği frekans konvertörü yardımıyla ayarlanmaktadır ve 1 ile 45 lt/sn arasında debi değerleri sabit olarak elde edilebilmektedir. Debi değerleri pompalardan gelen boru üzerine yerleştirilen 0.01 lt/s ölçüm hassasiyetine sahip ultrasonik debimetre ile ölçülmektedir. Açık kanal sisteminde suyun akışı, kanalın aralarına yerleştirildiği iki hazne yardımıyla sağlanmaktadır. İki adet paralel bağlanmış pompa, suyu 1. hazneden alarak borular vasıtasıyla 2. hazneye göndermektedir. 2. hazneye ulaşan ve maksimum seviye gelen su, taşarak açık kanal sistemine geçmekte ve kanal sonunda su tekrar 1. hazneye dökülmektedir.

Deneylerde kullanılan bent kapaklarında, e_1=2,5 cm ve e_2=5 cm olmak üzere 2 farklı net açıklık kullanılmıştır (Şekil 6). Bent kapakları 1 cm kalınlığında pleksiglas malzemeden imal edilmişlerdir. Suyun bent kapaklarının altından geçtiği kenar, düz kret şekline sahiptir ve kalınlığı kapağın kalınlığı olan 1 cm ye eşittir.

Şekil 5. Fiziksel deney düzeneği.
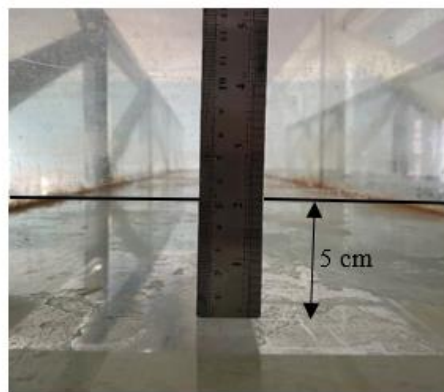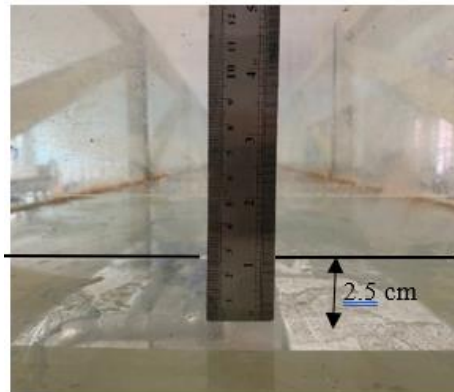
Şekil 6. Deneylerde kullanılan iki farklı kapak açıklığı e_1=2,5 cm ve e_2=5 cm.

Çalışmanın amacı hidrolik sıçramanın, debi ve kapak açıklığına bağlı olarak konumunun belirlenmesi olduğu için yapılan deneylerde serbest hidrolik sıçramanın oluşması amaçlanmıştır. Hidrolik sıçramanın oluşabilmesi için kapak altından geçen akımın rejiminin sel rejiminden nehir rejimine geçmesi gerekmektedir. Bu yüzden belirgin bir hidrolik sıçramanın olması amaçlanmıştır. Belirgin bir hidrolik sıçramanın oluşabilmesi için kapak altından geçen akımın rejiminin sel rejiminden nehir rejimine geçmesi gerekmektedir. Kapak altından sel rejiminde çıkan akım kanal sonuna kadar bir engel ile karşılaşmadığında rejim değiştirmemektedir. Rejim değişikliğini sağlamak için kanal sonuna 5 cm yüksekliğinde dikdörtgen doğrusal bir savak yerleştirilmiştir (Şekil 7). Bu savağın batık çalıştırılarak akım derinliğinin yükseltilip nehir rejiminin oluşması sağlanmıştır. Doğrusal savak, bent kapaklarından 450 cm ileriye yerleştirilmiştir. Bent kapağının arkasındaki toplam memba su derinliği (H), sıçramadan önceki derinlik (y_1) ve sıçramadan sonraki derinlik (y_2) olmak üzere 3 farklı noktada limnimeter ile derinlik ölçümü yapılmıştır.
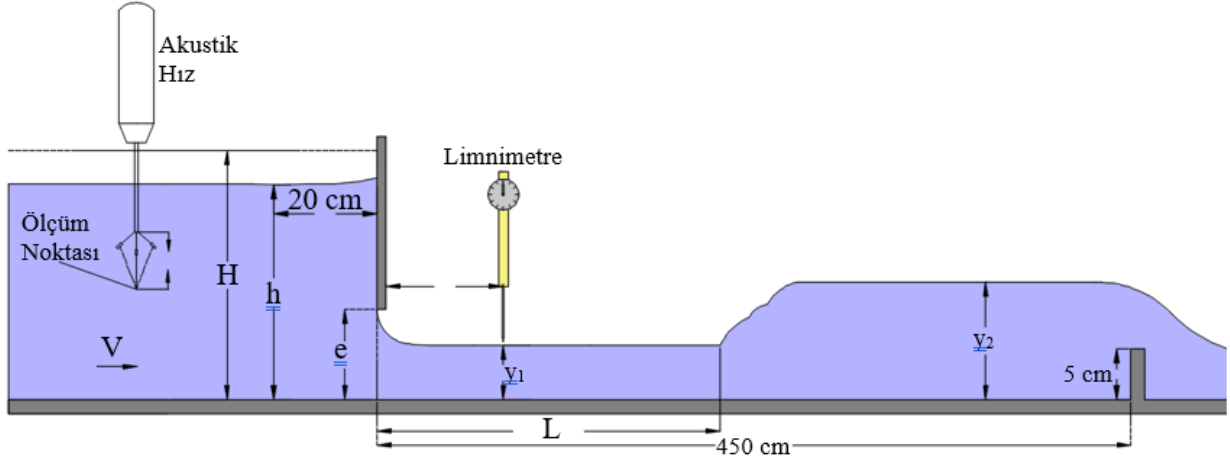
Şekil 7. Fiziksel deney düzeneğinin genel görünümü ve ölçüm yapılan noktalar.

Bent kapağının arkasındaki toplam memba su derinliği (yükü) (H), memba su derinliğinin (h) ve hız yükünün ($V^2/2 \times g$) toplamından elde edilmiştir. Kapağın arkasındaki piyezometrik derinlik (h) ve hız yük hesabında kullanılan hızlar, bent kapağının 20 cm gerisinde ölçülmüştür. Kapağın memba tarafı her ne kadar hazne gibi davransa da kapağa gelen suyun kapağa çarpmasından dolayı, kapağın hemen arkasında 7-10 cm bir mesafede kabarma meydana gelmektedir. Bu kabarmanın, derinlik ölçümünü etkilememesi için, ölçümler su yüzeyinin düz ve kabardığı 20 cm geride bir nokta seçilmiştir. Hız yükleri ($V^2/2 \times g$) hesabında kullanılan hız değerleri, akustik hız ölçer (ADV) ile ölçülmüştür. Akustik hız ölçer ile 3 eksende hız ölçümleri yapılabilmektedir fakat, akım +x yönünde aktığı için, hız yüklerinin ($V^2/2 \times g$) hesabında +x yönünde elde edilen hız değerleri kullanılmıştır.

2.3. Nümerik modelleme

Son yıllarda hidrolik problemlerin çözümünde, fiziksel modellenmenin yanında nümerik modelleme teknikleri de sıkça kullanılmaktadır (Gumus ve ark., 2016). Nümerik modelle elde edilen sonuçların güvenilirliğini belirlemek için çoğunlukla nümerik model ile fiziksel modelin sonuçları karşılaştırılır. Nümerik modelin doğruluk testinin yanı sıra bu karşılaştırmalar nümerik modelin kalibrasyonu için de kullanılmaktadır. nümerik ve fiziksel modeller arasında karşılaştırma yapılırken bunların hidrolik mühendisliği açısından değerlendirilmesi gerekmektedir.

Hesaplamalı Akışkanlar Dinamiği (HAD), akışkan hareketinin olduğu hidrolik problemlerinin çözümü için geliştirilmiş bir tür nümerik modelleme tekniğidir. HAD akışkan hareketinin mevcut olduğu birçok alanda kullanılır, akışkan-akışkan ve akışkan-katı etkileşimlerinin bulunduğu problemlerin çözümü yapılır. Açık kanal sisteminde oluşan hidrolik sıçramanın nümerik modellemesi ANSYS-Fluent programı ile yapılmıştır. Akışkanların, sonlu hacim yöntemi (VOF) yöntemi ve Navier Stokes denklemleri kullanarak, akışın basıncını, hızını ve su yüzeyi profili gibi değerleri elde etmek mümkündür. Akışın üzerinde hesaplar yapılırken, 3 boyutlu modellerde hacim, 2 boyutlu modellerde ise alan, daha küçük hacim ve alanlara ayrılır. Bu hacim ve alanlar mesh olarak adlandırılır. Bu meshler, üçgen, kare, dikdörtgen ve diğer şekillerde olabilmektedir. Meshin boyutuna ve sayısına bağlı olarak çözümün hassasiyeti ve elde edilen sonuçların doğruluğu artmaktadır. Dolayısıyla nümerik modelde seçilen meshin şekli, sayısı ve boyutları ağ oluşturmada önemlidir. ANSYS-Fluent kütle ve momentumun korunum denklemlerini çözer (Ansys Fluent, 2024).

Kütlenin korunumu veya süreklilik denklemi eşitlik 4 ile ifade edilebilir. Eşitlik 4 kütlenin korunumu denkleminin genel şekli olup sıkıştırılabilir ve sıkıştırılamaz akışlar için geçerlidir.

$$\frac{\partial \rho}{\partial t} + \nabla \times (\rho \vec{v}) = S_m \tag{4}$$

2 Boyutlu asimetrik geometriler için süreklilik denklemi eşitlik 5 ile verilir.

$$\frac{\partial \rho}{\partial t} + \frac{\partial}{\partial x}(\rho v_x) + \frac{\partial}{\partial r}(\rho v_r) + \frac{\rho v_r}{r} = S_m \qquad (5)$$

Ataletsel (ivmelenmeyen) bir referans çerçevesinde momentumun korunumu eşitlik 6 ile tanımlanır;

$$\frac{\partial}{\partial t}(\rho \vec{v}) + \nabla \times (\rho \vec{v} \vec{v}) = -\nabla P + \nabla \times (\vec{\tau}) + \rho \vec{g} + \vec{F} \qquad (6)$$

Burada; x eksenel koordinat, r radyal koordinatı, v_x eksenel hızı, v_r radyal hızı, ρ sıvının yoğunluğunu, S_m kütle değişimini, P statik basıncı, $\rho \vec{g}$ yerçekimi kuvveti, $\vec{F}$ dış kuvvet ve $\vec{\tau}$ stres tensörüdür.

Bent kapakları altından geçen akımın ve oluşan hidrolik sıçramanın nümerik modellenmesinde, fiziksel modelin bulunduğu ortam şartları ile aynı özellikteki sınır tabaka koşulları bilgisayar ortamında oluşturulmuştur. Deneylerle kullanılan debi (Q) değerlerinin aynısı, nümerik modele girilerek farklı kapak açıklıkları için analizler yürütülmüştür. Her analizin sonunda hidrolik sıçramanın konumu, akış derinlikleri ve su yüzeyi profilleri elde edilmiştir.

Fiziksel modelin nümerik modelde doğru şekilde temsil edilebilmesi için, akış alanının sınır tabaka koşullarının ve boyutlarının fiziksel deneylere uygun olarak programa girilmesi gerekmektedir. ANSYS-Fluent de akışın hareketinin VOF ve Navier Strokes denklemleri ile çözümü akış alanın içerisinde gerçekleştirilmektedir. Hidrolik sıçramanın oluştuğu, açık kanal sisteminin ANSYS-Fluent deki nümerik modelleri 2-boyutlu ve fiziksel deney düzeneği ile aynı ölçülerde oluşturulmuştur (Şekil 8). Analizlerde açık kanal akımını temsil etmesi için su ve havanın aynı anda bulunacağı şekilde 2 fazlı bir analiz yapılmıştır. Yapılan literatür çalışmalarına (Cassan ve Belaud, 2012; Daneshfaraz ve ark., 2021) göre k-ε RNG türbülans modeli bent kapaklarının nümerik modellenmesinde başarılı sonuçlar vermektedir. Bu yüzden analizlerde k-ε RNG türbülans modeli kullanılmıştır.

Akış alanının 4 yüzü bulunması sebebiyle, ana ızgara sisteminin dört farklı (+X, -X, +Y, -Y) sınır tabaka bulunmaktadır. Suyun kanala girdiği ve bent kapaklarının arkasındaki rezervuar görevi gördüğü memba sınır koşulu (-X), "mass flow inlet" debi girişi olarak tanımlanmıştır. Programda analizler iki boyutlu olarak yürütüldüğünde, akış alanının z eksenindeki uzunluğu yani kanalın genişliği 1 m olarak kabul edilmektedir. Girilecek debiler bu 1 m genişliğe göre yeniden hesaplanarak programa girilmesi gerekmektedir. Örneğin deneylerde 0,6 m kanal genişliğinde Q_{Deney}=31,20 lt/sn olarak ölçülen bir debi programa, Q_{Model}=31,20/0,6=52 lt/sn olarak girilmesi gerekmektedir. Suyun açık kanaldan çıktığı yüzey (+X), "pressure outlet" yani basınç çıkışı olarak tanımlanmıştır. Bu tabakadan hava ve su akış alanını engelsiz bir şekilde terk etmektedir. Kanalın taban yüzeyi "wall" duvar olarak tanımlanmıştır. Akış alanının üst yüzeyi (+Y) tanımlanırken iki farklı sınır tabaka koşulu kullanılmıştır. Bent kapağının arkasında bulunan ve hazne görevi görecek olan hacmin üstü "pressure outlet" olarak tanımlanırken, bent kapağından sonraki akış alanının üstü yüzeyi "wall" duvar olarak tanımlanmıştır. İki farklı tabaka kullanılmasının sebebi, su bent kapağının arkasında biriktikçe havanın akış alanını terk edeceği bir yüzey olmazsa sıkışacağıdır bu yüzden hava akış alanından çıkabilmesi için bu bölgenin üst yüzeyi yine basınç çıkışı olarak tanımlanmıştır. Bent kapakları, akış alanında 1 cm'lik boşluk bırakılarak tanımlanmıştır. Bu boşluğun etrafı duvar tanımlanarak bu açıklığın kapak gibi davranması sağlanmıştır. Nümerik analizde mesh şekli kare olarak ve boyutu Δx=Δy= 1 cm olarak seçilmiştir. Bu çalışmada optimum mesh boyutu belirlenmeden önce Grid Çözünürlük yöntemi kullanılarak mesh bağımsızlığı çalışması yapılmıştır. Tüm debi (Q) değerleri için nümerik modeller oluşturulmadan önce, bazı debi değerleri için 5 farklı mesh büyüklüğü (Δx=Δy=2,5, 2, 1,5, 1 ve 0,5 cm) ile analizler yürütülmüş ve sonuçlar deneylerle karşılaştırılarak ortalama hatalar hesaplanmıştır. Mesh boyutuna bağlı olarak elde edilen hata yüzdeleri Şekil 9'da gösterilmiştir. Nümerik model ile deneysel sonuçlar arasındaki hata yüzdesinin ne olması gerektiği tamamen hidrolik problemin fiziği ve önemi ile ilgilidir. Bu çalışmada bent kapaklarının nümerik modellerinden elde edilen sonuçların, deneysel modeller ile %10'luk bir hata payından daha az oranla tutarlı olması istenmektedir. Çünkü deneylerde akım yüksekliklerini ölçmek için kullanılan limnimetrenin hassasiyeti 0,1 cm'dir. Bu nedenle limnimetre ile yapılan ölçümlerde %10 hata payı olasılığı bulunmaktadır. Nümerik modelin başarılı olabilmesi için sonuçlarının istenen hata oranlarının altında olması, deneysel verilerle tutarlı olması ve problemin karmaşıklığına bağlı olarak analiz sürelerinin çok uzun olmaması gerekmektedir. 1 cm mesh boyutuna sahip analizin sonuçlandırılması 3 saat sürerken, 0,5 cm mesh boyutuna sahip modelin çözümlenmesi 9 saat sürmüştür. Bu nedenle 1 cm mesh boyutunun analizlerde kullanılması uygun görülmüştür (Şekil 9). Bütün analizlerde toplam 33315 mesh sayısı ile yapılmıştır. Bütün debi değerleri için toplam 34 adet nümerik model oluşturulmuştur.
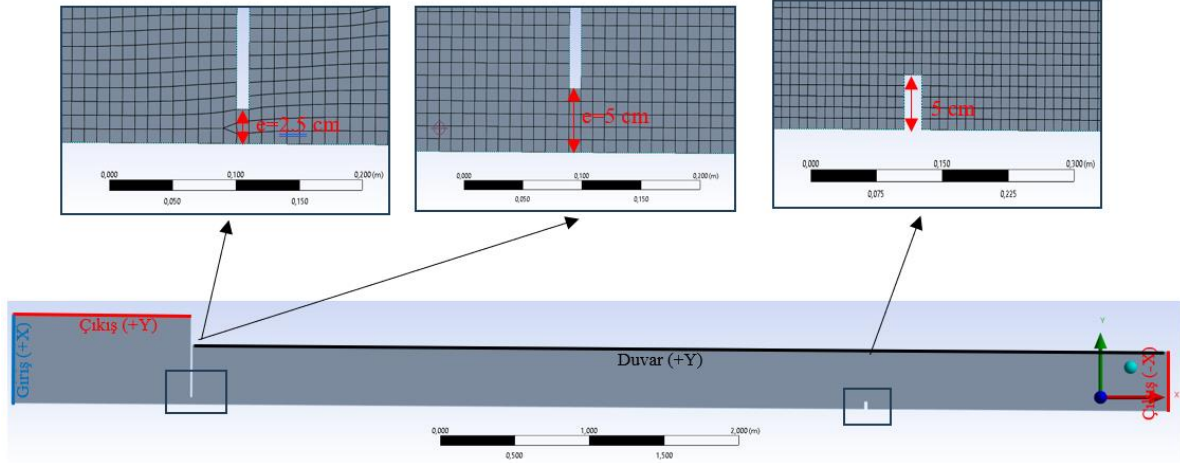
Şekil 8. Nümerik model analizlerinde kullanılan akış alanı ve özellikleri.
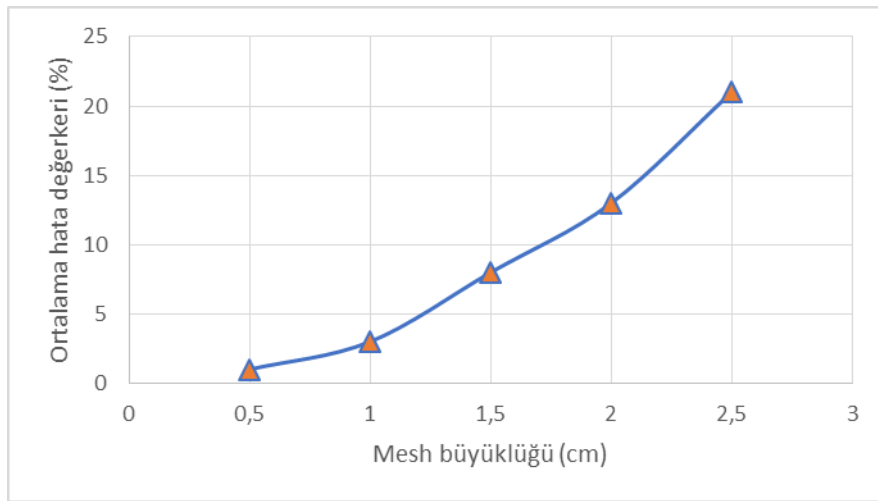
Şekil 9. Farklı mesh büyüklükleri için ortalama hataların hesaplanması.

3. Bulgular

Bu çalışmada, bir kapak altından geçen akımın, oluşturduğu hidrolik sıçramanın debiye ve kapak açıklığına bağlı olarak değişen konumu deneysel ve nümerik olarak incelenmiştir. Kapağın arkasındaki toplam memba akım derinliği (H), sıçramadan önceki derinlik (y_1) ve sıçramadan sonraki derinlik (y_2) olmak üzere 3 farklı noktada akım derinliği ölçülmüştür. Ayrıca, bu akım derinliklerine karşılık gelen hidrolik sıçrama konumları (L) ve debi (Q) değerleri de belirlenmiştir. Akım derinliği ölçümü yapılan noktalar ve fiziksel deney düzeneğinin genel şeması Şekil 7'de gösterilmiştir. Deneylerden elde edilen sonuçlar Tablo 1'de verilmiştir. Deneyler iki farklı kapı açıklığı (e_1=2,5 cm ve e_2=5 cm), 34 farklı debi (Q) değeri için tekrarlanmıştır. Çalışmada serbest hidrolik sıçramanın konum değişiminin araştırılması amaçlanmış olsa da, deneylerin başlangıcındaki batmış hidrolik sıçrama içinde veriler toplanmıştır. Hidrolik sıçramanın batmış veya serbest olma durumu Tablo 1'de belirtilmiştir.

Serbest hidrolik sıçramanın oluşmaya başladığı debi, kapak açıklığına bağlı olarak değişmektedir. e_1=2,5 cm kapak açıklığında serbest hidrolik sıçrama Q=14,73 lt/sn'de başlarken, e_2=5 cm kapak açıklığında Q=29,63 lt/sn debi değerinde gözlemlenmeye başlamıştır. Kapak altından geçen debi değeri arttıkça veya azaldıkça hidrolik sıçrama kapaktan uzaklaşmakta veya yakınlaşmaktadır ve bu mesafe L ile ifade edilmiştir. Bu durum hidrolik sıçramanın içsel atalet kuvvetlerinin ve momentumun dengelenmesinden kaynaklanmaktadır. İki farklı kapak açıklığına ve debi değerine bağlı olarak elde edilen hidrolik sıçrama konumları Şekil 10'da gösterilmiştir.

Oluşan serbest hidrolik sıçramanın konumu, kapak açıklığına ve debiye bağlı olarak değişmektedir. Farklı kapak açıklıklarında ve aynı konumdaki serbest hidrolik sıçramaların oluşması için gereken debi değerleri de farklı olmaktadır. Örneğin, e_1=2,5 cm kapak açıklığında, Q=20,20 lt/sn debi değerinde hidrolik sıçrama L=175 cm konumunda oluşurken, e_2=5 cm kapak açıklığında, L=176 cm konumunda hidrolik sıçramanın oluşması için gereken debi Q=36,54 cm lt/sn olmaktadır. Kapak açıklığı arttıkça, su seviyesine bağlı olarak artan statik basınç hidrolik sıçramanın daha ileri bir konumlarda oluşmasını sağlamaktadır. Şekil 10'dan görüleceği üzere hidrolik sıçramanın konum değişimi ile debi miktarı arasında

lineer bir bağlantı bulunmaktadır. Debi-hidrolik sıçrama konumu eğrileri üzerine lineer regresyon ile doğru belirlendiğinde bu doğruların, her iki kapak açıklığı içinde R^2 değeri 0,99 olmaktadır. Kapak açıklığı, hidrolik sıçramanın debiye bağlı olarak mansap tarafındaki ilerleme hızını da etkilemektedir. e_1=2,5 cm kapak açıklığında, bu oran ortalama olarak $(L_s-L_i)/(Q_s-Q_i)$=26,58 olurken, e_2=5 cm kapak açıklığında bu oran $(L_s-L_i)/(Q_s-Q_i)$= 22,73 olmaktadır. Bu durum artan debi ile birlikte hidrolik sıçramanın e_1=2,5 cm kapak açıklığında %17 daha hızlı ilerlediğini göstermektedir. Nümerik ve deneysel modellerden elde edilen hidrolik sıçrama konumlarının (L) karşılaştırılarak hata oranlarının hesaplanması Şekil 11'de gösterilmiştir. Deneylerden ve nümerik modelden elde edilen hidrolik sıçrama konumları (L), karşılaştırıldığında e_1=2,5 cm kapak açıklığı için %92,22 oranında bir tutarlılık gösterirken, e_2=5 cm kapak açıklığında %95,69 oranında

bir tutarlılık elde edilmiştir. e_1=2,5 cm kapak açıklığında en yüksek fark, Q=25,70 lt/sn için 16 cm olarak elde edilmiştir. e_2=5 cm kapak açıklığı için ise en yüksek fark Q=41,47 lt sn debi değeri için 19 cm olarak elde edilmiştir. Nümerik modelde hidrolik sıçramanın konumu daha net bir şekilde belirlenirken, yüksek miktardaki türbülanstan dolayı deneylerde bu konumu belirlemek daha zor olmaktadır. Yüksek debilerde oluşan farkın temel sebeplerinden bir tanesi de bu olmaktadır. Nümerik modellerden sonuçlar alınmadan önce sistem stabil oluncaya kadar analizler devam ettirilmiştir. Sistemin stabil hale gelmesi ise, akış alanının "outlet" yüzeyinden çıkan debinin sabit kalmasıyla ve giriş yani "inlet" yüzeyindeki debiye eşit olmasıyla anlaşılmaktadır. Bunun bir örneği olarak, e_2=5 cm ve Q=31,20 lt/sn için yapılan nümerik modelde "outlet" yüzeyinden zamana bağlı olarak çıkan debinin grafiği Şekil 12'de gösterilmiştir.

Tablo 1. e_1=2,5 cm ve e_2=5 cm kapak açıklığında elde edilen deney sonuçları

	Kapak Açıklığı e_1=2,5 cm						Kapak Açıklığı e_2=5 cm					
No	Q (lt/sn)	H (cm)	y_1 (cm)	y_2 (cm)	Sıçrama Durumu	L (cm)	No	Q (lt/sn)	H (cm)	y_1 (cm)	y_2 (cm)	Sıçrama Durumu	L (cm)
1	11,72	10,50	6,42	8,75	Batmış	-	1	17,47	9,55	7,95	10,25	Batmış	-
2	12,63	11,35	7,65	9,00	Batmış	-	2	19,54	10,40	8,35	10,75	Batmış	-
3	13,67	12,15	7,95	9,25	Batmış	-	3	21,55	11,35	8,75	11,20	Batmış	-
4	14,73	13,35	1,60	9,12	Serbest	20	4	23,66	12,35	8,90	11,65	Batmış	-
5	15,65	15,50	1,61	9,20	Serbest	54	5	25,60	13,25	8,95	11,95	Batmış	-
6	16,37	18,45	1,63	9,32	Serbest	80	6	27,58	14,35	7,05	12,35	Batmış	-
7	16,40	17,95	1,65	9,41	Serbest	85	7	29,63	15,55	3,10	12,01	Serbest	37
8	17,34	20,25	1,66	9,48	Serbest	110	8	31,60	17,45	3,12	12,70	Serbest	77
9	18,25	22,35	1,68	9,52	Serbest	130	9	32,58	18,40	3,17	13,02	Serbest	98
10	18,30	21,80	1,69	9,61	Serbest	125	10	33,55	20,45	3,25	13,35	Serbest	118
11	19,20	24,35	1,71	9,85	Serbest	145	11	34,53	21,45	3,42	13,40	Serbest	134
12	20,04	26,30	1,73	9,87	Serbest	175	12	36,54	22,35	3,55	13,85	Serbest	176
13	20,20	26,25	1,74	11,23	Serbest	165	13	37,45	23,05	3,61	14,75	Serbest	195
14	21,93	30,60	1,76	12,05	Serbest	232	14	37,54	23,45	3,66	13,70	Serbest	195
15	23,78	34,75	1,78	12,26	Serbest	270	15	38,45	24,45	3,72	14,02	Serbest	220
16	25,70	38,90	1,80	13,15	Serbest	320	16	39,49	25,35	3,75	14,52	Serbest	260
							17	40,53	26,65	3,81	14,85	Serbest	283
							18	41,47	27,85	3,85	15,10	Serbest	312
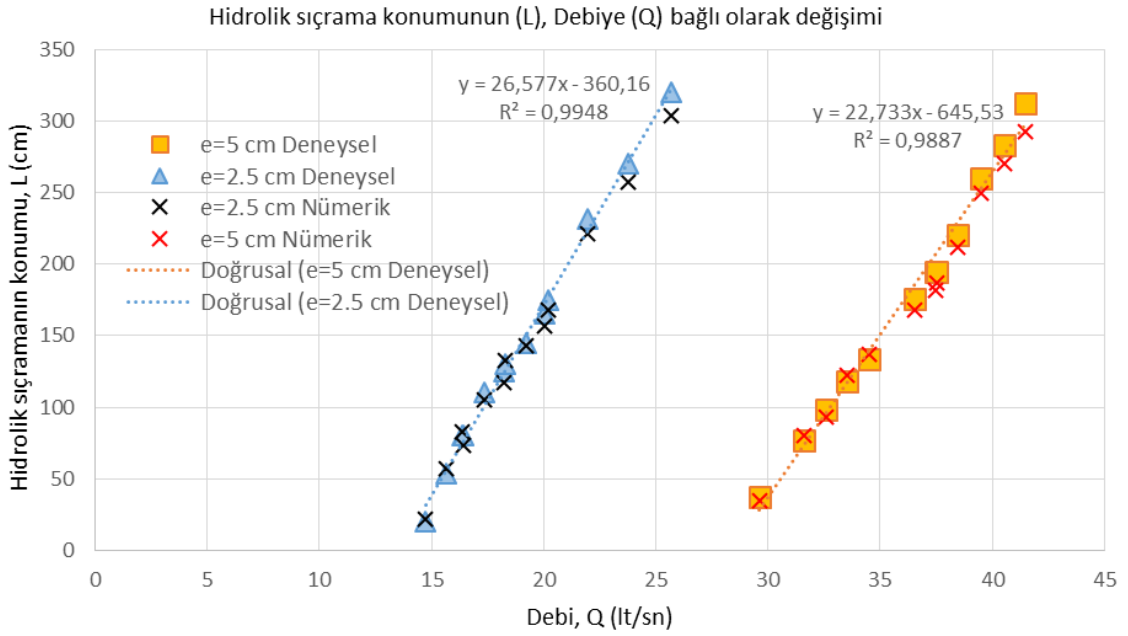
Şekil 10. e₁=2,5 cm ve e₂=5 cm kapak açıklıkları için elde edilen debi (Q) ve hidrolik sıçrama konumlarının (L) karşılaştırılması.
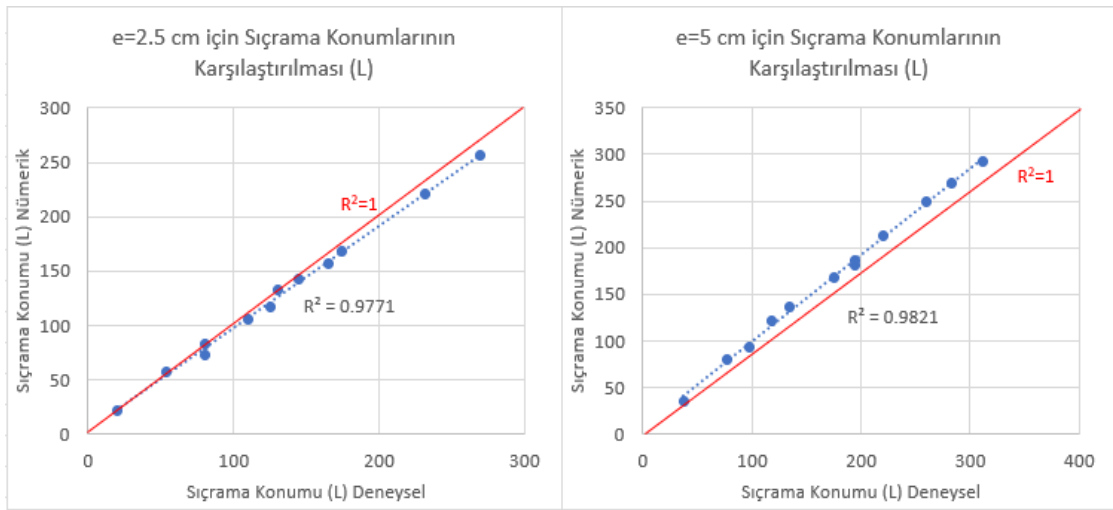
Şekil 11. e=2,5 cm ve e=5 cm için hidrolik sıçrama konumlarının (L) karşılaştırılarak hata oranlarının hesaplanması.
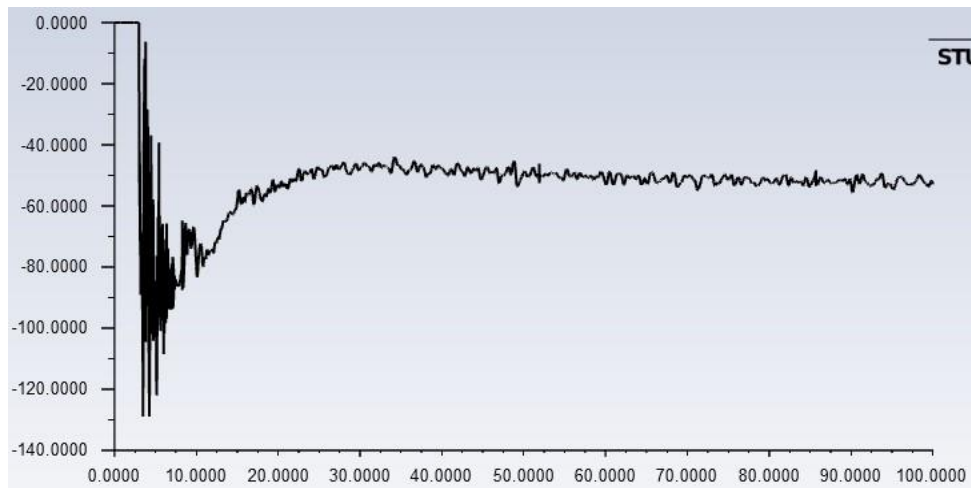
Şekil 12. e₂=5 cm ve Q=31,20 lt/sn (Q=52 lt/sn 2 boyuttaki 1 m genişlik) için yapılan nümerik analizlerde outlet debisinin zamana bağlı değişimi.

Çıkış debisinin sabitlenmesi ve hidrolik sıçramanın sabit yerde kalması için geçen süre analiz süresi 100 sn olarak belirlenmiştir. Programın 100 sn süresindeki bir analizi yapmak kapak açıklığına ve debi miktarına bağlı olarak 5-6 saat sürmektedir.

Bent kapağının memba tarafında bulunan ve kapak altından çıkan su için statik basıncı oluşturan, memba su seviyelerinin (H), iki farklı kapak açıklığı için karşılaştırılması Şekil 13'te gösterilmiştir. Nümerik modellerden elde edilen memba su seviyeleri de aynı grafik üzerinde Şekil 13'te verilmiştir. Artan debi (Q) miktarı ile su memba seviyesinin arasında lineer bir bağlantı olduğu görülmektedir. e_1=2,5 cm kapak açıklığında memba su seviyesinin(H), debi (Q) ile artış oranı $(H_s-H_i)/(Q_s-Q_i)$=2,30 olurken, e_2=5 cm kapak açıklığında bu oran $(H_s-H_i)/(Q_s-Q_i)$=0,99 olmaktadır. Artan debi değeri ile (Q), e_1=2,5 cm kapak açıklığında memba su seviyesi (H) artışı, e_2=5 cm kapak açıklığından %132 daha fazla olmaktadır. Memba su seviyesi karşılaştırmasında nümerik model ve deneyler %99 oranında tutarlılık göstermiştir. Hidrolik sıçrama öncesindeki su derinliklerinin (y_1) debiye bağlı olarak iki farklı kapak açıklığı için karşılaştırılması Şekil 14'te gösterilmiştir. Hidrolik sıçrama öncesindeki su derinliği kapak açıklığı tarafından sınırlanmaktadır ve bu derinlik

serbest hidrolik sıçramada kesinlikle kapak açıklığında fazla olamamaktadır. e_2=5 cm kapak açıklığında artan debi (Q) miktarı ile sıçrama öncesi su derinliği, e_1=2,5 cm kapak açıklığına göre 2,84 kat fazla artmaktadır.

Laboratuvarda yapılan hidrolik sıçrama deneyleri 3 boyutlu olmasına rağmen nümerik modeller 2 boyutlu olarak oluşturulmuştur. 2 boyutlu nümerik modeller ile analizler yapılırken, programın 2 boyutta kullandığı 1 m kanal genişliği dikkate alınarak debiler belirlenmiştir. Nümerik modeller ile deneysel veriler, hidrolik sıçramanın konumunun (L) belirlenmesi açısından %94 oranında tutarlı sonuçlar vermişlerdir. Ayrıca nümerik model ile fiziksel modelin su yüzeyi profili karşılaştırılmıştır. Görsel karşılaştırılmanın yapılmasındaki amaç, deneylerin ve nümerik modelin su yüzeyi profillerinin ne kadar tutarlı olduğunu belirlemektir. e_1=2,5 cm ve e_2=5 cm kapak açıklıklarında, Q=31,60 lt/sn ve Q=17,34 lt/sn debi değerleri için, nümerik model ve deneylerden elde edilen görsellerin karşılaştırılması Şekil 15'de gösterilmiştir. Nümerik model, fiziksel deney düzeneğinde olduğu gibi hidrolik sıçramayı başarılı bir şekilde analiz etmiştir. Nümerik modelde su, kapakların arkasında haznedeymiş gibi davranmakta ve kapak altından sel rejimi ile geçtikten sonra hidrolik sıçramaya sebep olmaktadır.
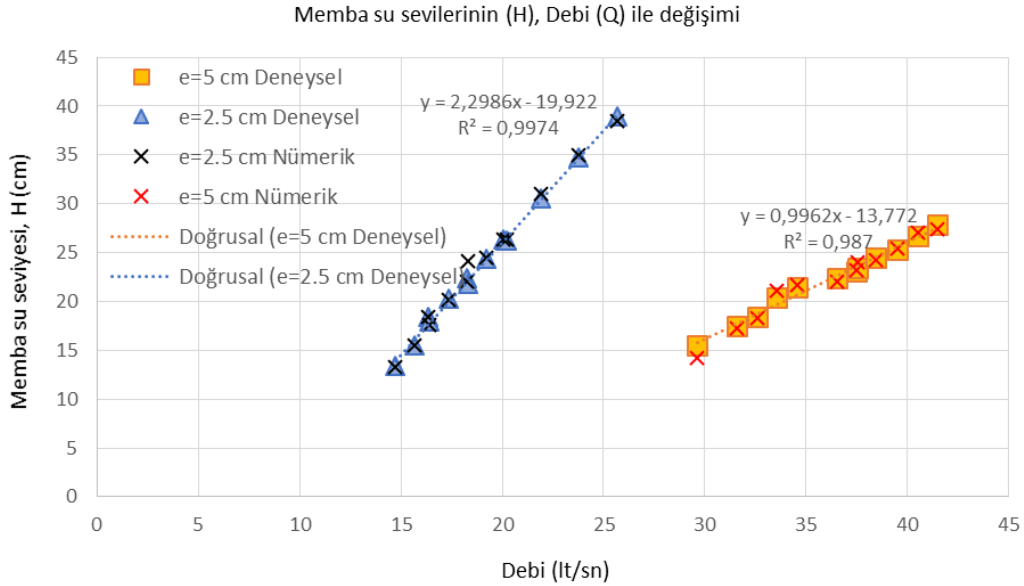
Şekil 13. e_1=2,5 cm ve e_2=5 cm kapak açıklıkları için elde edilen debi (Q) ve memba su seviyelerinin (H) karşılaştırılması.

Sıçrama öncesi su derinliklerinin (y₁), Debi (Q) ile değişimi
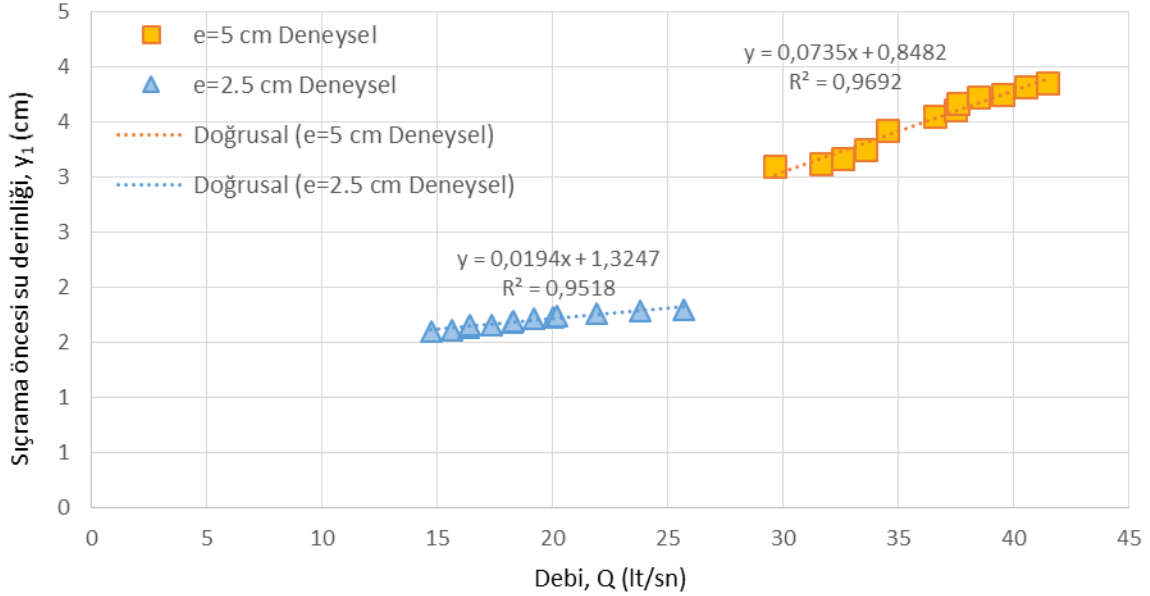
Şekil 14. e_1=2,5 cm ve e_2=5 cm kapak açıklıkları için elde edilen debi (Q) ve sıçrama öncesi su derinliklerinin (y_1) karşılaştırılması.
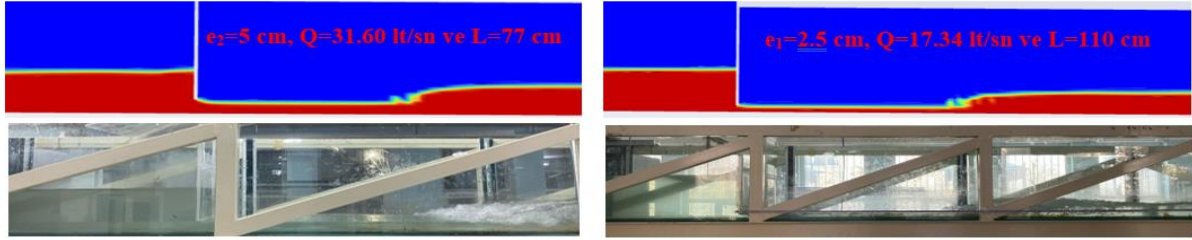
Şekil 15. Nümerik modelden elde edilen 2 boyutlu görsellerin, deneyler ile karşılaştırılması.

4. Sonuç

Bu çalışmada açık kanal sisteminde hidrolik sıçrama oluşturmak için bent kapağı ve doğrusal savak kullanılmıştır. Hidrolik sıçramanın ve su seviyelerinin değişken debi değerleri ile davranışı incelenmiştir. Öngörülemeyen ve oluşacağı konum tam olarak bilinmeyen bir hidrolik sıçrama hidrolik yapılar için tehlike arz etmektedir. Hidrolik sıçramanın meydana geleceği yer doğru tahmin edilmeli ve ek önlemler alınmalıdır. Deneylerden de görülebileceği gibi hidrolik sıçramanın konumu, debi, kapak açıklığı ve memba su seviyesi gibi hidrolik koşullara bağlı olarak değişmektedir. Çalışmada e_1=2,5 cm ve e_2=5 cm olmak üzere iki farklı kapak açıklığı kullanılmış ve kapaklar üzerinde toplamda 34 farklı debi değeri ile deneyler yürütülmüştür. Yapılan deneylerde hidrolik sıçramanın konumunun, debiye bağlı olarak değişimi incelenmiştir. Elde edilen sonuçlara göre, hidrolik sıçrama konumunun ve memba su seviyesinin artan debi değeri ile lineer orantılı olarak değiştiği görülmüştür. Kapak açıklığı arttıkça hidrolik sıçramanın mansap tarafında ilerleme hızı azalmaktadır. Kapak açıklığı azaldıkça ise memba su seviyesi daha hızlı yükselmektedir. Bu çalışmada Fluent gibi nümerik modelleme programlarının, bent kapağı altından geçen akımı ve oluşturduğu hidrolik sıçramayı simüle etmek için yeterince gelişmiş olduğunu göstermiştir. Ayrıca laboratuvar ortamında yapılan deneyler 3 boyutlu olmasına rağmen oluşturulan 2 boyutlu nümerik modeller, deneysel ile karşılaştırıldığında hidrolik sıçramanın konumu ve memba su seviyesi bakımından yüksek tutarlılık göstermiştir. Bu yapılan 2 boyutlu nümerik modeller zamandan tasarruf sağlayarak başarılı sonuçlar vermişlerdir.

Kaynaklar

Akoz MS, Kirkgoz MS, Oner AA. 2009. Experimental and numerical modeling of a sluice gate flow. J Hydraul Res, 47(2): 167-176.

Ansys® Fluent. 2023 Release 23.1, Help System, Chapter 1: Basic Fluid Flow, ANSYS, Inc., pp: 41.

Araz GBM, Hanif CM. 1991. Numerical simulation of hydraulic jump. J Hydraul Eng, 117(9): 1195-1211.

Aydın, MC, Ulu AE. 2017. Numerical modelling of sluice gates with different baffle types under submerged flow conditions. BEU J Sci Technol, 7(1): 1-6

Bakhmeteff BA, Matzke AE. 1936. The hydraulic jump in terms of dynamic similarity. T Am Soc Cıv Eng, 10(11): 630-647.

Bélanger JB. 1828. Essai sur la solution numérique de quelques problèmes relatifs au mouvement permanent des eaux courantes. Chez Carilian-goeury, Paris, Fransa, pp: 62.

Bidone G. 1819. Observation sur le hauteur du ressaut hydraulique en 1818. Royal Academy of Sciences, Turin, İtalya.

Bradley JN, Peterka AJ. 1957. Hydraulic design of stilling basins: hydraulic jumps on a horizontal apron (Basin I). J Hydr Eng Div-ASCE, 83(5): 1401-1424.

Cassan, L, Belaud G. 2012. Experimental and numerical ınvestigation of flow under sluice gates. J Hydraul Eng, 138: 367-373.

Cihan AM, Ulu AE. 2017. Numerical modelling of sluice gates with different baffle types under submerged flow conditions. BEU J Sci Technol, 7(1): 1-6.

Daneshfaraz R, Abbaszadeh H, Gorbanvatan P, Abdi M. 2021. application of sluice gate in different positions and ıts effect on hydraulic parameters in free-flow conditions. J Hydraul Stract, 7(3): 72-87.

Ead SA, Rajaratnam N. 2002. Hydraulic jumps on corrugated beds. J Hydraul Eng, 128(7): 656-663.

Gumus V, Simsek O, Soydan NG, Akoz MS, Kirkgoz MS. 2016. Numerical modeling of submerged hydraulic jump from a sluice gate. J Irrig Drain Eng, 142(1): 04015037-1-11.

Habibzadeh A, Vatankhah AR, Rajaratnam N. 2011. Role of energy loss on discharge characteristics of sluice gates. J Hydraul Eng, 137(9): 1079-1084.

Hager WH. 1992. Energy dissipators and hydraulic jump. Dordrecht. Springer, Water Science and Technology Library, London, UK, pp: 289.

Hager WH, Wanoschek R. 1987. Hydraulic jump in triangular channel. J Hydraul Res, 25(5): 549-564.

Karami S, Heidari MM, Rad MHA. 2020. Investigation of free flow under the sluice gate with the sill using Flow-3D Model. Ijst-T Cıv Eng, 44(1): 317-324.

Kubrak E, Kubrak J, Kiczko A, Kubrak, M. 2020. Flow measurements using a sluice gate; Analysis of applicability. Water, 12(3): 819.

Lazzarin T, Viero DP, Defina A, Cozzolino L. 2023. Flow under vertical sluice gates: Flow stability at large gate opening and disambiguation of partial dam-break multiple solutions. Phys Fluids, 35 (2): 024114.

Levy AG, Ellms JW, Gore W, Fales AL. 1927. The hydraulic jump as a mixing device. American Water Works Assoc, 17:1, 1-26.

Peterka AJ. 1984. Hydraulic design of stilling basins and energy dissipators. Bureau of Reclamation, Denver, Colorado, pp: 124.

Rajaratnam N, Subramanya K. 1968. Profile of the hydraulic jump, J Hydr Eng Div-Asce, 94(3): 663-674.

Retsinis E, Papanicolaou P. 2020. Numerical and experimental study of classical hydraulic jump. Water, 12(6): 1766.

Rouse H, Siao TT, Nagaratnam S. 1959. Turbulence characteristics of the hydraulic jump. T Am Soc Cıv Eng 124(1): 926-950.

Safranez K. 1929. Researches relating to the hydraulic jump, English translation by DP Barnes. Bureau of Reclamation, Denver, Colorado, USA, pp: 63.

Silvester R. 1964. Hydraulic jump in all shapes of horizontal channels, J Hydr Eng Div-ASCE, 90(1): 23-55.

Swamee PK. 1992. Sluicegate discharge equations. J Irrig Drain Eng, 118(1): 56-60.

ARALIK TİP-2 BULANIK TOPSIS YÖNTEMİ KULLANARAK DEPARTMAN MÜDÜRÜ SEÇİMİNE KARAR VERME

Kemal Gökhan NALBANT[1]*

[1]*İstanbul Beykent University, Faculty of Engineering and Architecture, Department of Software Engineering, 34396, İstanbul, Türkiye*

Özet: Yetenekli bir departman yöneticisinin belirlenmesi, bir departmanın süreçlerinin yönetilmesinde hayati önem taşıyan bir faktördür. Rekabetçi piyasada etkin bir şekilde yol alabilmek için yöneticilerin belirli bir dizi yeteneğe sahip olması gerekir. Bir departmanı yönetecek kişiyi seçmek, çok kriterli karar verme (ÇKKV) bağlamında zor bir görev olabilir. Teknik beceriler, iş deneyimi, kişisel özellikler ve diğer ilgili faktörler de dahil olmak üzere çeşitli yönleri kapsayan kapsamlı bir değerlendirme yapmak son derece önemlidir. Bu çalışmanın birincil amacı, departman yöneticisi seçiminde karşılaşılan zorlukları ele almaktır. Bu zorluğu ele almak için çalışma, ideal çözüme dayalı sıralama (TOPSIS) tekniği için aralık tipi 2 (AT2) bulanık yaklaşımını kullanarak departman yöneticilerini değerlendirmektedir. Departman müdürü seçim probleminde 4 alternatif arasından 6 temel kritere göre yamuk AT2 bulanık sayılar kullanarak çözüm yapılmış ve AT2 Bulanık TOPSIS metodolojisi uygulanmıştır. Bu yöntem ile alternatifler arasından en iyisi seçilmiştir.

Anahtar Kelimeler: Bulanık mantık, AT2 bulanık TOPSIS, Çok kriterli karar verme, Personel seçimi, Departman müdürü

Decision Making for Department Manager Selection Using Interval Type-2 Fuzzy TOPSIS Method

Abstract: Identifying a capable department manager is a vital factor in managing the processes of a department. In order to effectively navigate the competitive market, managers need to possess a certain set of skills. Selecting the person to manage a department can be a difficult task in the context of multi-criteria decision making (MCDM). It is extremely important to make a comprehensive assessment covering various aspects, including technical skills, work experience, personal characteristics, and other relevant factors. The primary objective of this study is to address the challenge of departmental manager selection. To address this challenge, the study evaluates departmental managers using the interval type 2 (IT2) fuzzy approach for the order of preference by similarity to the ideal solution (TOPSIS) technique. In the department manager selection problem, IT2 Fuzzy TOPSIS methodology was applied by using trapezoidal IT2 fuzzy numbers according to 6 main criteria among 4 alternatives. With this method, the best one among the alternatives was selected.

Keywords: Fuzzy logic, IT2 fuzzy TOPSIS, Multi-criteria decision making, Personnel selection, Department manager

1. GİRİŞ

İnsan kaynakları yönetimi (İKY), işe alma, personel seçimi, performans değerlendirmesi, teşvik yapıları ve eğitim ve geliştirme gibi faaliyetleri kapsayan, bir kuruluş içindeki bireylerin sistematik yönetimidir (Petrovic-Lazarevic, 2001). Etkili İKY uygulamalarının müşteri mutluluğu, kârlılık, inovasyon, kalite ve benzerlerine katkıda bulunarak kurumsal performansı artırdığı gösterilmiştir. Personel seçimi, ardından insan kaynakları planlaması ve işe alım, işletmelerin bireylerin doldurulması gereken işler için nitelikli olup olmadıklarını belirlemek için çeşitli yollar kullandıkları süreçtir (Boran ve ark., 2011).

İKY, istihdam ve personel seçimi, performans değerlendirme, teşvik sistemleri ve eğitim ve geliştirme dahil olmak üzere bireyleri yönetme sürecidir. Öznel ve nesnel süreçler, personel seçimindeki değerlendirme sürecinin sınıflandırılabileceği başlıca kategorilerdir. Öznel süreç kişilik değerlendirmelerini, stres ve yönetim modu envanterlerini, mülakatları ve amir değerlendirmelerini içerirken, nesnel süreç iş örneklerini, biyografik verileri (cinsiyet ve yaş gibi), durumsal yargı testlerini ve beceri testlerini içerir (Raj Mishra ve ark., 2020).

Şirketlerin, teknolojinin hızla ilerlemesi ve rekabetin küreselleşmesinin bir sonucu olan küresel pazarda rekabet edebilmeleri için profesyonel ve yüksek kaliteli insan kaynaklarına sahip olmaları gerekmektedir. Bir kuruluşun başarısı, bilgi, beceri ve yetenekleri de dahil olmak üzere çalışanlarının performansından önemli ölçüde etkilenir. Kuruluşların birincil hedefi, belirli bir çalışanı veya personeli çeşitli yetkinliklerine göre değerlendirmek için daha etkili yöntemler belirlemektir (Güngör ve ark., 2009).

Personel seçimi, işgücünün kalitesini doğrudan etkilediği için insan kaynakları yönetiminin çok önemli bir yönüdür. Personel seçimi konusu kapsamlı bir şekilde araştırılmıştır. Bir dizi seçenek arasından en uygun

kişileri seçme süreci, çok kriterli karar verme (ÇKKV) olarak bilinen çeşitli faktörlere dayalı kararlar vermeyi içeren bir zorluktur. Gerçek dünya durumlarında belirsizliğin ele alınması, çeşitli yaklaşımların ve teorilerin geliştirilmesine yol açan kalıcı bir araştırma konusu olmuştur (Afshari ve ark., 2014).

Politikaları, süreçleri, araçları ve yapıları tasarlayan, geliştiren, uygulanmasını denetleyen ve değerlendirenler her düzeydeki (taktik, operasyonel ve stratejik) yöneticilerdir. Bir kuruluşun refahı yöneticilerinin sorumluluğundadır. Bir kuruluşun gelişimi ve sürdürülebilirliği ya da başarısızlığı ve çöküşü yöneticilerinin kararlarına bağlıdır. Bir kuruluşta, yönetim becerilerini geliştirmek için eğitim ve gelişim programlarının yanı sıra pratik deneyim de uygulanabilir. Ancak ilk ve en kritik aşama, en azından bir dizi çağdaş yönetim becerisine sahip olan yöneticilerin titizlikle seçilmesidir (Kelemenis ve ark., 2011).

Bir departman yöneticisini işe alırken karşılaşılan sorunlar bazen adayın yeteneklerinin ve deneyiminin departmanın taleplerini ne kadar karşıladığını analiz etmekle başlar. Teknik uzmanlık ve liderlik özelliklerinin yanı sıra, adayın mevcut kültüre uyum sağlama kapasitesi de kritik önem taşır. Adayın liderlik tarzının mevcut ekip dinamiklerini ne kadar iyi tamamlayacağını ve mükemmel yönetim becerileri sergileyip sergilemeyeceğini önceden kestirmek mümkün değildir. Ayrıca, adayların motivasyonlarını ve uzun vadeli kariyer hedeflerini bilmek, hem birey hem de işletme için uzun vadeli mutluluğu sağlamak açısından kritik önem taşır. Adil ve objektif değerlendirme kriterlerinin belirlenmesi ve seçim sürecinde şeffaf bir iletişim stratejisi geliştirilmesi, prosedürün kabul edilebilirliğini ve başarısını etkiler. Yeni bir yöneticinin işe alınması mevcut ekipte çeşitli duyguların ortaya çıkmasına neden olabilir, bu nedenle geçiş sürecini yönetmek kritik önem taşır. Bir diğer sorun da uzun vadeli performans tahminleridir ve bu tahminlerin etkili bir şekilde yapılması zor olabilir. Ayrıca, yeni yöneticinin mevcut süreçlere uyum sağlaması ve eğitim alması gerekebilir ki bu da zaman alıcı ve maliyetli olabilir. İç ve dış adaylar arasında karar vermek de zor olabilir, çünkü her grubun avantajları ve dezavantajları vardır. Bu sorunların üstesinden gelmek için titiz bir değerlendirme süreci, iyi planlanmış geçiş stratejileri ve etkili iletişim planlarının oluşturulması gerekir.

Literatürde çok kriterli karar verme yöntemlerinin uygulandığı pek çok bulanık yöntem bulunmaktadır. AT2 bulanık TOPSIS kullanan çalışmalara literatürde çok fazla rastlanmamıştır. Bu çalışmadaki temel amaç literatüre katkı sağlayıp, literatürü bu alanda zenginleştirmektir.

Torfi ve Rashidi (2011) bulanık çok kriterli karar verme (FMCDM) modelini, önemli bir inşaat şirketinde proje müdürü pozisyonu için en uygun adayı belirlemek amacıyla bir vaka çalışmasında kullanmışlardır. İlk olarak, seçim için gerekli tüm kriterleri ve alt kriterleri derlemek için üst düzey yöneticilerin görüşleri alınmış ve

kriter öncelikleri niteliksel olarak belirlenmiştir. Daha sonra, Analitik Hiyerarşi Süreci (AHP), TOPSIS ve kriterlerin yaklaşık ağırlıkları adayları sıralamak için kullanılmıştır.

Baharin ve ark. (2021) çalışmalarında, bir şirkette orta düzey yönetici pozisyonu için yeni personel alımında TOPSIS yöntemi için bulanık tekniği önermişlerdir. Araştırmalarının amacı, Bulanık TOPSIS yöntemini kullanarak bir şirkette orta düzey yönetici seçimi için alternatifleri ve kriter ağırlıklarını değerlendirmektir. Bulanık TOPSIS yönteminin uygulanabilirliği, bir şirketteki orta düzey yönetici seçim problemine ilişkin gerçek dünya verilerinin uygulanması yoluyla gösterilmiştir. Çalışmada on iki seçilmiş kriter, üç seçilmiş alternatif (A1, A2, A3) ve üç karar verici bulunmaktadır. Mumcu ve Gök (2021) çalışmalarındaki amaç, tekstil endüstrisi işletme sahiplerinin yönetici seçerken önem verdikleri kriterleri belirlemektir. Bu kriterleri belirlemek için ÇKKV teknikleri kullanılmıştır. Şirket sahipleri için yönetici seçimi, mevcut küresel ve rekabetçi piyasa koşullarında birden fazla kriteri içeren çok değişkenli bir karar verme problemidir. İlk olarak, çalışmanın amaçları doğrultusunda, yönetici seçimine ilişkin kriterler bir literatür değerlendirmesi ile belirlenmiştir. Belirleyici kriterler, uzmanlarla yapılan görüşmeler yoluyla dört ana kriter oluşturmak için kullanılmıştır.

Nalbant (2022) çalışmasında terfi için en yetkin bireyler, birleştirilmiş Tutarlı Bulanık Tercih İlişkileri (CFPR) - Aralık Tip-2 (AT2) Bulanık TOPSIS metodolojisi kullanılarak belirlenmiştir. Türkiye'deki bir vaka çalışması için bireylerin sınıflandırılması bu metodoloji kullanılarak belirlenmiştir. Daha sonra, uzmanlar tarafından belirlenen kriterlerin ağırlığı CFPR tekniği ile bulunmuştur. Daha sonra, AT2 yamuk bulanık sayılar kullanılarak seçeneklerin sırasını belirlemek için AT2 Bulanık TOPSIS yöntemi kullanılmıştır. Böylece, terfi için en yetkin aday seçilmiştir.

Yan ve ark. (2023) Bulanık-DEMATEL yöntemini ve pişmanlık teorisini birleştirerek inşaat programı yöneticilerinin seçimine yönelik çok özellikli bir model oluşturmaktadır. Yönetici seçme ve değerlendirme endeks sistemi, altı yeterlilik unsurunun çıkarılmasından sonra oluşturulmuştur. İkinci olarak, karar vericilerin psikolojik özelliklerini simüle etmek için pişmanlık teorisi kullanılmıştır. Bu daha sonra her bir unsur için kapsamlı ağırlıkları belirlemek üzere Bulanık-DEMATEL ile birleştirilmiştir. Son olarak, tüm alternatifler düzenlendikten sonra yetkin alternatifler seçilmektedir. Geliştirilen modelin etkinliği bir vaka çalışması kullanılarak değerlendirilmiştir.

Nalbant (2024) bireyleri seçmek için yamuk aralık tip-2 (AT2) bulanık Karar Verme Deneme ve Değerlendirme Laboratuvarı (DEMATEL) - Analitik Ağ Süreci (ANP) metodolojisini kullanmıştır. Personel alımı ile ilgili hem birincil hem de ikincil kriterler için en iyi sonuçlar belirlenmiştir. Ayrıca, alternatifler arasından en iyisi seçilmiştir.

Çalışmanın 2. bölümünde kullanılan AT2 bulanık TOPSIS tekniğinden bahsedilmiştir. Ayrıca bu bölümde problemin çerçevesi ve yöntemin akış şeması ile aşamaları anlatılmıştır. 3. bölümde ise AT2 bulanık TOPSIS tekniğinin uygulanması ile hesaplamalar yapılmıştır. 4. bölümde yöntemin kısıtları ve gelecek ile ilgili çalışmalar açıklanmıştır. 5. bölüm ise çalışmanın sonlandırıldığı gelecekteki araştırmalar için önerilerde bulunulduğu ve bulguların sunulduğu sonuç bölümüdür.

2. Materyal ve Yöntem

Bu çalışmanın temel amacı, yönetici seçim sürecini incelemek ve bu karar verme sürecinde ortaya çıkan çeşitli zorlukların etkin bir şekilde üstesinden gelmenin önemini vurgulamaktır. Çalışmada yamuksal Aralık Tip-2 (AT2) bulanık TOPSIS tekniği kullanılmıştır. Bu araştırma, İstanbul, Türkiye'de bulunan bir şirket için departman müdürü seçimine odaklanmıştır. Karar vericiler, bir adayı departman yöneticisi rolüne terfi ettirecektir. Kararlar, kurum ve işletme içinde yetki ve sorumluluk pozisyonlarında bulunan üç kişi tarafından alınmıştır.

Bu çalışmada yamuk AT2 bulanık TOPSIS yaklaşımı kullanılmıştır (Chen ve Lee, 2010a; Kahraman ve ark., 2014; Senturk ve ark., 2017; Ozdemir ve ark., 2021). Bu bölümde, AT2 yamuk bulanık sayılar kullanılarak farklı departman müdürü alternatifleri için AT2 bulanık TOPSIS tekniği kullanılmıştır. Lee ve Chen (2008) AT2 bulanık TOPSIS adı verilen bir teknik sunmuştur. Lee ve Chen (2008) yamuk aralıklı Tip 2 bulanık kümelerinin sıralama değerlerini belirlemişlerdir (Lee ve Chen, 2008; Chen ve Lee, 2010b; Cengiz Toklu, 2018).

Problem, Tablo 1'de gösterildiği gibi bulanık sayılar içeren AT2 bulanık TOPSIS yaklaşımı uygulanarak çözülmüştür (Chen ve Lee, 2010b; Abdullah ve Najib, 2014; Cengiz Toklu, 2018).

AT2 bulanık sayılar, sıradan T2 bulanık sayılara göre doğal basitlikleri ve azalan işlem yükleri nedeniyle genellikle T2 bulanık sayılara tercih edilmektedir. Sonuç olarak, AT2 bulanık kümeleri mevcut araştırmalarda kullanılmaktadır.

Çalışmada her uzmana aynı ağırlıklar tahsis edilmiştir. Bu senaryoda, altı kritik kriter seçilmiş ve ardından her birine uygun ağırlık değerleri atanmıştır. Ayrıca, Şekil 1'de gösterildiği gibi, dört departman müdürü alternatifi (A1, A2, A3, A4) seçilmiş ve ilgili sorumluluklarıyla tutarlı ağırlıklar atanmıştır. Problemin hiyerarşisi Şekil 1'de oklar kullanılarak gösterilmiştir. Altı temel kriter vardır: yönetim (C1), organizasyon (C2), planlama (C3), güvenilirlik (C4), kontrol (C5), ve iletişim (C6).

Tablo 1. AT2 bulanık kümelerle ilişkili dilsel ifadeler

Dilsel İfadeler	Yamuk AT2 bulanık sayılar
Çok Düşük (ÇD)	((0, 0, 0, 0,1; 1, 1) (0, 0, 0, 0,05;0,9, 0,9))
Düşük (D)	((0, 0,1, 0,1, 0,3; 1, 1) (0,05, 0,1, 0,1, 0,2; 0,9, 0,9))
Orta Düşük (OD)	((0,1, 0,3, 0,3, 0,5; 1, 1) (0,2, 0,3, 0,3, 0,4; 0,9, 0,9))
Orta (O)	((0,3, 0,5, 0,5, 0,7; 1, 1) (0,4, 0,5, 0,5, 0,6; 0,9, 0,9))
Orta Yüksek (OY)	((0,5, 0,7, 0,7, 0,9;1; 1) (0,6, 0,7, 0,7, 0,8; 0,9, 0,9))
Yüksek (Y)	((0,7, 0,9, 0,9, 1; 1, 1) (0,8, 0,9, 0,9, 0,95; 0,9, 0,9))
Çok Yüksek (ÇY)	((0,9, 1, 1,1; 1, 1) (0,95, 1, 1,1; 0,9, 0,9))
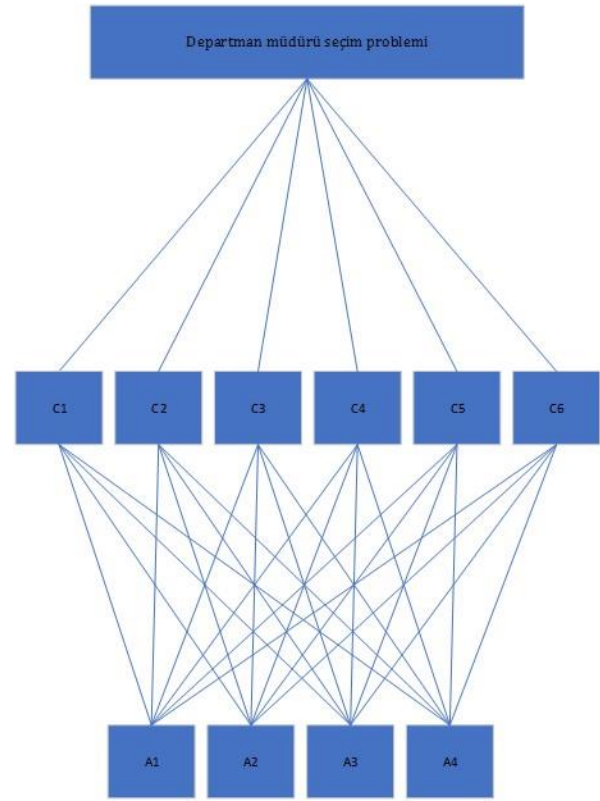
Şekil 1. Departman müdürü seçim probleminin hiyerarşik bir çerçevesi.
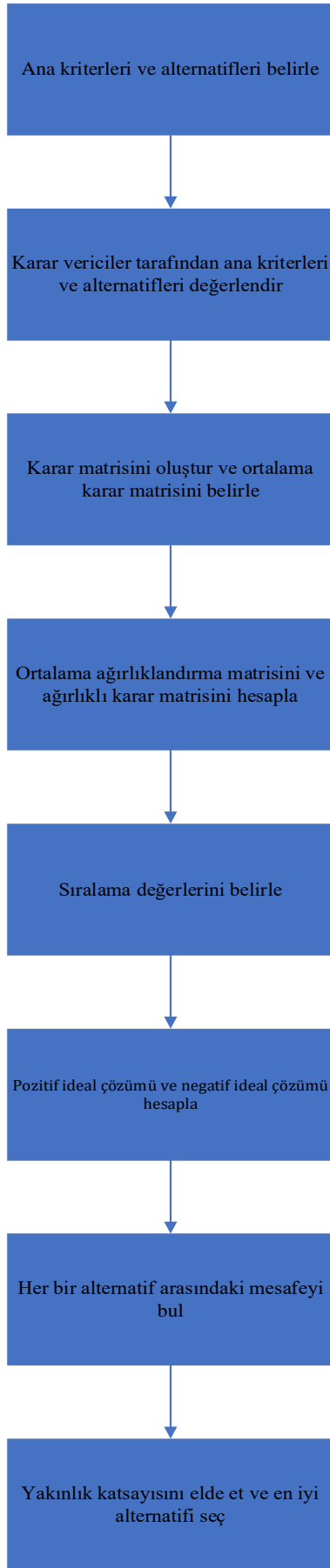
Şekil 2. AT2 Bulanık TOPSIS metodolojisi için uygulama akış şeması.

Bu çalışmada en uygun departman yöneticisini belirlemek için AT2 bulanık TOPSIS tekniği kullanılmıştır. Şekil 2'de uygulama senaryosunun yapısı gösterilmektedir.

İlk olarak problem belirlenmiştir. Daha sonra birincil kriterler ve alternatif seçenekler seçilmiştir. Yetki dağılımı oluşturuldu ve girdiler istendi. Değerlendirme yapmak için üç karar verici vardı. Tablo 1'de ana kriter ve alternatiflerin belirlenmesi sürecinde kullanılan dilsel ifadeler ve aralıklı bulanık sayılar gösterilmektedir. Model daha sonra AT2 bulanık TOPSIS metodolojisi kullanılarak oluşturulmuştur. Tüm alternatif seçim süreci için AT2 bulanık TOPSIS algoritması kullanılmıştır. Her bir kriterin önem ağırlıklarını içeren ortalama ağırlıklandırma yöntemi kullanılarak kapsamlı bir matris oluşturulmuştur. Daha sonra, verilen ağırlıklar kullanılarak karar matrisi hesaplanmıştır. Ayrıca, pozitif ideal çözüm (PIS) ve negatif ideal çözümün (NIS) hesaplanması gerçekleştirilmiştir.

Tablo 2 ve Tablo 3'de karar vericilerin temel kriterlere ve seçimlere ilişkin dil değerlendirmeleri gösterilmektedir. Karar vericiler sırasıyla K1, K2 ve K3'tür.

Tablo 2. Karar vericilerin alternatiflerin değerini farklı niteliklere göre değerlendirmesi

Kriterler	Alternatifler	K1	K2	K3
C1	A1	OY	O	OD
	A2	D	OD	D
	A3	Y	ÇY	OY
	A4	O	O	OD
C2	A1	O	Y	OD
	A2	OY	O	O
	A3	O	OD	OD
	A4	ÇY	Y	Y
C3	A1	OD	OD	O
	A2	OY	OY	Y
	A3	OD	O	OD
	A4	OY	OY	OY
C4	A1	OD	O	OD
	A2	O	O	O
	A3	OY	OY	Y
	A4	OY	OY	O
C5	A1	OY	OY	Y
	A2	Y	Y	O
	A3	D	OD	OD
	A4	O	OY	Y
C6	A1	OD	O	OY
	A2	OY	OY	O
	A3	Y	Y	OY
	A4	O	O	O

Tablo 3. Karar vericiler tarafından kriterlere atanan ağırlıklar

Kriterler	K1	K2	K3
C1	ÇY	Y	Y
C2	OY	Y	OY
C3	Y	OY	OY
C4	OY	Y	Y
C5	Y	Y	O
C6	OY	OY	Y

3. Bulgular

Departman müdürü seçimi konusunu ele almak için AT2 bulanık TOPSIS tekniği kullanılmıştır. AT2 bulanık TOPSIS tekniğinin uygulanması sonucunda ortaya çıkan ağırlıklı karar matrisi hesaplanmıştır. Tablo 4'de sıralama ağırlıklı karar matrisi gösterilmektedir. Ek olarak, pozitif ve negatif ideal çözümler Tablo 5'de hesaplanmıştır. Her bir olası seçenek arasındaki mesafeler belirlenir. Daha sonra yakınlık katsayısı hesaplanır ve en avantajlı seçeneği belirlemek için kullanılır.

Tablo 4. Sıralama ağırlıklı karar matrisi

	A1	A2	A3	A4
C1	6,44	4,68	8,42	6,08
C2	6,26	6,28	5,38	7,88
C3	5,38	7,15	5,38	6,87
C4	5,51	6,16	7,44	6,81
C5	7,14	7,13	4,80	6,84
C6	5,98	6,57	7,44	5,98

Tablo 5. Pozitif ve negatif ideal çözümler

Pozitif ideal çözümler	Negatif ideal çözümler
8.42	4,68
7.88	5,38
7.15	5,38
7.44	5,51
7.14	4,80
7.44	5,98

Tablo 6. AT2 Bulanık TOPSIS Sonuçları

	Ağırlıklar	Normalize Edilmiş Değerler
A1	0,345	18,73%
A2	0,409	22,19%
A3	0,622	33,75%
A4	0,467	25,33%

Tablo 6'daki verilerin de gösterdiği gibi gözlemlenen sıralama A3>A4>A2>A1 şeklindedir. Toplanan veriler göz önünde bulundurulduğunda, A3 alternatifinin en iyi alternatif olduğunu ve diğer seçeneklerin de rasyonellik açısından bunu takip ettiğini söylemek mümkündür.

4. Tartışma

Tip-1 (T1) bulanık kümelerin üyelik fonksiyonları iki boyuttan oluşurken, tip-2 (T2) bulanık kümelerin üyelik fonksiyonları üyelik fonksiyonu başına üç boyuttan oluşur. Daha fazla serbestlik derecesi sağlaması nedeniyle yeni eklenen üçüncü boyut, belirsizliğin fiziksel olarak temsil edilmesini mümkün kılmaktadır. T1 bulanık küme tekniğine kıyasla, T2 bulanık küme yaklaşımı esneklik sağlar ve belirsizliği temsil eder. Buna ek olarak, T2 bulanık kümesi belirsizlik bileşeninin doğru bir şekilde temsil edilmesini sağlar. Kural tabanlı bulanık mantık sistemleri, T2 bulanık mantık sistemleri sayesinde gecikmeleri modelleyebilmekte ve azaltabilmektedir (Senturk ve ark., 2016; Nalbant ve ark., 2024).

Önceki araştırmalarda olduğu gibi, bilgi toplama yöntemi zaman alıcı ve pahalıdır (yaklaşık yüz ikili karşılaştırma). Bu durum kullanılan yöntemin temel dezavantajıdır. Ayrıca, metodoloji genellikle çok sayıda uzmanın işbirliğini gerektirmektedir ki bu da yöntemin bir başka dezavantajıdır. Yöntemin bir diğer dezavantajı ise, uzmanın tercihleri konusunda şüphe veya anlaşmazlık yaratması ve bunun da belirsizlik yaratmasıdır.

Gelecekteki araştırmalardan aşağıdaki potansiyel sonuçların ortaya çıkması mümkündür: Önümüzdeki birkaç yıl içinde, kuruluşların karar alma prosedürlerini yürütme sürecini kolaylaştıracak yazılım araçları geliştireceği öngörülmektedir. Ayrıca, şirketler entegre yazılımlarla bağlantılı sınırların etkin bir şekilde üstesinden gelebilmektedir. İş ve yönetim sektörlerinde, sofistike yazılımların kullanımı, insan kaynaklarının seçimiyle ilgili zorlukların üstesinden gelme etkinliğini önemli ölçüde artırma potansiyeline sahiptir. Bu uygulama sayesinde bireyler, basitlik ve uzmanlık ile en büyük potansiyel faydayı sunan personel seçeneğini seçebileceklerdir. Bulanık ÇKKV tekniklerini AT2 bulanık TOPSIS ile birlikte kullanarak bu alana katkı sağlamak, gelecekteki araştırmalar için takip edilmesi gereken bir diğer hedeftir.

5. Sonuç

Bu araştırmanın temel amacı, departman müdürlerinin profesyonel kapasitelerindeki etkinliklerini değerlendirmektir. Yamuk AT2 bulanık TOPSIS tekniğinin kullanılması bu çalışmanın tamamlanmasını kolaylaştırmıştır. Yapılan analiz, departman müdürü alternatifleri için belirlenen ağırlıklara göre A3 alternatifinin %33,75'lik bir puana sahip olduğunu ve en iyi alternatif olduğunu göstermektedir. Buna karşılık, A4 alternatifi %25,33 puan alırken, A2 alternatifi %22,19 puan almıştır. Buna karşılık, A1 alternatifi %18,73'lük bir puan elde etmiştir.

İnsan kaynakları yönetimi alanı için gelecekteki araştırmalarda, DEMATEL-ANP, FANP, FAHP ve VIKOR gibi çeşitli AT2 bulanık yaklaşımlarının kullanılması mümkündür. Buna ek olarak, tüm farklı yolların etkinliğini analiz etmek için AT2 ile birleştirilmiş bulanık

yaklaşımlar da kullanılabilir. Departman müdürü seçim problemi, en etkili olduğu düşünülen strateji olan AT2 bulanık TOPSIS yöntemi kullanılarak çözülmüştür. AT2 yamuk bulanık TOPSIS tekniğinin etkili olduğu, değerlendirme prosedürünün optimize edilmesi sürecinde başarıyla uygulanmış olmasıyla gösterilmiştir. AT2 bulanık yaklaşımları, bulguları daha fazla araştırmayla genişletebilecek gelecekteki çalışmalar için potansiyel konuların odak noktasıdır. AT2 bulanık mantık yaklaşımları için hesaplama sürecini kolaylaştıracak programlar yazmak mümkündür. Bu programlar manuel olarak oluşturulabilir. Bu uygulamalar kullanıldığında, çözüm prosedürleri daha hızlı sonuçlar üretme potansiyeline sahiptir.

Katkı Oranı Beyanı

Yazar(lar)ın katkı yüzdesi aşağıda verilmiştir. Yazar(lar) makaleyi incelemiş ve onaylamıştır.

	K.G.N.
K	100
T	100
Y	100
VTI	100
VAY	100
KT	100
YZ	100
KI	100
GR	100

K= kavram, T= tasarım, Y= yönetim, VTI= veri toplama ve/veya işleme, VAY= veri analizi ve/veya yorumlama, KT= kaynak tarama, YZ= Yazım, KI= kritik inceleme, GR= gönderim ve revizyon.

Çatışma Beyanı

Yazar bu çalışmada hiçbir çıkar ilişkisi olmadığını beyan etmektedir.

Etik Onay Beyanı

Hayvanlar veya insanlar üzerinde herhangi bir çalışma yapılmadığı için bu çalışma için etik kurul onayı gerekmemiştir.

Kaynaklar

Abdullah L, Najib L. 2014. A new type-2 fuzzy set of linguistic variables for the fuzzy analytic hierarchy process. Expert Syst Appl, 41(7): 3297-3305.

Afshari AR, Cockalo D, Anisseh M. 2014. Linguistic project manager selection. In V International Symposium Engineering Management and Competitiveness, June 19 – 20, Zrenjanin: Serbia, pp: 41.

Baharin NH, Rashidi NF, Mahad, NF. 2021. Manager selection using Fuzzy TOPSIS method. J Physics Conf Ser, 1988(1): 012057.

Boran FE, Genç S, Akay D. 2011. Personnel selection based on intuitionistic fuzzy sets. Hum Factor Ergon Man, 21(5): 493-503.

Cengiz Toklu M. 2018. Interval type-2 fuzzy TOPSIS method for calibration supplier selection problem: A case study in an automotive company. Arab J Geosci, 11: 1-7.

Chen SM, Lee LW. 2010a. Fuzzy multiple attributes group decision-making based on the interval type-2 TOPSIS method. Expert Syst Appl, 37(4): 2790-2798.

Chen SM, Lee LW. 2010b. Fuzzy multiple attributes group decision-making based on the ranking values and the arithmetic operations of interval type-2 fuzzy sets. Expert Syst Appl, 37(1): 824-833.

Güngör Z, Serhadlıoğlu G, Kesen SE. 2009. A fuzzy AHP approach to personnel selection problem. Appl Soft Comput, 9(2): 641-646.

Kahraman C, Oztaysi B, Sari IU, Turanoglu E. 2014. Fuzzy analytic hierarchy process with interval type-2 fuzzy sets. Know Based Syst, 59: 48-57.

Kelemenis A, Ergazakis K, Askounis D. 2011. Support managers' selection using an extension of fuzzy TOPSIS. Expert Syst Appl, 38(3): 2774-2782.

Lee LW, Chen SM. 2008. Fuzzy multiple attributes group decision-making based on the extension of TOPSIS method and interval type-2 fuzzy sets. International Conference on Machine Learning and Cybernetics, July 12-15, Kunming, China, pp: 3260-3265.

Mumcu A, Gök M. 2021. Application of fuzzy Ahp and topsis methods for manager selection. Sos Bil Araş Derg, 16(2): 270-280.

Nalbant KG, Ozdemir S, Ozdemir Y. 2024. Evaluating the campus climate factors using an interval type-2 fuzzy ANP. Sigma J Eng Nat Sci, 42(1): 89-98.

Nalbant KG. 2022. Using an integrated consistent fuzzy preference relations and interval type-2 fuzzy TOPSIS methodology for personnel selection and promotion. WSEAS Trans Comput, 20: 158-164.

Nalbant KG. 2024. A methodology for personnel selection in business development: An interval type 2-based fuzzy DEMATEL-ANP approach. Heliyon, 10(1).

Ozdemir Y, Ozdemir S, Nalbant KG. 2021. A hybrid methodology for prioritizing of store plan alternatives produced with rule-based design. Int J Inf Tech Decis, 20(06): 1685-1709.

Petrovic-Lazarevic S. 2001. Personnel selection fuzzy model. Int T Oper Res, 8(1): 89-105.

Raj Mishra A, Sisodia G, Raj Pardasani K, Sharma K. 2020. Multi-criteria IT personnel selection on intuitionistic fuzzy information measures and ARAS methodology. Iran J Fuzzy Syst, 17(4): 55-68.

Senturk S, Binici Y, Erginel N. 2016. The theoretical structure of fuzzy analytic network process (FANP) with interval type-2 fuzzy sets. IFAC-Papers OnLine, 49(12): 1318-1322.

Senturk S, Erginel N, Binici Y. 2017. Interval type-2 fuzzy analytic network process for modelling a third-party logistics (3PL) company. J Mult-Valued Log S, 28: 311-333.

Torfi F, Rashidi A. 2011. Selection of project managers in construction Firms using analytic hierarchy process (AHP) and fuzzy Topsis: a case study. J Constr Dev Ctries, 16(1): 69-89.

Yan H, Yang Y, Lei X, Ye Q, Huang W, Gao C. 2023. Regret theory and fuzzy-DEMATEL-based model for construction program manager selection in China. Buildings, 13(4): 838.

DESIGN A COMPUTER CONTROLLED UNMANNED UNDERWATER VEHICLE THRUSTER USING SMART CLOSED LOOP CONTROLLER

Ihab ELAFF[1]*

[1]*Üsküdar University, Faculty of Engineering and Natural Sciences, Department of Computer Engineering, 34662, İstanbul, Türkiye*

Abstract: The first step of designing an Unmanned Underwater Vehicle (UUV) depends mainly on the selection of the thrusters, as UUVs require many thrusters to be installed onboard for smooth operation. The problems with the widely used thrusters in UUVs are the relatively large dimensions, and they just spin in the water without reporting any kind of important information such as the status of the thruster and the RPM of the motor. This project aims to design and implement a new computer-controlled thrusting system from end-to-end that fits various UUVs with more advantages including a smaller sized thruster, cheaper in price, and with more additional smart capabilities that report the thruster's instantaneous RPM, power consumption, proper operation, malfunctions, damages, and water stream blockage. The new thruster has Forward Thrust of 3.5 kgf, Reverse Thrust of 2.45kgf, and a maximum Power consumption 172.8 which is close to other widely used thrusters with the advantage of reporting operational status.

Keywords: Thruster, ETR100, UUV, Blue robotics, SeaBotix

1. Introduction

The discovery of the underwater world presents a big challenge to human limitations. Exploration of the underwater environment of the deep oceans is handled nowadays with Unmanned Underwater Vehicle (UUV) (Prasad and Sai Kiran, 2020). UUVs such as Remotely Operated Vehicle (ROV) (Capocci et al., 2017) and Autonomous Underwater Vehicle (AUV) (Sánchez et al., 2020) have recently become a promising growing field in the underwater environment exploration industry. Exploration includes: sea-floor reconstruction (Song and Choi, 2020), underwater life exploration (Macreadie et al., 2018), shipwreck exploration (Patterson et al., 2012), underwater-pipelines inspection (Ho et al., 2020), oil and gas exploration (Khojasteh and Kamali, 2017) etc. All those applications don't require fast motion and large torque. However, they require many thrusters for fine-motion control and low power consumption, while also small size is an important issues to be considered. Brushed DC motor such as SeaBotix BTD150 thrusters (Seabotix BTD150, 2024) or brushless DC motor such as Blue Robotics T200 thrusters (Blue Robotics, T200, 2024), and SAAB Seaeye thrusters (SAAB Seaeye, 2024) are widely used by many UUVs. Selection of suitable thruster for certain applications affects the whole design of the UUV. For motion control, UUV's designers usually support 4 to 8 thrusters at the corners with a titled angle on a plan inside or outside the UUV to obtain a smooth control of planner motion and 2 to 4 thrusters perpendicular to this plan for vertical motion. This relatively large number of thrusters affects the UUV body design and workspace, where thrusters with relatively large length will make its placement in the UUV somehow more difficult than the shorter length. Then, selection of the thruster is a critical aspect in designing the UUV body.

One important factor during UUV motion control is specifying the thrust of each thruster instantly to follow the desired trajectory. Thrust can be determined based on the motor's RPM, the parameters of the thruster's propeller and the water parameters. Measurement of the RPM in the widely used thrusters such as T200 and BTD150 is not present as an option. Doing that using a tachometer or an IR counter requires additional hardware to be installed on the thruster's body which will cause more drag and requires some additional wiring and caution to fit the underwater environment. Another important factor during UUV operation is power consumption, especially in AUVs. This requires measuring the current consumption in each thruster. This also is not present as a built-in option in the widely used thrusters. Knowing the RPM and the current of each thruster will help in evaluating the status of the system components and the working environment.

This project aims to design and implement a computer-controlled thrusting system from end-to-end that fits

various UUVs with more advantages including, smaller than existing thrusters, cheaper in price, and with more additional smart capabilities that report thruster's instantaneous RPM, power consumption, proper operation, malfunctions, damages, and water stream blockage.

2. Materials and Methods

The development process of the new thrusting system is divided into 4 layers (Figure 1): physical layer, mechanical layer, electrical/electronic layer and computer layer.
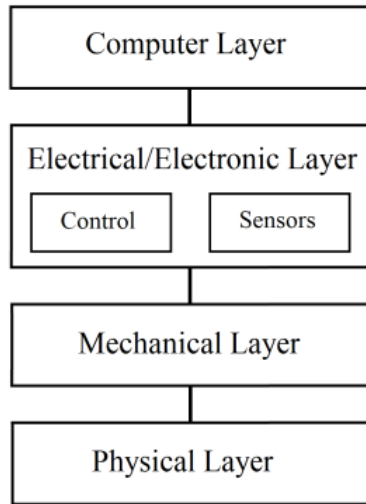
Figure 1. Thrusting system layers.

2.1 Physical Layer

Thruster is physically divided into 2 parts, the propeller and the casing. During thruster design, some issues have been taken into consideration, such as reliability, maintainability, usability, produceability, and affordability, scope of applications, targeted thrust, size of the thruster, number of propeller blades and safety.

For UUVs body design, the smaller the size of the thruster, the better to fit in the vehicle. Referring to the widely used thrusters such as BTD150 and T200, 100 mm outer diameter of the new thruster ETR100 has been selected as a starting point. Blue-Robotics and SeaBotix thrusters have relatively long motor casing extended outside the thruster head which adds some physical limitations to UUV design. In ERT100 thruster, it was taken into consideration to embed the motor inside the thruster casing saves a lot of space compared to other thrusters.

The propeller and the thruster casing have been designed using OpenProp (2024) which is used for design and analysis of marine propellers and horizontal-axis turbines. OpenProp can run on MATLAB or Octave (Epps, 2016; Epps and Kimball, 2013; OpenProp, 2024).

The number of blades and hub diameter are related to the required thrust and motor parameters (RPM, Current and Voltage). As selection of those design parameters is a recursive process, many trials with different parameters

have been tested until suitable values have been selected. EMAX CF2822 (2024) brushless motor is selected in the design, where the 2 blades propeller with 20 mm hub diameter has been selected to obtain a thrust of 4 kgf (Figure 2).
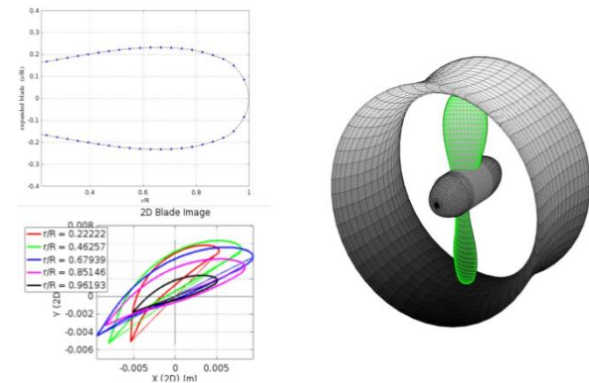
Figure 2. OpenProp design of ETR100 thruster

The generated blade profiles have been exported and reconstructed using FreeCAD (GNU) as 3D object (Figure 3). The hub has been split into 3 parts, namely: front nozzle, cylinder, and rear nozzle. To embed the motor inside the propeller's hub, the cylinder part of the hub has been modified to a frustum of 35 mm base diameter and 20 mm top diameter. An additional cylinder is added to the base of the frustum to cover the rest of the motor body which did not affect the forward thrust too much.
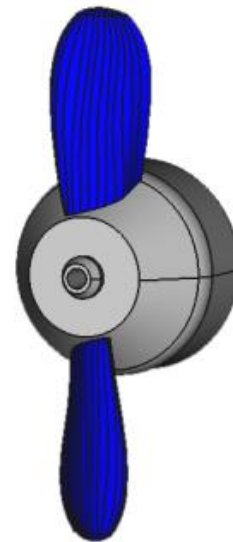
Figure 3. 3D model of ETR100 propeller.

The ETR100 thruster's casing is designed as a tube with front and rear supports to fix the motor in the center of that tube using 8 flat beams. Protection nets on both sides have been extended as edgy-rings through those flat beams (Figure 4). The inner profile of the thruster takes the same convex profile of the generated design from the OpenProp (Figure 2). However, the outer profile of the thruster is chosen to have a straight profile for alignment purposes on UUVs bodies. The front support takes the same profile of the 20mm propeller's hub's

nozzle; however, the rear support has been designed as a frustum of 35mm base diameter and 32 mm top diameter to hold the motor's base. Finally, the design has been realized using a 3D printer (PLA material) for testing and evaluation (Figure 5).
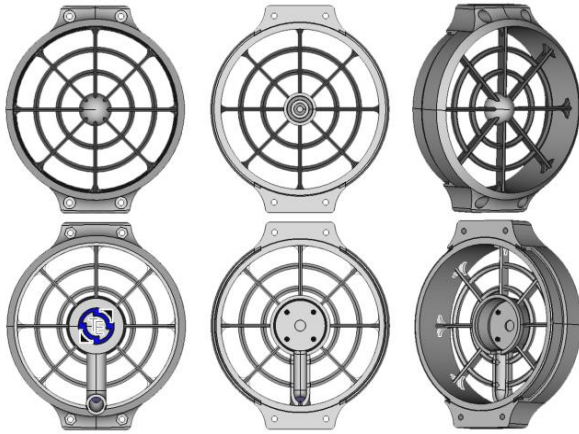
Figure 4. ETR100 front (top) and back (bottom) casing design.
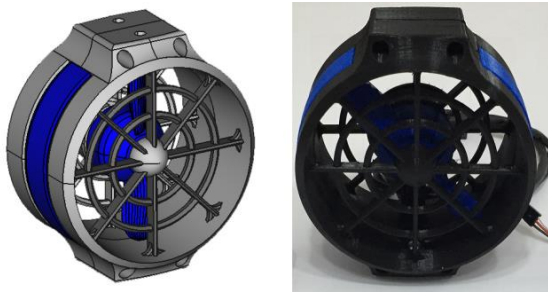
Figure 5. 3D model of ETR100 thruster (left) and 3D printed model (right).

2.2 Mechanical Layer

The main issue of the mechanical layer is to select a suitable motor for running the propeller inside the casing in a smooth and stable operation. Among different types of motor, a brushless motor has been selected because it is compact in size, light in weight, relatively low cost, run using DC supply at low voltage, provide good torque and speed without any gearbox, suitable for use in underwater environment directly without special sealing, and it can resist water pressure at large depths without special preparations. It should be noticed that the water density is much larger than air, which makes the propeller subjected to more reverse torque that will slow down motor rotation and implies the propeller slips if it is not supported properly on the motor's rotor. Because of that, among different brands of brushless motors, EMAX CF2822 has been selected because, in addition to the above advantages of brushless motors, its rotor part has 3 metallic shoulders which are used to rotate the propeller without slipping and without any additional support (reliability and produceability). It was sufficient to support the motor base using 4 nipples placed in the floor of the frustum of the back cover without any

screws. For stable operation, the tip of the rotor's axe is placed inside a bearing which is located in the cavity of the front cover's nozzle (Figure 6).
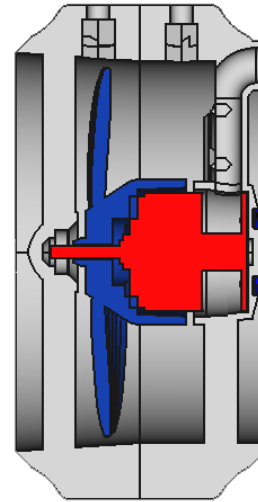
Figure 6. ETR100 thruster cross-sectional view showing inner casing profile and motor placement.

2.2 Electrical and Electronic Layer

The brushless motor is derived using Electronic Speed Controller (ESC) (Gorospe et al., 2017). In simple words, ESC is composed of a microcontroller, some MOSFETs pairs and a zero-crossing circuit. Each MOSFET pair is usually composed of P-MOS and N-MOS connected in series. Each wire of brushless motor is connected to an attachment point between the two MOSFETs. The MOSFET pair is responsible for connecting any motor's wire either to the supply's voltage or to the supply's ground. Such as any brushless motor, the motor will step according to a switching sequence of the MOSFET pairs. The MOSFET pairs sequencing operation is controlled by the ESC's microcontroller according to a Pulse Width Modulation (PWM) input signal from the deriving UUV controller. ESC is capable of measuring the completion of the mechanical action corresponding to a certain sequence by measuring the Back EMF (BEMF) of the free wire using a built-in zero-crossing measurement circuit. A complete rotation of the motor's rotor will be achieved after the zero-crossing circuit triggers a number of times equal to the number of the motor's poles.

Measuring the RPM of the motor while it is running will reflect the corresponding thrust of the propeller. Also, the ability to measure both the motor's RPM and its current consumption is useful in determining the rate of power consumption and the status of the thruster and ESC in case of any malfunctions or improper operating conditions such as blockage of the water stream or operation in the air that require halting the motor or intervention from the controller.

Measurement of the RPM under the water using a tachometer or an IR counter requires additional hardware to be installed on the thruster's body which will cause more drag and requires some additional

wiring and caution.

Developing an entire ESC that exporting sensor values is an unnecessary job because updating existing brands would be much easier and much more cost-effective. By adding an external zero-crossing measurement circuit to the ESC wires, the motor's RPM can be determined by the UUV controller from inside the air chamber without connecting extra components to the thruster itself. The EMAX CF2822 contains 12 poles which make one revolution being achieved after 12 triggers from the zero-crossing circuit. The following circuit (Figure 7) is capable of monitoring both the current consumed by the thruster and the zero-crossing pulsation. Also, combining readings from the RPM and the current will help to identify the status of the motor, the ESC and the working environment as stated earlier.
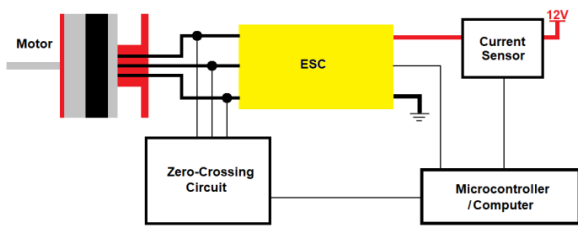
Figure 7. Circuit diagram of the motor's rotation position monitoring and current consumption monitoring

2.3 Computer Layer

The computer layer is concerned with 2 parts: the firmware of the ESC's microcontroller and the code in the UUV controller. The majority of ESC brands in the market derive the motor in one direction and very few brands work in both directions, where this depends on the firmware ability to shift MOSFET switching in both directions. There are two open-source firmware which can replace the original firmware of many ESC brands for a better, smoother and customizable operation; namely: SimonK (SimonK, 2024) (used by Blue Robotics' ESC deriver after some few updates) and BLHeli (2024). However, those firmwares are designed to work with drones that function according to air parameters. Using the ESC for the underwater environment requires some modifications for a slower response.

SimonK firmware has been used to re-program Hobbyking ESC20 (2024) for deriving the ETR100 thruster. Some updates have been done to the original SimonK firmware including: enabling to rotate the motor in both directions, adjusting the PWM input range between 1120 and 1865 uSec for controlling the ESC's output current (selection of those values will be discussed in results), adjusting dead band to be between 1450 uSec to 1550 uSec to avoid undesirable motor movement due to heating of the built-in crystal oscillator of the ESC's microcontroller during use, adjust initializing pulse to be at 1500 uSec, , limit the maximum throttle jump to try to prevent overcurrent, remove unnecessary beeps and disable error code of no operation for long time. The updated SimonK firmware is used instead of

the original firmware of the Hobbyking ESC20.

Violating the synchronization between mechanical action and electronic sequence causes SimonK firmware to halt the motor. So, reaching the desired RPM quickly in the underwater environment is not applicable to the original setting of SimonK firmware. Modifying the timeouts of the SimonK code was not successful after many trials. However, with the help of the external zero-crossing circuit, setting the suitable PWM for building-up to the required RPM could be achieved by monitoring the delay between each 2 successive pulses, which is in the case of the used components and water conditions is 397 uSec in the average at the maximum PWM. This will make the thruster operates with the maximum of 1048 RPM.

The current monitoring module combined with the RPM at any PWM input can indicate different conditions of the system according to the following table (Table 1), so the UUV controller can take proper actions for each case.

Referring to that table, the UUV controller could be programmed to take action by sending a warning to the user or disable the motor from running for a long time to protect the motor from possible damage.

Table 1. Thrusting system status

RPM Range	Current Range	Possible Problems
Normal	Normal	• No problems
Normal	Low	• thruster is still in the air • blades of the propeller are broken • The shaft of the motor is not connected to the propeller • The ESC is damaged
0 or very low	0	• Wire (s) of the motor not connected to ESC. • the power supply is low or not connected • The propeller or the motor is jammed.
Normal	High	• blockage in the inlet or the outlet of the thruster • fluid that surround the thruster is of higher viscosity (such as oil)
0 or very low	High	• Motor motion is blocked • Short circuit inside the ESC

3. Results

The thrust profile is generated by running the ETR100 thruster in sweet water in the room temperature using 12 VDC power supply and PWM timing adjusted (initially) to operate from 1100 uSec to 1900 uSec. The dead band has been adjusted at the beginning between

1450 and 1550 uSec is used as stop state, the timing band between 1550 and 1900 uSec is used for forward thrust and the timing band between 1100 and 1450 uSec is used for reverse thrust. Motor is initialized by sending PWM signal of 1500 uSec for a few seconds.

For thrust measurement, a mechanism has been developed as a class-I lever system where the thruster is placed on the tip of one side of the lever and the electronic mass scale on the other tip. The fulcrum of the lever has been supported at the top side of a water tank where the thruster is immersed entirely at a suitable height away from the tank floor and the electronic mass scale has been supported from its other side on a fixed reference point above the fulcrum.

Finally, the thrust profile and current profile have been created by measuring the thrust and the current consumption (Table 2) of the ETR100 during running at different PWM inputs from an external microcontroller many times and an average reading has been taken (Figure 8 and Figure 9).

Table 2. Measurements of the current and the thrust of ETR100 at different PWM

PWM (uSec)	Current (Amp.)	Thrust (kgf)
1100	17.72	-2.70
1150	13.66	-2.35
1200	9.96	-2.13
1250	6.52	-1.57
1300	3.72	-1.15
1350	1.63	-0.74
1400	0.43	-0.49
1450	0	0
1500	0	0
1550	0	0
1600	0.68	1.20
1650	2.18	1.7
1700	4.46	2.55
1750	7.48	3.14
1800	10.98	3.36
1850	14.77	3.53
1900	18.85	3.63
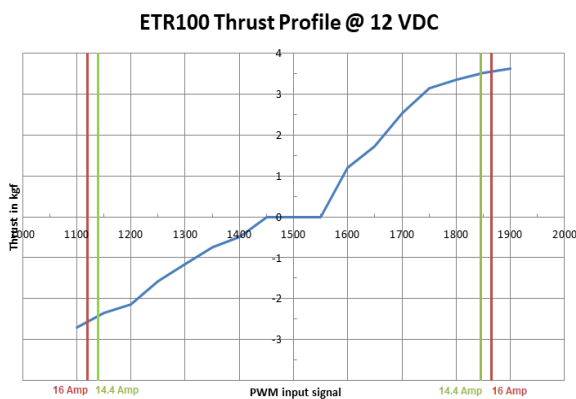
Figure 8. Thrust profile of ETR100 thruster.
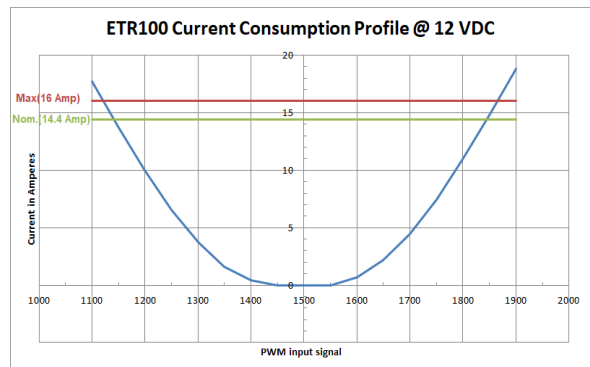
Figure 9. Current consumption profile of ETR100 thruster.

To control the maximum current that can be obtained from the ESC to derive the motor, the firmware of the ESC has been updated to truncate any input PWM signal outside the band 1120 and 1865 uSec. This truncation allows the ESC to supply up to 16 amperes, which is the maximum current of the EMAX CF2822; however, for long term operation of the thruster, the recommended maximum operating current is 14.4 Amps (10% lower than the maximum allowed current).

While the above testing is based on sweet water in the room temperature conditions, it is not the case when the UUV operates in seawater at different temperatures and with water stream currents flowing in unpredictable directions. So, determining the RPM using the external zero-crossing circuit would give a more accurate figure of the real generated thrust.

4. Discussion and Conclusion

A new thrusting system for UUVs has been developed to overcome some of the disadvantages of the other widely used brands and is equipped with smart capabilities. It is composed of the newly designed ETR100 thruster of compact size, regular ESC with modified firmware and additional modules to measure the current and the revolution speed of the motor. This system provides suitable thrust for exploration applications at standard 12 VDC supply and because of its smaller size compared to other thrusters (Figure 10) it will be much comfortable during the design of the UUV.

By comparing ETR100 to T200 and BTD150 (Table 3), ETR100 has a better advantage in size over the other 2 thrusters. For nominal operation, ETR100 is set to work at 90% of its maximum current (14.4 amperes). T200 produces more thrust for its nominal operation compared to ETR100; however, it consumes more power which causes the ESC to have higher temperature buildup during operation. Furthermore, BTD150 compared to ETR100, has lower thrusts and also lower power consumption, which makes ETR100 the middle performance between both thrusters. It is possible to run T200 thruster with up to 20 volts which produce more thrust and this is an advantage over the ETR100.

Because of the high current consumption of a brushless

motor, its temperature gets higher during the operation, which will cause the coil resistance to rise and affect motor performance. However, using the brushless motor underwater will make the surrounding water reduce motor temperature, which will keep the motor at high performance all the time.
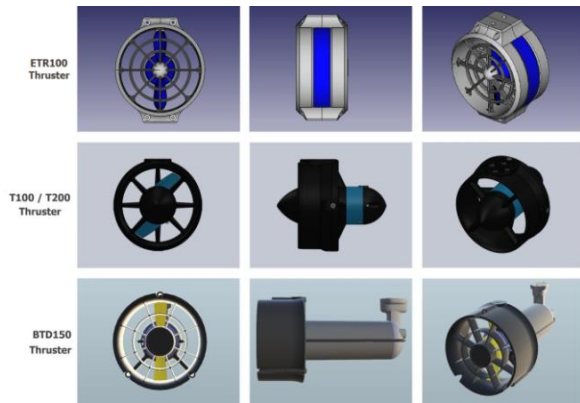
Figure 10. Comparison between ETR100, T100/T200 and BTD150 sizes.

Table 3. Comparison between ETR100, T200 and BTD150 performance parameters

Parameter	ETR100	T200	BTD150
Dimensions (mm)	D100 x 60	D100 x 113	D95 x 171
Motor Type	Brushless	Brushless	Brushed
Propeller Blades	2	3	2
Forward Thrust	3.5 kgf	3.71 kgf(@12V)	2.2 kgf
Reverse Thrust	2.45kgf	2.92 kgf(@12V)	-
Power in Watts	172.8	204 (@12V)	81
Operating Voltages	12 VDC	12, 16, 20 VDC	19.1 VDC
Current in Amp.	14.4	17	4.25

Developing a native firmware for ESC that works with water parameters is a very complicated task as many parameters and routines should be considered. It was much easier to adjust some settings in the ESC's firmware and complete the rest of tasks at computer layer level.

For realizing how a thruster's body causes a drag, a CFD simulation using OpenFOAM (2024) is used to generate surface pressure profiles for ETR100 and the other thrusters. All thrusters have been inserted inside a tube of 1000 mm in diameter and 2000 mm in length. Water flow in the tube was fixed at a magnitude of 10000 mm/sec (Figure 11). Then pressure drag is generated by the resolved components of the forces due to pressure acting normally on the surface at all points. It is

computed using ParaView (2024) utility as the integral of the flow direction component of the pressure forces acting on all points on the body.
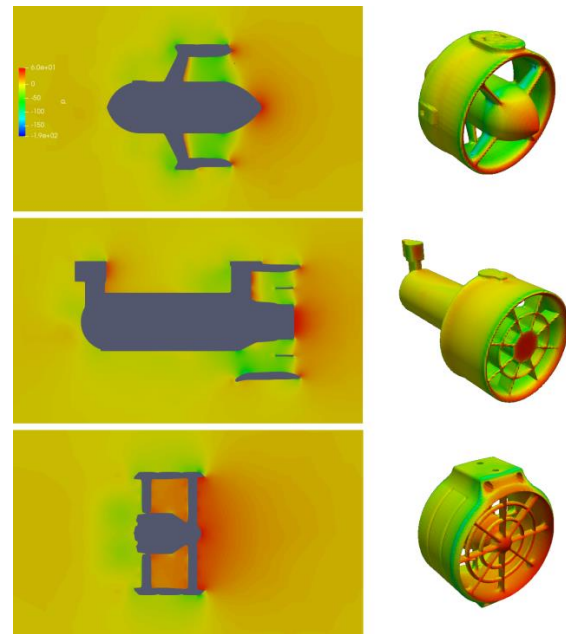
Figure 11. CDF simulation of pressure force for some thrusters (from the top) T200, BTD150 and ETR100.

Simulation results show that ETR100, T200 and BTD150 bodies give drag force -0.22N (-0.0223 kgf), -0.14N (-0.0138 kgf) and -0.15N (-0.0154 kgf) respectively. Even though ETR100 body gives relatively the highest drag, the worst case loss in thrust is extremely very low (0.64%) compared to the benefits of the safety network and the symmetric body design. As future work, more improvements to the thruster's body will be applied to reduce drag as well as use more blades for the propeller to improve efficiency.

Author Contributions
The percentages of the author contributions are presented below. The author reviewed and approved the final version of the manuscript.

	I.E.
C	100
D	100
S	100
DCP	100
DAI	100
L	100
W	100
CR	100
SR	100
PM	100
FA	100

C=Concept, D= design, S= supervision, DCP= data collection and/or processing, DAI= data analysis and/or interpretation, L= literature search, W= writing, CR= critical review, SR= submission and revision, PM= project management, FA= funding acquisition.

Conflict of Interest

The author declared that there is no conflict of interest.

Ethical Consideration

Ethics committee approval was not required for this study because of there was no study on animals or humans.

References

BLHeli. 2024. Firmware page. URL: https://github.com/bitdump/BLHeli. (accessed date: 9 August 2024).

Blue Robotics T200. 2024. Thruster specifications. URL: https://bluerobotics.com/store/thrusters/t100-t200-thrusters/t200-thruster-r2-rp/ (accessed date: 9 March 2024).

Capocci R, Dooly G, Omerdić E, Coleman J, Newe T. 2017. Inspection-class remotely operated vehicles—a review. J Marine Sci Engin, 5(1): 13.

EMAX CF2822. 2024. Brushless motor specifications. URL: https://emaxmodel.com/products/emax-cf2822-1200kv-brushless-motor-for-rc-airplane-multicopter (accessed date: 9 March 2024).

Epps B. 2016. On the rotor lifting line wake model. J Ship Prod Design, 32(3): 31-45.

Epps B, Kimball R. 2013. Unified rotor lifting line theory. J Ship Res, 57(4):181-201.

Gorospe G, Kulkarni C, Hogge E, Hsu A, Ownby N. 2017. A study of the degradation of electronic speed controllers for brushless DC motors. URL: https://ntrs.nasa.gov/api/citations/20200000579/downloads/20200000579.pdf (accessed date: 9 March 2024).

Ho M, El-Borgi S, Patil D, Song G. 2020. Inspection and monitoring systems subsea pipelines: A review paper. Struct Health Monitor, 19(2): 606-645.

Hobbyking ESC 20. 2024. Amperes specifications. URL: https://hobbyking.com/en_us/hobbyking-20a-2-4s-esc-3a-ubec.html?__store=en_us (accessed date: 9 March 2024).

Khojasteh D, Kamali R. 2017. Design and dynamic study of a ROV with application to oil and gas industries of Persian Gulf. Ocean Engin, 136: 18-30.

Macreadie P, McLean D, Thomson P, Partridge J, Jones D. 2018. Eyes in the sea: Unlocking the mysteries of the ocean using industrial, remotely operated vehicles (ROVs). Sci Total Environ, 634: 1077-1091.

OpenFOAM. 2024. URL:https://www.openfoam.com/ (accessed date: 9 March 2024).

OpenProp Software v3.3.4. 2024. Open-source software for the design and analysis of marine propellers and horizontal-axis turbines (2013). URL: https://www.epps.com/openprop. (accessed date: 9 March 2024).

ParaView. 2024. URL:https://www.paraview.org/ (accessed date: 9 March 2024).

Patterson M, Elliott J, Niebuhr D. 2012. A STEM experiment in informal science education: ROVs and AUVs survey shipwrecks from the American Revolution. Oceans, 2012: 1-8.

Prasad MPR, Sai Kiran P. 2020. Development of deep sea unmanned underwater robots: a survey. In: IEEE 17th India Council International Conference (INDICON); 10-13 December, New Delhi, India; pp: 1-7.

SAAB. 2024. Seaeye thrusters specifications. URL: https://www.saabseaeye.com/uploads/thrusters-group-datasheet-rev6.pdf. (accessed date: 9 March 2024).

Sánchez PJB, Papaelias M, Márquez FPG. 2020. Autonomous underwater vehicles: Instrumentation and measurements. IEEE Instrument Measure Magazine, 23(2): 105-114.

Seabotix BTD150. 2024. Thruster specifications. URL: http://ocean-innovations.net/OceanInnovationsNEW/SeaBotix/BTD150_Data_Sheet.pdf. (accessed date: 9 March 2024).

SimonK. 2024. Firmware page. URL: https://github.com/sim-/tgy. (accessed date: 9 March 2024).

Song Y, Choi S. 2020. Underwater 3D reconstruction for underwater construction robot based on 2D multibeam imaging sonar. J Ocean Engin Technol, 30(3): 227-233.

DC REGULATION AND LOOP GAIN ANALYSIS OF A DC-DC SWITCH MODE POWER SUPPLY: A CASE STUDY ON A SYNCHRONOUS PWM CONTROLLED BUCK CONVERTER

Cağfer YANARATEŞ[1], Aytaç ALTAN[2]*

[1]Gümüşhane University, Department of Electrical and Energy, Kelkit Aydın Doğan Vocational School, 29600, Gümüşhane, Türkiye
[2]Zonguldak Bülent Ecevit University, Department of Electrical Electronics Engineering, 67100, Zonguldak, Türkiye

Abstract: This study investigates the DC regulation of a DC-DC buck converter operating with pulse width modulation (PWM), taking into account the internal resistance of the coil and the on-resistance of the switching device. The effect of these parameters on the input/output disturbances is analyzed in continuous-conduction mode under constant frequency voltage mode control. The study also explores the effect on loop gain using the IRU3037 8-pin IC synchronous PWM controlled buck converter. The transfer function of the IRU3037 IC is derived from datasheet values using state-space averaging and AC small signal methods. A Type II compensator is then designed based on the derived transfer function. In addition, the step response characteristics of the open-loop and closed-loop circuits are investigated by time domain analysis.

Keywords: Switch mode power supply, IRU3037 IC, Synchronous PWM control, Loop gain analysis, Type II compensator

1. Introduction

Nowadays, effective electrical energy conversion is greatly facilitated by power electronic devices (Alavi et al., 2020; Samosir et al., 2023; Sangeetha et al., 2023). One of the most common circuit topologies for power processing is the second order pulse width modulation (PWM) DC-DC buck converter, which uses an inductor and a capacitor (Naik and Mehta, 2017). Its simple topology and strong frequency domain control characteristics, in particular the absence of non-minimum phase (right half-plane zero) is one of its main advantages, and this advantageous characteristic allows a wide bandwidth of the control loop, resulting in a fast transient response to changes in load and input voltage (Simmons and Tymerski, 2021; Boukerdja et al., 2020).

DC electrical power is converted by a DC-DC switch mode power supply (SMPS) to be used by other devices by changing the supply voltage. When designed to operate at high frequencies, an SMPS can achieve unity efficiency and become smaller in size. Both step-up and step-down conversion can be achieved by placing the switch, diode and inductor in different configurations. Regulation of the output voltage is required to use a feedback system. However, feedback raises the issue of stability (Zhou et al., 2024). In order for the converter to be stable, the compensation must be implemented correctly, otherwise the converter would be slow to respond (Yasuda and Itoh, 2024). In this respect, knowledge of the loop gain is

crucial for designing an effective compensation scheme (Lu et al., 2023; Hsieh and Lee, 2022; Beghou et al., 2021).

The loop gain is the sum of the gains around a feedback loop, either as a ratio or in decibels in electronics and control systems theory (Ravi and Ghosh, 2022). To control an SMPS, feedback loops are frequently employed in electronics such as amplifiers and oscillators, and more generally in both electronic and non-electronic control systems (Simmons and Tymerski, 2021). In a feedback loop, an output of the equipment is sampled and used to change the input, thereby improving the control of the output. The behaviour of the device is determined by the loop gain and the associated idea of loop phase shift, specifically whether the output is stable or unstable, which can cause oscillation (Chadha and Kazimierczuk, 2020).

An SMPS is classified as a PWM converter if its switching frequency f_sw is fixed, and the conversion ratio depends on duty ratios (Xie and Guo, 2019). A converter is considered pulse frequency modulated (PFM) if f_sw varies based on load or other factors to maintain the prearranged conversion ratio (Singh et al., 2020). SMPSs have two major advantages: they are relatively easy to analyze and simulate, and the switching harmonics are well known, so that switching noise can be dealt with systematically (Jing et al., 2022). The output of the SMPS is controlled and stabilized by negative feedback (Kapat

and Krein, 2020). However, the tendency to oscillate, known as converter instability, is a potential problem with the use of feedback and must be dealt with by compensation (Kobaku et al., 2020). The error in the system can be suppressed by having a large DC loop gain (Michal, 2016). However, large gain systems are more prone to instability. Therefore, a thorough loop gain analysis is required and the design of an efficient controller is crucial (Su and Li, 2020; Leoncini et al., 2022). By adjusting the values of the passive components, the transfer function of the compensator can be shaped in the loop gain analysis. Additionally, zeros, poles, and any DC gain can be achieved. Unlike linear systems, switching converters are time-varying non-linear systems whose loop gain is difficult to derive (Lu et al., 2023; Polivka et al., 1980; Lin et al., 2021). It is therefore necessary to obtain a time-invariant linear model. The dynamic (AC small signal) state space methodology, which is the most practical and widely used approach, is applied in this study (Suman et al., 2012; Herbst, 2019).

In this study, the effects of input and output disturbances on the DC regulation performance of a synchronous buck converter are investigated in detail. In addition, the commercially available IRU3037 8-pin synchronous PWM controlled buck converter is used as a case study. Parameters based on datasheet values are used to derive the transfer function. Using this transfer function, a PI controller is designed and comparative analysis is carried out by performing open-loop and closed-loop analyses.

The rest of the paper is structured as follows. The DC regulation principles of SMPS are discussed in Section 2, with particular emphasis on the methods used to achieve stable and efficient operation. Section 3 presents a detailed case study of the IRU3037 IC synchronous PWM controlled buck converter, highlighting its design and operating characteristics. The design process of the Type II (PI controller) compensator, including the rationale behind the selection of the parameters, is analyzed in detail in this section. Furthermore, this section presents the derivation of the system transfer function and gives an insight into the mathematical modelling and analysis techniques used in this study. Section 4 includes the simulation results and discussions, where the performance of the proposed design is evaluated and compared with existing methods. Finally, Section 5 concludes the paper with a summary of the main findings and suggestions for future work in this area.

2. DC Regulation of SMPSs

The closed-loop network of a DC-DC power supply consists of a power stage, a modulator for generating the pulses for the power stage with an output voltage V_{out}, a filter capacitor C_f, a divider leading to a compensator in which the reference voltage V_{ref} and the feedback voltage V_f are compared and the duty cycle D is produced accordingly (Rahimi and Emadi, 2008). The schematic

diagram of a DC regulator is shown in Figure 1.

The issue addressed in this study is that how the output of the system is affected by a step change (disturbance) in either the input voltage V_{in} or the load (output current) I_{out}. In many real applications, both are unavoidable. In the presence of the disturbances mentioned above, V_{out} will react in a similar way, but the issue is whether there will be a permanent shift away from the desired output or a return to the reference tracking value (Bryant and Kazimierczuk, 2006). The generic representation of the change in output is given in Figure 2.
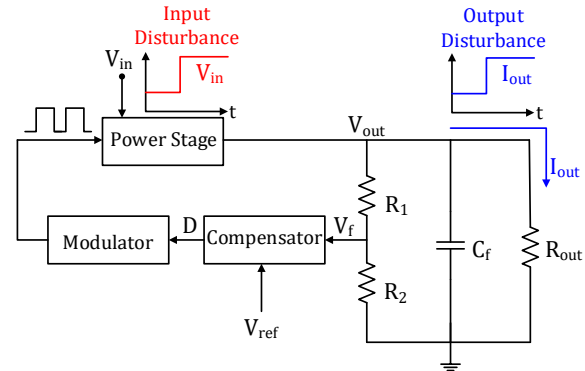
Figure 1. Schematic diagram of the closed loop network for a DC-DC power supply regulator.
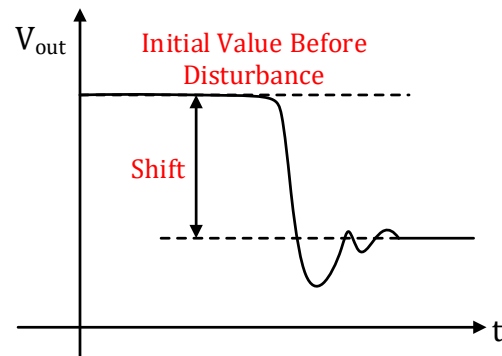
Figure 2. Generic representation of output response to step changes in input voltage or load current.

DC regulation analysis is used to observe the system to assess its behaviour and determine the amount of variation to be compensated. To understand the importance of DC regulation analysis, it can be said that the output of an electrical/electronic circuit consisting of many sub-systems is critical to the stability of the overall system as it is used as a reference in the other sub-systems. Apart from the dependence on a reasonably constant output, a robust system design captures not only the nominal or normal behaviour of the system, but also the degree of uncertainty and fluctuation (Linares-Flores et al., 2013). The voltage regulator with a feedback loop is given in Figure 3.
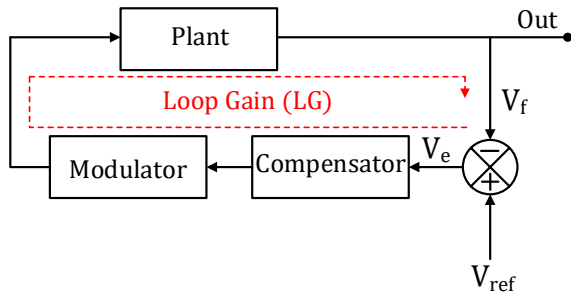
Figure 3. Voltage regulator with feedback loop for DC control analysis.

In addition to the main parts, it is shown with V_{ref}, a summation junction to compare the reference to the output, or a scaled output V_f through a divider which determined by the application and its limitations to calculate the error V_e.

The loop gain is a very important parameter that provides information for designing a reliable and robust compensator to ensure that the system will be stable at a desired bandwidth. The relationship between loop gain, V_{ref}, V_f and V_e is given by

$$Loop\ Gain = \frac{V_f}{V_e} \tag{1}$$

$$Error = V_e = V_{ref} - V_f \tag{2}$$

$$Error = V_{ref} - V_e * Loop\ Gain \tag{3}$$

The value of the loop gain in DC or extremely low frequencies is of interest, which typically have large values, certainly greater than 1. In this regard, V_e and $Loop\ Gain$ in DC are given by

$$V_e(DC) = \frac{V_{ref}}{1 + Loop\ Gain(DC)}\ ; Loop\ Gain(DC) \gg 1 \tag{4}$$

The block diagram including the effects of input and output disturbances, which can be modelled as additional inputs passing through transfer functions, is given in Figure 4. To derive the transfer functions $G_{input}(s)$ and $G_{output}(s)$, the implementations are carried out on a synchronous DC-DC buck converter topology by opening the loop (no feedback) for both cases: a step change in V_{in} and a step change in I_{out}. The generic circuit diagram of a synchronous DC-DC buck converter is shown in Figure 5.
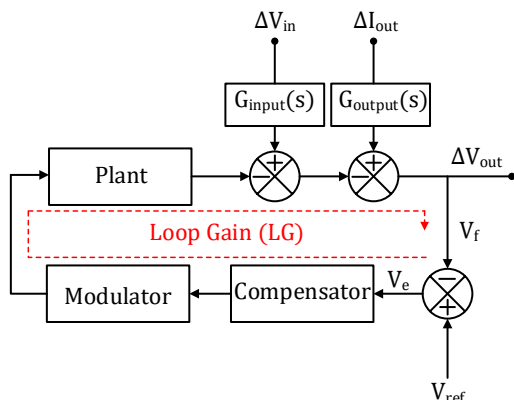
Figure 4. Block diagram showing the effects of input and output disturbances in a DC-DC buck converter.
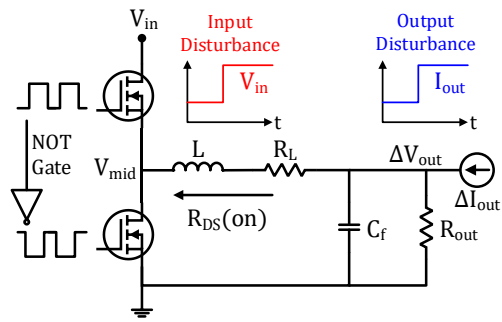
Figure 5. Generic circuit diagram of a synchronous DC-DC buck converter.

For a given operating point with a certain duty cycle, the change in V_{in} will modify V_{mid} and consequently be transmitted to V_{out}. Considering that the internal resistance of the inductor R_L is very small, close to 1, the value of V_{mid} is approximated as:

$$V_{mid} = V_{in}D \cong V_{out} \quad \Rightarrow \Delta V_{out} \cong \Delta V_{in}D \tag{5}$$

It is obvious that the transfer function $G_{input}(s)$ is the duty cycle D. Since the DC regulation of the converter is considered, the capacitor is open. The system includes R_L and the resistances of the $R_{DS}(on)$ transistors in parallel with R_{out}, which is much higher in real applications. In this respect, the relationship between ΔI_{out} and ΔV_{out}, and therefore the transfer function $G_{output}(s)$, is written as

$$\Delta V_{out} = \Delta I_{out}(R_L + R_{DS}(on)) // R_{out}) \tag{6}$$

$$\Delta V_{out} \cong \Delta I_{out}(R_L + R_{DS}(on)) \tag{7}$$

$$G_{output}(s) = R_L + R_{DS}(on) \tag{8}$$

3. A Case Study: IRU3037 IC Synchronous PWM Controlled Buck Converter

The IRU3037 8-pin synchronous PWM controlled buck converter is used as a case study, the schematic of which is shown in Figure 6. A key feature of the IRU3037 controller IC is its ability to provide cost-effective regulation for on-board DC-DC applications, including DDR memory source sink V_{TT} applications, graphics cards and hard disk drives. IRU3037 IC system parameters are listed in Table 1.
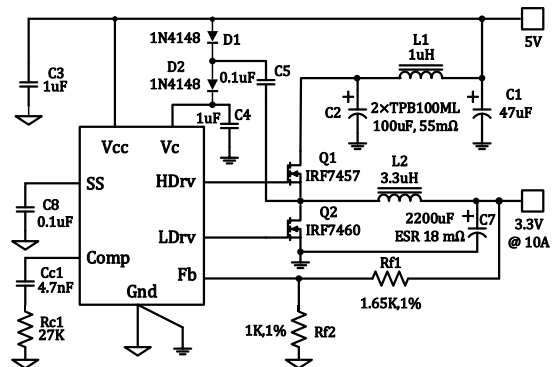
Figure 6. Schematic of the IRU3037 8-pin synchronous PWM controlled buck converter for on-board DC-DC applications.

Table 1. IRU3037 IC system parameters

IRU3037 IC System Parameters	
Input voltage	5 V
Output voltage	3.3 V
Output current	10 A
Switching frequency	200 kHz
Output inductor	3.3 μH
Output capacitor	2200 μF with 18 mΩ ESR
Peak to peak oscillator ramp voltage	$V_{OSC} = 1.25$ V
Reference voltage	$V_{REF} = 1.25$ V
Transconductance gain	$G_m = 0.6$ mA/V or 600 μmho

The zero-crossover frequency, or F_o, is the frequency at which the loop gain is unity. Its value is often between 1/10 and 1/5 of the switching frequency. F_o determines the speed at which the dynamic load response occurs. The higher the F_o, the faster the dynamic response. To obtain a stable system, the slope of the loop gain around F_o should be $-20\ dB$. A stable system often has a phase margin of $45°$ or more.

The output inductor and the output capacitor are the cause of the pole, so the power stage pole F_{PO} is determined as

$$F_{PO} = \frac{1}{2\pi \times \sqrt{L \times C_{OUT}}} \tag{9}$$

$$F_{PO} = \frac{1}{2\pi \times \sqrt{3.3\mu H \times 2200\mu F}} \cong 1.87\ kHz \tag{10}$$

The ESR of the output capacitor is the cause of the zero point F_{ZO}, and it is calculated as

$$F_{ZO} = \frac{1}{2\pi \times ESR \times C_{OUT}} \tag{11}$$

$$F_{ZO} = \frac{1}{2\pi \times 18m\Omega \times 2200\mu F} \cong 4\ kHz \tag{12}$$

The desired zero crossover frequency F_O is selected as 20 kHz according to the design criteria correlation between F_O and the switching frequency f_{sw} ($F_O \leq f_{sw}/5 \sim f_{sw}/10$). The standard process for designing compensators in practical circuits involves the use of an error amplifier in conjunction with a network; Type II and Type III compensators are the most commonly used, as Type I compensators exhibit poor performance. As shown in Table 2, the characteristics of the output capacitor and the location of the zero-crossover frequency determine the type of compensation. The Type II compensator, also known as a proportional-integral (PI) controller, is used in this case study because the integration of the derivative action into it causes high noise in the system control.

Table 2. Compensator type selection criteria based on output capacitor characteristics and zero crossover frequency

Compensator Type	Location of Zero Crossing Frequency	Typical Output Capacitor
Type II (PI)	$F_{PO} < F_{ZO} < F_O$ $< f_{sw}/2$	Electrolytic, Tantalum
Type III (PID)	$F_{PO} < F_O < F_{ZO}$ $< f_{sw}/2$	Tantalum, Ceramic

3.1. Type II Compensator Design Process

The configuration of the PI compensator, the desired loop gain and the bode plot of the buck converter power stage are shown in Figure 7.

(a)

(b)
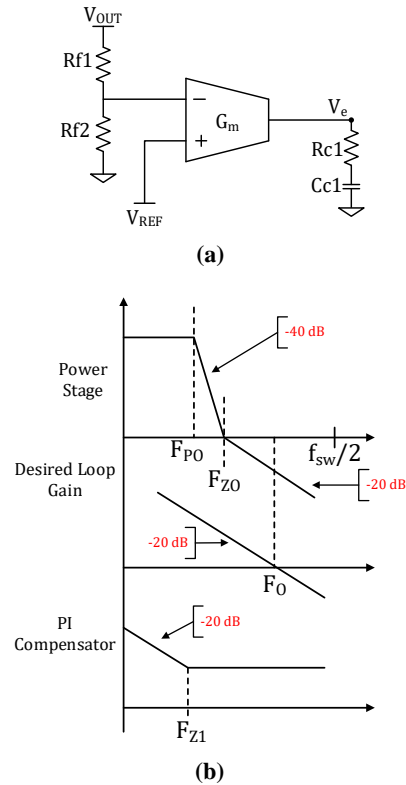
Figure 7. Configuration of **a)** the PI compensator with **b)** the desired loop gain and bode plot of the buck converter power stage.

A zero is present in a PI compensator at

$$F_{Z1} = \frac{1}{2\pi \times Rc1 \times Cc1} \tag{13}$$

The output voltage is calculated using resistors $Rf1$ and $Rf2$. This gives the output voltage and is expressed as

$$\frac{V_{OUT}}{V_{REF}} = \frac{Rf2}{Rf1 + Rf2} \tag{14}$$

The feedback pin of the error amplifier can be connected directly to the output voltage. This appears as

$$V_{OUT} = V_{REF} \tag{15}$$

The zero-crossover frequency is set by the resistor $Rc1$. It is calculated as

$$Rc1 = \frac{2\pi \times F_O \times L \times V_{OSC}}{ESR \times V_{IN} \times G_m} \times \frac{Rf1 + Rf2}{Rf2} \tag{16}$$

Combining Equation (14) with Equation (16), $Rc1$ is expressed as

$$Rc1 = \frac{2\pi \times F_O \times L \times V_{OSC}}{ESR \times V_{IN} \times G_m} \times \frac{V_{OUT}}{V_{REF}} \tag{17}$$

Assigning 75% of F_{PO} as the PI compensator zero:

$$F_{Z1} = \frac{1}{2\pi \times Rc1 \times Cc1} = 0.75 \times F_{PO} \tag{18}$$

Calculating the compensator capacitor $Cc1$ is as:

$$Cc1 = \frac{1}{0.75 \times 2\pi \times F_{PO} \times Rc1} = \frac{\sqrt{L \times C_{OUT}}}{0.75 \times Rc1} \tag{19}$$

The explanation above states that the desired locations for the zeros and poles of the chosen PI compensator are

$$F_{Z1} = 0.75 \times F_{PO} = 0.75 \times 1.87 \, kHz \tag{20}$$

$$F_{Z1} \cong 1.4 \, kHz \tag{21}$$

For the chosen PI compensator, based on the actual parameters, the resistor and capacitor are computed as

$$Rc1 = \frac{2\pi \times 20KHz \times 3.3\mu H \times 1.25}{18 \, m\Omega \times 5 \, V \times 0.6 \times 10^{-3}} \times \frac{3.3}{1.25} \tag{22}$$

$$Rc1 \cong 25.3 \, k\Omega \quad \Rightarrow selected \, as \, 27 \, k\Omega \tag{23}$$

$$Cc1 = \frac{\sqrt{3.3 \, \mu H \times 2200 \, \mu F}}{0.25 \times 27 \, k\Omega} \cong 4.2 \, nF \tag{24}$$

$$Cc1 \, selected \, as \, 4.7 \, nF \tag{25}$$

3.2. System Transfer Function Derivation

The transfer function model of the desired buck converter is obtained using the dynamic (AC small signal) state space methodology. Since the inductor and capacitor are the main energy storage components of the buck converter, the system state variables are inductor current i_L and capacitor voltage V_C. Accordingly, the system vector x is defined as

$$x = \begin{bmatrix} i_L \\ V_C \end{bmatrix} \tag{26}$$

The state variable vector x at the steady state operating point is rewritten using

$$X = -A^{-1}BV_{in} \tag{27}$$

$$X = -\frac{adj \begin{bmatrix} 0 & \frac{-1}{L} \\ \frac{1}{C_{OUT}} & \frac{-1}{R_{Load}C_{OUT}} \end{bmatrix}}{det \begin{bmatrix} 0 & \frac{-1}{L} \\ \frac{1}{C_{OUT}} & \frac{-1}{R_{Load}C_{OUT}} \end{bmatrix}} \begin{bmatrix} \frac{D}{L} \\ 0 \end{bmatrix} V_{in} \tag{28}$$

$$X = \begin{bmatrix} \frac{C_{OUT}{}^2 D V_{in}}{R_{Load}} \\ D V_{in} \end{bmatrix} \tag{29}$$

Here A, B are the system and input matrices, respectively. The load R_{Load} is chosen to be purely resistive with a value of 0.33 Ω. Applying the steady state vector, the average system, and input matrices, $\frac{\hat{x}(s)}{\hat{D}(s)}$ is obtained as

$$\frac{\hat{x}(s)}{\hat{D}(s)} = \frac{\begin{bmatrix} \hat{i}_L \\ \hat{V}_C \end{bmatrix}}{\hat{D}(s)} = \begin{bmatrix} \dfrac{V_{in}(C_{OUT}R_{Load}s + 1)}{C_{OUT}LR_{Load}s^2 + Ls + R_{Load}} \\ \dfrac{V_{in}R_{Load}}{C_{OUT}LR_{Load}s^2 + Ls + R_{Load}} \end{bmatrix} \tag{30}$$

The transfer functions connecting D to i_L and V_{OUT} can be obtained by substituting the values of the IRU3037 IC components into Equations (31) and (33).

$$\frac{i_L(s)}{D(s)} = \frac{V_{in}}{L} \frac{s + \dfrac{1}{R_{Load}C_{OUT}}}{s^2 + \dfrac{s}{R_{Load}C_{OUT}} + \dfrac{1}{LC_{OUT}}} \tag{31}$$

$$\frac{i_L(s)}{D(s)} = \frac{0.011s + 15.15}{7.26 \times 10^{-9}s^2 + 10^{-5}s + 1} \tag{32}$$

$$\frac{V_{OUT}(s)}{D(s)} = \frac{V_{in}}{C_{OUT}L} \frac{1}{s^2 + \dfrac{s}{R_{Load}C_{OUT}} + \dfrac{1}{LC_{out}}} \tag{33}$$

$$\frac{V_{OUT}(s)}{D(s)} = \frac{0.0075}{7.26 \times 10^{-9}s^2 + 10^{-5}s + 1} \tag{34}$$

4. Results and Discussions

Understanding the transient and steady state responses of systems requires an understanding of time domain analysis. It is essential to understand how a system operates in the initial stages of a disturbance and how it transitions to a stable state. The step response of the voltage transfer function $V_{OUT}(s)/D(s)$ is shown in Figure 8. Table 3 shows the step response characteristics of the open loop voltage transfer function of the IRU3037 IC.
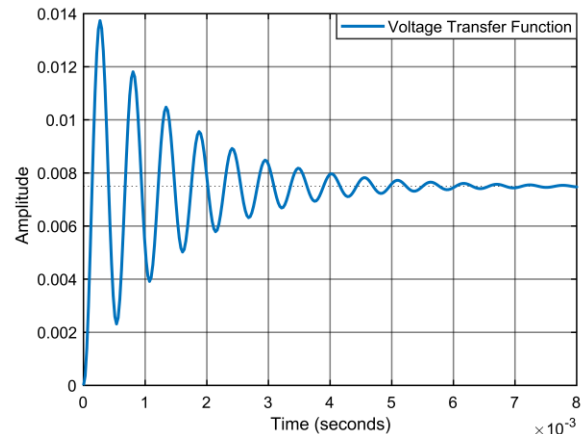
Figure 8. Step response of the voltage transfer function.

Table 3. Step response characteristics of the open-loop voltage transfer function for the IRU3037

Step Response Characteristics	IRU3037 IC Open Loop Voltage Transfer Function
Rise time (s)	9.2929e-05
Settling time (s)	0.0057
Settling minimum	0.0023
Settling maximum	0.0137
Overshoot (%)	83.1365
Undershoot (%)	0
Peak	0.0137
Peak time (s)	2.6768e-04

The step response of the current transfer function $i_L(s)/D(s)$ is given in Figure 9. Table 4 shows the step response characteristics of the open loop current transfer function of the IRU3037.

The step response of the closed loop voltage transfer function $V_{OUT}(s)/D(s)$ is given in Figure 10. Table 5 shows the step response characteristics of the closed loop voltage transfer function of the IRU3037 IC.
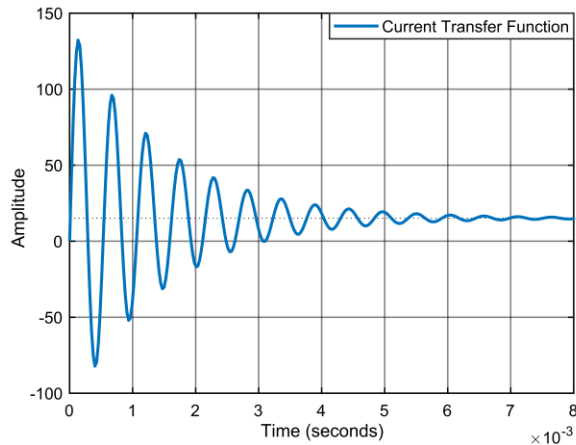
Figure 9. Step response of the current transfer function.

Table 4. Step response characteristics of the open loop current transfer function for the IRU3037

Step Response Characteristics	IRU3037 IC Open-Loop Current Transfer Function
Rise time (s)	8.1319e-06
Settling time (s)	0.0058
Settling minimum	-82.1559
Settling maximum	132.2361
Overshoot (%)	772.7586
Undershoot (%)	542.2288
Peak	132.2361
Peak time (s)	1.3384e-04
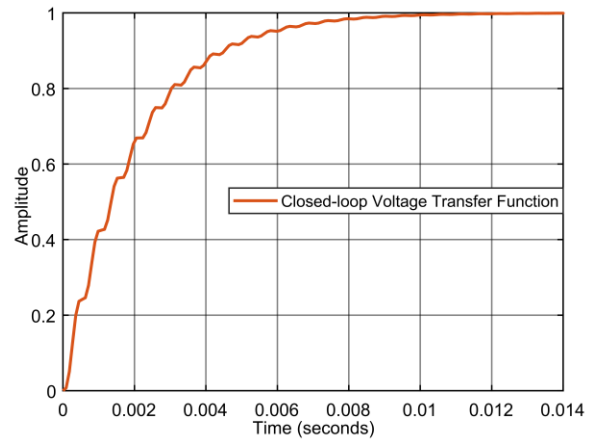
Figure 10. Step response of the closed loop voltage transfer function.

Table 5. Step response characteristics of the closed loop voltage transfer function for the IRU3037

Step Response Characteristics	IRU3037 IC Closed Loop Voltage Transfer Function
Rise time (s)	0.0043
Settling time (s)	0.0077
Settling minimum	0.9040
Settling maximum	0.9996
Overshoot (%)	0
Undershoot (%)	0
Peak	0.9996
Peak time (s)	0.0149

The step response of the closed loop current transfer function $i_L(s)/D(s)$ is given in Figure 11. Table 6 provides the step response characteristics of the closed loop current transfer function of the IRU3037 IC.

Table 7 shows the DC loop gain of the system as the product of the derived output voltage transfer function along the closed loop for various input and output disturbances, denoted as D_{in} and D_{out} respectively. The gain without any disturbance is obtained from the simulation result as 3.6.
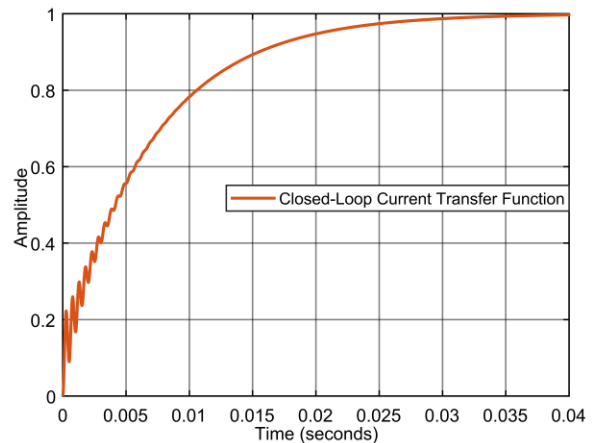
Figure 11. Step response of the closed loop current transfer function.

Table 6. Step response characteristics of the closed loop current transfer function for the IRU3037

Step Response Characteristics	IRU3037 IC Closed Loop Current Transfer Function
Rise time (s)	0.0153
Settling time (s)	0.0268
Settling minimum	0.9000
Settling maximum	0.9986
Overshoot (%)	0
Undershoot (%)	0
Peak	0.9986
Peak time (s)	0.0454

Table 7. DC loop gain for various input and output disturbances

Voltage Transfer Function DC Loop Gain				
Input Disturbance		Output Disturbance		Input & Output Disturbance
D_{in}	Loop Gain	D_{out}	Loop Gain	Loop Gain
0.1	3.465	1.0	2.530	2.450
0.2	3.337	1.5	2.162	2.036
0.3	3.217	2.0	1.864	1.711
0.4	3.103	2.5	1.617	1.448
0.5	2.995	3.0	1.410	1.232
0.6	2.892	3.5	1.232	1.051
0.7	2.795	4.0	1.079	0.898
0.8	2.702	4.5	0.946	0.765
0.9	2.614	5.0	0.829	0.650
1.0	2.530	5.5	0.725	0.549

5. Conclusion

Feedback loops are widely used in electronics and control theory, whether they are electronic or not, to regulate equipment and devices. Oscillators and amplifiers are two examples of such applications. A feedback loop modifies the input and amplifies the output control by using a sample of the output of a device, process or plant. The loop gain and the associated idea of loop phase shift control the behaviour of the device, in particular whether the output is stable and not prone to oscillation. In this context, the DC regulation of a buck converter, which is a DC-DC SMPS operating on a PWM signal, is carried out in this study. Particular attention has been paid to the internal resistance of the coil and the on-resistance of the controllable circuit element (switching device), which are essential in the system. It has been investigated how these parameters create disturbances in the input and output load of the system and how they affect the loop gain. The transfer function of the IRU3037 IC, which was used as a case study, was obtained using datasheet-based information and state-space averaging and AC small-signal methods. In addition to the loop gain analysis, a time domain analysis was carried out and the corresponding step response characteristics were analyzed for both open and closed loop circuits. Future work is concerned with developing different control techniques to obtain more reliable and robust results to minimize the effect of essential and undesirable parameters in switch mode power supply applications.

Author Contributions

The percentages of the authors contributions are presented below. The authors reviewed and approved the final version of the manuscript.

	C.Y.	A.A.
C	50	50
D	50	50
S	50	50
DCP	50	50
DAI	50	50
L	50	50
W	50	50
CR	50	50
SR	50	50

C=Concept, D= design, S= supervision, DCP= data collection and/or processing, DAI= data analysis and/or interpretation, L= literature search, W= writing, CR= critical review, SR= submission and revision.

Conflict of Interest

The authors declared that there is no conflict of interest.

Ethical Consideration

Ethics committee approval was not required for this study because of there was no study on animals or humans.

References

Alavi P, Babaei E, Mohseni P, Marzang V. 2020. Study and analysis of a DC–DC soft-switched buck converter. IET Power Electron, 13(7): 1456-1465.

Beghou L, Popat M, MacDonald S. 2021. PWM control of 3-phase PFC vienna rectifier derived from an average current-based control of single-phase PFC boost converter. In 2021 IEEE IEEE Energy Convers. Congr. Expo. (ECCE), October 10-14, Vancouver, Canada, pp: 3452-3459.

Boukerdja M, Chouder A, Hassaine L, Bouamama BO, Issa W, Louassaa K. 2020. H∞ based control of a DC/DC buck converter feeding a constant power load in uncertain DC microgrid system. ISAT, 105: 278-295.

Bryant B, Kazimierczuk MK. 2006. Voltage loop of boost PWM DC-DC converters with peak current-mode control. IEEE Trans Circuits Syst I, Reg Papers, 53(1): 99-105.

Chadha A, Kazimierczuk MK. 2020. Small-signal modeling of open-loop PWM tapped-inductor buck DC–DC converter in CCM. IEEE Trans Ind Electron, 68(7): 5765-5775.

Herbst G. 2019. A building-block approach to state-space modeling of DC-DC converter systems. J Multidiscip Sci J, 2(3): 247–267.

Hsieh YH, Lee FC. 2022. Improved three-terminal model for PWM converters with current-mode control. In 2022 IEEE IEEE Energy Convers. Congr. Expo. (ECCE), October 9-13, Detroit, USA, pp: 1-8.

Jing T, Maklakov A, Radionov A, Gasiyarov V, Liang Y. 2022. Formulations, solving algorithms, existing problems and

future challenges of pre-programmed PWM techniques for high-power AFE converters: A comprehensive review. Energies, 15(5): 1696.

Kapat S, Krein PT. 2020. A tutorial and review discussion of modulation, control and tuning of high-performance DC-DC converters based on small-signal and large-signal approaches. IEEE Open J Power Electron, 1: 339-371.

Kobaku T, Jeyasenthil R, Sahoo S, Ramchand R, Dragicevic T. 2020. Quantitative feedback design-based robust PID control of voltage mode-controlled DC-DC boost converter. IEEE Trans. Circuits Syst. II: Express Briefs, 68(1): 286-290.

Leoncini M, Melillo P, Bertolini A, Levantino S, Ghioni M. 2022. Integrated loop-gain measurement circuit for DC/DC boost converters with time-based control. In 2022 IEEE 17th Conf. Ph. D Res. Microelectron. Electron. (PRIME), June 12-15, Villasimius, Italy, pp: 253-256.

Lin J, Su M, Sun Y, Li X, Xie S, Zhang G, Blaabjerg F, Feng, J. 2021. Accurate loop gain modeling of digitally controlled buck converters. IEEE Trans Ind Electron, 69(1): 725-739.

Linares-Flores J, Méndez AH, García-Rodríguez C, Sira-Ramírez H. 2013. Robust nonlinear adaptive control of a "boost" converter via algebraic parameter identification. IEEE Trans Ind Electron, 61(8): 4105-4114.

Lu D, Zeng X, Hong Z. 2023. Accurate loop gain model of ripple-based constant on-time controlled buck converters. IEEE Trans Power Electron, 38(6): 7034-7048.

Michal V. 2016. Dynamic duty-cycle limitation of the boost DC/DC converter allowing maximal output power operations. In 2016 IEEE Int. Conf. Appl. Electron, September 6-7, Pilsen, Czech Republic, pp: 177-182.

Naik BB, Mehta AJ. 2017. Sliding mode controller with modified sliding function for DC-DC Buck Converter. ISA T, 70: 279-287.

Polivka WM, Chetty PRK, Middlebrook RD. 1980. State-space average modelling of converters with parasitics and storage-time modulation. In 1980 IEEE Power Electron Spec Conf, June 16-20, Atlanta, USA, pp: 119-143.

Rahimi AM, Emadi A. 2008. An analytical investigation of DC/DC power electronic converters with constant power loads in vehicular power systems. IEEE Trans Veh Technol, 58(6): 2689-2702.

Ravi D, Ghosh A. 2022. Voltage mode control of buck converter using practical PID controller. In 2022 IEEE Int. Conf. Intell. Control. Comput. Smart Power (ICICCSP), July 21-23, Hyderabad, India, pp: 1-6.

Samosir AS, Sutikno T, Mardiyah L. 2023. Simple formula for designing the PID controller of a DC-DC buck converter. Int J Power Electron Drive Syst, 14(1): 327-336.

Sangeetha S, Revathi BS, Balamurugan K, Suresh G. 2023. Performance analysis of buck converter with fractional PID controller using hybrid technique. Robotics Auton Syst, 169: 104515.

Simmons J, Tymerski R. 2021. Design and control of an alternative buck PWM DC-to-DC converter. J Power Energy Eng, 9(6): 43-61.

Singh R, Bose S, Dwivedi P. 2020. Closed loop control of flyback converter with PV as a source. In 2020 IEEE 9th Power India Int. Conf. (PIICON), February 28-March 01, Sonepat, India, pp: 1-6.

Su I, Li D. 2020. Understanding and simulation of loop stability test for DC/DC converters. URL: www.ti.com (accessed date: 28 July 2024).

Suman G, Kumar BP, Kumar MS, Babu BC, Subhashini KR. 2012. Modeling, analysis and design of synchronous buck converter using state space averaging technique for PV energy system. In 2012 IEEE Int Symp on Electronic System Design (ISED), December 19-22, Kolkata, India, pp: 281-285.

Xie H, Guo E. 2019. How the switching frequency affects the performance of a buck converter. Texas Instruments Incorporated: Dallas, TX, USA, pp: 53.

Yasuda T, Itoh JI. 2024. A power balancing control for large power unbalance in a modular multilevel multiport converter with phase-disposition PWM. IEEJ J Industry Appl, 13(1): 41-51.

Zhou S, Zhou G, He M, Mao S, Zhao H, Liu G. 2024. Stability effect of different modulation parameters in voltage-mode PWM control for CCM switching DC-DC converter. IEEE Trans Transport Electr, 10(2): 2408-2422.

FAST AND THERMAL NEUTRON REMOVAL CROSS-SECTION FOR CERAMIC GLASS ALUMINUM OXYNITRIDE

Aydın YILDIRIM[1]*

[1]*Proton Accelerator Facility, Nuclear Energy Research Institute (TENMAK-NÜKEN), 06980, Ankara, Türkiye*

Abstract: This study investigates the effectiveness of transparent aluminum oxynitride (AlON) in neutron shielding, focusing on both fast and thermal neutrons. Using conventional radiation attenuation parameters, the macroscopic neutron removal cross-sections of AlON were calculated for varying neutron energies and material thicknesses. The Geant4 simulation toolkit was employed to model and analyze the neutron interactions with AlON. The results indicate that AlON exhibits a high neutron shielding capacity for fast neutrons (2 MeV), with transmission factor values ranging from 0.783 to 0.260 for material thicknesses between 1 and 10 cm. These values are nearly identical to those for water, which range from 0.782 to 0.257, highlighting AlON's comparable performance. However, for thermal neutrons, AlON's performance was less effective, only surpassing lead but not concrete or water. The findings suggest that while AlON is highly effective for fast neutron shielding, it may require complementary materials to adequately shield thermal neutrons. This could involve using AlON in combination with other materials to create a more comprehensive neutron shielding solution. AlON shows significant potential as a neutron shielding material, particularly for fast neutrons. Its integration with additional shielding materials could enhance its overall effectiveness, making it suitable for various nuclear and radiation protection applications.

Keywords: Neutron, Attenuation, Shielding, Geant4, Cross-section

1. Introduction

Although encounters with neutron sources in daily life are relatively rare, the highly destructive nature of neutrons makes them significantly more hazardous than the more commonly encountered gamma rays. Moreover, neutrons are frequently utilized in nuclear reactors, accelerator facilities, and various industrial applications, where they can generate high fluxes. The high penetrative capability of neutrons, due to their lack of charge, necessitates enhanced and complicated protective measures for radiation workers operating in environments with neutron sources (Kim et al., 2014; Lakshminarayana et al., 2022; Alomayrah et al., 2024; Reda et al., 2024).

Given the increasing need for more effective radiation shielding, there is considerable motivation to develop new materials that surpass traditional methods in reducing biological damage (ALMisned et al., 2021; ALMisned et al., 2024a; Alzahrani et al., 2024a; Alzahrani et al., 2024b; Alzahrani et al., 2024c; Özdoğan et al., 2024). Advances in material science hold promise for innovative shielding solutions that can provide superior protection against neutron radiation (Al-Buriahi et al., 2020; ALMisned et al., 2024b, Alrowaili et al., 2024). For instance, Ali et al. (2024), investigated the use of unglazed ceramic materials in Boron Neutron Capture Therapy (BNCT), highlighting their dual effectiveness in both gamma attenuation and neutron beam shaping. Their study emphasized the potential of ceramics doped with Pb and Ba, which were found to attenuate gamma radiation without significantly affecting the neutron flux, aligning with International Atomic Energy Agency (IAEA) recommendations. Additionally, research by Katubi et al. (2024), explored the neutron and charged particle attenuation properties of Apatite-Wollastonite (AW) glass ceramics doped with B_2O_3. Their findings suggest that these materials are particularly suitable for absorbing fast and thermal neutrons, with fast neutron removal cross-section (FNRC) values measured at 0.0913, 0.0972, and 0.1024 for AW, AW-B10, and AW-B20 samples, respectively. The study indicates potential applications in neutron and ion beam therapy. Similarly, Zayed et al. (2024), studied the gamma and neutron shielding properties of heavy minerals such as hematite and barite. Their results revealed that while barite is superior in gamma attenuation, hematite excels in thermal neutron shielding, outperforming barite by 210%. However, barite demonstrated better performance for fast neutrons, illustrating the importance of material selection based on the specific type of radiation encountered.

As space travel becomes an increasingly discussed and attainable venture, the exposure of astronauts and space

travelers to cosmic ray-induced neutrons is expected to rise. The challenging space environment, with its heightened levels of neutron radiation, emphasizes the critical importance of advancing neutron shielding technologies (Tellili et al., 2014; Kaçal et al., 2019; Cherkashina et al., 2024). In the coming years, the necessity for effective neutron shielding will become even more pronounced, highlighting the urgency of research and development in this field.

Current shielding methods often rely on materials like boron, polyethylene, and heavy metals, which, while effective, come with limitations such as weight and material degradation over time (Singh and Badiger, 2014; Singh et al., 2014; Pavlenko et al., 2015; Fahmi et al., 2024). Novel materials, including polymer composites and nanomaterials, are being investigated for their potential to provide lighter and more effective neutron shielding (Pianpanit and Saenboonruang, 2024; Reda et al., 2024). Research into these advanced materials suggests they could offer substantial improvements in shielding efficiency, potentially revolutionizing protective measures in both terrestrial and extraterrestrial environments.

Aluminum oxynitride (AlON) is a material that finds numerous applications due to its excellent mechanical properties and optical transparency in the visible spectrum. AlON is produced by combining Al_2O_3 with AlN and is typically represented by the formula $Al_{(64+x)/3}O_{(32-x)}N_x$, where x can range from 0 to 8. Studies have shown that when x equals 5, the resulting aluminum oxynitride ($Al_{23}O_{27}N_5$) achieves its most stable and stoichiometric phase (Li et al., 2024). Some of the material properties of AlON, as reported by Salifu and Olubambi (2023), include a density of 3.67 g/cm^3, 80% transparency from the near-ultraviolet through the visible to the near-infrared regions, high durability, stability up to 1200 °C, three times the hardness of steel of the same thickness, scratch resistance, and excellent refractive index, along with large-scale homogeneity (Salifu and Olubambi, 2023). More generally, the mechanical and optical properties of AlON are summarized in Table 1 and Table 2.

Considering these mechanical and optical characteristics, AlON presents numerous potential applications. It could replace traditional glass in a range of products, from smartphone screens to automotive components. Moreover, AlON could play a significant role in the emerging space travel industry. It might be used in spacecraft windows, exterior coatings for radiation shielding and thermal insulation, protection of electronic equipment against cosmic radiation, and in astronaut suits during space missions or extravehicular activities. Additionally, AlON could be critical in protecting solar cells from radiation without obstructing visible light, which is essential for space exploration. In environments like the lunar surface, where the atmosphere is absent or extremely thin, and cosmic radiation can directly reach the surface, AlON could be suitable as a construction material. Its mechanical properties, comparable to concrete, and its optical characteristics make it particularly useful for transparent structural components.

Table 1. Some mechanical properties of the aluminum oxynitride (Ramisetty et al., 2013, Salifu and Olubambi, 2023)

Property	Value
Young Modulus	334 GPa
Poisson's Ratio	0.24
Knoop Hardness	1800 kg/mm^2
Shear Modulus	135 GPa
Compressive Strength	2.68 GPa
Fracture Toughness	2 MPa/m$^{1/2}$
Flexural Strength	0.38 – 0.7 GPa
Weibull Modulus	8.7
Thermal Conductivity at 25 °C	12.6 W/(mK)
Thermal Expansion Coefficient (30 – 900 °C)	7.5 $\times 10^{-6} K^{-1}$
Thermal Shock Resistance, $R' = \frac{\sigma(1-v)k}{\alpha E}$	1.2

Table 2. Some optical properties of the aluminum oxynitride (Ramisetty et al., 2013, Salifu and Olubambi, 2023)

Property	Value
Range of Transmission Wavelength	334 GPa
Typical clarity in the visible range	0.24
Typical haze in visible range	1800 kg/mm^2
Absorption coefficient at a wavelength of 3.39 μm	135 GPa
Refractive index at 0.5 μm wavelength	2.68 GPa
Typical transmittance (without AR coatings) in the visible range	2 MPa/m$^{1/2}$
Optical homogeneity achieved in a (15 in × 25 in) part having 3.4 in aperture	0.38 – 0.7 GPa
Weibull Modulus	8.7
Total integrated optical scatter at a wavelength of 0.64 μm, and sample thickness of ~5 mm	12.6 W/(mK)
dn/dT in the wavelength range 3 - 5 μm	7.5 $\times 10^{-6} K^{-1}$

Given these attributes, it is evident that AlON would be highly useful in neutron shielding applications if it also provides good radiation protection. Previous study indicating AlON's effective gamma radiation shielding suggests that its neutron shielding performance warrants investigation (Yıldırım, 2024). In this study, Yıldırım

(2024), investigated the gamma-ray shielding capabilities of AlON and presented the following results. As evidenced by the findings of the study, while AlON exhibits superior gamma-ray shielding properties compared to Ordinary Portland Concrete in its undoped form, its efficacy does not surpass that of lead. The mass attenuation coefficients (MACs) for AlON have been reported to range between 2×10^{-2} and $2 \times 10^{3}\ cm^{2}/g$. Furthermore, the study compared AlON with commercially available lead-equivalent glasses (e.g., RS-253, RS-253-G18, RS-323-G19, RS-360, RS-250), demonstrating that AlON offers superior shielding compared to non-lead alternatives, while exhibiting comparable performance to lead-containing options, particularly at higher energies. In addition to its potential applications in space, AlON's glass-like structure and transparency in the visible range make it a promising candidate for use as a lead-equivalent glass in radiation shielding, particularly in contexts such as nuclear power plants and healthcare facilities.

The aim of this study is to investigate the shielding performance of aluminum oxynitride against fast and thermal neutrons. The study proceeds as follows: Section 2 describes the interaction of neutrons with matter and discusses neutron shielding parameters and their calculation methods. Section 3 presents the results obtained for fast and thermal neutrons, comparing AlON's performance with traditional shielding materials and discussing its neutron shielding effectiveness. The final section summarizes the study and lists the conclusions.

2. Materials and Methods

2.1 Theoretical Calculations

In this study, the effective neutron removal cross-section of transparent aluminum oxynitride for fast and thermal neutrons was investigated using Geant4 simulations. The cross-section discussed here is not the true interaction probability cross-section but a useful parameter that can be calculated for materials with insufficient hydrogen content. It is generally lower than the true cross-section, approximately two-thirds of its value.

Neutrons interact with the medium primarily through absorption and scattering. The total cross-section (σ_T) is expressed as the sum of the absorption cross-section (σ_A) and the scattering cross-section (σ_S). The relationship between these cross-sections is outlined below (equation 1):

$$\sigma_T = \sigma_A + \sigma_S \tag{1}$$

To calculate the total macroscopic cross-section for a compound or mixture, we use the formula (equation 2):

$$\Sigma_T = \sum_i N_i \tag{2}$$

In this equation, N_i represents the number of nuclei per unit volume of the i_th element in the mixture (Akyıldırım, 2019). For the macroscopic neutron removal

cross-section (Σ_R), the calculation is performed using (equation 3):

$$\Sigma_R = \sum_i \rho_i \tag{3}$$

Here, ρ_i is the density of the i_th component, and refers to the neutron removal cross-section of the i_th component. Extending this to a material comprising multiple components, the generalized macroscopic neutron removal cross-section (Σ_R) can be determined as follows (equation 4):

$$\Sigma_{R_S} = \sum_{c=1}^{n} \rho_c (\Sigma_R/\rho)_c = \sum_{c=1}^{n} (F_w)_c \rho_S \tag{4}$$

In this expression, ρ_c denotes the density of the c-th component, $(\Sigma_R/\rho)_c$ signifies the mass removal cross-section of the c_th component, ρ_S is the overall density of the material, and $(F_w)_c$ represents the weight fraction of the c_th component (El-Khayatt, 2010; Gaylan et al., 2021).

In this study, the cross-section to be calculated is the macroscopic removal cross-section, based on the principle of measuring the fraction of incident neutrons that remain unaffected after passing through the material. This calculation is quite similar to the gamma attenuation coefficient and can be computed using the equation given below (equation 5):

$$I = I_0 e^{-\Sigma t} \tag{5}$$

Here, I_0 represents the number of incident neutrons, while I denotes the number of neutrons that pass through the material without interaction. The parameter t in equation 5 refers to the thickness of the material the neutrons traverse, and $\sum$ corresponds to the Σ_R parameter shown in equations 1 - 4. Another useful parameter for discussing equation 5 in the context of neutrons is the Transmission Factor (TF), defined by the equation below (equation 6):

$$TF = \frac{I}{I_0} \tag{6}$$

When considering equations 5 and 6, a relationship between TF and the neutron shielding effectiveness of the material can be observed; the smaller the TF, the better the material's neutron shielding capability (ALMisned et al., 2024b).

2.2 Geant4 Simulation Setup

The Geant4 simulation toolkit was utilized to calculate the macroscopic neutron removal cross-sections, thus providing detailed insights into the interaction of neutrons with aluminum oxynitride (AlON). Geant4 is a versatile and widely used simulation program that is particularly effective for modeling particle interactions across various domains, including nuclear physics, space science, high-energy physics, and accelerator physics (Agostinelli et al., 2003; Allison et al., 2006, 2016). The flexibility and precision of the tool make it an invaluable resource for optimizing the design and performance of

high-budget experiments. In this study, the simulation setup involved a detailed definition of the geometry of the test material. This included the specification of all constituent elements, compounds, or mixtures, along with the material's density, physical state, and spatial configuration relative to the neutron source. The accurate representation of AlON was achieved by incorporating 23 Al, 27 O, and 5 N atoms into the simulation model, with a density of 3.67 g/cm³ as reported in the literature (Johnson et al., 2012; Salifu and Olubambi, 2023). The experimental conditions were set to reflect typical room temperature and atmospheric pressure conditions, with the material in its solid state, in order to ensure that the simulation closely mimicked real-world conditions. The parameters used in simulations are given in Table 3. The SHIELDING physics list from Geant4 was selected for the simulations, a choice particularly suitable for neutron shielding studies due to its comprehensive treatment of neutron interactions. The physics list includes models for elastic and inelastic scattering, absorption, and capture, thus providing a robust framework for the analysis of neutron attenuation.

Table 3. Geant4 simulation parameters for AlON

Property	Value
Chemical Formula	$Al_{(64+x)/3}O_{(32-x)}N_x$ $\quad (0 \leq x \leq 8)$
Most Stable Form ($x = 5$)	$Al_{23}O_{27}N_5$
Density	3.67 g/cm³
Elemental Mass Fraction	55.28% Al, 38.48% O, 6.24% N
Elemental Abundance	41.82% Al, 49.09% O, 9.09% N

A critical aspect of the simulation was the configuration of the neutron source. The source was positioned 5 cm from the target, designed with a radius of 0.5 cm and a beam spread of 0.2 mm, directed along the +z axis. To achieve a narrow, focused beam, which is common in neutron shielding research, a beam-type source was utilized instead of a collimated point source. This approach ensures that the neutron flux impinging the target material is consistent with experimental setups typically used in neutron shielding studies. The simulation was run with 1,000,000 events per scenario to ensure statistical significance. This large number of events allows for a detailed analysis of neutron interactions within AlON, providing precise macroscopic neutron removal cross-sections. The high granularity of the data obtained from these simulations enables a thorough understanding of AlON's effectiveness as a neutron shielding material, which is crucial for its potential applications in nuclear and space environments. Moreover, post-simulation data analysis focused on evaluating the neutron attenuation characteristics of AlON across a range of neutron energies. The results were benchmarked against other common shielding materials, such as lead, water and standard concrete, to assess AlON's relative performance. This comparison highlights the strengths and limitations of AlON in practical shielding scenarios, offering valuable insights for its application in environments where neutron radiation is a concern.

The simulation for neutron removal cross-sections prepared with Geant4 is shown in Figure 1. In this figure, the red block represents the AlON material, which serves as the primary target for the neutron beam. The large blue block immediately behind it indicates the region where the energy losses of neutrons, after passing through the material, are recorded. This region is crucial for determining the degree of interaction the neutrons undergo as they traverse the AlON target. The green lines in the figure represent the neutrons that are sent in a well-collimated beam, ensuring a focused and uniform interaction with the target material. The simulation is designed to capture and record all possible interactions of neutrons with the material, including scattering, absorption, and transmission without interaction. Each of these interactions is significant as they contribute to the overall understanding of how AlON interacts with neutron radiation. However, for the specific calculation of neutron removal cross-sections, as defined in the literature, only the neutrons that pass through the material without any interaction are considered relevant (El-Khayatt, 2010). These non-interacting neutrons are essential for calculating the macroscopic removal cross-section, which is a measure of the material's effectiveness in attenuating or filtering out neutron radiation. Furthermore, the data recorded in the blue block is analyzed to determine the energy distribution of neutrons post-interaction, which provides insight into the material's shielding capabilities. The energy losses are directly related to the material's ability to absorb or scatter neutrons, which is critical for applications where neutron attenuation is required, such as in radiation shielding or nuclear reactors. By comparing the number of neutrons that pass through the material without interaction to the total number of neutrons sent in the beam, the macroscopic neutron removal cross-section can be accurately calculated, offering a quantitative measure of AlON's neutron shielding effectiveness.

These comprehensive simulations not only help in predicting the material's performance in various neutron-rich environments but also provide a basis for optimizing the material's composition and thickness to achieve desired neutron attenuation characteristics.
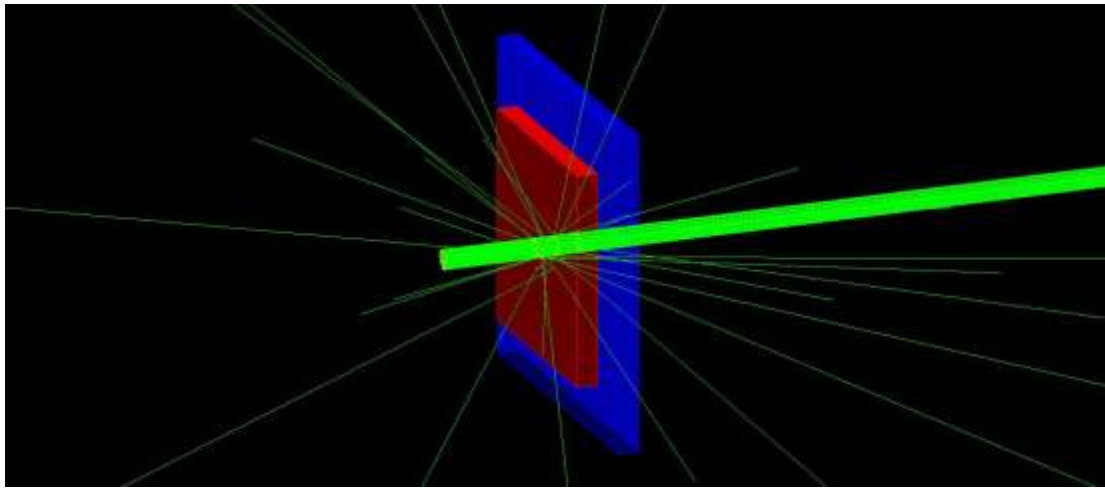
Figure 1. The image of the Geant4 simulation geometry. The red block presents the aluminum oxynitride while the blue block presents the neutron detector. The green lines represents the neutron beam. The incident and outgoing neutron flux can clearly be clearly seen in the figure.

3. Results and Discussion

In the study, the effectiveness of transparent aluminum oxynitride in stopping fast and thermal neutrons was calculated using conventional radiation attenuation parameters. As described in Section 2, the macroscopic neutron removal cross-section of AlON was calculated for different energies and thicknesses. Subsequently, for a fixed thickness and energy, the cross-sections of each element constituting AlON were considered, and the sum of these cross-sections was compared with the directly calculated cross-section.

First, we analyze the change in neutron removal cross-sections with increasing energy for fast neutrons. The graph shown in Figure 2 illustrates the variation of cross-sections with energy. Given that the neutrons in question are fast, the energy range is 2 to 10 MeV. The cross-sections obtained by varying the energy with 0.5 MeV intervals are plotted on the graph. As previously discussed, a larger macroscopic cross-section or a smaller transmission factor indicates superior shielding. As illustrated in Figure 2, while an increase in neutron energy is typically associated with a reduction in the macroscopic cross-section, the graph reveals a number of instances where the cross-section exhibits a sudden rise at specific intermediate energy values. For example, the macroscopic cross-section reaches its maximum value at approximately 3.5 MeV, after which it begins to decline and reaches a second maximum at approximately 6 MeV. These points may be indicative of resonance points for neutron capture or peak points for neutron scattering.

Expanding on the data in Figure 2, Figure 3 presents the variation in fast neutron removal cross-sections with respect to material thickness for selected neutron energy values. As seen in Figure 2, the values for 4 MeV and 6 MeV are lower than those for 3 MeV and 5 MeV, respectively. Here, since the vertical axis represents the transmission factor instead of the macroscopic removal cross-section, lower values correspond to better shielding properties. As an example, the removal cross-section values calculated for a neutron energy of 2 MeV are given in Table 4.
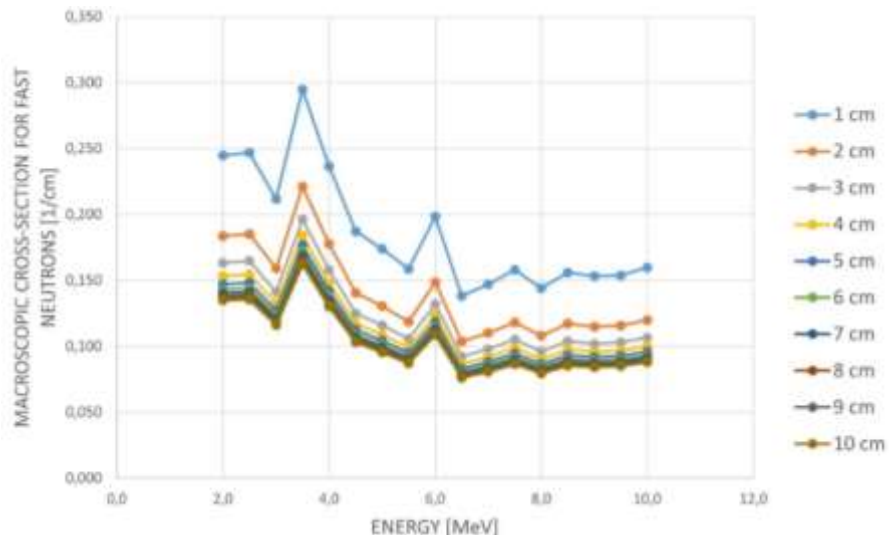
Figure 2. Comparison of macroscopic fast neutron cross-sections with increasing neutron energy.
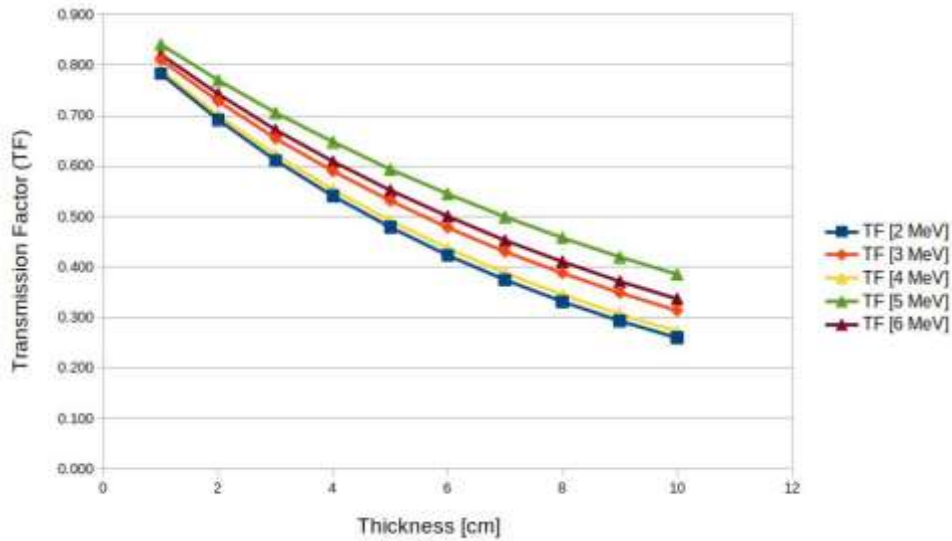
Figure 3. Comparison of transmission factors (TFs) with increasing target thickness. The graph also shows the effect of the neutron energy.

Table 4. The table shows the Macroscopic Neutron Removal Cross-Section for transparent aluminum oxynitride. It shows cross-section values for only 2 MeV neutron energy

Macroscopic Neutron Removal Cross-Section for 2 MeV									
Thickness [cm]	1	2	3	4	5	6	7	8	9	10
Cross-Section [1/cm]	0.245	0.184	0.163	0.153	0.147	0.143	0.140	0.138	0.136	0.135

For thermal neutrons, the TF values for AlON range from 0.663 to 0.104, proportional to the material thickness (lower values indicate better shielding). As expected, the best result is obtained at a thickness of 10 cm with a TF value of 0.104, whereas this value is 0.026 for concrete and 0.125 for lead. The same value is calculated as 0.000014 for water. Similarly, when AlON is evaluated for fast neutrons (2 MeV) over a thickness range of 1 to 10 cm, the TF values range from 0.783 to 0.260 (again, lower values indicate better shielding). These values are very close to the values calculated for water, which are 0.782 to 0.257, and it has been observed that AlON provides better shielding than both lead and concrete. As shown in Figure 4, water and AlON behave almost identically.
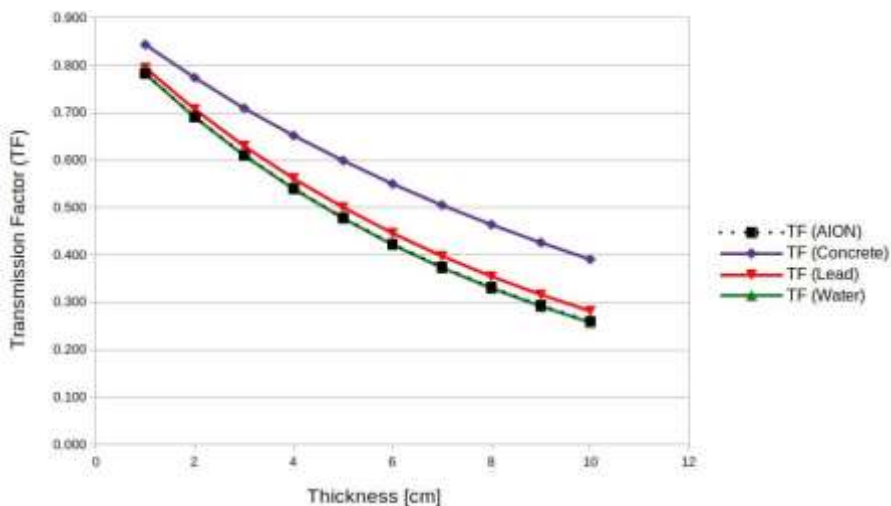
Figure 4. A comparison of conventional shielding materials with aluminum oxynitride for fast neutrons. The y-axis displays the transmission factor. In the case of fast neutrons, AlON is superior to concrete and lead, and is almost identical to water.

The last two graphs in this section compare the shielding capabilities of thermal and fast neutrons with other conventional shielding materials. First, the shielding capacity of AlON against fast neutrons is shown in Figure 4. In Figure 4, the change in the transmission factor with material thickness is shown for a constant fast neutron energy (2 MeV). Here, the neutron shielding capacity of AlON is compared with three other materials: concrete,

lead, and water. Their thicknesses were varied between 1 and 10 cm and compared with AlON. As can be seen in Figure 4, AlON provides superior performance in stopping fast neutrons compared to both concrete and lead. However, it yields nearly the same transmission factors as water. This indicates that AlON is a suitable material for neutron shielding when fast neutrons are concerned.

The graph in Figure 5 is an adaptation of the comparison for fast neutrons to thermal neutrons. The first noticeable feature is that AlON's excellent shielding performance for fast neutrons is not observed for thermal neutrons. Although it still provides better shielding than lead, it performs worse than both concrete and water.

According to the comparisons, transparent aluminum oxynitride demonstrates excellent shielding properties against fast neutrons but not for thermal neutrons. AlON, which provides better values than lead for thermal neutrons, may not be sufficient alone to stop or attenuate these neutrons. Neutron shielding has a more complex mechanism compared to gamma shielding and involves slowing down fast neutrons to thermal neutrons and then absorbing them to stop them (Ouardi, 2021). Therefore, ALON can be used either alone or as the initial shielding material to stop fast neutrons, depending on the application and conditions. The resulting thermal neutrons can then be stopped using a secondary material.
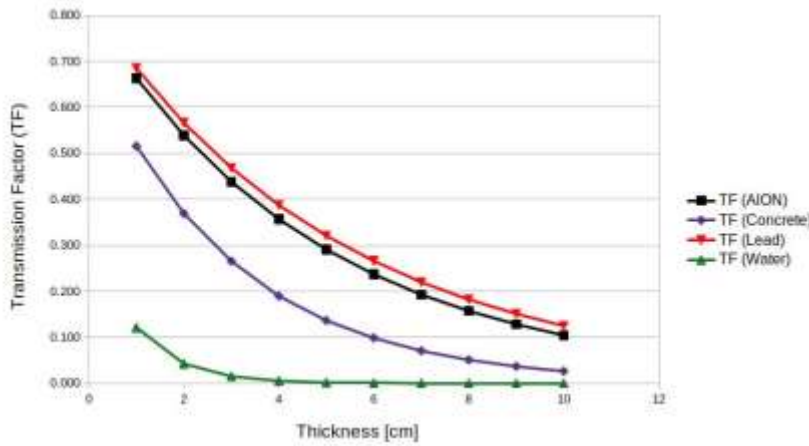
Figure 5. The figure presents the comparison of the four materials. Three of them are conventional radiation shielding materials while the third one is novel aluminum oxynitride. The AlON is superior to lead but worse than ordinary portland concrete and water for thermal neutrons.

4. Conclusion

This study investigated the neutron shielding effectiveness of transparent aluminum oxynitride (AlON) using a Geant4 Monte Carlo simulation. The macroscopic neutron removal cross-sections were calculated for various neutron energies and material thicknesses to assess AlON's performance. The results demonstrate that AlON has a high capacity for shielding fast neutrons, outperforming traditional materials like concrete and lead, and showing nearly identical performance to water. However, AlON's effectiveness in shielding thermal neutrons is more limited, only surpassing lead but falling short compared to concrete and water. Figures 4 and 5 further illustrate these findings. As shown in Figure 4, AlON proves superior to both concrete and lead in shielding fast neutrons, with performance almost equivalent to that of water. Conversely, Figure 5 reveals that while AlON outperforms lead in thermal neutron shielding, it does not match the effectiveness of Ordinary Portland Concrete or water. These findings suggest that AlON is a promising candidate for fast neutron shielding in various nuclear and radiation protection applications. However, its limited effectiveness against thermal neutrons highlights the potential need for a dual-material approach, where AlON could be combined with other materials to enhance overall neutron shielding efficiency.

While this study has provided valuable insights, several limitations must be acknowledged. The simulation results are contingent on the accuracy of the input parameters and the assumptions made, such as material purity and homogeneity. In real-world applications, these factors may vary, potentially affecting the material's performance. Future research could explore these limitations by conducting experimental validation of the simulation results and investigating the effects of impurities and material variations on AlON's shielding properties. Furthermore, studies could explore the potential of combining AlON with other materials to develop hybrid shielding solutions that offer enhanced protection against both fast and thermal neutrons.

Author Contributions

The percentages of the author contributions are presented below. The author reviewed and approved the final version of the manuscript.

	A.Y.
C	100
D	100
S	100
DCP	100
DAI	100
L	100
W	100
CR	100
SR	100
PM	100
FA	100

C=Concept, D= design, S= supervision, DCP= data collection and/or processing, DAI= data analysis and/or interpretation, L= literature search, W= writing, CR= critical review, SR= submission and revision, PM= project management, FA= funding acquisition.

Conflict of Interest

The author declared that there is no conflict of interest.

Ethical Consideration

Ethics committee approval was not required for this study because of there was no study on animals or humans.

References

Agostinelli S, Allison J, Amako KA, Apostolakis J, Araujo H, Arce P. 2003. Geant4 - a simulation toolkit. Nucl Instrum Methods Phys Res A, 506(3): 250-303.

Akyıldırım H. 2019. Calculation of fast neutron shielding parameters for some essential carbohydrates. Erzincan Üniv Fen Bilim Enst Derg, 12(2): 1141-1148.

Al-Buriahi M, Bakhsh EM, Tonguc B, Khan SB. 2020. Mechanical and radiation shielding properties of tellurite glasses doped with ZnO and NiO. Ceram Int, 46(11): 19078-19083.

Ali MS, Hassan GS, Shoraiet GM, Abdelmonem AM. 2024. Optimizing gamma-ray shielding for boron neutron capture therapy by using unglazed ceramic composites. Nucl Instrum Methods Phys Res B, 554: 165450.

Allison J, Amako K, Apostolakis J, Araujo H, Dubois PA, Asai M. 2006. Geant4 developments and applications. IEEE Trans Nucl Sci, 53(1): 270-278.

Allison J, Amako K, Apostolakis J, Arce P, Asai M, Aso T. 2016. Recent developments in geant4. Nucl Instrum Methods Phys Res A, 835: 186-225.

AlMisned G, Sen Baykal D, Elshami W, Susoy G, Kilic G, Tekin HO. 2024a. A comparative analysis of shielding effectiveness in glass and concrete containers. Open Phys, 22(1): 20240019.

AlMisned G, Susoy G, Tekin H. 2024b. Neutron transmission analysis in borated polyethylene, boron carbide, and polyethylene: Insights from MCNP6 simulations. Radiat Phys Chem, 218: 111585.

AlMisned G, Tekin HO, Kavaz E, Bilal G, Issa SA, Zakaly HM, Ene A. 2021. Gamma, fast neutron, proton, and alpha shielding properties of borate glasses: a closer look on lead (ii) oxide and bismuth (iii) oxide reinforcement. Appl Sci, 11(15): 6837.

Alomayrah N, Alrowaili Z, Alalawi A, Al-Buriahi M. 2024. Gamma and neutron attenuation of asm geopolymers for radiation shielding applications: Theoretical study. J Radiat Res Appl Sci, 17(2): 100876.

Alrowaili ZA, Alsaiari NS, İbrahimoğlu E, Çalışkan F, Olarinoye IO, Al-Buriahi MS. 2024. Physical, chemical and radiation shielding properties of metakaolin-based geopolymers containing borosilicate waste glass. Radiat Phys Chem, 224: 112075.

Alzahrani FMA, Basha B, Hammoud A, Tamam N, Alsufyani SJ, Kebaili I. 2024a. Gamma attenuation and nuclear shielding ability of $\llbracket TeO \rrbracket\_2/ \llbracket Bi \rrbracket\_2 O\_3/ \llbracket WO \rrbracket\_3$ glass system. Radiat Phys Chem, 223: 111985.

Alzahrani JS, Alrowaili ZA, Alalawi A, Alshahrani B, Al-Buriahi MS. 2024b. Gamma and neutron attenuation of $\llbracket Bi \rrbracket\_2 O\_3/CaO$ modified borovanadate glasses for radiation shielding applications. J Radiat Res Appl Sc, 17: 100887.

Alzahrani JS, Alrowaili ZA, Sriwunkum C, Al-Buriahi MS. 2024c. Radiation and nuclear shielding performance of tellurite glass system containing $\llbracket Li \rrbracket\_2 O$ and MoO_3: XCOM and FLUKA Monte Carlo. J Radiat Res Appl Sc, 17: 100923.

Cherkashina N, Pavlenko V, Shkaplerov A, Kuritsyn A, Sidelnikov R, Popova E, Umnova LA, Domarev S. 2024. Neutron attenuation in some polymer composite material. Adv Space Res, 73(5): 2638-2651.

El-Khayatt A. 2010. Calculation of fast neutron removal cross-sections for some compounds and materials. Ann Nucl Energy, 37(2): 218-222.

Fahmi AHM, Sazali MA, Yazid K, Bakar AAA, Ali NSM, Jamaluddin K, Sarkawi MS. 2024. Analysis of graphite-paraffin composite in neutron radiography, impact resistance, and thermal neutron attenuation. Radiat Phys Chem, 218: 111639.

Gaylan Y, Bozkurt A, Avar B. 2021. Investigating thermal and fast neutron shielding properties of b4c, b2o3, sm2o3, and gd2o3 doped polymer matrix composites using Monte Carlo simulations. Süleyman Demirel Üniversitesi Fen Edebiyat Fakültesi Fen Dergisi, 16(2): 490-499.

Johnson R, Biswas P, Ramavath P, Kumar R, Padmanabham G. 2012. Transparent polycrystalline ceramics: an overview. T Indian Ceram Soc, 71(2): 73-85.

Kaçal M, Akman F, Sayyed M. 2019. Evaluation of gamma-ray and neutron attenuation properties of some polymers. Nucl Eng Technol, 51(3): 818-824.

Katubi KM, İbrahimoğlu E, Çalışkan F, Alrowaili ZA, Olarinoye IO, Al-Buriahi MS. 2024. Apatite–Wollastonite (AW) glass ceramic doped with B_2 O_3: Synthesis, structure, SEM, hardness, XRD, and neutron/charged particle attenuation properties. Ceram Int, 50: 27139-27146.

Kim J, Lee BC, Uhm YR, Miller WH. 2014. Enhancement of thermal neutron attenuation of nano-b4c,-bn dispersed neutron shielding polymer nanocomposites. J Nucl Mater, 453(1-3): 48-53.

Lakshminarayana G, Tekin HO, Dong M, Al-Buriahi M, Lee DE, Yoon J, Park T. 2022. Comparative assessment of fast and thermal neutrons and gamma radiation protection qualities combined with mechanical factors of different borate-based glass systems. Results Phys, 37: 105527.

Li X, Cui D, Zou C, Ren C, Chen J. 2024. Neutron shielding analysis for a gadolinium doped nickel alloy. Mater Today Commun, 38: 107933.

Ouardi A. 2021. Neutron shielding calculations for neutron imaging facility at the maamora triga reactor. Appl Radiat Isotopes, 176: 109852.

Özdoğan H, Üncü YA, Akman F, Polat H, Kaçal MR. 2024. Detailed analysis of gamma-shielding characteristics of ternary composites using experimental, theoretical and Monte Carlo simulation method. Polymers, 16:1778.

Pavlenko V, Edamenko O, Cherkashina N, Kuprieva O, Noskov A. 2015. Study of the attenuation coefficients of photon and neutron beams passing through titanium hydride. J Surf Investig, 9: 546-549.

Pianpanit T, Saenboonruang K. 2024. Understanding neutron-shielding properties of self-healing poly (vinyl alcohol) hydrogels containing rare-earth oxides through simulations. Results Phys, 57: 107436.

Ramisetty M, Sastri S, Kashalikar U, Goldman LM, Nag N. 2013. Transparent polycrystalline cubic spinels protect and defend. Am Ceramics Soc Bull, 92(2): 20-25.

Reda AM, Ahmed R, Alsawah MA, El-Sabbagh SH, Elabd AA, Kansouh W. 2024. Radiation shielding effectiveness, structural, and mechanical properties of hdpe/b4c composites reinforced with fe2o3-al2o3-al-fe fillers. Phys Scr, 99: 035308.

Salifu S, Olubambi PA. 2023. Transparent aluminium ceramics: fabrication techniques, setbacks and prospects. J Korean Ceram Soc, 60(1): 24-40.

Singh VP, Badiger N. 2014. Gamma ray and neutron shielding properties of some alloy materials. Ann Nucl Energy, 64: 301-310.

Singh VP, Badiger N, Chanthima N, Kaewkhao J. 2014. Evaluation of gamma ray exposure buildup factors and neutron shielding for bismuth borosilicate glasses. Radiat Phys Chem, 98: 14-21.

Tellili B, Elmahroug Y, Souga C. 2014. Calculation of fast neutron removal cross sections for different lunar soils. Adv Space Res, 53(2): 348-352.

Yıldırım A. 2024. Radiation attenuation properties of transparent aluminum oxynitride: a comprehensive study. Eur Phys J Plus, 139(5): 383.

Zayed AM, El-Khayatt AM, Mahmoud KA, Petrounias P, Masoud MA. 2024. Evaluation of some heavyweight minerals as sustainable neutron and gamma-ray attenuating materials: comprehensive theoretical and simulation investigations. Arab J Sci Eng, Early Access, https://doi.org/10.1007/s13369-024-09300-2.

TİCARİ OLARAK SATILAN *Spirulina platensis*'İN ÜÇ FARKLI ÇÖZÜCÜ İLE ELDE EDİLEN EKSTRAKTLARININ SEÇİLMİŞ PATOJEN BAKTERİ VE MANTARLARA KARŞI ANTİMİKROBİYAL AKTİVİTELERİNİN BELİRLENMESİ

Aysel VEYİSOĞLU[1]*, **Abdulğani YEŞİLYER[1]**, **Demet TATAR[2]**

[1]*Sinop University, Vocational School of Health Services, Department of Medical Services and Techniques, 57000, Sinop, Türkiye*
[2]*Hitit University, Osmancık Ömer Derindere Vocational School, Department of Medical Services and Techniques, 19500, Çorum, Türkiye*

Özet: *Spirulina* cinsi üyelerinin, diğer birçok siyanobakteri türü gibi çok sayıda antimikrobiyal madde üretme potansiyeline sahip olduğu bilinmektedir. Çalışmamızda, ticari olarak satılan toz formundaki *Spirulina platensis*'in üç farklı çözücü (aseton, hekzan, metanol) kullanılarak elde edilen ekstraktlarının yedi bakteri suşu (*Bacillus cereus* ATCC 10987, *Bacillus subtilis* ATCC 6623, *Staphylococcus aureus* ATCC 25923, *Enterococcus faecalis* ATCC 29212, *Escherichia coli* ATCC 25922, *Klebsiella pneumoniae* ATCC 70060, *Pseudomonas aeruginosa* ATCC 27853) ve iki fungus türüne (*Candida albicans* ATCC 10231, *Aspergillus niger* ATCC 16404) karşı beş farklı konsantrasyonda (30 mg/ml, 15 mg/ml, 6 mg/ml, 3 mg/ml ve 1 mg/ml) disk difüzyon yöntemi kullanılarak antimikrobiyal aktivitesinin belirlenmesi amaçlanmıştır. Sonuçlarımıza göre, kullanılan çözücüler arasında en iyi sonucu metanolden elde edilen ekstraktın verdiği görülmüştür. Metanolden elde edilen ekstrakt *Bacillus cereus* ATCC 10987, *Bacillus subtilis* ATCC 6623, *Escherichia coli* ATCC 25922, *Klebsiella pneumoniae* ATCC 70060 ve *Pseudomonas aeruginosa* ATCC 27853 suşlarına karşı antimikrobiyal aktivite gösterirken, hekzandan elde edilen ekstrakt *Bacillus cereus* ATCC 10987 ve *Bacillus subtilis* ATCC 6623 suşlarına karşı aktivite göstermiş, asetondan elde edilen ekstrakt ise sadece *Pseudomonas aeruginosa* ATCC 27853 suşuna karşı antimikrobiyal aktivite göstermiştir. Metanol, aseton ve hekzandan elde edilen ekstraktlar kullanılan funguslara karşı aktivite göstermemiştir.

Anahtar kelimeler: *Spirulina platensis*, Antimikrobiyal aktivite, Ekstrakt, Disk difüzyon

Determination of Antimicrobial Activity of Commercially Sold *Spirulina platensis* Extracts Obtained with Three Different Solvents against Selected Pathogen Bacteria and Fungi

Abstract: Members of the genus *Spirulina*, like many other species of cyanobacteria, are known to have the potential to produce numerous antimicrobial substances. In our study, extracts of the commercial powder form of *Spirulina platensis* were tested using three different solvents (acetone, hexane, methanol) against seven bacterial strains (*Bacillus cereus* ATCC 10987, *Bacillus subtilis* ATCC 6623, *Staphylococcus aureus* ATCC 25923, *Enterococcus faecalis* ATCC 29212, *Escherichia coli* ATCC 25922, *Klebsiella pneumoniae* ATCC 70060, *Pseudomonas aeruginosa* ATCC 27853) and two fungal species (*Candida albicans* ATCC 10231, *Aspergillus niger* ATCC 16404) at five different concentrations (30 mg/ml, 15 mg/ml, 6 mg/ml, 3 mg/ml and 1 mg/ml) using the disc diffusion method. According to our results, it was observed that the extract obtained from methanol gave the best result among the solvents used. The extract obtained from methanol showed antimicrobial activity against *Bacillus cereus* ATCC 10987, *Bacillus subtilis* ATCC 6623, *Escherichia coli* ATCC 25922, *Klebsiella pneumoniae* ATCC 70060 and *Pseudomonas aeruginosa* ATCC 27853 strains, The extract obtained from hexane showed activity against *Bacillus cereus* ATCC 10987 and *Bacillus subtilis* ATCC 6623 strains, while the extract obtained from acetone showed antimicrobial activity only against *Pseudomonas aeruginosa* ATCC 27853 strain. The extracts obtained from methanol, acetone and hexane did not show activity against the fungi used.

Keywords: *Spirulina platensis*, Antimicrobial activity, Extract, Disc diffusion

1. Giriş

Artan bakteriyel enfeksiyonlar yüksek oranda ölüme neden olmaktadır (Kandhasamy ve Arunachalam, 2008). Hastalık salgınlarının önlenmesi, hastalığın ilaçlarla tedavi edilmesi veya tedavi edici aktiviteye sahip bileşiklerin seçilmesine yönelik tarama programlarının uygulanması bu soruna çözüm sunmaktadır. Bir diğer çözüm olarak antimikrobiyal aktiviteye sahip doğal bileşiklerin araştırılması, antibiyotiğe dirençli mikroorganizmaların enfeksiyon oranındaki artışı nedeniyle dünya çapında son yıllarda oldukça önem kazanmıştır. Doğal bileşiklerin yan etkilerinin sentetik

This work is licensed (CC BY-NC 4.0) under Creative Commons Attribution 4.0 International License

ilaçlardan daha az olması kimyasal ürünler yerine doğal ürünlere yönelimi artırmaktadır (Muteeb ve ark., 2023). *Spirulina platensis* yenilebilir mavi-yeşil bir algdir. İnsan gıdası ve evcil hayvan yemindeki faydalı rolü nedeniyle *Spirulina*, son yıllarda birçok disiplinde artarak ilgi görmektedir (Abdel-Moneim ve ark., 2022). Tüm esansiyel amino asitleri, esansiyel yağ asitlerini, mineralleri, pigmentleri, karotenoidleri ve vitaminleri içeren yüksek protein seviyelerini içermektedir (Mendiola ve ark., 2007; Abdel- Moneim ve ark., 2022).

Son zamanlarda *Spirulina platensis*, , yalnızca beslenme amacıyla değil, aynı zamanda rapor edilen tıbbi özellikleri nedeniyle de geniş çapta araştırılmakta olup, birçok çalışma *Spirulina* veya ekstraktlarının insanlarda ve hayvanlarda kanseri önleyebildiğini veya inhibe edebildiğini göstermiştir (Hirahashi ve ark., 2002; Subhashini ve ark., 2004) ve son yıllarda yapılan çalışmalarda kolesterolün azaltılması ve ağır metallerin nefrotoksisitesini, antikanser özelliklerini, radyasyona karşı korumayı ve bağışıklık sistemini güçlendirmeyi içeren terapötik etkilerinin araştırılmasına daha fazla önem verilmiştir (Belay ve ark., 1994; El-baz ve ark., 2013).

Çoğu *Spirulina* türünün, antialgal, antibakteriyel, antifungal ve antiviral aktivite gibi çeşitli biyolojik aktivitelere sahip hücre içi ve hücre dışı metabolitler ürettiği bilinmektedir (Noaman ve ark., 2004; El-Sheekh ve ark., 2008). *Spirulina* cinsi, sağlıklı gıda, yem ve medikal endüstrilerinde uluslararası bir talebe sahiptir (Becker, 1994). *Spirulina* sp.'nin farmakolojik aktiviteleri antiviral (Hernández-Corona ve ark., 2002), antibakteriyel (Özdemir ve ark., 2004), antiplatelet (Hsiao ve ark., 2005), antikardiyotoksik (Khan ve ark., 2005), hipokolesterolemik (Nagaoka ve ark., 2005), antinefratoksik (Khan ve ark., 2006) ve antihepatoksik etki sergilediği çeşitli araştırmacılar tarafından daha önce incelenmiştir (Mohan ve ark., 2006).

Çalışmamızda, ticari olarak satılan *Spirulina platensis*'in toz formundan üç farklı çözücü (metanol, aseton ve hekzan) ile ekstrakt elde edilip, ekstrakların yedi bakteri suşu ve iki fungus türüne karşı antimikrobiyal aktivitesinin araştırılması amaçlanmıştır.

2. Materyal ve Yöntem
2.1. Materyal
2.1.1. *Spirulina platensis* materyali
Çalışmada kullanılan *Spirulina platensis*'in toz halindeki formu ticari olarak yerel firmadan satın alınmıştır (Şekil 1) Toz numune çalışma yapılıncaya kadar oda sıcaklığında serin ve kuru ortamda muhafaza edilmiştir.
2.1.2. Bakteriyel suşlar
Antimikrobiyal aktivite çalışmasında kullanılan patojen mikroorganizmalar Amerikan Tip Kültür Koleksiyonundan (ATCC) temin edilmiştir. Gram-pozitif bakterilerden dört suş *Bacillus cereus* ATCC 10987, *Bacillus subtilis* ATCC 6623, *Staphylococcus aureus* ATCC 25923, *Enterococcus faecalis* ATCC 29212, Gram negatif

bakterilerden üç suş *Escherichia coli* ATCC 25922, *Klebsiella pneumoniae* ATCC 70060, *Pseudomonas aeruginosa* ATCC 27853, funguslardan ise iki suş *Candida albicans* ATCC 10231 ve *Aspergillus niger* ATCC 16404 olmak üzere dokuz patojen antimikrobiyal aktivite çalışmasında kullanılmıştır.
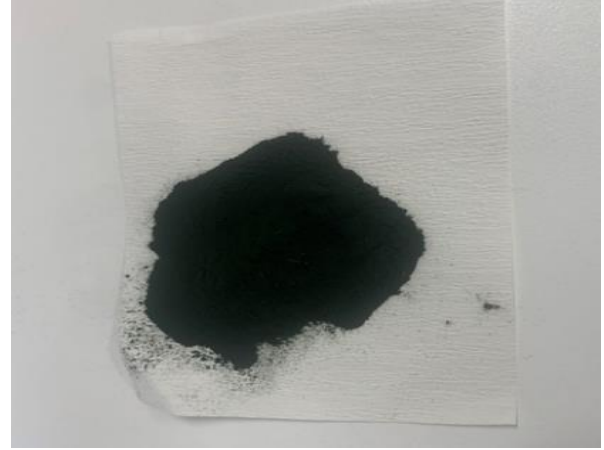
Şekil 1. *Spirulina platensis*'in toz formu.

2.2. Yöntem
2.2.1. Ekstraktların hazırlanması
Ticari olarak satın alınmış *S. platensis*'in toz formundan 40 g alındı ve 200 ml solvent (metanol, aseton ve hekzan) ile karışması için çalkalamalı inkübatörde 180 rpm'de bir gece bekletildi. Hassanin ve ark. (2020)'nin önerdiği yöntem modifiye edilerek ekstraksiyon yapılmıştır. Ekstraktlar, döner vakumlu evaporatör kullanılarak azaltılmış basınçla kuruyana kadar buharlaştırıldı ve elde edilen macun kıvamındaki ekstraktlar %25'lik dimetil sülfoksit (DMSO) ile seyreltilerek antimikrobiyal aktivite çalışmasına uygun hale getirildi (Hassanin ve ark., 2020, Saad ve ark., 2020).

2.2.2. In vitro antimikrobiyal aktivitenin saptanması
Disk difüzyon metodu
S. platensis'in antimikrobiyal aktivitesi disk difüzyon yöntemi kullanılarak değerlendirilmiştir (Collins ve ark., 1989; Bradshaw,1992). Bakteri kültürlerini aktifleştirmek için Muller Hinton Agar (MHA) ve funguslar için Sabouraud Dextrose Agar (SDA) (Difco) kullanıldı ve çalışmadan önce mikroorganizmalar, bakteriler için Muller Hinton Broth'a (MHB) ve funguslar (Difco) için Sabouraud Dextrose Broth'a (SDB) aktarılmış ve gece boyunca 37 °C'de (fungus için 28 °C) gelişmeye bırakılmıştır. Test suşlarının hazırlanan süspansiyonlarının bulanıklığı 0.5 McFarland'a eşdeğer ($1,5×10^8$ kob/ml) ayarlanmıştır ve agar plakasının yüzeyine 100 µl steril eküvyonlarla patojen mikroorganizmalar yayılmıştır ve beş dakika Laminar Flow'da kuruması için bekletilmiştir. Çözücüler (metanol, aseton ve hekzan) kullanılarak elde edilen *Spirulina platensis* ekstraktları (30 mg/ml, 15 mg/ml, 6 mg/ml, 3 mg/ml ve 1 mg/ml), 1 ml %25 dimetil sülfoksit (DMSO) ile karıştırılmıştır. Filtre kağıdı diskleri (6

mm)'ne ekstraktlar (30 mg/ml, 15 mg/ml, 6 mg/ml, 3 mg/ml ve 1 mg/ml) antimikrobiyal aktivitelerini kontrol etmek için 25 µl emdirilmiştir ve Laminar Flow'da kuruması için beş dakika bekletilmiştir. Kuruduktan sonra bakteri bulunan petriler gece boyunca 37 °C'de, fungus ekimi yapılan petriler 28 °C'de inkübasyona bırakılmıştır. Kör kontrol olarak %25 DMSO, pozitif kontrol için Amfisilin (AM10), Polimiksin B (PB300) ve funguslar için Nistatin (NS100) kullanılmıştır. İnhibisyon bölgesi gözlemlenmiş ve milimetre (mm) cinsinden ölçülmüştür. Çalışma üç kez tekrarlanmış ve elde edilen sonuçların ortalamaları alınmıştır.

3. Bulgular ve Tartışma

Spirulina, terapötik özellikleri ve biyoaktif bileşiklerin varlığı nedeniyle son yıllarda ilgi odağı olmuştur (Belay ve ark., 1994). Bitkilerde antimikrobiyal bileşiklerin varlığı bilimsel çalışmalarla gösterilmiştir ve bu bileşiklerin biyolojik sistemlerde antimikrobiyal aktiviteye sahip olduğu bilinmektedir. *Spirulina* ile beslenen hiperkolesteremik hastalarda kolesterol seviyelerinin azaldığı bildirilmiştir ve *Spirulina platensis*'ten çıkarılan fikobiliproteinlerin antimikrobiyal aktiviteye sahip olduğu çalışmalarla belirlenmiştir (Usharani ve ark., 2015).

Metanol, aseton ve hekzan çözücüleri daha önce yapılan çok sayıda çalışmada kullanılmış olup etkili oldukları tespit edilmiştir (Gümüş ve ark.,2018).

S. platensis'in toz formunun üç farklı çözücü kullanılarak hazırlanan ekstraktların disk difüzyon metodu ile belirlenen antimikrobiyal aktivite sonuçları Tablo 1'de verilmiştir. Elde edilen sonuçlar incelendiğinde en iyi antimikrobiyal aktiviteyi metanolden elde edilen ekstrakt göstermiştir. Metanolden elde edilen ekstrakt kullanılan yedi bakteriden beşine (*B. cereus*, *B. subtilis*, *E. coli*, *K. pneumoniae* ve *P. aeruginosa*) karşı antibakteriyel etki göstermiştir. Asetondan elde edilen ekstrakt sadece *P. aeruginosa* bakterisine karşı antibakteriyel etki gösterirken hekzandan elde edilen

ekstrakt *B. cereus* ve *B. subtilis* bakterisine karşı antibakteriyel etki göstermiştir. Üç farklı çözücü ile elde edilen ekstraktlardan hiçbirinin *A. niger* ve *C. albicans* funguslarına karşı antifungal aktivite göstermediği görülmüştür.

İnhibisyon zon çapları değerlendirildiğinde *S. platensis* ekstraktlarının bakterilere karşı inhibisyon zonu 30 mg/ml'de 12 mm ile 10 mm arasında değişmiştir. Metanol ekstraktının 15 mg/ml'de inhibisyon zonu oluşturduğu (*S. aureus* ve *E. faecalis* hariç) ancak daha düşük konsantrasyonlarda etki oluşturmadığı görülmüştür. Asetondan elde edilen ekstrakt yalnızca *P. aeruginosa* bakterisi üzerinde (1 mg/ml hariç) antibakteriyel etki göstermiş ve 30 mg/ml'de 10 mm inhibisyon zonu oluşturmuştur. Hekzandan elde edilen ekstrakt ise *B. cereus* (30 ve 15 mg/ml için) ve *B. subtilis* (30, 15 ve 6 mg/ml için) bakterilerine karşı antibakteriyel etki göstermiş, inhibisyon zon çapı *B. cereus*'a 15 mg/ml'de 9 mm iken *B. subtilis*'e 6 mg/ml'de 9 mm olarak belirlenmiştir (Şekil 2).

Kullanılan standart antibiyotiklerle karşılaştırıldığında metanolden elde edilen ekstrakt 30 mg/ml konsantrasyonda amfisilin standardından düşük, polimiksin B standardından ise daha iyi antimikrobiyal aktivite sergilemiştir. Hekzan ve asetondan elde edilen ekstraktlar ise polimiksin B ile eşit aktimikrobiyal aktivite göstermiştir.

Usharani ve ark. (2015) yaptığı çalışmada *S.platensis*'in beş farklı çözücü ile (metanol, aseton, etanol, hekzan ve petrol eteri) hazırladıkları ekstraktlarının on bir bakteri (*Staphylococcus aureus*, *Streptococcus epidermidis*, *Streptococcus pyogenes*, *Bacillus cereus*, *Proteus mirabilis*, *Escherichia coli*, *Pseudomonas aeruginosa*, *Vibrio cholerae*, *Salmonella typhi*, *Klebsiella pneumoniae* ve *Shigella flexneri*) ve altı fungusa (*Aspergillus flavus*, *Aspergillus niger*, *Aspergillus fumigatus*, *Candida tropicalis*, *Candida albicans* ve *Candida glabrata*) karşı antimikrobiyal aktivitesini disk difüzyon ve minimum inhibisyon konsantrasyonu ile belirlemiştir.

Tablo 1. Metanol, aseton ve hekzan çözücüleriyle hazırlanan *Spirulina platensis* ekstraktlarının antimikrobiyal aktivitesi

Mikroorganizmalar	*Spirulinaplatensis* ekstraktlarının (mg/ml) konsantrasyonları ve ortalama inhibisyon zonları (mm)															Pozitif kontrol			NK
	Metanol					Aseton					Hekzan					Amfisilin (AM10)	Polimiksin B (PB300)	Nistatir (NS100	% 25 DMSO
	30	15	6	3	1	30	15	6	3	1	30	15	6	3	1				
Bacillus cereus	12	9	-	-	-	-	-	-	-	-	10	9	-	-	-	30	10	-	-
Bacillus subtilis	12	10	-	-	-	-	-	-	-	-	10	9	9	-	-	30	10	-	-
Staphylococcus aureus	-	-	-	-	-	-	-	-	-	-	-	-	-	-	-	30	10	-	-
Enterococcus faecalis	-	-	-	-	-	-	-	-	-	-	-	-	-	-	-	30	10	-	-
Escherichia coli	12	9	-	-	-	-	-	-	-	-	-	-	-	-	-	22	15	-	-
Klebsiella pneumoniae	12	10	-	-	-	-	-	-	-	-	-	-	-	-	-	40	20	-	-
Pseudomonas aeruginosa	12	10	-	-	-	10	10	10	9	-	-	-	-	-	-	30	15	-	-
Candida albicans	-	-	-	-	-	-	-	-	-	-	-	-	-	-	-	-	-	20	-
Aspergillus niger	-	-	-	-	-	-	-	-	-	-	-	-	-	-	-	-	-	30	-

NK= negative kontrol

Şekil 2. Metanol ve hekzan çözücüleriyle *Spirulina*'dan elde edilen ekstraktların *Bacillus* cinsi üyelerine karşı oluşturduğu inhibisyon zonları.

Beş farklı çözücü ile hazırlanan ekstraktlar değerlendirmede kullanılan on bir bakteri ve altı fungusa karşı iyi antimikrobiyal aktivite göstermiştir. Rania ve ark. (2008), *S. platensis* üst sıvısını, metanol ve hekzan ekstraktlarını dört fungus türüne karşı (*Candida kefyr*, *Aspergillus fumigatus*, *Aspergillus niger* ve *Aspergillus fumigatus*) değerlendirmişler ve hekzan ekstraktının fungusların gelişimini engellemediği gözlemlemişlerdir. Bizim çalışmamızda da metanol, aseton ve hekzan ekstraktları *A. niger* ve *C. albicans* funguslarının gelişimini engellememiştir. El-Baz ve ark. (2013)'nın yaptığı bir çalışmada *S. platensis*'in etanol ekstraktlarının antibakteriyel ve antiviral etkisi test edilmiş ve *S. platensis*'in etanol ekstraktlarının farklı bakteri suşlarına (*Escherichia coli*, *Staphylococcus aureus*, *Salmonella typhi* ve *Enterococcus faecalis*) karşı antibakteriyel etkisini göstermek için disk difüzyon yöntemi kullanılmıştır. *Escherichia coli* ve *Salmonella typhi* (*Enterobacteriaceae* familyasından Gram negatif bakteriler) ve *Staphylococcus aureus* (*Micrococcaceae* familyasından Gram pozitif bakteri) ile inhibisyon bölgeleri oluşturmamasına rağmen *Enterococcus faecalis* ve *Candida albicans*'a karşı belirgin inhibisyon bölgeleri oluşturduğunu gözlemlemişlerdir.

4. Sonuç

Çalışmamızdan elde edilen sonuçlar ile diğer araştırmacıların elde ettikleri sonuçlar (Elnabris ve ark., 2013; Ramalingam ve Amutha, 2013; Gümüş ve Ünlüsayın, 2016) arasındaki farklılığın nedenleri arasında ekstraktın elde edilme yöntemi, ekstraktın kimyasal içeriğindeki bileşenler, çözücü çeşitliliği, kullanılan patojen mikroorganizma türünün veya aynı türün farklı suşlarının kullanılması gibi olası sebeplerden dolayı *Spirulina* özütleri farklı antibakteriyel ve antifungal aktivite sergileyebilmektedir. Çalışmamızda kullanılan ekstraktların, pozitif kontrol olarak kullandığımız amfisilin antibiyotiğinden düşük, polimiksin B antibiyotiğinden daha iyi, eşit veya düşük aktivite göstermesi diğer çalışmalarda ifade edildiği gibi özütlerin aktivitesinin ekstraksiyon yöntemi ve kullanılan doz artışına bağlı olarak değişebileceğinden, *Spirulina* ekstraktlarının antibiyotiklere ve geleneksel kimyasal ilaçlara alternatif olarak kullanılabileceğini umut ediyoruz.

Kaynaklar

Abdel-Moneim AE, El-Saadony MT, Shehata AM, Saad AM, Aldhumri SA, Ouda SM, Mesalam NM. 2022. Antioxidant and antimicrobial activities of *Spirulina platensis* extracts and biogenic selenium nanoparticles against selected pathogenic bacteria and fungi. Saudi J Biol Sci, 29(2): 1197-1209.

Becker EW. 1994. Microalgae, biotechnology and microbiology. Cambridge, Cambridge University Press; New York, US, pp: 291.

Belay A, Ota Y, Miyakawa K, Shimamatsu H. 1994. Production of high quality *Spirulina* at Earthrise Farms. In: Phang et al., eds. Algal Biotechnology in the Asia-Pacific Region. University of Malaya, Kuala Lumpur, Malezya, pp: 92-102.

Bradshaw LJ. 1992. Laboratory of microbiology. Saunders College Publishing, Saunders, US, pp: 435.

Collins CM, Lyne PM, Grange JM. 1989. Microbiological methods. Butterworths, London, UK, pp: 410.

El-Baz FK, El-Senousy WM, El-Sayed AB, Kamel MM 2013. In vitro antiviral and antimicrobial activities of Spirulina platensis extract. J Appl Pharm Sci, 3(12): 52-56.

Elnabris KJ, Elmanama AA, Chihadeh WN. 2013. Antibacterial activity of four marine seaweeds collected from the coast of Gaza Strip, Palestine. Mesopotamian J Marine Sci, 28(1): 81-92.

El-Sheekh MM, Dawah AM, Abd El-Rahman AM, El-Adel HM, Abd El-Hay RA. 2008. Antimicrobial activity of the cyanobacteria *Anabaena wisconsinense* and *Oscillatoria curviceps* against pathogens of fish in aquaculture. Annals Microbiolh, 58: 527- 534.

Gümüş B, Ünlüsayin M. 2016. Tüketilebilir iki makroalg ekstraktının antimikrobiyal aktivitelerinin belirlenmesi. Ege Üniv Su Ürün Derg, 33(4): 389-395.

Gümüş B, Ünlüsayın M, Gümüş E. 2018. A review on antimicrobial properties of marine macroalgae extracts. Ege J Fish Aquat Sci. 35(3): 343-351.

Hassanin AA, Saad AM, Bardisi EA, Salama A, Sitohy MZ. 2020. Transfer of anthocyanin accumulating *delila* and *rosea1* genes from the transgenic tomato micro-tom cultivar to antibacterial property of seaweeds of southeast coast of India. African J Biotech, 7(12): 1958-1961.

Hernández-Corona A, Nieves I, Meckes M, Chamorro G, Barron BL. 2002. Antiviral activity of *Spirulina maxima* against *Herpes simplex* virus type 2. Antiviral Research, 56(3):279-285.

Hirahashi T, Matsumoto M, Hazeki K, Saeki Y, Ui M, Seya T. 2002. Activation of the human innate immune system by *Spirulina*: Augmentation of interferon production and NK cytotoxicity by oral administration of hot water extract of *Spirulina platensis*. International Immunopharmacology, 2(4):423-434.

Hsiao G, Chou PH, Shen MY, Chou DS, Lin CH, Sheu JR. 2005. C-phycocyanin, a very potent and novel platelet aggregation inhibitor from *Spirulina platensis*. J Agric Food Chem, 53:7734–7740.

Kandhasamy M, Arunachalam KD. 2008. Evaluation of in vitro antibacterial property of seaweeds of southeast coast of India. African J Biotech, 7(12):1958-1961.

Khan M, Shobha JC, Mohan IK, Naidu MUR, Sundaram C, Singh S, Kuppusamy P, Kutala VK. 2005. Protective effect of *Spirulina* against doxorubicin-induced cardiotoxicity. Phytother Res,

19(12): 1030-1037.

Khan M, Shobha JC, Mohan IK, Naidu MUR, Prayag A, Kutala VK. 2006. *Spirulina* attenuates cyclosporine-induced nephrotoxicity in rats. J Appl Toxico, 26: 444-451.

Mendiola JA, Jaime L, Santoyo S, Reglero G, Cifuentes A, Ibañez E, Señoráns FJ. 2007. Screening of Functional Compounds in Supercritical Fluid Extracts from *Spirulina platensis*. Food Chem, 102(4): 1357-1367.

Mohan IK, Khan M, Shobha JC, Naidu MUR, Prayag A, Kuppusamy P, Kutala VK. 2006. Protection against cisplatin-induced nephrotoxicity by *Spirulina* in rats. Cancer Chemother Pharmacol, 58: 802-808.

Muteeb G, Rehman MT, Shahwan M, Aatif M. 2023. Origin of antibiotics and antibiotic resistance, and their impacts on drug development: A narrative review. Pharmaceuticals, 16(11): 1615.

Nagaoka S, Shimizu K, Kaneko H, Shibayama F, Morikawa K, Kanamaru Y, Otsuka A, Hirahashi T, Kato T. 2005. A novel protein C-phcocyanin plays a crucial role in the Hypocholesterolemic action of *Spirulina* platensis concentrate in rats. J Nutr, 135: 2425-2430.

Noaman NH, Khaleafa AM, Zaky SH. 2004. Factors affecting antimicrobial activity of *Synechococcus leopoliensis*. Microbiol Res, 159: 395-402.

Ozdemir G, Karabay NU, Dalay MC, Pazarbasi B. 2004. Antibacterial activity of volatile component and various extracts of *Spirulina platensis*. Phytotherapy Res, 18: 754-757.

Ramalingam A, Amutha C. 2013. Antibacterial activity of four seaweed collected from Thondi Coast, Tamilnadu, India. Int J Res Biol Sci, 3(1): 60-64.

Rania M, Abedin A, Taha HM. 2008. Antibacterial and antifungal activity of cyanobacteria and green microalgae. evaluation of medium components by placket-burman design for antimicrobial activity of *spirulina platensis*. Global J Biotechnol Biochem, 3(1): 22-31.

Saad AM, Mohamed AS, Ramadan MF. 2020. Storage and heat processing affect flavors of cucumber juice enriched with plant extracts. Int J Veg Sci, 2020: 1-11.

Subhashini J, Mahipal SV, Reddy M, Mallikarjuna Redd M, Rachamallu A, Reddanna P. 2004. Molecular mechanisms in C- phycocyanin induced apoptosis in human chronic myeloid leukemia cell line-K562. Biochemical Pharmacol, 68(3): 453-462.

Usharani G, Srinivasan G, Sivasakthi S, Saranraj P. 2015. Antimicrobial activity of *Spirulina platensis* solvent extracts against pathogenic bacteria and fungi. Biol Res, 9: 292-298.

IMAGED EXPERIENCES: MAPPING THE TRABZON CITY CENTER

Hare Kılıçaslan[1]*, Merve ULUÇAY TEMEL[2], Pınar TASLI[2]

[1]Karadeniz Technical University, Faculty of Architecture, Department of Architecture, 61080, Trabzon, Türkiye
[2]Karadeniz Technical University, Graduate School of Natural and Applied Sciences, Department of Architecture, 61080, Trabzon, Türkiye

Abstract: This research sets out from the cycle of impaired belonging between city dwellers and the cities they live in and the weakened perceptibility of urban identity in spatial experiences as a result of the chaos and rapid flow of daily life in today's cities that evolve around consumption culture. This cycle is addressed with experiential mapping applications, which prompt citizens to take a step back and slow down their rhythm of life as a way to connect with their city. Based on this, it is aimed to reveal the deepening of the relationship between city dwellers and the city through experiential mapping, which provides a more meaningful and conscious interaction with the urban environment. In this research, the urban identity formed between urban space and the user was analyzed by image analysis, taking the Theory of Imageability as a basis. The application process consisted of three main phases and was conducted with ten students studying at Karadeniz Technical University, Department of Architecture. The research findings show that experiential mapping and semantic rating, applied with a view to increasing the visibility of urban images peculiar to Trabzon city center, enabled the participants to direct their focus on and explore the spatial components of Trabzon city center, suggesting that experiential mapping can be an effective tool in exploring the potentials and problematic aspects of cities.

Keywords: Experiential map, Urban experiences, Urban images, Trabzon

1. Introduction

Cities are densely populated settlements that bring together large masses of different people and different functions. Cities, which developed into centers of production in the wake of the industrial revolution, are places where the effects of globalization made themselves felt the most intensely as they triggered a change in traditional social structures (Begel, 1996). Globalization has penetrated almost every area of the world from the 1980s onwards, and it has reshaped cities in many ways, leading to an inevitable transformation of cities with the effect of socio-cultural and economic developments. Once the "spaces of production", industrial cities evolved gradually into "spatial centers of social consumption" (Krätke, 2014). The emerging new production-consumption model and the urban policies that developed in parallel therewith focused largely on money spending patterns, and the spatial transformation of urban areas took place in the same direction (Yaylı, 2012). This consumption model went beyond mere consumption of goods and services and extended to consumption of urban spaces and social values because as the consumption habits of societies changed, new spatial needs came into play that triggered a transformation of the relationship between city dwellers and the city as well as the physical structuring of cities (Aliağaoğlu and Mirioğlu, 2020), causing the identities of

cities defined by their differences and authenticity to fade away (Giddens, 2012).

Globalization, a much-debated topic in a variety of aspects, led to an inevitable transformation of the cities in Türkiye, as in all other developing countries, which resulted in impaired urban identity and weakened bonding between city dwellers and the city in environments that have become centers of economic attraction during the process of urbanization. Most city dwellers find themselves trapped in a consumption-oriented and rapidly flowing circulation that prevents them from noticing the images they come across in the course of urban experiences.

In the physical sense, cities are defined as a set of streets that provide access from and to buildings and structures where large numbers of people live together and which create different meanings for these people (Milgram, 1970); and in the social sense, they are defined as a living organism that has the potential of bringing together urban city dwellers in different ways and give them the freedom of choice in various life scenarios (Šenk, 2021). The everyday life actions and behavior patterns of city dwellers come to life in this organism. On the other hand, for urban identity, the meaning attributed to the city by its dwellers is as important as the characteristics of the city itself. In other words, cities can be given meaning neither only by a physical environment nor only by the

presence of people living in the city. Cities are shaped by the interaction known to exist between humans and their environment and the behaviors that emerge as a result of this interaction (Özgen and Türkseven Doğrusoy, 2020). According to Gehl (2011), in low-quality public spaces, necessary activities take place first, while in high-quality public spaces, necessary activities take place with approximately the same frequency, but people prefer to do them for longer periods of time (Carmona et al., 2003). Improved physical conditions lead to a significant increase in the number of pedestrians, more time spent outdoors and a wider range of outdoor activities (Gehl, 2011).

The city is impregnated with endless mobility that feeds on everything and everyone that is part of the life it surrounds. If we traced back this mobility, the most befitting word to describe the identity of modern cities brought to life by the globalizing world would be speed. In today's cities, everything flows quickly and everyone moves quickly in a hurry to get somewhere (Alver, 2012). This speed and the urban experiences passing by faster than normal expose city dwellers to rapidly and constantly changing environmental stimuli, making it almost impossible for them to follow the changing images surrounding them, and impede their conscious interaction with their environment (Simmel, 2005). This, in turn, weakens both the city dwellers' contact with urban space and their bond with the city. Urban dwellers attach identity to their city to the extent they come into contact with it, and cities find their identity through a social synthesis of these individual identifications. However, urbanization problems and the hustle and bustle of daily life taking hold of many cities today have destroyed the time and space for people to take a step back and consciously listen to and notice their surroundings. The consequence of this is that city dwellers become less likely to attach meaning to the images they see around them, and cities become a mere object of consumption.

Within this accelerated life scenario, city dwellers are exposed to constant spatial experiences. Harvey's (2022) "The Urban Experience" starts with this question: "Who among us will refuse the opportunity on arriving in some unfamiliar city, to ascend to a convenient high point and look down upon the intricate landscape of streets and buildings and the restless flow of human activity among them? Why do we feel so curious to do what long-term residents rarely consider ... and what do we gain by it?" He attributes his reply to Michel de Certeau's (1984) thoughts on ascending to the heights of New York's World Trade Center. According to Certeau, the ascent lifts us out of the city's grasp, out of the feverish motion of street life, and allows us to become voyeurs. Thus, the bewitching world by which one was possessed is transformed into a readable text that lies before one's eyes (Harvey, 2022). This ascent is equivalent to an urban reading that corresponds to taking a step back and slowing down one's experience in the daily flow of a city.

Walking, which is an inevitable part of daily life, is also a way of experiencing a place and a city. Through daily walking, the individual develops a sense of place in the space they experience. In other words, daily walks, which differ in terms of purpose, speed and rhythm, enable creative and critical relationships with urban space. In this context, walking can be considered as an important and alternative research method in urban design (Matos Wunderlich, 2008). The pedestrian perspective in defining the urban fabric should not be limited to human visual capacity. Pedestrians can develop a more comprehensive understanding by experiencing the spatial diversity of the urban fabric as they move from one street to another (Araldi and Fusco, 2019).

Şenel's (2019) paper contains a heading that reads as *"passing a place every day and staying in that place for a day"*. This phrase gives many clues about the effectiveness of experiential mapping in urban experience. In other words, the act of experience is *"passing through a place every day"* in cognitive maps, while in experiential maps it is *"staying in that place for a day"*. To build and strengthen their bond and sense of belonging with their city, city dwellers should slow down the experiences they have in the hustle and bustle of their everyday lives, even if it is for a day, take a step back and get familiar with the identity of the city. This is where experiential mapping comes into play as an area of activity that promotes this slowdown.

Any human activity that involves physical and mental connection between an observed location and its environment describes a cognitive image of a given location. The message conveyed by the environment is ultimately based on individual interpretation and depends on the decoding and reconstitution of encrypted meanings (Rozman Cafuta and Sitar, 2017). With this in view, the aim of this research is to reveal how and to which extent experiential mapping can help city dwellers deepen their relationship with the city by entering into a more meaningful and conscious interaction with their urban environment. This paper uses experiential mapping as a tool to discuss Certeau's *ascent* in making sense of the city.

2. Materials and Methods

The research focuses on identifying city center images in the city center of Türkiye's Trabzon province through a slowed-down spatial experience, adopting an approach of concentrated experience and selective perception. For this, we employed experiential mapping, a method comprising successive philosophies such as slowing down the rhythm of life and experiencing everyday paths from a different perspective. To evaluate urban identity taking shape between urban space and the user, we used image analysis based on Lynch's Theory of Imageability.

According to Cosgrove (1985), when looking at the emergence and development process, maps have always served as an objective and observation-based document drawn up to create and finalize the knowledge of a place.

Şenel (2014) states that rather than a static representation of a place, the act of mapping has evolved into a process of sense-making and repositioning between the mapped place and the mapper. With this aspect, mapping holds an important position especially in architectural practice and is used as a tool for representing how the spirit of a place is influenced and reconstructed by human existence, spatial experiences and design actions. In this sense, it is seen that cognitive maps that can be applied with a large number of participants depending on the size of the study area have been employed in many studies from past to present (Cadwallader, 1979; Evans et al., 1984; Jang and Kim, 2019; Topcu and Topcu, 2012). Exploratory pursuits that contain original meanings and in which information is obtained through a bottom-up operational method rather than top-down are experiential mapping (Schoonderbeek, 2017). Experiential maps, on the other hand, involve more complex processes than cognitive maps as they use a multi-layered methodology that consists of several phases and analyze a broad set of verbal, written and visual data.

But studies employing experiential mapping are not only smaller in number but also in sample size. In Lynch's Image of the City, for example, the experiential phase of the two-phase research conducted in three different cities in 1960 was carried out by one observer, and the cognitive phase with a group of city dwellers (Lynch, 2022). Spencer and Weetman (1981) studied in their two-phase research 30 subjects who were new university residents without any prior experience of the city and asked them to draw sketch maps of the city center, the campus and their individual daily paths. The research by

Yorgancıoğlu and Çalak (2020) focusing on contacting real life, touching and interacting with space, and gaining a unique perspective and deep perception of a place was conducted with 20 architecture students. As in the studies above, each an example of experiential mapping applications involving complex stages, the number of participants in the present study using a multi-layered research design was kept limited.

A three-phase design was adopted for the implementation of the present research, seeking an answer to the research questions "How does experiential mapping allowing for a slowed down spatial experience affect the interaction between Trabzon city center and city dwellers?" and "What are the clues that the images reflected on experience maps give us about the potentials and problems of the city?". The hypotheses formulated for the purpose of this research are:

H_1. Slowed down and focused spatial experiences are an effective tool in unveiling the images that the participants have of Trabzon city center in their minds.

H_2. Experience maps allow to identify the potentials and problems associated with Trabzon city center from the perspective of city dwellers.

Unlike large-sample studies on urban identity that draw on statistical data and generalizations, the present research adopts a multi-layered research design that focuses on urban images unveiled through individual experiences and interpretations with a limited number of participants. Figure 1 shows the research model in which the study group consisted of ten students (6 female, 4 male), all in their third year at Karadeniz Technical University, Department of Architecture.
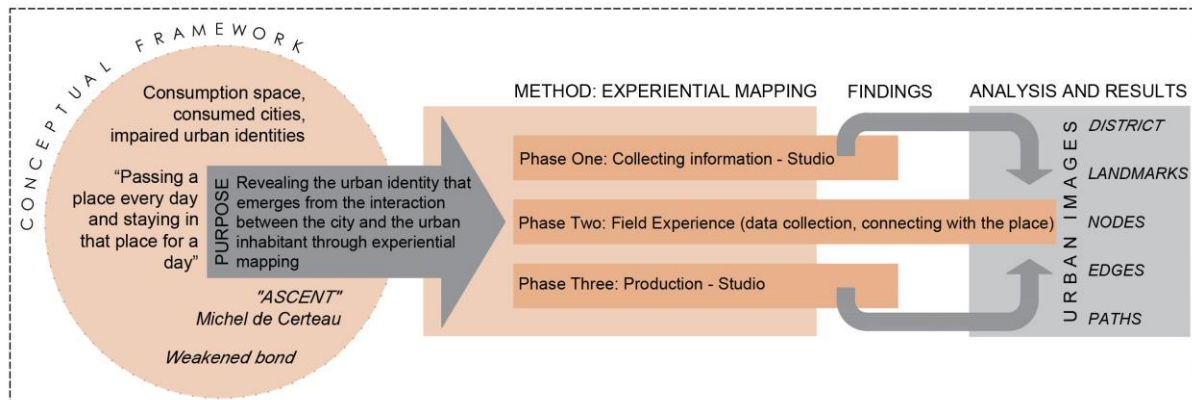
Figure 1. Research model.

The city center designated for the purpose of this research defined an area that started from Atatürk Square and extended all along Kahramanmaras Street, Uzun Street, Kunduracılar Street, including the secondary roads connecting these three axes (Figure 2). The area has a multi-layered structure that is home to many historical landmarks as well as shopping, leisure time, eating and drinking places. As such, the study area is a place where many city dwellers with different demographic characteristics can find something to their

taste and come into contact with the city. This area, which sets an example for urban centers that develop with a focus on consumption, had a good potential for giving us the data we needed for this research, as it mediated an urban experience focused on crowds, chaos and speed.
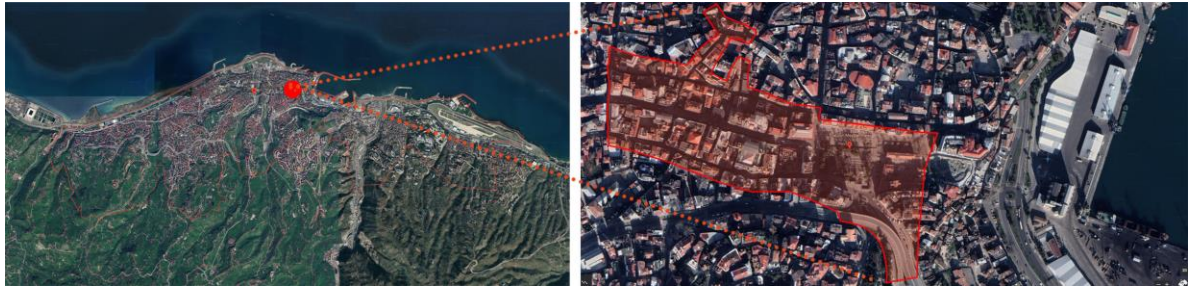
Figure 2. Satellite images of Trabzon city center.

2.1. Experiential Mapping Applications
2.1.1. Phase one: studio

In phase one, the participants were brought together in studio environment, and after briefing them about the purpose of research, they were asked to fill out an information collection form (Table 1). The purpose of the form was to do a memory reading before "generating an identity for a given place with a slowed-down experience". The form consisted of two parts. The first was aimed at gathering data about the participants' demographics, and the second was to determine their level of interaction with Trabzon city center, their level of familiarity with the city center, and the traces of the city center in their minds. A semantic rating scale aimed at measuring subjective spatial perception and evaluation responses was used to measure the participants' impressions of the city center before and after mapping.

2.1.2. Phase two: Trabzon city center

Phase two aimed at giving the participants "an experience that would raise their awareness of their own motion in the city" by discovering urban images in a fast-flowing urban space, in the presence of fast-flowing pedestrian motion, so as to make them attach identity and meaning to their city. Rather than trying to have the students draw a map, mapping was based on having the students record their experiences on sketch maps handed out to them, while discovering and imaging the spatial components steering their experiences. Each participant was provided with a sketch map to use while strolling through the city (Figure 3).

The participants were briefed on the research problem and the points to focus on while strolling through the city in order to have them collect data fit for the purpose, which they would need at the stage of mapping (Table 2).

Table 1. Information collection form questions

I	What is your age?
	How many years have you been living in Trabzon?
	Are you satisfied with living in Trabzon and why?
	For which purpose(s) do you visit Trabzon city center?
	How often do you visit Trabzon city center?
	How much time do you spend in Trabzon city center?
II	Does living in Trabzon make you feel good? Can you explain why?
	How does it make you feel when you have to go to Trabzon city center?
	What does Trabzon city center evoke in your mind? Please explain.
	Could you rate the images that Trabzon city center evokes in your mind, using the adjective pairs given below?

	-2	-1	0	1	2	
Congested						Spacious
Uninviting						Inviting
Tiring						Refreshing
Disturbing						Relaxing
Ordinary						Authentic
Boring						Exciting
Flowing/Uncontrollable						Controllable to the least detail
Disconnected/Intermittent						Fluent/Integrated
Dissatisfying						Satisfying
Consuming/Slipping by						Adopted/Memorised
Forces fast motion						Allows slow motion

Table 2. Information collection form questions

Problem description	Identifying images of the city center by way of a concentrated and slowed down spatial experience with an approach based on selective perception.
Instructions	The stroll should be as relaxed and internalized as possible, focusing on all the physical and mental spatial features around the participants that influence their behavior and shape their experience.
Terminology	Categorizing the spatial data that steered their stroll according to Lynch's Theory of Imageability (edges, nodes, landmarks and paths) and plotting the data on sketch maps.
Data collection	Photographing the imaged spaces, taking notes on sketch maps and making sketches/drawings to serve as data for experience maps.

Participants were instructed to focus on their daily paths rather than trying to stroll the entire area and to create a route according to the streets and spaces they use most frequently and the secondary roads connecting the three axes. Participants experienced their familiar routes in the city center, but this time from a different perspective and with a planned motive, gathered information and plotted the data on sketch maps (Figure 4).

2.1.3 Phase three: studio

In phase three, the participants were called back to studio environment for experiential mapping based on the notes taken on the sketch maps and the visual data obtained in the field study (Figure 5).

The materials used in this phase were provided by the researchers to maintain consistency and coherence across sketch maps. Students were given a blank map showing the boundaries of the area, pencils, cutters, glue sticks, acetate films, poster boards, pushpins and thread.

To facilitate categorization and analysis of experiential mapping data, students were instructed to use red materials for paths, blue for nodes, green for landmarks and yellow for edges. Students were told that in addition to these materials, they were free to use the area photographs taken in phase two, the notes they had taken on sketch maps and any of their sketches/drawings during mapping. The experience maps created in this phase are presented in Table 3.
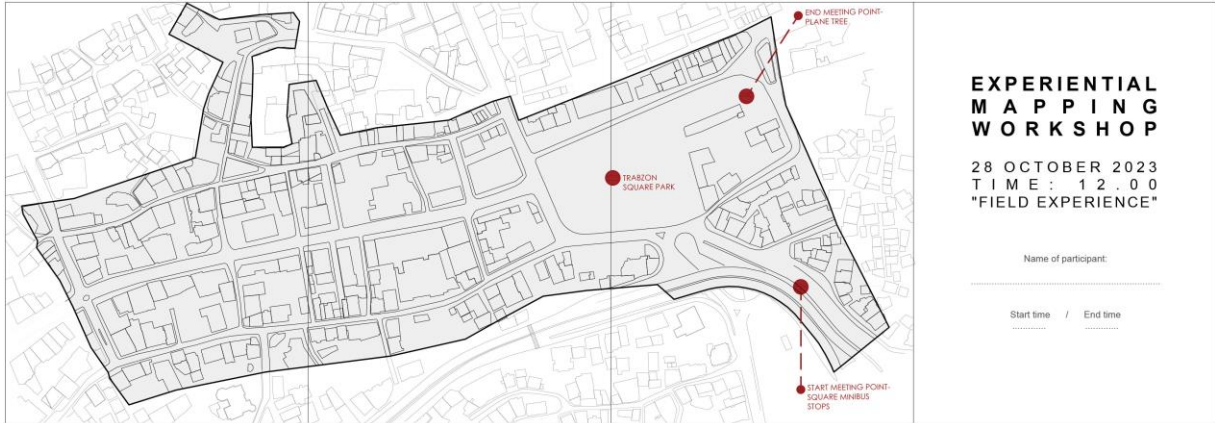
Figure 3. Sketch map of the study area
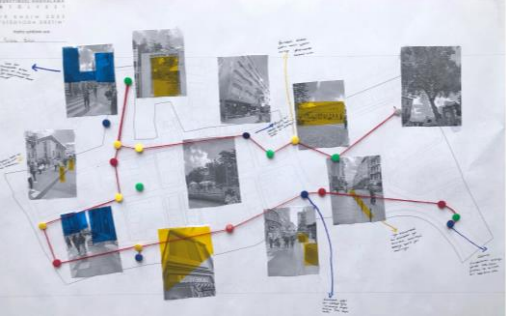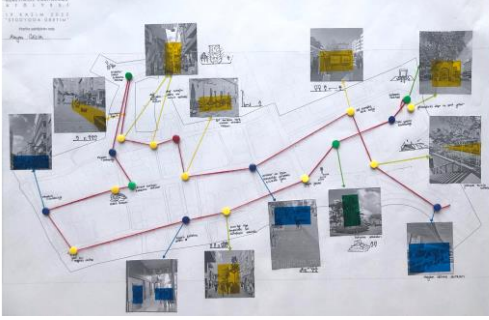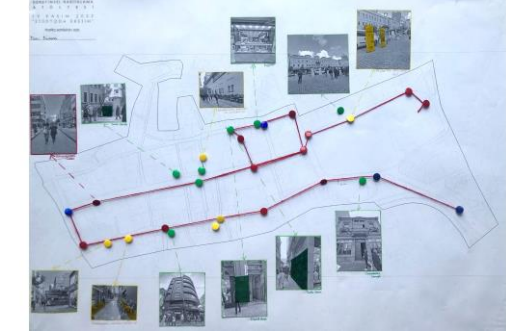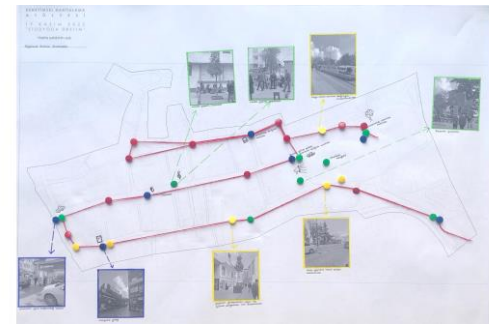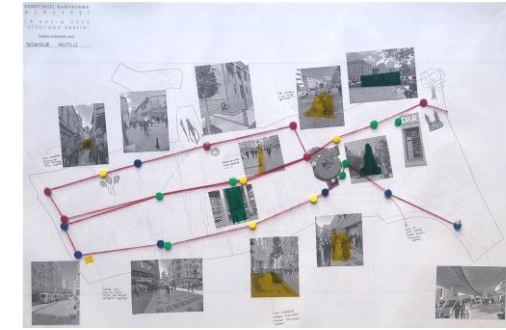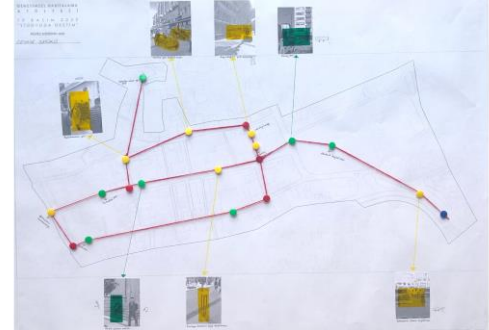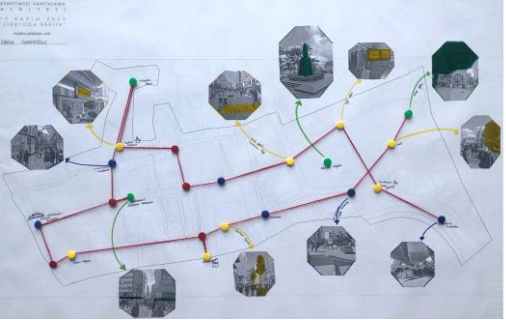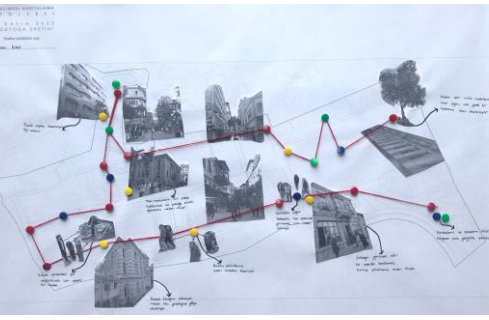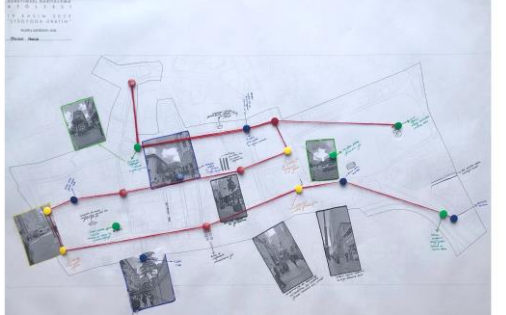
Figure 4. Field study photos.

Figure 5. Experiential mapping photos.

Table 3. Experiential maps

After mapping, a semi-structured interview form and semantic rating scale were applied to gain insight into the participants' impressions of the city and the changes that their perception of urban space had undergone as a result of the experience.

3. Results

Table 4 shows the distribution of the participants' demographics based on information obtained from the information collection forms in phase one. The participants' reasons for spending time in the city center

were shopping (9), sitting/resting (8), meeting with people (8), leisure time (3) and essential part of daily transportation (3).

Before the experience, the participants were asked whether they were satisfied with living in Trabzon in order to assess their general perception of the city. Only three out of 10 participants answered yes. Among those who responded positively, P1 and P8 had been living in the city for 2 years and responded that the reason for their satisfaction was mainly the nature of the city. P4, the third who answered yes, stated that the reason for their positive response was because they had been born and raised in Trabzon. P5 and P6, who had been living in Trabzon since they were born, responded negatively and described the city as boring. The participants' responses showed that their interaction with the city (visiting frequency and time spent in the city center) was high enough for the purpose of this study. The data obtained from part two of the information collection forms was analyzed by means of content analysis. The analysis of a total of 30 answers given to three questions showed, that 11 negative and 6 positive features dominated the answers to these questions. The images dominating the participants' answers are presented in Figure 6 with sample statements picked out from among the questions and the answers given to each of them. Words marked with gray on the figure represent negative images, whereas words marked with orange represent positive

ones. The participants described the existing urban identity in their minds with negative adjectives like non-inclusive (7), crowded (7), boring/constricting/oppressive (7), and congested/jammed (5). Another remarkable point was that the spatial features expressed positively revolved around consumption-related concepts, such as responding to needs (8) and availability of social activity spaces (6).

While analyzing the data obtained in phase three, the researchers examined each map created by participants and traced the images they had marked on them in writing or with photographs, sketches or collages. To exemplify the process steps followed in this analysis, the notes plotted on the maps and some of the images associated with them are given in Table 5. Based on the analysis results, the researchers categorized the participants' expressions as edges (8), nodes (5) and landmarks (11) and identified a total of 24 city center images.

Table 4. Demographics of participants

Participant	Age (years)	Time lived in Trabzon (years)	Satisfied with living in Trabzon; reasons	City center visiting frequency	Time spent in the city center per visit
P1	19	2	Yes; nature	1-3 times a month	1-4 hours
P2	19	8	No; non-inclusive	1-3 times a week	1-4 hours
P3	19	1	No; lack of belonging	1-3 times a month	1-4 hours
P4	21	21	Yes; hometown	Everyday	4 hours or more
P5	21	21	No; boring	1-3 times a week	1-4 hours
P6	20	20	No; boring	1-3 times a week	1-4 hours
P7	20	2	No; congested/jammed	1-3 times a week	1-4 hours
P8	19	2	Yes; nature	1-3 times a week	1-4 hours
P9	20	1	No; unplanned urbanization	1-3 times a month	1-4 hours
P10	22	2	No; congested/jammed	1-3 times a month	1-4 hours

Repetitive images	Sample statements
Suffocating/Depressing (2)	**Question: Does living in Trabzon make you feel good? Can you explain why?**
Poor transportation (2)	*"I think the city is very chaotic and jammed. It's like the buildings are piled on each other and it gives me cramped feeling."* (P5)
Estranging (2)	*"It doesn't give a city feeling. Transportation is poor. There are no activities. The climate is unfavorable. It's expensive. Long story short, it's not a student city."* (P3)
Disorganized (3)	*"It is not a city to live in for university students. In today's conditions, it is full of people that live here to serve tourists."* (P10)
Chaotic (4)	**Question: How do you feel when you have to go to Trabzon city center?**
Disturbing (4)	*"Very good because if I am going to the city center, I usually either meet someone or go shopping. I enjoy doing both."* (P1)
Historical assets not protected (4)	*"I feel stuck. The minibuses passing through the square all the time is disturbing."* (P7)
Congested/Jammed (5)	*"I feel suffocated and depressed."* (P9)
Non-inclusive (7)	*"I am very reluctant when I have to go because it can be very crowded. However, finding everything I'm looking for gives can be a great advantage."* (P6)
Crowded (7)	**Question: What does Trabzon city center evoke in your mind? Please explain.**
Boring/constricting/ oppressive (7)	*"If it were not like this, I would describe it as a center that draws me in with its complexity. A place that I can't stay without despite its disorder. Exploring places that have remained unknows to date has been an activity that I find very interesting."* (P2)
Responds to needs (8)	*"A city center that is so addictive that even the repulsiveness of its bad weather caused by the huge crowds of people cannot prevent people from hanging out there."* (P8)
Social activity space (6)	*"A common area where all people gather, socialize, shop and meet their needs. But it's the crowd that bothers me the most. The best feature is that there are shops where we can find all what we are looking for."* (P4)
Meeting venue (3)	
Dynamic (3)	
Attractive (1)	

Figure 6. Content analysis findings of data obtained from information collection forms.

Table 5. Analysis steps for identifying city center images

	Participant expressions plotted on the maps	City Center Images
Edges	Crowd forcing mass movement (P1), Pedestrian circulation (P2, P10), People (P3), Crowds of people (P5, P6, P8), Crowd (P6, P7), Human density (P9)	Crowd (10)
	Tables overflowing onto sidewalks (P2), Tables belonging to shops (P3, P9), Grocery stalls (P3), Stalls overflowing onto sidewalks (P6), Shoe store (P6), Office block columns (P3, P9), Seating areas of food and beverage shops (P3, P7), Street food (P8), Commercial spaces overflowing onto sidewalks (P10)	Commercial functions overflowing onto sidewalks (12)
	Lighting poles on Kahramanmaras street (P1, P5, P6, P10), Flower pots on Uzun street (P1, P2, P4, P5, P7, P9, P10), Garbage containers in the Square (P5), Seating elements (P10), Ornamental pools (P7), Planting spaces (P3, P4)	Urban landscape elements (flower pots, benches, pool, lighting, etc.) (16)
	Chaos at minibus stops (P1, P7, P8), Minibus stops in the Square (P2, P6), Minibus stops (P3, P9, P10)	Minibus stops, chaos (8)
Nodes	Vehicle density (P1), Vehicles (P2), Intersection of vehicle road and pedestrian road (P3), Traffic chaos caused by vehicles (P4), Car park entrances/exits (P4), Vehicle crowd (P2, P5), Crossroads (P4, P5, P7), Car park in narrow space (P2, P9), Traffic (P10)	Traffic (13)
	Entry to crowded streets (P1), Crowds of people (P2, P5), Crowd at Iskender Pasha Mosque (P2), People shopping (P4), Bustle of people at the banks (P2, P4), Mass motion of people (P5), People waiting for minibuses (P7, P8), Chaos at the crossroads (P9), Crowd (P10)	Crowd (14)
	Street music (P3*2 times), Street musicians (P4*2 times, P5, P6), Musicians (P8)	Street musicians (7)
	Street music (P3*2 times), Street musicians (P4*2 times, P5, P6), Musicians (P8)	Historical structures (12)
Landmarks	Suluhan (P1), Historical buildings (P1*3 times, P8*2 times, P10*2 times), Historical buildings in the Square (P3*2 times), Historical coffee shop (P1, P8)	Atatürk Statue (6)
	Atatürk Statue (P2, P4, P5, P10), Atatürk Statue in the Square (P6, P7)	Crowd (10)

To determine the density and distribution of identified city center images, the maps were transferred to CAD and then superposed. On the superposed map, red represents the paths, yellow represents the edges, blue represents nodes and green represents landmarks (Figure 7). The circles denoting the city center images are sized according to the frequency they were repeated by the participants.

When we look at the map distribution of identified images, it is seen that landmarks and nodes are concentrated at similar points, whereas edges are spread all over the area. The concepts that stand out among the edges are crowd (10), commercial functions overflowing onto sidewalks (12), urban landscape elements (16) such as design elements like flower pots, benches, lighting elements, pavement, and peddlers (7). It is seen that nodes are perceived as concepts that obstruct spatial legibility in the city center, and concepts such as minibus stops (8), traffic (13) and crowd (14) are imaged as the reason for this. When we look at landmarks, it is seen that they are predominated by historical buildings (12), followed by street musicians (7), the Atatürk Statue (6), and plane tree (5). When the experiential maps are evaluated in terms of the streets preferred by the participants, it is seen that all participants used the three main road axes in the area and made markings for these roads, whereas the usage rate of secondary roads remained quite low.
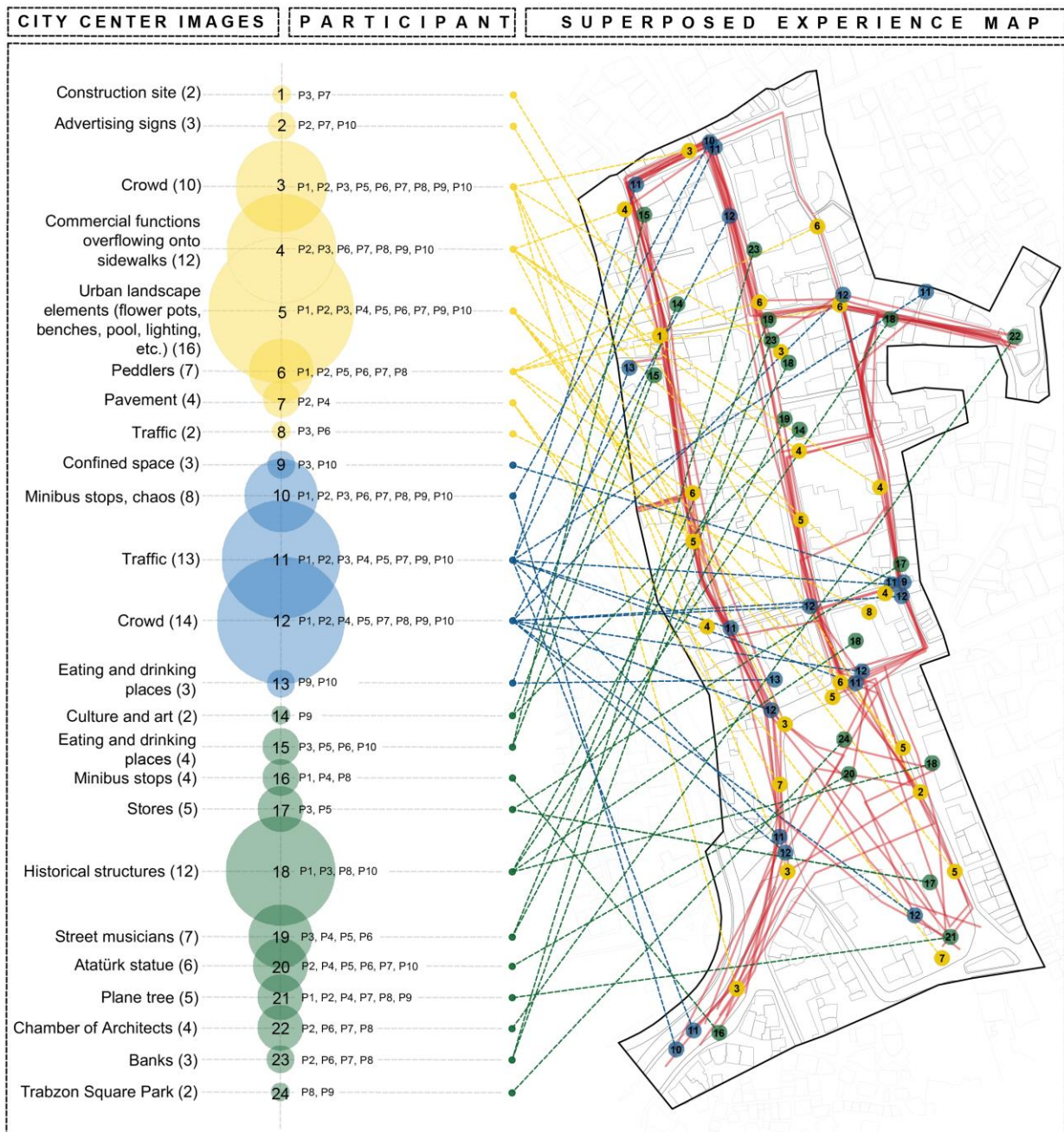
Figure 7. Experiential map analysis and findings.

Figure 8 shows a graph of the average values of the participants' responses to the semantic rating scale in phase one and at the end of phase three, respectively. In the graph, gray represents pre-experience data and orange represents post-experience data.
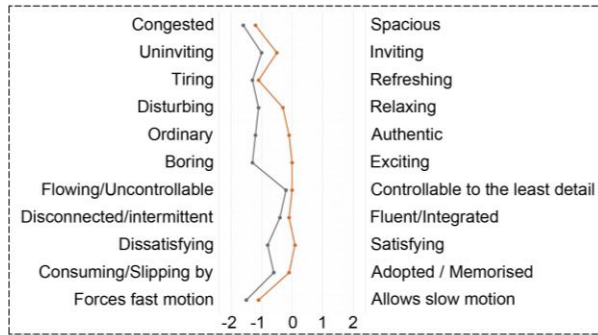
Figure 8. Semantic rating scale findings.

When we look at the pre-experience graph, it is seen that the participants had a negative perception of the city before the experience. This finding is supported by the mean values ranging between -1 and -2 for the statements "congested", "tiring", "ordinary", "boring" and "forcing fast motion". In contrast, the post-experience graph is largely neutral and shows a positive trend in all aspects, with a noteworthy positive differentiation in the adjective pairs "disturbing-relaxing", "ordinary-authentic", "boring-exciting", and "dissatisfying-satisfying".

4. Discussion

Information collection forms, a semantic rating scale and experiential mapping were used to analyze the participants' images of the city center. A collective interpretation of the findings shows that while the participants utilized 16 concepts (Figure 6) to describe their pre-experience impressions of the city, this number increased to 24 post-experience (Figure 7). While the pre-experience images mostly consisted of adjectives signifying the problems of the city and consumption-related statements; even though there were still some similar points, a semantic diversification was found in all post-experience aspects with the addition of different concepts such as spatial components that add value to the city and cultural elements that identify the city center. In other words, the experience enabled the participants to discover the reasons behind the negative ideas they had about the city such as suffocating, boring, congested, chaotic, and disorganized as well as the positive attributions referring to consumption. For instance, participants realized that their description of the city as congested was due to "commercial functions overflowing onto sidewalks", "peddlers", or "urban landscape elements" that made their experience difficult at times. Further, the participants' pre-experience description of the city center was a social activity and meeting venue that responded to needs, whereas post-experience they described it with place-specific components such as historical texture, landmarks, and street musicians, which suggests that experiential mapping made the participants develop an awareness of regional identity.

When the pre-experience and post-experience semantic differentiation graphs are interpreted in the context of the study design based on the premise "fast city, fast experience, weak bond", it is seen that the perceptual picture, which was negative before the experience, showed a relatively positive development after the experience (Figure 8), which is a significant finding when interpreted with a view to the research problem of "positive effect of slowed-down experience on the perception of urban space". In a similar vein, Knox (2005) argues that good walking infrastructure and people's use of it for their daily activities can contribute to enhancing the attractiveness and image of a place, which directly affects quality of life.

Analyzing map content, studying them in detail and trying to see them anew in the sense of stepping outside familiar ways of looking is reported to be a useful starting point (Pinder, 2003). Emphasizing the importance of reactions and preferences of experiencers to different spaces, Pocock (1971) states that the value of mapping stems from the fact that although each individual's image is unique, it allows common images to be recognized. Based on these views, we analyzed the experience maps in detail and determined the most prominent/most frequently repeated concepts and related themes as shown in Figure 9. Interpretation of the map samples of the spatial components imaged by the participants reveals that *edges* and *nodes* derive their own meanings, while the *landmarks* and *paths* are addressed with their original meanings.
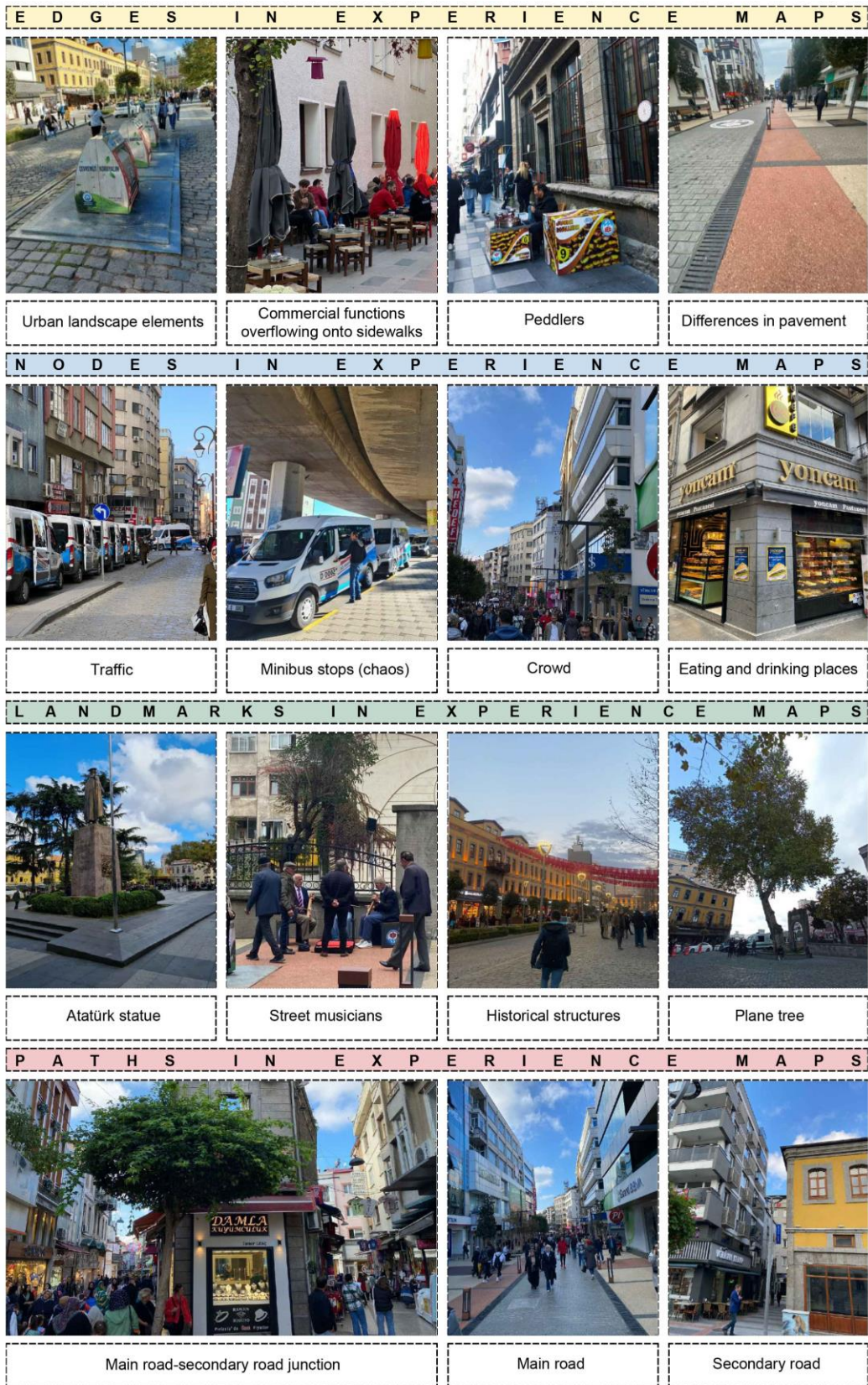
Figure 9. Prominent images in experience maps.

Acting as lateral references that define a perceived space in the mind of the experiencer, edges are usually thought of as walls that divide two regions or as connections that connect two regions (Lynch, 2022). But according to the participants' experiences within the scopes of this research, edges come to the fore as perceptual or physical boundaries that disrupt spatial experience and shape the route of the experiencer, which suggests that edges are not limited to physical barriers on the vertical plane but may also include various materials on the

horizontal plane. In other words, edges can be spatial guideposts that are created in the user's mind and differ according to the user's perception.

Defined by Lynch (2022) as foci that allow a city user to enter the city, such as junctions and intersections in the transportation system, it can be seen that the nodes on experience maps are concentrated in places with dense traffic and crowds, and that they derive meanings like confusion and chaos. Whilst dense people and vehicle presence come to the forefront, meeting venues (eating and drinking) and minibus stops are also described as nodes.

Defined as point-references that the observer does not enter within but assume the role of characterizing the urban identity (Lynch, 2022), the landmarks described in this research were Atatürk Statue that has evolved into a triangulation point in Trabzon Square Park, plane tree, and historical buildings. It is also seen that street musicians, who have become a symbol in the square, are also described as landmarks.

It is seen that edges and nodes were effective in shaping the participants' paths, i.e., "channels along which the observer customarily, occasionally, or potentially moves" (Lynch, 2022). The study shows that limiting factors on the main street such as commercial functions, peddlers and crowds sometimes caused participants to take secondary roads.

The findings obtained in line with the first hypothesis of the study show that slowed down spatial experiences had a positive effect on unveiling the images of Trabzon city center. The participants explored the city center with a deeper perception while creating their experience maps, which enabled them to unveil the city images more clearly. The findings related to the second hypothesis show that the experience maps helped to identify the potentials and problems of Trabzon city center from the perspective of the urban dweller. Mapping enabled the participants to look at the city from a participatory perspective and gave them the chance to express their visual and emotional evaluations. Accordingly, the research findings support both hypotheses. The research does not claim that images formed in the minds of users alone will be sufficient in representing urban identity. Indeed, given the multi-layered nature of urban identity, the topic can be enriched with research processes supported by different dimensions. Similarly, Belanche et al. (2017) argue that urban identity is a construct that consists of cognitive, affective and evaluative dimensions and that more research is needed to understand the development of these dimensions.

5. Conclusion

Each place penetrates differently into the perception of its constant users, first-time observers or people whose attention is drawn to that place for professional reasons or other motives. Urban identity is a synthesis of these different perceptions. But in the age we live in, cities are shaped under the shadow of consumer culture and city

dwellers are exposed to an accelerated spatial experience imposed by it. This makes the images of urban identity a matter of curiosity that can be unveiled in the minds of city dwellers through a slowed-down and planned experience.

This paper discusses the outputs of a field study carried out with a planned motive in the city center of Trabzon, a Turkish city that stands as an example of the fast-life scenario mentioned above. The pre-experience data collected in writing were compared with post-experience mapping results to study how spatial images were affected by experiential mapping. It was seen that the participants' pre-experience impression of the city was predominantly negative. The fact that most of the participants who had been living in the city for many years expressed negative opinions supports the idea that problematic urbanization has weakened the bond of belonging between the city and the city dwellers.

Edges such as the crowdedness of the city center, commercial functions overflowing onto sidewalks, and urban landscape elements, *nodes* such as traffic, narrow spaces, chaos, and *landmarks* such as historical buildings, street musicians, and plane tree identified by the participants show that experiential mapping increased their awareness of the city center. The fact that in the semantic rating scale, the pre-experience weighted average was predominated by negative adjectives such as boring, disturbing, ordinary, and consuming but turned towards rather positive ones such as exciting and relaxing after the experience supports the view that the experience strengthened the belonging between city dwellers and urban space. In conclusion, this study designed to create Certeau's *ascent* through experiential mapping revealed the importance of a slowed-down and focused experience in making sense of urban space. Even though the small number of participants constitutes a limitation of this study, it has been observed that even a short stroll taken by a small number of participants with a focus on *"taking a step back for a moment and think"* is effective in deriving many meaningful images of the city, suggesting that in a speed-oriented daily life depriving the urban dweller of their ability to develop sufficient awareness of a space they use almost every day, experiential mapping can be a good tool of analysis to guide future research by identifying the potentials and problems related to the city.

When we look at the literature, it is seen that there is only limited research into the effects of experiential mapping on the determination of urban identity or the interaction between the city and city dwellers. This research and the applications described in this paper are expected to provide a base for future urban research that will delve into topics like promoting urban literacy among city dwellers and unveiling the urban identity that emerges from the interaction between the city and the city dweller. We believe that this research, which places its focus on exploring spatial components through a slowed down urban experience, will make a genuine

contribution to the literature. The methodology created for the purpose of this research with a view enhancing the visibility of city images (whether of historical, cultural, artistic or other nature) peculiar to Trabzon city center through experiential mapping can serve as a valuable starting point for future research in this area. The methodology used in this study offers a novel perspective that can be used/built on when developing new approaches to planning and design of city centers and increasing urban literacy.

Author Contributions

The percentage of the author(s) contributions is presented below. The author reviewed and approved the final version of the manuscript.

	H.K	M.U.T	P.T
C	30	40	30
D	40	30	30
S	50	25	25
DCP	30	35	35
DAI	40	30	30
L	30	40	30
W	40	30	30
CR	50	25	25
SR	40	30	30
PM	30	35	35

C=Concept, D= design, S= supervision, DCP= data collection and/or processing, DAI= data analysis and/or interpretation, L= literature search, W= writing, CR= critical review, SR= submission and revision, PM= project management

Conflict of Interest

The authors declared that there is no conflict of interest.

Ethical Consideration

The authors confirm that the ethical policies of the journal, as noted on the journal's author guidelines page, have been adhered to. The experimental procedures were approved by the Science and Engineering Ethics Committee of Karadeniz Technical University, (approval date: 25 October, 2023, protocol code: E-82554930-050.01.04-440132).

References

Aliağaoglu A, Mirioğlu G. 2020. Urban identity of Balıkesir. Inter J Geograp Edu, 42: 374-399.

Alver K. 2012. Kent imgesi. Alver K, editor. Kent sosyolojisi. Hece Yayınları, Ankara, Türkiye, pp: 9-31.

Araldi A, Fusco G. 2019. From the street to the metropolitan region: Pedestrian perspective in urban fabric analysis. Environ Plan B: Urban Analyt City Sci, 46(7): 1243-1263.

Begel EE. 1996. Kentlerin doğuşu. Cogito, Yapı Kredi Yayınları, İstanbul, Türkiye, 8: 7-16.

Belanche D, Casaló LV, Flavián C. 2017. Understanding the cognitive, affective and evaluative components of social urban identity: Determinants, measurement, and practical consequences. J Environ Psychol, 50: 138-153.

Cadwallader M. 1979. Problems in cognitive distance. Environ Behav, 11(4): 559-576.

Carmona M, Heath T, Oc T, Tiesdell S. 2003. Public Places-Urban spaces. Routledge, London, UK, pp: 106-129.

Certeau M. de 1984. The practice of everyday life. University of California Press, Berkeley, USA, pp: 91-110.

Cosgrove D. 1985. Prospect, perspective and the evolution of the landscape idea. Transact Institute British Geograp, 10(1): 45-62.

Evans GW, Brennan PL, Skorpanich MA, Held D. 1984. Cognitive mapping and elderly adults: Verbal and location memory for urban landmarks. J Gerontol, 39(4): 452-457.

Gehl J. 2011. Life between buildings: Using Public Space. Island Press, Washington, USA, pp: 33.

Giddens A. 2012. Sosyoloji. Güzel C, editor. Kırmızı Yayınları, İstanbul, Türkiye, pp:978.

Harvey D. 2022. Kent deneyimi. Sel Yayıncılık, Istanbul, Türkiye, 4th ed, pp: 13.

Jang KM, Kim Y. 2019. Crowd-sourced cognitive mapping: A new way of displaying people's cognitive perception of urban space. PLOS ONE, 14(6): 1-18.

Knox PL. 2005. Creating ordinary places: Slow cities in a fast world. J Urban Design, 10(1):1-11.

Krätke S. 2014. Cities in contemporary capitalism. Inter J Urban Regional Res, 38(5): 1660-1677.

Lynch K. 2022. Kent imgesi. Is Bankası Kültür Yayınları, Istanbul, Türkiye, 16th ed, pp: 16-53.

Matos Wunderlich F. 2008. Walking and rhythmicity: Sensing urban space. J Urban Design, 13(1): 125-139.

Milgram S. 1970. The experience of living in cities. Sci, 167(3924): 1461-1468.

Özgen AI, Türkseven Doğrusoy I. 2020. İzmir-Karşıyaka'da çevresel algıyı çözümlemeye yönelik bir araştırma. Tasarım+ Kuram J, 16(29): 153-167.

Pinder D. 2003. Mapping worlds: Cartography and the politics of representation. In Blunt A, Gruffudd P, May J, Ogborn M, Pinder DP, editors. Cultural Geography in Practice. Arnold Publishers, London, UK, pp: 172-187.

Pocock DCD. 1971. Urban environmental perception and behaviour. Tijdschrift voor Economische en Sociale Geografie, 62(5): 321-326.

Rozman Cafuta M, Sitar M. 2017. Rethinking the city spatial identity through the eyes of the observer. Prostor, 25(2/54): 316-327.

Schoonderbeek M. 2017. A theory of "design by research"; Mapping experimentation in architecture and architectural design. Ardeth, 1: 63-79.

Spencer C, Weetman M. 1981. The microgenesis of cognitive maps: A longitudinal study of new residents of an urban area. Transact Instit British Geograph, 6(3): 375-384.

Šenk F. 2021. On the interaction of here and there. Places in the city. In Giombini L, Kvokačka A, editors. Everydayness. Contemporary aesthetic approaches. Roma TrE-Press, Rome, Italy, pp: 65-78.

Simmel G. 2005. Metropol ve zihinsel yaşam. In Aydoğan A, editor. Şehir ve cemiyet. Iz Yayıncılık, Istanbul, Türkiye, 2nd ed., pp: 167-184.

Şenel A. 2014. Haritalama: Bir anlama, elestirme ve tasarlama eylemi. In Şentürer A, Paker N, Berber Ö, Şenel A, editors. taarla: Projections on Istanbul. ITU architectural design research laboratory works. ITU Vakfı Yayınları, Istanbul, Türkiye, pp: 26-33.

Şenel A. 2019. Mimarlık eğitiminde haritalama: Geleneksel eril mimarlık üretimine yaratıcı bir eleştiri. In Aral EA, editor. Dosya 42: İlişkisel bir eylem olarak haritalama. TMMOB Mimarlar Odası Ankara Şubesi, Ankara, Türkiye, pp: 5-18.

Topcu KD, Topcu M. 2012. Visual presentation of mental images in urban design education: Cognitive maps. Proc - Soc Behav Sci, 51: 573 – 582.

Yaylı H. 2012. The effects of globalization on the cities: The case of Istanbul. The J Soc Econ Res,, 12(24): 331-356.

Yorgancıoğlu D, Çalak I. 2020. A methodological inquiry for re-structuring spatial knowledge derived from bodily-experience: Experiential mapping. Megaron, 15(1): 126-137.

OPTIMIZING CAPSULE NETWORK PERFORMANCE WITH ENHANCED SQUASH FUNCTION FOR CLASSIFICATION LARGE-SCALE BONE MARROW CELLS

Amina FARIS ABDULLA AL RAHHAWI[1], Nesrin AYDIN ATASOY[2]*

[1]Karabük University, The Institute of Graduate Studies, 78050, Karabük, Türkiye
[2]Karabük University, Faculty of Engineering, Department of Computer Engineering, 78050, Karabük, Türkiye

Abstract: Capsule networks (CapsNet) have emerged as a promising architectural framework for various machine-learning tasks and offer advantages in capturing hierarchical relationships and spatial hierarchies within data. One of the most crucial components of CapsNet is the squash function, which plays a pivotal role in transforming capsule activations. Despite the success achieved by standard squash functions, some limitations remain. The difficulty learning complex patterns with small vectors and vanishing gradients are major limitations. Standard squash functions may struggle to handle large datasets. We improve our methodology to enhance squash functions to address these challenges and build on our previous research, which recommended enhancing squash functions for future improvements. Thus, high-dimensional, and complex data scenarios improve CapsNet's performance. Enhancing CapsNet for complex tasks like bone marrow (BM) cell classification requires optimizing its fundamental operations. Additionally, the squash function affects feature representation and routing dynamics. Additionally, this enhancement improves feature representation, preserves spatial relationships, and reduces routing information loss. The proposed method increased BM data classification accuracy from 96.99% to 98.52%. This shows that our method improves CapsNet performance, especially in complex and large-scale tasks like BM cells. Comparing the improved CapsNet model to the standard CapsNet across datasets supports the results. The enhanced squash CapsNet outperforms the standard model on MNIST, CIFAR-10, and Fashion MNIST with an accuracy of 99.83%, 73%, and 94.66%, respectively. These findings show that the enhanced squash function improves CapsNet performance across diverse datasets, confirms its potential for real-world machine learning applications, and highlight the necessity for additional research.

Keywords: Capsule networks, Enhanced squash function, Imbalanced dataset

1. Introduction

Bone marrow (BM) cells affect human health. They facilitate the correct functioning of human blood. Many cell types make up human blood. These cells support tissue repair and stop bleeding and infection resistance in the body (Girdhar et al., 2022). The human immune system depends critically on blood cells to defend the body against bacteria and infections (Çınar and Tuncer, 2021). Although making up just 1% of the blood volume overall, white blood cells (WBCs) are essential to immunity. Carrying oxygen, red blood cells (RBCs) make up a noteworthy 45% of the blood volume (Tamang et al., 2022). Besides, white blood cells shield the body from viruses and parasites. Regarding the human immune system, they are essential (Stock and Hoffman, 2000). WBCs are mostly of five types: monocytes, lymphocytes, basophils, neutrophils, and eosinophils (Yao et al., 2021). Every type serves a different purpose in shielding the body from various germs and promoting general health and well-being. The cytoplasm of these cells contains nuclei, which sets them apart. Often used to evaluate the

effectiveness of radiation and chemotherapy (Kutlu et al., 2020), blood tests are an essential diagnostic tool for many diseases (Long et al., 2021). Polio, tuberculosis, measles, HIV, and chickenpox are only a few of the illnesses that can lower lymphocyte counts. On the other side, leukemia, brucellosis, liver disease, and Bordetella pertussis disease can all raise lymphocyte levels. Leukemia, the illness, polio, and pertussis-borne diseases can cause lymphocyte counts to rise; polio, tuberculosis, measles, HIV, and chickenpox can cause them to fall. WBCs, RBCs, and plasma, platelets are considered the peripheral blood cells (PBCs) (Balasubramanian et al., 2022). Anemia, malaria, and leukemia can all be diagnosed with a PBC test (Hegde et al., 2019a). Unlike more homogeneous forms of platelets and RBCs, WBCs are the subject of much research because of their varied shape and unique subtypes (Dhal et al., 2023). The diversity of WBCs makes them of special interest for medical image segmentation and classification (Agustin et al., 2021). Hematologists' workload has been much reduced by computer-aided automated white blood cell

classification. Masses of data can be processed quickly and accurately by these methods. These automated techniques can be categorized essentially into three groups. Known as TIP, the first technique extracts feature from WBC images by means of threshold functions derived from mathematical relationships and preset parameters. With the aid of these cutoffs, classification of various white blood cell types is facilitated. Over time, several TIP approaches have been honed and enhanced; these include pixel template matching techniques as in (Ghosh et al., 2010; Hegde et al., 2019b; Mohamed et al., 2012; Rezatofighi et al., 2009), fuzzy divergence, modified thresholding, Grayscale contrast, and Gram-Schmidt orthogonality. Second, machine learning: As computing power has increased and conventional image processing has shown flaws, researchers have started using machine learning (ML) algorithms such as support vector machines (SVM), Bayesian classifiers, and random forest models for WBC classification (Gautam et al., 2017; Mirmohammadi et al., 2021). These techniques enhance classification accuracy by making use of unique morphological features of WBCs. Statistical, geometric, wavelet and textural features are extracted from images through analysis. The most pertinent features are chosen through a feature selection process that runs through all these features. To achieve accurate identification, the features that were chosen are subsequently fed into classifiers like Bayesian and SVM. Third, DL: convolutional neural networks (CNNs) and other deep learning structures have recently seen a surge in popularity for WBC classification jobs. Deep learning techniques automatically extract features from images, leading to improved classification accuracy (Aydin Atasoy and Faris Abdulla Al Rahhawi, 2024; Dayı et al., 2023), in contrast to conventional ML methods that depend on human feature extraction.

Historically, the classification of WBCs has been carried out manually, resulting in a slow, laborious, and error-prone procedure. Hence, it is essential to develop algorithms and automated diagnostic systems to classify WBC quickly and accurately (Liu et al., 2019). The motivation behind this study is that Capsule networks (CapsNet) exhibits potential in capturing intricate data relationships but faces challenges when dealing with huge complex data sets due to limitations in traditional squash functions. This article introduced an enhanced squash function to improve CapsNet performance, especially when dealing with high-dimensional and complex datasets. We aim to improve feature representation and classification accuracy by optimizing the fundamental operations, focusing on BM cell classification tasks. This research represents a significant extension of our previous contributions (Aydın Atasoy and Faris Abdulla Al Rahhawi, 2024), improving the effectiveness and applicability of CapsNet in real-world applications. The contributions of the presented model are as follows:

- We present an enhanced squash function optimized for CapsNet. The improved function addresses the limitations of standard squash and improves feature representation.

- Our methodology significantly improved the classification of 21 BM cells, which increased the classification accuracy for bone marrow cells from 96.99% to 98.52%. This success is an essential step in the process of diagnosing hematological disorders.

- Imbalance classes issue have been solved using SMOTE oversampling.

- Extending evaluation to MNIST, Fashion MNIST, and CIFAR-10 datasets demonstrates that our CapsNet architecture with the enhanced squash function has consistently improved performance.

- A wide comparison is conducted between our proposed methods and several previous CapsNet architectures.

This paper is organized and arranged as follows: Section 2 presents the literature review. In Section 3, dataset details and selected CapsNet methods are introduced. The classification performance results of the proposed models are evaluated in Section 4. The conclusion and future works are discussed in Section 5.

1.2. Literature Review

Nowadays, deep learning has proven to be effective in many classification tasks (Somuncu and Aydın Atasoy, 2022; Taşdelen and Ugur, 2021). Further, it has been used to classify images using various fields and methods. A multilayer feedforward artificial neural network like CNN is one of the most popular deep learning models. It is easy to use, runs in parallel, and achieves high success levels. CNN comes in many types, including VGGNet, AlexNet, GoogleLeNet, ResNet, EfficientNet, and ConvNeXt (Arjun Ghosh et al., 2022). CNNs consist of convolution, pooling, and a fully connected layer (LeCun et al., 2015). Kernels filter input data in the convolution layer to extract feature maps and learn image regional patterns. The pooling layer reduces feature map dimensionality by applying pooling operations, but this can lose information (Somuncu and Aydın Atasoy, 2022). Finally, the fully connected layer's activation function processes weighted inputs from each neuron in the previous layer to determine output.

It is a significant challenge to train a model to perform all possible combinations of enlargement, rotation, inversion, cropping, and zooming; it requires a substantial amount of time and data. However, the resulting model may not yield optimal outcomes. The CNN model may cause data loss during the feature extraction when filters are applied to datasets created through rotation. CNNs can handle translational invariance but cannot do so with rotational invariance (Kwabena Patrick et al., 2022; Muhammad et al., 2023; Nair et al., 2021; Ren et al., 2019) and are not sufficiently successful in training large and unbalanced data (Singh et al., 2021). CapsNet employs dynamic routing methods to prevent data loss in the pooling layer (Zhao and Huang, 2019).

Recent advancements in BC classification have led to the

development of advanced deep-learning techniques. Girdhar et al. (Girdhar et al., 2022) developed a new CNN structure for the WBC classification. An investigation was conducted on the blood cell count and detection (BCCD) dataset to evaluate the effectiveness of the CNN method as presented. The CNN method achieved a classification accuracy of 98.55% after 20 epochs. Long and colleagues (Long et al., 2021) presented BloodCaps, a capsule-based model aimed at precisely categorizing a broad spectrum of blood cells for PBC classification. Eight classes of human peripheral blood cells made up a large dataset for which the BloodCaps method was used. Its remarkable 99.3% total accuracy beats that of convolutional neural networks like InceptionV3 (98.4%), ResNet18 (95.9%), VGG16 (97.8%), and AlexNet (81.5%). Sengur et al. (2019) presented in their work a hybrid method for the WBC count that combines deep learning methods with image processing. Among the image processing methods used by the WBC images are morphological procedures, thresholding, filtering, color-to-grayscale conversion, and RGB to HSV conversion. Later, the long-short-term memory (LSTM) approach is used to classify WBC. Analyzing the experiment findings on the BCCD dataset, the proposed hybrid approach produced a 92.89% classification accuracy. Patil et al. (2021) proposed a deep learning method for the WBC classification by combining LSTM and CNN through canonical correlation analysis. The official correlation analysis enhances the accuracy of the input image by extracting multiple overlapping features, surpassing other comparable deep learning methods. The classification accuracy achieved for the applications on the BCCD dataset is 95.89%. Baghel et al. (2022) designed a new CNN model to enhance the precision of WBC classification. After 1000 epochs, their analysis of the BCC dataset resulted in a classification accuracy of 98.91%. Basnet et al. (2020) introduced a technique for precise WBC classification by employing the CNN structure. The researchers employed a dataset of 10,000 images categorized into five classes to assess their deep CNN classification accuracy, achieving an impressive 98.92% accuracy. Baydilli and Atila (2020) proposed a new method that utilizes capsule networks to categorize white blood cells into five distinct types. The researchers evaluated the precision of their capsule networks by conducting tests on the Leukemia Image Segmentation Challenge (LISC) dataset. This dataset consists of 263 blood cell images and is considered relatively small. Their efforts resulted in an accuracy rate of 96.86%. Ha et al. (2022) introduced a new semi-supervised model called Fine-grained Interactive Attention Learning (FIAL) for the classification of WBC. This model involves two essential elements; firstly, the Semi-Supervised Teacher-Student modules utilize a limited number of labeled WBC images to train a network called the "teacher". The "teacher" network subsequently directs the learning process of a "student" network using a vast collection of unlabeled WBC samples, resulting in the generation of estimated probability vectors for these

samples. Secondly, the Fine-Grained Interactive Attention mechanism enhances the attention within the network by highlighting the informative regions of the WBC images, leading to improved accuracy in classification. they achieved an overall accuracy of 93.2% when evaluating the FIAL model on the publicly available BCCD dataset. Hosseini et al. (2022) proposed a new CNN structure that is specifically tailored for the classification of four different types of WBCs: neutrophils, monocytes, eosinophils, and lymphocytes. Their approach stands out because they utilize a mix of random and grid search optimization algorithms to adjust the model's hyperparameters precisely. Following evaluation using the BCC dataset, their CNN achieved an accuracy rate of 97%. Vigueras-Guillén et al. (2021) focused on developing an innovative "parallel CapsNets" framework tailored specifically for the classification of WBCs. By utilizing a branching strategy, this architecture can isolate capsules that are utilized to identify distinct cell types. When evaluated on a 15-class dataset of acute myeloid leukemia images, their parallel CapsNets demonstrated superior performance to the baseline CNN, owing to enhanced stability and rotational invariance. Although the precise accuracy was not explicitly stated, its performance exceeded that of the foundational CNN. Various publications have employed CapsNets to execute various tasks using medical images. Many researchers utilized Sabour et al.'s network (2017) on small patches to carry out various tasks. These tasks include detecting diabetic retinopathy in fundus images, identifying mitosis in histology images (Hand E), and classifying breast cancer (Anupama et al., 2019; Iesmantas and Alzbutas, 2018) (Hoogi et al., 2019).

As seen in the literature, many studies have tried to improve CapsNet using different methods, often pre-training techniques. However, much must be done to strengthen the core CapsNet components, particularly the squash function. This paper will focus on improving the squash function, an important part of CapsNet.

2. Materials and Methods

This section presents two implementations: one employing the standard squash function and the other utilizing an enhanced squash to conduct a comparative analysis of the performance of these two employments within the CapsNet architecture, as shown in Figure 1.

2.1. Baseline capsnet theory

The concept of CapsNet was initially proposed by Sabour et al. (2017) . These networks represent images in a whole vector format, which allows them to encode internal properties, including the pose of entities within an image. In contrast to CNNs, which rely on pooling for output routing, CapsNet aims to preserve information to achieve equivariance, particularly in handling viewpoint changes. This preservation is facilitated through dynamic routing, which replaces the pooling mechanism. Lower-level capsules representing specific features are hierarchically routed to parent capsules to capture part-

whole relationships via linear transformations. This approach is based on the concept of inverse graphics, which suggests that the neural system deconstructs images into their inherent hierarchical properties. A capsule is a group of neurons that perform a diverse range of internal computations and subsequently encode the results of these computations into an n-dimensional vector. The vector is the output of the capsule. The length of this output vector indicates the vector's probability and direction, indicating certain properties about the entity. Using initial convolutional layers in capsule networks permits the reuse and replication of learned knowledge across different parts of the receptive field. An iterative Dynamic Routing algorithm is employed to determine the inputs to the capsules. The output of each capsule is then compared with the actual production of the higher-level capsules. In the case of a match between the outputs, the coupling coefficient between the two capsules is increased. Let i represent a lower-level capsule and j a higher-level capsule. The prediction vector is calculated as follows in equation 1 (Sabour et al., 2017).

$$\hat{u}(j|i) = W_{ij}u_i \qquad (1)$$

The W_{ij} trainable weighting matrix and the u_i output pose vector from the $(i-th)$ capsule to the $(j-th)$ capsule are employed in this context. The coupling coefficients are calculated using a SoftMax function as follows in equation 2 (Sabour et al., 2017).

$$C_{ij} = \text{SoftMax}(b_{ij}) = \frac{\exp(b_{ij})}{\sum_k \exp(b_{ik})} \qquad (2)$$

The log probability of capsule i coupled with capsule j, denoted by b_{ij}, is initialized with zero values. The total input to capsule j is a weighted sum of the prediction vectors, calculated as follows in equation 3 (Sabour et al., 2017):

$$s_j = \sum_i C_{ij}\, \hat{u}_{j|i} \qquad (3)$$

In capsule networks, the length of the output vector is employed to represent the probability for the capsule. Consequently, a non-linear activation function, the squashing function, is used. The squashing function is defined as follows in equation 4 (Sabour et al., 2017):

$$V_j = Squash(s_j) = \frac{||s_j||^2}{1 + ||s_j||^2} \frac{s_j}{||s_j||} \qquad (4)$$

The dynamic routing algorithm can update the c_{ij} values in each iteration. In this case, the objective is to optimize the V_j vector. In the dynamic routing algorithm, the b_{ij} vector is updated in every iteration according to equation 5 (Sabour et al., 2017):

$$b_{ij} = b_{ij} + V_j\, \hat{u}_{j|i} \qquad (5)$$
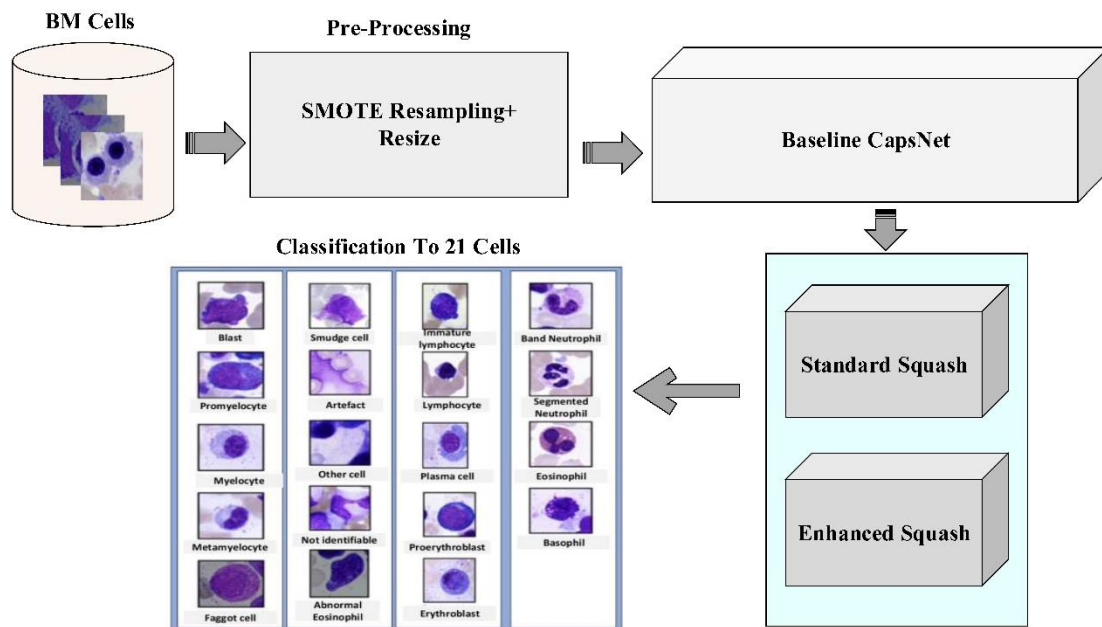
Figure 1. General steps for classification.

2.2. Dataset

The BM cell dataset (Matek et al., 2021) includes various hematological disease cell microscopic images consisting of more than 170000 de-identified, expert-annotated cells from bone marrow smears of 961 patients stained using the May-Grünwald-Giemsa/Pappenheim stain. The institutional review board at the Munich Leukemia Laboratory (MLL) has given its permission to use this dataset. Sample microscopic images from the dataset are shown in Figure 2.
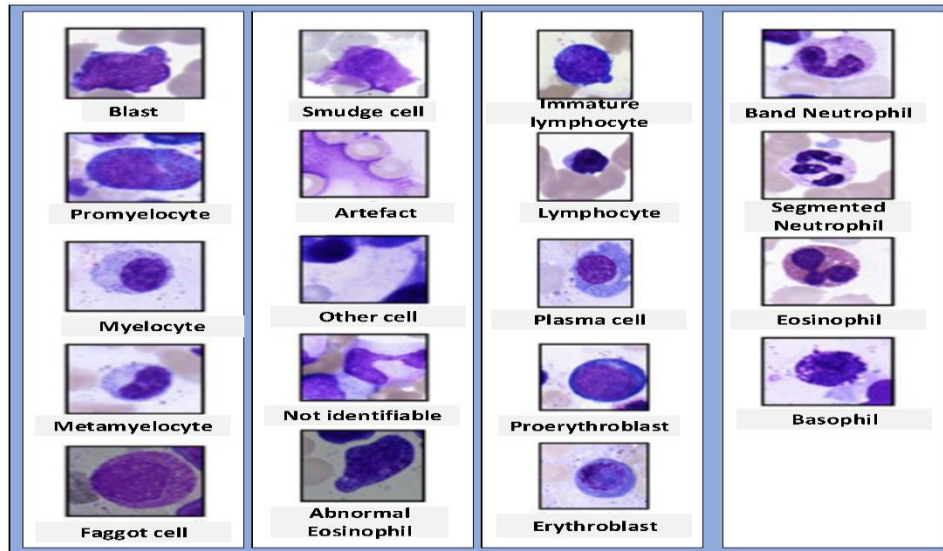
Figure 2. Morphological appearance of BM cell classes.

2.3. Pre-processing

As seen in Figure 3, imbalances in the distribution of some BM cell dataset classes cannot reach the expected target. SMOTE (Chawla et al., 2011), Adaptive Synthetic (ADASYN) (He et al., 2008), SMOTEBoost (Nitesh V. Chawla et al., 2003), and DataBoostIM (Guo and Viktor, 2004) sampling approach techniques are used to avoid these imbalances.

In this study, SMOTE, which is preferred over other sampling approximation techniques (Bajer et al., 2019; Maldonado et al., 2019) is used to create synthetic instances of the minority class by interpolating between class instances of an imbalanced dataset(Elreedy and Atiya, 2019) using equation 6 (Juanjuan et al., 2007; Reza and Ma, 2019). In this equation, t is the true minority value; k is the number of nearest neighbors of the true value; n is the nearest neighbor value $(n-t)$does Euclidean distance obtain the difference; $random(0,1)$Is the number value that allows the addition of different feature values. In this study, k=5 for each minority class.

$$smote(t, k) = t + random(0,1) * (n - t) \qquad (6)$$

Minority classes were rounded to 5000 images, and classes with over 5000 images were rounded up. This over-sampling technique improved overall classification performance and representation of the minority classes. Figure 4 shows the change in the number of data after the SMOTE process. In addition, all images are rescaled using Bicubic Interpolation (Keys, 1981). This technique is a non-adaptive interpolation algorithm and uses polynomial techniques to sharpen and enlarge digital images.

2.4. CapsNet Architecture with Standard Squash

The input images of the baseline CapsNet model were resized as 32 × 32 pixels to reduce the training time and then designed as shown in Figure 5.

The proposed model takes three arguments: the input image, the number of classes, and the number of routing iterations. After input images are preprocessed as in previous steps, fed to the convolutional layer to extract low-level features with filters is 256, kernel size is 9, and strides is 1. Then, these features are grouped into primary capsules with filters of 8 × 32, kernel of 9 × 9, and stride of 1 to reduce the model size, each representing a part or aspect of an object. Each capsule in the convolutional layer corresponds to a capsule in the primary capsule layer. A routing-by-agreement approach boosts learning capability and captures the relationships between different parts of an object. Each capsule in a higher-level layer sends its output to capsules in the layer above based on the agreement (compatibility) between their outputs. The routing process consists of iteratively updating the connection weights between capsules based on the match between their outputs. Thus, dynamic routing makes the capsules in higher layers focus on the most relevant capsules in the layer below; the ReLU activation function, a non-linear function in deep neural networks, is used to reduce dimension. The output of the capsule network is obtained by measuring the length of the output vectors of the capsules in the top layer. This length indicates the probability that a given class or object is present in the input image. Standard squash is applied to squash the vectors of the primary capsules as a non-linear activation function. It aims to ensure that short vectors are reduced to a length close to zero and

long vectors are reduced to a length close to 1. Then, adjusting the hyperparameter, the learning rate is initially determined to be 0.001, and the Adam (Kingma and Ba, 2015) optimization algorithm is used to change it dynamically. The model is run with a decay ratio of 0.9 and a routing of 3 for 100 epochs. The CapsNet model train accuracy is calculated at 96.99% on the BM dataset.

2.5. Squashing Vectors Improvement

Standard squash function proposed by (Sabour et al., 2017)represents a key component within the context of CapsNet. It refers to a non-linear activation function applied to the output of capsule layers to normalize the output vectors of capsules within the range [0, 1], ensuring consistent representation across different capsules. These layers process features and encode not only the presence of an entity but also its orientation. This normalization allows the magnitude of the output vector to be interpreted as the probability of the presence of an entity and its pose parameters. In addition, by scaling the vectors, the squash function prevents short vectors from vanishing and long vectors from becoming overly large. Additionally, there are still a few restrictions even with the succeeding standard squash function. It first has the vanishing gradient issue, which gets harder to ignore as vectors reach their maximum length. Training can proceed slowly or unstable because the squash function's gradient tends to get very small as the vectors reach 1. Squash functions aim to squash vectors into the range of 0 to 1. Moreover, very small norm vectors can be difficult for the traditional squash function to manage. Numerical instability or errors can arise when gradients must be computed precisely during training. Furthermore, the squash function has a sensitive behavior to initialization; a wrong initialization can cause problems like exploding, jeopardizing the training process's stability and convergence. Recording intricate relationships and patterns in the data is insufficient, to sum up. These drawbacks highlight the need to resolve these issues and improve the functionality of capsule networks in a range of applications by means of improvements or novel squash function formulations. This paper offers a better squash function that uses layer normalization to address these problems and offers more accurate and effective CapsNet training. Upon entering this normalization layer, the input vectors are scaled. Conversely, the commonly used squash function normalizes input vectors only by considering their squared norm. The normalization layer approach stabilizes the learning process by successively normalizing the activations of each capsule across the feature dimension. The computed mean and variance statistics are first applied by the improved squash function to normalize the input vectors. The following illustrates the mathematical procedures. The scaling factor is computed as (equation 7):

$$Scale = \frac{\alpha \left|\left|\frac{sj}{5}\right|\right|^2}{1 + \alpha \left|\left|\frac{sj}{5}\right|\right|^2} \tag{7}$$
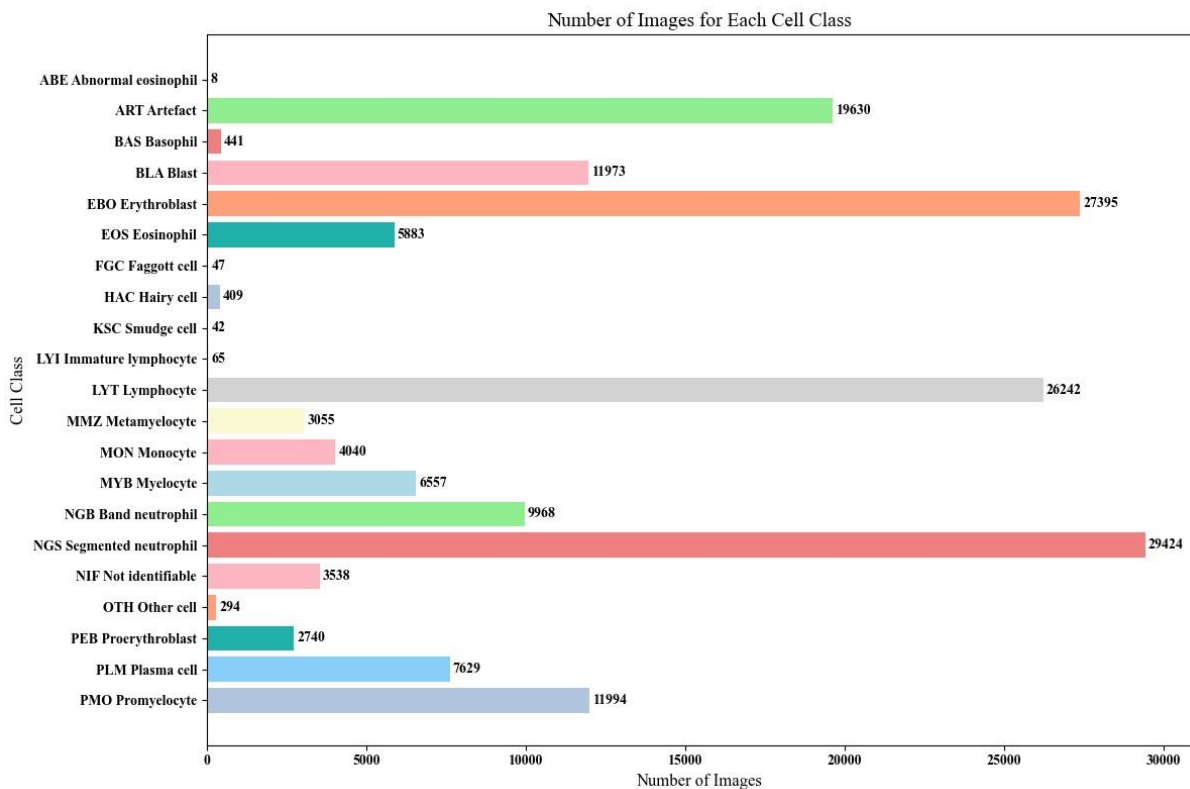
Figure 3. BM cell dataset features.
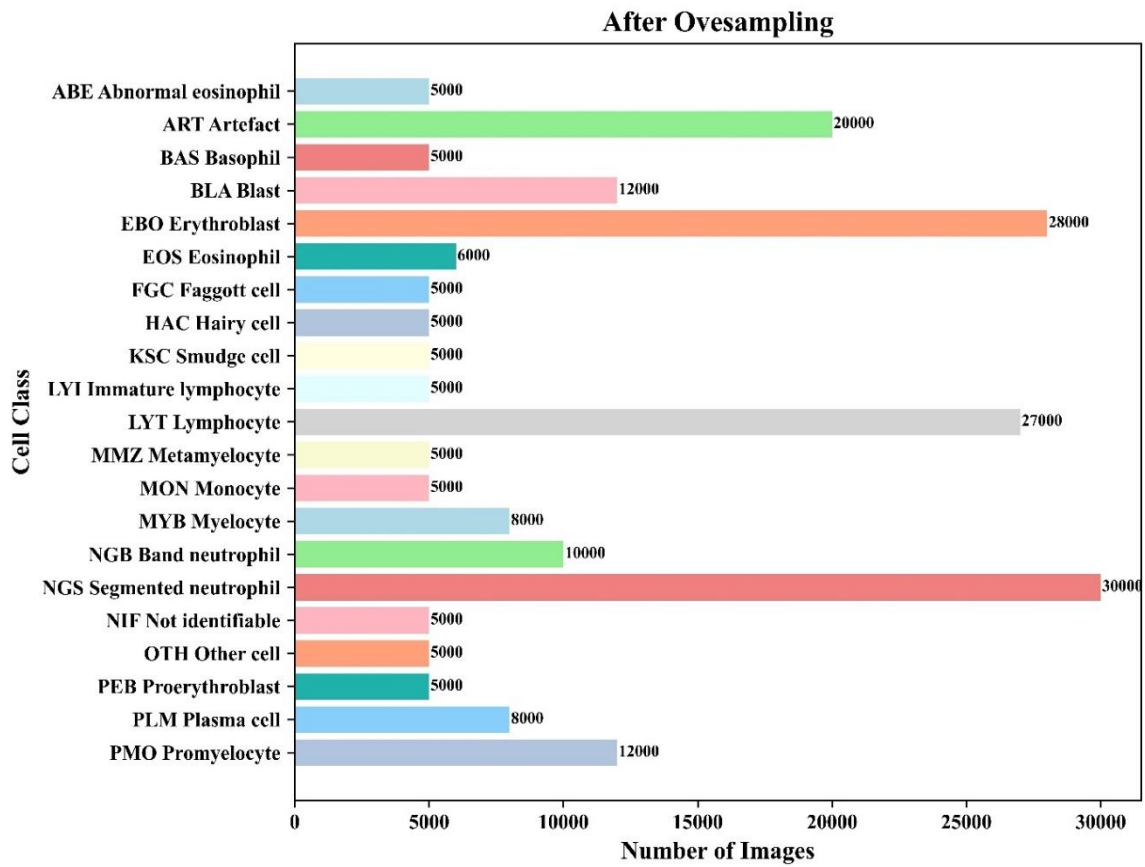
Figure 4. After Oversampling BM cell dataset features.
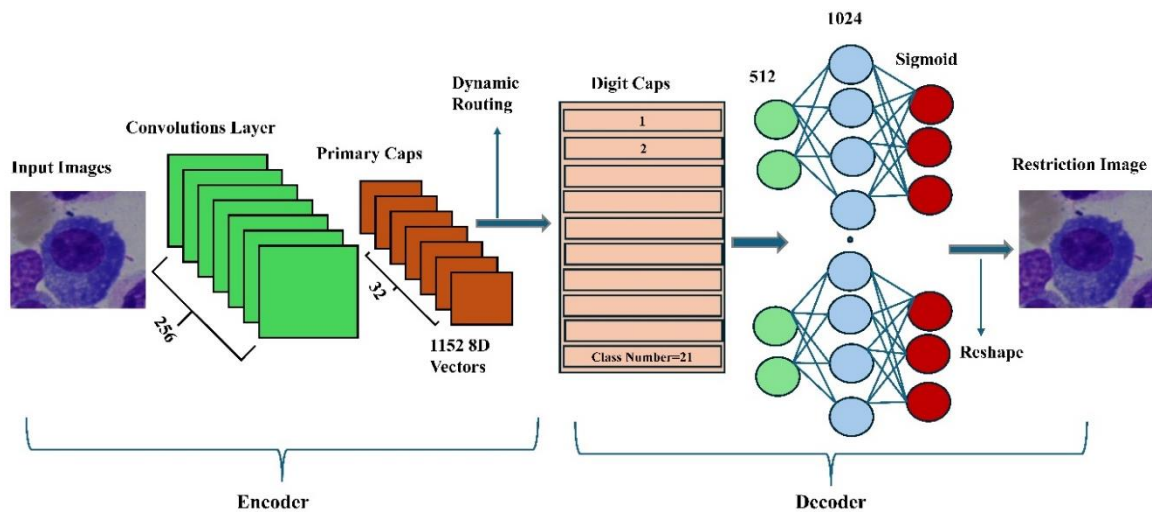
Figure 5. General structure of proposed CapsNet on BM dataset.

This equation defines the scale squash function; it transforms an input vector sj to extract informative features while discarding less informative ones. $||\frac{s_j}{5}||^2$: This computes the input vector sj's squared L2 norm. The vector's length, or norm, equals its size. Input vectors can be stabilized by dividing them by 5 which will also improve optimization convergence and reduce issues like exploding or disappearing gradients. In addition, it indicates relative feature relationships over true values, so promoting scale invariance and strengthening the network against changes in feature magnitude. By focusing on features within a suitable range of magnitude, this normalization prevents the network from being unduly influenced by the values of extreme features. It allows it to extract meaningful patterns more successfully. Controlling the degree of the squashing is the scaling factor $\alpha > 0$, which is set to 0.5. Moreover, the model became more robust to noisy or unstable input data at $\alpha = 0.5$. The model demonstrated superior validation and tested dataset performance by capturing essential features and patterns. Thus, reduced bias,

improved gradients, and potentially more stable training often overcome the potential drawbacks. After calculating the scaling factor, the function performs layer normalization on the input vectors. It is a technique employed to normalize a layer's activations, ensuring that the mean is zero and the variance is one. This facilitates the stabilization of the learning process and accelerates convergence. The normalization layer is based on mean and variance instead of simply normalizing the input vectors based on their squared norm (as in the standard squash function); this step helps to capture more information about the distribution of the input vectors than just their squared norm. The equation for layer normalization is represented as (equation 8):

$$\text{vectors} = \frac{sj - \mu}{||sj|| \ \sqrt{\sigma^2 + \varepsilon}} \tag{8}$$

First, layer normalization efficiently centers the input vectors around the zero mean by removing the mean (μ) from each one. This step can be used to lessen the variance of the input distribution to prevent too large or too small gradients during back-propagation. Every element of the input vectors has its distribution changed when the mean is subtracted from it. The effect of different mean values amongst samples is reduced by this method, which ensures that the transformed vectors mean close to 0. By focusing and scaling the activations around zero mean and unit variance, respectively, this normalization method improves the convergence and stability of the training process.

By normalizing activations within each layer, the improved squash function improves gradient flow by lowering variability across the feature dimension, and it additionally decreases the network's sensitivity to the layer addition of parameters. Through the enhancement of capsule networks' expressiveness and robustness, the squash function enables them to capture complex patterns and relationships more successfully in the data, which may lead to better performance on tasks like pose estimation, object detection, and image classification. The final enhanced equation is represented as (equation 9):

$$\text{Enhanced squash} = \text{scale} * \text{vector} \tag{9}$$

$$= \frac{\alpha \ |\left|\frac{sj}{5}\right||^2}{1 + \alpha \ |\left|\frac{sj}{5}\right||^2} \ \frac{sj - \mu}{||sj|| \ \sqrt{\sigma^2 + \varepsilon}}$$

3. Results and Discussion

The experiment results in this work were obtained using an NVIDIA RTX 3070 GPU with 64 GB of VRAM. Our focus was on creating models specifically made to manage the difficulties of handling huge datasets and highly complex features. Our method focused mainly on adding a better squash function to the CapsNet core. On three more datasets MNIST, Fashion MNIST, and CIFAR-10, we carefully evaluated the performance of our proposed models. These tests showed how flexible our models could be and how they might be used for purposes other than the BM dataset that was first used.

Using extensive publicly available datasets, this section examines our improved models for BM cell classification. Utilizing over-sampling techniques, the SMOTE method was used to address the class imbalance in the BM dataset successfully. During training, the SMOTE application significantly improved our models' overall accuracy. Rebalancing the distribution of the data, SMOTE over-sampling methods guaranteed a strong evaluation and validation process. BM images totaling 216,000 were produced after SMOTE was applied to the original 171,374-image BM dataset. The dataset was next split into three subsets, as shown in Table 1, 70% for training, 10% for validation, and 20% for testing. Moreover, we investigated three more datasets: the MNIST, Fashion MNIST, and CIFAR-10 datasets, each of which presented important difficulties and revealed the effectiveness of our model in different domains. The handwritten numbers in the MNIST dataset are used as a standard for image categorization tasks. A further feature of the Fashion MNIST dataset is grayscale photos of accessories and clothing. With the more difficult classification task provided by the Fashion MNIST dataset than the MNIST dataset, our models can distinguish between minute details and minute variations in fashion items. Ten classification classes with a wider range of object classes including animals, cars, and commonplace objects represented in colored photos make up the CIFAR-10 dataset. The complexity and variation of CIFAR-10 present difficulties. Table 2 provides details of these three data sets.

Table 1. Splitting BM dataset

Total BM cells	After applying SMOTE	Training data (70%)	Validation (10%)	Test data (20%)
171374	216000	151200	21600	43200

Table 2. Details of the dataset

Dataset	Image Size	Channels	Classes	Train Set	Test Set
MNIST	(28, 28)	1	10	60,000	10,000
Fashion-MNIST	(28, 28)	1	10	60,000	10,000
CIFAR10	(32, 32)	3	10	50,000	10,000

3.1. Evaluation Process of Models

We evaluated the performance of our models using an array of metrics to get an extensive understanding of their effectiveness. F1-score was one of the metrics applied, together with specificity, recall, and precision. Much of evaluating the model's ability to accurately reduce false positives while identifying true positive instances was precision, which indicates the accuracy of positive predictions. Conversely, recall gauged how sensitively the model caught each positive occurrence in the data. Conversely, specificity assessed how well a model might recognize instances of negativity. Furthermore, the general performance of the model was fairly evaluated by the harmonic mean of recall and precision, or F1-score. We were driven to enhance and optimize the performance of our models for different applications by our thorough knowledge of their benefits and drawbacks, which we attained by combining these metrics. Equations (10, 11, 12 and 13) are applied as follows (Bharathi, 2024):

$$Precision = \frac{TP}{TP + FP} \qquad (10)$$

$$Specificty = \frac{TN}{TN + FP} \qquad (11)$$

$$Recall = \frac{TP}{TP + FN} \qquad (12)$$

$$F1 - score \qquad (13)$$
$$= \frac{2 * (Precision * Recall)}{Precision + Recall}$$

4. Discussion

The CapsNet model's outcomes using the conventional squash function are shown in Table 3 for a variety of classes in the BM dataset. It reports the precision, recall, specificity, and F1-score of the model, which demonstrates its correct classification of various cell types. The model is robust in identifying positive and negative instances, demonstrated by the high precision and recall it shows across most classes.

It is shown in Table 4 and Figure 6 that combining the suggested CapsNet architecture with an "enhanced squash" function works well. More precisely, the improved squash function outperforms CapsNet versions using standard squash functions from previous studies with an excellent classification accuracy of 98.52% on the BM dataset. This remarkable development highlights how important the improved squash function is to the model's capacity to identify and classify intricate patterns in the dataset. To optimize the performance of CapsNet, we have also methodically included several improved squash functions into our model architecture and carefully included enhancements recommended by previous studies. Through conducting extensive testing and comparison of the BM dataset, we evaluated the efficacy of each of these variations. Our results clearly demonstrate the superiority of our model over alternative approaches, confirming its ability to identify the most efficient squash function for capsule networks.

Table 3. Performance metrics of the CapsNet model using standard squash

Class Name	Precision (%)	Recall (%)	Specificity (%)	F1-score (%)
Abnormal eosinophil (ABE)	100	100	100	100
Artefact (ART)	100	100	100	100
Basophil (BAS)	100	100	100	100
Blast (BLA)	99.92	100	100	99.96
Erythroblast (EBO)	99.89	99.96	99.98	99.93
Eosinophil (EOS)	100	99.5	100	99.75
Faggott cell (FGC)	100	100	100	100
Hairy cell (HAC)	100	100	100	100
Smudge cell (KSC)	100	100	100	100
Immature lymphocyte (LYI)	100	100	100	100
Lymphocyte (LYT)	99.17	99.59	99.88	99.38
Metamyelocyte (MMZ)	95.03	89.8	99.89	92.34
Monocyte (MON)	89.01	89.1	99.74	89.06
Myelocyte (MYB)	92.57	93.37	99.71	92.97
Band neutrophil (NGB)	91.74	85	99.63	88.24
Segmented neutrophil (NGS)	94.19	97.47	99.03	95.8
Not identifiable (NIF)	91.86	86.9	99.82	89.31
Other cell (OTH)	97.35	99.1	99.94	98.22
Proerythroblast (PEB)	95.35	92.3	99.89	93.8
Plasma cell (PLM)	93.28	86.75	99.76	89.9
Promyelocyte (PMO)	91.83	97	99.49	94.35

Table 4. Comparison of our proposed with the previous optimized squash functions for the CapsNet on the BM dataset

References	Year	Equations	Accuracy %	Number of epochs
(Sabour et al., 2017)	2017	$Squash(sj) = \dfrac{\|\|sj\|\|^2}{1 + \|\|sj\|\|^2} \dfrac{sj}{\|\|sj\|\|}$	96.99	100
(Xi et al., 2017)	2017	$F(x) = (1 - \dfrac{1}{\exp(\|\|x\|\|)}) \dfrac{x}{\|\|x\|\|}$	91	100
(Afriyie et al., 2022a)	2022	$Squash(sj) = \dfrac{\|\|sj\|\|^2}{1 + \|\|sj\|\|^2} \dfrac{sj}{2\|\|sj\|\|^2}$	94.05	100
Proposed (Enhanced squash)	2024	$Squash(sj) = \dfrac{\alpha \|\|\frac{sj}{5}\|\|^2}{1+\alpha \|\|\frac{sj}{5}\|\|^2} \dfrac{sj-\mu}{\|\|sj\|\|\sqrt{\sigma^2+\varepsilon}}, \alpha = 0.5$	98.52	100

Figure 6. Accuracy comparison of standard vs enhanced squash functions on BM dataset.

A comprehensive comparison between the baseline CapsNet, which employs conventional squash functions, and our enhanced model is shown in Table 5. Multiple datasets are utilized for the comparison, such as MNIST, Fashion-MNIST, and CIFAR-10. The results show that, on various image classification tasks, the improved squash function significantly enhances CapsNet's performance. On the MNIST dataset, our proposed model achieved 99.83% accuracy compared to the baseline CapsNet accuracy of 99.23%. This shows that the improved squash function successfully optimized CapsNet's performance by a significant 0.5% percent on this commonly used dataset for handwritten digit classification. With a 94.66% accuracy on the Fashion-MNIST dataset, our improved model outperformed the foundational CapsNet's 92.49% accuracy. The significant accuracy increase (2.17%) observed is strong evidence that the squash function enhancement improves CapsNet's performance on tasks involving fashion item categorization. Moreover, the performance of our suggested model was much enhanced when it was applied on the CIFAR-10 dataset, which is a very difficult classification problem because of its large number of real-life images. At 73%, the CapsNet model we improved outperformed the baseline CapsNet's accuracy (67.81% by 5.19%). The substantial accuracy increase shows the robustness and adaptability of the improved squash function, which allowed CapsNet to classify complicated images correctly in various datasets. The results demonstrate the flexibility and promise of the enhanced squash function to support CapsNet's performance in a range of image categorization tasks. We show that our model is flexible and capable of handling different data types and challenges by routinely outperforming the original CapsNet on a variety of datasets. The results show how our improved CapsNet architecture can be useful in practical situations requiring precise and efficient image categorization.

Table 5. Comparison baseline CapsNet and enhanced our model on different datasets

Dataset	Standard Squash (%)	Enhanced Squash (%)
MNIST (Sabour et al., 2017)	99.23	99.83
Fashion MNIST (Afriyie et al., 2022b)	92.49	94.66
Cifar10 (El Alaoui and Gadi, 2021)	67.81	73

Figure 7, Figure 8 and Figure 9 show how the enhanced squash function on the training data improved over 100 epochs. This shows how the model learns and how its accuracy improves.

Figure 10 shows a confusion matrix of the model's performance for Bone Marrow, Fashion MNIST, and CIFAR-10 dataset. The actual and predicted classes of a classification model are shown in a confusion matrix. Each row of the matrix represents actual class instances, while each column represents predicted class instances. The matrix cells show the number of true and false positives. Analyzing the confusion matrix allows us to evaluate the model's accuracy and detect misclassification patterns across classes in each dataset

as shown Table 6.

4.1. Comparison of Our Models with State-of-The-Art Methods on Same Dataset

Table 7 briefly compares different methods on the BM dataset the studies on this BM dataset are limited because is new and huge unbalanced data, but in our proposed models these issues have been solved, showing the performance metrics achieved by different approaches. It shows that our proposed methods outperform existing state-of-the-art methods in terms of accuracy. These results highlight the effectiveness and superiority of our proposed methods for biomedical image classification tasks on the BM dataset.
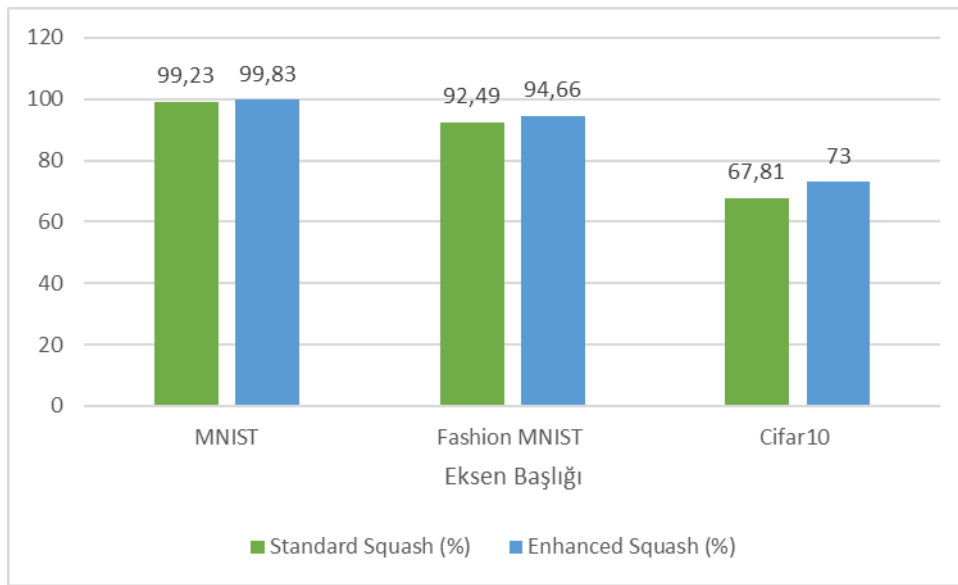
Figure 7. Accuracy comparison of standard vs enhanced squash functions on different datasets
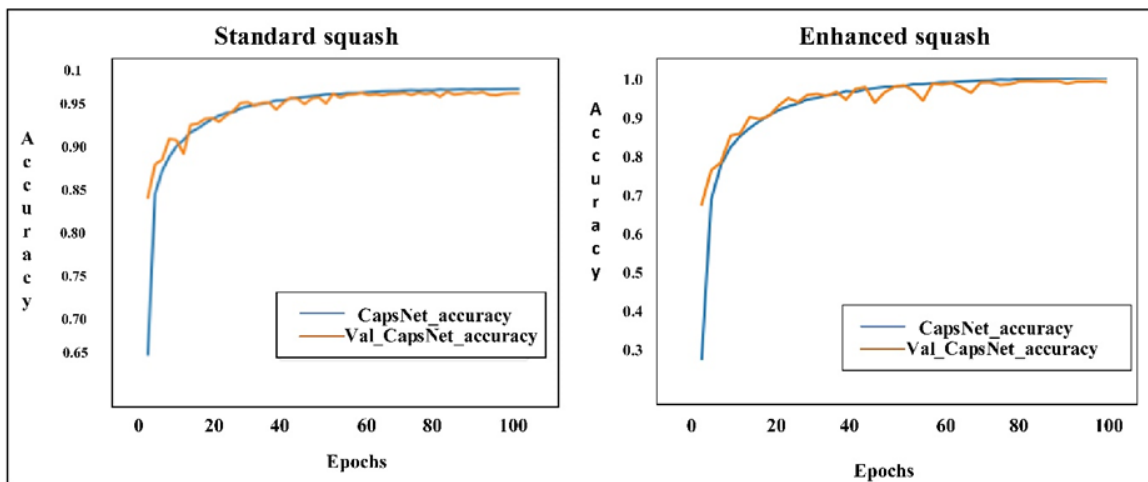
Figure 8. Accuracy curve comparison: standard vs enhanced squash functions on BM dataset
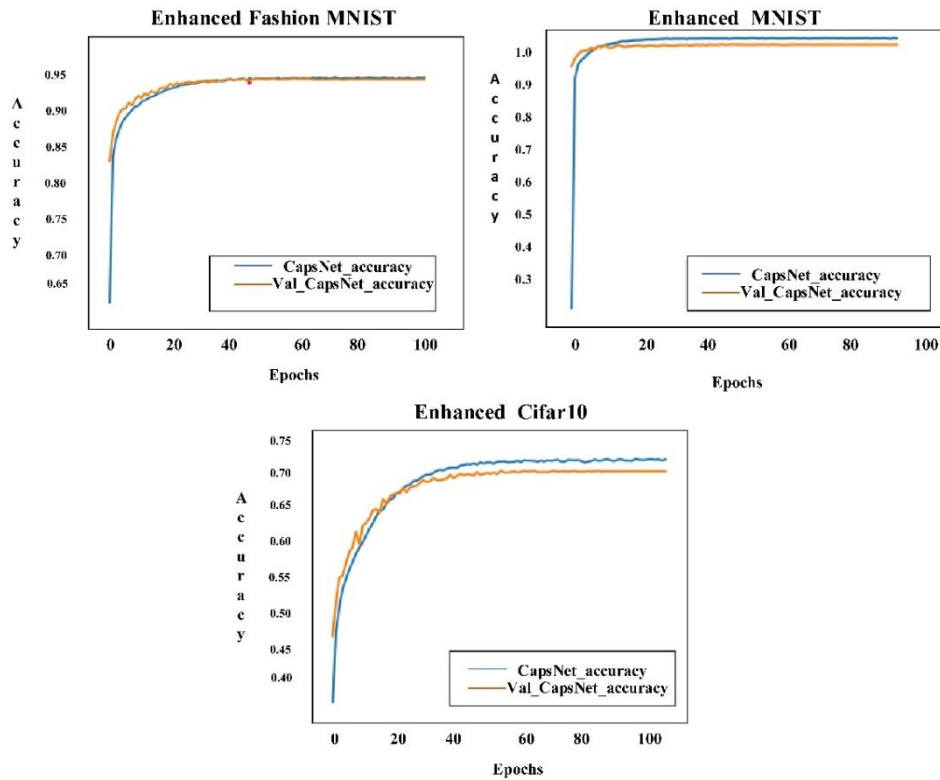
Figure 9. Accuracy comparison: standard vs enhanced squash functions on a different dataset.
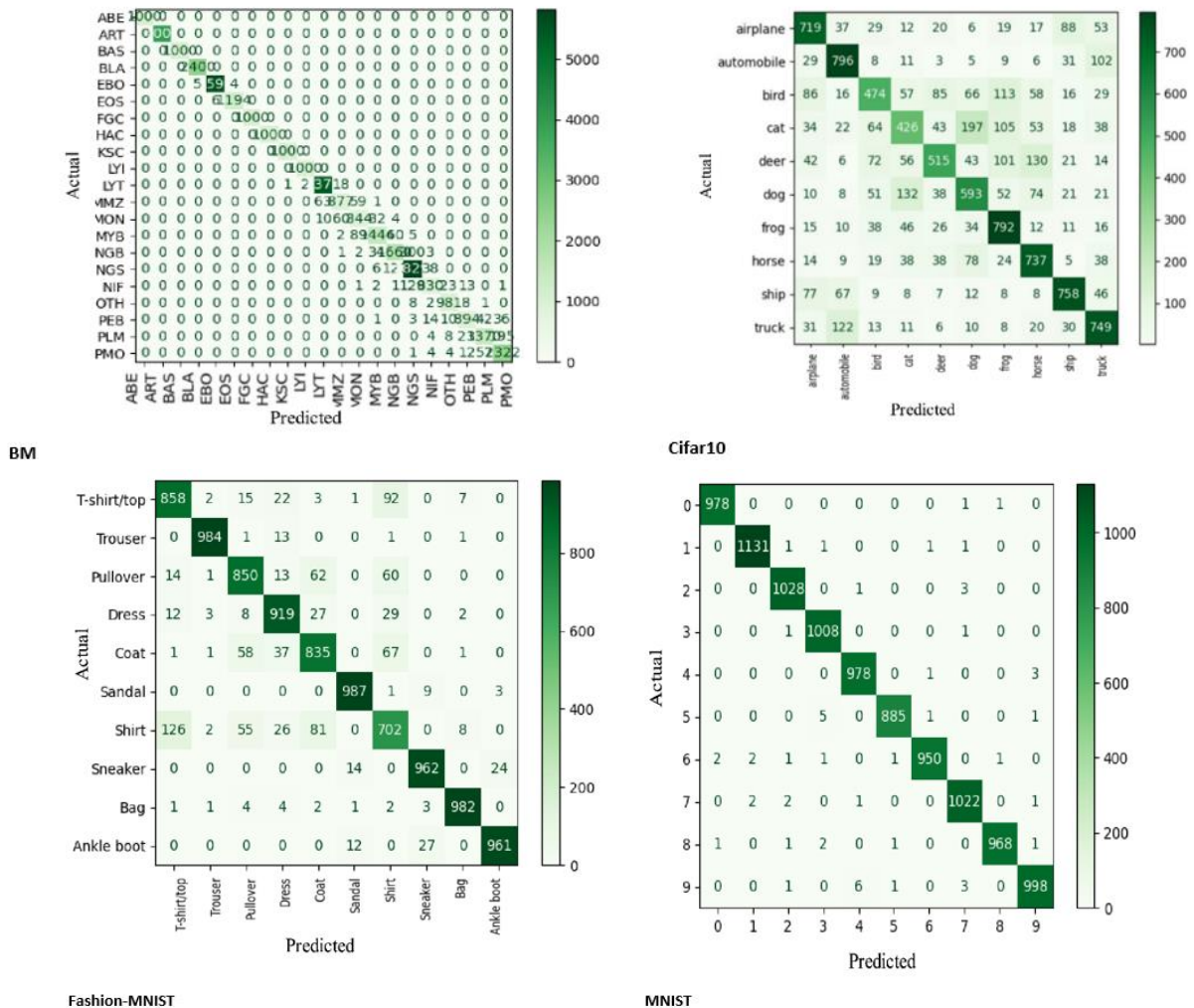
Figure 10. Confusion matrix analysis across four types of datasets

Table 6. Performance Comparison of Various CapsNet Architectures on MNIST, Fashion MNIST, CIFAR-10, and BM Datasets.

Methods	MNIST (%)	Fashion MNIST (%)	Cifar10(%)	BM (%)
ShallowNet (Mensah et al., 2021)	-	92.70	75.75	-
CapsNet (Sabour et al., 2017)		90.72	62.91	-
64 Capsule Layers (Xi et al., 2017)	68.93	-	64.67	-
Multi-lane (Chang and Liu, 2020)	99.73	92.63	76.79	-
MS-CapsNet (Xiang et al., 2018)		92.70	75.70	-
ResCapsNet (Goswami, 2019)		-	78.54	-
CFC-CapsNet (Shiri and Baniasadi, 2021)	-	92.86	73.15	-
Fast Inference (Zhao et al., 2019b)	99.43	91.52	70.33	-
Max–min (Zhao et al., 2019a)	99.55	92.07	75.92	-
MLSCN (Chang and Liu, 2020)	99.73	-	76.79	-
MLCN (do Rosario et al., 2021)	-	92.63	75.18	-
Quick-CapsNet (QCN) (Shiri et al., 2020)	99.28	88.84	67.18	-
(Afriyie et al., 2022a)	-	92.80	75.42	-
Proposed Model Enhanced Squash CapsNet	99.83	94.66	73	98.52

Table 7. Performance comparison of our proposed method with the existing state-of-the-art on the same BM dataset

Reference	Year	Method	Performance Metric	Result Rate
(Ananthakrishnan et al., 2022)	2022	CNN + SVM , CNN + XGB.	Accuracy	32%,28%
		Siamese neural	Accuracy	91%
		Supervised method (ResNeXt-50)	(Avg) F1-Score	62 %
			Precision	68.24%
			Recall	72.92%
(Fazeli et al., 2022)	2022	Self-supervised method (SW AV)	(Avg) F1-Score	73%
			Precision	78%
			Recall	70%
		Supervised Contrastive	(Avg) F1-Score	69 %
			Precision	75%
			Recall	66%
Our proposed Methods	2024	Baseline CapsNet	Accuracy	96.99 %
		Enhanced Squash CapsNet	Accuracy	98.52 %

4. Conclusion

Our research demonstrates that a CapsNet architecture with a novel function designated "enhanced squash" is highly efficacious. This yielded superior outcomes compared to preceding CapsNet methodologies on the selected BM dataset. This evidence substantiates the pivotal role of the Enhanced Squash function in enabling the model to effectively learn and classify intricate patterns within the data. The enhanced squash function is also effective in other datasets. The enhanced squash function facilitated superior performance of the model on datasets such as MNIST, CIFAR-10 and Fashion-MNIST, demonstrating its versatility in handling diverse image types. The enhanced squash function handles complex data well. It improves the accuracy of CapsNet models in real-world applications. Implementing our enhanced squash function improved the accuracy of bone marrow cell classification. Our experiments have shown that the Enhanced squash feature improves accuracy on various datasets, including MNIST, CIFAR-10 and Fashion-MNIST. The model achieved 99.83% accuracy on the MNIST dataset, 73% on the CIFAR-10 dataset, and 94.66% on the Fashion MNIST dataset.

In the future, we can look at the math behind the enhanced margin loss function in more detail. This will help us understand how it affects the model and improves classification accuracy. We can also compare CapsNet with other image classification architectures to see how the enhanced squash function affects its performance and whether it can be used for other image classification tasks.

Author Contributions

The percentages of the author contributions are presented below. The author reviewed and approved the final version of the manuscript.

	A.F.A.A.R.	N.A.A
C	50	50
D	60	40
S		100
DCP	100	
DAI	100	
L	100	
W	50	50
CR	50	50
SR		100
PM		100

C=Concept, D= design, S= supervision, DCP= data collection and/or processing, DAI= data analysis and/or interpretation, L= literature search, W= writing, CR= critical review, SR= submission and revision, PM= project management.

Conflict of Interest

The author declared that there is no conflict of interest.

Ethical Consideration

Ethics committee approval was not required for this study because of there was no study on animals or humans.

References

Afriyie Y, Weyori BA, Opoku AA. 2022a. Classification of blood cells using optimized capsule networks. Neural Process Lett. 54: 4809–482.

Afriyie Y, Weyori BA, Opoku AA. 2022b. Comparative evaluation performances of capsule networks for complex image classification. J. Data Inf. Manag, 4(3–4): 267-276.

Agustin RI, Arif A, Sukorini U. 2021. Classification of immature white blood cells in acute lymphoblastic leukemia L1 using neural networks particle swarm optimization. Neural Comput Appl, 33(17): 10869-10880. doi: 10.1007/S00521-021-06245-7/TABLES/5.

Ananthakrishnan B, Shaik A, Akhouri S, Garg P, Gadag V, Kavitha MS. 2022. Automated bone marrow cell classification for haematological disease diagnosis using siamese neural network. Diagnostics (Basel), 13(1): 3390. doi: 10.3390/DIAGNOSTICS13010112.

Anupama MA, Sowmya V, Soman KP. 2019. Breast cancer classification using capsule network with preprocessed histology images. In: Proceedings of the IEEE International Conference on Communication and Signal Processing, ICCSP, April 4-6, Melmaruvathur, India, pp: 143-147.

Aydın Atasoy N, Al Rahhawi AFA. 2024. Examining the classification performance of pre-trained capsule networks on imbalanced bone marrow cell dataset. Int J Imaging Syst Technol, 34(3): e23067. doi: 10.1002/IMA.23067.

Balasubramanian K, Ananthamoorthy NP, Ramya K. 2022. An approach to classify white blood cells using convolutional neural network optimized by particle swarm optimization algorithm. Neural Comput Appl, 34(18): 16089-16101. doi: 10.1007/S00521-022-07279-1/TABLES/13.

Baghel N, Verma U, Nagwanshi KK. 2022. WBCs-Net: type identification of white blood cells using convolutional neural network. Multimed Tools Appl, 81(29): 42131-42147. doi: 10.1007/S11042-021-11449-Z/TABLES/11.

Bajer D, Zonc B, Dudjak M, Martinovic G. 2019. Performance analysis of SMOTE-based oversampling techniques when dealing with data imbalance. In: Proceedings of the International Conference on Systems, Signals, and Image Processing, June 5-7, Osijek, Croatia, pp:265-271.

Basnet J, Alsadoon A, Prasad PWC, Al Aloussi S, Alsadoon OH. 2020. A novel solution of using deep learning for white blood cells classification: enhanced loss function with regularization and weighted loss (ELFRWL). Neural Process Lett, 52(2): 1517-1553. doi: 10.1007/S11063-020-10321-9.

Baydilli YY, Atila Ü. 2020. Classification of white blood cells using capsule networks. Comput Med Imaging Graph, 80: 101699. doi:10.1016/J.COMPMEDIMAG.2020.101699.

Chawla NV, Bowyer KW, Hall LO, Kegelmeyer WP. 2011. SMOTE: synthetic minority over-sampling technique. J Artif Intell Res, 16: 321-357.

Chawla NV, Lazarevic A, Hall LO, Bowyer KW. 2003. SMOTEBoost: improving prediction of the minority class in boosting. In: Proceedings of the 7th European Conference on Principles and Practice of Knowledge Discovery in Databases, September 22-26, Cavtat-Dubrovnik, Croatia, pp: 107–119.

Chang S, Liu J. 2020. Multi-lane capsule network for classifying images with complex background. IEEE Access, 8: 79876-79886.

Confusion Matrix for Multi-Class Classification 2024. URL: https://www.analyticsvidhya.com/blog/2021/06/confusion-matrix-for-multi-class-classification/ (accessed date: June 13, 2024).

Çınar A, Tuncer SA. 2021. Classification of lymphocytes, monocytes, eosinophils, and neutrophils on white blood cells using hybrid Alexnet-GoogleNet-SVM. SN Appl Sci, 3(4): 1-11. doi: 10.1007/S42452-021-04485-9/TABLES/4.

Dayı B, Üzen H, Çiçek İB, Duman ŞB. 2023. A novel deep learning-based approach for segmentation of different type caries lesions on panoramic radiographs. Diagnostics, 13(2): 202. doi: 10.3390/DIAGNOSTICS13020202.

Dhal KG, Rai R, Das A, Ray S, Ghosal D, Kanjilal R. 2023. Chaotic fitness-dependent quasi-reflected Aquila optimizer for superpixel based white blood cell segmentation. Neural Comput Appl, 35(21): 15315-15332. doi: 10.1007/S00521-023-08486-0/TABLES/10.

do Rosario VM, Breternitz M, Borin E. 2021. Efficiency and scalability of multi-lane capsule networks (MLCN). J Parallel Distrib Comput, 155: 63-73. doi: 10.1016/J.JPDC.2021.04.010.

El Alaoui-Elfels O, Gadi T. 2021. EMG-CapsNet: Elu multiplication gate capsule network for complex images classification. In: Proceedings of the 13th International Conference on Soft Computing and Pattern Recognition (SoCPaR 2021), Online, December 15 – 17, pp: 97–108.

Elreedy D, Atiya AF. 2019. A comprehensive analysis of synthetic minority oversampling technique (SMOTE) for handling class imbalance. Inf Sci (N Y), 505: 32-64.

Fazeli S, Samiei A, Lee TD, Sarrafzadeh M. 2022. Beyond labels: visual representations for bone marrow cell morphology recognition, ArXiv, 111-117. doi: 10.1109/ichi57859.2023.00025.

Gautam A, Singh P, Raman B, Bhadauria H. 2017. Automatic classification of leukocytes using morphological features and Naïve Bayes classifier. In: Proceedings of the IEEE Region 10 Annual International Conference, TENCON, November 5-8, Penang, Malaysia, pp: 1023-1027. doi: 10.1109/TENCON.2016.7848161.

Girdhar A, Kapur H, Kumar V. 2022. Classification of white blood cells using convolution neural network. Biomed Signal Process Control, 71: 103156. doi: 10.1016/J.BSPC.2021.103156.

Ghosh M, Das D, Chakraborty C, Ray AK. 2010. Automated leukocyte recognition using fuzzy divergence. Micron, 41(7): 840-846. doi: 10.1016/J.MICRON.2010.04.017.

Ghosh A, Jana ND, Mallik S, Zhao Z. 2022. Designing optimal convolutional neural network architecture using differential evolution algorithm. Patterns, 3(9):100567. doi: 10.1016/j.patter.2022.100567.

Guo H, Viktor HL. 2004. Learning from imbalanced data sets with boosting and data generation: the DataBoost-IM approach. SIGKDD Explor, 6(1): 30-39.

Goswami D. 2019. Application of capsule networks for image classification on complex datasets.URL: https://hdl.handle.net/2142/105694 (accessed: May 26, 2024).

Ha Y, Du Z, Tian J. 2022. Fine-grained interactive attention learning for semi-supervised white blood cell classification. Biomed Signal Process Control, 75: 103611. doi: 10.1016/J.BSPC.2022.103611.

He H, Bai Y, Garcia EA, Li S. 2008. ADASYN: adaptive synthetic sampling approach for imbalanced learning. In: Proceedings of the International Joint Conference on Neural Networks, June 1-8, Hong Kong, China, pp:1322-1328.

Hegde RB, Prasad K, Hebbar H, Singh BMK. 2019a. Comparison of traditional image processing and deep learning approaches for classification of white blood cells in peripheral blood smear images. Biocybern Biomed Eng, 39(2): 382-392. doi: 10.1016/J.BBE.2019.01.005.

Hegde RB, Prasad K, Hebbar H, Singh BMK. 2019b. Feature extraction using traditional image processing and convolutional neural network methods to classify white blood cells: a study. Australas Phys Eng Sci Med, 42(2): 627-638. doi: 10.1007/S13246-019-00742-9/FIGURES/11.

Hosseini M, Bani-Hani D, Lam SS. 2022. Leukocytes image classification using optimized convolutional neural networks. Expert Syst Appl, 205: 117672. doi: 10.1016/J.ESWA.2022.117672.

Hoogi A, Wilcox B, Gupta Y, Rubin DL. 2019. Self-attention capsule networks for object classification. URL: https://arxiv.org/abs/1904.12483v2 (accessed: May 03, 2024).

Juanjuan W, Mantao X, Hui W, Jiwu Z. 2007. Classification of imbalanced data by using the SMOTE algorithm and locally linear embedding. In: Proceedings of the International Conference on Signal Processing, ICSP, November 16-20, Guilin, China, pp: 1741- 1745.

Keys RG. 1981. Cubic convolution interpolation for digital image processing. IEEE Trans Acoust, 29(6): 1153-1160.

Kingma DP, Ba JL. 2015. Adam: a method for stochastic optimization. In: Proceedings of 3rd International Conference on Learning Representations, ICLR, May 7-9, San Diego, pp:13.

Kutlu H, Avci E, Özyurt F. 2020. White blood cells detection and classification based on regional convolutional neural networks. Med Hypotheses, 135: 109472. doi: 10.1016/J.MEHY.2019.109472.

LeCun Y, Bengio Y, Hinton G. 2015. Deep learning. Nature, 521(7553): 436-444. doi: 10.1038/nature14539.

Liu Y, Fu Y, Chen P. 2019. WBCaps: a capsule architecture-based classification model designed for white blood cells identification. In: Proceedings of the Annual International Conference of the IEEE Engineering in Medicine and Biology Society, EMBS, July 23-27, Berlin, Germany, pp:7027-7030. doi: 10.1109/EMBC.2019.8856700.

Long F, Peng JJ, Song W, Xia X, Sang J. 2021. BloodCaps: a capsule network-based model for the multiclassification of human peripheral blood cells. Comput Methods Programs Biomed, 202: 105972. doi: 10.1016/J.CMPB.2021.105972.

Iesmantas T, Alzbutas R. 2018. Convolutional capsule network for classification of breast cancer histology images. In: Proceedings of the 15th International Conference, ICIAR 2018, June 27–29, Póvoa de Varzim, Portugal, pp 869–876 DOI: 10.1007/978-3-319-93000-8_85

Maldonado S, López J, Vairetti C. 2019. An alternative SMOTE oversampling strategy for high-dimensional datasets. Appl Soft Comput, 76: 380-389.

Matek C, Krappe S, Münzenmayer C, Haferlach T, Marr C. 2021. Highly accurate differentiation of bone marrow cell morphologies using deep neural networks on a large image data set. Blood, 138(20): 1917-1927. DOI: 10.1182/blood.2020010568

Mensah PK, Weyori BA, Ayidzoe MA. 2021. Evaluating shallow capsule networks on complex images. Int J Inf Technol (Singapore), 13(3): 1047-1057. doi: 10.1007/S41870-021-00694-Y/FIGURES/6.

Mirmohammadi P, Ameri M, Shalbaf A. 2021. Recognition of acute lymphoblastic leukemia and lymphocytes cell subtypes in microscopic images using random forest classifier. Phys Eng Sci Med, 44(2): 433-441. doi: 10.1007/S13246-021-00993-5/TABLES/2.

Mohamed M, Far B, Guaily A. 2012. An efficient technique for white blood cells nuclei automatic segmentation. In: Proceeding of IEEE International Conference on Systems, Man, and Cybernetics (SMC), October 14-17, Seoul, Korea (South), pp: 220-225. doi: 10.1109/ICSMC.2012.6377703.

Muhammad A, Arserim M, Ömer T. 2023. Compare the classification performances of convolutional neural networks and capsule networks on the Coswara dataset. DUJE, 14(2): 265-271. doi: 10.24012/dumf.1270429.

Nair P, Doshi R, Keselj S. 2021. Pushing the limits of capsule networks. URL: http://arxiv.org/abs/2103.08074 (accessed: May 03, 2024).

Patil AM, Patil MD, Birajdar GK. 2021. White blood cells image classification using deep learning with canonical correlation analysis. IRBM, 42(5): 378-389. doi: 10.1016/J.IRBM.2020.08.005.

Patrick MK, Adekoya AF, Mighty AA, Edward BY. 2022. Capsule networks – a survey. J King Saud Univ Comput Inf Sci, 34(1): 1295-1310. doi: 10.1016/J.JKSUCI.2019.09.014.

Ren H, Su J, Lu H. 2019. Evaluating generalization ability of convolutional neural networks and capsule networks for image classification via Top-2 classification. URL: https://arxiv.org/abs/1901.10112v4 (accessed: May 10, 2024).

Reza MS, Ma J. 2019. Imbalanced histopathological breast cancer image classification with convolutional neural network. In: Proceedings of the 14th IEEE International Conference on Signal Processing (ICSP), August 12-16, 8, Beijing, China, pp: 619-624.

Rezatofighi SH, Soltanian-Zadeh H, Sharifian R, Zoroofi RA. 2009. A new approach to white blood cell nucleus segmentation based on gram-schmidt orthogonalization. In: Proceedings of the international Conference on Digital Image Processing, ICDIP, March 7 – 9, Bangkok, Thailand, pp:107-111. doi: 10.1109/ICDIP.2009.19.

Sabour S, Frosst N, Hinton GE. 2017. Dynamic routing between capsules. In: preceding of the 31st Conference on Neural

Information Processing Systems (NIPS 2017), December 5 - 7, Long Beach, CA, USA, pp: 3859–3869. doi.org/10.48550/arXiv.1710.09829

Sengur A, Akbulut Y, Budak U, Comert Z. 2019. White blood cell classification based on shape and deep features. In: Proceeding of International Conference on Artificial Intelligence and Data Processing Symposium, IDAP, September 21-22, Malatya, Turkey, pp 1-4.

Singh R, Ahmed T, Kumar A, Singh AK, Pandey AK, Singh SK. 2021. Imbalanced breast cancer classification using transfer learning. IEEE/ACM Trans Comput Biol Bioinform, 18(1): 83-93. doi: 10.1109/TCBB.2020.2980831.

Shiri P, Baniasadi A. 2021. Convolutional fully connected capsule network (CFC-CapsNet). In : Proceeding of the International Conference of Workshop on Design and Architectures for Signal and Image Processing (DASIP) - 14th edition, January 18-20, Budapest, Hungary, pp:19.

Shiri P, Sharifi R, Baniasadi A. 2020. Quick-CapsNet (QCN): a fast alternative to capsule networks. In: Proceedings of IEEE/ACS International Conference on Computer Systems and Applications, AICCSA, November 2-5, Antalya, Turkey, pp:1-7. doi: 10.1109/AICCSA50499.2020.9316525.

Somuncu E, Atasoy Aydın N. 2021. Realization of character recognition application on text images by convolutional neural network. J FAC ENG ARCHIT GAZ, 37(1):17-27.doi: 10.17341/gazimmfd.866552.

Stock W, Hoffman R. 2000. White blood cells 1: non-malignant disorders. Lancet, 355(9212): 1351-1357. doi: 10.1016/S0140-6736(00)02125-5.

Tamang T, Baral S, Paing MP. 2022. Classification of white blood cells: a comprehensive study using transfer learning based on convolutional neural networks. Diagnostics, 12(12).

Tasdelen A, Ugur AR. 2021. Artificial intelligence research on COVID-19 pandemic: a bibliometric analysis. In: Proceedings of 5th International Symposium on Multidisciplinary Studies and Innovative Technologies, ISMSIT, October 21-23, pp: 693-699. doi: 10.1109/ISMSIT52890.2021.9604573.

Vigueras-Guillén JP, Patra A, Engkvist O, Seeliger F. 2021. Parallel capsule networks for classification of white blood cells. In: preceding of the International Conference on Medical Image Computing and Computer Assisted Intervention (MICCAI), September 27 to October 1, Strasbourg, France, pp: 743-752. doi.org/10.48550/arXiv.2108.02644

Xi E, Bing S, Jin Y. 2017. Capsule network performance on complex data. URL: https://arxiv.org/abs/1712.03480v1 (accessed: May 16, 2024).

Xiang C, Zhang L, Tang Y, Zou W, Xu C. 2018. MS-CapsNet: a novel multi-scale capsule network. IEEE Signal Process Lett, 25(12): 1850-1854.

Yao X, Sun K, Bu X, Zhao C, Jin Y. 2021. Classification of white blood cells using weighted optimized deformable convolutional neural networks. Artif Cells Nanomed Biotechnol, 49(1): 147-155. doi: 10.1080/21691401.2021.1879823.

Zhao L, Huang L. 2019. Exploring dynamic routing as a pooling layer. In: Proceeding of IEEE/CVF International Conference on Computer Vision Workshop (ICCVW),October 27-28, Seoul, Korea, pp: 738 – 742.

Zhao Z, Kleinhans A, Sandhu G, Patel I, Unnikrishnan KP. 2019. Capsule networks with max-min normalization. URL:http://arxiv.org/abs/1903.09662 (accessed: May 26, 2024).

Black Sea Journal of Engineering and Science

ELEKTRİKLİ ARAÇ ŞARJ İSTASYONU KONUM TASARIMINDA, DİGSİLENT YAZILIMI KULLANILARAK KOCAELİ ÜNİVERSİTESİ UMUTTEPE KAMPÜSÜ İÇİN ÖRNEK UYGULAMA

Ayşe Tuğba YAPICI[1]*, Nurettin ABUT[1]

[1]Kocaeli University, Faculty of Engineering, Electrical Engineering, 41100, Kocaeli, Türkiye

Özet: Ulaşım konusunda tüm dünyanın üzerinde durduğu elektrikli araçlar oldukça hızlı yaygınlaşmaktadır. Bu hızlı yayılma ile birlikte aracın sorunsuz yol alabilmesi için belirli aralıklarla şarj edilmesi gerekmektedir. Dolayısıyla, elektrikli araçlar için şarj istasyonları ve bunların enerji şebekesine entegrasyonunun önemi gündeme gelmiştir. Yapılan bu çalışmada Kocaeli Üniversitesi Umuttepe Yerleşkesi için gerçek veriler Digsilent Power Factory programına aktarılarak mevcut enerji dağıtım sisteminin elektrikli araç şarj istasyonu tasarım sorunu detaylı olarak ele alınmıştır. Böylece yakın gelecekte kampüste kurulması beklenen şarj istasyonları için çalışma rehber niteliğinde olacaktır. İlk olarak mevcut dağıtım sisteminin trafolarının % 80 yüklendiği bilindiği için bu yüklenme yüzdesi ile yük akışı elde edilmiştir. Böylece mevcut sisteme herhangi bir iyileştirme yapılmadan ne kadar şarj istasyonu eklenebileceği görülmüştür. Mevcut sisteme eklenebilecek maksimum şarj istasyonu sayısının gelecekte yetersiz olabileceği ön görülerek iki farklı yöntem önerisi ile şarj istasyonu sayısının artırılması hedeflenmiştir. İlk olarak sisteme uygun yeni trafo merkezleri eklenerek şarj istasyonu sayıları ve noktaları gösterilmiştir. Daha sonra ise oldukça popüler olan yenilenebilir enerji kaynaklarından güneş enerjisi ile kampüs için bir güneş panelli şarj istasyonu tasarlanmıştır. Yapılan tasarım Digsilent Power Factory programı ile mevcut sisteme entegre edilerek şarj istasyonu sayısı ve noktaları gösterilmiştir. Yapılan her bir simülasyon çalışması detaylı olarak incelenmiş ve mevcut sisteme etkisi gösterilmiştir.

Anahtar kelimeler: Elektrikli Araç, Hızlı şarj istasyonu, Güneş paneli

Sample Application for Kocaeli University Umuttepe Campus, in Electric Vehicle Charging Station Location Design, Using Digsilent Software

Abstract: Electric vehicles, which the world focuses on in terms of transportation, are becoming widespread very rapidly. With rapid growth, the vehicle needs to be charged periodically to drive without problems. Therefore, the issue of charging stations has also come to the fore with electric vehicles. In the study, real data for Kocaeli University Umuttepe Campus was transferred to the Dig Silent Power Factory program and the electric vehicle charging station issue of the current system was discussed in detail. Thus, the study will be a guide for charging stations expected to be installed on campus in the near future. Firstly, since it is known that the existing system transformers are loaded at 80%, the load flow was obtained with this loading percentage. Thus, it was seen how many charging stations could be added without making any improvements to the existing system. Considering that the maximum number of charging stations that can be added to the current system may be insufficient in the future, it is aimed to increase the number of charging stations with two different method suggestions. First, additional transformers are added to the system and the number and points of charging stations are shown. Later, a solar panel charging station was designed for the campus, using solar energy, one of the most popular renewable energy sources. The design was integrated into the existing system with the Dig Silent Power Factory program and the number and points of charging stations were shown. Each simulation study was examined in detail and its effect on the current system was shown.

Keywords: Electric vehicle, Fast charging station, Solar panel

1. Giriş

İnsanlık tarihinde, tekerleğin icadından başlayarak gelişen ekonomiler ve teknolojik durumlara bağlı olarak ulaşım sürekli gelişmektedir (Oral ve Kıpkıp, 2019; Parades ve ark., 2020). Günümüzde, dünya genelinde toplam enerji tüketiminde ulaşımın payı yaklaşık %34'ünü oluşturmaktadır (Koç ve ark., 2018). Hem kırsal hem de kentsel alanlarda insanların yaşam kalitesinin en önemli unsurlarından biri verimli ve erişilebilir bir ulaşım sistemidir (Simarro ve ark., 2023a). İçten yanmalı araçların dünya genelinde, çevreye vermiş olduğu zararlara nazaran elektrikli araçların durumu oldukça kıymetlidir (Akmal ve ark., 2018). Dünya genelinde ulaşım için ağırlıklı yakıt olarak petrol kullanılmaktadır (Gündoğan, 2022). Bu sebeple petrol türevli yakıt kullanan araçlara alternatif olabilecek elektrikli araçlar

sıfır emisyon özelliği ile oldukça cazip bir alternatif olmuştur (Kılıçarslan ve Çam, 2021). İçten yanmalı araçların yakıt ihtiyacını karşılayan petrol istasyonlarının yerini elektrikli araç şarj istasyonları alacaktır. Bu sebeple elektrikli araçların kullanımının yaygınlaşmasını teşvik edebilmek için, yakıt talebini karşılayabilme konusunda tüketicinin zihninde herhangi bir tereddüt kalmaması adına şarj istasyonu sayısının çok hızlı olarak artırılması gerekmektedir (Mastoi ve ark., 2022).

Elektrikli araç şarj alt yapısı son yıllarda iyileşme göstermiş olsa da, mevcut büyüme hızı ile ilerleme olursa önümüzdeki birkaç yıl içinde kurulacak halka açık şarj istasyonu sayısı , ulaşılması hedeflenen elektrikli araç sayısının şarj talebi büyüklüğünü beslemek için yetersiz olabilecektir (Simarro ve ark., 2023b). Bu yeni yükün, enerji dağıtım şebekesi üzerinde etkileri olacağından kamu hizmeti şirketlerinin bu yeni yükün dağıtım şebekesi üzerindeki olası etkilerini anlamak için kapsamlı çalışmalar yapması ve buna göre planlama yapması gerekmektedir (Nour ve ark., 2018). Sonuçta elektrikli araçların yaygınlaşması için gerekli şarj altyapı ağının oluşturulması kaçınılmazdır (Micari ve ark., 2017). Bununla beraber şebekeye eklenecek ek yükün etkilerini önceden öğrenip buna göre hazırlık yapılması için konu üzerinde yapılacak çalışmalar oldukça kıymetlidir (Kumar ve ark., 2021).

Yapılan çalışmada uygulama alanının tek hat şeması üzerinde, Digsilent Power Factory paket programı kullanılarak modelleme yapılmış ve mevcut sistemin yük akışı elde edildikten sonra şarj istasyonu ile ilgili çalışmalar yapılmıştır (Simarro ve Villena, 2022). Yapılan çalışmalarda modelleme yapmak, gerçek uygulama öncesi oldukça kıymetlidir. Çünkü yapılan modelleme üzerinde en iyi sonuca ulaşana kadar defalarca deneme, değişiklik yapma imkanı vardır. Bu nedenle modelleme yapılarak planlanan çalışma için en uygun olan konumlar seçilmelidir (Aydın ve ark., 2017). Yapılan çalışmada şebeke analizinde baralar, hatlar ve trafolar için gerçek uygulamayla birebir modelleme yapılabilen paket programlardan biri olan Digsilent Power Factory seçilmiştir (Özçelik ve ark., 2018). Böylelikle modelleme yapılırken seçilen elemanların etiket bilgileri, gerilim, frekans gibi değerler kullanılabilmektedir.

Dünya geneline bakıldığında sera gazının olumsuz etkilerini ulaşım sistemlerinde azaltmak için, çevreye olumsuz olarak etkisi olmayan elektriğin kullanımı en iyi alternatif çözüm olarak görünmektedir (Kerem ve Gürbak, 2020). Bu sebeple elektrikli araç kullanımına hızlı bir dönüşüm olması için tüm hazırlıkların hızlıca yapılması gerekmektedir. Bu hazırlık aşamasını değerlendirmek gerekirse, öncelikli olarak şarj istasyonlarının yeterli sayıya artırılması gerekmektedir (Metais ve ark., 2022). Şarj istasyonu sayısını arttırmak için mevcut şebekenin buna ne kadar elverişli olduğu belirsizdir (Durmuş ve Kaymaz, 2020). Şarj istasyonu kurulumunda talebi karşılamak için uygun istasyon dağılımı yapmak oldukça önemlidir (Ge ve ark., 2011). Çünkü ülke geneli olarak düşünüldüğünde araç kullanımı

her şehirde aynı yoğunlukta olmayacaktır (Dörtköşe ve ark., 2022). Şehirler açısından, gün içerisinde araç yoğunluğu bölgesel olarak farklılık göstereceğinden, şarj istasyonu kurulumunda talebi karşılayacak doğru yerleştirme tasarımı yapılması gerekmektedir. Bu sebeple her şehir ve her şehrin içinde de talebi karşılayacak yeterli sayıda şarj istasyonu kurulması birinci hedef olurken mevcut sistemin bu ek yükten nasıl etkileneceği konusu da oldukça önemlidir (Bashaireh ve ark., 2023). Dolayısıyla bölgesel şarj istasyonu ve mevcut enerji dağıtım sistemlerinin durumu ile ilgili yapılacak çalışmalar oldukça önemlidir (Abaspahic ve Saric, 2021). Yapılan çalışma ile seçilen planlama alanındaki mevcut sisteme entegre edilebilecek maksimum sayıda, şarj istasyonu konumlandırması yapılmıştır. Şarj istasyonu talebinin ilerleyen zamanda artacağının kaçınılmaz olduğu düşünülerek mevcut sistem üzerinde kurulabilecek şarj istasyonu sayısı konusunda iyileştirme önerileri sunulmuştur.

2.1. Literatür İncelemesi

Elektrikli araç ve şarj istasyonu konuları kendi içlerinde farklı alt başlıklar ile detaylandırılabilir. Konunun şarj istasyonu başlığına odaklanılacak olunursa konu ile ilgili çalışmalar ilk olarak gerçek uygulama alanları ve gerçek olmayan uygulama alanları üzerinde olmak üzere konum olarak ikiye ayrılabilir. Gerçek uygulama alanları üzerindeki çalışmalar ise gerçek verileri barındıran veya tahmini senaryolar üzerinden ilerleyebilir. Bu çalışmalara bakıldığında her biri çözümlemeye giderken farklı yaklaşımlardan faydalanmıştır. Yapılan çalışmalardan birinde, İtalya karayolu üzerinde araç akışı, bölgede tercih edilen elektrikli araç modelleri ve bataryaları göz önünde bulunarak şarj istasyonu noktalarının belirlenmesi hedeflenmiştir (Micari ve ark., 2011). Çalışmada çözüme ulaşmak için bazı değişkenler seçilerek matematiksel denklemler üzerinden elde edilen sonuçlar değerlendirilmiştir. Turino bölgesi üzerinde yapılan bir diğer çalışmada gerçek uygulama alanı seçilmiş ve mevcut araç kullanımı üzerinden şarj istasyonu talebi hakkında sayısal verilerle fikir oluşturulmuştur (Sica ve Deflorio, 2023).

Burada çalışma alanı bölgelere ayrılarak araç yoğunluğunun olduğu noktalar belirlenerek şarj talebi hakkında tahminde bulunulmuştur. Sakarya ili üzerinde yapılmış bir çalışmada ise yollar ve bu yol güzergahları üzerindeki akaryakıt istasyonları konum ve sayı olarak belirtilmiştir (Dörtköşe,2022). Bu akaryakıt istasyonları potansiyel elektrikli araç şarj istasyonu olarak değerlendirilmiş ve kurulumu için konum ve maliyet belirtilmiştir. Yapılan bir diğer çalışmada elektrikli araç şarj istasyonun enerji yönetimi konusunu ele alınmıştır (Paredes ve Pozo, 2020). Burada şarj istasyonun güneş panelinden beslenmesi ve gün içerisindeki yoğunluğa bağlı olarak oluşabilecek enerji talebi için elektrikli aracın şebekeyi de besleme durumu ele alınmıştır Çalışma alanı olarak Kırıkkale seçilmiş bir çalışmada bölgenin trafo ve hat durumu incelenerek şarj altyapısı için uygunluk incelenmiştir (Kılıçarslan ve Çam, 2021).

Yunanistan'da bir bölge için elektrikli araç şebeke araç entegrasyonu konusunu ele alan bir çalışmada her defa farklı sayıda elektrikli aracın kullanıldığı düşünülen senaryolar için üzerinde çalışılan bölgenin şebekesi incelenmiştir (Simarro ve ark., 2023b). Yapılan bir diğer çalışmada gerçek bir konut üzerinde çalışarak farklı senaryolar oluşturarak elektrikli araç şarj işleminin mevcut sitem üzerindeki olası etkilerini trafo ve hat yüklenmesi üzerinden değerlendirilmiştir (Nour ve ark., 2018). Mostar Şehri üzerine yapılan bir çalışmada mevcut şebeke yük akışı incelenmiş ve şarj istasyonu eklenmesi durumunda şebekenin nasıl etkileneceği değerlendirilmiştir (Medogorac ve ark., 2022). Bir otoyol boyunca karşılıklı olarak yerleştirilen hızlı şarj istasyonlarının şebekeye etkisini incelendiği çalışmada öneri olarak batarya değiştirme istasyonları önerilmiştir (Farkas ve ark., 2013).

Tayland üzerinde belirlenen uygulama alanı için dört trafo merkezi seçilmiştir (Pothinun ve Premrudeepreechacharn, 2018). Sisteme eklenecek şarj istasyonlarının bu dört trafo merkezi üzerindeki etkisi, harmonik distorsiyonu günlük saat dilimleri üzerinde incelenmiştir. İtalya'da bir çalışma alanı üzerinde şarj istasyonları sisteme entegre olduktan sonrası için oluşabilecek yüklenmelere karşı çözüm önerileri sunulmuştur (Mancini ve ark., 2020). Kolombiya'da seçilen çalışma alanı üzerinde, bölgede tercih edilen araçlar ve sayıları baz alınarak günlük alınabilecek mesafeler ve şarj ihtiyacına bağlı olarak talep edilecek şarj istasyonu sayıları yorumlanmıştır (Betancur ve ark., 2021). Pamukkale Üniversitesi Kınıklı Yerleşkesi için elektrik dağıtım şebekesi Digsilent Powerfactory programı ile modellendiği çalışmada, şebeke üzerinden seçilen üç trafo merkezi üzerinde sisteme entegre edilebilecek şarj istasyonu sayısı ve olası etkileri incelenmiştir (Tunçer ve Çetin, 2023).

Konuyla ilgili literatür incelendiğinde farklı çalışma alanları üzerinde benzer ya da farklı yaklaşımlar kullanılarak şarj istasyonu kurulumu ile ilgili çeşitli çalışmalar yapılmıştır. Bu çalışmaların her biri kendi içinde sadece farklı çalışma alanları seçilmiş olmasından dolayı bile özgün çalışma olarak nitelendirilebilir. Çünkü elektrikli araç konusunda çalışmalar henüz çok uzun bir geçmişe sahip değildir ve çok hızlı yaygınlaşması hedeflenmektedir. Bu hedefe ulaşabilmek için tüketicinin konu ile ilgili herhangi bir tedirginliğinin kalmaması gerekir. Bu sebeple ilk olarak ihtiyaç duyulan anda erişimi sağlanabilecek yakınlıkta şarj istasyonuna ulaşımı sağlamak gerekir. Bu ihtiyacı karşılamak için şarj istasyonları doğru sayıda ve doğru konuma yerleştirilmelidir. Bu nedenle konu ile ilgili gerçek uygulama alanları üzerinde yapılan her çalışmaya ihtiyaç vardır.

Bu sebeple şarj istasyonu kurulumu öncesi özellikle ilk etapta araç yoğunluğunun fazla olduğu, şehirlerin belli bölgeleri için gerçek uygulama alanları üzerinde yapılan çalışmalar oldukça kıymetlidir. Çünkü bu çalışmalar şarj istasyonu gerçek kurulumu öncesi ön fikir oluşturarak

doğru nokta belirleme, mevcut sistemin bu ek yüke ne kadar hazır olduğu, nasıl etkileneceği ve maliyet konusunda fazlaca katkı sağlayacaktır.

Yapılan çalışmanın yukarıda belirtilen literatür çalışmasındaki Digsilent Power Factory paket programı ile yapılan modellemelerden farklılıkları bakılacak olunursa, seçilen uygulama alanı üzerinde daha önce herhangi bir elektrikli araç şarj istasyonu çalışması yapılmamıştır. Ayrıca diğer çalışmalardan farklı olarak mevcut sistemdeki bağlantı noktalarına ek trafolar eklenerek çok daha fazla sayıdaki şarj istasyonuna erişim için öneri sunulmuştur. Yapılan çalışma ile bir önceki maddede önerilen ek trafo tahsisinden hariç günümüzde oldukça popüler olan yenilenebilir enerji kaynaklarından güneş enerjisinin elektrikli araç şarj istasyonu için enerji kaynağı olması durumu önerilmiştir. Burada kampüs için güneş panelli elektrikli şarj istasyonu tasarlandıktan sonra sisteme Digsilent Power Factory programında entegre edilmiştir.

Yapılan çalışmada seçilen uygulama için mevcut sistem gerçek verileri ile ele alınmıştır. Bu sebeple uygulama alanına yakın gelecekte şarj istasyonu kurulurken, bu çalışma konu üzerinde öngörü oluşturacaktır.

2. Materyal ve Yöntem

Çalışmada Kocaeli Üniversitesi Umuttepe Kampüsü yerleşkesi üzerinde planlanan elektrikli araç şarj istasyonu simülasyon çalışmaları ve sonuçları irdelenmektedir.

Burada, kampüs üzerinde ilk defa elektrikli araç şarj istasyonu kurulumu planlanmaktadır. Kısa vadede Kampüste, mevcut sistem kapasitesine bağlı olarak şarj istasyonu kurulumu için fikir oluşturulacak olsa da, beklenen elektrikli araç kullanımının hızlı yaygınlaşması için uzun vadede sayıca yetersiz kalacaktır. Bu sebeple uzun vadede kalıcı çözüm için iki farklı öneri sunulmuştur. Bu bağlamda önerilen birinci seçenekte ek trafolar ile şarj istasyonu sayısının maksimum sayıda olması hedeflenirken ekonomik olarak maliyet azaltılması için, alternatif olabilecek ve yenilenebilir enerji kaynaklarından biri olan güneş enerjisinden faydalanılan ikinci bir yöntem önerilmektedir. Böylece hem uygulama alanıyla hem de farklı alternatif seçenekleriyle çalışma oldukça özgünleştirilmiştir. Bu sebeple, dört farklı simülasyon çalışması yapılarak şarj istasyonu konusu detaylı olarak incelenmektedir. İlk simülasyon çalışması ile mevcut sistemin yük akışını elde etmek hedeflenmiştir. İkinci simülasyon ile mevcut sistemdeki trafoların maksimum yüklenerek, dışarıdan herhangi bir maliyet artışı ve iyileştirme işlemi olmaksızın, hangi bağlantı noktasına ne kadar şarj istasyonu yerleştirilebileceği gösterilmiştir. Üçüncü simülasyonda ise mevcut sisteme eklenebilecek şarj istasyonuna ilave olarak sisteme entegre edilen ek trafolar ile yeni şarj istasyonu sayıları bağlantı noktaları ile gösterilmiştir. Son simülasyon ile mevcut sisteme eklenebilecek şarj istasyonuna ilave olarak, yeni trafo merkezleri tahsisi ile eklenen şarj istasyonları

olmaksızın, sisteme entegre edilen güneş panellerinden beslenen şarj istasyonlarının bağlantı noktaları ve sayıları gösterilmiştir. Simülasyon çalışmalarının sonuçları, sonraki bölümde gösterilmekte ve irdeleme değerlendirilmesi sonuç kısmında yapılmaktadır.

2.1. Çalışmada Kullanılan Parametreler ve Sayısal Değerler

Kocaeli Üniversitesi Umuttepe Yerleşkesi tek hat şeması Digsilent Power Factory paket programda aktarılmış hali Şekil 1.'de incelendiğinde 9 adet indirici trafo bulunduğu görülmektedir. Trafoların 8 adedi 2MVA gücünde 1 adedi ise 1 MVA gücündedir. Tablo 1'de trafolar ile ilgili bilgiler

gösterilmiştir.

Yapılan çalışmada temel amaç kampüs için şarj istasyonları noktalarını ve sayılarını belirlemektir. Bu şekilde yapılması planlanan çalışma için en ideal şarj istasyonu, şarj işlemini en hızlı yapan seçenektir. Burada şarj istasyonunun gücü belirleyicidir. Ancak istenilen her noktaya yüksek güçlü şarj istasyonu yerleştirmek mevcut şebekenin bu ek yüke ne kadar hazır olduğu ile ilgilidir. Yapılan çalışmada mümkün olduğunca şarj işlemini hızlı yapabilecek yüksek güçlü şarj istasyonları seçilmiştir. Yapılan çalışmada kullanılan şarj istasyonları Tablo2'de gösterilmiştir.

Tablo 1. Trafo parametreleri

Trafo İsmi	Trafo Gücü(MWA)	Nominal Gerilim(Kv)
TR-1	2	34,5/0,4
TR-2	2	34,5/0,4
TR-3	1	34,5/0,4
TR-4	2	34,5/0,4
TR-5	2	34,5/0,4
TR-6	2	34,5/0,4
TR-7	2	34,5/0,4
TR-8	2	34,5/0,4
TR-9	2	34,5/0,4

Tablo 2. Kullanılan şarj istasyonları

Uygulama çalışması ismi	Şarj istasyon tipi	Şarj istasyon gücü(MVA)
Mevcut Sisteme Eklenecek Şarj İstasyonları	DC Yüksek Hızlı Şarj İstasyonu	200
Ek Trafo Tahsisi ile Eklenecek Şarj İstasyonları	DC Yüksek Hızlı Şarj İstasyonu	200
Güneş Paneli Eklenerek İlave Edilecek Şarj İstasyonları	DC Yüksek Hızlı Şarj İstasyonu	200-50

2.2. Umuttepe Yerleşkesi Tek Hat Şeması Digsilent Powerfactory Modeli İle Yük Akışı

Yapılan çalışma gerçek bir uygulama alanı üzerinde gerçekleştirildiğinden Umuttepe Yerleşke alanı seçilmiştir. Umuttepe Yerleşkesinin tek hat şeması kullanılarak ilk olarak kampüsün mevcut yük akışı oluşturulmuş ve orta gerilim elektrik şebekesi modeli Digsilent Power Factory paket programı yazılımını kullanarak gerçekleştirilmiştir. Şekil 1'de sistemin tek hat şemasının Digsilent Power Factory paket programda tasarlanmış şekli gösterilmektedir. Sistem tasarımında trafoların, yüklerin, iletkenlerin, baraların bağlantıları ve bunların tüm değerleri mevcut sistemin tek hat şemasına birebir bağlı kalarak yapılmıştır. Böylelikle trafoların mevcut durumu değerlendirilerek herhangi bir değişiklik yapmadan mevcut sisteme entegre edilebilecek şarj istasyonu sayısının hesaplanması sağlanacaktır.

Şekil 1'de 9 adet indirici trafo bulunmaktadır. Trafoların 8 adedi 2MVA gücünde 1 adedi ise 1 MVA gücündedir. Şekildeki model sistemin yük akışı için çalıştırılmış iken alınan ekran görüntüsüdür. Trafolar turuncu renkte görülmektedir. Şebekedeki transformatör yüklenme oranı %80 alınmıştır.%100 yüklenme durumunda ise renk kırmızıya dönüşmektedir.

2.3. Umuttepe Yerleşkesi Tek Hat Şeması Digsilent Powerfactory Modeli İle Yük Akışı

Simülasyon ile, mevcut sistemin yük akışını doğru olarak elde etmek hedeflenmiştir. Şekil 1'e bakıldığında sistem hata vermeden doğru yüklenmeyi göstermektedir. Bu sebeple ilk olarak mevcut sistemde trafoların maksimum yüklenme durumu için kaç adet şarj istasyonunun hangi noktaya eklenebileceği incelenmektedir. Daha sonra buna ek olarak olumlu katkı sağlayacak öneri modellerini uygulamaktır. Şekil 2'de mevcut yüklerin bulunduğu trafo bağlantı noktalarındaki dağıtım merkezlerinin bulunduğu her bir noktaya mevcut sisteme maksimum sayıda şarj istasyonu eklenmiş Digsilent Power Factory Modeli ekran görüntüsü gösterilmektedir.

Her bir yükün yanına ek yük olarak eklenen şarj istasyonları her bir şarj istasyonunu ayrı ayrı olarak değil, eklenen şarj istasyonları sayısını toplu olarak ifade etmektedir. Sisteme, gerçek uygulama aşamasına gelindiğinde, daha çok tercih edile bilineceği öngörülerek DC yüksek hızlı şarj istasyonları seçilmiştir. Bu sebeple Tablo2'de belirtildiği üzere tüm şarj istasyonları DC yüksek hızlı 200kW gücünde şarj istasyonlarıdır. Şekil 2'de görüleceği gibi, şarj istasyonları eklendiğinde trafoların kırmızı renkte olduğu görülmektedir. Bunun nedeni ise her bir trafonun %100 olarak yüklenmiş olmasıdır. Böylelikle mevcut sisteme eklenebilecek maksimum sayıdaki şarj istasyonu sayısı elde edilmiştir.
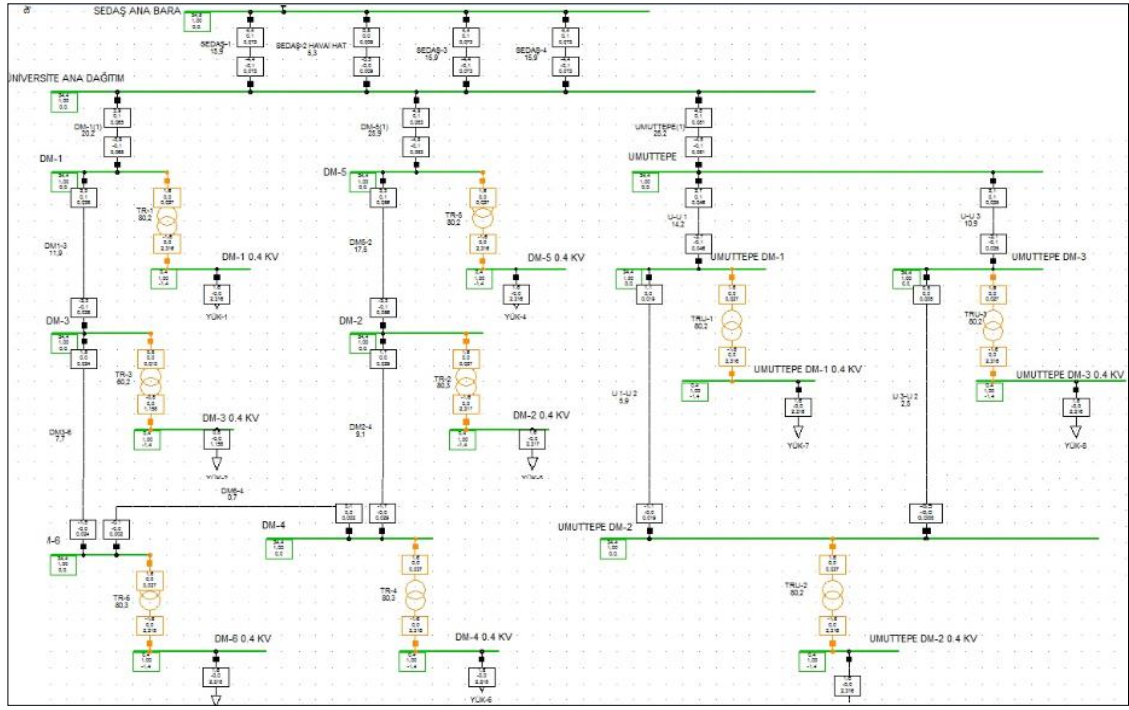
Şekil 1. Kocaeli Üniversitesi Umuttepe kampüsü yerleşkesi tek hat şeması Digsilent Power Factory modeli.
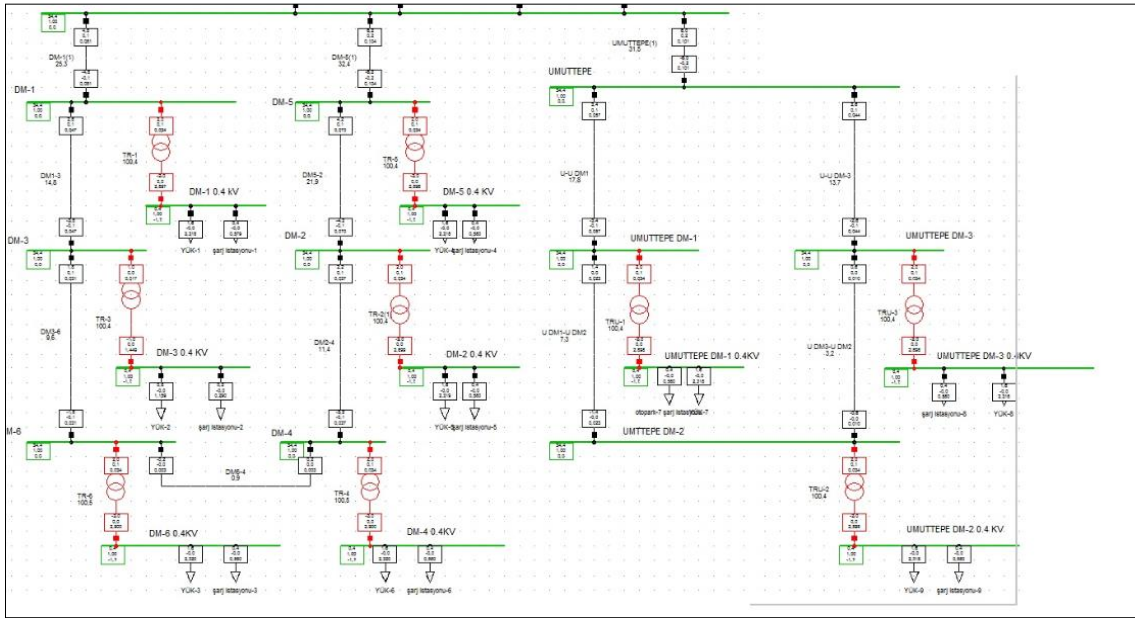
Şekil 2. Kocaeli Üniversitesi Umuttepe kampüsü yerleşkesi şarj istasyonu eklenmiş Digsilent Power Factory modeli.

2.4. Umuttepe Yerleşkesi Ek Trafo Tahsis Edilmiş DigSilent Powerfactory Modeli

Bu uygulamada, çalışmaya kampüs için şarj istasyonu tasarımında sayıca istasyon olarak yetersiz görülmesiyle öneri ve fikir oluşturmaya katkı sağlayacak şekilde mevcut sistem üzerinde senaryolar oluşturulmuştur. İlk olarak şarj istasyonu sayısının yetersiz görülmesi durumunda yapılabilecek seçeneklerden birisi olan ek trafo tahsisidir.

Şekil 3 incelendiğinde bir önceki şekilden farklı olarak mevcut trafolar ve buna sistemin müsade edebildiği şarj istasyonuna ek olarak mevcut trafoların yanına eklenmiş trafolar ile maksimum sayıda sisteme entegre edebilecek

şarj istasyonları görülmektedir. Eklenen trafolar mevcut sistemdeki trafolar ile birebir aynı olacak güç seviyesine sahip 2MVA ve 1 MVA gücünde seçilmiştir. Eklenen şarj istasyonları ayrı ayrı şarj ünitesi olarak değil her bir bağlantı noktasında maksimum sayıda olabilecek şekilde toplu olarak gösterilmiştir. Eklenen şarj istasyonları Tablo 2'de belirtildiği gibi tüm şarj istasyonları DC yüksek hızlı 200kW gücünde olacak şekilde seçilmiştir.

Şekil 3 incelendiğinde hem mevcut trafolar hem de eklenen trafoların kırmızı renkte olduğu görülmektedir. Bunun nedeni ise her bir trafonun %100 olarak yüklenmiş olmasıdır.

2.5. Umuttepe Yerleşkesi Güneş Paneli Entegre Edilmiş DigSilent Powerfactory Modeli

Kampüse şarj istasyonu kurulması aşamasına gelindiğinde ilk olarak mevcut sistemin üzerinde çalışma yapılarak şarj istasyonu kurulacaktır. Ancak mutlaka zamanla ek şarj istasyonu talep edilecektir. Bahsedilen ek trafo tahsisi bunun için bir seçenektir ancak çalışmada günümüzde oldukça rağbet gören ve gelecek vadeden yenilebilir enerji kaynaklarından biri olan güneş enerjisi konusu ile ilgili de bir çalışma yapılarak önerilere eklenmiştir (Mastoi ve ark., 2022).

Güneş paneli önerisi ile ilgili yapılan çalışmada her bir trafonun olduğu bağlantı noktasına ek olarak güneş paneli eklenmiştir. Sisteme entegre edilen paneller ile ek olarak kurulmak istenen şarj istasyonu güçlerinin mevcut

sistemden değil sadece panellerden karşılanması hedeflenmiştir. Önerilen bu sistemin tasarımı Şekil 4'deki gibi yapılmıştır. Burada her bir panelin olduğu bağlantı noktasına 3 adet şarj istasyonu eklenmiştir. Yapılan çalışma ile eklenen paneller ile her bir şarj istasyonunda 2 adet 200kW, 1 adet 50kW gücünde 3 er adet şarj ünitesi olacak şekilde istasyonlar önerilmiştir. Burada seçilen şarj istasyonları için güç seçimi yaparken, hızlı şarj istasyonu seçilme sebebi günümüzde daha çok tercih edilmesidir. Bunun sebebi ise şarj işlem süresinin daha kısa olmasıdır. Ek olarak AC şarj istasyonu da seçilmiştir. Bunun sebebi ise kampüs alanında uzun süre duran sürücüler için önerilmiştir. Çünkü AC şarj istasyonlarında şarj işlemi daha uzun sürelidir.
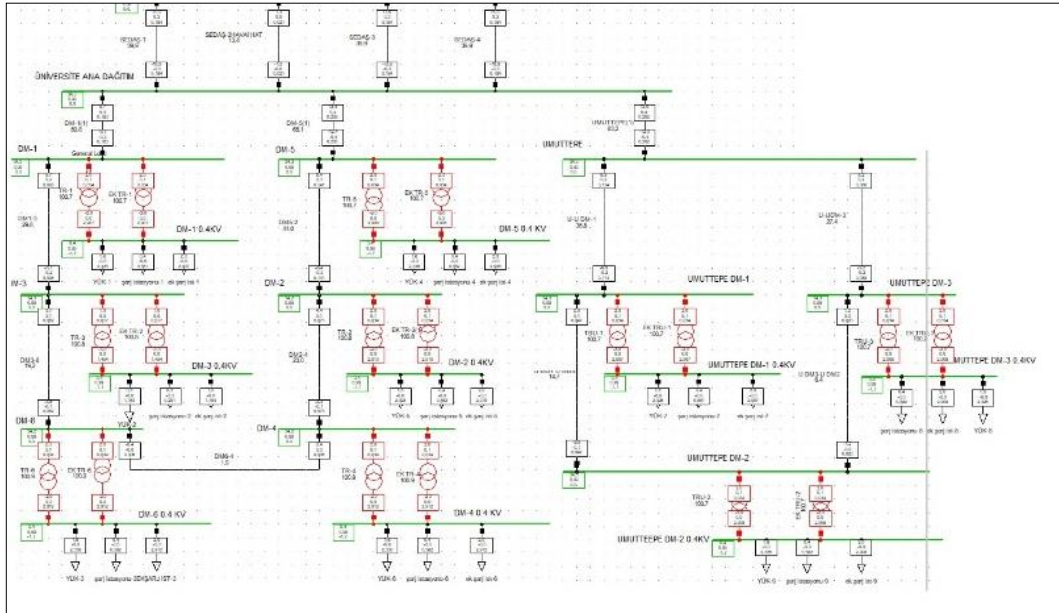
Şekil 3. Kocaeli Üniversitesi Umuttepe kampüsü yerleşkesi ek trafo tahsis edilmiş Digsilent Power Factory modeli.
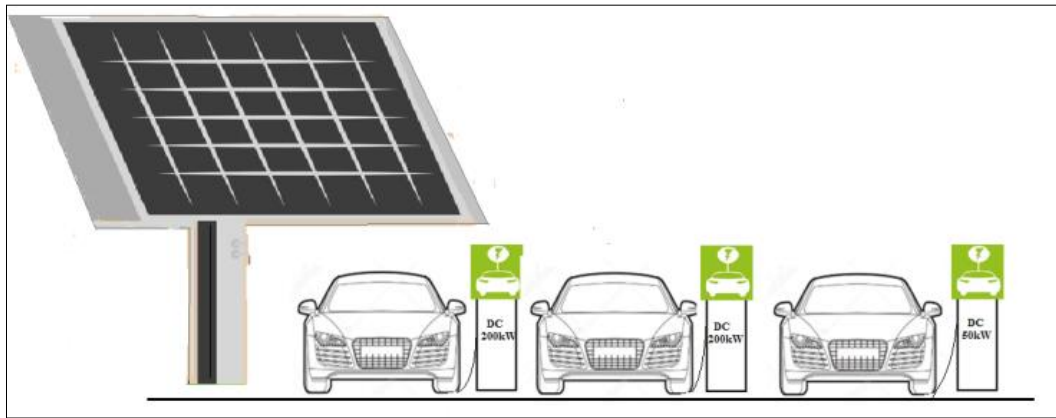
Şekil 4. Güneş Paneli ile Şarj İstasyonu Modeli

Şekil 4'de tasarlanan panel sisteminin kampüse entegre edilmiş modellemesi, Şekil 5'de gösterilmiştir. Yapılan öneride mevcut sistemin trafolarına eklenebilecek şarj istasyonları muhafaza edilerek bu sayının üzerine şarj ünitesi eklenmesi hedeflenmiştir. Böylelikle mevcut sisteme ek bir yük eklenmesinin önüne geçilmektedir.

Eklenen panellerin gücü şekildeki şarj ünitelerinin gücünü sağlayacak şekilde 450 kW olarak ayarlanmıştır. Daha fazla sayıda güneş paneli ile çok daha fazla sayıda şarj istasyonu önerilebilir. Ancak kampüs alanı çok fazla sayıda güneş paneli için uygun değildir. Önerilen güneş paneli sistemi için ilk etapta bataryasız, sadece güneş

olduğu esnada enerji üreten bir sistem önerilmektedir. Çünkü başlangıçta şarj istasyonları maliyeti göz önüne alındığında daha sonra bataryalı sistem önerilebilir. Şekil 5'de sistemde 9 adet trafo bağlantı noktasında

güneş panelleri bağlantıları şarj istasyonların yanına eklenmiştir. Böylelikle mevcut sistem için önerilen şarj istasyonlarına ek olarak eklenen güneş panellerinin şarj istasyonu sayısını arttırdığı görülmektedir.
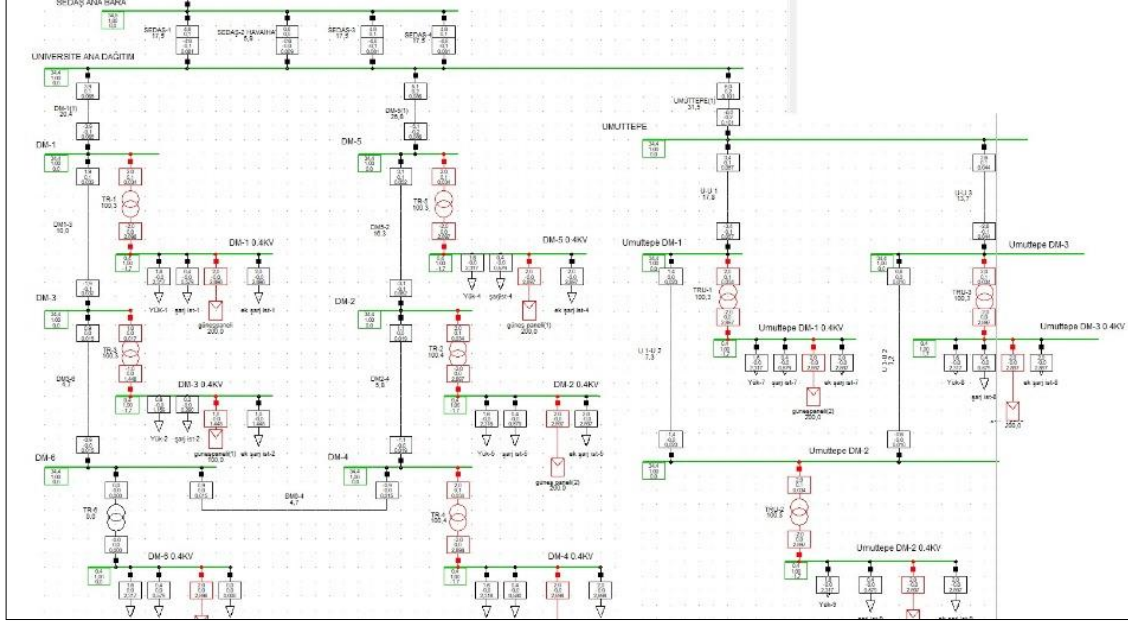
Şekil 5. Kocaeli Üniversitesi Umuttepe Kampüsü Yerleşkesi Güneş Paneli Eklenmiş Digsilent Power Factory Modeli.

3. Bulgular

Önceki bölümde sadece Digsilent Power Factory program modellemeleri gösterilen uygulama çalışmalarının sonuç verileri tablolar şeklinde eklenerek karşılaştırılıp sonuçları yorumlanmaktadır. Mevcut sisteme eklenen şarj istasyonları ile elde edilen sonuçlar, ek trafo tahsis edilen sistemin sonuçları ve son olarak güneş paneli eklenmiş sistemin sonuç tabloları olarak değerlendirilmiştir.

3.1. Umuttepe Yerleşkesi Tek Hat Şeması Digsilent Power Factory Modeli Simülasyon Sonuçları

Şekil 1'de Kocaeli Üniversitesi Umuttepe Kampüsü için tek hat şeması Digsilent Power Factory Modeli gösterilmişti. Tablo 3'de kampüs için trafoların %80 yüklenmiş durumda elde edilen verileri gösterilmektedir. Burada elde edilen sonuçlar mevcut sistemin şuan için yük akışını göstermektedir. Bu sebeple hem mevcut sisteme eklenecek şarj istasyonlarını hem önerilen yöntemler için şarj istasyonlarını belirlemede Tablo 3'deki veriler kullanılmaktadır. Tablo 4'de ise mevcut durum için yük verileri gösterilmiştir.

3.2. Umuttepe Yerleşkesi Şarj İstasyonu Eklenmiş Digsilent Power Factory Modeli Simülasyon Sonuçları

Şekil 2'deUmuttepe Yerleşkesi şarj istasyonu eklenmiş Digsilent Power Factory Modeli gösterilmiştir. Tablo 4'de ise, Şekil 2'de gösterilen mevcut sistemde şarj istasyonları eklenmiş durum için yapılan modellemenin sonuçları gösterilmektedir.

Tablo 5'de elde edilen sonuçlar kampüs için yakın gelecekte kurulacak şarj istasyonu kurulum aşamasında mevcut sistemin buna ne kadar uygun olduğu konusunda rehberlik edebilecektir.

3.3. Umuttepe Yerleşkesi ek trafo tahsis edilmiş digsilent power factory modeli simülasyon sonuçları

Şekil 3'de Umuttepe Yerleşkesi ek trafo tahsis edilmiş Digsilent Power Factory Modeli gösterilmiştir. Tablo 6'da Şekil 3'de gösterilen mevcut sistemde şarj istasyonları eklenmiş duruma ilave olarak ek trafo tahsisi ile sisteme eklenebilecek şarj istasyonlarını gösteren modellemenin sonuçları gösterilmektedir.

Tablo 6'da elde edilen sonuçlar kampüs için yakın gelecekte kurulacak şarj istasyonlarının bir süre sonra araç şarjı konusunda yetersiz kalması durumunda alternatif olarak önerilmiştir.

Tablo 3. Mevcut sistemin hat iletim verileri

Hat ismi	Bara X'den	Bara Y'ye	Hat akımı(kA)	Hat aktif gücü (MW)	Hat reaktif gücü (Mvar)	Hat yüklenme yüzdesi %
Sedaş-1	Sedaş Ana Bara	Üniversite Ana Dağıtım	0.073	4.4	0.1	15.9
Sedaş-2	Sedaş Ana Bara	Üniversite Ana Dağıtım	0.009	0.5	0.0	5.3
Sedaş-3	Sedaş Ana Bara	Üniversite Ana Dağıtım	0.073	4.4	0.1	15.9
Sedaş-4	Sedaş Ana Bara	Üniversite Ana Dağıtım	0.073	4.4	0.1	15.9
DM-1	Üniversite Ana Dağıtım	DM-1	0.065	3.9	0.1	20.2
DM1-3	DM-1	DM-3	0.038	3.9	0.1	11.9
DM3-6	DM-3	DM-6	0.024	1.5	0.0	7.7
DM-5	Üniversite Ana Dağıtım	DM-5	0.083	4.9	0.1	25.9
DM5-2	Üniversite Ana Dağıtım	DM-5	0.056	3.3	0.1	17.5
DM2-4	DM-2	DM-4	0.029	1.7	0.0	9.1
DM6-4	DM-6	DM-4				0.7
UMUTTEPE	Üniversite Ana Dağıtım	Umuttepe	0.081	4.8	0.1	25.2
U-U 1	Umuttepe	Umuttepe DM-1	0.046	2.7	0.1	14.2
U-U 3	Umuttepe	Umuttepe DM-3	0.035	2.1	0.1	10.9
U 1-U 2	Umuttepe DM-1	Umuttepe DM-2	0.019	1.1	0.0	5.9
U 3-U 2	Umuttepe DM-3	Umuttepe DM-2	0.008	0.5	0.0	2.5

Tablo 4. Mevcut sistemin yük verileri

Yük ismi	Bağlantı noktası	Yük akımı (kA)	Yük aktif gücü (MW)
Yük-1	DM-1 0.4 kV	2.316	1.6
Yük-2	DM-3 0.4 kV	1.158	0.8
Yük-3	DM-6 0.4 kV	2.318	1.6
Yük-4	DM-5 0.4 kV	2.316	1.6
Yük-5	DM-2 0.4 kV	2.317	1.6
Yük-6	DM-4 0.4 kV	2.318	1.6
Yük-7	UMUTTEPE DM-1	2.316	1.6
Yük-8	UMUTTEPE DM-3	2.316	1.6
Yük-9	UMUTTEPE DM-2	2.316	1.6

Tablo 5. Mevcut sisteme şarj istasyonu eklenmiş hat iletim verileri

Hat ismi	Bara X'den	Bara Y'ye	Hat akımı(kA)	Hat aktif gücü (MW)	Hat reaktif gücü (Mvar)	Hat yüklenme yüzdesi %
Sedaş-1	Sedaş Ana Bara	Üniversite Ana Dağıtım	0.092	5.5	0.2	19.9
Sedaş-2	Sedaş Ana Bara	Üniversite Ana Dağıtım	0.011	0.6	0.0	6.7
Sedaş-3	Sedaş Ana Bara	Üniversite Ana Dağıtım	0.092	5.5	0.2	19.9
Sedaş-4	Sedaş Ana Bara	Üniversite Ana Dağıtım	0.092	5.5	0.2	19.9
DM-1	Üniversite Ana Dağıtım	DM-1	0.081	4.8	0.1	25.3
DM1-3	DM-1	DM-3	0.047	2.8	0.1	14.8
DM3-6	DM-3	DM-6	0.031	1.8	0.1	9.6
DM-5	Üniversite Ana Dağıtım	DM-5	0.104	6.2	0.2	32.4
DM5-2	Üniversite Ana Dağıtım	DM-5	0.070	4.2	0.1	21.9
DM2-4	DM-2	DM-4	0.037	2.2	0.1	11.4
DM6-4	DM-6	DM-4	0.003	0.2	0.0	0.9
UMUTTEPE	Üniversite Ana Dağıtım	Umuttepe	0.101	6.0	0.2	31.5
U-U 1	Umuttepe	Umuttepe DM-1	0.057	3.4	0.1	17.8
U-U 3	Umuttepe	Umuttepe DM-3	0.044	2.6	0.1	13.7
U 1-U 2	Umuttepe DM-1	Umuttepe DM-2	0.023	1.4	0.0	7.3
U 3-U 2	Umuttepe DM-3	Umuttepe DM-2	0.010	0.6	0.0	3.2

Tablo 6. Ek trafo tahsis edilmiş durumda hat iletim verileri

Hat ismi	Bara X'den	Bara Y'ye	Hat akımı(kA)	Hat aktif gücü (MW)	Hat reaktif gücü (Mvar)	Hat yüklenme yüzdesi %
Sedaş-1	Sedaş Ana Bara	Üniversite Ana Dağıtım	0.184	11.0	0.3	39.9
Sedaş-2	Sedaş Ana Bara	Üniversite Ana Dağıtım	0.021	1.3	0.0	13.4
Sedaş-3	Sedaş Ana Bara	Üniversite Ana Dağıtım	0.184	11.0	0.3	39.9
Sedaş-4	Sedaş Ana Bara	Üniversite Ana Dağıtım	0.184	11.0	0.3	39.9
DM-1	Üniversite Ana Dağıtım	DM-1	0.163	9.7	0.3	50.8
DM1-3	DM-1	DM-3	0.095	5.7	0.2	29.8
DM3-6	DM-3	DM-6	0.062	3.7	0.1	19.2
DM-5	Üniversite Ana Dağıtım	DM-5	0.208	12.4	0.4	65.1
DM5-2	Üniversite Ana Dağıtım	DM-5	0.141	8.4	0.3	44.0
DM2-4	DM-2	DM-4	0.073	4.4	0.1	23.0
DM6-4	DM-6	DM-4	0.006	0.4	0.0	1.9
UMUTTEPE	Üniversite Ana Dağıtım	Umuttepe	0.202	12.0	0.4	63.2
U-U 1	Umuttepe	Umuttepe DM-1	0.114	6.8	0.2	35.8
U-U 3	Umuttepe	Umuttepe DM-3	0.088	5.2	0.2	27.4
U 1-U 2	Umuttepe DM-1	Umuttepe DM-2	0.047	2.8	0.1	14.7
U 3-U 2	Umuttepe DM-3	Umuttepe DM-2	0.020	1.2	0.0	6.4

3.4. Umuttepe Yerleşkesi Güneş Paneli Eklenmiş Digsilent Power Factory Modeli Simülasyon Sonuçları
Şekil 5'de Umuttepe Yerleşkesi sistemine güneş paneli entegre edilmiş DigSilent Power Factory Modeli gösterilmiştir. Tablo 7'de,Şekil 5'de gösterilen mevcut sistemde şarj istasyonları eklenmiş duruma ilave olarak güneş paneli entegre edilmiş sisteme eklenebilecek şarj istasyonlarını gösteren modellemenin sonuçları gösterilmektedir.

Tablo 7'de elde edilen sonuçlar kampüs için yakın gelecekte kurulacak şarj istasyonlarının bir süre sonra araç şarjı konusunda sayıca yetersiz kalması durumunda ikinci bir alternatif olarak önerilmiştir. Çünkü yenilenebilir enerji kaynaklarının mümkün olan her alanda kullanılması artık kaçınılmazdır. Bu sebeple ek şarj istasyonu talebi gündeme geldiğinde muhtemelen ilk tercih edilen seçenek olacaktır.

Tablo 7. Güneş Panelli sistem hat iletim verileri

Hat ismi	Bara X'den	Bara Y'ye	Hat akımı(kA)	Hat aktif gücü (MW)	Hat reaktif gücü (Mvar)	Hat yüklenme yüzdesi %
Sedaş-1	Sedaş Ana Bara	Üniversite Ana Dağıtım	0.092	5.5	0.2	19.9
Sedaş-2	Sedaş Ana Bara	Üniversite Ana Dağıtım	0.011	0.6	0.0	6.7
Sedaş-3	Sedaş Ana Bara	Üniversite Ana Dağıtım	0.092	5.5	0.2	19.9
Sedaş-4	Sedaş Ana Bara	Üniversite Ana Dağıtım	0.092	5.5	0.2	19.9
DM-1	Üniversite Ana Dağıtım	DM-1	0.081	4.8	0.1	25.3
DM1-3	DM-1	DM-3	0.047	2.8	0.1	14.8
DM3-6	DM-3	DM-6	0.031	1.8	0.1	9.6
DM-5	Üniversite Ana Dağıtım	DM-5	0.104	6.2	0.2	32.4
DM5-2	Üniversite Ana Dağıtım	DM-5	0.070	4.2	0.1	21.9
DM2-4	DM-2	DM-4	0.037	2.2	0.1	11.4
DM6-4	DM-6	DM-4	0.003	0.2	0.0	0.9
UMUTTEPE	Üniversite Ana Dağıtım	Umuttepe	0.101	6.0	0.2	31.5
U-U 1	Umuttepe	Umuttepe DM-1	0.057	3.4	0.1	17.8
U-U 3	Umuttepe	Umuttepe DM-3	0.044	2.6	0.1	13.7
U 1-U 2	Umuttepe DM-1	Umuttepe DM-2	0.023	1.4	0.0	7.3
U 3-U 2	Umuttepe DM-3	Umuttepe DM-2	0.010	0.6	0.0	3.2

4. Tartışma
Önceki bölümde yapılan uygulama çalışmalarının sonuçları irdelenmektedir. Mevcut sistemin elektrikli araç şarj istasyonu kapasitesini belirlemede, elde edilen veriler oldukça faydalı olmakla beraber, önerilen yöntemlerle kampüs için şarj istasyonu değerlendirilmesi çok daha kapsamlı bir hale gelmiştir.

Bölüm 4'te elde edilen uygulama çalışması sonuçlarını yorumlamadan önce, mevcut sistemin durumu ve eklenen şarj istasyonunun etkileri mevcut sistemin sonuçları ile kıyaslayarak yorumlamak daha doğru olacaktır. Böylelikle ek yük olarak sisteme eklenecek şarj istasyonları ile kıyaslandığında mevcut sisteme etkileri görülebilmektedir. Bu sebeple mevcut sistemin üzerine gelen her bir yükün sistemde oluşturduğu etki gözlemlenirken, bölüm 4'te elde edilen sonuç tablolarındaki hat yüklenme yüzdeleri göz önüne alınır. Burada sistem etkisi, hat yüklenme yüzdeleri tablosu ile görsel anlaşılırlığı hedeflenmiştir. Tablo 8 incelendiğinde

ilk sütunda mevcut sistemdeki yüklerin hat üzerinde oluşturduğu yüklenme yüzdeleri görülmektedir. Mevcut sistemdeki trafolar %100 yüklenecek şekilde yüksek hızlı şarj istasyonu eklendiğinde hatlardaki yüklenme ikinci sütunda görülmektedir. Eklenen şarj istasyonlarının bir miktar artış yapması beklenen bir durumdur. Sonuca bakılarak yapılacak değerlendirmeyi bu artışın mevcut sistem için aşırı yüklenmeye sebep olma durumuna bakarak yapmak daha sağlıklı olacaktır. Böylece, artışların yüklenme yüzdelerinde %100 yaklaşmayan değerler olması mevcut sistem için kurulacak şarj istasyonlarına elverişli olduğunu göstermektedir. Üçüncü sütunda ise ek yük gelmesi durumunda mevcut sistemdeki yüke göre artış oranlarını gösterir.

Tablo 8 de mevcut sistem ve şarj istasyonu eklenmiş durum için hat yüklenmeleri incelenerek hat uygunluğu ile entegre edilebilecek şarj istasyon sayısını ve bu istasyonların bağlantı noktalarını göstermektedir.

Tablo 8. Mevcut sistem ve şarj istasyonu eklenmiş durumda hat yüklenme yüzdeleri

Hat ismi	%80 yüklü durum hat yüklenme yüzdesi	Şarj istasyonu eklenmiş durum yüklenme yüzdesi	% 80 yüklü durum hat yüklenme yüzdesine göre artış miktarı
Sedaş-1	15.9	19.9	0.092
Sedaş-2	5.3	6.7	25.15
Sedaş-3	15.9	19.9	26.41
Sedaş-4	15.9	19.9	25.15
DM-1	20.2	25.3	25.15
DM1-3	11.9	14.8	25.24
DM3-6	7.7	9.6	24.36
DM-5	25.9	32.4	24.67
DM5-2	17.5	21.9	25.09
DM2-4	9.1	11.4	25.14
DM6-4	0.7	0.9	25.27
UMUTTEPE	25.2	31.5	28.57
U-U 1	14.2	17.8	25
U-U 3	10.9	13.7	25.35
U 1-U 2	5.9	7.3	25.68
U 3-U 2	2.5	3.2	23.72

Tablo 9'da mevcut sistem üzerinde yapılan çalışmalar ve değerlendirmeler sonucunda kampüsteki trafoların %80 yüklenme yüzdesi üzerinden yüksek hızlı DC 200 kW gücü şarj istasyonları sayısı bağlantı noktalarıyla verilmiştir. Sonuçtan görüldüğü gibi, şuan için kampüse toplam 17 adet yüksek hızlı şarj istasyonu eklenebilmektedir. Burada kampüs trafolarının %100 yüklenmesi ile maksimum sayıda şarj istasyonu önerilmiştir. Ancak arz-talep dengesine bağlı olarak bu sayı azaltılabilir. Önerilen şarj istasyonları DC hızlı şarj istasyonudur. Şarj süresi aracın batarya gücüne bağlı olarak değişmektedir. Ancak bu güçte şarj istasyonları ile ortalama bir süre verilmek istenirse, ortalama 20 dakika gibi bir sürede şarj işlemi tamamlanmaktadır.

Kısa bir süre için yeterli olabilse de elektrikli araç konusunda öngörülen araç sayısına çok kısa sürede ulaşılma hedefi düşünülürse yakın gelecekte ek şarj istasyonu talebi, çalışma alanı olan Kampüste ihtiyaç olacaktır. Bu nedenle mevcut sistemdeki yüklenmeyi olumsuz olarak etkilemeyecek alternatiflere ihtiyaç vardır. Yapılan çalışmada ilk öneri olarak ek trafo tahsisi sunulmuştur. Tablo 10 incelendiğinde ilk sütunda mevcut sistemdeki yüklerin hat üzerinde oluşturduğu yüklenme yüzdeleri görülmektedir. Mevcut sisteme ek olarak trafolar ile aynı güç seviyesinde yeni trafolar eklenerek şarj istasyonu sayısı arttırıldığında mevcut sistem etkisi, ikinci sütunda ek trafo tahsisi ile hat yüklenme yüzdeleri görülmektedir. Hat yüklenme yüzdelerinde mevcut sisteme göre hızlı bir artış olmuştur. Bu durum üçüncü sütunda görülmektedir.

Sisteme eklenen trafolar ile kampüste kurulabilecek en fazla sayıdaki yüksek hızlı DC 200 kW gücünde şarj istasyonu toplam sayısı mevcut sisteme eklenen ile birlikte 102 adettir.

Tablo 11 incelendiğinde ek trafo tahsis edilmesi ile toplamda 85 adet şarj istasyonu kurulabilirken mevcut sistemekurulabilen 17 adet şarj istasyonu ile birlikte bu rakam 102 olmuştur. Şarj istasyonu sayısı arttırılmaktadır.Bu sebeple önerilen yöntem şarj istasyonu sayısını artırmak için oldukça iyi sonuç vermiştir.

Şarj istasyonu sayılarını arttırmak için ilk olarak trafo tahsisi önerilmektedir.Ancak oldukça yaygın kullanılan güneş panelleri sisteme entegre edildiğinde ek yük olarak sistemi etkilemediği için ek trafo tahsisinden daha önce tercih edilebilir.Güneş paneli eklenmiş sistemde, Tablo 7 incelendiğinde, hat yüklenme yüzdelerinin Tablo 5 ile aynı olduğu görülmektedir.Burada mevcut sisteme eklenen trafolardan hariç ek bir yük gelmemiştir.Şarj istasyonu eklenmesi ile ilgili yapılan çalışmalarda şarj üniteleri DC 200kWseçilmiştir. Güneş paneli ile uygulamada ise her bir nokta için üç adet şarj ünitesi seçilmiş, bunlardan ikisi DC 200kW gücünde iken bir adedi ise DC 50kW gücündedir. Bu nedenle ek şarj istasyonları iki ayrı başlık altında tabloya eklenmiştir. Tablo 12'ye bakıldığında her bir nokta için 3'er adet şarj ünitesi olmak üzere 9 bağlantı noktasına 27 adet şarj ünitesi eklenebilir. Mevcut sistem için ise 17 adet olduğu daha önceden hesaplanmıştır. Böylece güneş paneli eklenmiş sistemde toplam 44 adet şarj istasyonu sisteme dahil edilebilir.

Tablo 12'deki şarj istasyonu sayısı mevcut sisteme ek yük eklenmeden elde edilmiş olduğu için iyi bir alternatif olmaktadır.

Tablo 9. Mevcut sistem ve şarj istasyonu eklenmiş durumda hat yüklenme yüzdeleri

Şarj istasyonu ismi	Şarj istasyonu bağlantı noktası	Şarj istasyonu gücü (kW)	Şarj istasyonu sayısı
Şarj istasyonu-1	DM-1 0.4 kV	200	2
Şarj istasyonu-2	DM-3 0.4 kV	200	1
Şarj istasyonu-3	DM-6 0.4 kV	200	2
Şarj istasyonu-4	DM-5 0.4 kV	200	2
Şarj istasyonu-5	DM-2 0.4 kV	200	2
Şarj istasyonu-6	DM-4 0.4 kV	200	2
Şarj istasyonu-7	UMUTTEPE DM-1	200	2
Şarj istasyonu-8	UMUTTEPE DM-3	200	2
Şarj istasyonu-9	UMUTTEPE DM-2	200	2
			Toplam:17

Tablo 10. Mevcut sistem ve şarj istasyonu eklenmiş durumda hat yüklenme yüzdeleri

Hat ismi	%80 yüklü durum hat yüklenme yüzdesi	Ek trafo eklenmiş durum yüklenme yüzdesi	% 80 yüklü durum hat yüklenme yüzdesine göre artış miktarı
Sedaş-1	15.9	39.9	150.94
Sedaş-2	5.3	13.4	152.83
Sedaş-3	15.9	39.9	150.94
Sedaş-4	15.9	39.9	150.94
DM-1	20.2	50.8	151.48
DM1-3	11.9	29.8	150.42
DM3-6	7.7	19.2	149.35
DM-5	25.9	65.1	151.35
DM5-2	17.5	44.0	151.42
DM2-4	9.1	23.0	152.74
DM6-4	0.7	1.9	171.42
UMUTTEPE	25.2	63.2	150.79
U-U 1	14.2	35.8	152.11
U-U 3	10.9	27.4	151.37
U 1-U 2	5.9	14.7	149.15
U 3-U 2	2.5	6.4	156.00

Tablo 11. Ek trafo tahsisi ile şarj ünitesi sayısı ve bağlantı noktaları

Şarj istasyonu ismi	Şarj istasyonu bağlantı noktası	Şarj istasyonu gücü (kW)	Şarj istasyonu sayısı
Şarj istasyonu-1	DM-1 0.4 kV	200	2
Ek Şarj İstasyonu-1	DM-1 0.4 kV	200	10
Şarj istasyonu-2	DM-3 0.4 kV	200	1
Ek Şarj İstasyonu-1	DM-3 0.4 kV	200	5
Şarj istasyonu-3	DM-6 0.4 kV	200	2
Ek Şarj İstasyonu-1	DM-6 0.4 kV	200	10
Şarj istasyonu-4	DM-5 0.4 kV	200	2
Ek Şarj İstasyonu-1	DM-5 0.4 kV	200	10
Şarj istasyonu-5	DM-2 0.4 kV	200	2
Ek Şarj İstasyonu-1	DM-2 0.4 kV	200	10
Şarj istasyonu-6	DM-4 0.4 kV	200	2
Ek Şarj İstasyonu-1	M-4 0.4 kV	200	10
Şarj istasyonu-7	UMUTTEPE DM-1	200	2
Ek Şarj İstasyonu-1	UMUTTEPE DM-1	200	10
Şarj istasyonu-8	UMUTTEPE DM-3	200	2
Ek Şarj İstasyonu-1	UMUTTEPE DM-3	200	10
Şarj istasyonu-9	UMUTTEPE DM-2	200	2
Ek Şarj İstasyonu-1	UMUTTEPE DM-2	200	10
			TOPLAM:102

Tablo 12. Güneş paneli entegre edilmiş sistem şarj ünitesi sayısı ve bağlantı noktaları

Şarj istasyonu ismi	Şarj istasyonu bağlantı noktası	Şarj istasyonu gücü (kW)	Şarj istasyonu sayısı
Şarj istasyonu-1	DM-1 0.4 kV	200	2
Ek Şarj İstasyonu-1	DM-1 0.4 kV	200	2
Ek Şarj İstasyonu-1	DM-1 0.4 kV	50	1
Şarj istasyonu-2	DM-3 0.4 kV	200	1
Ek Şarj İstasyonu-2	DM-3 0.4 kV	200	2
Ek Şarj İstasyonu-2	DM-3 0.4 kV	50	1
Şarj istasyonu-3	DM-6 0.4 kV	200	2
Ek Şarj İstasyonu-3	DM-6 0.4 kV	200	2
Ek Şarj İstasyonu-3	DM-6 0.4 kV	50	1
Şarj istasyonu-4	DM-5 0.4 kV	200	2
Ek Şarj İstasyonu-4	DM-5 0.4 kV	200	2
Ek Şarj İstasyonu-4	DM-5 0.4 kV	50	1
Şarj istasyonu-5	DM-2 0.4 kV	200	2
Ek Şarj İstasyonu-5	DM-2 0.4 kV	200	2
Ek Şarj İstasyonu-5	DM-2 0.4 kV	50	1
Şarj istasyonu-6	DM-4 0.4 kV	200	2
Ek Şarj İstasyonu-6	DM-4 0.4 kV	200	2
Ek Şarj İstasyonu-6	DM-4 0.4 kV	50	1
Şarj istasyonu-7	UMUTTEPE DM-1	200	2
Ek Şarj İstasyonu-7	UMUTTEPE DM-1	200	2
Ek Şarj İstasyonu-7	UMUTTEPE DM-1	50	1
Şarj istasyonu-8	UMUTTEPE DM-3	200	2
Ek Şarj İstasyonu-8	UMUTTEPE DM-3	200	2
Ek Şarj İstasyonu-8	UMUTTEPE DM-3	50	1
Şarj istasyonu-9	UMUTTEPE DM-2	200	2
Ek Şarj İstasyonu-9	UMUTTEPE DM-2	200	2
Ek Şarj İstasyonu-9	UMUTTEPE DM-2	50	1
			Toplam:44

Literatürde DigSilent power factory yazılımı ile yapılmış şarj istasyonu konumlandırması konusunda birkaç örnek bulunmaktadır. Ancak yapılan çalışmayı benzerlerinden ayıran en temel farklardan birisi uygulama alanıdır. Kampüs alanı üzerinde herhangi bir şarj istasyonu kurulumu mevcut değildir. Bu nedenle yapılan çalışmanın kampüs alanı üzerinde yapılacak kurulum ve benzer çalışma yapacaklar için örnek olması hedeflenmektedir. Ayrıca çalışmanın benzerlerinden ayrılan bir diğer noktası yenilenebilir enerji kaynaklarından güneş paneli mevcut alana şarj istasyonu kurulumunda önerilmiştir. Böylece kampüs alanı için mevcut şebekeyi destekleyecek bir enerji kaynağı da önerilmiştir. Gelecek çalışmlarda bu kurulumun üzerine güncel teknoloji uygulamaları eklenerek çalışma genişletilebilir.

5. Sonuç

Çalışmanın geneli kısaca değerlendirilecek olunursa hedeflenen tüm aşamalar başarılı olarak tamamlanmıştır. Böylelikle Kocaeli Üniversitesi Umuttepe Kampüsü için detaylı bir elektrikli araç şarj istasyonu çalışması yapılmıştır. Çalışmanın yakın gelecekte şarj istasyonu konusunda rehber olması hedeflenmektedir.

Katkı Oranı Beyanı

Yazar(lar)ın katkı yüzdeleri aşağıda verilmiştir. Tüm yazarlar makalenin son halini incelemiş ve onaylamıştır.

	A.T.Y.	N.A.
K	50	50
T	60	40
Y	20	80
VTI	80	20
VAY	50	50
KT	50	50
YZ	60	40
KI	10	90
GR	50	50
PY	20	80
FA	50	50

K= kavram, T= tasarım, Y= yönetim, VTI= veri toplama ve/veya işleme, VAY= veri analizi ve/veya yorumlama, KT= kaynak tarama, YZ= Yazım, KI= kritik inceleme, GR= gönderim ve revizyon, PY= proje yönetimi, FA= fon alımı.

Çatışma Beyanı

Yazarlar bu çalışmada hiçbir çıkar ilişkisi olmadığını beyan etmektedirler.

Etik Onay Beyanı

Bu araştırmada hayvanlar ve insanlar üzerinde herhangi bir çalışma yapılmadığı için etik kurul onayı alınmamıştır.

Kaynaklar

Abaspahic A, Saric M. 2021. Impact of complementary integration of electricvehicle charging stations and photovoltaics onvoltage quality and voltage stability. 20th International Symposium Infoteh-Jahorına , 17-19 March, East Sarajevo, Bosnia and Herzegovina, pp:1-6.

Akmal M, Jawad A, Tarabsheh A. 2018. Design and simulation of solar grid-connected charger for electric vehicle. 20th International Conference on Computer Modelling and Simulation, 27-29 Mart, Cambridge, UK, pp: 108-113.

Aydın A, Şeker M, Memmedov A. 2017.Bingöl orta gerilim şebekesinin teknik kayıpların analizi için digsilent power factory yazılımı ile bilgisayar destekli şebeke modeli. Mesleki Bilim Derg, 6(1): 10-15.

Bashaireh A, Obeidat D, Almehizia AA, Shalalfeh L. 2023. Optimal placement of electric vehicle chargingstations: a case study in Jordan. 2023 IEEE Texas Power and Energy Conference, 13-14 February, College Station, TX, USA, pp: 1-6.

Betancur D, Duarte LF, Revollo J, Restrepo C, Diez AE, Isaac IA, Lopez GJ,Gonzalez JW. 2021. Methodology to evaluate the impact of electric vehicles on electrical networks using Monte Carlo. J Ener,14(5): 1-16.

Dörtköşe S. 2022. Elektrikli araç şarj istasyon yerlerinin belirlenmesi. Yüksek Lisans Tezi,Sakarya Üniversitesi, Fen Bilimleri Enstitüsü, Sakarya, Türkiye, ss.49.

Dörtköşe S, Yazgan HR, Cömert S.2022. Elektrikli araç şarj istasyon yerlerinin akış yakıt ikmal yer modeli kullanılarak belirlenmesi. Erciyes Üniv Fen Bilim Enstit Derg, 38(2):371-382.

Durmuş FS, Kaymaz H. 2020. Elektrikli araç şarj yöntemleri. Akıllı Ulaşım Sistem Uyg Derg, 3(2): 123-139.

Farkas C, Szücs G, Prikler L. 2013. Grid impacts of twin EV fast charging stationsplaced alongside a motorway. 4th International Youth Conference on Energy , 06-08 June, Budapest, Hungary, pp:1-6.

Ge S, Feng L, Liu H. 2011.The planning of electric vehicle charging station based on grid partition method. International Conference on Electrical and Control Engineering, 16-18 September, Yichang, China, pp: 2726-2730.

Gündoğan AE, 2022. Türkiye'deki ulaşımda enerji talebinin sağlam istatistiksel yöntemler ile araştırılması. Nicel Bilim Derg, 4(19): 85-95.

Kerem A, Gürbak H. 2020. Fast charging station technologies for electric vehicles. Gazi Üniv Fen Bilim Derg, 8(3): 644-661.

Kılıçarslan OM, Çam E. 2021. Investigation on the electrical vehicles effects on the electrical power grid. El-Cezerî Fen Mühen Derg, 8(1):21-35.

Koç A, Yağlı H, Koç Y, Uğurlu İ. 2018. Dünyada ve Türkiye'de enerji görünümünün genel değerlendirilmesi. Mühen Mak Derg, 59(692):86-114.

Kumar G, Gautam D, Kumar P. 2021. Optimal charging schedule for electric vehicles in a microgrid with renewable energy sources using digSilent power factory and matlab. Universities Power Engineering Conference, 24-26 September, Kollam, India, pp: 1-5.

Mancini E, Longo M, Yaici W, Zaninelli D. 2020. Assessment of the impact of electric vehicles on the design and efectiveness of electric distribution grid with distributed generation. J Applied Sci, 10(15): 5125-5158.

Mastoi M, Zhuang S, Munir H , Haris M, Hassan M, Usman M, Bukhari S, Ro J. 2022.An in depth analysis of electric vehicle charging station infrastructure, policy implications, and future trends .J Energy Rep,8(1): 11504-11529.

Medogorac M,Capuder T, Bago D,Susac S,Marijanovic M. 2022. Impact of charging stations for electric vehicles on the power distribution network. J B&H Elect Engin, 16(2): 30-36.

Metais MO, Jouini O, Perez Y, Berrada J, Suomalainen E. 2022. Too much or not enough? Planning electric vehicle charging infrastructure: A review of modeling options. J Renew Sustain Energy Rew, 153: 1-29.

Micari S, Polimenib A, Napolia G, Andaloroa L, Antonuccia V. 2017. Electric vehicle charging infrastructure planning in a road network. J Renew Sustain Energy Rew, 80: 98–108.

Nour M, Ali A, Farkas C. 2018. Evaluation of electric vehicles charging impacts on a real low voltage grid. Inter J Power Engin Ener, 9(2):837-842.

Oral C, Kıpkıp E. 2019. Ulaştırma sektörünün önemi üzerine kavramsal bir yaklaşım. Oğuzhan Sosyal Bilim Derg, 1(1): 58-64.

Özçelik B, Tör O, Cebeci M, Ünver G, Özen K. 2018. Elektrik iletim operatörleri için digsilent powerfactory ve siemens simatic wincc scada yazılımı entegrasyonu ile geliştirilen eğitim simülatörü. Fırat Üniv Fen Bilim Derg, 30(3): 23-29.

Paredes L, Pozo M. 2020. Energy management model for an electric vehicle charging station in the environment of a microgrid. J Revista Tecnica Energia, 17(1): 32-42.

Pothinun T, Premrudeepreechacharn S. 2018.Power quality ımpact of charging station on MV distribution networks: a case study in PEA electrical power system. 53rd International Universities Power Engineering Conference, 04-07 September, Glasgow, UK, pp: 1-6.

Sica L, Deflorio F. 2023. Estimaq"tion of charging demand for electric vehicles by discrete choice models and numerical simulations: applications to a case study in Turin. J Green

Energy Intel Transport, 2(2): 1-11.

Simarro GA, Villena RR, Honrubia EA, Gomez LE. 2023a. Effect of penetration levels for vehicle-to-grid integration on a power distribution network. J Machines, 11(4): 452-456.

Simarro GA, Villena RR, Honrubia EA, Gomez LE. 2023b. Impact of electric vehicle integration on an industrial distribution network: case study based on recent standards. 11th International Conference on Smart Grid Conference, 04-07 June, France, Paris, pp: 1-5.

Simarro GA, Villena RR. 2022. Impacts of electric vehicle charging stations on a Greek distribution network. CIRED Porto Workshop 2022: E-mobility and power distribution systems Conference, 02-03 June, Porto, Portugal, pp:452-456.

Tunçer B, Çetin E. 2023. Elektrikli araç şarj istasyonlarının dağıtım şebekesi üzerindeki etkilerinin örnek bir saha üzerinde incelenmesi.VII. Elektrik Tesisleri Ulusal Kongre ve Sergisi, 1-3 Kasım, İzmir, Türkiye, ss: 54.

THE METHOD THAT MAKES OILS AND FATS HEALTHIER: INTERESTERIFICATION

Batuhan İNANLAR[1], Filiz ALTAY[1]*

[1]*İstanbul Technical University, Faculty of Chemical-Metallurgical Engineering, Department of Food Engineering, Maslak, 34469, Sarıyer, İstanbul, Türkiye*

Abstract: Interesterification is a versatile modification technique with significant benefits for health, the environment, and the economy. It serves as an advantageous alternative to partial and full hydrogenation, preventing the formation of trans fatty acids and saturated fats. While more research is needed to fully understand its health impacts, existing studies suggest that the health effects may stem from end products rather than the process itself. This method is particularly valuable in producing alternatives to breast milk, enriching foods with omega-3 fatty acids, and contributing to food safety through applications like edible film production. From an environmental standpoint, enzymatic interesterification is especially advantageous due to its ability to reuse enzymes and minimize waste, thus reducing environmental impact. The process also offers energy savings and increased efficiency, which are both environmentally and economically beneficial. By preserving food quality, aiding in the production of trans fat free margarine, and reducing the need for hydrogenation, interesterification supports the food industry while indirectly contributing to lower health expenditures. Despite its advantages, interesterification is influenced by factors such as fatty acid composition, triacylglyceride stereochemistry, temperature, process duration, catalyst usage, and the condition of the oil mixture. Challenges such as acyl migration and residue formation can arise. While both chemical and enzymatic methods are utilized, enzymatic interesterification has become more popular due to its efficiency and environmental benefits. Future research should focus on enzymatic interesterification to optimize its applications. Given its widespread use, it is recommended that interesterification undergo thorough risk assessments by national and international authorities to ensure safety, particularly concerning its health effects.

Keywords: Interesterification, Margarine, Trans fatty acids, Hydrogenation

*Corresponding author: İstanbul Technical University, Faculty of Chemical-Metallurgical Engineering, Department of Food Engineering, Maslak, 34469, Sarıyer, İstanbul, Türkiye
E mail: lokumcu@itu.edu.tr (F. ALTAY)

Batuhan İNANLAR	(iD)	https://orcid.org/0000-0002-9511-6182
Filiz ALTAY	(iD)	https://orcid.org/0000-0002-5484-866X

1. Introduction

Fats and oils are indispensable parts of human life and are used for various purposes in food production. They primarily affect the organoleptic properties of food. They can improve the texture and mouth feel of food and its appearance and taste. Features such as the stability of air bubbles in products like cakes, absorbency to prevent the absorption of water from flour in bakery products like biscuits, extending shelf-life due to moisture retention, providing a shiny appearance when poured into hot foods and having an efficient heat transfer ability lead to the use of oils (Spessato et al., 2023).

Edible oils are a complex mixture of triacylglycerides, containing variety of saturated, unsaturated and trans fatty acids. They also have minor components such as phospholipids, pigments, tocopherols. Although fat components provide functionality to foods, saturated and trans fats can adversely affect human health (Oroian, 2024). Many important scientific authorities recommend that saturated fat and trans fat should be reduced. According to Harvard Health Publishing, saturated fat intake in diets should not exceed 10%. It states that there is no safe consumption limit for trans fat. It also emphasizes that including monounsaturated and polyunsaturated fatty acids in the diet instead of saturated fat and trans fatty acids will positively affect human health (Harvard Health Publishing, 2022).

There are slight differences between the sequences of fatty acids. Fatty acids have hydrocarbon groups of different lengths and methyl and carboxylic groups at both ends. Depending on the double bond between the carbon groups in fatty acids, they are divided into saturated, monosaturated and polysaturated (Karageorgou et al., 2023). Saturated fats have not any double bonds in its carbon chain. In contrast, monounsaturated fats have one double bond, polyunsaturated fats have more than one double bond in their carbon chain (DiNicolantonio and O'Keefe, 2022). Mono and polyunsaturated fatty acids have cis or trans isomers. In cis isomers, H atoms are positioned at the same side of the carbon double bond. On the other hand, trans isomers have H atoms on the opposite side of the carbon double bond. Trans fatty acids provide better adherence and cell penetration. For this reason, no studies were conducted on removing trans fatty acids from oils for many years, and a method called partial

hydrogenation was used. However, in the 1990s, with the understanding of the negative effects of trans fatty acids on health, a method to remove trans fatty acids from oils was sought (Shah and Thadani, 2019).

Interesterification, one of the modification methods for reducing trans fatty acids in oils, has become increasingly widespread. Although its applications are increasing in the industry, there are significant gaps in the literature. According to the data of the National Library of Medicine (NIH), there are 321 articles using the term "interesterification" between 2004-2024; 89 of them (approximately 28%) belong to the years 2020-2024 (NIH, 2024). Moreover, in the Web of Science (WoS) database, there are 782 studies in the field of food science technologies that include the term "Interesterification" from the last 20 years, while there are 169 (almost 22%) studies from the last 5 years (WoS Database, 2024). The purpose of this review is to provide information about the application of the interesterification method, its effects on health, and legal regulations. The review will be a guide for future studies.

2. Modification Methods

Fats and oils that have not undergone any modification process do not always have the required properties. Fats and oils with the desired ideal properties are limited because they are expensive or raw materials that are available in limited quantities. Modification techniques offer a solution at this point. These techniques alter the physical and chemical properties of fats and oils and are effective in imparting desired properties to foods such as stability, melting point. They may also support consumer health by helping to regulate fatty acid ratios. In short, modification methods have an impact on fats and oils in terms of economy, technology and health. (Zbikowska et al., 2023).

2.1. Hydrogenation

The oldest modification technique used in oils is hydrogenation. This method, which started to be used in industry at the beginning of the 20th century, allowed the solidification of liquid oils. Hydrogenation is a process that involves saturating oil with hydrogen as a catalyst, typically Ni, and maintaining a temperature range of 160-200 °C. During hydrogenation, the double bonds of unsaturated fatty acids are saturated with hydrogen atoms, resulting in a product that has a relatively high content of saturated fatty acids. Hydrogenation extends shelf life by reducing the polyunsaturated fatty acid content and improving the functionality of oils for use in certain applications by converting them. The reaction is terminated when the product reaches the desired fat content and melting point. However, nickel catalysts cause the formation of trans fats and leave residues. This can pose a risk to both human health and product quality. Therefore, alternative catalysts to nickel can be used in hydrogenation. Palladium catalysts, although quite effective, tend to inactivate themselves, while platinum is less active and produces less trans fatty acids.

Hydrogenation is not only affected by the type of catalyst. Factors such as the initial oil composition, amount of catalyst, reaction temperature, pressure, time and reaction type also affect the reaction. There are three types of hydrogenation: selective, partial and full (Rasor and Duncan, 2014; Troncoso et al., 2022).

In selective hydrogenation, a small amount of hydrogenation is performed to increase the oil stability before it becomes a solid. In some cases, this technique has also been applied to soybean and canola oils, which include too much linolenic acid, to increase their stability. The cis- to trans-isomerization can be reduced by keeping the reaction temperature low and by a selective catalyst such as platinum, in contrast to the standard hydrogenation process (Rasor and Duncan, 2014).

Partial hydrogenation is defined as the process in which the unsaturaed fatty acids in the oil are not completely removed. If the final iodine number, which is used as a measure of unsaturation, is greater than 4, it is interpreted as partial hydrogenation, and if it is small, it is interpreted as complete hydrogenation (Bhandari et al., 2020). During partial hydrogenation, temporary half-hydrogenated molecules are formed before the completion of the process, the loss of a hydrogen atom from the unsaturated fatty acid molecule and the conversion of the double bond to the trans configuration occur more easily than the addition of another hydrogen to the saturated form. Therefore, trans fatty acids are significantly formed under partial hydrogenation conditions (Zbikowska et al., 2019). The World Health Organization reported that consuming excessive amounts of trans fatty acids increasesthe risk of death for any reason by 34% and that of death from coronary heart disease by 28%. As a result, studies are being conducted worldwide to minimize trans fat consumption (WHO, 2018).

In recent years, the use of cold plasma for hydrogenation has attracted attention because it is both sustainable and reduces the amount of trans fat. Although the use of this technology creates secondary lipid products, it can be used as a new method in oil modification over time (Thirumdas, 2023).

2.2. Fractionation

Fractionation is a widely used process in the oil industry, which allows the separation of low and high melting triacylglycerols under controlled cooling conditions, and olein and stearin fractions with different chemical and physical properties are obtained. Fractionation is used in the modification of various oils, including margarine, frying oil and cocoa butter substitutes using palm oils. Because fractionation helps to obtain stearin and olein with the desired quality and distribution (Tong et al., 2021). Fractionation can be done through three different methods: dry fractionation, solvent fractionation, and detergent fractionation. Dry fractionation which is the most common fractionation method enables thermomechanical separation of a mixture of acylglycerols by crystallization of the melt followed by

separation of the fractions by vacuum filtration. It does not use any additives. The disadvantage of dry fractionation is that a greater amount of olein is usually trapped in the stearin. (Papchenko et al., 2021).

Solvent fractionation has high efficiency, effectively separates components at low temperatures and provides purer products than other fractionation methods. However, it has high operating costs. However, solvent fractionation produces high value-added products containing certain triacylglycerides (Hasibuan et al., 2021). In solvent fractionation, solvents such as acetone reduce the viscosity of the oil during the process and increase the heat transfer coefficient. This also provides benefits such as controlled triglyceride distribution and high purity. However, there is a health risk due to the possibility of solvent residue in solvent fractionation (Tong et al., 2021).

Detergent fractionation is done by adding a detergent such as sodium lauryl sulfate to facilitate the separation of the liquid fraction olein and the solid fraction stearin. This method offers the advantages of shortening the fractionation time and producing a harder stearin. Nevertheless, detergent fractionation is rarely used today because detergent residue is problem (Tong et al., 2021). Excessive use of detergent increases the possibility of residue as well as waste. Insufficient use slows down the separation of solid and liquid fractions, and may cause the surface of the crystals formed to be rough and narrow, reducing quality (Hasibuan et al., 2018).

2.3. Interesterification

The properties of fats and oils are determined by their fatty acid composition and the stereochemistry of triacylglycerides, which consist of three fatty acids and one glycerol. The physicochemical properties of triacylglycerides vary depending on factors such as fatty acid chain length, degree of saturation, and the position of fatty acids in the glycerol backbone. While their functionality is limited in the natural state, triglyceride esters are redistributed on the glycerol bond and become functional with interesterification. The interesterification process consists of two stages: first, hydrolysis, followed by esterification (Zhang et al., 2020). This change in the TAG molecular structure plays a role in thermal or physicochemical properties such as melting point, crystallization behavior, solid fat ratio, oxidative stability, while trans fatty acids are not produced and the degree of unsaturation of fatty acids is preserved. (Zhang et al., 2022). The interesterification method is divided into two: chemical and enzymatic interesterification.

2.3.1. Chemical interesterification

In chemical interesterification, fatty acid transfer is carried out in the presence of chemicals such as sodium methylate (CH_3ONa) in the range of 80-120 °C. This method has been used since the 1920s (AOCS, 2021a).

Since the sodium methylate used as a catalyst reacts with H_2O and free fatty acids, the oil mixture should be dry and neutral. To achieve this, neutralized components are used, an amount of KOH is added to the reaction vessel,

and any moisture present is evaporated by vacuum. Some color formation can be observed during interesterification. The bleaching process is subsequently applied; therefore, RBD oils should not be used as raw materials. The oil mixture to be interesterified was dried before the catalyst was added. An amount of 0.05% by weight is adequate for sodium methylate. Although the reaction is too fast, it is generally allowed to continue for up to thirty minutes. The catalyst is deactivated by the addition of water, which results in soap formation. The use of water, which includes some acid for inactivation, results in the formation of free fatty acids instead of soap. Both soap and free fatty acids cause loss of efficiency, which is detrimental for chemical interesterification. Using more catalysts will further increase this yield loss (AOCS, 2021a).

2.3.2. Enzymatic interesterification

Enzymatic interesterification is gaining popularity in industrial applications as an effective method for lipid modification due to advances in immobilized enzyme technologies. It offers several advantages, including higher specificity, reduced environmental pollution, and basic post-processing processes. In addition, immobilized enzyme can be reused multiple times in carefully optimized interesterification processes, reducing costs (Cui et al., 2022).

Enzymatic interesterification is done by using enzymes to alter the fatty acid composition and distribution within triacylglyceride molecules. This process can be random or specific depending on the enzyme used. When a nonspecific lipase enzyme is used, the fatty acids are randomly redistributed between positions in the triacylglyceride molecule, resulting in changes in its physical properties. In contrast, a specific enzyme, like a sn-1,3-specific lipase, is designed to hydrolyze only the sn-1 and sn-3 positions, ideally leaving the sn-2 position unchanged. However, during application, acyl migration can occur and alter the fatty acid at the sn-2 position. Acyl migration involves the positively charged carbonyl carbon in TAG being attracted by the reaction catalyst, forming a tetrahedral intermediate, the diacylglyceride anion (DAG). This DAG anion then attacks a second activated triacylglyceride ester bond, forming an intermediate complex. The complex eventually dissociates, forming the newly interesterified molecule but it can cause loss of specialty (Singh et al., 2022).

A vertical column is used in the enzymatic interesterification process. This column contains the immobilized lipase enzyme. The oil mixture to be esterified is pumped from the upper part of the column and the feeding continues from above during the process. The oil that has been made interesterifying is extracted from the base. This process was carried out continuously at 70°C. However, when using a single reactor oxidized oils or citric acid and mineral acid residues may decrease the activity of the enzyme. To prevent this, more than one reactor should be used in the process, refining should be applied to the oils before interesterification or the

amount of residue should be controlled before the process (AOCS, 2021b).

2.3.3. Uses of interesterification and regulations

The main use of interesterification is the production of margarine. Trans fat is formed because of partial hydrogenation, which is an old production method. Many countries, including Türkiye, have applied legal regulations in response to the negative health effects of trans fats to prevent the presence of trans fat in foods, with the discovery that trans fat causes cardiovascular diseases. At this point, interesterification has become an option for partial hydrogenation. The interesterification method allows the production of vegetable oils that are trans fat free, while the initial amount of unsaturated fatty acids is preserved (Sivakanthan and Terrence, 2020).

Another application area is breast milk substitutes. Breast milk fat is essential as a source of nutrition and energy for infants. Therefore, alternative oils are needed to meet these needs, such as the inability to breastfeed. However, the fatty acid composition of breast milk varies from person to person, depending on factors such as diet, and interesterification studies have been carried out on palmitic acid, which is the richest saturated fatty acid in breast milk (Wei et al., 2019).

Third, the addition of new fatty acids during interesterification results in the production of structured lipids with increased nutritional value and potential health benefits. For example, omega-3 fatty acids can be incorporated into oils in this way (AOCS, 2021b). Among nutrients, low-calorie structured lipids, which can be considered another derivative of structured lipids, reduce the caloric value of most energy-giving fats (9 kcal/g) to intervene in increasing obesity worldwide. The caloric value is reduced by relatively reducing the density of medium-chain fatty acids or by reducing the intestinal absorption of long-chain fatty acids (Zárate et al., 2017).

The area where interesterification has just begun to be used is edible films. Edible films include carbohydrates, fats and proteins. The animal or vegetable oils contained in these films provide moisture barrier properties. In addition, unsaturated fatty acids reduce surface tension. A high oleic acid content of lipids resulting from interesterification is also considered more suitable for edible film production (Moore and Akoh, 2017).

Owing to the cost of cocoa butter, which is characteristic of chocolate, the search for a substitute for cocoa butter or equivalent oil has begun. The aim of interesterification at this point is to obtain alternatives with the lowest cost, easy availability and fatty acid composition, such as cocoa butter

There is no direct regulation on the areas where interesterification can be used. The European Commission (EC), in its 'EC working paper' on food processes using food enzymes, emphasises that food enzymes can be used to rearrange the position of fatty acids in triacylglycerols, thereby changing their physical properties (melting point) without creating trans

isomers and/or altered sensory properties, typically using lipases, and that interesterification is operated as a continuous process with immobilised lipases (EFSA, 2023).

In United States Food and Drug Administration (FDA) regulations, it is mentioned that sucrose in sucrose oligoesters can be produced by interesterification with methyl esters of fatty acids derived from edible oils and fats (including hydrogenated oils and fats), lipase enzyme obtained from culture filtrate obtained from pure culture fermentation of a pathogenic and toxin-free strain of *Rhizopus niveus* can be used in interesterification of oils. (FDA, 2023; FDA, 2024a).

On the other hand, there are many regulations in the world regarding the reduction of trans fat provided by interesterification. The first regulation study on the elimination of trans fat was carried out in Denmark in 2003. In the regulation applied since January 1, 2004, the amount of trans fat per 100 grams of fat or oil could not exceed 2 grams (Bjoernsbo et al., 2022). In 2020, Bangladesh, India, Paraguay, the Philippines and Ukraine adopted industrial trans fat limits, followed by Brazil, Peru, Singapore, Türkiye, the United Kingdom and the European Union in 2021 (WHO, 2021). According to the regulation that came into force in the European Union, the amount of trans fat, other than trans fat naturally found in animal fat, has been determined as 2 grams per 100 grams of fat (European Union, 2019). In 2015, the FDA determined that partially hydrogenated oils (PHOs), the main source of artificial trans fats in the food supply, were no longer "Generally Recognized As Safe" (GRAS). In 2021, partially hydrogenated oils were removed from the U.S. market. Also, on nutrition labels, trans fatty acids must be listed as "Trans fat" or "Trans" on a separate line below the saturated fat list (FDA, 2024b).

3. Recent Studies

With the increasing prevalence of interesterification, studies on the development of technology are increasing, along with studies on health. Table 1. shows recent the studies carried out on this topic. Current studies show that both enzymatic and chemical interesterification methods can be used on different oil mixtures and are a versatile modification method. It is observed that enzymatic interesterification is generally carried out at lower temperatures and thus higher tocopherol content is preserved. This can be interpreted as a reason why the enzymatic method provides better nutritional value preservation under less harsh processing conditions and therefore is preferred more than chemical interesterification. Because chemical interesterification can generally result in unwanted side effects with higher temperatures and catalyst usage. It can lower the melting point of oils and lead to the formation of undesirable crystal structures. For example, in a study comparing chemical and enzymatic interesterification, it was concluded that the oil mixtures that did not undergo interesterification had higher peroxide values and were

less stable than those that were interesterified, compared to animal-vegetable oil mixtures used at different ratios. It was also observed that enzymatic interesterification had less trans fat content, more free fatty acids and melting points than chemical interesterification (Okcu and Aktas, 2024). In another study, investigating the effect of enzymatic interesterification on the physicochemical properties and rheological behavior of *Cinnamomum camphora* seed kernel oil, *Pangasius bocourti* stearin and perilla seed oil mixtures, differences were observed on fatty acid distribution and physicochemical properties. As a result of interesterification, the crystal polymorphological form was transformed from - $\beta > \beta'$ to $\beta < \beta'$ and a more stable structure was obtained. It also decreased the crystallization onset temperature and peak temperature of low melting triacylglycerides. It was observed that spreadability and mouthfeel were improved compared to noninteresterified oil mixtures (Tian et al., 2024).

Table 1. Current studies on interesterification

Study	TI	Used Blend	Process Conditions	Result	References
Modification of palm oil mixture by interesterification and investigation of physicochemical properties, crystallization behaviors, oxidative stability	Enzymatic and chemical	Palm olein (50%), palm kernel oil (30%), palm stearin (20%)	Enzymatic: Fat fed with 60°C/100 mL/min flow, presence of lipozyme Chemical: 105°C/30 min, presence of 0.3% sodium methoxy catalyst	Enzymatic interesterification has reduced the fat content, and spreadability has improved. Fats with enzymatic interesterification at a lower temperature than chemical interesterification, crystallized faster than oils with chemical interesterification, and their tocopherol content is preserved.	(Zhen et al., 2021)
The impact of enzymatic interesterification on the nutritional and textural characteristics of butter containing milk fat.	Enzymatic	Milk fat and palm olein mixture (100:0, 80:20, 60:40, 40:60, 20:80, 0:100)	Enzymatic: 70°C/6 hours in the presence of 5% lipase	Enzymatic interesterification has added spreadability to the oil containing probiotics. The butter containing milk fat were improved by interesterification, which rised the oil bases unsaturation degree.	(Santos et al., 2020)
Chemical intersterifications impact on the production of cocoa butter substitutes using palm kernel stearin, coconut oil, and fully hydrogenated palm stearin mixtures.	Chemical	Palm Kernel stearin, coconut oil, hydrogenated palm stearin (10:10:80, 20:10:70, 30:10:60, 40:10:50, 50:10:40, 60:10:30, 70:10:20, 80:10:10)	Chemical: 88±2 °C, 1 hour, in the presence of 0.3% sodium methoxy catalyst and bubbling N_2	While the obtained oils have fine crystals in the desired β' polymorph, they have a lower solid fat value than cocoa butter. The melting behavior of oils originated from the interesterification of 60:10:30 and 70:10:20 mixtures showed a different melting characteristic and almost all melted at body temperature.	(Ornlaied et al., 2021)
Examination of Soybean Oil Interesterified with Propylene Glycol in Supercritical CO_2 Using NMR Spectroscopy.	Enzymatic	17 g of soybean oil with an equal amount of not more than 0.5% water	Enzymatic: Under 276 bar supercritical CO_2, in the presence of 17 g 1-2 propanediol/oil, in the presence of 0.3% lipozyme, 70°C/15 min	The use of interesterified soybean oil containing 1,2-propanediol can cause more environmentally friendly fats with lower trans fat content compared to commercially available soybean oils.	(Vafaei et al., 2020)
Generating trans fatty acids free using enzyme-catalyzed interesterified rice bran oil and fully hydrogenated rice bran oil.	Enzymatic	Rice bran oil and fully hydrogenated rice bran oil (9 blends alternating at 10% intervals 10:90...)	Enzymatic: Incubation for 24 hours at 60°C, 200 rpm in the presence of 10% lipozyme.	Interesterification has produced new triacylglycerides with moderate degree of unsaturation and suitability. These alterations affected the thermal behavior of the products, decreasing their melting points and fat content.	(Campioni et al., 2021)

TI= type of interesterification

Table 1. Current studies on interesterification (continuing)

Study	TI	Used Blend	Process Conditions	Result	References
Synthesis and characterization of behenic acid-rich lipid by enzymatic interesterification	Enzymatic	Mixture containing olive oil, soybean oil and fully hydrogenated thyme oil in a percentage of 43:43:14 (w/w) in 500 g mixture	Enzymatic: In the presence of 10% lipozyme, continued for 0,1,2,3,4 hours at different times, 60°C, under vacuum, in a 350 rpm mixer	Processing conditions did not affect tocopherol and chlorophyll a level, but increased carotenoid losses. When only olive oil, soybean oil or fully hydrogenated thyme oil and the mixture of these raw materials were compared in terms of oxidative stability, it was observed that interesterification did not cause any difference.	(Moreira et al., 2020)
Preparing trans fat-free bakery products by using margarine containing palm stearin and rice bran oil.	Chemical	Palm stearin, rice bran oil composition (50:50, 70:30, 60:40, 40:60)	Chemical: 90°C/1 hour, 0.8 bar absolute pressure, mixer speed 300 rpm	Chemical interesterification decreased the peroxide value of the mixtures and increased the free fatty acid value. Noninteresterified margarine samples showed fat separation during storage.	(Sewwandi and Arampath, 2022)
Producing trans-free oil through lipase-catalyzed interesterification of rice bran oil with hydrogenated cottonseed oil	Enzymatic	Rice bran oil-hydrogenated cottonseed oil blend (60:40, 70:30, 80:20, 90:10)	Enzymatic: At 50-55-60°C for/6 hours, presence of lipase enzyme at different rates (2.5%, 5%, 7.5% and 10%)	It was observed that the solid fat content decreased with the increase of the lipase enzyme concentration. Higher fat content was obtained at lower reaction temperature.	(Neeharika et al., 2015)

TI= type of interesterification

The process conditions of interesterification (temperature, presence of catalyst, duration, etc.) can also affect the chemical and physical properties of oils. It has been observed that chemical interesterification at high temperatures reduces the solid fat content of oils and increases their spreadability. The behavior of different oil mixtures after interesterification is also important for different process conditions and plays a critical role in the production of products such as margarine. For example, it was observed that the chemical interesterification of solid oil, carried out at 80°C, in which the deep eutectic solvent potassium carbonate was pretreated with glycerol, was more efficient than in the noninteresterified and untreated states of glycerol, the melting point of the solid oil increased significantly, and finer and more regular snowflake-like spherical crystals were formed in the interesterified oil (Meng et al., 2023).

3.1. Health Effects of Interesterification

There are very few investigations on interesterification health effects. Studies on the health effects of interesterification are given in Table 2. Existing health studies on interesterified oils generally examine short-term effects and do not provide definitive information about long-term health outcomes. Interesterification does not significantly affect the digestion of fats, sugar balance and insulin resistance. However, some interesterified fats may negatively affect metabolism not because of the process but because of their fatty acid content. They can particularly reduce insulin secretion and cause inflammation in white adipose tissue. Moreover, interesterification may alter the bioavailability of fats. The absorption of fats with high melting points may be delayed, which may lead to different processing of fats in the body.

Several human studies have shown that consuming interesterified oils for 3-6 weeks has no significant effect on blood lipids compared with noninteresterized oils. On the other hand, it can potentially contribute to reducing saturated fat intake to promote healthier dietary options. Nevertheless, reaching these bounds to the frequency and amount of consumption of products containing interesterified oil by different groups in the population. In addition, partial hydrogenation can produce trans fatty acids, while full hydrogenation can produce oils with a high saturated fat content. World Health Organization (WHO) recommends reducing trans fatty acid consumption and recommends that saturated fatty acid intake should not exceed 10% of the daily diet. WHO, which aims to decrease the consumption of trans fats that cause cardiovascular disease worldwide by 2023, recommends interesterified oils that do not contain trans fats as options for oils containing trans fatty acids (Berry et al., 2019; WHO, 2019). The effects of hydrogenation and interesterification on health make a significant difference in the content produced. It can be said that interesterification is a preferable fat modification method in terms of health because it prevents the production of

trans fat and reduces the saturated fat rate. Since fractionation is preferred as an intermediate stage, studies on health are insufficient to make a comprehensive assessment.

3.2. Effects of Interesterification on the Environment

When comparing the impacts of chemical and enzymatic interesterification on the environment, the energy consumption is greater in chemical interesterification, which has more process steps and occurs at higher temperatures.

In addition, less loss occurs during production in enzymatic interesterification. Thus, enzymatic interesterification is considered more environmentally friendly because of the minimum loss of energy, the main saving source, and the catalysts reused during production (AOCS, 2021b).

Table 2. Studies on the effect of interesterification on health

Study	Materials and Method	Effects on Health	References
Comparing the effect of interesterified oil on in vivo postprandial and in vitro lipid metabolism compared to a nonequivalent oil with a reference oil	Subject: Healthy adults aged 45-75 years (n=20) Tested oils: interesterified 80:20 palm stearin/palm kernel oil noninteresterified 80:20 palm stearin/palm kernel oil Experiment time: 8 hours Measurement: Triglyceride and lipoprotein values after consumption of 50 g fat for 4 weeks with 1-week intervals	The interesterification process does not affect the digestion of fats.	(Mills et al., 2021)
Investigation of the effects of interesterified palm oil on blood sugar balance and livers of rats.	Subject: Mice (n=72) Tested oils: palm oil, interesterfied palm oil Interesterified palm oil, which is given at a level to meet 10% of the energy in the daily diet. Interesterified palm oil, which is given at a level to meet 60% of the energy in the daily diet. Measurement: For 8 weeks: Insulin tolerance (4-hour intervals), pyruvate level in liver, body weight (once a week).	Consumption of interesterified fats may have an adverse impact on metabolic properties and insulin secretion, and a high-fat diet can cause inflammation in white adipose tissues. It has been stated that these oils cause the same results in rodents and humans, but there is no clear result.	(Miyamoto et al, 2020)
Investigation of the effects of diets rich in interesterified, noninteresterified and trans fats on the biochemical parameters and oxidative status of mice.	Subject: Mice (n=24) Tested oils: Interesterified oil rich in palmitic acid (39%) Noninteresting oil blend Partially hydrogenated vegetable oil (with trans fatty acid (20%) and linolenic acid (6%)) Experiment period: 75 days Measurement: At the end of the 75. day, triglyceride and cholesterol values in the blood	To conclude the change in the triglyceride structure of the fats with interesterification, the cholesterol values in the blood of the mice were found to be higher than the partially hydrogenated vegetable oil.	(de Lima et al., 2020)
Investigation of the effects of chemical interesterified oils rich in palmitic (C16:0) and stearic (C18:0) acids on insulin resistance using natural palm olein rich in C16:0.	Subject: Overweight, healthy adults (n=85) Tested oils: interesterified palm oil rich in palmitic acid (C16:0) Interesterified palm oil rich in stearic acid (C18:0) Natural palm olein rich in palmitic acid (C16:0) Experiment duration: 8 weeks Measurement: Nutrition was carried out to take 35% of the daily diet from fat, and blood sugar and insulin resistance measurement at 0, 6 and 8 weeks	Interesterified oils do not have a significant effect on insulin resistance.	(Ng et al., 2018)
Investigation of interesterification on the bioavailability of fatty acids in lipids (in flaxseed oil and palm stearin blends) using structured (sn-1,3 stereospecific lipase) effects	Subject: Mice (n=48) Tested oils: Blends of interesterified and noninteresterified linseed oil and palm stearin (70-30, 60-40, 50-50 ratios) Experiment duration: After 1 time fasting for 18 hours Measurement: Fat profile of plasma lipids at 0,1.5,3,4.5, 6 and 12 hours	Its high melting point delays lipid absorption. Interesterification changes the bioavailability of oils.	(Farfán et al., 2013)

Table 2. Studies on the effect of interesterification on health (continuing)

Study	Materials and Method	Effects on Health	References
Impact of intersterification of palmitic acid-rich triglyceride on postprandial lipid	Subject: Healthy people (n=38) Tested oils: Interesterified palm oil, crude palm oil, sunflower oil with high oleic acid Experiment Period: 3 days Measurement: Measurement of insulin, lipoprotein and triglyceride in the blood after meals (measurement in 1-hour intervals after the first 2 hours 30 minutes until the 6th hour)	Consumption of interesterified oils causes lower lipoprotein and triglyceride levels compared to crude palm oil and sunflower oil containing high oleic acid. Insulin concentration was not affected by oil.	(Berry et al., 2007)
Impact of interesterification on acute metabolic risk factors for stearic acid-rich spreadable oil	Subject: Health people (n=24) Tested oils: High oleic acid Sunflower oil – fully hydrogenated canola stearin (70-30%) oil is noninteresterified, chemically interesterified (0.3% sodium methoxy – 85°C) and enzymatic interesterified (5% Candida antarctica lipase – 60°C) Experiment time: 3 days Measurement: Individuals who consume 25% of the total energy in the diet with fat, 0-60. 15 min interval between min, 60-90. HDL cholesterol, total cholesterol, free fatty acid and glucose measurement in the blood with 30 minutes intervals between minutes and 60 minutes after 90 minutes	No interesterification method has been found to affect glucose, insulin or free fatty acids and triglycerides.	(Robinson et al., 2009)
Effect of interesting palm olein on postprandial glucose-dependent response in type 2 diabetes	Subject: People with type-2 diabetes (n=23) Tested oils: Palm olein, interesterified palm olein, sunflower oil with high oleic acid Experiment period: 1 year Measurement: Between 0-360. min after consumption of 50 g of oil per week. Measurement of lipid and glucose level in the blood	Interesterified fat has no effect on glucose balance in type-2 diabetes subjects.	(Mo et al., 2019)
Effects of interesterified palm oil on inflammation of white adipose tissues and metabolic disturbances	Subject: Mice (n=60) Tested oils: Soybean oil (4%), palm oil (23.8%), lard and interesterified palm oil Experiment period: 8 weeks Measurement: The control group (C) was fed a standard diet with 4% soybean oil, the high-fat group (HF) was fed 23.8% lard, the high palm oil fat group (HFP) was fed 23.8% palm oil, and the high interesterified palm oil fat group (HFI) was fed 23.8% interesterified palm oil.	The adverse effects of a high-fat diet do not differ whether interesterification in lipid sources is present or not. Adverse effects have been observed in mice regarding white adipose tissue hypertrophy, hepatic steatosis, and insulin resistance. However, human studies are needed.	(Martins et al., 2024)
Comparison of postprandial lipid and vascular responses of an interesterified palmitic acid-rich margarine to functionally equivalent noninteresterified margarine and butter.	Subject: Healthy people (n= 50 (25 men, 25 women; 35–75 years)) Tested Oils: Interesterified, noninteresterified palm based fats, butter Experiment period: 1 week Measurement: Between 07:30-09:00 a consumption 50 g of oil a week. Measurement of blood samples.	The long-term implications of these differences in postprandial markers of cardiometabolic health are unclear. However, commercial interesterified oil may have a neutral postprandial effect when compared with similar products without interesterified oil in healthy adults. An interesterified oil containing 17% palmitic acid causes similar postprandial lipemia to an oil containing 28% palmitic acid and spreadable butter.	(Hall et al., 2024)

4. Conclusion

In conclusion, interesterification is a modification method that makes human life easier in terms of health, environment and economy, can be considered advantageous. Although more research is needed on the health effects, the health effects of trans fatty acids that may form in partial hydrogenation and saturated fatty acids that may form in full hydrogenation can be prevented by interesterification. Studies that especially show that the processing of oil does not affect health show that the effect may not be due to the process but to the end products that may be formed as a result of the process. In addition, products made as an alternative to breast milk, enriching foods with omega 3 fatty acids, and contributing to food safety by using them in edible film production also have a positive effect on health.

When examined from an environmental perspective, the fact that the enzyme can be reused and leaves little waste in enzymatic interesterification makes an important contribution. Process residues can negatively affect the environment. In addition, energy saving and efficiency also contribute to being environmentally friendly. Energy saving and reuse of the catalyst contribute not only environmentally but also economically. Moreover, it provides significant contributions to the food sector by preserving the quality of food, helping to obtain the desired product, and helping to produce trans fat-free margarine. It is also a good solution to partial hydrogenation, which the FDA has banned in order to limit trans fat. It also contributes to the reduction of health expenditures by indirectly minimizing the negative effects on health.Interesterification is affected by issues such as fatty acid composition and stereochemistry of triacylglycerides, temperature, process time, catalyst usage, and the condition of the oil mixture, and acyl migration and residue problems may be encountered. Although both interesterification methods are used, enzymatic interesterification has become more preferred in recent years. We recommended that researchers who will work on this subject in the future should work on enzymatic interesterification.

Although interesterification makes life easier in many ways, more studies are needed, especially in the health field. We recommend that such a widely used method be risk assessed by national and international authorities.

Author Contributions

The percentage of the author(s) contributions is presented below. All authors reviewed and approved the final version of the manuscript.

	B.İ.	F.A.
C	50	50
D	20	80
S		100
DCP	50	50
DAI	50	50
L	80	20
W	90	10
CR	20	80
SR	50	50
PM	20	80
FA	50	50

C= concept, D= design, S= supervision, DCP= data collection and/or processing, DAI= data analysis and/or interpretation, L= literature search, W= writing, CR= critical review, SR= submission and revision, PM= project management, FA= funding acquisition.

Conflict of Interest

The authors declared that there is no conflict of interest.

References

American Oil Chemists' Society (AOCS). 2021a. Chemical interesterification. URL: https://lipidlibrary.aocs.org/edible-oil-processing/chemical-interesterification (accessed date: August 28, 2024).

American Oil Chemists' Society (AOCS). 2021b. Enzymatic interesterification. URL: https://lipidlibrary.aocs.org/edible-oil-processing/enzymatic-interesterification (accessed date: August 28, 2024).

Berry S, Bruce H, Steenson S, Stanner S, Buttriss L, Spiro A, Gibson S, Bowler I, Dionisi F, Farrell L, Glass A, Lovegrove JA, Nicholas J, Peacock E, Porter S, Mensink P, Hall W. 2019. Interesterified fats: What are they and why are they used? Nutr Bull, 44(4): 363-380. https://doi.org/10.1111/nbu.12397

Bhandari SD, Delmonte P, Honigfort M, Yan W, Dionisi F, Fleith M, Iassonova D, Bergeson L. 2020. Regulatory changes affecting the production and use of fats and oils: Focus on partially hydrogenated oils. J Am Oil Chem Soc, 97(7): 797-815. https://doi.org/10.1002/aocs.12366

Bjoernsbo KS, Joensen AM, Joergensen T, Lundbye-Christensen S, Bysted A, Christensen T, Fagt S, Capewell S, O'Flaherty M. 2022. Quantifying benefits of the Danish transfat ban for coronary heart disease mortality 1991-2007: Socioeconomic analysis using the IMPACTsec model. PLoS One, 17(8): e0272744. https://doi.org/10.1371/journal.pone.0272744

Campioni NC, Pereyra LS, Ribier APB, Alpuy IJ. 2021. Zero-trans fats designed by enzyme-catalyzed interesterification of rice bran oil and fully hydrogenated rice bran oil. OCL, 46: 1-11. https://doi.org/10.1051/ocl/2021036

Cui H, Li J, Xu X, Li J, Lu M, Song H, Wang S, Yang L, Zhu D, Liu H. 2022. Enzymatic interesterification of beef tallow/coconut oil blends to produce a superior margarine base stock. J Food Sci

Technol, 57(2): 908-919. https://doi.org/10.1111/ijfs.15314

de Lima EE, Castro W, Grinevicius A, Hilbig J, Mota S, Zeferino RC, da Silva RC, Jachmanián I, da Silva EL, Pedrosa RC, Block JM. 2020. Effect of a diet rich in inter-esterified, non-inter-esterified, and trans fats on biochemical parameters and oxidative status of Balb-c mice. Food Nutr Sci, 11(11): 1032-1052. https://doi.org/10.4236/fns.2020.1111073

DiNicolantonio JJ, O'Keefe JH. 2022. Monounsaturated fat vs saturated fat: Effects on cardio-metabolic health and obesity. Mo Med, 119(1): 69-73. PMID: 36033137; PMCID: PMC9312452.

European Food Safety Authority (EFSA). 2023. Scientific opinion on the safety of interesterified oils in food. EFSA J, 21(7): Article 8094. https://doi.org/10.2903/j.efsa.2023.8094

European Union. 2019. Regulation (EU) 2019/649 of 24 April 2019 amending Annex III to Regulation (EC) No 1925/2006 of the European Parliament and of the Council as regards trans fats, other than trans fats naturally occurring in fat of animal origin. J European Union, L 110: 17-20. https://eur-lex.europa.eu/legal-content/EN/TXT/PDF/?uri=CELEX:32019R0649&from=EN

Farfán M, Villalón MJ, Ortíz ME, Nieto S, Bouchon P. 2013. The effect of interesterification on the bioavailability of fatty acids in structured lipids. Food Chem, 139(1-4): 571-577. https://doi.org/10.1016/j.foodchem.2013.01.024

Hall WL, Alkoblan A, Gibson PS, D'Annibale M, Coekaerts A, Bauer M, Bruce JH, Lecomte B, Penhoat A, Laugerette F, Michalski MC, Salt LJ, Wilde PJ, Berry SE. 2024. Postprandial lipid and vascular responses following consumption of a commercially-relevant interesterified palmitic acid-rich spread in comparison to functionally-equivalent noninteresterified spread and spreadable butter: A randomized controlled trial in healthy adults. Food Funct, 15(5): 2733-2750. https://doi.org/10.1039/d3fo05324e

Harvard Health Publishing. 2022. The truth about fats: The good, the bad, and the in-between. Harvard Health. URL: https://www.health.harvard.edu/staying-healthy/the-truth-about-fats-bad-and-good (accessed date: August 28, 2024).

Hasibuan HA, Sitanggang AB, Andarwulan N, Hariyadi P. 2021. Solvent fractionation of hard palm stearin to increase the concentration of tripalmitoylglycerol and dipalmitoyl-stearoyl-glycerol as substrates for synthesis of human milk fat substitute. J Food Sci Technol, 56(9): 4549-4558. https://doi.org/10.1111/ijfs.15206

Hasibuan VR, Aini N, Febriyanti F, Pane, SAA. 2018. The effect of additional detergent in crude palm oil in the process of separation stearin. In: International Conference on Innovation in Education, Science and Culture, November 8–9, Medan, Indonesia, pp: 64. https://doi.org/10.1088/1742-6596/970/1/012020

Karageorgou D, Rova U, Christakopoulos P, Katapodis P, Matsakas L, Patel A. 2023. Benefits of supplementation with microbial omega-3 fatty acids on human health and the current market scenario for fish-free omega-3 fatty acid. Trends Food Sci Technol, 136: 169-180. https://doi.org/10.1016/j.tifs.2023.04.018

Martins BC, da Silva Ribeiro M, Teixeira AVS, et al. 2024. Consumption of interesterified palm oil leads to inflammation of white adipose tissue and triggers metabolic disturbances in mice on a high-fat diet. Sci Reports, 14: 12530. https://doi.org/10.1038/s41598-024-63488-9

Meng E, Li J, Liu W, Yang G, Yang R, Liang S, Sun C. 2023. Deep eutectic solvent-inspired solid alkali carbonate for highly efficient interesterification of lard. LWT, 186: 115232. https://doi.org/10.1016/j.lwt.2023.115232

Mills CE, Harding SV, Bapir M, Mandalari G, Salt LJ, Gray R, Fielding BA, Wilde PJ, Hall WL, Berry SE. 2021. Palmitic acid-rich oils with and without interesterification lower postprandial lipemia and increase atherogenic lipoproteins compared with a MUFA-rich oil: A randomized controlled trial. Am J Clin Nutr, 113(5): 1221-1231. https://doi.org/10.1093/ajcn/nqaa413

Miyamoto JE, Reginato A, Portovedo M, dos Santos RM, Stahl MA, Le Stunff H, Milanski M. 2020. Interesterified palm oil impairs glucose homeostasis and induces deleterious effects in liver of Swiss mice. Metabolism, 112, 154350. https://doi.org/10.1016/j.metabol.2020.154350

Mo SY, Lai OM, Chew BH, Ismail R, Bakar AS, Jabbar NA. 2019. Production and characterization of a trans-free interesterified blend prepared from palm stearin and rice bran oil. Food Chem, 288: 126-132. https://doi.org/10.1016/j.foodchem.2019.02.106

Moore MA, Akoh CC. 2017. Enzymatic interesterification of coconut and high oleic sunflower oils for edible film application. J Am Oil Chem Soc, 94(4): 567-576. https://doi.org/10.1007/s11746-017-2969-z

Moreira DKT, Gandra RL, Zuin JC, Ract JNR, Ribeiro APB, Macedo JA, Gambero A, Akil E, Torres GA, Macedo GA. 2020. Synthesis and characterization of structured lipid rich in behenic acid by enzymatic interesterification. Food Bioprod. Process. 122, 303-310. https://doi.org/10.1016/j.fbp.2020.06.005

National Library of Medicine (NIH). 2024. "Interesterification". URL: https://pubmed.ncbi.nlm.nih.gov/?term=Interesterification (accessed date: August 28, 2024).

Neeharika SVR, Rallabandi R, Ragini Y. 2015. Lipase catalyzed interesterification of rice bran oil with hydrogenated cottonseed oil to produce trans free fat. . J Food Sci Technol, 52: 4905–4914. https://doi.org/10.1007/s13197-014-1563-8

Ng YT, Voon PT, Ng TK, Lee VKM, Sahri M, Esa N, Ong SH, Ong ASH. 2018. Interesterified palm olein (IEPalm) and interesterified stearic acid-rich fat blend (IEStear) have no adverse effects on insulin resistance: A randomized control trial. Nutrients, 10(8): 1112. https://doi.org/10.3390/nu10081112

Okcu BN, Aktas AB. 2024. Characterization of structured lipids produced through interesterification of blends comprising beef tallow, milk, and vegetable oil using infrared spectroscopy. J Am Oil Chem Soc, 101(3): 309–320. https://doi.org/10.1002/aocs.12801

Ornlaied P, Podchong P, Sonwai S. 2021. Synthesis of cocoa butter alternatives from palm kernel stearin, coconut oil, and fully hydrogenated palm stearin blends by chemical interesterification. J Sci Food Agric, 102(4): 1619-1627. https://doi.org/10.1002/jsfa.11498

Oroian M. 2024. A new perspective regarding the adulteration detection of cold-pressed oils. LWT, 198: 116025. https://doi.org/10.1016/j.lwt.2024.116025

Papchenko V, Matveeva T, Khareba V, Khareba O. 2021. Fractionation of oil from a new line of sunflower seeds. Food Sci. Technol, 15(3): 71-79. https://doi.org/10.15673/fst.v15i3.2117

Rasor AS, Duncan SE. 2014. Fats and oils - Plant based. In: Clark S, Jung S, Lamsal B, editors. Food processing: Principles and applications. Wiley Blackwell, 2nd ed., pp: 457-481. ISBN: 978-0-470-67114-6.

Robinson DM, Martin NC, Robinson LE, Ahmadi L, Marangoni AG, Wright A. 2009. Influence of interesterification of a stearic acid-rich spreadable fat on acute metabolic risk factors. Lipids, 44: 17–26. https://doi.org/10.1007/s11745-008-3253-7

Santos, C. S., Kanup, R. F., Albuquerque, M. A. C., Bedani, R., Santos CS, Kanup RF, Albuquerque MAC, Bedani R, Souza CHB, de Gioielli LA, Saad SMI, Ract JNR. 2020. Effect of enzymatic interesterification on the textural and nutritional properties of a probiotic table spread containing milk fat. LWT, 124: 109129. https://doi.org/10.1016/j.lwt.2020.109129

Sewwandi SDC, Arampath PC. 2022. Preparation of trans fat-free bakery margarine with rice bran oil and palm stearin. World J. Food Sci Technol, 6(2): 31-38. https://doi.org/10.11648/j.wjfst.20220602.12

Shah B, Thadani U. 2019. Trans fatty acids linked to myocardial infarction and stroke: What is the evidence? Trends Cardiovasc Med, 29(5): 306-310. https://doi.org/10.1016/j.tcm.2018.09.01

Singh PK, Chopra R, Garg M, Dhiman A, Dhyani A. 2022. Enzymatic interesterification of vegetable oil: A review on physicochemical and functional properties, and its health effects. J Oleo Sci, 71(12): 1697-1709. https://doi.org/10.5650/jos.ess22118

Sivakanthan S, Terrence M. 2020. Current trends in applications of enzymatic interesterification of fats and oils: A review. LWT 132: 109880. https://doi.org/10.1016/j.lwt.2020.109880

Spessato A, Rivero Meza S, Cañizares L, Timm N, Mardade C, Rombaldi C, Oliveira M. 2023. Effect of industrial bleaching on the physicochemical and nutritional quality of non-allergenic lecithin derived from rice bran oil (Oryza sativa L.). Biocatal. Agric Biotechnol, 51: 102768. https://doi.org/10.1016/j.bcab.2023.102768

Thirumdas R. 2023. Partial hydrogenation of oils using cold plasma technology and its effect on lipid oxidation. J Food Sci Technol, 60(7): 1674–1680. https://doi.org/10.1007/s13197-022-05434-z

Tian W, Yan X, Zeng Z, Xia J, Zhao J, Zeng G, Yu P, Wen X, Gong D. 2024. Enzymatic interesterification improves the lipid composition, physicochemical properties and rheological behavior of Cinnamomum camphora seed kernel oil, Pangasius bocourti stearin and perilla seed oil blends. Food Chem, 430: 137026. https://doi.org/10.1016/j.foodchem.2023.137026

Tong SC, Tang TK, Lee YY. 2021. A review on the fundamentals of palm oil fractionation: Processing conditions and seeding agents. Eur J Lipid Sci Technol, 123(12): 2100132. https://doi.org/10.1002/ejlt.202100132

Troncoso FD, Costilla IO, Tonetto GM. 2022. Hydrogenation of vegetable oil using highly dispersed Pt/γ-Al2O3 catalyst: Effects of key operating parameters and deactivation study. J Am Oil Chem Soc, 99(8): 697–710. https://doi.org/10.1002/aocs.12614

U.S. Food and Drug Administration (FDA). 2023. Decision 172.869: Oxystearin. Code of Federal Regulations Title 21. URL:https://www.accessdata.fda.gov/scripts/cdrh/cfdocs/cfcfr/CFRSearch.cfm?fr=172.869 (accessed date: August 28, 2024).

U.S. Food and Drug Administration (FDA). 2024a. Decision 184.1420: Methyl stearate. Code of Federal Regulations Title 21. URL: https://www.accessdata.fda.gov/scripts/cdrh/cfdocs/cfcfr/CFRSearch.cfm?fr=184.1420 (accessed date: August 28, 2024).

U.S. Food and Drug Administration (FDA). 2024b. Trans fat. U.S. Food and Drug Administration. URL: https://www.fda.gov/food/food-additives-petitions/trans-fat (accessed date: August 28, 2024).

Vafaei N, Eskin MNA, Rempel CB, Jones PTJ, Scanlon MG. 2020. Interesterification of soybean oil with propylene glycol in supercritical carbon dioxide and analysis by NMR spectroscopy. Appl. Biochem. Biotechnol, 191: 905–920. https://doi.org/10.1007/s12010-019-03200-0

Web of Science (WoS) Database. 2024. "Interesterification". URL: https://0-www-webofscience-com.divit.library.itu.edu.tr/wos/woscc/analyze-results/097f2189-581d-49b9-b9ee-20247a4103ce-010472f488 (accessed date: August 28, 2024).

Wei W, Jin Q, Wang X. 2019. Human milk fat substitutes: Past achievements and current trends. Prog Lipid Res, 74: 69-86. https://doi.org/10.1016/j.plipres.2019.02.001

World Health Organization (WHO). 2018. Nutrition: Trans fat. URL: https://www.who.int/news-room/questions-and-answers/item/nutrition-trans-fat (accessed date: August 28, 2024).

World Health Organization (WHO). 2019. Replace Trans Fat: Promote (No. 2, pp. 15-17). URL: https://cdn.who.int/media/docs/default-source/nutritionlibrary/replace-transfat/replace-module-2-p.pdf?sfvrsn=e9f83030_4 (accessed date: August 28, 2024).

World Health Organization (WHO). 2021. Countries with regulations protecting people from industrially produced trans fat tripled over the past year. World Health Organization. URL: https://www.who.int/news/item/07-12-2021-countries-with-regulations-protecting-people-from-industrially-produced-trans-fat-tripled-over-the-past-year (accessed date: August 28, 2024).

Zárate R, El Jaber-Vazdekis N, Tejera N, Pérez JA, Rodríguez C. 2017. Significance of long chain polyunsaturated fatty acids in human health. Clin Transl Med, 6(1): 25. https://doi.org/10.1186/s40169-017-0153-6

Zbikowska A, Onacik-Gür S, Kowalska M, Rutkowska J. 2019. Trans fatty acids in Polish pastry. J Food Prot, 82(6): 1028-1033. https://doi.org/10.4315/0362-028X.JFP-18-497

Zbikowska A, Onacik-Gür S, Kowalska M, Zbikowska K, Feszterová M. 2023. Trends in fat modifications enabling alternative partially hydrogenated fat products proposed for advanced application. Gels, 9(6): 453. https://doi.org/10.3390/gels9060453

Zhang Z, Lee WJ, Wang Y. 2020. Evaluation of enzymatic interesterification in structured triacylglycerols preparation: A concise review and prospect. Crit Rev Food Sci Nutr, 61(19): 3145-3159. https://doi.org/10.1080/10408398.2020.1793725

Zhang Z, Xie X, Lee WJ, Zhao G, Li C, Wang Y. 2022. The effects of interesterification on the physicochemical properties of Pangasius bocourti oil and its fractions. Food Chem, 371: 131177. https://doi.org/10.1016/j.foodchem.2021.131177

Zhen Z, Jing Y, Wan JL, Casimir CA, Aijun L, Yong W. 2021. Modification of palm-based oil blend via interesterification: Physicochemical properties, crystallization behaviors, and oxidative stabilities. Food Chem, 347: 129070. https://doi.org/10.1016/j.foodchem.2021.129070

ARTIFICIAL INTELLIGENCE IN MEDICINE; OPPORTUNITIES AND CHALLENGES

Tahmineh DARVISHMOHAMMADI[1], Ayşe ÖZKAL[2]*, Ahmet Selim ÖZKAL[3]

[1]*Pamukkale University, Faculty of Natural and Applied Sciences, Department of Biology, Denizli, Türkiye*
[2]*Pamukkale University, Faculty of Engineering, Department of Textile Engineering, 20070, Denizli, Türkiye*
[3]*Gazi University, Faculty of Medicine, Department of Internal Medicine, 06570, Ankara, Türkiye*

Abstract: Currently, artificial intelligence (AI) is used in many fields of medicine such as cardiology, endocrinology, neurology, and particularly gastroenterology where AI increases the quality of images obtained from related imaging techniques. Also, medical diagnosis is greatly affected by AI algorithms and deep learning techniques. AI shows potential for not only monitoring and managing treatment plans but also promises accurate diagnosis and prediction of diseases. This paper aims to review the future opportunities and challenges of AI applications in medicine. The results show a bright future with multiple opportunities in medical diagnosis, radiology, and pathology fields with increasing accuracy, image quality, and decreasing radiation dose. Additionally, AI will facilitate medical research studies which is a great contribution to the medical world. Challenges and ethical limitations will be mostly related to the validity and reliability of data, bias, responsibility issues, risks and unpredictable consequences, and equitable application which need establishing clear guidelines and regulations. This paper suggests a more extended educational program for both healthcare professionals and patients to achieve the best result.

Keywords: Artificial intelligence, Medical technologies, Medicine, Medical diagnosis

1. Introduction

Artificial intelligence (AI) is a field that aims to fabricate machines that can perform human-like tasks such as decision-making, problem-solving, language processing and learning from data. A wide range of disciplines, including technology, psychology, neuroscience, biology, mathematics, social sciences and philosophy, fall within the scope of AI and AI aims to solve complex problems by imitating human cognitive abilities (Velagaleti, 2023).

The first use of the artificial intelligence (AI) concept (computers think as intelligent as humans) was raised as early as 1950. Although AI applications in medicine experienced a slow development trend compared to engineering, it has revolutionized medicine (Kaul et al., 2020). AI in healthcare can save time, reduce costs, and improve patient management, while also supporting recruitment and retention of healthcare professionals in rural areas rural health facility recruitment and retention. However, challenges include delayed adoption, a lack of ongoing implementation of technology within the healthcare system and insufficient consideration of user perspectives and feedback (Sunarti et al., 2021).

As a result, personalized medicine has emerged replacing the old version of algorithm-based medicine (Kaul et al., 2020). Generally, AI has the potential to predict diagnoses and therapeutic response in medicine. To mention some examples of AI in predicting and diagnosing diseases, we can refer to its potential to detect early-stage Alzheimer's disease using Support Vector Machines (SVM) and statistical tools. Other examples include analyzing retinal fundus images in diabetic patients using Convolutional Neural Networks (CNN), identifying brain lesion segmentation by multi-scale 3D CNN, and predicting ischemic stroke thrombolysis using a combined approach of CNN and Artificial Neural Networks (Kamdar et al., 2020). Although, it can increase the accuracy of diagnosis which leads to better efficacy of therapeutic processes (Ruffle et al., 2019), the development of AI in medicine has raised questions about how this technology might affect trustworthy relationships in clinical settings (McDougall, 2018).

The importance of this study lies in its potential to bridge the gap between emerging technologies in computer science and their applications in medical care systems, particularly in diagnosis, disease control, and management. As AI continues to reshape the medical landscape and shift decision-making processes towards data-centric insights (Filipp, 2019), understanding its implications and challenges is critical not only for patient care but also for informing medical education. Therefore, the broader impact of AI-based technologies on the

medical community and patient outcomes underscores the significance of this review paper.

This paper aims to review the current applications of AI in various fields of medicine, particularly in medical diagnosis, and also to explore the opportunities, challenges, ethical implications, and future directions in this area.

1.1. Current Application of AI in Different Fields of Medicine

Artificial intelligence (AI) is transforming the healthcare industry through improvements in patient outcomes, therapeutic planning, diagnostic accuracy, and operational efficiency. Large volumes of medical data are analyzed using AI and machine learning (ML) technologies to find patterns and anomalies that can be used for personalized medication and early disease diagnosis (Kuwaiti et al., 2023). The use of these technologies enhances administrative efficiency, resource allocation, and patient engagement with virtual assistants and chatbots (Velagaleti, 2023). Additionally, AI helps healthcare practitioners by combining human knowledge with analytical skills, guaranteeing a human-in-the-loop strategy for high-quality and safe healthcare services. The transformative influence of artificial intelligence (AI) on healthcare delivery and patient outcomes is demonstrated by its use in medical imaging, diagnostics, virtual patient care, drug development, patient engagement, and rehabilitation. Incorporating AI into healthcare systems presents several ethical, social, and technical concerns that must be addressed through with effective governance (Sezgin, 2023).

Currently, AI is applied in multiple medical fields. In cardiology, AI is not only applied to FDA-approved ECG monitoring and atrial fibrillation applications but also can significantly predict the risk of cardiovascular diseases. It is shown that AI-based systems can identify incidents of atrial fibrillation more than routine clinical care and can subsequently impact the lower incidence of ischemic strokes (Halcox et al., 2017). In endocrinology fields, AI has been applied to glucose monitoring systems which helps the patients to obtain better control of their blood glucose (Christiansen et al., 2017). In addition, in neurology, AI plays an important role in disease management. For example, wearable technology can detect epilepsy seizures and report them on mobile applications (Regalia et al., 2019). Another example is the assessment of gait, posture, and tremors in multiple sclerosis, Parkinson's disease or Huntington's disease (Dorsey et al., 2018). AI also plays a crucial role in diagnostic medicine, particularly in increasing the accuracy of cancer histopathology. It is demonstrated that it is feasible to develop and deploy a robust computational decision support system for pathology that can scale to large datasets and integrate into clinical workflows, improving diagnostic efficiency and accuracy (Campanella et al., 2019).

There are great advancements in AI in different fields of medicine. However, special improvements in the field of gastroenterology were observed (Kaul et al., 2020). In this field, artificial intelligence and deep learning help increase the quality of images obtained from endoscopy (Yang and Bang, 2019) and colonoscopy in a way that can revolutionize gastroenterological practice for prediction, personalization, and automation in diagnostics and treatment (Ruffle et al., 2019). For example, AI successfully differentiates chronic pancreatitis from pancreatic cancer which has been a challenge in the field (Zhu et al., 2013). AI has particularly advanced AI-assisted endoscopy for more accurate detection of gastrointestinal polys or lesions (Hoogenboom et al., 2020). AI-assisted systems have gone beyond by predicting bleeding, increasing the survival rate of cancer, and metastasis in colorectal cancer and can significantly reduce the rate of unnecessary additional surgeries (Ichimasa et al., 2018). The summary of these studies on the application of AI in various medical fields, including aims, technology, and results is demonstrated in Table 1.

1.2. AI Application in Medical Diagnosis

The application of AI in medical diagnosis has been particularly successful. Specifically, multiple AI algorithms and deep learning techniques have been used successfully in diagnosing diseases such as Alzheimer's, Parkinson's, skin cancer, and stroke. Also, image analysis has had a significant impact on. For example, new techniques have been employed in analyzing medical images like mammograms, MRI scans, and anatomical images for stroke diagnosis. Additionally, Natural Language Processing (NLP) has been utilized to extract information from clinical notes and radiology reports for the identification, classification, and prediction of diseases (Kamdar et al., 2020). For example, the first NLP was introduced by Fiszman which was a device to read X-ray language on the chest (Fiszman et al., 2000). Also, in another study least square support vector machine (LSSVM) was introduced to detect cancer at an early stage (Sweilam et al., 2010). In 2017, NLP was used to differentiate between peripheral arterial diseases and other arterial diseases with more than 90% accuracy (Afzal et al., 2017). The three main domains of AI application in medical diagnosis are illustrated in Figure 1.

Table 1. Summary of studies on the application of AI in various medical fields, including aim, technology, and results. AI had a great impact on diagnosis and managing the treatment process in multiple fields of medicine such as cardiovascular, endocrinology, neurology, gastroenterology and oncology

Field of Medicine	Aim of the study	Technology	Result	Reference
Cardiovascular Diseases	Evaluating the effectiveness of monitoring using an AI-based electrocardiographic capture system, compared to routine clinical care in diagnosing atrial fibrillation (AF) in individuals over 65 years age with ≥1 additional stroke risk factor	AliveCor Kardia device, a smartphone/tablet-based single-lead electrocardiographic capture system	Screening with this method can significantly identify incidents of atrial fibrillation more than routine clinical care and can impact on AF detection and the lower incidence of ischemic strokes	Halcox et al. (2017)
Endocrinology	Evaluating the performance, safety, and accuracy of an AI based glucose sensor, particularly when used in conjunction with an insulin pump, mobile device application, or glucose sensor recorder (GSR), in individuals with type 1 or type 2 diabetes	Guardian Sensor 3 glucose sensor	Demonstrated accuracy and precision across a range of glucose levels (hypoglycemic, euglycemic, and hyperglycemic)	Christiansen et al. (2017)
Neurology	Evaluating the effectiveness of generalized tonic-clonic seizure (GTCS) detection and monitoring using AI-based wearable devices.	These devices use a machine learning algorithm to recognize the physiological signatures of GTCS events based on accelerometer (ACC) and electrodermal activity (EDA) data.	Showed effective with high sensitivity (over 92%) and a low false alarm rate (FAR), especially during rest, making them promising tools for seizure detection.	Regalia et al. (2019)
Diagnosis of Cancer in Histopathology	To develop a decision support system for pathology that overcomes the limitations of traditional methods using an AI-based system that only use the reported diagnoses as labels for training, so avoiding the time-consuming and expensive process of pixel-wise manual annotation.	A deep learning framework that combines convolutional neural networks with RNNs under a multiple-instance learning approach	Showed the feasibility to develop and deploy a robust computational decision support system for pathology that can scale to large datasets and integrate seamlessly into clinical workflows, improving diagnostic efficiency and accuracy.	Campanella et al. (2019)
Gastroenterology	A review to evaluate potential applications of AI and machine learning to improve predictive modelling, personalize medicine, and enhance diagnostic and therapeutic interventions in gastroenterology.	Machine learning (ML), deep learning and computer vision	Showed advanced tools can revolutionize gastroenterological practice for prediction, personalization, and automation in diagnostics and treatment.	Ruffle et al. (2019)
Colorectal Cancer	To Evaluate whether AI could predict the presence of lymph node metastasis in patients with T1 colorectal cancer after endoscopic resection, with the goal of reducing the need for unnecessary additional surgeries.	An AI model was developed using machine learning techniques to analyze 45 clinicopathological factors and predict the presence or absence of lymph node metastasis	The AI model showed better performance in predicting lymph node metastasis compared to existing guidelines, significantly reducing the rate of unnecessary additional surgeries.	Ichimasa et al. (2018)
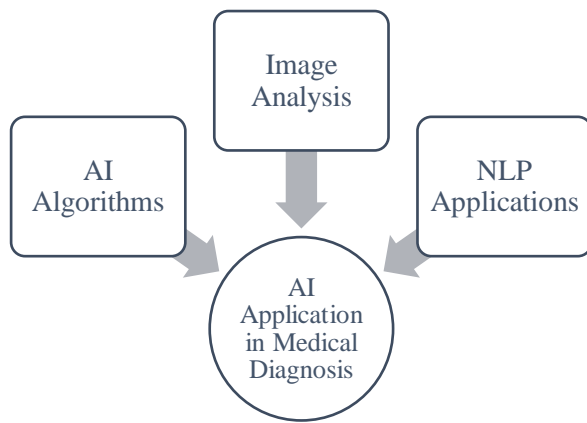
Figure 1. Three main domains of AI application in medical diagnosis.

As seen from Figure 1, the AI algorithm is used to diagnose multiple diseases, Image Analysis is also used to increase the accuracy of medical imaging techniques. Finally, Natural Language Processing NLP is used to extract data from medical notes and reports.

AI offers a wide range of opportunities for healthcare professionals to be involved in everyday practice. AI consultation is an example of an AI opportunity in medical practice. An AI system can easily use patients' medical records and databases to offer them the best medical care decisions (Tursunbayeva and Renkema, 2022). Another important use of AI is acting as a healthcare assistant to monitor patients' symptoms, manage their medication, and follow up on their compliance (Kim, 2018). Additionally, AI tools make it easier easy for untrained healthcare professionals to perform cardiac ultrasound imaging with high-quality images. In addition, AI can design treatment plans by analyzing medical records and guidelines to provide treatment options and plans (Zauderer et al., 2014). Moreover, AI-based technologies not only can be applied in doctors' practice, but also in helping pharmaceutical companies but they can also help pharmaceutical companies to develop new molecules at a higher speed compared to traditional methods. This can significantly affect the medical world in terms of time and cost (Meskó and Görög, 2020).

2. Review

Literature sources were Google Scholar, PubMed, and Scopus. The inclusion criteria were the relevancy to the topics of artificial intelligence, machine learning, and application in medicine. Also, new and most updated resources were preferred. Papers with poor citations and those published before 2000 were excluded from the sources. Mostly review articles were chosen as they were closer to the nature of the topic, but there was no limitation on the study design of the papers. The search strategy was mostly based on "relevancy" on topics and keywords "AI in medicine", "AI in medical diagnosis" and, "AI opportunity in medicine" were used. Only papers published in journals were reviewed in this article and the book chapter was not used to obtain the more recent ideas of AI in medicine.

3. Findings

Out of the reviewed literature, 10 articles discussed the future opportunities and challenges of AI in different fields of medicine. The key results of the studies highlight the fact that AI can not only be applied to collecting medical records, follow-up, and managing treatment plans, but it is particularly the subject of study in the diagnosis field. Studies show the promising results of AI's potential for successful diagnosis with a high level of accuracy and reliability. Few articles were discussed about the question of whether AI can replace doctors or not. Lastly, other articles focused on the challenges and ethical limitations of AI applications in medicine. The key findings include the need to educate and train healthcare professionals, the great challenge of validity and reliability of AI outcomes, bias, responsibility, risks and unpredicted results, and equitable issues.

AI has been shown to assist in designing predictive models that use electronic health record data to generate accurate and scalable predictions for numerous medical events that can help with collecting medical records, follow-ups, and using neural networks to identify relevant information from the patient's chart (Rajkomar et al., 2018). Also, articles reviewed machine learning and deep learning technologies and algorithms to assess whether they are patient-centric and improve the process of care (Kim, 2018). Additionally, medical diagnosis has been a major focus in articles discussing how AI could significantly improve accuracy and sensitivity. Papers provide technical knowledge on methods, algorithms, and applications in the medical diagnosis field, particularly in medical imaging systems such as endoscopic diagnosis (Kamdar et al., 2020). In endoscopy, AI has helped make the endoscopic process more efficient, leading to the more accurate categorization of risk in patients with common gastroenterology symptoms, such as bleeding (Kaul et al., 2020).

Furthermore, an issue raised in the literature is whether AI could replace doctors. The findings suggest that this is unlikely to happen. Instead, the technology is intended to assist medical professionals rather than replace them (Briganti and Moine, 2020).

In case of challenges, although AI offers many opportunities, the reliability of generative AI is under question. There are concerns about whether these systems are tailored to meet the needs and requirements of medical professionals and healthcare systems (Zhang and Boulos, 2023). Additionally, literature studies focus on ensuring that AI in medicine prioritizes patient care. It is essential to develop clear guidelines and regulations to address the ethical implications of AI, such as maintaining patient privacy (Canales, 2020).

Lastly, from the healthcare professional's perspective, the need for designing AI-enabled jobs was highlighted to

ensure the contribution of healthcare professionals in this field. This includes better adaptation of doctors to their roles and learning skills that will be useful in the future, such as social and related soft skills, to ensure a smooth transition (Tursunbayeva and Renkema, 2022). Also, for this need, articles and educational materials are currently being written as guides for medical professionals including definitions of AI, various methods in practice, potential challenges, and insights into what the future may hold (Meskó and Görög, 2020).

3.1. Opportunities

In the field of medical diagnosis, a future trend discussed involves designing a method to assess the reliability of classifiers on a case-by-case basis which focuses on increasing the reliability of disease diagnosis considerably. Another discussed future scenario was the use of AI in complementary medicine. As this branch of medicine needs further evaluation and verification, AI can play an important role in facilitating the verification process (Kononenk, 2001).

In the radiology field, AI applications can result in increased image quality, decreased radiation dose, and MRI scanner time, and reduced cost. All of these could result in a higher technical quality of radiology examinations (Lakhani et al., 2018). To be more specific, possibilities and perspectives in the radiology field are anticipations of the diagnosis of cancerous lesions in oncologic patients using texture analysis, prediction of treatment response to therapies for tumors, such as intra-arterial treatment for hepatocellular carcinoma, and evaluation of the biological relevance of borderline cases (Abajian et al., 2018).

In the pathology field, there are challenges regarding quantifying and standardizing clinical results and AI shows a promising role in accurate grading, staging, classifying, and quantifying responses to treatment (Vamathevan et al., 2019). Also, as AI can learn from any kind of data, it can assist in clinical settings by collecting electronic health records and accurately predicting medical events (Rajkomar et al., 2018).

Additionally, employing the capability of AI in imaging techniques is also under-studied. There are promising developments related to using AI-based PET models to improve the monitoring and management of rare diseases (Hasani et al., 2022).

Lastly, AI will have an enormous effect on the biological and medical research field. Automation offers the opportunity to accelerate the drug discovery process which remains a great challenge (Filipp, 2019).

3.2. Can Artificial Intelligence Replace Doctors?

Despite all the developments, the question that has been raised is whether doctors be replaced by artificial intelligence or not. The answer to this question would be probably "No". There is no chance of replacing doctors and healthcare systems with AI. The technology-based AI is complementary to medicine, not the replacement of it (Briganti and Moine, 2020). Recently, the question and worries about removing radiologists from medicine after AI applications have been raised. The fact is that it is not possible to remove radiologists from medicine, particularly after AI application in medicine. Radiologists were the first medical professionals who adopt technology and computer science in their work, so radiologists will be further strengthened by emerging new technologies (Pesapane et al., 2018).

3.3. Challenges

One of the future trends of applying AI in medicine will likely be the need to have educated and trained healthcare professionals. Some medical universities have already started adding to add AI-technology-related courses to their curriculum to prepare the students for real practice of the future (Briganti and Moine, 2020). Additionally, academic papers and guides are being written to inform and educate healthcare professionals to fulfil this need (Meskó and Görög, 2020).

Another challenge with the use of AI in medicine is the clinical validation of AI applications in medical practice. Although a large number of articles have been published comparing the non-AI technology diagnosis with AI-driven diagnosis, they lack sufficient number, sample size, or proper study design (Briganti and Moine, 2020). For generative AI tools such as ChatGPT, the unpredictability seems to cause trust and validation problems because it is not exactly clear when the answers are completely correct, wrong incorrect, or even misleading. There is a phenomenon related to generative AI called "AI hallucinations" which refers to making up information, references, or academic papers that do not exist (Zhang and Boulos, 2023).

Moreover, Healthcare professionals have several concerns and resistance regarding AI integration. These include concerns about safety, particularly related to the risk of errors that could potentially endanger patient safety, leading to increased skepticism in healthcare settings. Additionally, fears of losing professional autonomy and difficulties integrating AI into existing workflows are widely reported barriers. To address these challenges, effective training programs and involving end-users in the development and technical processes of AI systems are essential (Lambert et al., 2023).

Lastly, studies frequently emphasize the clinical benefits of AI without adequately addressing the associated costs and technical requirements. This lack of transparency can lead to incomplete conclusions about the financial barriers and economic impact of AI in medicine. To gain a clearer understanding of AI's financial implications, future research should focus on detailing the investments required for AI technologies and evaluating the expected return on investment. By improving the reporting of these financial aspects, researchers can provide more accurate evaluations of AI's cost-effectiveness and its potential to enhance healthcare delivery. This will facilitate better decision-making and support more strategic investments in AI technology (Rossi et al., 2022).

3.4. Ethical Complications

The use of AI in medicine must aligned with ethical

principles to ensure that patient care remains the top priority. Achieving this requires the development of clear guidelines and regulations for the use of artificial intelligence in healthcare. Additionally, healthcare professionals must be trained to understand the ethical implications of artificial intelligence and how to use it responsibly. This includes understanding the limitations and potential biases of the technology, also the importance of maintaining patient privacy. Finally, transparency and accountability are crucial in ensuring that the use of artificial intelligence in medicine aligns with ethical and moral principles. This includes ensuring that patients are fully informed about the use of artificial intelligence in their care and that healthcare providers are held accountable for any errors or biases that may arise (Canales, 2020). Main challenges to AI algoritms in medicine are shown in Figure 2
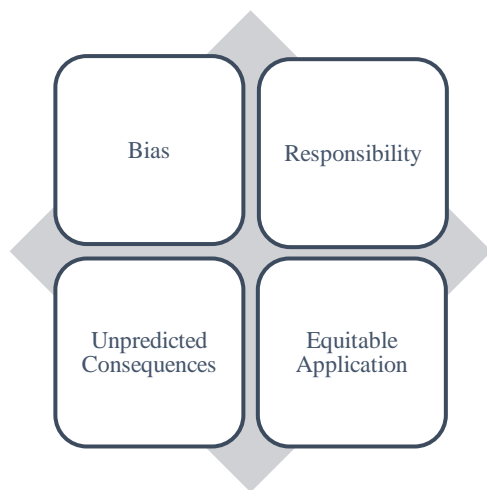
Figure 2. The key ethical challenges to AI algorithms in medicine.

From Figure 2, it is seen that the key limitations and ethical challenges related to the use of artificial intelligence in medicine include bias (artificial intelligence algorithms can inherit biases from the data they are trained on), responsibility (as artificial intelligence becomes more autonomous, determining responsibility for medical errors becomes more complex), unpredicted consequences (the introduction of artificial intelligence may lead to unpredicted results and new risks for patients, requiring constant monitoring of its proper functioning) and equitable application (there is a need to ensure that artificial intelligence is applied equitably across communities and healthcare systems to avoid further limiting access and outcomes for certain patient populations). These ethical limitations of AI application in medicine are illustrated in Figure 2. Addressing these limitations and ethical challenges is crucial to gaining the potential benefits of AI in medicine (McKinney et al., 2020).

4. Results and Suggestions

As the application of AI increases day by day, it is crucial to become more informed and discuss how AI is affecting the healthcare environment. It seems that engineering and computer science or technology-related fields are already advancing in integrating AI usage and despite the advancement in AI application medicine, a long journey remains.

Results of the studies performed by 2023 indicate that generally, the future of AI in medicine is very bright. Several promising studies show that clinical decision support is one of the most important opportunities for the application of AI in medicine. It is the process of making decision for healthcare professionals more effective and quick. The process is particularly important in emergency medicine where quick and accurate decisions can save lives. Soon, we expect that clinical decision-making will be more efficient, saving time, money, and energy with more accurate results. Furthermore, image analysis has been positively affected and continues its advancement in recent years. In recent years, imaging techniques have been influenced by computer science adopting many analysis software and applications. It is highly probable that AI will bring be a new revolution in image analysis fields producing not only high-quality and high-resolution images but also making them more accessible to patients.

Additionally, AI also contributes significantly to disease detection and diagnosis area which is a considerable advancement in the medical world. It is now clearly known that the key to treatment is diagnosis. This is why a large amount of research and science budget is dedicated to the diagnosis section. Predictive models have been the potential to facilitate the early detection and diagnosis of diseases. Lastly, personalized disease treatment and simplification of administrative tasks in the healthcare system are two other areas in which AI improves efficiency, leading to and leads to time and cost savings.

Regarding challenges in AI application in medicine, the main ones are related to the challenge of validation of data. Since well-designed studies are still limited in this area, the reliability and validity of data might need more information and data at this time.

Our suggestion for the future of AI in medicine would be to increase educational problems in universities, companies, and private training sessions. It is not possible to apply all the changes to the healthcare environment without having enough knowledge. This era is more than just using computer science in medicine, we are encountering fast-evolving technology that has no boundaries in advancement and innovation. To obtain the best result, more education is still needed for both healthcare professionals and patients.

5. Conclusion

This review highlights three critical takeaways for readers and researchers. First of all, AI shows great promise in enhancing medical diagnosis and treatment planning particularly in areas like radiology, pathology, and clinical decision support. However, AI is intended to augment rather than replace medical professionals. Secondly, significant challenges remain in validating AI systems, addressing ethical concerns, and ensuring equitable implementation across healthcare settings. These issues require future ongoing research and careful consideration. Thirdly, there is an urgent need for increased education and training on AI in healthcare, both for current professionals and future medical students.

These points are crucial from both scientific and practical perspectives. The potential of AI to improve patient outcomes and healthcare efficiency could revolutionize medical practice, but only if implemented responsibly. The challenges identified underscore the need for accurate validation studies and ethical guidelines to ensure patient safety and equitable care. The emphasis on education highlights the evolving nature of medical practice and the importance of preparing the healthcare workforce for technological integration.

Lastly, for medical students and their educators, this research highlights the importance of incorporating AI-related coursework into the medical curriculum. Students must develop not only technical skills but also critical thinking abilities to evaluate AI tools, their opportunities and ethical implications. Besides, Education policymakers should consider revising medical education standards to include AI competencies, ensuring future physicians are prepared for an increasingly tech-driven healthcare environment. On the other hand, practitioners should be aware of both the potential benefits and limitations of AI in their fields, actively seeking opportunities for continuing education to be updated with AI advancements. Furthermore, for data scientists and engineers, this research highlights the critical need for collaboration with healthcare professionals to develop clinically relevant AI solutions. It also emphasizes the importance of addressing issues like bias, transparency, and interpretability in AI systems. Last but not least, for patients and the public, this research suggests a future where AI could lead to more accurate diagnoses and personalized treatments and highlights the need for informed consent regarding AI use in their care. Addressing these implications across various stakeholders will lead to realizing the full potential of AI in medicine while reducing its risks and challenges.

Author Contributions

The percentage of the author(s) contributions is presented below. All authors reviewed and approved the final version of the manuscript.

	T.D.	A.Ö.	A.S.Ö.
C		100	
D	80	20	
S		100	
DCP	80	20	
DAI	30		70
L	80		20
W	20	20	20
CR	20	20	60
SR		100	
PM	20	80	

C= concept, D= design, S= supervision, DCP= data collection and/or processing, DAI= data analysis and/or interpretation, L= literature search, W= writing, CR= critical review, SR= submission and revision, PM= project management.

References

Abajian A, Murali N, Savic LJ, Laage-Gaupp FM, Nezami N, Duncan JS, Schlachter T, Lin M, Geschwind J, Chapiro J. 2018. Predicting treatment response to ıntra-arterial therapies for hepatocellular carcinoma with the use of supervised machine learning: an artificial ıntelligence concept. J Vasc Interv Radiol, 29(6): 850-857.

Afzal N, Sohn S, Abram S, Scott CG, Chaudhry R, Liu H, Kullo IJ, Arruda-Olson AM. 2017. Mining peripheral arterial disease cases from narrative clinical notes using natural language processing. J Vasc Surg, 65(6): 1753–1761.

Briganti G, Moine OL. 2020. Artificial intelligence in Medicine: Today and tomorrow. Front Med, 7: 27.

Campanella G, Hanna MG, Geneslaw Miraflor A, Silva VWK, Busam KJ, Brogi E, Reuter VE, Klimstra DS, Fuchs TJ. 2019. Clinical-grade computational pathology using weakly supervised deep learning on whole slide images. Nat Med, 25(8): 1301–1309.

Canales C, Lee C, Cannesson M. 2020. Science without conscience is but the ruin of the soul: the ethics of big data and artificial intelligence in perioperative medicine. Anesth Analg, 130(5): 1234–1243.

Christiansen MP, Garg S K, Brazg R, Bode BW, Bailey TS, Slover RH, Sullivan A, Huang S, Shin J, Lee SW, Kaufman FR. 2017. Accuracy of a Fourth-Generation subcutaneous continuous glucose sensor. Diabetes Technol Ther, 19(8): 446–456.

Dorsey ER, Glidden AM, Holloway MR, Birbeck GL, Schwamm L H. 2018. Teleneurology and mobile technologies: the future of neurological care. Nat Rev Neurol, 14(5): 285–297.

Filipp FV. 2019. Opportunities for Artificial intelligence in advancing precision Medicine. Current Curr Genet Med Rep, 7: 208–213.

Fiszman M, Chapman WW, Aronsky D, Evans RS, Haug PJ. 2000. Automatic detection of acute bacterial pneumonia from chest X-ray reports. J Am Med Inform Assoc, 7(6): 593–604.

Halcox JPJ, Wareham K, Cardew A, Gilmore M, Barry JP, Phillips

C, Gravenor MB. 2017. Assessment of remote heart rhythm sampling using the AliveCor heart monitor to screen for atrial fibrillation. Circ Cardiovasc Interv, 136(19): 1784–1794.

Hasani N, Farhadi F, Morris MA, Nikpanah M, Rhamim A, Xu Y, Pariser A, Collins MT, Summers RM, Jones E, Siegel E, Saboury B. 2022. Artificial intelligence in medical imaging and its impact on the rare disease community: threats, challenges and opportunities. PET Clin, 17(1): 13–29.

Hoogenboom SA, Bagci U, Wallace MB. 2020. Artificial intelligence in gastroenterology. The current state of play and the potential. How will it affect our practice and when? Tech Innov Gastrointest Endosc, 22(2): 42–47.

Ichimasa K, Kudo S, Mori Y, Misawa M, Matsudaira S, Kouyama Y, Baba T, Hidaka E, Wakamura K, Hayashi T, Kudo T, Ishigaki T, Yagawa Y, Nakamura H, Takeda K, Haji A, Hamatani, S, Mori K, Ishida F, Miyachi H. 2018. Artificial intelligence may help in predicting the need for additional surgery after endoscopic resection of T1 colorectal cancer. Endoscopy, 50(03): 230–240.

Kamdar JH, Praba JJ, Georrge JJ. 2020. Artificial intelligence in medical diagnosis: methods, algorithms and applications. Springer, Cham, New Delhi, India, 13, pp: 27–37.

Kaul V, Enslin, S, Gross S A. 2020. History of artificial intelligence in medicine. Gastrointest Endosc, 92(4): 807–812.

Kim JT. 2018. Application of machine and deep learning algorithms in intelligent clinical decision support systems in healthcare. J Health Med Inform, 9: 5.

Kononenko I. 2001. Machine learning for medical diagnosis: history, state of the art and perspective. Artif Intell Med, 23(1): 89–109.

Kuwaiti AA, Nazer K, Al-Reedy A, Al-Shehri S, Almuhanna A, Subbarayalu AV, Al-Muhanna D, Al-Muhanna F. 2023. A Review of the role of artificial intelligence in healthcare. J Pers Med, 13(6): 951.

Lakhani P, Prater AB, Hutson RK, Andriole KP, Dreyer KJ, Morey J, Prevedello LM, Clark TJ, Geis JR, Itri JN, Hawkins CM. 2018. Machine learning in radiology: applications beyond image interpretation. J Am Coll Radiol, 15(2): 350–359.

Lambert SI, Madi M, Sopka S, Lenes A, Stange H, Buszello C, and Stephan A. 2023. An integrative review on the acceptance of artificial intelligence among healthcare professionals in hospitals. NPJ Digit Med, 6(111).

McDougall RJ. 2018. Computer knows best? The need for value-flexibility in medical AI. J Med Ethics, 45, 156 - 160.

McKinney SM, Sieniek M, Godbole V, Godwin J, Антропова НВ, Ashrafian H, Back T, Chesus, M, Corrado G, Darzi A, Etemadi M, Garcia-Vicente F, Gilbert FJ, Halling-Brown M, Hassabis D, Jansen S, Karthikesalingam A, Kelly C, King D, Ledsam J R, Melnick D, Mostofi H, Lily P, Reicher JJ, Romera-Paredes B,Sidebottom R, Suleyman M, Tse D, Young KC, Fauw JD, Shetty S. 2020. International evaluation of an AI system for breast cancer screening. Nature, 577(7788): 89–94.

Meskó B, Görög M. 2020. A short guide for medical professionals in the era of artificial intelligence. NPJ Digit Med, 3: 126.

Pesapane F, Codari M, Sardanelli F. 2018. Artificial intelligence in medical imaging: threat or opportunity? Radiologists are again at the forefront of innovation in medicine. Eur Radiol Exp, 2(1): 35.

Rajkomar A, Oren E, Chen K, Dai A M, Hajaj N, Hardt M, Liu PJ, Liu X, Marcus J, Sun M, Sundberg P, Yee H, Zhang K, Zhang Y, Flores G, Duggan GE, Irvine J, Le Q, Litsch K, Mossin A, Tansuwan J, Wang D, Wexler J, Wilson J, Ludwig D, Volchenboum SL, Chou K, Pearson M, Madabushi S, Shah NH, Butte A J, Howell MD, Cui C, Corrado GS, Dean J. 2018. Scalable and accurate deep learning with electronic health records. NPJ Digit Med, 1: 18.

Regalia G, Onorati F, Lai M, Caborni C, Picard RW. 2019. Multimodal wrist-worn devices for seizure detection and advancing research: Focus on the Empatica wristbands. Epilepsy Res, 153: 79–82.

Rossi JG, Feldberg B, Krois J, Schwendicke F. 2022. Evaluation of the clinical, technical, and financial aspects of cost-effectiveness analysis of artificial intelligence in medicine: scoping review and framework of analysis. JMIR Med Inform, 10(8): e33703.

Ruffle JK, Farmer AD, Aziz Q. 2019. Artificial intelligence-assisted gastroenterology, promises and pitfalls. Am J Gastroenterol, 114(3): 422–428.

Sezgin E. 2023. Artificial intelligence in healthcare: Complementing, not replacing, doctors and healthcare providers. Digit Health, 2023: 9.

Sunarti S, Rahman FF, Naufal M, Risky M, Febriyanto K, Masnina R. 2021. Artificial intelligence in healthcare: opportunities and risk for future. Gac Sanit, 35(1): S67-S70.

Sweilam NH, Tharwat AA, Moniem NKA. 2010. Support vector machine for diagnosis cancer disease: A comparative study. Egypt Inform J, 11(2): 81–92.

Tursunbayeva A, Renkema M. 2022. Artificial intelligence in health-care: implications for the job design of healthcare professionals. Asia Pac J Hum Resour, 61(4): 845–887.

Vamathevan J, Clark D, Czodrowski P, Dunham I, Ferrán E, Lee G, Li B, Madabhushi A, Shah P, Spitzer M, Zhao S. 2019. Applications of machine learning in drug discovery and development. Nat Rev Drug Discov, 18(6): 463–477.

Velagaleti SB, Krishna AV, Lakshmi DS. 2023. Improving performance of clinical and operational workflows in health tech domain using artificial intelligence. IJRASET, 11(6):3929-3932.

Yang Y J, Bang C S. 2019. Application of artificial intelligence in gastroenterology. World J Gastroenterol, 25(14): 1666–1683.

Zauderer MG, Gucalp A, Epstein AS, Seidman AD, Caroline A, Granovsky S, Fu J, Keesing J, Lewis SM, Co HT, Petri J, Megerian M, Eggebraaten T, Bach PB, Kris MG. 2014. Piloting IBM Watson Oncology within Memorial Sloan Kettering's regional network. J Clin Oncol, 32: e17653-e17653.

Zhang P, Boulos MNK. 2023. Generative AI in medicine and healthcare: promises, opportunities and challenges. Future Internet, 15(9): 286.

Zhu M, Xu C, Yu J, Wu Y, Li C, Zhang M, Jin Z, Li, Z. 2013. Differentiation of pancreatic cancer and chronic pancreatitis using Computer-Aided Diagnosis of Endoscopic Ultrasound (EUS) images: a diagnostic test. PLoS One, 8(5): e63820.